UNSW SYDNEY | Australia's Global University

Thesis/Dissertation Sheet

Surname/Family Name	:	**Pakkiam**
Given Name/s	:	**Prasanna**
Abbreviation for degree as give in the University calendar	:	**PHYS9103 – Research Thesis Physics F/T**
Faculty	:	**Science**
School	:	**Physics**
Thesis Title	:	**On a scalable RF-probed Si-P quantum computational architecture**

Abstract 350 words maximum: (PLEASE TYPE)

A scalable quantum computer requires high-fidelity qubits arranged in a 2D array to form a fault-tolerant quantum error correction code. One of the challenges in implementing such a system is the large number of leads per qubit used to create, control and readout the qubit. By utilising the natural confinement potential of P-donors in silicon, we can integrate single-gate RF readout into existing control gates with a minimum gate density of 2 gates per qubit. This thesis investigates the realisation of singlet-triplet qubits in silicon using P-donor qubits with minimal gate density.

We created a coupled singlet-triplet Si-P qubit device with scanning tunnelling microscope (STM) lithography with only 2 gates per qubit. Using a custom designed electrostatic model with a charge-stability diagram simulator we designed and characterised electrostatic couplings in this device. Using a triangulation technique, we not only verified the physical locations of the dots but were able to identify the location of charge traps in the device and correlate them with STM images to determine their cause. Using single lead RF read-out we demonstrated an inter-dot tunnel coupling of 39 GHz, with a s_0-t_- decay time of 2 ms, and a large inter-qubit coupling of 5 GHz.

We then focused on the development of two compact RF sensors. The first, an RF single-lead quantum dot (SLQD) sensor used the nonlinear quantum capacitance to detect charge movement ~100nm away. A nanoscale Si-P SLQD patterned using STM-lithography demonstrated a sensitivity equivalent to an integration time of 550 ns to detect a single charge with a signal-to-noise ratio of 1. We then extended this work to a single-gate RF sensor and demonstrated single-gate single-shot RF spin readout for the first time. We achieved a readout fidelity of 85.77% at a 3.3 kHz bandwidth and showed how to extend this to >99% fidelity.

Finally, we discussed the theoretical development of scalable singlet-triplet architectures using P-donor qubits. We focussed on specific device parameters required for high-fidelity single and two qubit gates and how to integrate these into 1D and 2D arrays.

ORIGINALITY STATEMENT

'I hereby declare that this submission is my own work and to the best of my knowledge it contains no materials previously published or written by another person, or substantial proportions of material which have been accepted for the award of any other degree or diploma at UNSW or any other educational institution, except where due acknowledgement is made in the thesis. Any contribution made to the research by others, with whom I have worked at UNSW or elsewhere, is explicitly acknowledged in the thesis. I also declare that the intellectual content of this thesis is the product of my own work, except to the extent that assistance from others in the project's design and conception or in style, presentation and linguistic expression is acknowledged.'

Signed …….....

Date …….....

INCLUSION OF PUBLICATIONS STATEMENT

UNSW is supportive of candidates publishing their research results during their candidature as detailed in the UNSW Thesis Examination Procedure.

Publications can be used in their thesis in lieu of a Chapter if:

- The candidate contributed greater than 50% of the content in the publication and is the "primary author", ie. the candidate was responsible primarily for the planning, execution and preparation of the work for publication
- The candidate has approval to include the publication in their thesis in lieu of a Chapter from their supervisor and Postgraduate Coordinator.
- The publication is not subject to any obligations or contractual agreements with a third party that would constrain its inclusion in the thesis

Please indicate whether this thesis contains published material or not:

☐ This thesis contains no publications, either published or submitted for publication
(if this box is checked, you may delete all the material on page 2)

☒ Some of the work described in this thesis has been published and it has been documented in the relevant Chapters with acknowledgement
(if this box is checked, you may delete all the material on page 2)

☐ This thesis has publications (either published or submitted for publication) incorporated into it in lieu of a chapter and the details are presented below

CANDIDATE'S DECLARATION

I declare that:

- I have complied with the UNSW Thesis Examination Procedure
- where I have used a publication in lieu of a Chapter, the listed publication(s) below meet(s) the requirements to be included in the thesis.

Candidate's Name	Signature	Date (dd/mm/yy)
Prasanna Pakkiam		

COPYRIGHT STATEMENT

Signed …….....

Date …….....

AUTHENTICITY STATEMENT

‘I certify that the Library deposit digital copy is a direct equivalent of the final officially approved version of my thesis.’

Signed …….....

Date …….....

On a scalable RF-probed Si-P quantum computational architecture

Prasanna Pakkiam

A thesis submitted for the degree
Doctor of Philosophy
in the School of Physics of UNSW

25 September 2019

Abstract

A scalable quantum computer requires high-fidelity qubits arranged in a 2D array to form a fault-tolerant quantum error correction code. One of the challenges in implementing such a system is the large number of leads per qubit used to create, control and readout the qubit. By utilising the natural confinement potential of P-donors in silicon, we can integrate single-gate RF readout into existing control gates with a minimum gate density of 2 gates per qubit. This thesis investigates the realisation of singlet-triplet qubits in silicon using P-donor qubits with minimal gate density.

We created a coupled singlet-triplet Si-P qubit device with scanning tunnelling microscope (STM) lithography with only 2 gates per qubit. Using a custom designed electrostatic model with a charge-stability diagram simulator we designed and characterised electrostatic couplings in this device. Using a triangulation technique, we not only verified the physical locations of the dots but were able to identify the location of charge traps in the device and correlate them with STM images to determine their cause. Using single lead RF read-out we demonstrated an inter-dot tunnel coupling of 39 GHz, with a s_0-t_- decay time of 2 ms, and a large inter-qubit coupling of 5 GHz.

We then focused on the development of two compact RF sensors. The first, an RF single-lead quantum dot (SLQD) sensor used the nonlinear quantum capacitance to detect charge movement $\sim$100 nm away. A nanoscale Si-P SLQD patterned using STM-lithography demonstrated a sensitivity equivalent to an integration time of 550 ns to detect a single charge with a signal-to-noise ratio of 1. We then extended this work to a single-gate RF sensor and demonstrated single-gate single-shot RF spin readout for the first time. We achieved a readout fidelity of 85.77% at a 3.3 kHz bandwidth and showed how to extend this to >99% fidelity.

Finally, we discussed the theoretical development of scalable singlet-triplet architectures using P-donor qubits. We focussed on specific device parameters required for high-fidelity single and two qubit gates and how to integrate these into 1D and 2D arrays.

Acknowledgements

Firstly, I would like to thank my supervisor Professor Michelle Y. Simmons for the opportunity to undertake a PhD in CQC^{2}T, UNSW. I thank her for all the help and guidance given during the course of the PhD. Additionally, I would like to thank her for providing opportunities to expand my network and productivity via conferences and collaborations with Professor Lloyd Hollenberg in Melbourne University and Professor Amir Yacoby in Harvard.

I would then like to thank Dr. Matthew G. House for offering a project that had a lot of potential for exploration that resulted in noteworthy publications. His support and guidance during the experiments were invaluable.

I would also like to thank Dr. Matthias Koch for effectively starting the project on the fabrication level. Dr. Koch took time out of his work to help me realise my first P-donor devices and eventually helped me gain independence in the fabrication pipeline.

I would like to thank Dr. Charles D. Hill from Melbourne University for his insightful feedback on my whitepapers. Dr. Hill also provided many insightful discussions around general theoretical physics, qubit architecture design and interpretations of experimental data.

I would also like to thank the following members of our group (both past and present) with whom I collaborated during my project:

- Ian Stuart Bartlett for the useful discussions (from the perspective of a fellow engineer) and support in both the experimental and theoretical work involving the SLQD experiment.

- Dr. Lukas Fricke for the useful discussions as well as valuable support and supervision when Stuart and I worked on the wet dilution fridge.

- Dr. Eldad Peretz for support with the initial device fabrication and processing.
- Anubhav Dixit for support in the cleanroom.
- Dr. Sven Rogge, Dr. Joost van der Heijden and Dr. Takashi Kobayashi for the useful discussions involving RF readout.
- Felix Krauth for providing valuable feedback on my whitepapers. In addition, I appreciate the valuable support and discussions on general quantum mechanics involving the rotating wave approximation, STM and device processing.
- Michael Jones for providing valuable feedback on my whitepapers.
- Dr. Andrey Timofeev for proving valuable feedback on my whitepapers. In addition, Andrey entertained insightful discussions in both theoretical and experimental physics. In addition, I thank Andrey for unlocking the high quality factor of the superconducting inductor by advising the removal of PMMA.
- Mark R. Hogg for the useful discussions and support in the single-shot single-gate RF readout experiments.
- Dr. Yousun Chung for useful advice and support in the cleanroom.
- All the technical staff (Dr. Otte Homan, David Barber and Dr. Rodrigo Ormeno-Cortes) for their valuable advice and support in running the dilution fridges.
- All other group members who were not directly involved with my experiments but have provided noteworthy suggestions during the thesis such as (but not limited to): Daniel Keith, Sam Hile, Sam Gorman, Dr. Matthew Broome, Ludwig Kranz and Dr. Arne Laucht.

I would also like to thank Lucas Orona and Professor Amir Yacoby (and the members of his group in Harvard) for their valuable advice and insightful discussions on singlet-triplet qubits.

Finally, I would like to thank my close family and friends for both showing interest and providing valuable support during my PhD.

Contents

List of Figures

Nomenclature

$\sigma_x, \sigma_y, \sigma_z$	Pauli x, y and z matrices
e	Euler's constant (approx. 2.7182818)
e	Elementary positive ($1.602176634 \times 10^{-19}\,\mathrm{C}$)
h	Planck constant ($6.62607015 \times 10^{-34}\,\mathrm{J \cdot s}$)
k_B	Boltzmann constant ($1.380649 \times 10^{-23}\,\mathrm{J/K}$)
ε_0	Permittivity of free space (approx. $8.854187817 \times 10^{-12}\,\mathrm{Fm^{-1}}$)
μ_e	Bohr magneton (approx. $9.274009994 \times 10^{-24}\,\mathrm{J/T}$)
DQD	Double quantum dot
ST	Singlet-Triplet
DNP	Dynamic nuclear spin polarisation
RF	Radio frequency
STM	Scanning tunnelling microscope
SET	Single electron transistor
QPC	Quantum point contact
TJCS	Tunnel junction charge sensor
SLQD	Single lead charge sensor
PCB	Printed circuit board
SMD	Surface-mounted device
RWA	Rotating wave approximation
$(\mathbf{M})_{mn}$	Entry in row m and column n of matrix $\mathbf{M}$
$(\mathbf{M})_{*n}$	Column vector taken from column n of matrix $\mathbf{M}$

Chapter 1

Motivation and thesis organisation

Chemical sciences has a great impact on human society by providing exotic technologies ranging from contributions such as that in renewables, medicine and agriculture. However, the methods to create new materials with exotic properties tend to be empirical and employ random heuristics. It is difficult to know the optimal chemical compositions required for specific outcomes as simulations tend to be computationally expensive. In fact, even the simple crystalline unit-cell cannot be solved or simulated exactly given current computational technologies. For example, consider a $3 \times 3 \times 3$ cube of atoms that may represent a cubic unit-cell in a crystal. If one were to study the magnetic properties and dynamics of strongly interacting electrons on all 27 atoms, then one needs to store 2^{27} values to represent the answer and an additional $2^{27} \times 2^{27}$ values to store the matrix that needs to be diagonalised during the computation. The raw memory usage to store the matrix of values is 64 petabytes (if using 32-bit floating-point numbers); approximately quarter the 250 petabyte storage capacity of the most powerful supercomputer at the time of writing the thesis[1]. With the computational complexity of diagonalisation using SVD (singular value decomposition) being $\mathcal{O}(n^3)$ [1], one would require in the order of 200 days of computation time[2]. With nonlinear dynamics of general molecules requiring multiple diagonalisations, the idea of exactly simulating larger and more complex chemical compounds a priori using conventional computers is unrealistic. The reason for the large computational complexity is a result of the large state-space that a heavily entangled quantum state may traverse during its time evolution. Thus, the solution to solve systems governed by quantum mechanics is to build a computer

[1] The data is based on the top supercomputer *Summit* as catalogued by the *TOP500* project

[2] An optimistic lower bound estimate given the approximately 148.6 petaflops in computation speed (1 FLOP is one floating point operation per second) of the fastest supercomputer *Summit*.

that specifically exploits quantum mechanics to solve computational problems as first proposed by Feynman [2]. Further interest gathered in quantum computing when explicit algorithms were developed to solve a certain class of useful problems; most notably the Shor's algorithm [3] for integer factorisation and Grover's algorithm [4]. Experimental work to date has shown the formation and control of qubits (a two-level system representing a unit of quantum information) with some cases explicitly implementing the Shor's algorithm to factorise small integers [5–7]. However, nobody has created a full-scale quantum computer that can solve useful commercial problems that cannot be achieved on a classical computer. One of the key issues is that quantum information is difficult to isolate as any interaction the qubit has with another particle from its environment will disperse its quantum information. Thus, a lot of effort goes into the research and development of creating isolated qubits and then having them interact to perform inter-qubit gate operations without interacting with the environment. However, even with the creation of high quality isolated qubits, the required error rates to compute useful algorithms with multiple qubits is prohibitively low and thus, one requires many qubits to build up redundancy and lower the effective error rate. Current state-of-the-art quantum error correction codes propose up to 10^8 qubits, where the redundant physical qubits collectively form approximately 4000 logical qubits to demonstrate Shor's algorithm in factorising a 2000-bit number [8]. A current challenge in creating a useful quantum processor therefore lies in creating high fidelity qubits that are isolated from their environment and high-fidelity two-qubit gate operations that can scale up to millions or billions of interconnected physical qubits. There are now signs of significant investment into the realisation of a useful quantum processor with higher qubit numbers reported. A startup IonQ has claimed up to 160 qubits [9] in a trapped ion quantum computer while IBM and Google have claimed up to 50 qubits [10] and 72 qubits [11] when using superconducting transmon qubits. Despite this, a fault-tolerant implementation where the use of redundant qubits showed a dramatic decrease in the qubit error rates is yet to be demonstrated.

One possible approach in which to eventually realise a scalable and useful quantum computer is to make qubits using electron spins trapped in nano-scale quantum dot structures [12–18]. With the electron spins operated under cryogenic temperatures, one suppresses interactions the qubits may have with their environment. Quantum dot implementations are in their infancy requiring the latest nanofabrication technologies to reach device sizes $\lesssim$10-100 nm. As such, they have not yet shown low enough qubit error rates as seen in their trapped ion systems or superconducting counterparts. Experimental and theoretical results however suggest that the

strong interactions between qubits, unique to quantum dots due to the close proximity of the qubits [19], should enable error rates comparable to that of trapped ion implementations while allowing fast gate operations comparable to that found with transmon qubits. As with ion traps and superconducting qubits, quantum dots do not have a straightforward method to scale up to many qubits. One significant obstacle is the gate density required to create and control the small nano-scale qubits. For example, with gate-defined GaAs quantum dots the gate density can extend up to 11 gates per qubit [14]. However, a class of quantum dots using atoms such as P-donors in silicon do not require extra confining gates to create the quantum well that traps the electron spin qubit and offers a pathway to significantly reduce the gate density. Whilst the use of atomic qubits is still in its infancy, a lot of effort has been made to develop the fabrication techniques to be able to atomically place both single and multiple P-donors in quantum dot qubits in specific locations in silicon using hydrogen-mask STM (scanning-tunnelling-microscope) lithography [15, 20–27]. Utilising the advantages of the lower gate density in P-donor qubits, a pathway has been mapped out to scale up to many qubits in a 2D array with gate densities of $\sqrt{n}$ for n qubits [28]. This 2D Si-P surface code architecture requires great uniformity of qubit placement as the low gate density was achieved by sharing a given gate across many qubits.

This thesis considers an alternate proposal using two-electron singlet-triplet qubits (rather than single-spin qubits) in which one may scale up to many qubits using atomic qubits in silicon with a gate density of two gates per qubit. Since every qubit has its own set of control gates, the fabrication precision of the qubits is relaxed as each qubit can be independently tuned to overcome potential offsets or device defects. Furthermore, a key development in the thesis was the reduction of the gate density by replacing the conventional 3-lead qubit sensor (the single electron transistor) with a single-gate RF (radio frequency) sensor that takes up no additional space real-estate in the nano-scale device as it integrates directly into pre-existing control gates in the device. Here, we demonstrated single-shot single-gate RF spin readout for the first time.

The thesis is divided into four main results chapters including a theoretical proposal for a scalable singlet-triplet qubit architecture. These are outlined below:

- **Design and realisation of a quadruple quantum dot device in Si-P capable of hosting two singlet-triplet qubits** [29]. This chapter covers the theoretical modelling and optimisation of a coupled singlet-triplet device. Capacitance modelling simulations and a custom charge stability diagram sim-

ulator were used to simulate multiple P-donor quantum dots in silicon. A quadruple quantum dot device designed to host 2 singlet-triplet qubits (across 2P-2P and 3P-4P donor double quantum dots) was then fabricated in Si-P using STM lithography and measured in a dilution fridge. The device was characterised using a TJCS (tunnel junction charge sensor) and a single-gate RF sensor. A triangulation technique using charge stability diagrams and finite-element models was developed to verify the location of all four quantum dots. Interestingly, this technique was also used to identify the location and source of a nearby charge trap; something that will provide useful information in fabricating further devices. A singlet-triplet spin state was formed between the 3P-4P dots and the singlet to triplet-t_- lifetime (which limits the available RF sensor measurement time) was measured to be 2 ms; much larger than previously measured (60 ns [30]), owing to our design to reduce the coupling of the quantum dots to their reservoirs. Furthermore, the improved electrostatic model for larger P-donor quantum dots was successfully benchmarked against experimental measurements of the gates' differential lever-arms and the inter-qubit coupling. The device provided a large inter-qubit coupling of 5 GHz, optimised for fast high-fidelity two-qubit gate control. We found that the device had too transparent a tunnel barrier between the dots hosting the singlet-triplet qubit such that the exchange J between the dots could not be turned off. However, the electrostatic control demonstrated in this device suggested that with inter-dot tunnel couplings less than 10 GHz, it would be possible to use this design to achieve a high-fidelity singlet-triplet qubit.

- **Theoretical and experimental development of a compact RF SLQD (single-lead-quantum-dot) charge sensor** [31]. This chapter outlines the advantages of RF techniques, and the possibility to reduce the lead count of a conventional SET charge sensor to a single lead with a dedicated quantum dot. The operation of the SLQD was first modelled theoretically to both understand the nonlinear components of the SLQD response and to find the optimal regimes of operation. This includes the first predictions of a saturation in the SLQD response at high input RF powers away from the linear regime to achieve larger readout signal strengths. The SLQD sensor was then fabricated using STM lithography to pattern a Si-P device and the theoretical predictions were experimentally verified. The SLQD sensor was shown to operate with peak sensitivity (using a 244.8 MHz RF resonator with an effective quality factor of approximately 100) and shown to detect charge movement approximately

44 nm away. Indeed we show how the SLQD can act as a long range (∼100 nm) compact high-fidelity charge sensor for P-donor qubits in silicon where typical qubit sizes are within 12 nm.

- **Theoretical and experimental development of a scalable single-gate RF singlet-triplet sensor** [32]. Following on from the SLQD sensor we outline the developments of a single-gate RF sensor that requires no dedicated lead (and in this case no dedicated quantum dot) and integrates directly into the pre-existing control gates within the device. To understand the optimal operating regimes, the single-gate RF sensor was modelled theoretically using Hamiltonian modelling of the 'adiabatic quantum capacitance' and 'tunnelling capacitance' modes of operation. A unique feature of this modelling is the investigation into the use of larger input RF voltage amplitudes to enter the nonlinear capacitance regime. Although the RF response does not saturate as with the SLQD sensor, the analytic models provided important bounds for optimal operation in both the adiabatic quantum capacitance (where the driving frequency must be much smaller than the tunnel coupling frequency) and in the tunnelling capacitance (driving frequency must match twice the tunnel coupling frequency) regimes. The single-gate RF sensor was used to measure a 6-electron singlet-triplet state with a 39 GHz tunnel coupling across a 3P-4P double quantum dot separated by approximately 12.5 nm. The device design allowed us to extend to the singlet to triplet-t_- relaxation time to 2 ms. The resonator circuit was then optimised for maximal readout signal strength, by increasing the internal quality factor of the RF resonator by replacing the surface mount chip inductor with a custom low-loss NbTiN superconducting inductor with an internal quality factor of ∼800. Using this single-gate RF sensor, we achieved single-shot readout for the first time with a fidelity of 85.77% at a 3.3 kHz readout bandwidth; thereby confirming we could make sensitive measurements of the electron spins without affecting the spin dynamics of the qubit state under measurement. The results implied the compatibility of the single-gate RF sensor with the large-scale qubit architectures proposed in this thesis.

- **Fundamental design and optimisation of high-fidelity single and two qubit gates for scalable 1D and 2D arrays of singlet-triplet qubits using Si-P**. In the final results chapter, we use the detailed understanding of Si-P devices obtained from experimentally benchmarked electrostatic models to optimise critical device parameters (such as the inter-dot tunnel coupling,

the inter-qubit coupling and the operational points in qubit exchange) for one and two qubit gates using singlet-triplet qubits. We focus on the CZ gate fidelity under the presence of charge noise, since it can be used to realise both the ZZ and XX parity measurements required in the fault-tolerant surface code. A unique aspect of the modelling developed, lies in the exploitation of the large inter-qubit couplings present in Si-P quantum dots due to their small size and close packing when compared to equivalent gate-defined quantum dot implementations. Most works in the literature involving two-qubit gates with singlet-triplet qubits have been in the pertubative (with respect to the inter-dot tunnel coupling) inter-qubit coupling regime [33–35]. Using the electrostatic models developed with the optimal device parameters established for high fidelity single and two qubit gates, we propose scalable 1D and 2D singlet-triplet qubit arrays using P-donors in silicon.

Looking forwards, we have proposed scalable designs that require 2 gates per qubit with each qubit hosted on asymmetric 1P-2P donor quantum dots. It is important to investigate the nuclear spin dynamics in P-donors to ensure a stable magnetic field gradient (across the quantum dots) and that the system migrates to isotopically purified ^{28}Si to minimise magnetic noise from the substrate. Whilst there are still technical challenges, this thesis provides both a guide and critical understanding in the choice of device parameters required for scalable singlet-triplet architectures using P-donors in silicon and provides a roadmap ahead.

Chapter 2

Architectures for singlet-triplet qubits in Si-P

In developing a scalable architecture for a solid-state quantum computer, a qubit structure with a low lead density is desirable as it reduces the interconnect crosstalk and complexity [36, 37]. Solid state qubits exist on the nano-scale and must be placed in close proximity to each other at the nano-scale to enable high-fidelity inter-qubit gate operations. Typically, each solid state qubit requires leads to perform qubit operations, qubit initialisation, qubit readout and, in some systems, to form the qubit trapping potential itself. This can lead to a very large lead density with challenges to route all gate electrodes under the constraints of limited space and reduce inter-lead crosstalk.

The qubit unit-cell proposed in this thesis eliminates the need for additional confining gates (to form the qubit trapping potential) by using P-donors in silicon. The P-donors' Coulombic potential well naturally confines the qubit electrons. The nuclear spin-half P-donors can also be used to encode long-lived qubit information [38, 39]. Additionally, the spin-half P-donor nuclei can be polarised to form local magnetic field gradients for qubit control [40, 41]. Importantly, the gates required for conventional qubit sensing structures are eliminated by integrating the sensor into one of the pre-existing mandatory gates in the device (see Section 3). The result is a linear array of qubit unit-cells that only requires two leads per qubit as shown in Figure 2.1. Since each quantum dot in this unit-cell has a matching gate, one has a full degree of freedom in controlling the electrostatic potentials of each individual dot. Thus, the proposed qubit architecture does not compromise qubit tunability or require the large device uniformity of architectures where any single gate is tasked

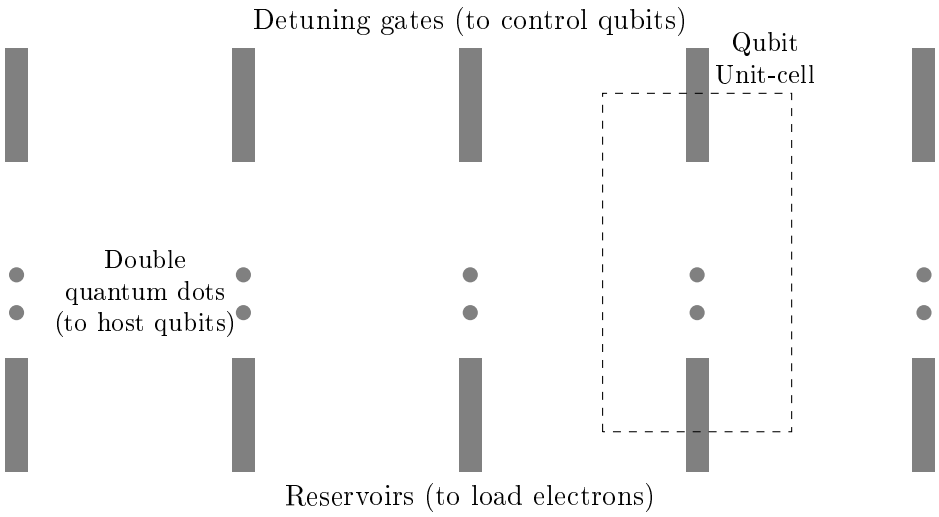

Figure 2.1: Proposed architecture to host a linear array of singlet-triplet qubits using Si-P quantum dots. The qubits are arranged in a linear array of qubit unit-cells each consisting of a reservoir (to load electrons), a detuning gate (for qubit control) and a double-quantum dot to host a two-electron singlet-triplet spin qubit. Single qubit gates are performed by moving electrons between a given double-quantum dot (Pauli-x rotations when the electrons are on separate dots and Pauli-z rotations when the electrons are pushed towards the same dot) while two-qubit gates are mediated via the electric dipole coupling between adjacent double quantum dots.

with controlling many quantum dots simultaneously [28]. The singlet-triplet qubit unit-cell was developed in this thesis by taking advantage of the features unique to STM patterned P-donor dots[1]. An initial geometry was investigated using a simple electrostatic model. Based on these simulations, a quadruple quantum dot device was fabricated using P-donor quantum dots in silicon [29]. To characterise the device, an electrostatic triangulation method was developed and implemented to verify that the four P-donor dots were present. The geometry enabled independent control of all four dots with the ability to load electrons onto each of the four dots. In addition, the proposed unit-cell geometry was shown to be compatible with a linear array of singlet-triplet qubits by demonstrating a strong inter-qubit coupling (required for two-qubit gates) of 5 GHz between adjacent double quantum dots. Finally, a singlet-triplet spin state across one of the double quantum dots was read out in single-shot using RF technology as discussed later in Section 3.

[1] The small size of the P-donor dots enables close qubit packing, thereby allowing stronger inter-qubit interactions. In addition, local P-doped leads patterned as close as 11 nm to the quantum dots enables greater gate tunability (in the form of a greater gate-to-dot lever-arm α) of electrons on the quantum dots when compared to larger gate-defined quantum dot counterparts.

2.1 Introduction to quantum dot spin qubits

A qubit is a controllable two-level quantum system where information is embedded into the overall, possibly superposed, quantum state. In spin-based quantum computing, the two-level system is that due to the particle's spin. For example, in single-spin qubit proposals, the two-level system is an electron or nuclear spin that is either aligned or anti-aligned with an applied magnetic field. One may concatenate multiple spinful particles to create a larger state-space upon which a two-dimensional subspace acts as an enhanced qubit such as the singlet-triplet qubit which has a qubit subspace protected from global magnetic field noise [12–14, 42]. In all cases, there is a need to trap and isolate a single spin from the environment.

2.1.1 Confinement potential for qubits

It can be shown from Maxwell's equations that electrostatic fields cannot have a global minimum upon which charge may settle; coined Earnshaw's theorem [43]. However, one may still have saddle points, which if rotated (via two orthogonal coils producing AC sinusoidal electric fields in a configuration known as a 'rotating Paul-trap') can form an electric field minimum that may trap charge [44–46]. Another method to circumvent Earnshaw's theorem is to restrict the degrees of freedom in which the electron may reside. In the case of gate-defined quantum dots such as that in GaAs or SiGe, a thin doped layer within the heterostructure creates a plane of high electron mobility in which electrons are restricted to form a two-dimensional-electron-gas (2DEG). With one degree of confinement provided freely by the heterostructure formed on the semiconductor substrate, one may use surface gates (on a layer above the 2DEG) to provide static electric fields that confine the electrons laterally in the 2D plane to a small area [13, 17, 47]. On tuning the gates, the confinement potential of the quantum dot can be modified to allow a single electron to be trapped. The nearby gates can then be used to shape the confinement potential to manipulate the electron spin qubits and couple adjacent qubits. In this way, gate defined quantum dots offer tunability in terms of system parameters such as electron-electron exchange coupling J, but come with the disadvantage that they have a high gate densities that can tally up to 11 gates per qubit [14]. Ultimately, the higher the gate density, the more likely there will be a problem in scaling up to many qubits due to the fanning out of the large number of gate lines.

One method to reduce the gate density in semiconductor qubits is to use atom donors in the silicon substrate. The donors naturally trap electrons in their atomic

valence bands of Coulombic potentials. However, this advantage comes at the cost of reduced qubit tunability. For example, the inter-dot tunnel rate between two donor quantum dots is set upon fabrication and cannot be strongly tuned using a gate like with gate-defined quantum dots [13, 14]. This is because the inter-dot distances for donor quantum dots are in the order of 12 nm and thus, any gate that tunes the tunnel barrier (and not the on-site potentials of the dots) will need to be near the centre of the double quantum dot; at this point the gate is too close to the quantum dots and the gate electrons will interfere with the qubit state.

2.1.2 Types of quantum dot spin qubits

With the electrons confined within their Coulomb potential wells, one must create a two-level system in which to manipulate. One simple two-level system is to apply a magnetic field. The electron spin will Zeeman split into two states to form a 'single-spin' qubit: an excited state with the spin anti-aligned with the magnetic field and the lower energy ground state aligned with the magnetic field. This magnetic field naturally gives a Hamiltonian with a Pauli-z term that lets it precess the spin about the z-axis (defined as the direction of the applied magnetic field). To get Pauli-x terms in a similar way, one would need to tilt the magnetic field. However, magnetic fields are generated by large coils which will have large inductances that forbid quick changes in the magnetic field. A more elegant solution is to create the magnetic field via an electromagnetic wave, for RF pulses can be switched on and off quickly. Known as electron spin resonance (ESR), a sinusoidal time-varying perpendicular magnetic field, which if the frequency matches the Zeeman energy splitting, performs Pauli-x operations [48]. This yields the spin-qubit Hamiltonian:

$$\mathbf{H}_{\text{spin-qubit}} = \frac{g_e \mu_e B_z}{2}\sigma_z + \frac{g_e \mu_e B_x}{2}\cos(\omega_0 t)\sigma_x, \tag{2.1}$$

where g_e is the gyromagnetic ratio for electron spins, μ_e is the Bohr magneton, B_x is the orthogonal magnetic field strength, B_z is the global magnetic field and ω_0 is the driving frequency of the orthogonal RF drive. When the drive frequency matches the Zeeman splitting, $\hbar\omega_0 = g_e\mu_e B_z/2$, the Hamiltonian yields pure x-rotations when the system is in the so-called 'weak-driving' regime [49]: $g_e\mu_e B_x \ll g_e\mu_e B_z + \hbar\omega_0 = 2g_e\mu_e B_z$. In the case of semiconductor quantum dots, this involves integrating a metal antenna in close proximity to the qubits [16, 50]. Similar qubit control has been shown using low-loss superconducting coplanar striplines where the ability to achieve higher current densities in the antenna enables larger amplitude driving fields [51]. The challenge in using antennas lies in obtaining a large enough

magnetic drive amplitude at the location of the electron spin (typically only up to $\sim$1 MHz [52]). The difficulty in gathering a large drive amplitude arises from the RF engineering challenge for the high frequencies involved[2]. The coaxial lines going into the fridge must be thermalised via attenuators and this sets a limit on the maximum signal that may physically reach the device for a given high frequency microwave generator. In addition, large RF powers sent to the antenna cause dissipative heating that may warm the device and increase thermal excitations on the spin qubit. Thus, given a limited input power, the challenge for ESR driven spin rotations lies in shaping the antenna such that it converts as much of the RF power into an orthogonal magnetic field that can drive coherent rotations [53]. As the drive amplitude, $g_e\mu_e B_x/2$, determines the precession frequency of the Pauli-x gate, this limits the gate speed. Nonetheless, antenna-based driving of electron spins hyperfine-coupled to nuclei (such as ion-implanted P-donors) to drive nuclear spin qubits has yielded a promising route to single qubit control with long coherence times[3] of up to $T_2^* = 600\,\text{ms}$ for the nuclear spins as opposed to $T_2^* = 270\,\mu\text{s}$ measured for electron spin qubits on P-donors [39].

One approach taken to overcome the slow speed of the magnetic drive (in the order of a few megahertz) when using antennas, is to use micromagnets [18, 47, 54, 55]. Here, groups typically evaporate cobalt under a magnetic field to create a patch of magnetised material near the quantum dots. When engineered properly, the micromagnet produces a magnetic field gradient (perpendicular to the globally applied magnetic field) across the quantum dot. Now using the control gates to shape the potential well, the electron can be physically moved sinusoidally back and forth within this magnetic field gradient (or forced between different spatial orbital states [47]). This means that the electron feels a sinusoidal time-varying magnetic field that can be used to perform resonant Pauli-x gates as before, but with much larger driving amplitudes of up to 40 MHz [18].

The long-term issue with single-spin implementations is that they easily decohere in the presence magnetic field noise since all the Hamiltonian components strongly couple to external magnetic fields as seen in Equation 2.1. To combat this issue and

[2] The frequencies range to 40 GHz as the single spin readout mechanism requires a large Zeeman splitting for high-fidelity state readout. This leads to choosing the maximum workable frequency, when using coaxial cables, at approximately 40 GHz [16]

[3] The coherence time is the exponential time constant in which the spin population, when undergoing free precession (that is, identity operations), on average drops by $1/e$. The drop in population is due to the shot-to-shot inconsistencies in the precession frequency (for example, due to noise in the B-field for single spin qubits). The coherence time effectively limits the number of possible consecutive gate operations one may perform before the qubit. Thus, the ratio of the coherence time to the gate operation time is ideally large for a high-fidelity qubit.

thereby avoid the hassle of patterning micromagnets or antennas, aligned to the single spin qubits, initial semiconductor spin qubits were also created by concatenating two different electron spins to form a 'singlet-triplet qubit' [12–14]. The two-spin Hilbert space can be decomposed into the singlet-triplet basis:

$$\begin{cases} s_0 = \frac{1}{\sqrt{2}}\left(|\uparrow\downarrow\rangle - |\downarrow\uparrow\rangle\right) \\ t_0 = \frac{1}{\sqrt{2}}\left(|\uparrow\downarrow\rangle + |\downarrow\uparrow\rangle\right) \\ t_- = |\downarrow\downarrow\rangle \\ t_+ = |\uparrow\uparrow\rangle \end{cases} . \tag{2.2}$$

The arrows indicate the state of the individual electron spins (up or down). The first two states, s_0 and t_0, form the two-level system subspace for the qubit, while the final two states, t_- and t_+, are considered leakage states. Notice that the qubit subspace has anti-aligned spins and thus, the full Zeeman splitting is zero as these spins have an overall zero z-spin-projection. Thus, these qubits are immune to global common-mode (that is, the magnetic field component common to both dots) magnetic field noise. In addition, they allow full electrical control in the sense that there is no need for a high-frequency driving magnetic field using an antenna or waveguide. In fact, qubit control lies in establishing a magnetic field gradient ΔB_z and controlling the two-electron spin exchange J:

$$\mathbf{H}_{\mathrm{ST}} \equiv \frac{1}{2} J\sigma_z + \Delta B_z \sigma_x. \tag{2.3}$$

That is, in the singlet-triplet basis, s_0 and t_0, the singlet-triplet Hamiltonian offers x rotations mediated by ΔB_z and z-rotations via the exchange J. The exchange refers to the singlet-triplet energy splitting that manifests from energy considerations as two electron spins are forcibly overlapped via electric fields from local gates. The magnetic field gradient ΔB_z arises from a difference in the local magnetic fields across the two dots. This gradient can be formed by many methods ranging from the polarisation of a bath nuclear spins [40] to the placement of a permanent micromagnet [17] as discussed in Section 2.1.5.

For completeness, when discussing semiconductor qubits, it is worth noting the existence of charge qubits. These qubits ignore the spin of the electron and place the electron charge across two dots with the two qubit levels being the occupancy of the first or second dot. Spin qubits are often chosen over charge qubits since their qubit lifetimes (or T_1) are significantly longer. For example, electron and nuclear spin qubits have had lifetimes in the order of tens of seconds to minutes compared with a

few nanoseconds as seen with charge qubits [39, 56, 57]. However, the gate operations on charge qubits are typically much faster with gate operations times ranging in the order of several gigahertz [58]. Thus, there are proposals where one concatenates three electron spins across two dots to form the 'exchange-only qubit' [59], 'hybrid qubit' [60] or the 'quadrupole qubit' [61]. A key feature of these qubits is that like single-spin qubits, they are immune to electric field noise (singlet-triplet qubits are susceptible to electric field noise as discussed later in Section 5.4 for CZ gates in the strong inter-qubit coupling regime) and like singlet-triplet qubits they are also immune to global magnetic field noise. However, the qubit subspaces, for these more exotic qubits, typically require manipulation of sensitive silicon valley coupling terms[4], which may become increasingly difficult when having to simultaneously tune and control many qubits. In addition, the two-qubit gates for these exotic qubit types involve many additional subsidiary gate operations which may negate the advantage gained by having enhanced noise immunity (that is, the gained coherence time via operation in the low-noise regimes may be negated by the longer net gate times). Thus, given all the advantages and disadvantages of different qubit types, this thesis will focus on quantum computing architecture proposals incorporating the singlet-triplet qubit both for its simplicity of design and operation.

2.1.3 Two qubit gates

In Section 2.1.2, the spin qubits were discussed in terms of single-qubit gates and qubit lifetimes. However, another important criterion for a qubit processor is its ability to perform multi-qubit entangling operations. Although the development of fault-tolerant two-qubit gates are yet to be demonstrated in quantum dots, there has been recent progress in increasing the two-qubit gate fidelities [14, 34, 54, 55, 66].

For single spin qubits, the mechanism for a two qubit gate utilises the same setup as that used for single-qubit operations on a singlet-triplet qubit. That is, one sets up a magnetic field gradient between the two dots hosting the single-spin qubits upon which to perform the two-qubit gate. To run the actual two-qubit gate, one increases the electron-electron exchange J between the two spin qubits to perturb the energy level splitting such that there is a different ESR frequency between the $|\downarrow\downarrow\rangle$ and $|\uparrow\downarrow\rangle$ states[5] when compared to that between the states $|\uparrow\uparrow\rangle$ and $|\downarrow\uparrow\rangle$. Thus, for example if one probes the ESR frequency between the $|\uparrow\uparrow\rangle$ and $|\downarrow\uparrow\rangle$ states, the first electron

[4] The valley coupling terms have been shown to be sensitive to crystal strain [62], local electric fields [52, 63], oxide interface engineering [64], silicon interface roughness [65]

[5] Without loss in generality, $|\uparrow\downarrow\rangle$ is taken to be lower than $|\downarrow\uparrow\rangle$ as the magnetic field gradient is directed such that it is stronger on the right dot

spin only rotates if the second electron spin is spin-up. This operation is a controlled Pauli-x gate (or CX gate) and often labelled as the CROT gate. The gate was first demonstrated in Si-MOS quantum dot devices [67]. Later the CROT gate was again demonstrated with higher fidelities of approximately 78-85% in SiGe [54, 55] and up to 98% in Si-MOS [66]. The dominant issue to overcome in the two-qubit gate performance is decoherence due to charge noise[6]. Although single qubit gates for single spin qubits are predominantly limited by magnetic field noise, the reliance on J to perform the two-qubit gate operations ultimately makes charge noise the limiting factor in scaling up to many single spin qubits since J is sensitive to the electric field gradient across the quantum dots.

For singlet-triplet qubits, two qubit gates have been successfully demonstrated in GaAs quantum dots via the electric dipole interaction between adjacent singlet-triplet qubits [14]. This mechanism utilises Pauli-spin blockade between the two electrons hosted on the double quantum dot. That is, only the singlet state allows both electrons to occupy a single quantum dot (the two electrons must reside on separate dots when in the triplet t_0 state). In addition, note that J is a function of the electric field around the double quantum dot. Thus, one may arrange adjacent singlet triplet qubits (that is, two double quantum dots) such that there is a significant difference in the electric field sensed by the 'target' qubit when the 'control' qubit is in the singlet state (both electrons occupy one of the dots in the control qubit's double quantum dot) and the triplet state (both electron separated across the dots in the control qubit's double quantum dot). The resulting difference in electric fields (around the target qubit) due to the control-qubit's electric dipole yields a state-dependent perturbation on the target qubit's J. As J mediates Pauli-z rotations, the electric-dipole interaction can be used to form a CZ gate. In the regime of weak electric dipole coupling with respect to the speed of J-mediated Pauli-z gates (for example, when J was set to $\sim$300 MHz for Pauli-z rotations in GaAs quantum dots, a 1 MHz shift was present in J [14]), one may utilise AC driving methods [34, 35]. In the AC drive method, one sinusoidally drives J to perform Pauli-z rotations (similar to the AC driving used in electron spin resonance experiments). The advantage of AC driving is that the net working point in J is set to $J \approx 0$ and thereby reduces the impact of charge noise as charge noise is minimal at $J \approx 0$ [17, 34, 69]. AC driving has been used to demonstrate two-qubit gates with fidelities of up to 90% for GaAs quantum dots. The idea of using large, non-perturbative inter-qubit couplings (large

[6] The exact source of charge noise is still unknown. However, there are speculations that the noise is due to intrinsic 'two-level fluctuators' caused by electrons hopping between two sites; for example, crystal or interface defects [18, 68, 69].

shifts in target qubit's J with respect to the target qubit's J used for Pauli-z gates) has not been studied in detail as it is difficult to realise in gate-defined quantum dot structures. The reason why larger shifts are a challenge in gate-defined structures, compared to Si-P structures, is because the dots cannot be brought close enough to realise a large enough electric dipole. Thus, to enhance the inter-qubit coupling in gate-defined structures, one needs to utilise more exotic schemes such as coupling two GaAs singlet-triplet qubits via a superconducting resonator [70]. The strong inter-qubit coupling regime realisable in atomic scale qubits will be a focus of this thesis as large inter-qubit couplings in excess of 5 GHz have been measured in Si-P quantum dots [29]. A large inter-qubit coupling implies the potential to realise faster, therefore higher fidelity, two-qubit gates.

2.1.4 Using P-donors in silicon as a qubit platform

Singlet-triplet qubits in semiconductors have been demonstrated in gate-defined quantum dots in both GaAs and SiGe [14, 17]. However, these implementations typically require a large gate density, of up to 11 gates per qubit, since singlet-triplet qubits require two dots per qubit. The two electrons forming the singlet-triplet qubit are confined across the two dots, where upon the electron-electron exchange J (required for Pauli-z qubit rotations) is tuned by bringing both electrons onto one dot (large J) or separating them onto separate dots (low J). To have full independent control of the potentials on the dots, one requires a minimum of two gates per qubit[7]. Some of the additional gates in the gate-defined implementations are present to help create the confinement potential; these gates can be eliminated in P-donor architectures in silicon. Since the phosphorus atoms naturally confine electrons in their valence bands, it shall be shown in this thesis, that it is be possible to reduce the number of required gates down to two gates per qubit. The remaining gates in gate-defined quantum dots are typically present for the qubit sensor. These gates can also be eliminated (in both donor quantum dots and gate-defined quantum dots) by utilising a single-gate RF sensor that integrates into the pre-existing mandatory control gates in the device as discussed further in Section 3.

Donor based Si-P quantum dots can be created in multiple ways: one is via ion-implantation and another via STM (scanning tunnelling microscope) lithography. In ion-implantation one implants phosphorus ions into a silicon crystal at $\sim$keV energies and then anneals the substrate to remove the damage caused by the passage

[7] Sometimes full independent control is not necessary to achieve all required control on the quantum computer, for one exploits geometric symmetries like in one of the surface code proposals using single-spin qubits [28]

of the phosphorus ions below the silicon surface. To manipulate the implanted P-donor potentials, one incorporates metallic gates patterned on the surface of the silicon crystal via EBL (electron-beam-lithography) on a SEM (scanning-electron-microscope).

With STM lithography one can place individual P-donors in silicon [15, 20–22, 25]. Here, one starts creates a hydrogen mask where each silicon atom on the surface is bonded to one hydrogen atom. One can remove hydrogen atoms by pulsing a high voltage on the STM tip, causing vibrational excitation, in sites where one wishes to place phosphorus donors. The wafer is exposed to phosphine gas which binds to non-hydrogen-passivated sites. Upon heating the wafer to approximately 320 °C, the phosphorus donors incorporate into the top layer of the silicon surface within the patterned regions. Finally the wafer is encapsulated with an approximately 40 nm layer of silicon via a silicon-sublimation source. Unlike ion-implantation, the control gate leads are patterned on the same atomic plane as the dopants using STM lithography. The metallic gates are formed by creating large patches of highly P-doped silicon with a large density of states. One connects to these buried P-doped silicon patches via conventional metallic electrodes patterned on the top of the encapsulated silicon.

A critical advantage of STM lithography is that one can place the P-donors in silicon with atomic precision while ion implantation introduces errors in the lateral position and depth that depend on the energy of the implantation process. The typical error in depth is approximately 8 nm when using 12 keV. In addition, the implanted ions can channel back to the surface and become electrically inactive, such that multiple donors need to be implanted to ensure that there is a viable donor to form a qubit [71]. A possible disadvantage of STM lithography is that the silicon encapsulation layer must be grown at low temperatures to avoid dopant diffusion. It remains an open question if low temperature epitaxial growth, required to avoid dopant diffusion, affects the crystalline quality of the encapsulation layer. It is possible that defects may occur during the low temperature growth that can potentially form sites to trap charge that may arbitrarily charge or discharge. This can become a source of noise (where one will have diminished stability in the control of the electron spin states) in the system in the form of random electric field fluctuations. Typically the creation of a low-defect silicon surface requires annealing temperatures reaching 1100 °C. However, temperatures above 450 °C during incorporation causes loss of phosphorus on the surface via $PH_2 \rightarrow PH_3$ recombination [72, 73]. In addition, higher temperatures lead to the formation of electrically inactive P_2 dimers. Any excess heating will cause diffusion and segregation of the phosphorus atoms

that scramble the locations of the placed phosphorus atoms [74]. Diffusion refers to the random movement of the highly energetic phosphorus atoms through the silicon crystal. Segregation refers to the steady-state configuration where the phosphorus atom, given enough energy, may switch places with the silicon atom above it to enter a lower energy state in the lattice. Thus, while diffusion can occur over all directions, segregation is a vertical movement towards the surface of the silicon crystal. Current fabrication processes have optimised the growth rates and temperatures to minimise dopant diffusion and segregation whilst achieving full dopant activation. One can grow at higher temperatures to ensure a low-defect encapsulation layer by making use of 'locking layers' which reduce the impact of segregation and diffusion [75]. Locking layers are silicon encapsulated using low temperatures for the first few nanometres of encapsulation while heating remaining layers to the higher temperatures required for the formation of a low-defect silicon crystal. In fact, applying rapid thermal anneals after growing approximately 70 nm, required for creating a new flat surface for multilayer STM lithography, show strong indications of preserving the integrity of the buried device layer [76].

Although ion-implanted and STM fabricated architectures share some similarities, it is of note that the systems operate under different physical conditions. For example, in the case of ion-implanted donors, the donors are very close to the surface (up to approximately 20 nm). Thus, one needs to consider surface effects while STM patterned donors can be patterned either close to the surface or further away where they can be considered to be P-donors in an effectively bulk silicon crystal. Donors near the surface have the potential of better tuning of the hyperfine interaction (proportional to the electron wavefunction overlap with the phosphorus nucleus) when compared to isolated donors in a bulk crystal[8] [77]. However, this has yet to be confirmed experimentally.

In this thesis, STM lithography was used to reliably place multiple donors with atomic precision and control every aspect of the Si-P device geometry, in contrast to ion-implantation techniques. In addition, the atomic precision in placement of the metallic phosphorus control gates allows for greater flexibility in the shape, size and

[8] This is because the electrons on a donor are tightly confined to the potential well formed by the phosphorus nucleus (an s-orbital in the ground state). When applying a strong electric field, the actual perturbations on the wavefunction are small before the electron becomes free from the donor's potential (that is, ionisation). Having a strong barrier potential nearby (such as that of donors placed near the surface) allows one to exceed the ionisation energy to yield wavefunctions that have a large probability density near the barrier while retaining a smaller probability density across the nucleus. Note that the transition in hyperfine tuning is still a steep function that changes rapidly with electric field when near the ionisation energy [38, 77, 78]

placement of the gates while, MOS gates are limited to 10 nm in precision[9]. At the time of publishing this thesis, the technology for atomic-scale fabrication was well-developed and therefore appropriate to enable the demonstration of unit-cells capable of hosting singlet-triplet qubits. Previous results include the activation of a single-donor transistor device [15] and successful demonstration of phosphorus wires that are as thin as 2 atomic rows [27, 79]. Spinful behaviour of electrons confined within the phosphorus doped quantum dots had also been successfully demonstrated [50, 80–82]. An additional advantage of STM lithography, compared to ion implantation, is the ability to pack multiple donors into a single dot; thereby strengthening the quantum dot's confinement potential. This offers the advantage of better electrostatic tunability (lower voltage required on gates to move electrons onto or between quantum dots) and provides more local P-nuclei for stronger or tunable hyperfine interactions [40, 83, 84].

2.1.5 Generating ΔB_z for singlet-triplet qubits

As shown in Section 5.3, singlet-triplet qubits require a magnetic field gradient ΔB_z across the two dots to enable Pauli-x rotations. Such a magnetic field gradient has been realised in SiGe systems via micromagnets, where one evaporates ferromagnetic material (for example, cobalt) while under a magnetic field [17, 85]. However, this gradient is fixed on fabrication. An alternate approach is to use dynamic nuclear spin polarisation (DNP) where one may controllably polarise the nuclear spins within the substrate to realise a tunable magnetic field gradient like that shown in GaAs [40, 41]. By running a similar DNP protocol in Si-P, the polarisation of the phosphorus donors used to create the very dots themselves could create the required magnetic field gradient. This is because the confined electrons on the respective dots will experience a different hyperfine interaction depending on the nuclear spin state of the phosphorus donors in the different dots. A strong magnetic field gradient is desirable as it gives rise to faster Pauli-x gates. Therefore, dots with larger clusters of P-nuclei dot could prove useful for producing large magnetic field gradients. However, to date it remains unknown if larger P-donor dots can produce a stable ΔB_z since the dots may contain many spin configurations. It should be noted that the hyperfine interaction is of the form $A\mathbf{I}_\mathrm{n} \bullet \mathbf{S}$ (where $\mathbf{I}_\mathrm{n}$ is the nuclear spin operator, $\mathbf{S}$ is the electron spin operator and A is the contact hyperfine constant that is proportional to the electron wavefunction overlap with the nuclear spin). Thus, any changes in the

[9] The MOS gates however, can handle larger voltages between adjacent gates without current leaking between them due to the presense of an insulating oxide layer

electron spin, even when not intentionally performing DNP, will impact the nuclear spin. In the case of a micromagnet, one flipped spin in the magnetic domain will not significantly impact the ΔB_z (and this spin will likely flip back on its own due to thermal statistics). However, a flipped nuclear spin in a gradient formed by P-donors will strongly impact the ΔB_z. In addition, it has recently been shown that the act of placing an electron on a P-donor dot decreases its nuclear spin coherence time and can affect the nuclear spin states by either tilting or flipping the nuclear spins [39, 50]. The net impact of nuclear spin dynamics remains an area of ongoing research and remains outside the scope of this thesis.

The expected magnitude of ΔB_z due to the different number of P-nuclei in each dot can be estimated from electron spin resonance (ESR) experiments that probe the hyperfine energy splitting of electrons confined to P-donor dots of differing number of P-nuclei [39, 50]. For the first electron the hyperfine splitting (that is, between the nuclear spin pointing up and down) of a single electron on a 1P donor dot is approximately 58 MHz [50]. Thus, a 1P donor dot will contribute exactly have this value (that is, 29 MHz) to the magnetic field gradient. Therefore, between two 1P donors, if the nuclei are anti-parallel, the magnitude of the magnetic field gradient will be 58 MHz. For larger dot clusters created from more than one P-donor, the hyperfine interaction depends on the configuration of the phosphorus nuclei within the dot. For example, in a 2P cluster, if the nuclei are anti-parallel, the magnetic field contribution is approximately zero. If both P-nuclei are parallel, the field contribution of a 2P dot is approximately double that of a 1P dot at 58 MHz. However, this is strongly dependent on the spatial arrangement of the two P-donors within the silicon lattice with variations ranging from 71.9 MHz to 14.3 MHz when varying donor separation (∼0.5-5 nm) and arrangement with respect to the Si crystal axis [83]. Similarly larger 3P or 4P clusters can yield magnetic field contributions of up to triple or quadruple that of a 1P cluster for the first electron (for example, ∼87 MHz when arranging 4 donors in a tightly packed square). When adding more electrons to the dot, the outer valence electron is more weakly bound and thus, its probability density is lower at the site of the P-nuclei. Thus, the valence electron has a weaker hyperfine coupling and therefore, a significantly lower magnetic field contribution. It was shown in a simulation that a 2P cluster in a given arrangement in the silicon lattice can yield up to 50.9 MHz in the magnetic field contribution for the first electron. However, when adding 3 electrons to the dot, the outer valence electron yielded a magnetic field contribution of 5.25 MHz. This lower hyperfine contribution on adding more electrons could in fact, be used as an additional strategy to guarantee a stable non-zero magnetic field gradient. For example, one could have a double dot where the

donor clusters are 1P and 2P respectively. By loading one electron onto the 1P dot and three electrons onto the 2P dot, the difference in the magnetic field gradients could be approximately 24 MHz or 35 MHz given the spin of the nuclei.

2.1.6 Magnetic field noise in the substrate

Single-spin qubits utilise global magnetic fields for Pauli-z rotations while singlet triplet qubits utilise local magnetic field gradients for Pauli-x rotations. Due to this reliance on magnetic fields, any stochastic noise in the magnetic fields that fluctuate the magnetic field values will become a source of decoherence. To reduce magnetic field noise from the global magnet, affecting single-spin qubits, one may decouple the magnet from its power supply by placing it in persistence mode where the coil currents keep circulating due to the superconducting state of the magnet. However, magnetic field fluctuations may also come from the substrate. For example, GaAs has different isotopes containing non-zero nuclear spins that create magnetic field fluctuations which manifest as magnetic field noise. In the case of singlet-triplet qubits, this changes the magnetic field gradient across the two quantum dots causing decoherence in the Pauli-x qubit operations. The magnetic field gradient noise can be countered by making the value of the magnetic field gradient large (to reduce the fraction of the magnetic field gradient noise standard deviation to the overall magnetic field gradient) via dynamic nuclear spin polarisation [40]. When dynamically measuring the magnetic field gradient and setting up a feedback loop to stabilise the gradient, one can also reduce long-term fluctuations [41]. The success of using DNP in GaAs has been highlighted as the magnetic field noise no longer limits qubit fidelities. That is, single-qubit fidelities have exceeded 99% while the two-qubit gate fidelity currently remains limited to 90% due to intrinsic charge noise [34, 69].

A materials-level solution to overcome the fluctuating nuclear spins in the substrate is to utilise silicon; a substrate that has naturally fewer non-zero nuclear spins present. Approximately 5% of natural silicon ($^{\text{nat}}$Si) consists of ^{29}Si atoms which have a nuclear spin of 1/2. This is known to be a source of decoherence for single spin electron qubits in silicon [16, 50]. Although singlet-triplet qubits reject global magnetic field noise (unlike their single-spin qubit counterparts), they are still susceptible to close range ^{29}Si nuclei in the form of magnetic field gradient noise as in GaAs. The long term solution is to utilise isotopically purified ^{28}Si (Si nuclei with zero spin). Single-spin ESR experiments have shown that the bare decoherence time (T_2^*) of single-spin qubits rose from 55 ns to 270 µs when changing the host material from $^{\text{nat}}$Si to ^{28}Si [39]. Thus, one may posit that isotopically purified silicon

can lead to large coherence times in singlet-triplet qubits when performing Pauli-x rotations without the need for specialised nuclear spin polarisation protocols like in GaAs (although not a technical hindrance, the DNP sequences will add an extra layer of complexity to the control protocols).

2.2 Design and demonstration of a Si-P singlet-triplet unit-cell

Before optimising the qubit unit-cell for a many-qubit processor in Si-P, it is important to verify that the one can control electrons across two P-donor quantum dots to form a singlet-triplet qubit. For a singlet-triplet qubit, formed by two electrons across two quantum dots, one drives Pauli-x rotations by tuning the electron-electron exchange J to $J \approx 0$ where the electrons reside on separate dots. To drive Pauli-z rotations, one applies gate voltages to ensure $J \gg \Delta B_z$ where both electrons start to reside on the same dot. Therefore, for full qubit control, one needs to be able to controllably add one electron to each quantum dot with the ability to independently move one of the electrons to join the other electron on the adjacent quantum dot; a level of controllability that has already been demonstrated in Si-P quantum dots [81, 86]. However, the electrostatic controllability must be demonstrated on a device geometry that is compatible, in the long-term, with a scalable many-qubit architecture. That is, one needs to demonstrate an array of qubit unit-cells with the level of control required for individual qubit operations along with the ability to perform two-qubit operations between adjacent qubits.

The initial geometry to demonstrate a singlet-triplet qubit unit-cell using P-donors in silicon was designed using finite-element electrostatic models. The resulting design was then fabricated in Si-P using STM lithography and subsequently characterised in a dry dilution refrigerator [29].

2.2.1 Overview of techniques for modelling quantum dots

Electrostatic control of Si-P quantum dots fundamentally requires control of the electron occupancy on the quantum dots. The charge occupancy of the quantum dots is controlled by tuning the electrostatic potentials on the dots via voltages applied to local gates. Applying a voltage on a given gate creates a non-zero electrostatic potential on the entire structure. Tuning the electrostatic potential on the site of a quantum dot directly tunes its energy level. The general methodology to relate

the applied voltages on all the gates to the electrostatic potentials at the sites of the quantum dots and thus, the resulting charge occupancy requires one to solve a 'tight-binding' problem [81, 84, 87]. In the tight-binding method, one first calculates the electrostatic potential due to the gates and any other sources (for example, phosphorus donors provide a Coulombic potential well) by numerically solving the Poisson's equation. Then one solves the Schrödinger's equation with the interaction terms (such as the inter-site tunnel coupling, on-site potentials and electrostatic inter-electron terms) discussed in Appendices E.1 and E.2. To simplify the spin components, one can separately solve each of the singlet-triplet states while taking care to write the wavefunction solutions in the appropriate symmetric or antisymmetric manner to satisfy the overall antisymmetry of the wavefunction. The spatial wavefunction solutions may be found numerically solving the Schrödinger's equation. Now individual electrons also have electric fields that will affect the overall confinement of the other electrons. One calculates the resulting Coulombic potentials from the electrons (achieved by integrating the Coulomb potential of a point charge across the wavefunction's probability density) to create a new confinement potential. Finally, one solves the Schrödinger's equation as before and iterates until the electron wavefunction no longer changes as the trial solution has found a fixed point. The wavefunction solution can be used to extract the charge occupancy on the dots given the initial set of gate voltages. One may enhance the analysis by introducing an orbital component to the wavefunction where the basis of wavefunctions would be a linear combination of atomic orbitals (LCAO[10]). One may also include silicon valley contributions and lattice strain effects [15, 27]. This self-consistent Poisson-Schrödinger solver, especially when tempered with experimental data, provides the most accurate simulation of a device. However, this approach is very time consuming and only provides the electron occupancy solution for one combination of gate voltages. This makes resulting simulation of 'gate maps' (electron occupancy as a continuous function of two gate voltages) extremely time consuming. Thus, one typically adopts a semi-classical approach known as the 'constant interaction model' or the 'capacitance model' [88–90].

[10] If no electric fields are to be considered, the initial ground-state wavefunction can be found by weighting the orbital wavefunctions and finding the weights that minimise the overall energy

2.2.2 Adapting capacitance modelling for Si-P quantum dot devices

In a simple capacitance model, one ignores strong electron-electron interactions. In fact, only electrostatic contributions due to the gates' electric fields are considered while electron tunnelling and spin effects (that is, due to the Pauli exclusion principle) are discarded. Note that if the tunnelling and spin interaction strengths (of electrons between quantum dots) are much stronger than the typical on-site confinement potentials (termed 'strongly interacting systems'), this model is not applicable[11] [91]. In the capacitance model, one finds the relationship between the gate voltages and the electrostatic potentials on the dots along with the strength of electrostatic repulsion amongst electrons between every pair of dots. The natural abstraction to convert the voltages on the gates to the resulting charge states on the dots is to treat the transfer of an electron to a dot (or between any two dots) as the charging of a capacitor. A zero capacitance implies that no matter what voltage is applied to the gate, there is no interaction or relationship between the gate and the dot's voltage. On constructing capacitors for all interlinking nodes (gates and dots), one obtains a capacitance network. Figure 2.2 shows one such example for a double-dot system (D1 and D2) controlled by two gate leads (G1 and G2). Due to the high carrier density of P-doped silicon, the gates and dots can be considered as metallic objects upon which one applies a voltage [27]. All capacitances shown in Figure 2.2b are geometric capacitances that may be found in a numeric simulation via FEA (finite-element analysis).

Figure 2.2c shows the resulting capacitance matrix. As shown in Appendix A.1.1, this matrix has algebraic properties that relate the node voltages $\mathbf{V}$ to the nodal charges $\mathbf{Q}$ starting with: $\mathbf{Q} = \mathbf{CV}$. Appendix A.1 shows how, after some basic algebra, the capacitance matrix can be used to find the energies on the dots given the electron occupancies and gate voltages. The electron occupancy that yields the lowest energy, for a given set of gate voltages, is the ground-state charge state of interest. Subsequently, one may find hyperplanes in gate-voltage space that divide two charge states and thus, one may simulate the charge transitions (transfer of electrons onto or off the dots) that would occur on sweeping the gate voltages. Given simulations of the charge transitions with respect to the voltages on the gates, one may optimise device geometries (of the P-doped leads and P-donor quantum dots)

[11] As shown in Appendix E.2, it is clear that if the interacting terms are removed from the singlet-triplet Hamiltonian, the solutions to the Hamiltonian describing the double quantum dot system become diagonal; that is, the dot energies are all independent and linear.

(a) Example double-quantum dot device

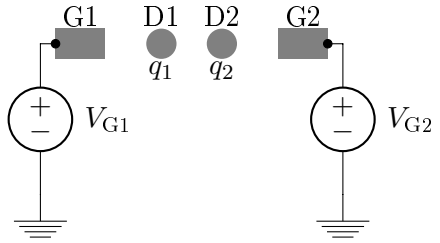

(b) Equivalent capacitance network

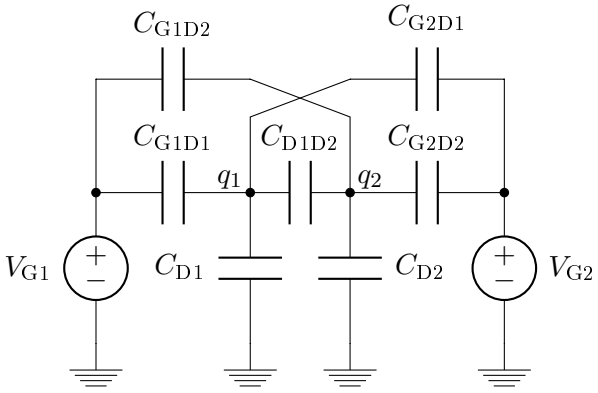

(c) Equivalent capacitance matrix

$$\mathbf{C} = \begin{pmatrix} 0 & 0 & -C_{\mathrm{G1D1}} & -C_{\mathrm{G1D2}} \\ 0 & 0 & -C_{\mathrm{G2D1}} & -C_{\mathrm{G2D2}} \\ -C_{\mathrm{G1D1}} & -C_{\mathrm{G2D1}} & C_{\mathrm{D1}} + C_{\mathrm{G1D1}} + C_{\mathrm{G2D1}} & -C_{\mathrm{D1D2}} \\ -C_{\mathrm{G1D2}} & -C_{\mathrm{G2D2}} & C_{\mathrm{D1D1}} & C_{\mathrm{D2}} + C_{\mathrm{G1D2}} + C_{\mathrm{G2D2}} \end{pmatrix}$$

Figure 2.2: An example of converting a device to an equivalent capacitance model. **(a)** shows the top-down view of an example device that consists of a two dots (D1 and D2) and two gates (G1 and G2). The voltages on the gates are tuned by voltages sources V_{G1} and V_{G2}. Applying different voltages on the gates changes the electrostatic potential environment around the dots and thus, tunes their energy levels. **(b)** shows the equivalent capacitance network that helps analyse the dots' energy levels. The key concept is that all nodes in the network represent dots or gates from the original device. **(c)** shows the equivalent capacitance matrix where the on-diagonal components indicate the total capacitance branching off a given node while the off-diagonal components indicate the inter-nodal capacitances. The intra-gate capacitances are irrelevant (as the charges on the gates will be actively compensated by the voltage sources to ensure they remain at a fixed voltage) in the context of device operation and left at zero for convenience.

to achieve the charge states required for the electrostatic control required to perform singlet-triplet operations.

One of the important device parameters to consider is the gate lever-arm α_{gd}. The lever-arm is a dimensionless scaling factor that links the energy change ΔU_d on dot d to the change in a applied voltage V_g on gate g via:

$$\Delta U_d = -e\alpha_{gd}\Delta V_g. \tag{2.4}$$

The lever-arm α_{gd} is a geometric scaling factor between 0 and 1. One may calculate the matrix of lever-arms using the capacitance matrix via:

$$\boldsymbol{\alpha} = -\mathbf{C}_{\mathrm{GD}}\mathbf{C}_{\mathrm{DD}}^{-1}, \tag{2.5}$$

where $\mathbf{C}_{\mathrm{GD}}$ is the block matrix in $\mathbf{C}$ describing the capacitances between the gate indices G and the dot indices D, while $\mathbf{C}_{\mathrm{DD}}$ is the inter-capacitance block matrix between the quantum dots. The element α_{gd} in $\boldsymbol{\alpha}$ is the lever-arm between the gate g and dot d. By its definition, it is easy to show that the sum of lever-arms for a given dot is also bound by 1. For example, if two gates are symmetrically arranged close to a dot, the gates individually have a lever-arm of at most 0.5. However, if these gates are at a larger distance away from the dot (such that the dot's self-capacitance starts to greatly dominate the gate-to-dot capacitances), then the gate lever-arms on the dot tend to zero. It is important to maximise the lever-arm of a gate designated to control a given dot as this minimises the required voltage swing to bring the dot to the desired energy level. A lower voltage range (needed to control the quantum dot) is important as the available range of gate voltages is limited by gate-to-gate current leakage. However, a higher lever-arm implies that the gates are in closer proximity to the dots and thus, ideally one needs to optimise the distance between the dot and gates to achieve an acceptable voltage range without current leakage. Currently, there exists no model to predict the gate voltage range in which no current leakage occurs. Therefore, one must rely on current leakage data from previous devices to optimise the device geometry and operating conditions.

In addition to the charge stability diagram simulations, it is of note that the electrostatic simulations used to generate the capacitance matrix differs from that used previously to model Si-P devices [28, 86, 92, 93]. The capacitance matrix was previously generated from electrostatic finite-element simulations of the device geometries where the leads were treated as planar metallic elements with a thickness of 3.6 nm (taken from the simulated Bohr radius of P-donors in silicon [94, 95]) while the donor dots were treated as metallic spheres with a radius of 1.4 nm to

match the 45 meV charging energy of single P-donors [15]. The finite-element solver then calculates the resulting capacitances between all gates and dots to generate the capacitance matrix. However, with double quantum dots and gates placed in a line (like in Figure 2.2a), the model will underestimate the lever-arm of the gate with the opposite dot due to the electrostatic screening of the second dot in between as discussed in Appendix A.3 (for example, in Figure 2.2a, dot D1 will screen dot D2 from gate G1 and thus the capacitive model will underestimate the gate lever-arm of G1 to dot D2). However, a charge neutral P-donor could be inferred to be similar to that of a nearby silicon atom; that is, the P-donor may not necessarily act as a metallic sphere (specifically a perfect electrical conductor in a continuous silicon dielectric as in previous simulations). Thus, the electrostatic simulations were modified to remove the dots' screening effects by removing the dots from the FEA simulation. Here, one infers the gate lever-arms by considering the electrostatic potentials of the gates at the positions of the dots. That is, since the dots are point-like objects, the potential energy change on a given dot is indeed proportional to the electrostatic potential (of the gate) at the dot's position on applying a given voltage on the gate. Compilation of all the lever-arms can be used to generate the gate-to-dot capacitance block matrix $\mathbf{C}_{\mathrm{GD}}$ via Equation 2.5. Similarly, the potential energy shifts on one dot when loading electrons to the other dots can be inferred by viewing the shift in the dot's potential energy due to the electrostatic potential of an electron charge placed on the other dots. On compiling all the potential energy shifts between all pairs of dots one may generate the dot-to-dot capacitance block matrix $\mathbf{C}_{\mathrm{DD}}$. The mathematical details along with the exact algorithm used in the modified capacitance model simulations (of Si-P quantum dots near P-doped leads) shown in this thesis are discussed in Appendix A.3.

2.2.3 Electrostatic design of a Si-P singlet-triplet qubit unit-cell

The proposed scalable singlet-triplet unit-cell contains two gates per qubit hosted on a double quantum dot. A two-qubit gate between two singlet-triplet qubits has already been shown in GaAs and thus, aspects of that experiment's particular device design were worth investigating. As shown in Figure 2.3a, the two GaAs singlet triplet qubits (hosted on the double quantum dots LL/LR and RL/RR) are arranged in a line to maximise the inter-qubit coupling. For example, consider a singlet-triplet spin state hosted on the dots LL/LR. When moving both electrons onto the dot LR (note this only occurs if the electron spins are in the singlet state), the repulsive force (of both electrons on LR) would maximally push the electrons across the singlet-

triplet state on RL/RR (to cause a maximal shift in J on the singlet-triplet qubit hosted on RL/RR). Thus, having the four dots in a linear geometry maximises the inter-qubit coupling. A key observation in the GaAs device architecture is the gate density of 11 gates per qubit (counting the gates for the RF-QPC qubit readout sensors in red and the blue gates reserved for confinement and qubit control). This large gate density (of more than 1 gate per qubit) may ultimately create challenges in qubit scale-up [37].

One method to reduce the gate density is to replace the gate-defined dots (which require many confinement gates) with P-donor dots which provide free self-confinement such as the device shown in Figure 2.3b. Here, the device consists of a double quantum dot (D1 and D2) with the resulting singlet-triplet state loaded and measured via a SET charge sensor (source S, drain D and tuning gate GSET). The dots' potentials are tuned via the gates G1, G2 and GT. As a long-term scalable unit-cell beyond two singlet-triplet qubits, the geometry is not ideal due to the space taken up by the three-lead sensor. Thus, the geometry used in this thesis was adapted from a different Si-P double quantum dot device (shown in Figure 2.3c) designed to measure electrons in transport [81]. The transport device loaded electrons onto the dots (D1 and D2) to form the singlet-triplet state via electron transport through the source and drain leads (S and D respectively). To tune the two dots' potentials, two extra gates (G1 and G2) were required as using S and D to manipulate the dots' potentials would cause electron current flow. Unlike the GaAs device shown in Figure 2.3a or the SET Si-P device shown in Figure 2.3b, there were no charge sensors patterned nearby and thus, the spin states were deduced via electron transport [81, 86, 89, 92]. Later a resonator was attached on the drain lead to measure the two-electron singlet-triplet state via RF reflectometry [30]. In the reflectometry experiment, it was successfully shown that the single-gate RF sensor (that integrates onto a pre-existing lead in the device; in this case, the drain lead D) could indeed measure the singlet-triplet spin state hosted across the double quantum dot. However, the immediate geometry was not ideal to use as a scalable unit-cell design for two reasons. The first reason was that the design required four leads to form and control the singlet triplet state (for example, a single-spin qubit hosted on a P-donor dot and measured with a three-lead SET would require the same number of leads per qubit). More importantly, the second reason was that the strong coupling of the dots to their reservoirs (S and D) resulted in very low spin life times of 60 ns. That is, the large tunnel rate of electrons between the dots and their nearby reservoirs caused one of the electrons in the singlet-triplet state to swap with electrons in the reservoir (via a second order quantum co-tunnelling process) thereby destroying the initial two-electron singlet-

(a) Quadruple quantum dot GaAs device used to show coupled singlet-triplet qubits [14, 34]

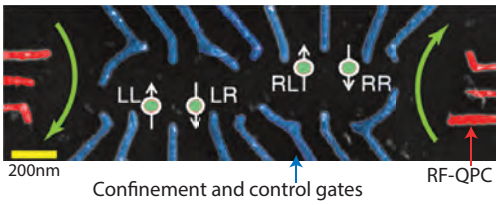

(b) Double quantum dot Si-P device measured with an SET [86]

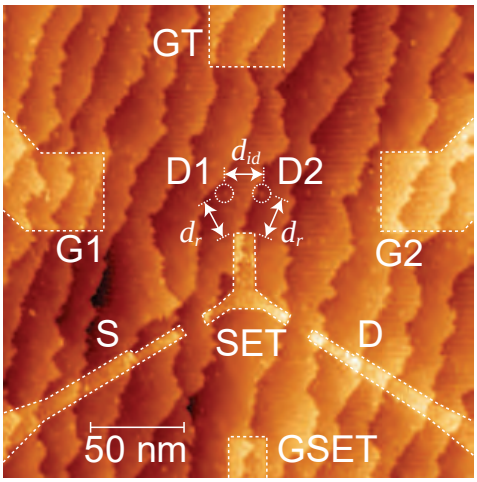

(c) Double quantum dot Si-P device measured with a single-gate RF sensor [30, 81]

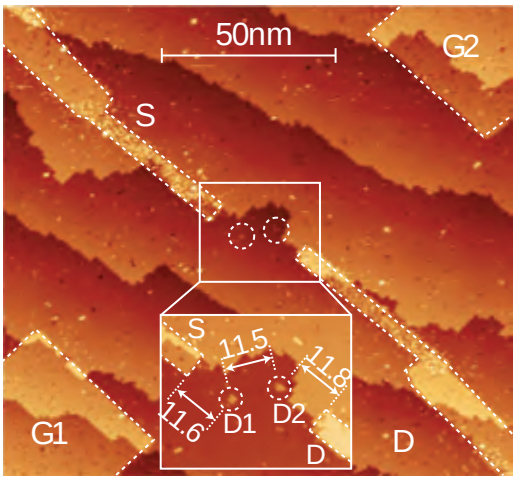

Figure 2.3: Previous devices to consider when designing a quadruple quantum dot device in Si-P. With the aim to demonstrate a scalable singlet-triplet qubit unit-cell in Si-P, it was important to look at previous designs. **(a)** A 4-dot gate-defined GaAs device used to show high fidelity two-qubit gates between two singlet-triplet qubits [14, 34]. The red structures highlight two RF-QPC sensors used to read out the qubit states, while the blue structures indicate confinement and qubit control gates. The green dots indicate approximate locations of the four dots. **(b)** A 2-dot Si-P device (D1 and D2) used to measure singlet-triplet spins via a SET (source S, drain D and SET tuning gate GSET). The dots' potentials are tuned via gates G1, G2 and GT. The SET acts as a reservoir for the two P-donor dots with a dot-to-reservoir distance of d_r∼21 nm and d_r∼22 nm for D1 and D2 respectively. The inter-dot distance was $d_i = 20$ nm. **(c)** A 2-dot Si-P device used to measure singlet-triplet spins in transport [81]. The dots were loaded with source (S) and drain (D) leads. The dots' energies were tuned via gates G1 and G2. The singlet-triplet spin states hosted across the dots D1 and D2 were later measured with RF reflectometry with a resonator attached to D [30].

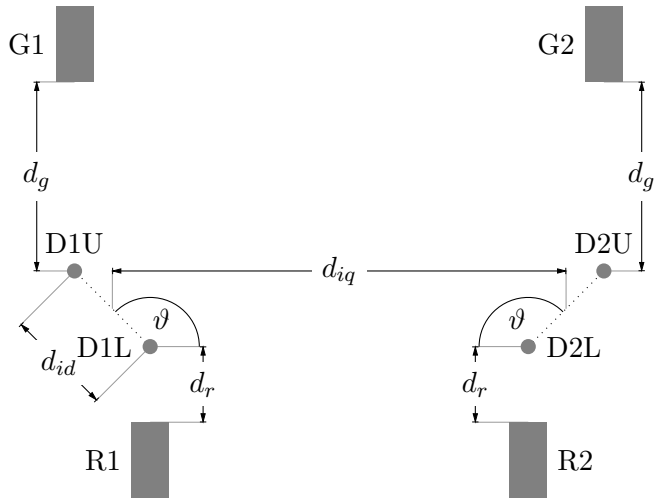

Figure 2.4: Schematic of the 4-dot device with minimal gate leads to host two singlet-triplet qubits. The qubits are to be hosted on the double quantum dot pairs D1L/D1U and D2L/D2U. Each double quantum dot is separated by the inter-dot distance d_{id} and tilted at an angle ϑ. Electrons are loaded onto the two qubits via reservoirs R1 and R2 spaced d_r away from the double quantum dots. Control gates G1 and G2 are placed d_g away from the double quantum dots to perform qubit operations via fast voltage pulses. The double quantum dots are separated by the inter-qubit distance d_{iq}.

triplet spin state. The singlet to triplet t_- lifetime of 60 ns was a time-frame too short for both qubit readout (via single-gate RF sensors) and high-fidelity qubit gate operations (with Pauli-x gate times expected to be ∼30 ns). The following discussion highlights the conversion of this Si-P device, designed predominantly to measure electrons in transport, into a low lead-count device where the double-dots could be used to host singlet-triplet qubits while working towards the demonstration of the singlet-triplet two-qubit gate previously shown using GaAs quantum dots. The main change (per singlet-triplet qubit hosted on a double quantum dot) was to remove the tuning gates (G1 and G2) and designate the S and D leads as the new qubit tuning gates. To disable direct electron transport through the dots, the source lead S was pulled away from the dots. The drain lead was kept close to the dots (still much further than 11.7 nm to avoid spin lifetime-limiting cotunnelling processes) to act as a reservoir of electrons to load onto the dots.

Figure 2.4 shows a schematic of the initial device design in a wedge formation. Each unit-cell has two dots to host the two electrons for the singlet-triplet qubit (the pairs D1L/D1U and D2L/D2U), a reservoir (R1 and R2) to provide electrons to load onto the quantum dots and a qubit control gate (G1 and G2) to tune the

charge occupancy on the quantum dots (required for qubit gate operations). The double-quantum dots (hosting the qubits) are placed on a wedge formation at an angle ϑ from the line forming the linear array. An angle of 0° would replicate the inter-qubit coupling geometry utilised in the GaAs coupled singlet-triplet qubit experiments shown in Figure 2.3a. If the angle were at 90°, then one would expect maximal differential gate lever-arms (defined as the difference in a gate's lever-arms across both dots) in which the tuning gates would be able to maximally tilt the potential across the dots to better tune the electron-electron exchange J (that is, moving from the state where electrons are on separate dots to both electrons being on the same dot). The optimisation procedure requires that there is sufficient electrostatic control to access the required singlet-triplet states while ensuring maximal inter-qubit coupling (required for two-qubit gates) and differential gate lever-arms (required for single-qubit control). The geometric distances that need to be optimised include the gate-to-dot distance d_g, inter-dot distance d_{id}, reservoir-to-dot distance d_r and the inter-qubit distance d_{iq}. Each of these parameters were originally chosen from a combination of new electrostatic simulations and the results from previous experiments performed on Si-P devices.

The inter-dot distance (within a double quantum dot hosting a singlet-triplet qubit) d_{id} is an important parameter since it determines the tunnel coupling of electrons between the two quantum dots[12]. The inter-dot tunnel coupling impacts both qubit control and readout. A device with too small an inter-dot tunnel coupling impedes one from obtaining coherent qubit operations due to charge noise. The issue is that too small an inter-dot tunnel rate makes the qubit exchange sensitive to small fluctuations in gate voltages. Ideally, one smoothly varies the electron-electron exchange J when moving both electrons, initially on separate dots, onto the same dot. A large tunnel coupling ensures a smooth transition in J with respect to the applied gate voltage (as there will be residual electron wavefunction overlap even when the electrons are on separate dots), rather than a sudden change in J when the electrons both enter the same dot. In previous experiments using Si-P quantum dots, the tunnel coupling was too small, at $<$100 MHz, for coherent interactions between two single-spin electrons[13]. Numerical simulations have predicted that the required tunnel coupling to achieve coherent Pauli-z rotations must be at least 2 GHz [82]. In this device [82], similar to that shown in Figure 2.3b, the dots were comprised of 1P and 2P P-donor dots (separated by 16 nm) with a tunnel coupling of under

[12]The inter-dot tunnel coupling is half the minimum energy splitting between the ground and excited singlet charge states.

[13]The goal was to show a two-qubit SWAP gate between two single-spin qubits. Nonetheless, the physical mechanism is the same as z-rotations for a singlet-triplet qubit.

100 MHz. In addition to qubit control, the inter-dot tunnel coupling is important in obtaining qubit readout using a single-gate RF sensor (as required by the architecture proposal where the sensors integrate into pre-existing leads in the device). As with the adiabatic quantum capacitance approach (discussed in detail when modelling the single-gate RF sensor in Section 3.3), the inter-dot tunnel rate (between the two dots in the singlet-triplet qubit) must be much larger than the RF driving frequency (typically in the order of 100 MHz) to enable the singlet-triplet qubit to respond to the RF drive. A large tunnel coupling in a Si-P device (for compatibility with single-gate RF readout) was demonstrated in the device shown in Figure 2.3c. Here, the Si-P device had 2P and 3P P-donor dots separated by 11.5 nm to give a tunnel coupling of 22 GHz [30, 81]. However, it is noted that if the tunnel coupling is too large it will impede qubit control as one may not be able to switch off J as the electrons are now too strongly interacting across the two dots. One can estimate the lower bound in the required voltage magnitude to turn off J by considering how far one must pulse (in gate voltage space) to tilt the singlet-triplet qubit's axis to 45° (the Hadamard point) where $J = \Delta B_z$. As derived later, the voltage pulse required to reach this Hadamard point is:

$$V_{\text{Hadamard}} = \left| \frac{4\Delta B_z^2 - t_c^2}{2\Delta B_z e \Delta\alpha} \right|. \tag{2.6}$$

Taking $\Delta B_z \approx 29$ MHz (the hyperfine interaction of a 1P donor dot) and the parameters from the Si-P experiment (22 GHz tunnel coupling and differential lever-arm of $\Delta\alpha = 0.16$ [30]), the required voltage magnitude to reach the Hadamard point would have been 220 mV. Noting that one would need to pulse further to apply a large enough electric field to separate the electrons enough to make $J \ll \Delta B_z$, the tunnel coupling in this device would appear to be too large as the large amplitude voltage pulses are not only impractical when considering the experimental apparatus, but one also risks entering a voltage region where current starts to leak between leads in the device. With no physical reason to have such a large tunnel coupling, the initial device was designed to aim for a slightly smaller tunnel coupling of approximately 10 GHz. To lower the tunnel coupling[14], the dots were set to a nominal distance of 12.5 nm with the idea to iterate over multiple devices to obtain the optimal tunnel

[14]The tunnel coupling is a non-trivial function of the P-donor dot sizes, the number of electrons forming the equivalent singlet-triplet state and the inter-dot distance. However, one may approximately note that the inter-dot tunnel coupling increases with decreasing inter-dot distance (the electron wavefunctions increase overlap between dots), increasing electron numbers on the dots (weaker confinement of the outer electron yields greater interaction between dots) and decreasing the P-donor dot sizes (larger dots have greater confinement leading to lesser electron wavefunction overlap between dots).

coupling. The chosen distance was to ensure that the inter-dot tunnel rate was above 1-2 GHz while not being so large (that is, > 22 GHz) that one cannot turn off J.

$d_r\,(nm)$	No. donors	No. electrons	Tunnel rate
21	3	1	480 Hz [86]
22	2	1	170 Hz [86]
21	3	2	$>$ 500 kHz [86]
22	2	2	9.6 kHz [86]
22	2	3	$>$ 250 kHz [86]
18	1	1	50 Hz [82]
18	2	1	240 Hz [82]
17	2-3	1	50 kHz [96]
11.6	2	1	1 GHz [81]
11.8	3	1	250 MHz [81]
11.8	3	3	11 GHz [81]
11.8	3	4	22 GHz [81]

Table 2.1: Reservoir-to-dot electron tunnel rates of previously measured Si-P devices. The table shows tunnel rates for P-donor dots at different distances from their reservoirs d_r, different dot sizes and a different number of electrons on the dot (the number of electrons refers to the valence electron; for example, 3 electron implies the $2 \leftrightarrow 3$ electron charge transition). Note that all data above $d_r = 16$ nm had the SET quantum dot act as the reservoir for the dot.

The distance d_r, from the reservoir to the dot, is important as it determines the time taken to load new electrons onto the dots. That is, a closer distance between the dot and the reservoir (for example, R1 and D1L) yields a faster tunnel rate and thereby a faster loading time. Faster loading times are beneficial if one desires to utilise dynamic nuclear spin polarisation (DNP) to set and stabilise magnetic field gradients across the two quantum dots during qubit operation [40, 41]. However, the DNP pulse sequence must be run over many cycles per second to overcome the rate of thermal diffusion of the nuclear spins resetting the magnetic field gradients. By considering the cycle rates used in GaAs and noting that DNP requires one to freshly load new electron spins onto the quantum dots, one can estimate that the tunnel rate needs to be at least 1 MHz. However, too large a tunnel rate implies a stronger coupling of the electron wavefunction on the dot to its reservoir which

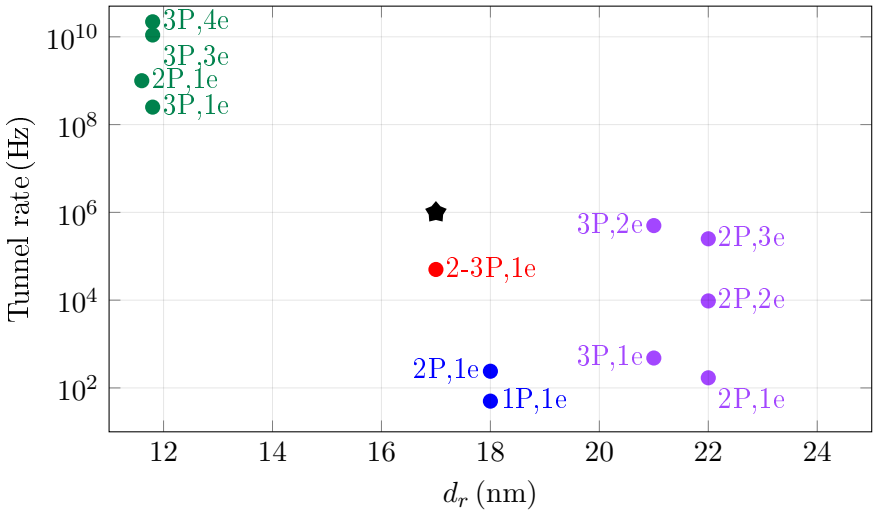

Figure 2.5: Plot of the reservoir-to-dot electron tunnel rates of previously measured and published Si-P devices. The tunnel rates are plotted against the dot to reservoir distance d_r. The labels show the number of donors in the P-donor dot and the number of electrons on the dot (the number of electrons refers to the valence electron; for example, 1e implies the $0 \leftrightarrow 1$ electron charge transition). Note that all data above $d_r = 16\,\text{nm}$ had the SET quantum dot act as the reservoir for the dot. The star indicates the point to aim for the first iteration of the quadruple quantum dot device. The colours indicate the different devices and publications from which the data points were extracted: green [81], red [96], blue [82], purple [86].

could lead to second order co-tunnelling effects where an electron on the quantum dot swaps with that in the reservoir. The co-tunnelling destroys the coherent singlet-triplet qubit state before operations can occur or indeed before the qubit state can be detected by read-out. A lower qubit lifetime due to a large reservoir to dot tunnel rate was observed in the 2P-3P device shown in Figure 2.3c where the reservoir-to-dot distances were 11.6 nm and 11.8 nm [30, 92]. The measured singlet to triplet lifetime for reservoir-dot tunnel rates in the order of ∼1-10 GHz was 60 ns; a figure much lower than the typically long spin state lifetimes of ∼1 s expected for electrons hosted on P-donors in silicon [56, 97]. Thus, tunnel rates well below 1 GHz are desired. The reservoir to dot tunnel rates previously measured in other Si-P devices are shown in Table 2.1 with the plot of the data shown in Figure 2.5. The tunnel rates gathered from the linear transport device (with d_r = 11.6-11.8 nm) were estimated from transport measurements and by noting the tunnel rate dependence on the RF readout signal strength when using the single-lead-quantum-dot (SLQD) sensor[15].

[15] As discussed in the modelling of the SLQD sensor in Section 3.3, the RF readout signal strength for reservoir-to-dot transitions has a $\Gamma_0^2/(\Gamma_0^2 + \omega^2)$ factor where Γ_0 is the reservoir-to-dot tunnel rate and ω is the driving frequency of the resonator.

Here, for a 2P donor dot 11.6 nm from its reservoir (the source S), the tunnel rate was 1 GHz. For a 3P cluster at a similar distance from its reservoir (11.8 nm from drain D), the tunnel rate was lower at 250 MHz as expected from the tighter confinement offered by a larger P-donor dot. The reservoir-to-dot tunnel rate increased with increasing electron number with the tunnel rate reaching 22 GHz at 4 electrons on the dot.

The remaining samples employed an SET to perform single-spin readout via the spin-to-charge conversion method on devices with the geometry given in Figure 2.3b. Here, the SET acts as a reservoir for electrons to load onto the P-donor dots. At a reservoir-to-dot distance of 21 nm, the tunnel rate on a 3P dot started from 480 Hz for the first electron and rose beyond 500 kHz after adding 2 electrons [86]. For a 2P dot at a distance of 22 nm, the tunnel rates started from 170 Hz for the first electron and rose beyond 250 kHz only after adding 3 electrons [86]. From that device, it was not clear whether the dot size or the distance from the reservoir that played a significant factor in the tunnel rate. However, there was a clear monotonic increase in the tunnel rate on adding more electrons to the dot. On another similar device with 1P and 2P donor dots both placed 18 nm from the reservoir, the tunnel rates were 50 Hz and 240 Hz respectively [82]. The result appears counter-intuitive as the 2P cluster would be expected to confine the electron more tightly, resulting in a much slower tunnel rate to the reservoir. However, the two tunnel rates were within an order of magnitude of each other and there may have been slight differences in the distances with regards to the position where the electron was confined on each dot. Finally, on another similar device; for a 2-3P P-donor dot at a distance of 17 nm from the reservoir, the tunnel rate was above 50 kHz for the first electron [96]. Thus, with the desired tunnel rate being 1 MHz (a nominal value much lower than 1 GHz where cotunnelling effects may start, but fast enough to perhaps run DNP), d_r was set to 17 nm as pinned by the star in Figure 2.5. Noting the non-trivial spread of tunnel rates (highlighted in Figure 2.5), given electron number and dot sizes, one may start to optimise the distances in future device iterations as more devices are fabricated and measured.

With the parameters d_{id} and d_r set by estimations from previous experimental results, the geometry only requires one to optimise the gate-to-dot distance d_g, the dot-pair angle ϑ and the inter-qubit distance d_{iq}. These three geometric parameters need to be optimised to maximise electrostatic tunability of electrons across the individual double quantum dots for single qubit operations while maintaining a strong inter-qubit coupling for two-qubit gates.

The first investigation used the improved electrostatic modelling (as discussed

in Appendix A) to study the impact of the parameters d_g and ϑ on maximising the differential lever-arm of gates and reservoirs onto the double quantum dot. The differential lever-arm measures the difference in energy across a double quantum dot on changing the voltage on a gate. A large differential lever-arm implies that one can better tilt the potential across the double quantum dot given the same voltage change on the gate. Therefore, the differential lever-arm is important in the context of qubit control as it describes the ability to bring the electrons together onto one dot ($J \gg \Delta B_z$ for Pauli-z rotations) and separate them ($J \approx 0$ for Pauli-x rotations). The smaller voltage range required to achieve both qubit operations, offered by a large differential lever-arm, is desirable as one can better avoid gate-to-gate current leakage and having large voltage pulses sent down the fridge. Gate-to-gate current leakage is undesirable as direct current flowing across the device will certainly disrupt or destroy any electron qubit formed on the dots [86, 92]. Regarding large high-speed voltage pulses, arbitrary waveform generators have a limited voltage range of typically $\pm 1.5\,\mathrm{V}$; the range is further limited (to approximately $\pm 470\,\mathrm{mV}$) due to the thermalising attenuators (minimum recommended 10 dB [33]) placed along the coaxial lines going into the dilution fridge. In addition to a strong gate differential lever-arm (needed for good qubit control), a strong reservoir differential lever-arm is desirable as one attaches the resonator of the single-gate RF sensor to the reservoir. When oscillating electrons between the dots (when the electrons are in a singlet state), a current forms on the reservoir that is picked up by the resonator. The current on the reservoir (proportional to the reservoir differential lever-arm as discussed in the modelling of the single-gate RF sensor in Section 4.1) is proportional to the readout signal strength and thus, a large differential lever-arm on the reservoir is desirable for maximal readout fidelity.

Capacitance model simulations were used to generate the differential lever-arms for the reservoir R and control gate G. Since the gates from adjacent unit-cells are required to be set further than 30 nm away (the typical minimum distance between device leads to avoid significant gate-to-gate current leakage), the electric fields from adjacent unit-cells' gates will not significantly perturb the final differential lever-arms of the reservoir and gate within a given qubit unit-cell. Thus, the capacitance matrices, used to extract the reservoir and gate differential lever-arms, were simulated for a single unit-cell model shown in Figure 2.6a; from which the differential lever-arms (defined for a lead as $\alpha_{\mathrm{D1L}} - \alpha_{\mathrm{D1U}}$) were extracted. The trends in the reservoir and gate differential lever-arms are shown in Figures 2.6b-c. Note that by definition of the differential lever-arm and noting that R has a stronger lever-arm to D1L, the differential lever-arms will be positive for R. Similarly, noting that G has a stronger

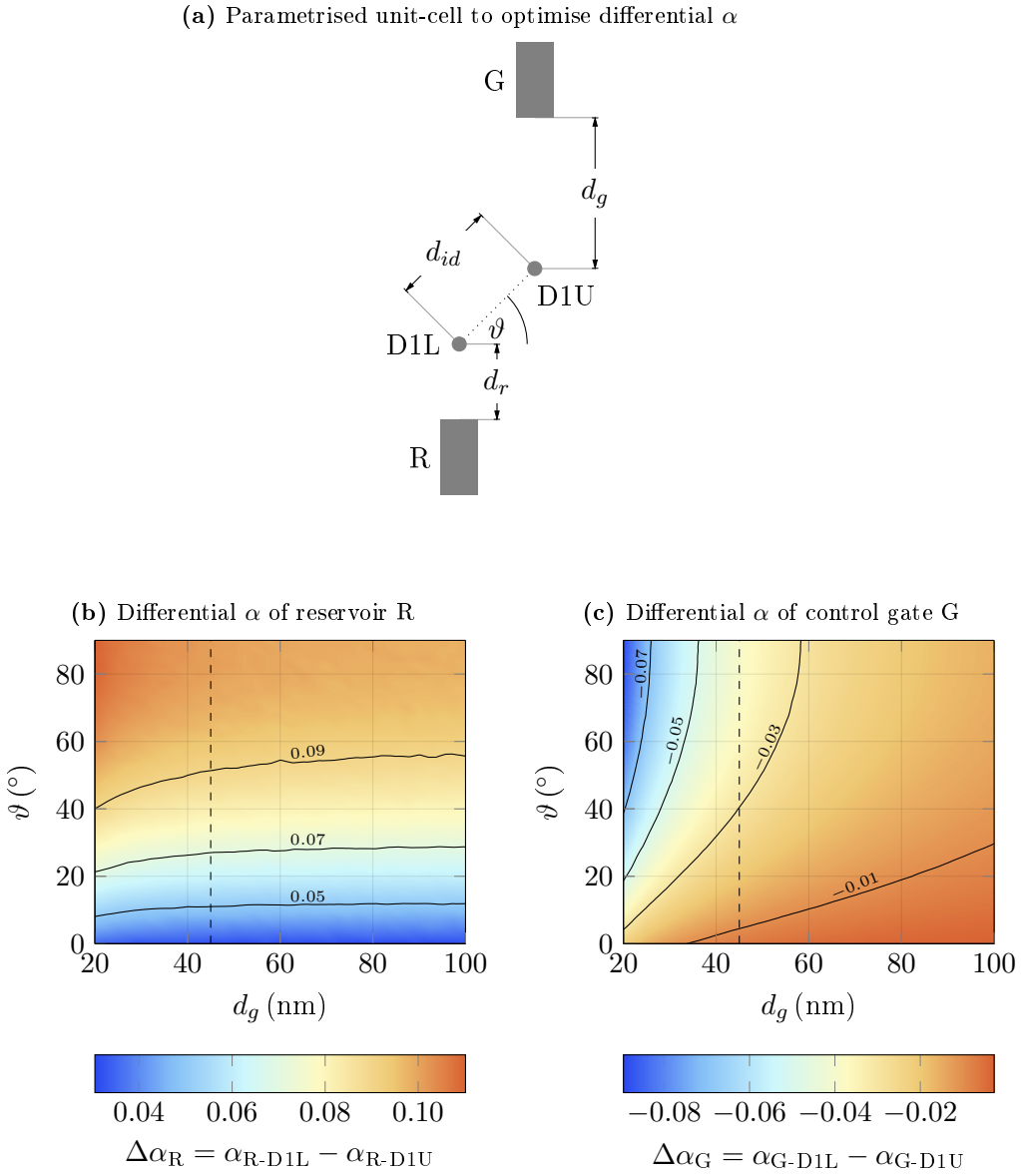

Figure 2.6: Differential lever-arm simulations on a single qubit unit-cell used to fix the gate to dot distance. The simulations used $d_r = 17\,\text{nm}$ and an encapsulation layer thickness of 45 nm. **(a)** shows the parametrised model used in the simulation. **(b)** shows the differential lever-arm for the reservoir R ($\Delta\alpha_R$) as a function of the gate distance d_g and inter-dot angle ϑ, while **(c)** shows the same variation for the differential lever-arm of the control gate G ($\Delta\alpha_G$). The contours in both plots are shown for clarity. Note that differential lever-arm for a lead (R or G) is defined as $\alpha_{D1L} - \alpha_{D1U}$. Since the coupling of the bottom dot D1L is stronger to R1 (and the top dot D1U is stronger to G1), the sign of the differential lever-arm is positive for the reservoir and negative for the gate. Note that $90° < \vartheta \leqslant 180°$ is not shown as this region is geometrically equivalent to $180° - \vartheta$. The dotted lines on both plots indicate the 40 nm gate distance. At 40 nm, the reservoir differential lever-arms (for a given ϑ) start to approach the maximum value with respect to increasing d_g.

lever-arm to D1U, the differential lever-arms will be negative for G.

Increasing the gate distance d_g causes a decrease in the control gate (G) differential lever-arm (seen in Figure 2.6c) as the larger distance lowers the magnitude of the lever-arms of G onto both dots. The reservoir (R) differential lever-arm remains mostly constant (as the geometric distance to the dots remains the same) with slightly lower differential lever-arms when the gate G comes into closer proximity (at $d_g \lesssim 30\,\text{nm}$) and perturbs the electric fields of reservoir R as shown in Figure 2.6b. For both the reservoir and the gate (R and G), the differential lever-arm has a strong dependence on the inter-dot angle ϑ. At a flat angle $\vartheta = 0$, both dots are closer to being equidistant to either R and G and thus, the differential lever-arms are close to zero. At $\vartheta = 90°$, the individual leads have the largest difference in the individual lever-arms to the dots due to the geometry placing the dots parallel with both leads. The simulations however show no true optimal point for the differential lever-arm. In fact, the simulations suggest to bring the gate G indefinitely closer (to the dots) while setting the angle at $\vartheta = 90°$ to maximise the differential lever-arms on the control gate G. Nonetheless, at $d_g = 45\,\text{nm}$ (indicated by the dashed line), the reservoir differential lever-arm approaches a maximum (required for high-fidelity single-gate RF readout) before becoming indifferent to the gate distance as seen by the contours flattening. In addition, at $d_g = 45\,\text{nm}$, the tunnel rate between the dots and the gate G will be negligible (that is, the electrons will only load from reservoir R) as required to prevent accidental electron transport between R and G. In addition, $d_g = 45\,\text{nm}$ should provide a sufficient distance to avoid gate leakage between R and G [86, 92]. It is noted that if there was a model for gate leakage, then one would be able to truly optimise the maximal qubit control (that is, the increasing differential lever-arm) with the decreasing gate voltage range as gate G is brought closer to the dots. Although one could set $\vartheta = 90°$ for maximal differential lever-arms on both G and R, one also needs to consider the inter-qubit coupling.

The inter-qubit distance d_{iq} and the dot-pair angle ϑ are optimised in the context of two-qubit control. The key parameter of interest is the inter-qubit coupling Δ_Δ between two adjacent singlet-triplet qubits. To describe the significance of Δ_Δ, one needs to consider the concept of detuning on each qubit Δ. The detuning describes the qubit electrons' shift in potential energy as one moves between the charge states where electrons are separated on each dot (with the $(1,1)$ charge occupancy across the two dots where $J \approx 0$) to the electrons being on the same dot (with the $(0,2)$ charge occupancy across the two dots where $J \gg \Delta B_z$). Specifically the detuning on each qubit is the energy level separation from when the two states (electrons together on the same dot $(0,2)$ and when fully separated $(1,1)$) are degenerate:

$$\Delta = \frac{U(1,1) - U(0,2)}{2}. \tag{2.7}$$

where $U(m,n)$ is the total potential energy when there are m electrons on the first dot and n electrons on the second dot. The inter-qubit coupling Δ_Δ is the change in detuning Δ on a 'target' qubit when one moves an electron between the two dots in the adjacent 'control' qubit unit-cell. That is, Δ_Δ is the change in the target qubit's detuning when the control qubit changes from the $(1,1)$ triplet state (the triplet is $(1,1)$ due to Pauli spin blockade) to the $(0,2)$ singlet state. The shift in detuning mediated by Δ_Δ causes a shift in J to create an entangling gate [14, 42]. One may determine Δ_Δ by calculating the shift in detuning when the control qubit is in the triplet state (the $(0,2)$ charge state) and singlet state (the $(1,1)$ charge state):

$$\Delta_\Delta = \left[\underbrace{\frac{U(0,2,1,1) - U(0,2,0,2)}{2}}_{\text{Target } \Delta \text{ when control is singlet}}\right] - \left[\underbrace{\frac{U(1,1,1,1) - U(1,1,0,2)}{2}}_{\text{Target } \Delta \text{ when control is triplet}}\right]. \tag{2.8}$$

Here the potential energies U are given as a function of the number of electrons in the dots (D1L, D1U, D2L, D2U), with the control qubit hosted across D1L/D1U and the target qubit hosted across D2L/D2U. Note that all device gates are held at a constant voltage and thus, the influence of gate voltages cancel out when taking the differences in the energies. An important property of Δ_Δ is that it is symmetric about both qubits. That is, the coupling parameter is invariant if the control and target qubits were swapped[16]. In addition, Δ_Δ will flip in sign if the dot in which both electrons are held in the $(0,2)$ charge state for the target or control qubit were to be changed, while Δ_Δ remains invariant if the dots holding both electrons in the $(0,2)$ charge state were swapped for both qubits as illustrated in Table 2.2 for $\vartheta = 0$. This is because the direction in which the control qubit pushes the target qubit's electrons (whether it is towards the $(1,1)$ or $(0,2)$ charge state on the target qubit) changes in sign when changing the dot with both electrons occupied.

From the potential energy difference given in Equation A.8 (derived in Appendix A.1), Δ_Δ can be written in terms of the capacitance model parameters:

$$\Delta_\Delta = \frac{e^2}{2}\left(\left(\mathbf{C}_{\mathrm{DD}}^{-1}\right)_{14} - \left(\mathbf{C}_{\mathrm{DD}}^{-1}\right)_{13} - \left(\mathbf{C}_{\mathrm{DD}}^{-1}\right)_{24} + \left(\mathbf{C}_{\mathrm{DD}}^{-1}\right)_{23}\right), \tag{2.9}$$

[16] Consider the target and control qubits being swapped: $2(\Delta_\Delta)_{\mathrm{swap}} = [U(1,1,0,2) - U(0,2,0,2)] - [U(1,1,1,1) - U(0,2,1,1)] \equiv 2\Delta_\Delta$.

Control $(0,2)$	Target $(0,2)$	Configuration	Δ_Δ
D1L	D2U	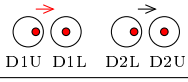	$\lvert\Delta_\Delta\rvert$
D1U	D2U	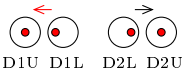	$-\lvert\Delta_\Delta\rvert$
D1L	D2L	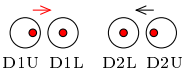	$-\lvert\Delta_\Delta\rvert$
D1U	D2L	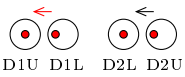	$\lvert\Delta_\Delta\rvert$

Table 2.2: How charge configurations on each dot determine the sign of the inter-qubit coupling. The configurations are arranged when $\vartheta = 180°$. The control $(0,2)$ indicates the dot in which both electrons are occupied when the control qubit is in the singlet state. The target $(0,2)$ indicate the dot both electrons occupy when in the $(0,2)$ charge state. The red arrow indicates the direction the electrons move when the control qubit is in the singlet state (with the electrons remaining separated on different dots when in the triplet state). The black arrow indicates the direction both electrons move to occupy the $(0,2)$ charge state on the target qubit. The resulting inter-qubit coupling Δ_Δ is purely dependent on the geometry, but it changes in sign as given by the dot to which both electrons occupy in the respective qubits (as determined by the voltages set on the gates).

where $\mathbf{C}_{\mathrm{DD}}^{-1}$ is the inverse of the 4×4 inter-dot capacitance matrix of the four dots. For clarity the indices $(1,2,3,4)$ indicate the dots (D1L, D1U, D2L, D2U). Once again, note that the coupling may have a change in sign depending on the orientation of the $(0,2)$ charge states on the qubits as shown in Table 2.2. As described in Appendix A.3, P-donor dots are point-like objects in which one may rewrite the inter-dot capacitances in terms of scalar potentials:

$$\Delta_\Delta = \frac{e}{2}\left(\phi_{14} - \phi_{13} - \phi_{24} + \phi_{23}\right), \tag{2.10}$$

where ϕ_{mn} denotes the electrostatic potential on dot n when placing one electron on dot m. Now the potential of a single electron at a distance r is well-known via Coulomb's law:

$$\phi_r = \frac{e}{4\pi\varepsilon_0\varepsilon_r r}, \tag{2.11}$$

where ε_r is the relative permittivity (approximately 11.7 in silicon). Under the assumption that the nearby leads are far away from the dots such that their effect on the electrostatic potentials is weakly perturbative, one may simply use Coulomb's law to calculate the inter-qubit couplings without resorting to long finite element

simulations. That is, the coupling can be approximated as:

$$\Delta_{\Delta} = \frac{e^2}{8\pi\varepsilon_0\varepsilon_r}\left(\frac{1}{r_{14}} - \frac{1}{r_{13}} - \frac{1}{r_{24}} + \frac{1}{r_{23}}\right), \tag{2.12}$$

where r_{mn} is the distance between dots m and n. Substituting the geometric distances from Figure 2.4, the coupling strengths (under the Coulomb's law approximation) gives:

$$\Delta_{\Delta} = \frac{e^2}{8\pi\varepsilon_0\varepsilon_r}\left(\frac{2}{\sqrt{d_{iq}^2 + d_{id}^2\sin^2(\vartheta)}} - \frac{2d_{iq}}{d_{iq}^2 - d_{id}^2\cos^2(\vartheta)}\right). \tag{2.13}$$

Taking the inter-dot distance of $d_{id} = 12.5\,\text{nm}$, the inter-qubit coupling is plotted as a function of the inter-qubit distance d_{iq} and the double dot angle ϑ in Figure 2.7a. The inter-qubit coupling is non-zero over the parameter space with the magnitude being approximately inversely proportional to the inter-qubit distance d_{iq}. The inter-qubit coupling is also negative (when taking D1U and D2U to be the dots being occupied when the first and second qubits enter the $(0, 2)$ charge state). The negative inter-qubit coupling is best seen geometrically when considering the configuration with the double quantum dots being horizontal at $\vartheta = 180°$ like with the diagram in the second row of Table 2.2. That is, moving one of the two qubits into the $(0, 2)$ charge state lowers the detuning on the other dot unless the $(0, 2)$ charge state has the electrons gathering in D1L for the first qubit and D2U for the second qubit (or vice versa).

By inspection of Figure 2.4, for a constant d_{iq} (measured between the centres of each double-dot), the inter-qubit coupling is symmetric about the angle $\vartheta = 90°$ as the dot positions are geometrically mirrored (the pivot position for the angles is taken at the centre of each double dot pair). However, the analytic formula assumes that there are no electric field perturbations from metallic structures like the nearby reservoirs. Using a reservoir to dot distance of 17 nm and a gate-to-dot distance of 40 nm, the inter-qubit coupling was extracted numerically using Equation 2.9 from FEA simulations as shown in Figure 2.7b. The contours from the analytic model are overlaid with the numeric model (the dashed lines) and one observes a small departure from the symmetry about $\vartheta = 90°$. In addition, the numeric simulations differ at the larger angles $\vartheta > 90°$, where the reservoirs are arranged near the two inner dots. The angular asymmetry in the inter-qubit coupling can be explained by the reservoirs perturbing the electrons' electric fields (more pronounced when near the inner two electrons for $\vartheta > 90°$). Otherwise, the analytic model neatly captures

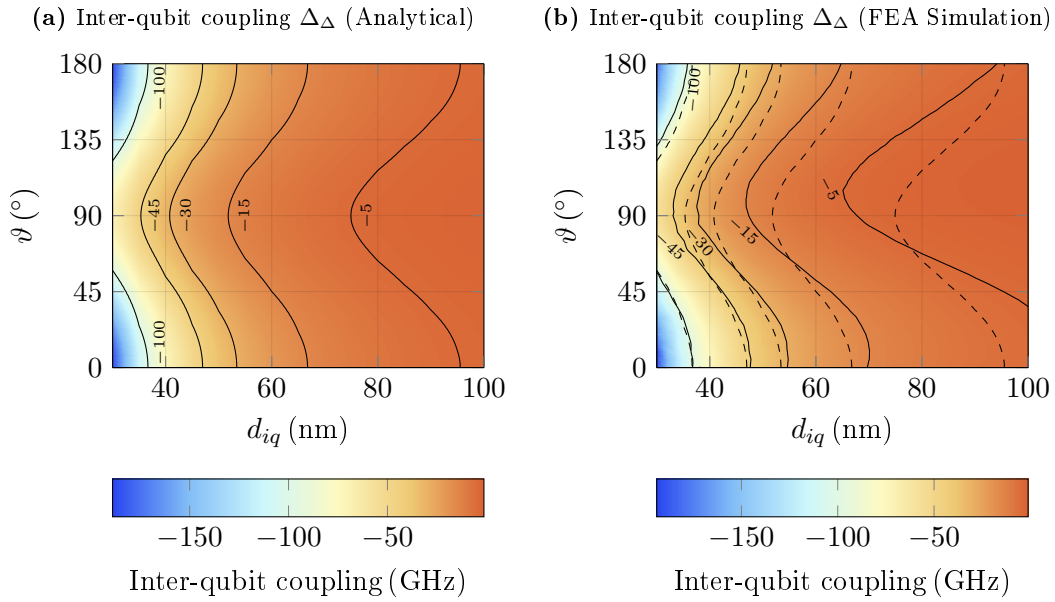

Figure 2.7: Optimising the inter-qubit coupling (Δ_Δ) as a function of inter-qubit distance (d_{iq}) and the double quantum dot angle. Previous experiments in GaAs had Δ_Δ∼300 MHz [14]. **(a)** Plot of the analytic approximation of the inter-qubit coupling Δ_Δ given by using Coulomb's law in Equation 2.13 over different inter-qubit distances d_{iq} and dot-pair angles ϑ. The contours, highlighted for clarity, give the inter-qubit coupling in gigahertz. **(b)** Plot of the inter-qubit coupling when running a FEA simulation with $d_r = 17$ nm, $d_{id} = 12.5$ nm, $d_g = 45$ nm and an encapsulation layer thickness of 45 nm. As in (a), the contours give the inter-qubit coupling in gigahertz. The dashed lines are contours from the analytic approximation in (b). The analytic model captures the FEA simulation at low angles where the contours overlap, while there is a slight discrepancy at higher angles where the analytic calculation overestimates the inter-qubit coupling for a given distance due to the electron's electric fields being perturbed by the reservoir leads.

the behaviour of the inter-qubit coupling especially at lower angles. Nonetheless, the suggested inter-qubit couplings are all in the order of many gigahertz; a figure much larger than the approximately ∼300 MHz (perturbative with respect to a ∼5 GHz tunnel coupling) measured in previous GaAs devices [14]. The larger inter-qubit coupling, seen in the simulations here, is likely due to the smaller inter-dot spacing (12.5 nm as opposed to ∼100 nm in GaAs quantum dots) and the smaller inter-qubit spacing (of approximately ∼30-100 nm as opposed to 100-200 nm in GaAs quantum dots). The inter-qubit coupling is maximal when the dots are lined up at $\vartheta = 0°$ in an arrangement similar to the previous GaAs device shown in Figure 2.3a [14]. Nonetheless, a flat angle of $\vartheta = 0°$ is not ideal for the proposed Si-P qubit unit-cell as the gates' differential lever-arms tend to zero as shown in Figure 2.6, thereby weakening gate control on the qubits (that is, one will need to apply larger voltage pulses to perform qubit gate operations). If one were to operate in the low inter-qubit coupling regime as in the previous GaAs experiments, one may set the dots to be vertical at $\vartheta = 90°$ and separate the qubits by over 80 nm to experience maximal ease in routing the leads and a generally larger gate voltage range before gate-to-gate current leakage occurs. However, with the aim of achieving strong inter-qubit couplings (with the intent to achieve faster high-fidelity two-qubit gate operations), the region with inter-qubit couplings below 5 GHz was avoided. To ensure that the device was above the 5 GHz contour, the inter-qubit distance was nominally set to 60 nm and the dot angle was set to 135°. Note that whilst 135° is equivalent to 45°; the angle 45° was not chosen to ensure that the control gates (G1 and G2 in Figure 2.4) could be far apart as possible to ensure maximal gate voltage range when attempting to perform qubit operations. An angle of 135° also compromises (for the first iteration) between having a large the differential gate lever-arm (close to 90° for good gate control) and a large inter-qubit coupling (close to 0° to ensure fast two-qubit gates).

With the geometric parameters optimised (summary given in Table 2.3), it is important to ensure that the device can indeed achieve the required charge occupancies on the dots before fabricating the device. Specifically, each pair of dots must achieve the $(1, 1)$ and $(0, 2)$ charge states[17] with the ability to change both charge states via the inter-dot crossing[18]. To control electron numbers on quantum dots, one controls the electrostatic potentials on the dots by applying the appropriate voltages to the gates. In large gate-defined quantum dots which have dots spaced approximately

[17] Note that the dot in the $(0, 2)$ charge state to which both qubit electrons occupy may be either of the two dots.

[18] A nice introduction to inter-dot charge crossings and the resulting 'honeycomb' structures is given in a review by W. G. van der Wiel [89]

Parameter	Value	Key considerations
Inter-dot distance (d_{id})	12.5 nm	Tunnel coupling needs to be 1 GHz $< t_c <$ 22 GHz to enable qubit control, single-gate RF readout and tunability of J [27, 82, 86].
Dot-to-reservoir distance (d_r)	17 nm	Reservoir-to-dot tunnel rate must be less than ∼1 GHz to ensure cotunneling does not degrade qubit lifetimes. Qubit reloading times need to be at least ∼1 MHz for DNP [14, 27, 30, 40, 82, 86, 96].
Dot-to-gate distance (d_g)	45 nm	A gate distance above ∼45 nm gives close to maximal reservoir differential lever-arm. Any further simply degrades the control gate lever-arm (see Figure 2.6).
Inter-qubit distance (d_{iq})	60 nm	Chosen to guarantee at least 5 GHz to large with respect to a ∼5 GHz tunnel coupling (see Figure 2.7).
Dot angle (ϑ)	135°	Chosen as a compromise in giving as large a differential lever-arms (on reservoir and gate) while ensuring inter-qubit coupling is larger than 5 GHz and control gates are maximally spaced for maximum gate voltage range (see Figure 2.7).

Table 2.3: Summary of design parameters optimised for the initial two qubit singlet-triplet device. The design parameters are drawn on the schematic in Figure 2.4. The extended discussion on the reasons is given in Section 2.2.3.

100 nm in scale, it is possible to pattern additional gates in between and near individual dots such that the gates can independently shape the electrostatic potentials on given dots without affecting adjacent dots[19]. Thus, one can easily adjust the potential to move electrons between dots. With Si-P quantum dots, the spacing between quantum dots is approximately 12.5 nm and thus, it is not easy to place gates such that the electrostatic potentials on the dots can be individually controlled (equivalently stated, it is difficult to achieve a large differential lever-arm on all the gates). Thus, inter-dot charge transitions like the singlet-triplet $(1,1)$-$(0,2)$ may not be as easily accessible within the voltage range available on all the gates. One method to overcome this limitation is to realise that only certain charge states need to be accessed for full qubit operation. It is then possible to engineer different sized P-donor dots (that is, dots with more than one P-donor) such that the required

[19] There is still finite back-action of these gates to other dots to which one must compensate [55]

inter-dot transitions can be reached with minimal voltage ranges on the gates.

Consider a symmetric double quantum dot system in the 1P-1P configuration such as that shown in Figure 2.8a (the geometry is used to illustrate the advantage of using asymmetric P-donor dots). Here, the in-plane gates give a certain degree of independent control across the dots since any voltage applied to a gate is likely bring the potentials of both dots downwards and thus, electrons enter both the dots. One can see the symmetric loading of electrons onto the dots in the numerically simulated stability diagram[20] in Figure 2.8b by noting that at 0 V on the left and right gates (L and R), the charge state (on the dots DL and DR) is $(0, 0)$. On increasing the voltage on both gates equally one enters the $(1, 1)$ charge state. With slight increases on the left or right gate voltages, one may enter the $(1, 1)$ via the $(1, 0)$ or $(0, 1)$ charge states respectively. However, there is a large energy penalty, specifically $U_{02}/2$, that must be paid to move electrons into the singlet-triplet subspace: the $(1, 1)$-$(0, 2)$ charge transition (requiring differential gate voltages, between gates L and R, above 0.5 V where gate-to-gate current leakage may start to occur as highlighted by the green window). To overcome the lack of differential gate lever-arms, one may engineer the dots to provide an extra tilting potential by adding a P-donor to the second dot to make it a 2P [82, 84]. Figure 2.8c shows the stability diagram for 1P-2P configuration where a combination of the dots' tilting potential and the lowering U_{02} with higher electron numbers results in an even parity transition $(1, 3) \leftrightarrow (2, 2)$ accessible within the 0.5 V differential gate voltage window. The $(1, 3) \leftrightarrow (2, 2)$ transition is equivalent to the $(1, 1) \leftrightarrow (2, 0)$ singlet-triplet subspace (two spin-paired electrons on the right dot do not affect the valence electrons across the two dots forming the singlet-triplet state). Note that the ultimate goal is to find inter-dot transitions where one has one electron on each dot that may interact to form the required singlet-triplet state. Thus, by using a combination of different P-donor dot sizes and electron numbers, it is possible to engineer inter-dot crossings of even parity; that is, a transition where the number of electrons on both dots sum to an even number. With all lower energy electrons spin-paired (thus, not participating in the electron-electron physics), one may form a singlet-triplet state with the outer valence electron on each dot. Finally, to perform two qubit gates, it is important to be able to simultaneously form two singlet-triplet qubits (each formed by accessing the singlet-triplet spin state) on adjacent double-quantum dots. This implies that for a given set of voltages

[20] The stability diagrams are inferred from the capacitance matrix extracted from a numerical FEA solver as described in Appendix A. As described in the derivation of the stability diagram simulator, the capacitance matrix holds information regarding the placement of the charge transitions [89]. Different donor cluster sizes were simulated by taking the potential offsets resulting from tight-binding calculations [81].

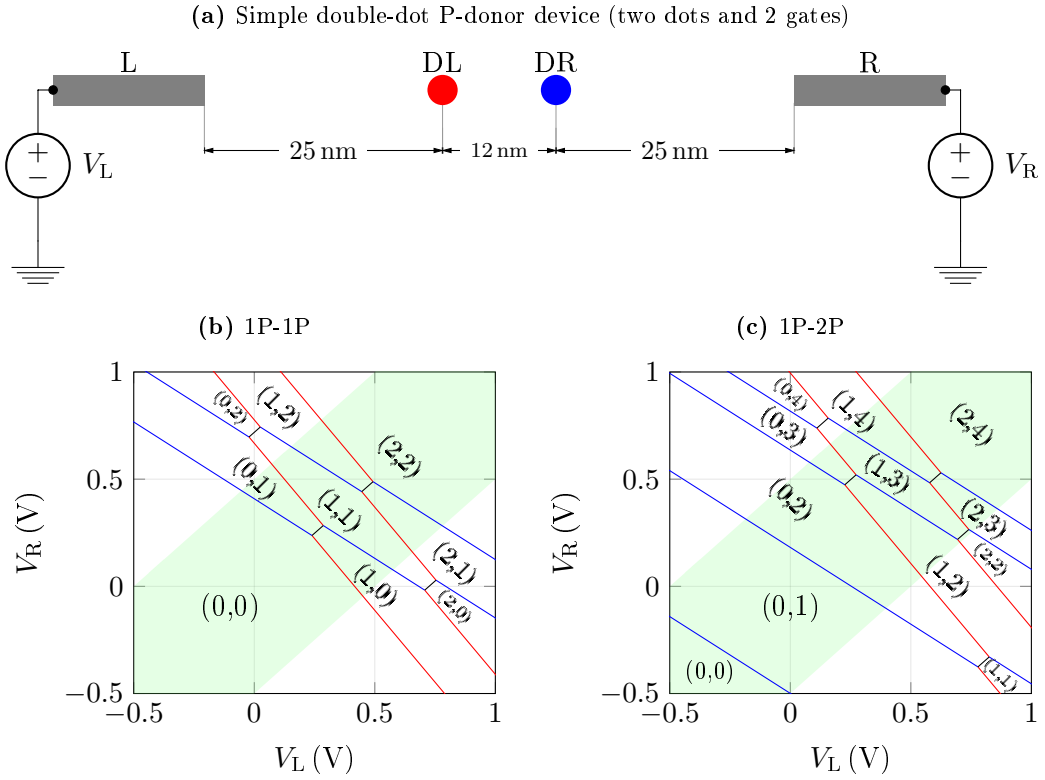

Figure 2.8: Using different P-donor dot sizes to access singlet-triplet states on a simple double quantum dot system in Si-P. **(a)** Schematic of a simple double quantum dot system under simulation. The device includes a double quantum dot (formed by P-donor dots DL and DR) and two control gates (L and R). **(b)** Simulated stability diagram when sweeping the voltages on the gates L and R. The ordered pairs in each charge-stable region indicate the electron numbers on DL and DR. Here, the dots DL and DR are both taken to be 1P donor dots. The green window indicates the region where the differential voltage between the gates is L and R is within 0.5 V. The even-parity inter-dot transitions ($(0,2) \leftrightarrow (1,1)$ and $(2,0) \leftrightarrow (1,1)$) require differential gate voltages above 0.5 V. **(c)** When replacing DR with a 2P donor dot, the even parity inter-dot transition $(1,3) \leftrightarrow (2,2)$ is now accessible within the 0.5 V differential voltage window with $(V_L, V_R) \approx (690, 220)$ mV. Note that both stability diagram simulations limit the electron numbers to be a maximum of 2 for 1P dots and 4 for 2P dots.

applied to the gates, one must be able to overlap the inter-dot crossings for each singlet-triplet pair.

Figure 2.9 shows some simulated stability diagrams for the quadruple quantum dot device (schematic shown in Figure 2.4 and geometric parameters summarised in Table 2.3) under different P-donor dot sizes. The electron numbers of each charge stable region in voltage space is given as a quadruplet for the number of electrons in the dots D1L, D1U, D2L and D2U respectively. Figure 2.9a-b show simulated stability diagrams for a symmetric 1P-1P-1P-1P cluster configuration. With all the gates set to zero voltage, there are no two even parity inter-dot transitions[21] and two odd parity inter-dot transitions (labelled EP and OP respectively) visible on sweeping the gates V_{G1} and V_{G2}. One can only overlap adjacent even parity transitions (labelled EP in Figure 2.9b), required to perform a two-qubit gate, on tuning the other gates and ultimately setting the gate voltages up to 1.25 V. Such high gate voltages will give rise to current leakage between the gates and thus, the 1P-1P-1P-1P arrangement is not a feasible configuration to observe gates between multiple singlet-triplet qubits.

Figures 2.9c-d show the stability diagrams when using asymmetric numbers of P-donors within the quantum dots where each double-dot pair is in the 1P-2P configuration. Figure 2.9c shows two even-parity inter-dot transitions (labelled EP) within the gate voltage space. With mild tuning of the gate voltages on R1 and R2, one may overlap even parity transitions across the two different singlet-triplet qubits, required for the two-qubit gate. The simulation shows that one may achieve the charge configuration for a two-qubit gate with all the gate voltages within 0.7 V in magnitude as shown in Figure 2.9d. For the even parity transitions overlapped in Figure 2.9d, both dot pairs are in the equivalent singlet-triplet $(1,3)$-$(0,4)$ inter-dot charge transition. Here, two electrons on the 2P dot spin-pair, while a third (valence) electron interacts with the single electron on the 1P dot to form a singlet-triplet spin state. Thus, the 1P-2P donor-dot was the chosen candidate for achieving a singlet-triplet two-qubit gate. The inset in Figure 2.9d shows the zoomed overlap of the inter-dot crossings and the subsequent points of interest when performing qubit operations. For this device, the bottom-left quadrant represents the $(1,3,1,3)$ charge state where both qubits have their electrons on separate dots. The inter-dot transitions $(1,3,1,3) \leftrightarrow (0,4,1,3)$ (in blue) and the $(1,3,1,3) \leftrightarrow (1,3,0,4)$ (in red)

[21] Odd parity inter-dot crossings are those where the sum of the electrons across both dots adds to an odd number. Here, all electrons are spin-paired and one valence electron moves between the dots; thereby not forming a two-electron singlet-triplet state. Even parity transitions have an even number of electrons both dots in which one valence electron on each dot come together to interact and form a singlet-triplet state

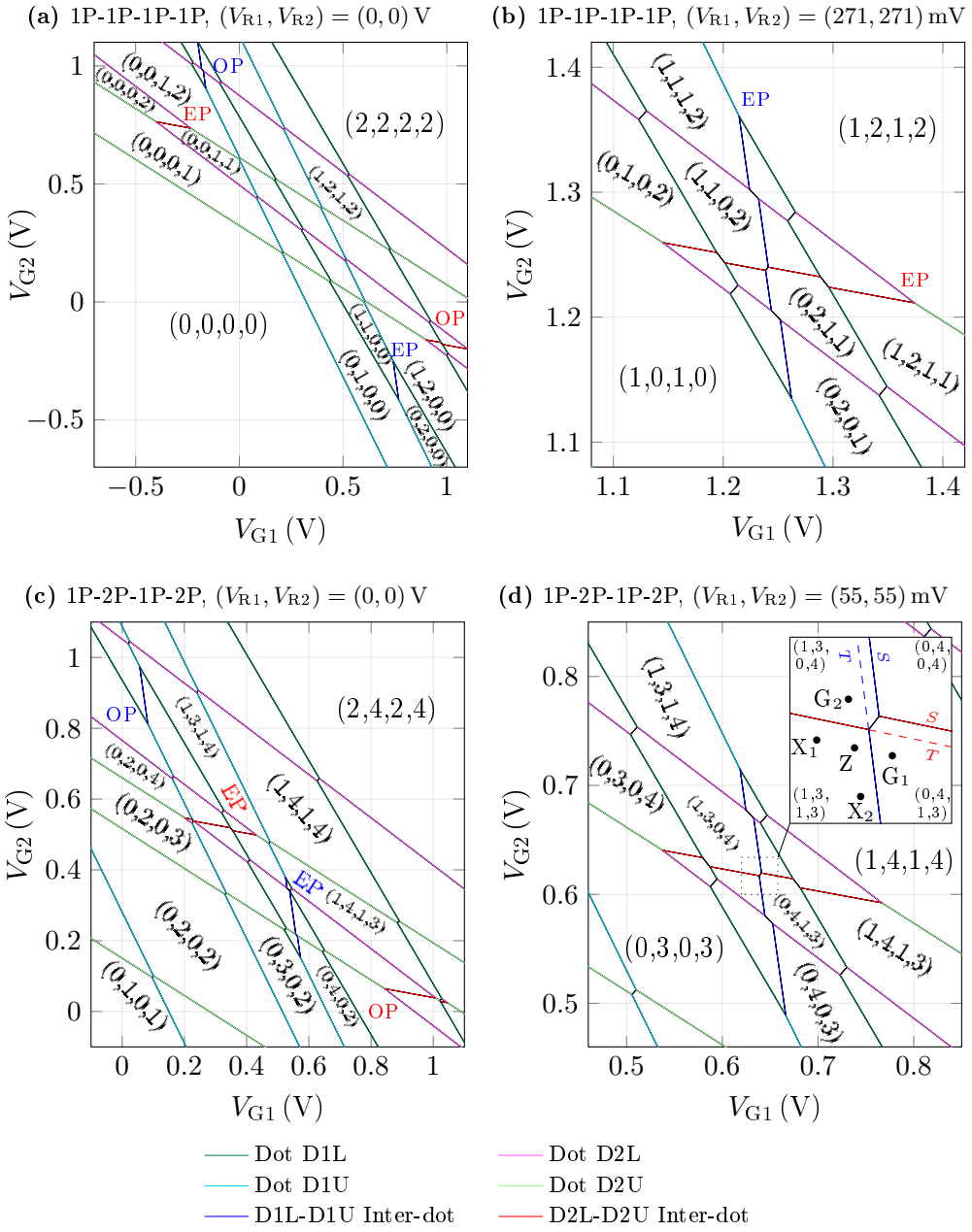

Figure 2.9: Stability diagram simulations for different P-donor cluster configurations. The goal is to overlap two even-parity singlet-triplet inter-dot transitions on adjacent dots (D1L/D1U in blue and D2L/D2U in red) to setup a two-qubit gate. The electron numbers on dots are shown as (D1L, D1U, D2L, D2U). The inter-dot transitions of odd parity are labelled OP while the transitions of even parity (for singlet-triplet operation) are labelled EP. **(a)-(b)** A symmetric donor cluster arrangement where each dot within the double-dot pair has the same number of P-donors. In order to overlap adjacent singlet-triplet charge transitions, one must apply voltages of up to 1.25 V on the gates. **(c)-(d)** However, when using asymmetric dot sizes such as a 1P-2P on each double-dot pair, the two-qubit gate charge transition can be set with all gate voltages below 0.7 V in magnitude. The inset in (d) shows the qubit operating points when overlapping of the inter-dot transitions. For single-qubit operations, Z is the qubit idle point for both qubits while X_1 and X_2 are the operating points for Pauli-x operations for the first and second qubit respectively. For a two-qubit CZ gate, one moves to G_1 or G_2 if choosing the first or second qubit to be the control qubit respectively. The red and blue dotted lines show the zero-detuning line of the second and first qubits when using the first and second qubits as the control qubits in the triplet state respectively. The solid lines indicate the zero-detuning positions for the target qubit when the respective control qubit is in the singlet state.

represent the nominal zero-detuning position for the first and second qubit respectively. Slightly into the $(1,3,1,3)$ charge region, where the electrons are separated, one chooses the idle point Z where $J \gg \Delta B_z$ for both qubits. At point Z, the qubits rotate about their respective Pauli-z axes. To perform individual single qubit Pauli-x rotations, one must keep the detuning on the other qubit constant, while moving the current qubit's detuning towards negative detuning where the electrons are fully separated to achieve $J \approx 0$. Thus, one moves from point Z to X_1 (parallel with the red inter-dot line to ensure the second qubit is left untouched kept rotating about its Pauli-z axis at the same frequency) to perform Paui-x operations on the first qubit. Similarly, one moves to X_2 to perform Paui-x operations on the second qubit. To perform a simple two-qubit gate, one needs to first select a control qubit. Without loss of generality, consider the first qubit to be the control qubit. One moves to point G_1 where the first qubit is pushed into positive detuning. If the first qubit is in the triplet state (electrons are on separate dots due to Pauli-blockade), then the distance from G_1 to the zero detuning line for the second qubit (red dotted line labelled T) remains the same as that at point Z and thus, the second qubit continues to precess about the Pauli-z axis at the same frequency. If the first qubit were in a singlet state, both electrons in the first qubit may enter the same dot. Thus, the non-zero inter-qubit coupling manifests in a shift in the second qubit's detuning (red line labelled S) shifting to a lower value (the distance from G_1 has increased) where the new J is lower (noting that $\Delta_\Delta < 0$ for the simulated design) and thus, the second qubit now precesses at a lower frequency. Waiting for a fixed period of time, if the difference in frequencies causes a π phase shift to occur on the second qubit conditional on the first qubit being in the singlet or triplet state, one has a CZ gate. Using a similar argument, one can perform a CZ gate where the second qubit is the control qubit by moving to point G_2. Note that here, the first qubit's zero-detuning remains the same at the blue dotted line labelled T if the second qubit is in the triplet state and moves to the solid blue line labelled S if the second qubit is in the singlet state.

It should be noted that the simulated voltage offsets on the charge transition lines given by different P-donor sizes (manifested for example as the 'y-intercept' in the stability diagram) vary significantly when the donor dots are placed close to reservoirs. For example, D1L is placed close to the reservoir while D1U is far from its reservoir. Thus, experimental measurements of the gate voltage offset on the D1L charging lines may differ from the theoretical estimates and thereby the predicted positions of the line intersections, where the inter-dot charge crossings form, may differ. The experimental differences in the gate voltage offsets is due to

the breakdown of the metallic lead approximation where one needs to consider the individual P-donors in the leads [15, 98]. Here, there is a possibility that on applying a positive voltage to the reservoir, the reservoir becomes depleted of electrons. The extent of the metallic region of the gate changes, resulting in a lower lever-arm on the dot and thus, a different voltage will be required to charge or discharge the dot. The influence of the reservoir on the voltage offsets could be empirically modelled via experimental data with different P-donor dots near reservoirs or via time-consuming tight-binding models. Nonetheless, the theoretical simulations suggest that the donor dots must contain a different number of P-donors in each dot within a given qubit unit-cell's double quantum dot to ensure electrostatic accessibility of the required singlet-triplet inter-dot charge transitions.

2.2.4 Fabrication of a quadruple Si-P quantum-dot device

To experimentally demonstrate the electrostatic operation of a single singlet-triplet unit-cell along with its interaction with an adjacent singlet-triplet unit-cell, a Si-P quadruple quantum dot device was created using the parameters estimated by the simulations. The device shown in Figure 2.10 was created using standard Si-P fabrication techniques. The wafers were Si-100 with a 0.1° cut, P-type boron doped and had an approximate resistivity of 5-10 Ωcm. Registration markers were created on the wafer using EBL and a TMAH wet-etch after which they were cleaned with SP (sulphuric acid and hydrogen peroxide) and RCA2 (hydrochloric acid and hydrogen peroxide). The wafer was then taken into an STM. After outgassing the wafer via direct current heating, the wafer was direct current flash annealed to 1100°C with surface reconstruction at approximately 780°C. The surface was then passivated with monatomic hydrogen. Using the STM tip at low current (∼70 pA), the surface can be imaged, while applying larger currents of ∼8 nA can vibrationally excite the hydrogen off the silicon surface to create openings. These patterned structures appear as lighter regions as seen in the STM image in Figure 2.10 due to the height of the dangling bonds out of the surface. Small openings (for example, D1L, D2U, D2L and D2U) make space to form small P-donor dots while larger openings are used to form metallic leads via the tight packing of many P-donors. The opened regions were filled with phosphorus by dosing the wafer with phosphine gas. The incorporation of the phosphorus into the silicon crystal was performed via another small direct current heating anneal. The surface was then encapsulated with 47 ± 3 nm of silicon via a silicon sublimation source (SUSI) at a temperature of 250°C and growth rate of 0.131 nm/min. The P-doped leads were contacted to ohmic pads on the surface of

the silicon via standard cleanroom processing. Holes were etched into the phosphorus pad via a SF_6 reactive ion etcher and then contacted to aluminium Ohmic surface contacts via physical vapour deposition. The sample was then transferred onto a PCB and bonded via an ultrasonic Al wedge bonder.

To aid in the electrostatic characterisation of the 4-dot device, the 2×1 array of double-dots was terminated, on both ends, with tunnel junction charge sensors (TJCS) [99]. The TJCS works by applying a voltage across the tunnel junction such that any changes in the electrostatic environment around the tunnel junction will affect the tunnel barrier and thereby cause a change in the current through the TJCS. Although in the long term, a full-scale singlet-triplet architecture will not have space (or indeed require the extra charge sensors), the two TJCSs in this particular device provide a useful diagnostic tool to characterise the device since they are sensitive to all charge transitions within the device. Note that in general the single-gate RF sensors are only sensitive to transitions with fast tunnel rates as the electrons must respond in time with the high frequency RF excitation as discussed in Section 3. The TJCS structures were placed approximately 80 nm away from the singlet-triplet dots as shown in Figure 2.10. The TJCS distance was chosen to ensure that the TJCS structures did not strongly affect the local electric fields around the dots (that is, these structures are further away than adjacent unit-cells in a larger array) while ensuring sufficient signal for charge detection. Previous experiments using TJCSs [99] showed a signal to noise ratio of approximately 15-20 at a distance of 50 nm; so it is estimated that the same sensor at 80 nm would yield enough signal to detect all charge transitions onto the four quantum dots with a signal to noise ratio of approximately 10-14. The TJCS dimensions were chosen to yield a greater junction conductivity from the previous TJCS experiment (8.5 nm lead width and 17.2 nm gap size) by lowering the gap size to ensure sufficient sensitivity [99]. However, previous studies on tunnel gaps have shown that the gap resistance varies over eight orders of magnitude when changing the gap aspect ratio (lead width divided by gap size) from approximately 0.5 to 3.0 [100]. Thus, two TJCS structures were deliberately patterned with different gap sizes to provide additional redundancy. In the end, the 5.6 nm lead width and 5.8 nm gap size of T1 was too conductive and failed to show gap-like behaviour as shown in Figure 2.10. However, T2 (8.8 nm lead width and 10.8 nm gap size) showed gap-like behaviour; since this gap could be tuned via electric fields, T2 functioned as a TJCS. The maximum resistance of the TJCS T2 was 600 kΩ; more than three orders of magnitude lower than the previously published TJCS with a maximum gap resistance of 1 GΩ [99].

The fabricated device was patterned with the geometric distances suggested by

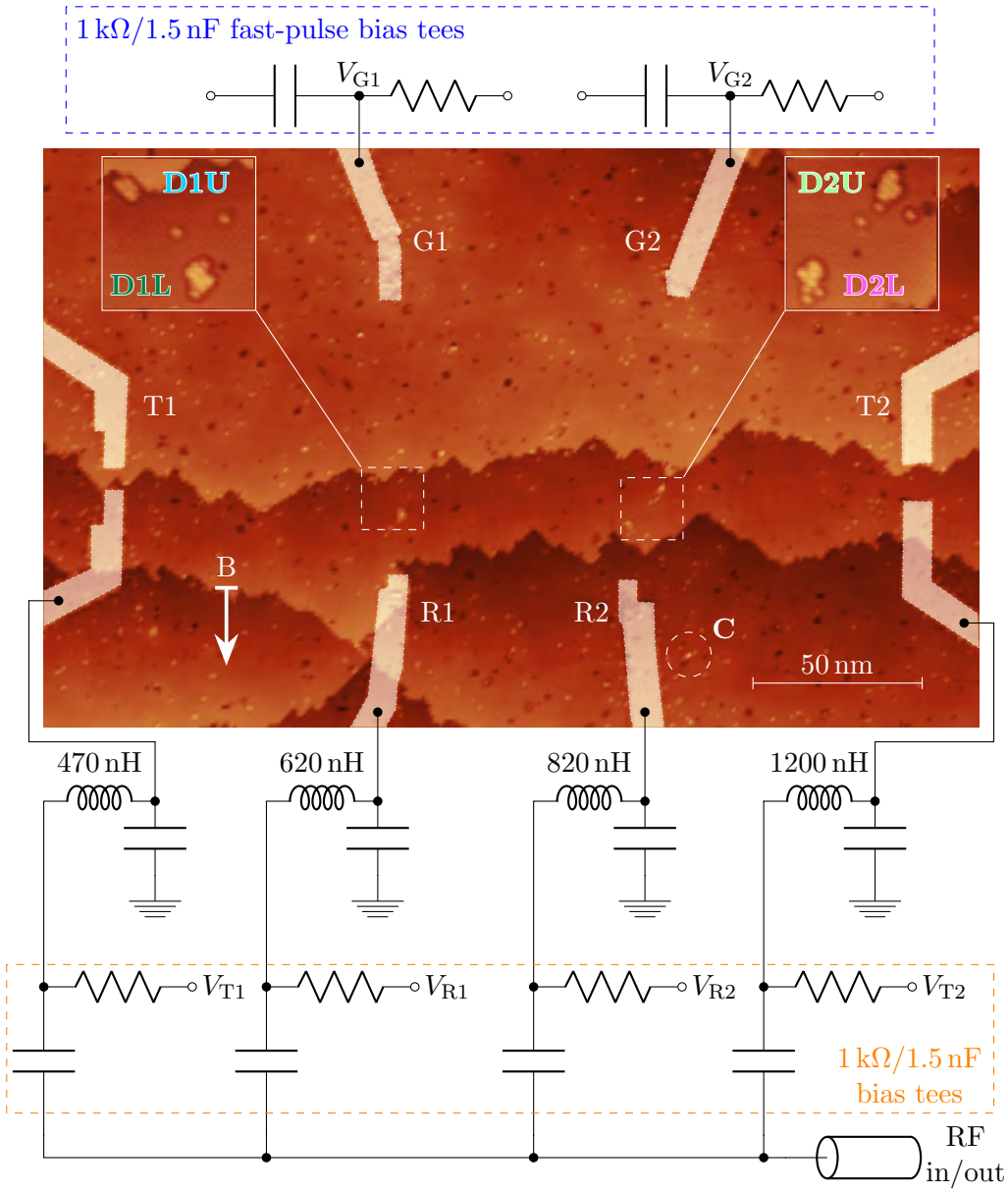

Figure 2.10: Donor based quadruple quantum dot device with multiplexed RF resonator readout. The STM image shows the silicon surface lithography where the lighter regions have been desorbed from the lithographic hydrogen mask. These areas are dosed with phosphorus to form metallic electrodes [27]. Zoomed images of the four dots (D1U, D1L, D2U and D2L) before the dosing of phosphine are shown in the insets. Two of the frequency multiplexed line of resonators, connected to R1 and R2, measure the singlet-triplet states across their respective dot pairs, while the remaining two lines are connected to tunnel junction charge sensors T1 and T2. Reservoirs R1 and R2 are used to load their respective pairs of dots with electrons while the gates G1 and G2 are used to manipulate the singlet-triplet detuning of the dot pairs. C highlights a lithographic defect where a portion of the tungsten STM tip deposited on the surface. The vector B is the direction of the in-plane magnetic field applied on the device during measurements in the dilution refrigerator.

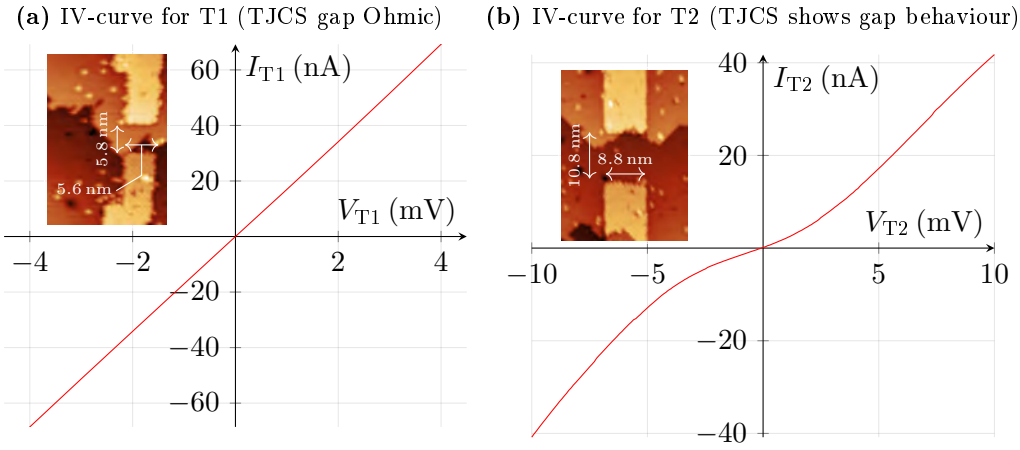

Figure 2.11: IV curves of TJCSs T1 and T2 in the fabricated 4-dot device. At a temperature of 4 K, the current response as a function of the voltage across the TJCS was taken for T1 and T2 shown in Figure 2.10. **(a)** T1 (STM image shown in inset) was found to be too Ohmic with a resistance of ∼60 kΩ. **(b)** T2 (STM image shown in inset) showed gap-like behaviour (with a maximum resistance of $\sim 600k\Omega$) that could be tuned with electric fields and thus, appropriate for charge sensing [99].

the simulations in Section 2.2.3 with additional increases in the distance between leads (approximately above 50 nm) to be able to attain larger gate voltage ranges (before gate-to-gate current leakage occurs) as summarised in Table 2.4. The extra gate-range was to provide a buffer if there were any unpredicted offset potentials that shifted the even parity singlet-triplet inter-dot charge transitions. The parameters that were left unchanged (with any differences due to unintentional variations in the STM fabrication) were the the inter-dot distances d_{id} (both at 12.5 nm), the dot-to-reservoir distances d_r (18 nm and 17 nm for the first and second unit-cells) and the dot angles ϑ (128° and 139° for the first and second unit-cells). The dot-to-gate distances d_g were increased from 45 nm to 52 nm and 55 nm (for the first and second unit-cells). The increased distance from 40 nm was predicted to result in an approximately 1% drop in the differential lever-arm for the gate as shown by the simulations in Figure 2.6. The inter-qubit distance $d_{iq}$was increased to 75 nm to ensure that the reservoir leads (the closest leads) were spaced by at least 50 nm. At this greater inter-qubit distance the simulations shown in Figure 2.7 still suggest an inter-qubit coupling of ∼5 GHz as desired for non-perturbative inter-qubit couplings.

Since the state of the art (at the time of publishing this thesis) method to incorporate P-donors in silicon was stochastic, the exact donor numbers could not be precisely controlled within the P-donor dots. That is, previous heuristic studies showed that the incorporation by heating yields a histogram of possible P-donor dot

Parameter	Simulation	Fabrication	Reason for change
d_{id}	12.5 nm	12.5 nm and 12.5 nm	N/A
d_r	17 nm	18 nm and 17 nm	Unintentional.
ϑ	135°	128° and 139°	Unintentional.
d_g	45 nm	52 nm and 55 nm	Intentional.
d_{iq}	60 nm	75 nm	Intentional.
P-Donors	1P-2P	∼2P-2P and ∼3P-4P	Unintentional

Table 2.4: Summary of changes to the geometry made during fabrication. The simulation column refers to the parameters suggested by simulations in Table 2.3. The fabrication column refers to the parameters measured from the STM image of the fabricated device with dual entries referring to the parameters in the first and second unit-cells (D1L/D1U and D2L/D2U respectively). The final column describes the reasons for the discrepancies where 'unintentional' refers to variations in the STM patterning of the fabricated device while 'intentional' refers to increases in the geometric distances to reduce gate-to-gate current leakage.

sizes depending on the temperature of incorporation and the size of the lithographic patch opened on the hydrogen mask [86, 101]. Thus, the dots were patterned to be asymmetric (as required for feasible electrostatic access of the even parity inter-dot charge transitions) 1P-2P donor dots. From the size of the openings on the hydrogen mask for dots (from the STM images in the insets of Figure 2.10), one may make the initial estimate of the dot sizes to be 2-6P, 1-4P, 2-6P, 2-6P (for the dots D1L, D1U, D2L and D2U respectively) given previous statistical studies performed on the incorporated P-donor dot sizes [101]. The final estimations on the size of the fabricated P-donor dots came from counting the number of charge transitions in the stability diagrams and the positions of inter-dot transitions in the gate voltage space. That is, if N electron transitions onto a dot are seen, then the dot has at least $N/2$ donors. In addition, as discussed in the next section, the electrostatic inaccessibility of the even parity inter-dot transitions on the first double quantum dot (D1L and D1U) suggest that the dots D1L and D1U have the same number of P-donors and thus, are symmetric. The ease in electrostatic accessibility of the even parity transitions on the second double quantum dot (D2L and D2U) suggest an asymmetric number of donors on these dots. Thus, the eventual dot sizes were estimated to be 2P, 2P, 3P and 4P for dots D1L, D1U, D2L and D2U respectively.

2.2.5 Electrostatic triangulation and verification of the P-donor dots

The first task when electrostatically characterising devices is to ensure that all four quantum dots are present. This is to both verify the success of fabrication process and provide statistics to benchmark the 'atomic engineerability' of the STM fabrication process. The presence and location of the dots can be verified by observing multiple charge transitions in the device when electrons are added onto the dots when changing the electrostatic potential around the dots by changing the voltages applied on the gates. The charge transitions on each dot can be detected using the TJCS T2 by measuring fluctuations in its junction DC current. The TJCS was measured using RF reflectometry due to the enhanced signal to noise ratio comparable to that when using a DC cold amplifier and a lock-in amplifier as outlined in Section 3.1.2. The *LC* resonator was created via a *Coilcraft 1206CS-122XJE* surface mount chip inductor (the capacitance being created via the geometric parasitic capacitance of the inductor) with a resonant frequency[22] of 215.4 MHz.

On measuring the RF response of T2 while sweeping the voltages on the reservoirs, V_{R1} and V_{R2}, one obtains the charge stability diagram shown in Figure 2.12. When sweeping any gate, R1 or R2, the tunnel barrier T2 is continuously changed by the electric fields on the gates, while the presence of electron charging events discretely shift the barrier strength. To highlight the charge transitions in the RF response of T2 from the linear background caused by the swept gate voltages, a numerical derivative was taken along both the x and y axes. Charge transitions belonging to the same dot have the same slope as highlighted by the presence of sets of parallel lines. The two sets of steeper lines (indicating a stronger coupling to R1 when compared to R2) highlighted by blue and dark green correspond to charge transitions on dots D1U and D1L respectively. The two sets of shallower lines (indicating a stronger coupling to R2 when compared to R1) highlighted by green and magenta correspond to charge transitions on D2L and D2U respectively. As both axes correspond to voltages being swept on the dots' reservoirs, electrons leave the dot when applying a more positive voltage. Thus, the top-right quadrant is labelled nominally as the (0,0,0,0) charge state (assuming no further charge transitions are to follow). The separation of the lines (in gate voltage space) is proportional to a non-trivial function of the electron charging energies on each donor dot. The initial

[22] The resonant frequency was selected for compatibility with on-site IQ demodulator used in the room temperature RF circuitry. The *Polyphase AD0105B* IQ demodulator was specified to work for frequencies from 100-500 MHz

(a) Backward scan (←) to empty electrons from dots (D2L,D2U)

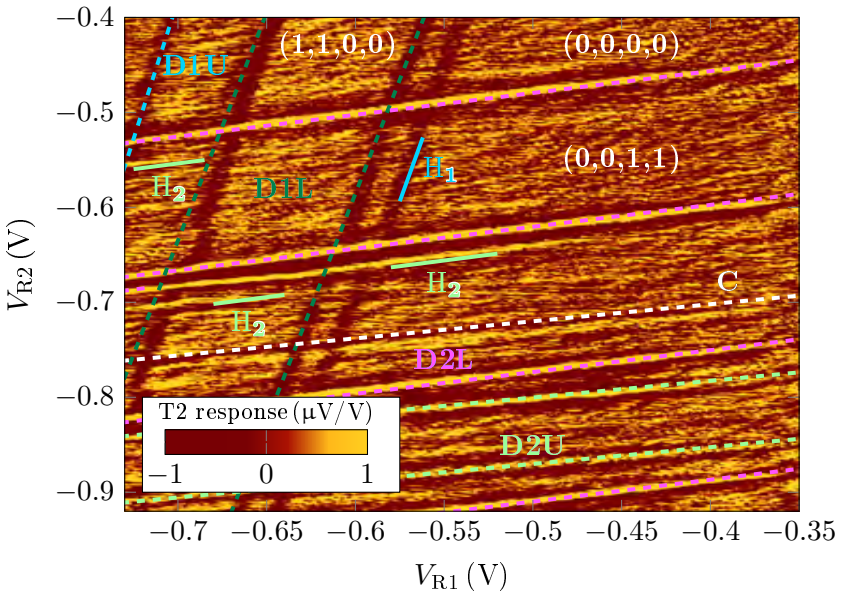

(b) Forward scan (→) to empty electrons from dots (D1L,D1U)

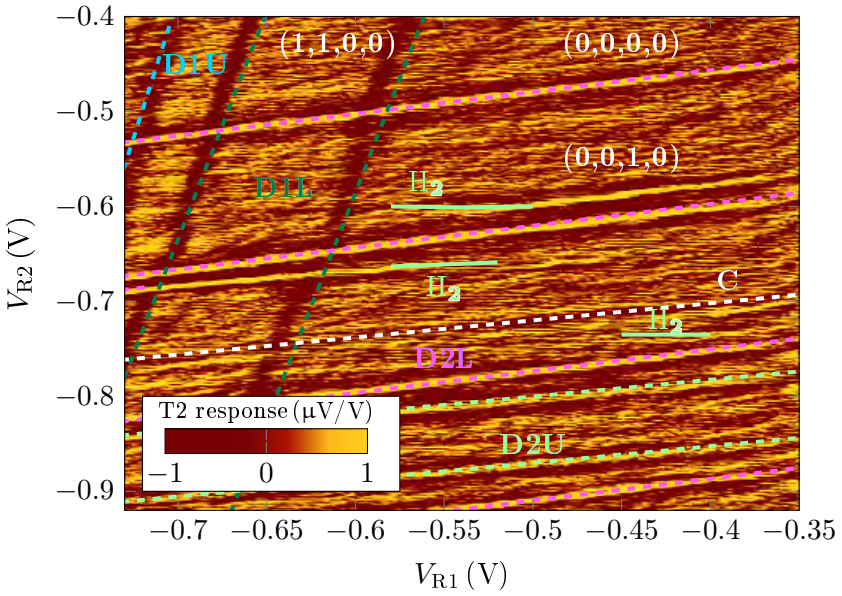

Figure 2.12: Charge stability diagram of all four dots in the 4-dot device taken using the TJCS T2. A numerical derivative of the RF response was taken along the x and y axes. The electron numbers for different charge stable regions in voltage space are shown for the dots (D1L, D1U, D2L, D2U). The two sets of steeper lines highlighted by blue and dark green represent transitions onto the dots D1U and D1L respectively. Similarly, the shallower green and magenta lines are due to electrons hopping on or off the right hand dots D2L and D2U. The lines labelled H_1 and H_2 are due to hysteretic transitions onto the dots D1U and D2U respectively. They match the slopes of D1L and D2L, due to the slow tunnel rates (of the first few electrons) from the reservoir onto the dots D1U and D2U causing them to load through the dots D1L and D2L respectively [102]. **(a)** and **(b)** show the reverse (adds electrons onto D1L/D1U and empties electrons on D2L/D2U) and forward (adds electrons onto D2L/D2U and empties electrons on D1L/D1U) scans where each horizontal line was scanned (taking 10.5 s per line direction) by decreasing and increasing V_{R1}. C is an unintended charge trap. The voltages on the other gates were: $(V_{G1}, V_{G2}, V_{T1}, V_{T2}) = (-0.1, 0.0, -0.2, -0.13)$ V.

electrons have a larger separation between charge transitions (with larger separations for larger P-donor dots) while the lowering confinement strength of later electrons usually yields smaller charging energies [81]. The stability diagram shows hysteretic behaviour where the charge transitions look different (or go off the scanning range) depending on the voltage scan direction. The hysteretic lines occur as there are dots further away from the reservoir (labelled H_1 and H_2 for transitions onto D1U and D2U respectively), which have slow dot-to-reservoir tunnel-rates that exceed the scanning time. Thus, the far dots (D1U and D2U) are charged and discharged by having electrons flow through the near dots (D1L and D2L). Note the charge transitions on the dots near the reservoirs have fast electron tunnel rates to the reservoir and do not exhibit hysteresis in the forward and reverse scans. Since the dot-to-reservoir tunnel rates increase when more electrons on the dots, the hysteresis effect disappears for higher electron transitions (for example, the two D2U lines in the bottom of each scan). The hysteresis is discussed in detail later in this section with details shown in Figure 2.14. Finally, there is a charge transition highlighted by C which was due to a charge-trap caused by a lithographic defect in Figure 2.10. The detailed justification of the charge stability diagram also includes the triangulation of the charge transition lines to the four patterned dots and the recognition of the charge-state hysteresis on dots D1U and D2U.

To verify that the multiple charge transition lines are due to electrons moving on the same quantum dot, many stability diagrams with a different combination of gate voltages (on the axes) were taken. The slope of the charge transition line indicates a ratio of the lever-arm of the gates (on the x and y axes) to the quantum dot associated with the charge transition line. Since the lever-arms relate to the gate geometry, the slopes remain invariant with electron number. Thus, multiple charge transition lines onto a given dot should remain parallel across different stability diagrams. By taking groups of transition lines with the same slope and verifying that they still had matching slopes over different stability diagrams, a family of four parallel lines of different slope were shown to arise from the four separate quantum dots as shown in Figure 2.12 under the colour-coded labels for D1L, D2U, D2L and D2U. A fifth line, that did not consistently match the slopes of the four families of transition lines across all stability diagrams, is marked C. An electrostatic triangulation method was then employed to infer the origin of the transition lines to the patterned quantum dots.

The slopes of charge transition lines on a given charge stability diagram yield information on the dot couplings of the gates swept along the x and y axes respectively. All charge transition lines were observed over multiple stability diagrams taken with

a different combination of gate voltages swept along the x and y axes. From Equation A.29 in Appendix A.2.1, the gradient of a charge transition line, when sweeping the gate voltages V_x and V_y on the x and y axes respectively, is:

$$\frac{dV_y}{dV_x} = -\frac{K_x - \alpha_x}{K_y - \alpha_y}, \tag{2.14}$$

where α_x and α_y are the gate lever-arms to the dot associated with the transition line for the gates x and y respectively. The constants K_x and K_y are 1 if the gate (x or y respectively) is the reservoir for the given dot and 0 otherwise[23]. As long as the dot does not have multiple reservoirs[24], it is evident from this equation that charge transitions lines for a given dot have negative gradient if, and only if, the gates used on the x and y axes are not reservoirs for the given dot. For example, the positive slope of the charge transitions suggest that R1 and R2 are reservoirs for the given quantum dots as expected (R1 is the reservoir for dots D1L and D1U while R2 is the reservoir for dots D2L and D2U).

Given a family of lines from the same dot (each line corresponds to an electron moving onto the dot), it is important to verify that the charging site is one of the intentional quantum dots (as opposed to unintentional quantum dots that can occur for example in MOS type devices [55, 103]) patterned during fabrication. Equation 2.14 shows that the slope of the charge transition line when sweeping the gates x and y (on the x and y axes respectively) that are not reservoirs for a given dot is $-\alpha_x/\alpha_y$. That is, the slope is the ratio of the gates' electrostatic influence on the given quantum dot. Now the lever-arm of a gate due to a point-like quantum dot (like a small P-donor dots in silicon) is numerically equal to the electrostatic potential due to the gate at the position of the quantum dot when applying 1 V to the gate (as discussed in further detail Appendix A.3.1 in the context of better capacitance matrix simulations). Therefore, the slope of a charge transition line on a stability diagram is indeed equal to the ratio of the electrostatic potentials of the gates (when individually applying some voltage V and grounding all other gates) at the site of the dot. By taking the exact structure of the gates from the STM image in Figure 2.10 and transferring it into a FEA simulation (as discussed in detail in Appendix A.3.3), one may simulate the electrostatic potentials of the

[23] K_m accounts for the changing level of the reservoir on sweeping a reservoir's voltage. That is, a more positive voltage on a gate will lower the dot's energy level: $\Delta U_d = -e\alpha_{gd}\Delta V_g$ but leave the reservoir untouched. However, a change the voltage on the reservoir itself lowers the reservoir energy level by $e\Delta V_g$, thereby raising the dot's energy level with respect to its reservoir by $\Delta U_d = e(1 - \alpha_{gd})\Delta V_g$

[24] Devices are typically designed to have single reservoirs to avoid current flow through the dots via multiple reservoirs [86, 92].

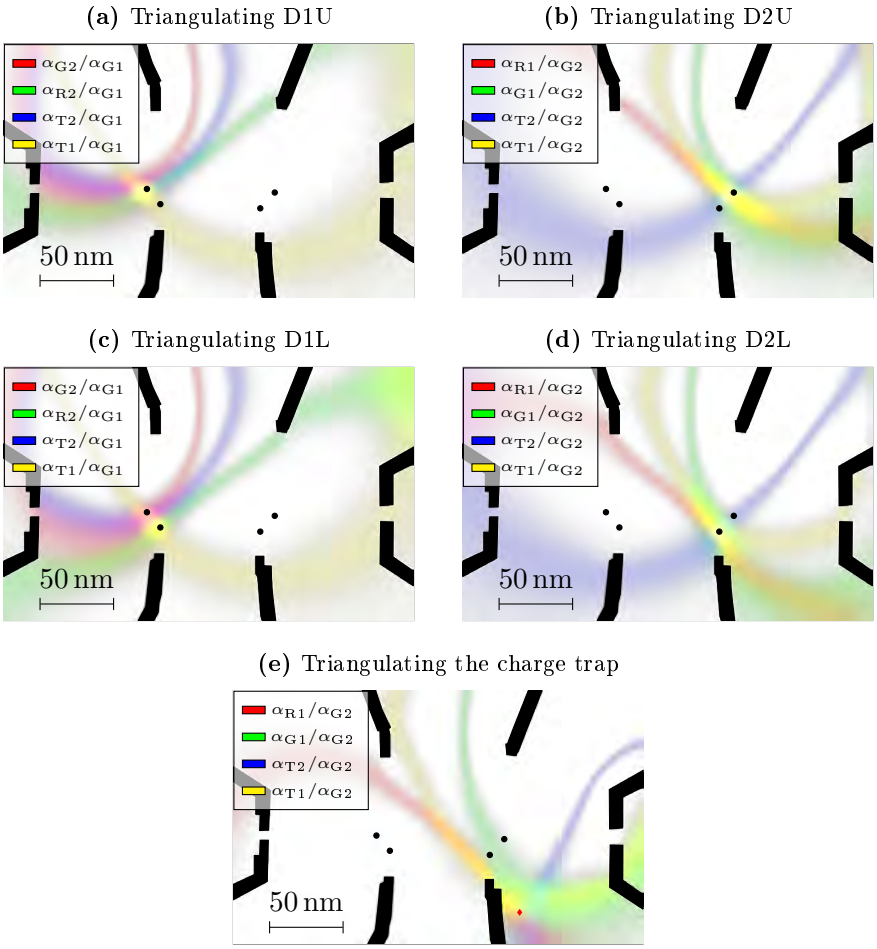

Figure 2.13: Electrostatic triangulation to verify the locations of the STM-patterned P-donor quantum dots. Each map shows the triangulation of the origin of each transition line observed in Figure 2.12. The black regions in each map represent electrodes in the device, while the four black dots represent the patterned locations of the dots in the STM. Each map, for a given dot, shows four shaded regions generated by taking the slopes of the dot transition over four different gate map combinations. The red cross marked on the final map represents the location where a lithographic defect due to a piece of the tip on the surface was observed in the STM image. The loci were generated by matching the ratio of slopes across different gate maps with simulated ratios of electrostatic potentials. Taking a 10% uncertainty in the measured slope, the regions were given a Gaussian spatial uncertainty.

individual gates and then calculate the locus of all points where the ratio of the electrostatic potentials of gates x and y match the slope dV_y/dV_x of the transition line in a given stability diagram. One may repeat this for the same transition line slope across different stability diagrams (taken with a different combination of gates on the x and y axes) to generate multiple loci and effectively triangulate the position of the quantum dot as shown in Figure 2.13. The loci are intentionally smeared by considering a 10% uncertainty in the measured slopes of the charge transition lines in the charge stability diagrams. That is, the intensity of each coloured locus at position $\mathbf{r}$ is given by a Gaussian distribution:

$$\ell(\mathbf{r}) = \exp\left[\frac{-1}{2\sigma_s^2}\left(\frac{\phi_x(\mathbf{r})}{\phi_y(\mathbf{r})} - |s|\right)^2\right], \tag{2.15}$$

where σ_s is the standard uncertainty in the transition line slope s. The position dependent functions ϕ_x and ϕ_y are the electrostatic potentials when applying 1 V to gates x and y respectively (while grounding all other gates in each case). Note that the combinations of gates used for each transition line were chosen to give lines of negative slope; that is, the gates swept along the x and y axes in the charge stability diagrams were not the reservoir for the dot under concern. This was to avoid complications that may arise when the simple electrostatic model does not accurately predict the lever-arm of a given dot when in close proximity to the reservoir [98]. Importantly, our results show that this technique, using the four loci for each family of transition lines, successfully triangulates the position of the measured dots to the positions of the four STM patterned dots as shown in Figure 2.13. In addition, this technique has the added advantage of being able to triangulate unintentional quantum dots (also known as 'charge traps'). In this case the transition line, marked C in Figure 2.12, is consistently triangulated to the position of a lithographic defect that occurred during fabrication before dosing as shown in the STM image of the device in Figure 2.10 by the label C. In the future, this triangulation technique can be iterated over new devices, so that the location and origin of unintentional charge traps can be identified, leading to a better understanding and subsequent elimination of such defects.

With the charge transitions successfully matched to the location of the STM-patterned dots in the device, one can label the electron charge state in the regions between the charge transition lines. To deduce the side (left/right or above/below a given charge transition line) with more electrons, one may examine the action of the gates. When increasing the voltage on a gate, the electrostatic potential on the dot becomes more positive and thus, electrons enter the dot. However, when increasing

the voltage on a reservoir, electrons deplete from the reservoir and lower the overall Fermi-level. Consequently, increasing the voltage on a reservoir effectively raises the dot's energy level (with respect to its reservoir) and thereby depletes charge on the dot. As shown by Equation 2.14, one may easily deduce that one of the gates being swept in the charge stability diagram is a reservoir to the dot if the slope of the charge transition line is positive. All lines in the stability diagram in Figure 2.12 are of positive slope. Thus, the dots all have R1 or R2 as their electron reservoirs. To deduce which of the gates (R1 or R2) is the reservoir for a given dot, one needs to consider the geometry. As R1 is closer, than R2, to dots D1U and D1L, R1 is the reservoir to the dots D1L and D1U. Similarly, R2 is the reservoir to the dots D2L and D2U. Thus, the region in the top-right corner of the stability diagram in Figure 2.12 with the most positive gate voltage on R1 and R2, has no further charge transition lines present and corresponds to the depleted charge region with the electron numbers labelled as $(0, 0, 0, 0)$ on all four dots[25]. When moving to more negative voltages on R1, one crosses charging lines on D1L or D1U as electrons are added to the respective dot. Since R2 is not a reservoir to the dots D1L and D1U, an electron is only added when crossing the charge transition line at a more positive gate voltage. Similarly, moving to more negative voltages on R2 loads electrons onto the dots D2L and D2U while a more negative voltage on R1 depletes those dots.

Finally, on labelling all the charge transitions and electron numbers from the depleted charge state, it is of note that two sets of transition lines in Figure 2.12, labelled with H_1 and H_2, changed slopes and positions depending on the direction of the voltage scan. Although the lines labelled H_1 and H_2 in the reverse scan in Figure 2.12a share the same slope as the the bottom dots in the reverse scan (for example, H_1 has the same slope as D1L and H_2 has the same slope as D2L), the slopes do not remain the same as the bottom dots' slopes in the forward scan in Figure 2.12b. This charge hysteresis effect is better observed in a simpler case when probing the first electron on the dots D2L and D2U (seen in Figure 2.12) using the gates R2 and G2 in Figure 2.14. The charge transition lines in both charge stability diagrams are positively sloped as R2 is the reservoir for the dots D2L and D2U. The two stability diagrams were taken by decreasing the voltage on R2 (reverse scan where electrons are added to the dots) and increasing R2 voltage (forward scan where electrons are depleted on the dots) with the charge stable regions labelled as the number of electrons in (D2L, D2U) respectively.

[25]Note that there may be more electrons present in the dots D1U and D2U. They may indeed never fully deplete due to their slow tunnel rates to their respective reservoirs. Thus, the exact electron numbers still remain as estimates.

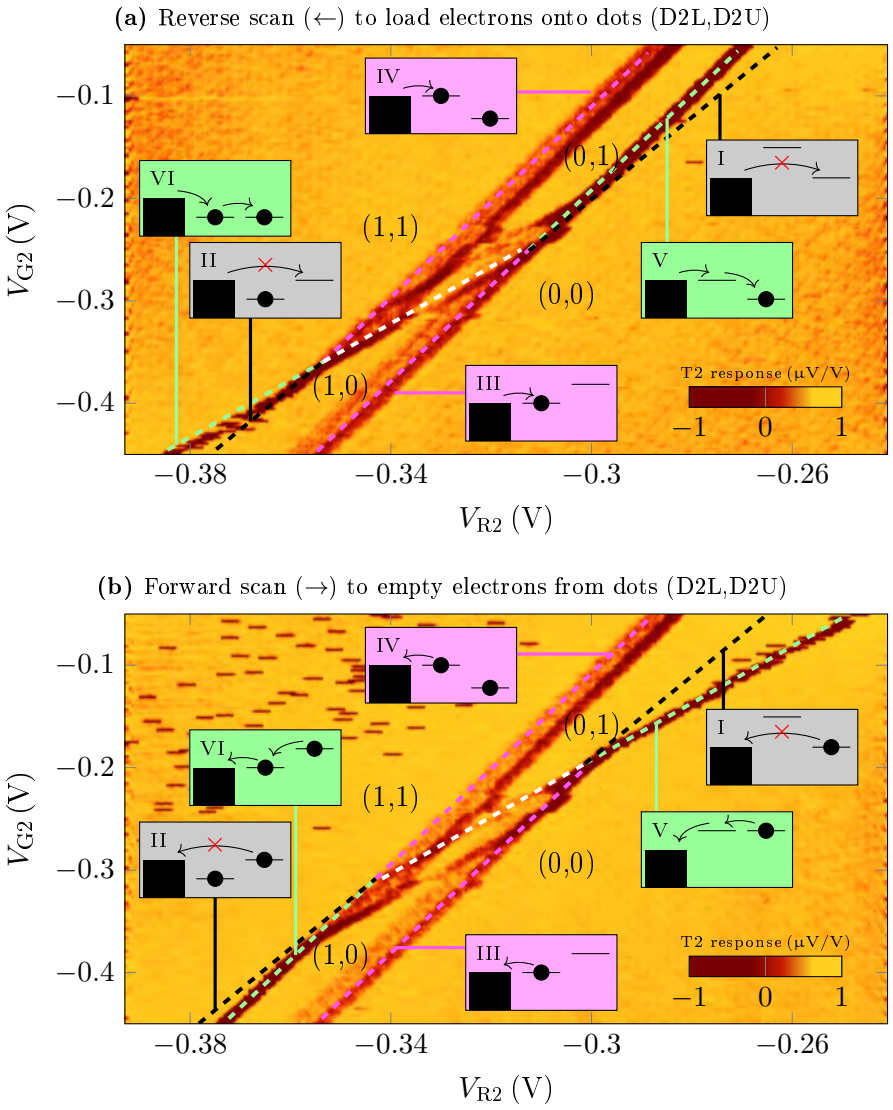

Figure 2.14: Hysteresis in the charge stability diagram, taken with sensor T2, due to asymmetric coupling of the dots D2L and D2U to reservoir R2. The tunnel rate from the reservoir R2 to dot D2U is extremely slow (compared to the tunnel rate between R2 and D2L) and thus, electrons emptying or loading dot D2U must move through dot D2L. This leads to a different slope for the D2U charge transition line when taking the gate map by scanning backwards **(a)** and forwards **(b)**. The slope of D2U transition (green) does not follow the expected slope (black lines), but instead follows the slope of the D2L transition line (magenta) or the inter-dot transition line (pink) depending on the required configuration of the D2L energy level to load or empty electrons on D2U. The labelled ordered pairs represent the number of electrons, in D2L and D2U, in the given charge stable regions. The energy diagrams have three columns representing the energy levels of the Fermi-level reservoir R2, dot D2L and dot D2U. The voltages on the other gates were set to 0 V except $V_{R1} = -0.2$ V. To process the data from T2, a numerical derivative was taken along the x-axis. Note that a high RF power was used in this gate map scan and thus, charge transitions involving R2-D2L (magenta) and D2L-D2U (white) were broadened as a result. Charge transitions on D2U were not broadened as the electron may not move back and forth once the charge transition has occurred due to the charge state hysteresis. The small horizontal lines seen in the (1,1) charge region in (b) are due to another charge transition.

By tuning the voltage on G2 one may change the dots' energy levels such that one adds or removes electrons (in the forward or reverse scans) onto the dots D2L and D2U as seen by the magenta $(0,0) \rightarrow (1,0)$ and green $(0,0) \rightarrow (0,1)$ charge transition lines respectively. On moving to lower voltages on R2, the dot that wasn't initially loaded receives an electron to finally enter the $(1,1)$ charge state. The intermediate region between which one loads to the D2L or D2U first is the odd-parity $(1,0) \leftrightarrow (0,1)$ inter-dot crossing shown in white where an electron moves between the dots. The black lines indicate the expected slope of charge transitions on D2U. However, there is a hysteresis effect where the slopes of the charge transition onto dot D2U (green) has a slope depending on the direction of the voltage scan. The gate voltage hysteresis effect has been previously observed in systems with asymmetric tunnel rates of two quantum dots to their reservoir [102] with some groups exploiting the hysteresis to prolong spin states for higher fidelity readout [104]. In our case, the tunnel rate between the reservoir R2 and D2U is too slow to load or empty directly in the time-frame of the gate map scans (approximately 56 s per line for a given scan). Thus, D2U can only be loaded or depleted by moving the electrons through D2L (instead of loading directly from the reservoir as seen by the grey panels I and II). However, D2L can be loaded fast directly (when the dot energy level aligns with the reservoir Fermi-level as seen in the magenta panels III and IV) and thus, the charge transition lines do not undergo any hysteresis.

Figure 2.14a shows electrons being added onto the dots. On the charge transition $(0,0) \rightarrow (0,1)$, the electron on the reservoir cannot enter D2U through D2L as D2L is too high in energy (grey panel I). On moving collinear with the $(0,0) \rightarrow (1,0)$ charge transition line, D2L is aligned with the Fermi-level on reservoir R2. Thus, electrons may now move onto D2U via D2L (green panel V). Similarly, on the charge transition $(1,0) \rightarrow (1,1)$, the electron on D2L cannot move onto D2U until D2U lowers its energy level to match that of D2L (grey panel II). Thus, this charge transition adopts the same slope as the inter-dot transition line $(1,0) \leftrightarrow (0,1)$ (green panel VI).

Figure 2.14b shows the case when removing electrons on the dots. On the $(1,1) \rightarrow (1,0)$ transition, the electron may not directly tunnel through D2L as the electron on D2L cannot tunnel out as the associated energy level on R2 is filled (grey panel II). In order to have two electrons on the dot D2L, the electron on D2U will need to tunnel onto a much higher energy level on D2L. Thus, the level on D2L must be raised such that it is at least in line with the Fermi-level on reservoir R2 (green panel VI). Thus, the slope of the charge transition is co-linear with the D2L transition line $(1,1) \rightarrow (0,1)$. Finally, on the $(0,1) \rightarrow (0,0)$ charge transition line, D2L is once more

too high in energy for the electron to tunnel out (grey panel I). Thus, the energy level on D2U must be raised align with the energy level on D2L (green panel V). Therefore, the charge transition line adopts the same slope as the inter-dot transition line $(1,0) \leftrightarrow (0,1)$.

By grouping the charge transition lines that remain parallel across multiple gate maps, then triangulating the transitions to match them to the dots and identifying the hysteresis effects on multiple reservoirs, one can completely label the charge stable states shown in Figure 2.12. Note we assume that the dots are capable of being fully depleted and all resulting electrons entering the dots were observed in the stability diagrams.

2.2.6 Effectiveness of electrostatic simulations in predicting differential gate lever-arm and inter-qubit couplings

Control of electron-electron exchange J in a singlet-triplet qubit (achieved by separating or moving both electrons together across the double quantum dot) of a given gate is gauged by the gate's differential lever-arm across the two quantum dots hosting the singlet-triplet qubit as discussed in Section 2.2.3. It is important to verify that the differential lever-arms match simulations in order to confidently optimise more complex singlet-triplet qubit systems. The differential lever-arm across two quantum dots can be inferred by mapping out the singlet-triplet electron energy levels as a function of magnetic field using the single-gate RF sensor [29, 30, 105]. Detailed discussion of the characterisation and optimisation of the single-gate RF sensor on R2 and the subsequent magnetic field measurements are shown later in Section 4.2.2. Nonetheless, the RF sensor requires inter-dot tunnel rates (for electrons in the singlet-triplet state across the two quantum dots) to be much larger than the driving frequencies of ∼100 MHz set by the resonators[26] connected to the reservoirs R1 and R2. The inter-dot tunnel rates across dots D1L and D1U were found to be too slow to respond to the drive frequencies of the single-gate RF sensors on R1 and R2 of 300.1 MHz and 261.5 MHz respectively. Thus, the differential lever-arms of the gates were only measured with respect to the dots D2L and D2U where the inter-dot tunnel coupling was approximately 39 GHz when measured using the $(3,3) \leftrightarrow (2,4)$ charge transition (for electrons on D2L and D2U respectively).

[26] As discussed in the design of RF readout sensors in Section 3, the readout sensor must be fast with respect to the qubit error rate to enable error detection and correction (approximately ∼270 µs for single-spin qubits; so error rates are ∼100 kHz). High fidelity readout requires high resonator quality factors $Q \gg 100$. Noting that the readout resonator bandwidth is $\sim f_0/Q$ (f_0 the resonant frequency of resonator), 100 MHz at least yields up to 1 MHz of usable bandwidth.

Lever-arm α	Experimental Value	Model
$\Delta\alpha_{\text{R2}}$	0.13 ± 0.05	0.12
$\Delta\alpha_{\text{G2}}$	-0.05 ± 0.02	-0.03
$\Delta\alpha_{\text{R1}}$	0.02 ± 0.01	0.01
$\Delta\alpha_{\text{G1}}$	-0.008 ± 0.005	-0.006
$\alpha_{\text{R1-D2L}}$	0.12 ± 0.07	0.07
$\alpha_{\text{R1-D2U}}$	0.10 ± 0.05	0.06
$\alpha_{\text{G1-D2L}}$	0.08 ± 0.04	0.04
$\alpha_{\text{G1-D2U}}$	0.08 ± 0.04	0.05
$\alpha_{\text{R2-D2L}}$	0.5 ± 0.2	0.34
$\alpha_{\text{R2-D2U}}$	0.4 ± 0.2	0.22
$\alpha_{\text{G2-D2L}}$	0.11 ± 0.07	0.07
$\alpha_{\text{G2-D2U}}$	0.16 ± 0.07	0.10

Table 2.5: Comparison of experimentally measured gate lever-arms with predictions from electrostatic simulations. The experimental measurements were only possible on the right-hand dot pair D2L and D2U. For a given gate G, the differential lever-arm α_{G} (defined as $\alpha_{\text{G-D2L}} - \alpha_{\text{G-D2U}}$) was measured directly from magnetic field measurements, while the remaining absolute lever-arms onto the dots were inferred by considering the differential lever-arms in conjunction with the slopes of the charge transition lines in the charge stability diagrams. The 'model' refers to the predictions made when importing the STM image into a FEA simulation and then calculating the expected gate to dot lever-arms as discussed in Appendix A.3.

From the magnetic field measurements shown later in Section 4.2.2, the differential lever-arms of the reservoir R2 and gate G2 were $\alpha_{\text{R2-D2L}} - \alpha_{\text{R2-D2U}} = 0.13 \pm 0.05$ and $\alpha_{\text{G2-D2L}} - \alpha_{\text{G2-D2U}} = -0.04 \pm 0.02$ respectively. The ratio of the differential lever-arms for the gates R2 and G2 (0.13/0.04) is consistent with the slope of the inter-dot charge transition across dots D2L and D2U in the stability diagram (with R2 and G2 on the x and y axes) of 2.6 ± 0.03 seen in Figure 2.14. The individual gate lever-arms can be found by taking the slopes of the transition lines in stability diagrams and applying Equation 2.14 which links the slopes to the ratio of lever-arm alphas. For example, the slopes of the D2L and D2U transitions on a R2-G2 stability diagram were $(1 - \alpha_{\text{R2-D2L}})/\alpha_{\text{G2-D2L}} = 4.67 \pm 0.05$ and $(1 - \alpha_{\text{R2-D2U}})/\alpha_{\text{G2-D2U}} = 4.01 \pm 0.05$ respectively. Thus, knowing the differential lever-arm (from the magnetic field measurements) and the ratio of lever-arms (taken from the slopes of transition lines in the stability diagrams), one may solve a linear system of equations to find the absolute lever-arms of the gates to each individual dot:

$$\begin{pmatrix} 1 & -1 & 0 & 0 \\ 0 & 0 & 1 & -1 \\ 1 & 0 & 4.67 & 0 \\ 0 & 1 & 0 & 4.01 \end{pmatrix} \cdot \begin{pmatrix} \alpha_{\text{R2-D2L}} \\ \alpha_{\text{R2-D2U}} \\ \alpha_{\text{G2-D2L}} \\ \alpha_{\text{G2-D2U}} \end{pmatrix} = \begin{pmatrix} 0.13 \\ -0.05 \\ 1 \\ 1 \end{pmatrix}. \tag{2.16}$$

By repeating this process for all the gates, one may infer the absolute lever-arms of all the gates R1, R2, G1 and G2 to the dots D2L and D2U as shown in Table 2.5.

The measured lever-arms on the dots D2L and D2U were compared with electrostatic simulations. The electrostatic model was the same model used in Section 2.2.5 but now the real device geometry (from the STM image in Figure 2.10) was imported into the simulation. The lever-arms were extracted from the simulations using the methods outlined in Appendix A.3. From Table 2.5, it would appear that the electrostatic FEA model predicts the differential lever-arm alphas correctly to within experimental uncertainty[27]. In addition, the FEA model correctly predicts the absolute lever-arm alphas within experimental uncertainty. However, the FEA model appears to slightly underestimate (although captured within uncertainty) the absolute lever-arms for R2 ($\alpha_{\text{R2-D2L}}$ and $\alpha_{\text{R2-D2U}}$); a lead that is in close proximity to the dots. When considered with the peculiarity that dot D2L (with approximately 3 P-donors) is depleted at 0 V and requires −0.28 V on R2 to fill with the first electron (3P dots in previous devices have shown at least one electron on the dot when setting all gate voltages to zero [81]), the explanation may require tight-binding simulations (beyond the scope of this thesis).

The final important parameter to be characterised in this device was the inter-qubit coupling Δ_Δ required for two-qubit gates. The coupling strength is defined as the shift in the target qubit's detuning when the control qubit moves from the $(1,1)$ charge state into the $(0,2)$ charge state (if in the singlet state and remains in $(1,1)$ otherwise). Thus, to operate the two qubit-gate one must simultaneously realise singlet triplet states on both pairs of quantum dots; that is, overlapping the inter-dot charge transitions across both dot pairs in voltage space as discussed in Section 2.2.3. Thus, to measure the inter-qubit coupling, one aligns the two inter-dot crossings across the dot pairs D1L/D1U and D2L/D2U respectively on top of one another to observe the resulting shift in the target-qubit's inter-dot crossing (as in the simulated charge stability diagrams in Figure 2.9). However, while the inter-dot crossing across dots D2L/D2U could be viewed via the single-gate RF sensor

[27] The uncertainties were calculated using standard propagation of uncertainties. The experimental uncertainties include the uncertainties in measured charge transition slopes (approximately 10%) in the stability diagrams and the uncertainties in the best-fit curves from the magnetic field measurements (for example, in Figure 4.2d) discussed in Section 4.2.2.

R2 and the TJCS T2, there was no mechanism to view the inter-dot crossing across the dots dots D1L/D1U. That is, the single-gate RF sensors R1 and R2 could not measure inter-dot crossings across D1L/D1U as the inter-dot tunnel rate was too slow to respond to the drive frequencies of the single-gate RF sensors on R1 and R2 of 300.1 MHz and 261.5 MHz respectively[28]. In addition, the charge sensor T2 could not detect the inter-dot transition as the dots (D1L and D1U) was too far from the sensor to detect the small electric dipole. However, the inter-qubit coupling could still be measured by the shift in detuning induced on the adjacent qubit. Here, the shift in the right qubit's detuning due to an inter-dot transition on the left qubit is equivalent to the difference in the charge shifts on freshly introducing an electron onto the dots D1L and D1U respectively (since by the electrostatic superposition principle, the shift is equivalent to an inter-dot charge shift on the left qubit). That is, the inter-qubit coupling (given by Equation 2.8 in the design discussions in Section 2.2.3) is defined as the shift in the right qubit's detuning (hosted on D2L/D2U) on shifting the left qubit from the singlet to triplet state (that is, moving a charge between the dots D1L and D2U).

Since the right qubit's shift in detuning is required, the even parity singlet-triplet inter-dot charge transition $(3,3) \leftrightarrow (2,4)$ (across the dots D2L and D2U) was chosen for the measurement. The singlet-triplet inter-dot crossing on the right qubit was aligned with two charging lines on the dots D1L and D1U as shown in Figure 2.15a. The stability diagram was taken using a lock-in amplifier to enhance the signal and automatically take the derivative of the signal by applying the lock-in excitation on top of the voltage applied to R2. When individually moving an electron onto D1L and D1U, the right qubit's singlet-triplet inter-dot crossing shifted by 702 µV and 529 µV respectively (along the R2 voltage axis). Note that the shift that occurs due to electrons moving onto D1U is smaller (than the shift due to D1U) by virtue that D1U is further away from the dots D2L and D2U. The difference in the shifts on right qubit's inter-dot crossing was 170 ± 60 µV. Taking the experimentally measured differential lever-arm for R2 across the dots D2L and D2U ($\alpha_{R2} = 0.13 \pm 0.05$), the resulting energy shift is $\Delta_\Delta = 5 \pm 2$ GHz. Using the electrostatic model of the device based directly on the STM image to calculate the capacitance matrix and thus, the resulting inter-qubit coupling (given in Equation 2.9), the estimated inter-qubit coupling from the electrostatic simulations was $\Delta_\Delta = 4.25$ GHz. Thus, the expected value was within the bounds of experimental uncertainty. Thus, once again the validity of the model was verified and predicted that even at inter-qubit distances

[28] The single-gate RF sensor requires the tunnel rate needs to be much larger than the drive frequency as discussed in Section 4.1.2.

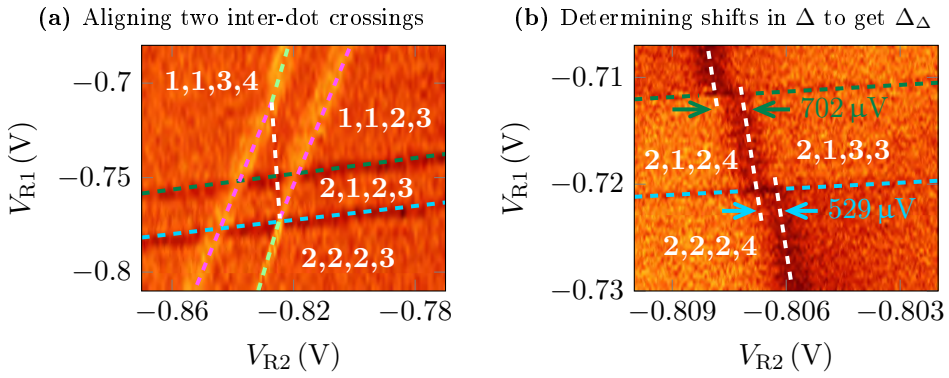

Figure 2.15: Experimental measurement the inter-qubit coupling Δ_Δ. (a) Stability diagram measured with T2 showing charge transitions onto all four dots. The response of T2 was measured with a lock-in amplifier. The horizontal lines represent charge transition transfer lines onto the dots D1L and D1U while the vertical lines represent that onto the dots D2L and D2U. The stability diagrams shown represent the response of the T2 sensor as measured with a 4 mV lock-in excitation applied to R2. The quadruplets show the electron numbers as in Figure 2.12. The white line represents an inter-dot singlet-triplet transition on the right hand dot pair. The voltages on the other gates were: $(V_{G1}, V_{G2}, V_{T1}, V_{T2}) = (0.05, -0.13, -0.05, -0.023)$ V. (b) Aligning charge transitions onto D1L and D1U on top of the white inter-dot transition line. Charge transitions onto D1L and D1U shift the inter-dot line by 702 μV and 529 μV respectively. The difference in the shifts in detuning is gives the inter-qubit coupling (that is, the shift in the target qubit's detuning when the control qubit moves both electrons onto the same dot when shifting from the triplet to singlet state). The resulting difference was 170 ± 60 μV; which translated to an inter-qubit coupling of 5 ± 2 GHz. Note that the all the charge transition lines in this stability diagram, unlike that in (a), were broadened heavily, to ensure an adequate signal strength, achieved by applying the lock-in excitation to both R1 and R2.

of $d_{iq} = 75\,\text{nm}$, one may obtain inter-qubit couplings in the excess of a few gigahertz. The verification of the model is important as it predicts that one may obtain larger inter-qubit couplings if desired for faster two-qubit gate operations (for example, inter-qubit couplings of 45 GHz and above can be achieved if the dots were brought closer at 40 nm as shown in Figure 2.7). Alternatively, one may place the qubits further apart if one wishes to operate the singlet-triplet qubits in the perturbative regime with AC driving as in previous experiments performed in GaAs [34, 35]. Increasing the spacing between qubits would have the advantage of reducing the complexity of lead fan-out and increasing the gate voltage range before current leaks between the leads.

2.3 Summary and outlook for future devices

Basic electrostatic modelling of Si-P devices using realistic experimental parameters yielded a device design to form four quantum dots with accessible even parity singlet-triplet inter-dot transitions as required for the demonstration of a two-qubit gate between two singlet-triplet qubits. This modelling matched the experimentally measured results by correctly predicting key system parameters, while noting the subtle discrepancies for dots placed in close proximity to the reservoirs. In addition, the models and measured data indicate strong inter-qubit couplings that were not possible to realise in previous quantum dot experiments in other systems such as GaAs. The smaller inter-qubit coupling of gate-defined quantum dot systems likely arises from the lower electric dipole coupling caused by the ~100 nm size of the double dots (unlike 12.5 nm), being spaced further apart at approximately 100-200 nm unlike 30-100 nm here with Si-P dots. The utilisation of this strong inter-qubit coupling (with respect to the inter-dot tunnel coupling) to perform two qubit gates is discussed in later in the development of the proposed singlet-triplet architecture in Section 5.

Further experimental development requires the realisation of adjacent singlet triplet qubits to perform a two-qubit gate. However, in this device, the dots D1L and D1U formed a symmetric P-donor cluster configuration and thus, yielded no accessible singlet-triplet transitions. As expected, the asymmetric P-donor clusters on dots D2L and D2U enabled access to a singlet-triplet transition. However, the inter-dot tunnel coupling was overshot at 39 GHz implying that the exchange J could not be turned off with reasonable voltage pulses. The magnitude of the voltage pulse to set $J = \Delta B_z$ is given by Equation 2.6 (used during the design discussion in Section 2.2.3):

$$V_{\text{Hadamard}} = \left| \frac{4\Delta B_z^2 - t_c^2}{2\Delta B_z e \Delta\alpha} \right|. \tag{2.17}$$

Note that V_{Hadamard} is the lower-bound to reaching $J \approx 0$; a lower bound that was found to be $\sim$2.2 V when taking $\Delta B_z \approx 29$ MHz and the differential lever-arm for the designated control gate G2 of $\Delta\alpha_{\text{G2}} = 0.05$. With the gate voltage ranges (before gate-to-gate leakage occurs) usually below 1 V, the required voltage pulse to turn J off is therefore unrealistic. Had the inter-dot tunnel coupling (between dots D2L and D2U) been close to 10 GHz, the required voltage would have been experimentally realisable at 180 mV. Thus, in the future regarding a scalable array, research and experimental development is required in creating accurately reproducible inter-dot tunnel couplings. Other system parameters, such as the inter-qubit coupling Δ_Δ, are not significantly altered by small perturbations in the device geometry and should be reliably reproduced.

Although a qubit was not realised in the experiments run during the thesis, there were several positive results regarding the design, fabrication and characterisation of the quadruple quantum dot device:

- General geometric layout enabled electrons to be loaded onto four quadruple quantum dots
- TJCS T2 showed good charge sensitivity, including the ability to detect charge transitions on dots up to 160 nm.
- Electrostatic models showed exceptional validity in matching the experimental measured lever-arms and inter-qubit coupling
- A triangulation technique was developed to match the measured charge transitions to the patterned dots on the device. The triangulation technique should prove useful in the future when diagnosing defect sites that give rise to unintentional charge traps such as the lithographic defect triangulated in this experiment.
- The large inter-qubit coupling of 5 GHz measured in the experiment verified that large non-perturbative (with respect to the tunnel coupling) inter-qubit couplings between singlet-triplet qubits can be realised when using Si-P quantum dots.

Despite these positive results, we did not observe a singlet-triplet qubit as J could not be turned off due to the large 39 GHz inter-dot tunnel coupling. However, the

experiment did provide some key focus points regarding the next device. Although one may take the optimal distances in the context of a large-scale architecture as discussed in Section 5, the next device should utilise similar geometric parameters to the current device. That is, one should opt for a large gate voltage ranges and experimental flexibility when there are many unknown parameters (as discussed below) still remaining in the system as opposed to using the tighter dimensions that require precise donor numbers and inter-dot tunnel couplings. Nonetheless, the geometric parameters that may remain the same for the next device (based on the results of this experiment) are:

- TJCS to dot distance: 80 nm. The TJCS appeared to be sensitive enough to detect all four dots alone from this distance. There is no need to change this distance.
- Primary TJCS dimensions: 10.8 nm gap size and 8.8 nm gap width. The TJCS T2 yielded a good charge sensor with the ability to sense electrons on all four dots.
- Dot-to-reservoir distance: $d_{id} = 17$ nm. As discussed in the characterisation of the single-gate RF sensor later in Section 4.2.2, there was no evidence of a strongly coupled reservoir (inducing cotunnelling processes) causing small spin life times (specifically the $s_0 \rightarrow t_-$ relaxation time that limited the available qubit readout time). In fact, the spin life time was 2 ms [29] instead of the previously measured 60 ns [30]. Thus, the dot-to-reservoir distance shall remain the same.

The measured inter-qubit coupling matched the electrostatic predictions. Given that one may now trust the simulations, one may reproduce the strong inter-qubit coupling of above 5 GHz for any dot angle ϑ by bringing the inter-qubit distance to 60 nm (as shown in Figure 2.7). Note that this change may reduce the gate voltage range and remove experimental flexibility in accessing useful even parity inter-dot charge transitions. However, by relaxing the angle from $\vartheta = 135°$ to $\vartheta = 90°$, where the dots are vertical, one may enhance the differential lever-arms of the control gate and reservoir. Thus, some recommended changes to the geometry include:

- Inter-qubit distance $d_{iq} = 60$ nm. The gate voltage range may drop slightly, but one would be able to retain the large $\Delta_\Delta > 5$ GHz for any dot angle.
- Dot angle $90° < \vartheta < 135°$. Pushing the dots to be vertical will enable the largest differential lever-arm on the qubit control gates. A larger differential

lever-arm increases the safety net on the maximum inter-dot tunnel coupling that can be used to form a qubit.

- Dot-to-gate distance: $d_g = 45\,\text{nm}$. In the next device one of the control gates could be brought closer by 5 nm to enhance the differential lever-arm. One should take note of the resulting lower gate voltage range and observe if the electrostatic accessibility of even parity inter-dot transitions is affected. If the accessibility is not affected, then one may continue bringing the control gates closer to the dots in future devices for a greater differential lever-arm.

- Secondary TJCS dimensions: 8 nm gap size and 6 nm lead width. The TJCS T1 was too Ohmic. Thus, the gap size can be widened to investigate the possibility of a more conductive TJCS than the sensor T2 in this experiment. With the gap size above 6 nm, the aspect ratio (gap width divided by gap size) is below one. Thus, one would expect gap-like behaviour once more [100].

In DC pulsing we aim to turn off the exchange coupling within an experimentally realisable value of the pulse amplitude. If one wishes to manipulate the singlet-triplet states via AC driving, as opposed to the faster 2-qubit gates investigated in Chapter 5, the inter-qubit coupling must be made perturbative with respect to the gigahertz tunnel coupling between the individual double quantum dots: $\Delta_\Delta \ll 1\,\text{GHz}$. The perturbative coupling is required to satisfy the perturbative approximation[29] used in deriving the AC-driven two-qubit gate [14, 34, 35]. AC driving also requires operation at J close to zero (as required to precess about the Pauli-x axis whereby Pauli-z rotations are realised with AC driving of the detuning). To achieve this in singlet-triplet donor qubits we could first set the dot angle to $\vartheta = 90°$ (that is, making the double quantum dots parallel to their respective gates) to maximise the differential lever-arm of the control gates with respect to their double quantum dots and subsequently maximising the ability to turn off J. Then one may set the inter-qubit distance to be greater than 120 nm to give inter-qubit couplings less than 1 GHz. To find the distances for smaller inter-qubit couplings, we note the approximate $\Delta_\Delta \sim 1/d_{iq}^3$ dependence seen in the numerical simulations when setting $\vartheta = 90°$.

The final geometric parameter is the inter-dot distance (d_{id}), which is set more specifically by the inter-dot tunnel coupling. An inter-dot tunnel coupling below 10 GHz is desirable for qubit control. However, the inter-dot tunnel coupling is

[29] The inter-qubit coupling needs to be much smaller than the driving AC amplitude $\Delta_\Delta \ll \Delta_{ac}$. To satisfy the rotating wave approximation, the driving amplitude must be smaller than the tunnel coupling $\Delta_{ac} < t_c$.

a non-trivial function of the P-donor dot size, configuration of the donors within each dot, electron number and the inter-dot distance. Unfortunately the amount of data we currently have is insufficient to estimate the optimal distances given the large size of the parameter space. Since the tunnel coupling changes with the P-donor dot sizes and the configuration of the donors within the dot, the inter-dot distance should remain at 12.5 nm. Setting a constant distance will at least enable a controlled experimental study. Regarding the choice of 12.5 nm, one should consider the fact that a 22 GHz tunnel coupling was observed for a 4-electron 2P-3P double quantum dot separated by $d_{id} = 11.5$ nm. Given the ideal double quantum dot is to be 1P-2P for the ease in electrostatic accessibility (from the simulations in Section 2.2.3), the tunnel coupling would have been much higher than 22 GHz for 4 electrons. Thus, increasing the distance to 12.5 nm would be advisable. Although the current experiment should have yielded a smaller tunnel coupling given the larger inter-dot distance and larger dot sizes, the larger electron number may have enhanced the tunnel coupling to be a higher value. Therefore, there is no reason to recommend a different distance for the next device.

In the vain of achieving higher device reproducibility, the ability to access even parity inter-dot charge transitions (by ensuring asymmetric P-donor dots) and optimising the tunnel coupling; any techniques to guarantee the P-donor dot sizes on fabrication would be welcome. That is, the development of on-site incorporation such as tip-induced incorporation [106] to guarantee the P-donor dot configuration and size would be beneficial in developing a many singlet-triplet qubit device. In addition, easy access to tight-binding simulations on optimal donor configurations would help with faster prototyping by being able to produce deterministic experimental designs for devices.

Chapter 3

Compact RF sensors for Si-P qubits

One of the key criteria for a working quantum computer is its ability to readout the state of its qubits [107]. It becomes difficult to reserve space for the qubit readout sensors in a scalable array of qubits when the spin qubits themselves need to be spaced at distances in the order of 10-100 nm required for electron-electron exchange and electron-electron dipole interactions typically used in two-qubit gates [28, 34, 78, 108]. One method to overcome the difficulty in placing the qubit sensors is to reduce the lead count by replacing the conventional 3-lead (and one quantum dot) single electron transistor (SET) sensor with a single-lead-quantum-dot (SLQD) sensor capable of reading out both single-spin and singlet-triplet qubits [31]. The SLQD sensor requires the detection of a small AC 'quantum capacitance' using an RF resonator. Thus, an exact analytic model (expressed in terms of purely experimentally measurable parameters such as the parasitic capacitance, internal quality factor and external quality factor) of the resonator was first developed. This circuit model description of the readout signal strength was also applicable to the quantum capacitance measurements using the more compact single-gate RF sensor discussed later in Chapter 4 [32]. The SLQD sensor was then investigated theoretically using rate equation models. In particular, this model investigated the SLQD operation in the nonlinear regime and made the first analytic predictions of the peak saturation of the RF readout signal strength at high input RF powers compared to previous similar works in the literature [109, 110]. In addition, this model was experimentally verified via a SLQD sensor fabricated in Si-P. This chapter also outlines the new techniques developed to both operate and characterise the SLQD sensor (for example, the reservoir to dot lever-arms in the SLQD cannot be deduced via conventional Coulomb oscillation techniques as there are no source and drain leads).

3.1 Overview of RF qubit sensors

RF qubit sensors have been implemented to sense solid state qubits for almost two decades. The evolution of RF qubit sensors started with simple enhancements on conventional charge sensors to unique single-gate sensors. The prior development of RF sensors shall be summarised in this section.

3.1.1 Overview of conventional charge sensors

Conventional solid-state sensors rely on detecting the charge state of a quantum dot (that is, the presence or absence of an electron) to measure the qubit state. Charge detection is sufficient for qubit-readout as most solid-state qubit states can be mapped onto a charge state [12, 13, 80, 111, 112]. For example, in the case of charge qubits, a charge sensor that senses the location of the electron immediately measures the qubit state [58]. In the case of two-electron singlet-triplet qubits, one utilises 'Pauli-spin blockade readout' where the electric potential across the two quantum dots is tilted such that both electrons are forced onto the same dot. The charge sensor must distinguish between the singlet state s_0 which allows both electrons to enter the same dot, with the triplet t_0 state where both electrons remain on separate dots due to Pauli-blockade [12–14].

To read the qubit state for single-spin qubits, one utilises a spin-to-charge conversion process by first aligning the energy level of the dot (holding the electron spin to be measured) to the Fermi level of its reservoir and then applying a magnetic field. The resulting Zeeman splitting of the electron implies that a spin-up electron (now higher than the Fermi-level) may tunnel off the dot (onto the reservoir) while a spin-down electron remains on the dot and may not tunnel off the dot as the corresponding states on the reservoir are filled. Detecting this change in the charge state of the dot when a spin-up electron tunnels off the dot enables single-shot single-spin readout [18, 80, 111].

An alternative method to measure single-spins using a charge sensor is to use a double quantum dot where the first dot holds a spin-down electron and the target electron is held on the second dot. On performing readout, the electric potential is tilted across the two quantum dots to bring both electrons onto the same dot. If the target electron is spin-down, then the resulting two-electron spin state is the $t_- = |\downarrow\downarrow\rangle$ state which forbids both electrons entering the same dot due to Pauli-blockade. If the target electron is spin-up, the resulting two-electron spin state $|\uparrow\downarrow\rangle$

maps onto the singlet s_0 state where both electrons may enter the same dot[1]. Thus, by mapping the single-spin state onto a two-electron singlet-triplet state one may employ Pauli-blockade readout to readout single-spin qubits [108, 113, 114].

Given that a charge state measurement can measure electron spins, it is important to review viable charge sensors. Several solid-state charge sensors have been realised experimentally to infer the charge state of a given dot. The earliest solid-state charge sensor is the single-electron-transistor or SET [115]. The SET consists of a large quantum dot tunnel-coupled to 'source' and 'drain' leads. Current flows from source to drain via the quantum dot when one applies a small bias voltage to the source lead. However, due to the discrete energy levels on the quantum dot, current may only flow when the energy level of the quantum dot is in between the the source and drain Fermi-levels as shown in Figure 3.1a. When no SET quantum dot energy level is in between the source and drain energy levels, the lack of current flow is termed 'Coulomb blockade'. A third gate lead is required to apply a potential on the quantum dot to tune its energy levels such that the SET is in a conductive state (when current flows) or in a 'Coulomb blockade' state (when no current flows). Just as the SET gate may tune the energy levels on the quantum dot, the scalar potential of electrons on a target dot can also shift the energy level of the SET quantum dot. When electrons enter or leave the target dot, the electrons' scalar potential field will shift the energy level of the SET quantum dot. The electrostatic coupling between the SET quantum dot and the dot hosting the target electron must be strong enough to toggle the SET into conduction and Coulomb blockade modes when changing the charge state on the target dot to yield a sufficient signal to noise ratio in the current readout signal.

Figure 3.1b shows a typical SET (seen by the quantum dot labelled SET along with its three leads SRC, DRN and G_{SET}) designed to sense single electron spins on a nearby P-donor dot (as seen by the quantum dot labelled D along with its control gate G_{DOT}). Using the spin-to-charge conversion technique, spin-up electrons (Zeeman split into the higher energy level placed above the Fermi-level) are detected via the electron tunnelling off the P-donor dot and onto the SET quantum dot and finally the drain lead. A spin-down electron, being Zeeman split below the Fermi-level,

[1]The four basis spin states, ordered in terms of energy levels, map onto the singlet-triplet states as follows: $(|\downarrow\downarrow\rangle, |\downarrow\uparrow\rangle, |\uparrow\downarrow\rangle, |\uparrow\uparrow\rangle) \rightarrow (t_-, s_0, t_0, t_+)$. To ensure that $|\uparrow\downarrow\rangle$ maps onto the singlet s_0 state on tilting the electric potential, as opposed to the $|\downarrow\uparrow\rangle$ state, $|\uparrow\downarrow\rangle$ is made lower in energy by directing the magnetic field gradient across the two dots to be stronger on the first dot (holding the spin-down electron). The singlet s_0 state is electrostatically lower in energy than the triplet state t_0, when both electrons enter the same dot on tilting the electric potential. Thus, on an adiabatic ramp where electrons initially separated are brought together onto the same dot, the lower energy state $|\downarrow\uparrow\rangle$ maps adiabatically maps onto the s_0 state.

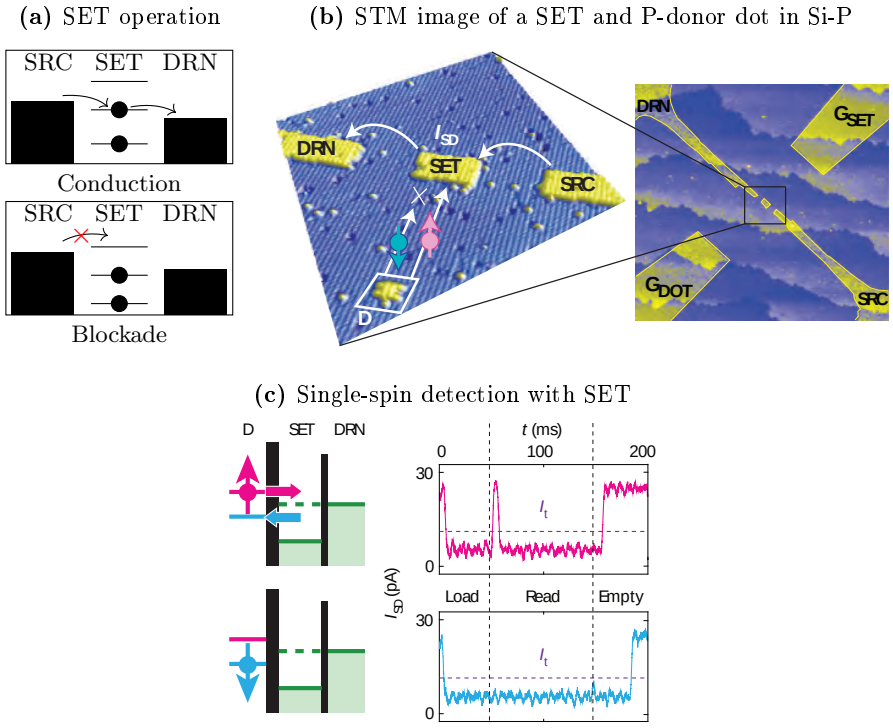

Figure 3.1: Single-electron-transistor measuring single spins in Si-P. **(a)** The single-electron-transistor consists of a source SRC, drain DRN, a gate G_{SET} and a quantum dot labelled SET. The SET energy level can be tuned via a gate or a nearby charge transfer to bring it into the conduction regime (when a SET energy level is in-between the SRC and DRN energy levels) and the blockade regime where there is no current flow (there are no SET energy levels in-between the SRC and DRN energy levels). **(b)** STM image of the first SET to perform single-spin readout on electrons hosted on STM patterned P-donor dots [80]. The yellow regions highlight regions of P-doping. **(c)** Resulting time-traces of the SET current I_{SD} [80]. If the electron on dot D is spin-up, the electron tunnels out and a new electron tunnels in to fill the lower spin-down state on dot D to create a blip in the current during the read phase. If the electron on dot D is spin-down, no charge transfer occurs and the read signal remains constant near zero as the SET is tuned into Coulomb blockade.

may not tunnel off the P-donor dot. Thus, only spin-up electrons cause a change in the SET current as seen by the current moving away from zero, during the read-phase in Figure 3.1c, for a spin-up electron while remaining zero for the spin-down electron. The non-zero current for a spin-up electron returns back to zero current as a spin-down electron eventually tunnels onto the P-donor dot to bring the SET back into Coulomb blockade. If the time-frame of the non-zero current is too small, one may not have sufficient time to detect the presence of the spin-up electron over the background noise. Thus, one may extend the time of this non-zero current signal via a 'latched-readout' mechanism which utilises an extra quantum dot (tunnel coupled

to the main quantum dot holding the target electron). The extra quantum dot has a slow tunnel rate to its reservoir and thus, electrons may only enter this auxiliary quantum dot via the main quantum dot. By utilising the resulting hysteresis effect, similar to that observed in the fabricated 4-dot device discussed in Section 2.2.5, one may trap spin-up electrons onto the auxiliary quantum dot upon which one has a longer time to read out the presence of a spin-up electron [104]. The latched readout mechanism thus, relaxes the high bandwidth requirements to enable high-fidelity sensing of high tunnel rate (between the reservoir and the main quantum dot) spin-up electrons that register fast blips in the current signals. A fast electron tunnel rate between the reservoir and the main quantum dot is desirable in the context of fast qubit state initialisation.

The second prominent charge sensor used to detect electron spins in solid-state quantum dots is the quantum-point-contact (QPC). The QPC consists of a source lead, drain lead and a tuning gate. The leads are setup such that there is ballistic conduction between the source and drain leads on applying a voltage bias across the two leads. A third lead is used to tune the sensitivity of the QPC by changing the electrostatic barrier of the constriction. At low temperatures, on changing the gate voltage, quantised steps are observed in the conductance with the separation given by the conductance quantum $2e^2/h$ as shown in Figure 3.2a [116]. For high sensitivity spin readout, the abrupt change in the QPC current at the step-edge between two quantised current steps is used for charge sensing. When a electron enters or leaves the target quantum dot, the resulting change in the electrostatic potential at the QPC pushes the QPC into one of the two quantised steps in conductance. Thus, the QPC current can be mapped to the charge state on a quantum dot. When combined with single-spin to charge conversion or the two-electron Pauli-blockade readout, the QPC can be used to measure single or two electron spin states [12–14, 111, 117].

A critical requirement of a QPC is the requirement for ballistic conduction across its channel to form the discrete steps in the current. For ballistic conduction to occur the channel length must be much shorter than the mean free path of the electron [116, 118–120]. The electron mean free path in 2D GaAs systems have been shown to range from 1 µm to 1000 µm [121]. However, 2D Si-P δ-layers are disordered conductors where conduction occurs directly through the dopants and as a consequence have a shorter mean free path of 4-6 µm [122]. An alternative sensor similar to a QPC, available in Si-P systems, is the tunnel junction charge sensor (TJCS). The TJCS has two leads: source and drain. However, the electron transport across the gap gives rise to a tunnel resistance rather than quantised current steps seen in the operation of a QPC. The conductance of a TJCS is sensitive to the

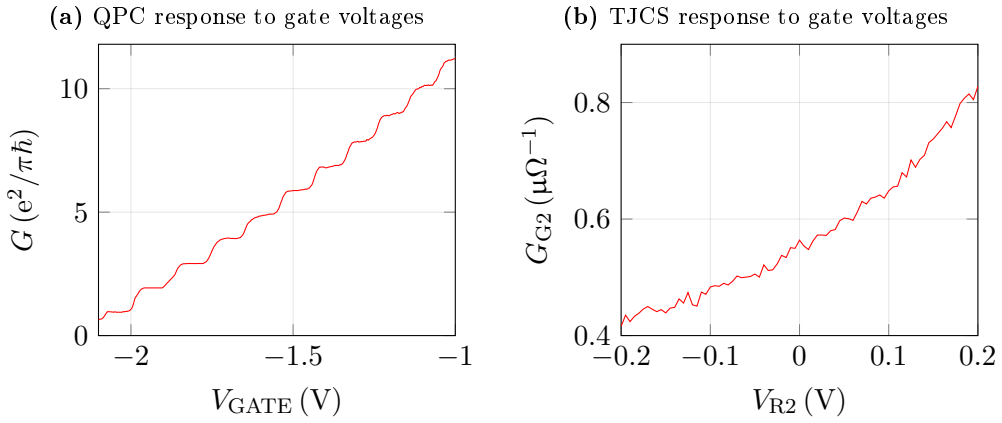

Figure 3.2: Comparing gate responses of quantum-point-contacts and tunnel-junction-charge-sensors. **(a)** Gate voltage conductance (after subtracting contact resistance) of a QPC formed across a GaAs 250 nm-wide channel [118]. The signature response is the quantised conductance steps to which one tunes when using a QPC as a charge sensor. **(b)** Minimum conductance (with respect to the source-drain voltage across the TJCS) of the TJCS T2 in the fabricated 4-dot device discussed in Section 2.2.4 as a function of the voltage applied on R2.

local electrostatic environment as seen by the typical conductance response shown in Figure 3.2b of a TJCS when sweeping the voltage on a gate close to the tunnel junction. Thus, any charges entering or leaving nearby quantum dots perturb the conductance of the tunnel barrier in the TJCS. As there is no quantised step to which one must tune the TJCS, there is no need for a third gate; leaving the TJCS a two-lead sensor [29, 99]. However, the sensitivity is much lower as the change in conductance is gradual rather than abrupt like with a QPC as shown in Figure 3.2.

3.1.2 Development of RF qubit sensors

Resolution of the qubit state must be performed at high speed as the measurement must occur at time-scales much shorter than the qubit decoherence time T_2^*. In the context of modern error correction codes that rely on multiple measurements on the qubits, the measurement time must be much faster than the average qubit error rate to enable one to detect the single qubit errors as they occur [8]. Conventional charge sensors, like the SET or QPC, which rely on measuring DC current across two junctions have their measurement speeds limited by the parasitic capacitance of the wire loom inside the cryogenic dilution refrigerator. The measured DC current is bandwidth limited as the signal must travel up a wire loom over a few metres before it can be amplified at room temperature. This wire loom has a parasitic capacitance of ap-

proximately 2 nF with junction resistances of an SET or QPC ranging approximately 100 kΩ [86, 118]. Since the transimpedance amplifier to convert the current signal into a readable voltage signal is outside the dilution fridge, the measurement bandwidth is approximately 800 Hz. One strategy to overcome the bandwidth limitation is to place the transimpedance amplifier before the wire loom by using a cryogenic DC transimpedance amplifier (with a low output impedance) near the device [123]. One could additionally use a lock-in amplifier to move the signal bandwidth to a region of low noise to improve the signal to noise ratio (SNR); thereby unlocking greater measurement bandwidths [124, 125]. An alternate strategy that achieves equivalent gains in SNR (in combining a cryogenic amplifier with a lock-in amplifier) is to use RF readout where one may utilise the coaxial cables in the dilution fridge as opposed to the DC wire loom to pass the measurement signals [117, 126, 127]. To utilise RF readout, one attaches an LC (inductor-capacitor) resonator to the lead that one would typically utilise to measure DC current of the charge sensor. The resonator acts as a bandpass filter that only allows signals in the range $\omega_0 \pm \Delta\omega$ (where ω_0 is the resonant frequency of the resonator and $\Delta\omega$ is the resonator bandwidth). On applying an RF excitation at frequency ω_0 to the resonator, the RF signal enters the lead associated with the charge sensor and causes the electrons to oscillate across the tunnel junction (whether it is an SET or a QPC). The dissipation caused by the electron oscillations across the resistive tunnel junction changes the quality factor of the resonator to result in a change in the RF signal reflectance. The resonator helps match the charge sensor's impedance to the coaxial line and thereby circumvents any bandwidth issues that would be present when using the DC loom. Low-noise cold amplification[2] can be achieved via readily available cryogenic RF amplifiers [128]. The use of a high frequency resonator upconverts the signal information to a high frequency region given by the passband of the resonator and thereby achieves the lock-in effect.

The dominant mechanism at play in the use of RF resonators with conventional DC charge sensors is the change in the quality factor due to the resistive load of the nano-scale charge sensor. As a resistive load, the applied AC voltage is in phase with the current as shown in Figure 3.3a. The tunnel rate of the electrons across the junction of the charge sensor (for example, the tunnel rate across the source

[2] The purpose of the low-temperature amplification here is not to overcome bandwidth restrictions like with the DC loom, but rather the second use of cryogenic amplifiers. Johnson noise is lower at lower temperatures and thus, the same signal would have a larger SNR at lower cryogenic temperatures when compared to that in room temperature. A cryogenic amplifier helps maintain the larger SNR by amplifying the signal at lower temperatures before the signal arrives at room temperature.

and drain leads in a QPC) is slow when compared to the RF voltage input drive. Thus, the lagging charge movement yields a current (time-derivative of charge) in-phase with the input voltage; a dissipative AC circuit element modelled well via the 'Sisyphus' resistance [109, 110]. However, a different mode of operation is to consider nano-scale sensors that have the current 90° out of phase with the voltage to create a non-dissipative, but reactive load as shown in Figure 3.3b. Here the tunnel rate of the electron oscillation between two sites (for example, between two dots) is much faster than the driving frequency of the input voltage drive. Thus, the charge movement is in-phase with the voltage drive and therefore, the current leads the voltage drive by 90°; modelled well with an AC 'quantum capacitance' circuit element C_q. Conceptually one may consider this AC capacitance to be a perturbation on the capacitor in the LC resonator circuit causing a change in the resonant frequency from $1\sqrt{LC}$ to a lower $1\sqrt{L(C+C_q)}$. When sending in a voltage signal tuned to the original resonant frequency, the resulting shift in the resonant frequency (due to the electron oscillations) causes a change in the reflectance as the initial probe signal at the resonant frequency is now off-resonant to the shifted resonant frequency. Readout by probing shifts in the reactance of the resonator was first applied in superconducting qubits where the qubit perturbs the inductance of the LC resonator [129], while in solid-state qubits, the perturbation is on the capacitance of the LC resonator in the form of a quantum capacitance [30, 32, 57].

One class of sensors utilising the quantum capacitance is the single-lead-quantum-dot (SLQD) sensors where the applied RF voltage oscillates electrons between a reservoir lead and a quantum dot [31, 109, 110, 130]. The SLQD sensor can be used as a charge sensor where, similar to an SET or QPC, nearby charging events tune the dot's energy level away from the reservoir Fermi-level to disable the electron oscillations. Thus, measuring the presence of the oscillations or the lack thereof, via the signal reflectance, one may infer charging events which leads to spin detection via spin to charge conversion methods discussed in Section 3.1.1. The advantage of the SLQD sensor is that it only requires one dedicated quantum dot and one reservoir lead and thereby has reduced the lead count from the conventional SET or QPC from three to one. In addition, the inherent heat dissipation of these sensors is lower than that in a SET as the equivalent load presented by the sensor is typically capacitive rather than the dissipative resistive loads presented by the SET or QPC. The development, optimisation and experimental demonstration of the SLQD sensor in P-doped silicon is discussed in Sections 3.3 and 3.4.

A variation in the SLQD method is to use the reservoir lead strongly tunnel-coupled to one of the two quantum dots hosting a two-electron singlet-triplet qubit (as

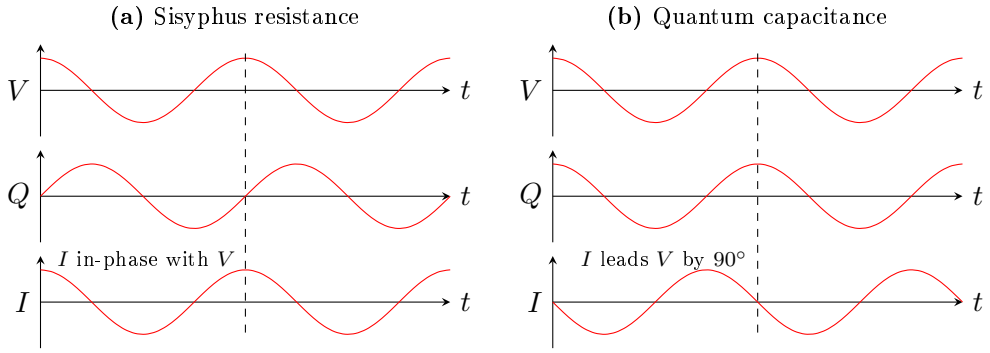

Figure 3.3: Tunnel rates of nano-scale sensor giving rise to AC resistive or capacitive responses. The nano-scale sensors are probed with an RF voltage drive V of frequency ω. The resulting charge movement Q and the current $I \equiv Q'$ are then plotted alongside. **(a)** For typical charge sensors, the RF response in the current is resistive where the current is in phase with the voltage. The charge movement lags the voltage pulse due to a slow tunnel rate of the oscillating electrons (for example, the junction tunnel rate for a QPC). **(b)** When probing typical gate-based sensors, the electron tunnel rate (for example, that between two dots) is much faster than the driving frequency. Thus, the charge movement is in phase with the probe voltage drive. Here, the current leads the voltage by 90°; therefore, one may consider the equivalent circuit element of the nano-scale sensor as an AC capacitance.

opposed to a dedicated quantum dot) to perform singlet-triplet qubit readout [130]. Here, electrons on a singlet-triplet qubit are pushed onto the first dot conditional on the electrons being in a singlet state to enable a third electron to oscillate between a nearby reservoir and the second dot. A possible disadvantage of using the SLQD sensor to probe singlet-triplet states is that the strong tunnel coupling between the reservoir to the second quantum dot, required for the sensor to ensure the fast tunnel rates to obtain the quantum capacitance, may degrade the qubit lifetimes and coherence times as observed in a previous experiment [30]. Nonetheless, the SLQD sensor has been shown to perform spin readout at temperatures of up to 1 K [130] (note that if a high-fidelity qubit can be formed at 1 K, this negates the need for a dilution fridge to operate the devices).

The final class of sensors that take advantage of the quantum capacitance is the single-gate RF sensor which requires no dedicated quantum dot and is used to detect the two-electron singlet-triplet qubit state hosted across two quantum dots [29, 30, 57, 105, 131, 132]. Single-gate RF sensors require no additional control leads and integrate into existing single gates in the device (for example, gates required to form or tune the qubit). The input RF voltage oscillates one of the two electrons (forming the singlet-triplet qubit) between the two quantum dots to

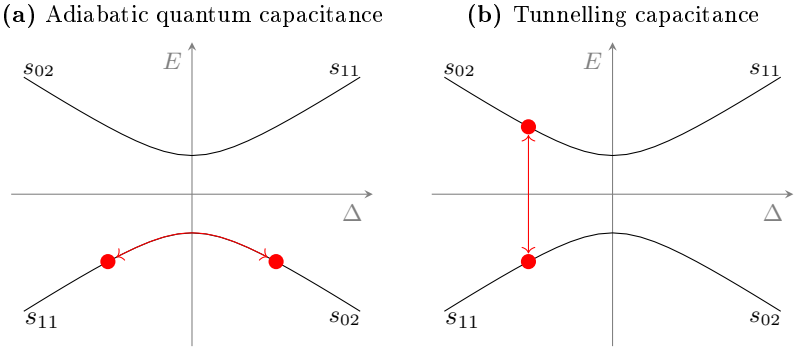

Figure 3.4: Comparing the tunnelling and quantum capacitance modes of operation for single-gate RF readout. The energy diagrams show the singlet branches relevant for single-gate RF readout (triplets forbid electron oscillations) where electrons may oscillate by moving between the s_{11} and s_{02} charge states. **(a)** Quantum capacitance mode of operation where one adiabatically oscillates between the two ground states about either side of zero detuning. **(b)** Tunnelling capacitance mode of operation where one oscillates between the two charge states via the ground and excited states.

separate and bring both electrons onto the same dot. The oscillations only occur, to form the quantum capacitance, if the qubit is in the singlet state as the triplet state forbids the electrons entering the same dot due to Pauli spin blockade. The electrons oscillated by switching between the two singlet-charge states s_{11} and s_{02} as shown in the simplified energy diagrams (triplet states omitted for clarity) in Figure 3.4. Typical operation of the single-gate RF sensor operates in the 'adiabatic quantum capacitance' regime shown in Figure 3.4a. Here, one adiabatically cycles between the two charge states via the ground state eigenstate; a technique that has successfully demonstrated single-shot spin readout [32, 132]. The single-gate RF sensor has also been shown to operate in the 'tunnelling capacitance' mode shown in Figure 3.4b where one resonantly drives the electrons between the ground and excited charge states. The resonant tunnelling method has been used to show single-shot qubit readout using SiGe quantum dots [133]. The advantages and experimental implications of using the two different modes are discussed in Section 4.1.2.

For completeness one should note the cQED (circuit quantum electrodynamics) implementations of the single-gate RF sensors that are desirable by-products in implementing single photon mediated long-distance qubit couplers. Here, one couples the charge state of an electron across two quantum dots, an electric dipole, to a single photon inside a resonant RF cavity [134, 135]. The disadvantage of this method is the need for high quality factor resonators (>5000 [136]) and quantum-limited amplifiers (as a noisy amplifier will destroy the coherence of the single photon in

the cavity). High quality factor resonators and quantum-limited amplifiers typically tend to use superconducting circuitry that cannot operate at the high magnetic fields required for spin qubit operation. Nonetheless, if one could utilise the long-distance spin-photon coupling across two double-quantum-dots, the qubits could be spaced further apart, making it easier to connect to the leads for qubit control [70].

A convenience of using RF reflectometry, common across all the summarised sensor types, is that the input and output signal lines can be combined into a single line via frequency multiplexing [29, 31, 57, 137]. That is, each qubit sensor (to be measured with RF reflectometry) is attached to a separate LC resonator with a different resonant frequency. All the resonators are then connected onto a single transmission line. If one wishes to address a given sensor, then the Rf input voltage is sent to match the frequency of the resonator attached to the sensor. The other resonators will block this RF input voltage signal as the frequency is off-resonant, or out of band, to their LC resonators. Since the probe signals encode information across different frequencies, one may probe multiple frequencies (to address different resonators) to perform simultaneous readout across gates connected to multiple resonators via a single pair of coaxial cables routed to the mixing chamber.

The first long-term challenge of using RF qubit sensors is the construction of low-loss (high quality factor) resonators required for high-fidelity readout. The accepted solution for low-loss resonators is to use superconducting inductors [32, 138]). In addition to the low-loss superconducting resonator, one needs to engineer matching circuitry (for example, via a parallel capacitor [139]) to ensure that there is not a large impedance mismatch between the superconducting resonator (interfacing with the nano-scale device) and the input transmission line to ensure sufficient signal can enter the nano-scale device (via the resonator). Collectively the superconducting resonator and its matching circuitry take up large footprints ($\sim$4 mm^2) mainly due to the need for bond-pads [32, 137, 138]. Therein lies the second long-term challenge of using RF qubit sensors over a large network of multiplexed resonators. That is, larger resonators imply that the resonators will inevitably be further away from the nano-scale device due to the packing geometries. It is important to have the resonators close to the device to avoid large geometric parasitic capacitances that reduce RF readout sensitivity as discussed later in Section 3.2. The proposed solution is to use multilayer lithography and superconducting vias, where it is predicted that one should be able to pattern the resonators with thinner tracks and tighter spacings to achieve a density of thousands of resonators per square centimeter [137].

3.1.3 Comparison of readout fidelities of solid-state qubit sensors

When operating a quantum processor via modern error correction codes, the need for fast high-fidelity single-shot measurements is desirable. Single-shot readout refers to the immediate resolution of a given qubit state in one measurement as opposed to taking the average state over many measurements. In the latter case, one will need to prepare the state identically many times in order to perform the multiple measurements. In general, there are implementations that suggest that one repeats the quantum algorithm and averages the read state over many repetitions to obtain the solution such as the quantum computing proposals using linear quantum optics [140, 141]. However, most modern proposals for universal quantum computers rely on real-time detection of qubit errors and thus, require single-shot detection [8, 142]. The measurement fidelity of a single-shot measurement is the average probability of correctly resolving the basis qubit states[3]. That is, the measurement fidelity is defined as:

$$F_{\text{meas}} = \frac{F_{|0\rangle} + F_{|1\rangle}}{2}, \tag{3.1}$$

where $F_{|0\rangle}$ is the probability of correctly measuring the basis state $|0\rangle$ given a qubit in state $|0\rangle$ and $F_{|1\rangle}$ is the probability of correctly measuring the basis state $|1\rangle$ given a qubit in state $|1\rangle$. Here, $|0\rangle/|1\rangle$ are the measurement basis states for the qubit (for example, $|\downarrow\rangle/|\uparrow\rangle$ for single-spin qubits and singlet-s_0/triplet-t_0 for singlet-triplet qubits). Given fault tolerant measurement fidelities above 99.9%, it is additionally important that the readout time is as fast as possible; specifically, the measurement time must be faster than the average qubit error rate to enable one to enable the real-time error detection required by modern error-correction codes [142]. Table 3.1 lists the fidelities and measurement times of some common experimental demonstrations of single-shot readout in solid-state quantum dots.

The first experimental demonstration of single-shot spin readout in solid-state quantum dots was achieved using a DC-QPC in GaAs where single electron spin-states were resolved with an average measurement fidelity of 83% [111]. Later in an ion-implanted Si-P quantum dot system, a DC-SET implementation achieved a measurement fidelity of 96% [112]. Further work in STM-patterned SETs in Si-P pushed the measurement fidelity of single-spins towards the required fault-tolerant levels (for example, in a surface code) at 99.8% [56]. The measurement fidelity of single-spin readout using the spin-to-charge conversion method shown in Figure 3.1 is given by

[3] That is, the states are not some superposition of the basis states. Thus, only the basis states which do not change on applying the collapse operator shall be considered

the electrical visibility and the tunnelling statistics of the electron between its reservoir and its hosted quantum dot. The electrical visibility refers to the SNR (of the SET or QPC output) of the charge transfer signal (when an spin-up electron tunnels off the quantum dot and a spin-down electron tunnels onto the quantum dot) of a spin-up electron when compared to the steady background that occur on detecting a spin-down electron. The visibility can be improved by increasing the electrostatic coupling between the charge sensor and the quantum dot hosting the target electron spin. That is, a stronger electrostatic coupling implies a larger shift in the tuning on the charge sensor to thereby better utilise the full signal contrast; the full signal contrast is between conduction and blockade in the context of SETs and that between two quantised current steps in the context of QPCs. The electrostatic coupling can be increased by bringing the target quantum dot closer to the charge sensor. One of the reasons why STM-patterned Si-P quantum dots can achieve near fault-tolerant measurement fidelities is because of the ability to place the target quantum dot closer to the charge sensor (up to ∼20 nm in distance) to achieve a large electrostatic coupling between the SET and the target quantum dot, such that the charge-transfer signal brings the SET into complete Coulomb blockade and maximum conduction

Sensor	Platform	Type	Leads	Fidelity	t_{meas}	SNR
DC-QPC	GaAs	Single-spin	3	83% [111]	500 µs	3
RF-QPC	GaAs	Singlet-triplet	3	97-98% [14]	1 µs	3
DC-SET	Si-P	Single-spin	3*	96% [112]	100 µs	4
DC-SET	Si-P	Single-spin	3*	93% [80]	40 ms	5
DC-SET	Si-P	Single-spin	3*	98.4% [143]	1 ms	5
DC-SET	Si-P	Single-spin	3*	99.8% [56]	55-65 ms	3
RF-SET	Si-P	Single-spin	3*	91% [96]	15 ms	12
SLQD	Si-P	Single-spin	1*	N/A [31]	$<$ 1 µs	1-2
SLQD	Si-MOS	Singlet-triplet	1†	98% [130]	500 µs	2
SG-RF(a)	Si-P	Singlet-triplet	1†	83% [32]	300 µs	2
SG-RF(a)	Si-MOS	Singlet-triplet	1†	73% [132]	2 ms	1
SG-RF(t)	SiGe	Singlet-triplet	1†	98% [133]	6 µs	2

Table 3.1: Experimentally measured spin-readout fidelities in quantum dot systems. The reported results are listed across different platforms. The sensor types include quantum-point-contact (QPC), single-electron-transistor (SET), single-lead-quantum-dot (SLQD) and the single-gate RF (SG-RF) sensors. Note that the lead counts with $*$ indicate an extra dedicated quantum dot for the sensor. The † on the lead counts indicates leads that are multi-purposed and must already be present for qubit control. The listed fidelities are that for single-shot spin readout, while t_{meas} is the associated measurement time and SNR is the approximate signal-to-noise ratio. SG-RF(a) refers to the use of adiabatic quantum capacitance while SG-RF(t) refers to the use of the tunnelling capacitance.

regimes unlike gate-defined quantum dots (>100 nm). An additional improvement to the visibility can come from low-temperature DC amplification[4] or via the use of a cryogenic RF amplifier coupled to an RF-SET [96]. High electron visibility implies high SNR and thus, one may increase the measurement speed (with the noise scaling by square-root of the bandwidth, one may increase the bandwidth as long as SNR is much larger than one). However, the measurement fidelity and readout times are also a function of the tunnelling statistics. For example, the measurement fidelity will be limited if the electron charge transfer signal is too short to resolve in time given the available bandwidth due to fast electron tunnel rates between the quantum dot and its associated reservoir. Similarly, long tunnel times between the quantum dot and its associated reservoir implies that one needs to wait longer to ensure that any spin-up electrons have tunnelled off the quantum dot. Therefore, high-speed, high-fidelity measurements of single-spin electrons requires optimisation of the electron tunnel rates (between its host quantum dot and reservoir), maximisation of the electrostatic coupling (between the quantum dot and the charge sensor) and maximisation of the available signal to noise ratio on the charge sensor (either via larger charge sensor conductivity or using specialised circuitry like that in an RF-SET). The SET and QPC have large lead counts and require an extra dedicated quantum dot in the case of the SET. To reduce the lead count (to make it easier on scaling up to many qubits), one may use the SLQD sensor (with a dedicated quantum dot) which has shown the capability to achieve high electron visibility in under 1 µs in the context of spin-readout as shown by the results discussed in this thesis in Section 3.4 [31]. Experimental demonstration of single-shot single-spin readout with a SLQD sensor has recently been demonstrated by a current PhD student Mark R. Hogg.

High-fidelity singlet-triplet readout for the two-electron spin state hosted across two quantum dots has also been experimentally demonstrated. In GaAs, RF-QPCs have been shown measurement fidelities of up to 98% with measurement times of $1\mu s$ by using standard Pauli-spin blockade techniques [14]. In reducing the lead counts from 3 dedicated leads to a single multi-purposed lead (that is, integrating the sensor into a mandatory control gate), the single-gate RF (using adiabatic quantum capacitance) sensor successfully showed single-shot readout in Si-P at a measurement fidelity of 83% [32]. Single-gate RF sensing (using adiabatic quantum capacitance) was also shown in Si-MOS with a measurement fidelity of 73% [132]. By using the tunnelling capacitance mode of measurement, single-gate RF sensing was also shown in single-shot using SiGe quantum dots at a measurement fidelity of

[4] Johnson noise increases with temperature. Thus, to maintain good SNR, the signal should be amplified while in the low-temperature environment.

98% [133]. By utilising the SLQD sensor in Si-MOS where the sensor dot was one of the two dots hosting the singlet-triplet qubit, a measurement fidelity of 98% has also been recently demonstrated [130], as predicted by previous experiments [31]. The SLQD sensor operating in the configuration using the quantum dot hosting the singlet-triplet qubit may not a desirable long-term solution as the strong reservoir to dot coupling required in operating the SLQD sensor may degrade the singlet-triplet qubit coherence times [30]. Thus, the single-gate RF sensor is proposed in large-scale architectures[5] [29, 108]. As discussed in this thesis, the physics governing the SLQD sensor is different to that of the single-gate RF sensor and thus, optimisation is different. Nonetheless, to improve the single-gate RF sensor measurement fidelities towards fault-tolerance, a simple change is to utilise resonators with high quality factors (such as resonators using low-loss superconducting inductors instead of PCB surface-mount chip inductors [32, 138]). A high quality factor resonator implies a narrow peak and thus, any shift in the resonance peak due to the quantum capacitance will cause a larger shift in the signal reflectance as discussed in the next section.

3.2 Resonance circuitry for detecting quantum capacitance

Before designing or operating the low-lead count SLQD and single-gate RF sensors, it is useful to separate the PCB electronics from the quantum physics governing the nano-scale qubit sensor when trying to maximise the measurement fidelities. As both the SLQD and single-gate RF sensors utilise a quantum capacitance during readout, the actual circuit model description is universal across both sensors. That is, the qubit sensors produce an AC quantum capacitance that is detected via resonator circuitry external to the nano-scale device. Thus, the resulting circuit model (of the macroscopic resonator and quantum capacitance from the nano-scale device) enables one to design with optimal resonator parameters (for example, overall quality factor or the resonant frequency) to maximise the measurement fidelity by only considering the PCB electronics. Finally, on building the equivalent circuit model of the surrounding PCB electronics, proper methods of analysis shall be established to clarify misconceptions that may be gathered from literature. For example, the

[5] The SLQD can still operate as a high-fidelity qubit sensor (for both single-spin qubits via spin-to-charge conversion or singlet-triplet qubits via Pauli blockade) when using a dedicated quantum dot. However, its use for singlet-triplet readout when using one of the dots forming the singlet-triplet qubit is not considered a long-term solution.

proper definition of the RF readout signal shall be discussed in terms of the IQ plane [29, 31, 32, 57, 139] rather than the phase response alone as implied in previous works found in the literature [30, 105, 110, 131, 132].

3.2.1 Equivalent circuit model of resonator and quantum dot

To create the electron oscillations that yield a measurable quantum capacitance, an RF voltage drive must be injected into the corresponding lead of the device to electrostatically drive the electron between the two sites (reservoir and quantum dot in the case of a SLQD sensor and between two quantum dots in the case of the single-gate RF sensor). To measure the small AC quantum capacitance, one attaches an LC resonator to the gate lead as shown in Figure 3.5. The resonator is typically implemented by connecting an inductor L between the coaxial line and the device lead. The capacitance element C_p of the LC resonator comes from the geometric parasitic capacitance of the inductor rather than that of a physical dedicated circuit element. The resonator will have internal losses modelled via a series resistance R. In the case of surface mount inductors, R is dominated by the resistance of the wire winding in the inductor. One may reduce the internal losses R, by using superconducting inductors. In the case of superconducting inductors R is dominated by dielectric losses, radiative losses and/or defects in the superconducting films [144, 145]. Finally, the discussion in Section 3.1.2 highlighted that from the tunnelling response of electrons between two sites can lead to a resistive circuit element (in the case of tunnel rates being slower than the input voltage drive frequency) and a capacitive element. Thus, in general the current response of the nano-scale sensor is best modelled via a resistor R_q and capacitor C_q as shown in Figure 3.5. Note that the entire circuit is the equivalent[6] AC-domain circuit involving the resonator interfacing between the coaxial lines in the fridge to the lead corresponding to the nano-scale sensor.

3.2.2 Using the resonator to detect electron oscillations

Given the equivalent circuit model of the resonator and the nano-scale sensor in Figure 3.5, this section will discuss how the resonator apparatus can be used to detect electron oscillations. It is first instructive to study the characteristics of the interface

[6] Note that this circuit model is simply the application of linear circuit theory where this is the equivalent circuit model for the system at hand. Thus, any details such as resistive losses in the inductor, stray capacitances and other minor corrections are absorbed into this single equivalent model.

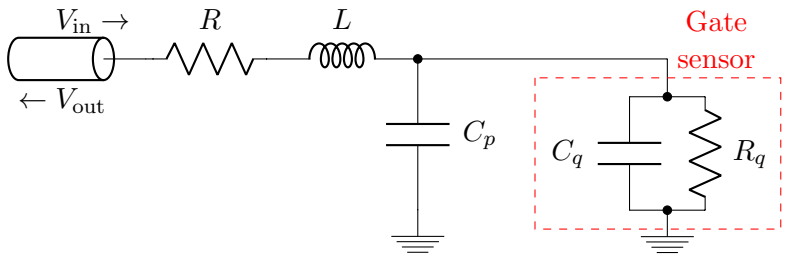

Figure 3.5: Equivalent circuit model of a resonator used to detect single electron oscillations in a nano-scale device. The resonator consists of the inductor L and its associated capacitor, typically parasitic due to the resonator geometry, C_p. The resistance R represents internal losses intrinsic to the resonator itself. The resonator attaches itself to a transmission line from which one sends or receives RF voltage signals. One connects the resonator (via bond wires) to the gate lead of a nano-scale device (for example, a SLQD sensor or a single-gate RF sensor). The resulting electron oscillations can be modelled via a quantum capacitance C_q (for electron oscillation currents leading the RF input voltage by 90°) and the Sisyphus resistance R_q (for electron oscillation currents in-phase with the RF input voltage).

between the coaxial line and the resonator in terms of quality factors. Quality factors are directly measurable quantities of a resonator that abstract away the values of individual circuit elements. This simplification enables the experimenter to design and characterise resonators using general quantities that are agnostic to the many ways one may model the equivalent circuit of the resonator on the PCB [30, 109, 110, 146]. The choice of quality factors (internal and external) strongly influences the measured readout signal strength as discussed below. It is important to realise how the choice of quality factors give rise fo the different operating regimes.

Now consider a general series RLC circuit (a resistor, inductor and capacitor connected in series). By definition the quality factor Q is 2π times the ratio of the energy stored to the power dissipated per cycle. Thus, one notes that $\text{Q} \equiv \omega \cdot \frac{\text{Energy Stored}}{\text{Power Loss}}$. For a series RLC circuit, the energy stored is $\frac{1}{2}LI^2$ and the power loss is I^2R. Thus, the quality factor for a series RLC circuit is:

$$\text{Q} = \frac{\omega_0 L}{R}, \tag{3.2}$$

where $\omega_0 = 1/\sqrt{LC}$ is the resonant frequency of the RLC resonant circuit. The resulting bandwidth of the bandpass filter formed by the RLC circuit can be shown to be $\sim\omega_0/\text{Q}$. Thus, a high quality factor implies that the signal bandwidth will be restricted (that is, a narrow peak in the frequency response transfer function). In experiments the RLC resonator circuit shown in Figure 3.5 is connected an external

transmission line. Upon loading the RLC circuit to a transmission line of impedance[7] Z_e, the 'effective quality factor' (taking into account the total impedance of the circuit[8]) is now:

$$\mathrm{Q_{eff}} = \frac{\omega_0 L}{R + Z_e}. \tag{3.3}$$

Now one distinguishes the 'internal' quality factor $\mathrm{Q_{int}}$ and the 'external' quality factor $\mathrm{Q_{ext}}$ as follows:

$$\mathrm{Q_{int}} \equiv \frac{\omega_0 L}{R} \tag{3.4}$$

$$\mathrm{Q_{ext}} \equiv \frac{\omega_0 L}{Z_e} \tag{3.5}$$

$$\mathrm{Q_{eff}^{-1}} = \mathrm{Q_{int}^{-1}} + \mathrm{Q_{ext}^{-1}}. \tag{3.6}$$

$$\mathrm{Q_{eff}} \equiv \frac{\mathrm{Q_{ext}}\mathrm{Q_{int}}}{\mathrm{Q_{ext}} + \mathrm{Q_{int}}}. \tag{3.7}$$

The internal quality factor $\mathrm{Q_{int}}$ represents the total losses within the resonator circuit itself, with a low internal quality factor representing high internal losses. The external quality factor relates to the coupling interface between the resonator circuit and the external transmission line. The significance of the external quality factor $\mathrm{Q_{ext}}$ is best understood in terms of the circuit reflectance. That is, any AC voltage signal sent through the transmission line will observe an impedance presented by the resonator circuit. An impedance mismatch will result in signal reflection while perfect impedance matching results in the AC signal getting completely absorbed by the resonant circuit. In the context of getting the RF signal to enter the gate lead of the qubit sensor, one should be close to perfect impedance matching. However, as discussed below, perfect impedance matching may not be desirable in the context of obtaining maximal readout signal strength for high fidelity qubit readout. Now noting the impedance of a series RLC circuit $Z = R + j\omega L + \frac{1}{j\omega C}$ and the definition of voltage reflectance $\rho \equiv \frac{Z - Z_e}{Z + Z_e}$, it is easily shown that:

$$\rho \equiv -\frac{1 - \frac{\mathrm{Q_{ext}}}{\mathrm{Q_{int}}}\left(1 + j\mathrm{Q_{int}}\left(\frac{\omega}{\omega_0} - \frac{\omega_0}{\omega}\right)\right)}{1 + \frac{\mathrm{Q_{ext}}}{\mathrm{Q_{int}}}\left(1 + j\mathrm{Q_{int}}\left(\frac{\omega}{\omega_0} - \frac{\omega_0}{\omega}\right)\right)}. \tag{3.8}$$

[7] It is stressed that this is not necessarily the characteristic 50 Ω-impedance of the transmission line but the net impedance of the object to which the resonator couples. In practice, the coupling to the external transmission line may be modified via the resonator geometry or adding extra circuit elements such as a parallel capacitor [139, 146].

[8] The external impedance is considered to have a negligible reactance term in this analysis.

The reflectance is given as a complex phasor where the real and imaginary parts are termed the in-phase (I) and quadrature-phase (Q) components. The magnitude of the complex vector is the amplitude of the reflected voltage signal with respect to the input voltage signal, while the complex argument is the phase of the reflected voltage signal with respect to the input voltage signal. The resulting reflectance responses are plotted in Figure 3.6. The plots show, as a function of input signal frequency, the reflected amplitude and phase responses. The phasor representations of the amplitude and phase values are also plotted in the IQ-plane. Now one may investigate three regimes where the resonator is to be termed 'under-coupled' if $Q_{ext} > Q_{int}$, 'critically-coupled' if $Q_{ext} = Q_{int}$ and 'over-coupled' if $Q_{ext} < Q_{int}$ [147]. Note that the effective quality factors are kept the same in all three regimes for clarity.

The first regime shown in Figure 3.6a is the under-coupled regime. Here the external quality factor dominates the internal quality factor and thus, implies that the losses in the resonator are much greater than the equivalent external losses to the transmission line. Equivalently stated, the impedance of the resonator is much greater than that of the transmission line. In the extreme limit where $Q_{ext} \gg Q_{int}$, the resonator circuit looks like an open circuit termination to the transmission line. The boundary condition for an open-circuit termination is given by Kirchoff's current law which states that current cannot escape; thus, the reflected current (moving in the opposite direction to the incident current) must be equal in amplitude and phase to the incident current yield zero net current. As voltage along the transmission line is proportional to the current, the voltage must also be equal in amplitude and phase to the incident voltage signal. Thus, at resonance, one expects the relative phase difference between the incident and reflected voltage signals to be zero. Due to the impedance mismatch, the resonator does not show full absorption (that is, zero amplitude response) at resonance. The characteristic signature of the under-coupled regime is the positive phase slope at resonance.

The second regime shown in Figure 3.6b is the critically-coupled regime. Here, the internal and external quality factors are equal and thus, due to the impedances being matched, there is no signal reflection at boundary between the transmission line and the resonator circuit when at resonance. The characteristic signature of the critically-coupled regime is the zero reflected amplitude response at resonance. The phase is undefined in the critically coupled regime due to the null reflected signal.

The third regime shown in Figure 3.6c is the over-coupled regime. Here, the internal quality factor dominates the external quality factor. Equivalently stated, the impedance of the resonator is much smaller than that of the transmission line. In the extreme limit where $Q_{int} \gg Q_{ext}$, the resonator circuit looks like a short circuit

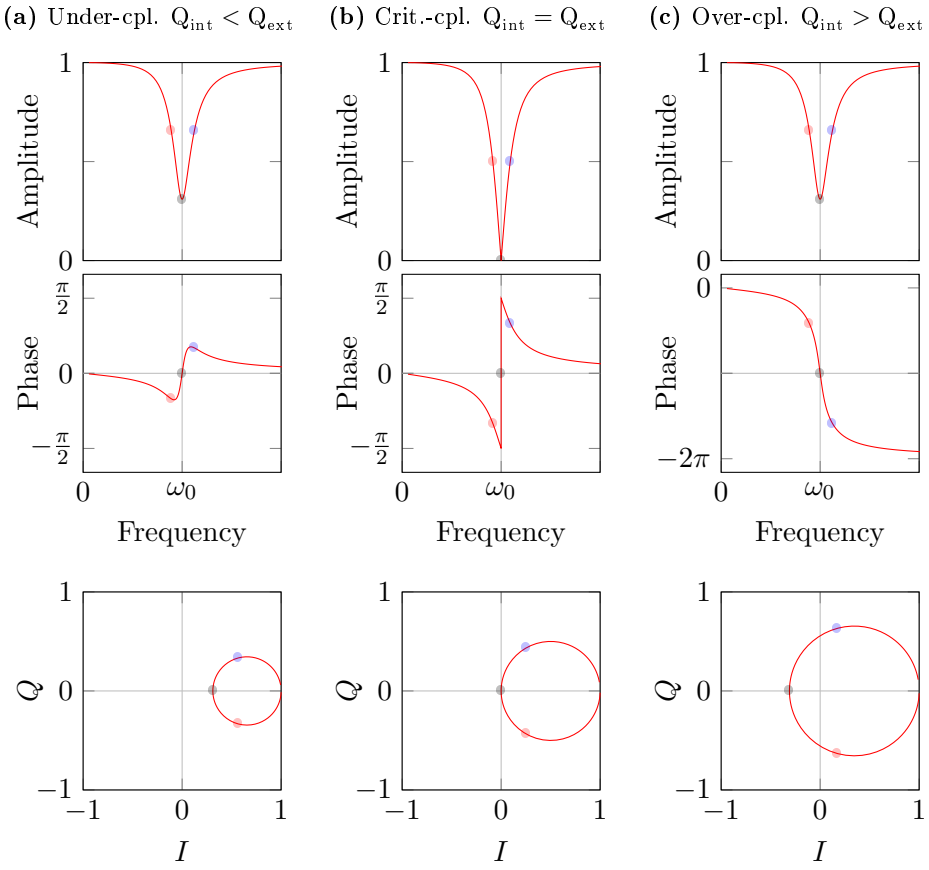

Figure 3.6: Resonator reflectance for different quality factor coupling regimes. For each coupling regime, the reflected amplitude and phase responses are plotted as a function of frequency. The IQ associated response is then plotted on the IQ-plane. The resonators have a resonant frequency ω_0. The resonator only undergoes full absorption of the input signal at resonance if the impedances of the transmission line and the resonator match; that is, at critical coupling when $Q_{int} = Q_{ext}$. The black dot indicates the resonant frequency in each plot, while the red and blue dots indicate the lower and upper frequency bands when the amplitude is half-way between its minimum reflection and maximum reflection of unity. Note that the effective quality factor is kept the same across all three regimes for clarity. **(a)** Under-coupled regime where the external quality factor dominates the internal quality factor. A characteristic signature of the under-coupled regime is the positive phase slope at resonance. **(b)** Critically-coupled regime where the internal and external quality factors match. Here the phase at resonance is undefined. **(c)** Over-coupled regime where the internal quality factor dominates the external quality factor. A characteristic signature of the over-coupled regime is the negative phase slope at resonance.

termination to the transmission line. The boundary condition for a grounded termination is that the voltages must sum to zero. Unlike the open-circuit termination where the voltage at the end is twice that of the input voltage (as the reflected signal has the same phase as the input signal), the reflected voltage must be the negation of the incident voltage wave. A negated voltage translates to a phase change of π as seen by the IQ curves encircling the origin in the IQ plane unlike that in the under-coupled regime in Figure 3.6a. Due to the impedance mismatch, the resonator does not show full absorption (that is, zero amplitude response) at resonance. The characteristic signature of the over-coupled regime is the negative phase slope at resonance.

For each regime in Figure 3.6, there are red and blue dots indicating the points in the IQ plane where the amplitude response is at half its peak height. One must note that although the effective quality factors are the same in the plots showing the under-coupled and over-coupled regimes, the resonator response traces out wider margins in the IQ-plane for the over-coupled case. The wider spread of the over-coupled response on the IQ-plane is important as shown later when selecting the best quality factors in detecting a quantum capacitance.

When using the resonator with a device, the nano-scale sensor either degrades the internal quality factor on presenting a Sisyphus resistance or shifts the resonant frequency due to a quantum capacitance. In the case of a Sisyphus resistance (for example, that presented by a SET or QPC), the junction resistance itself will degrade the internal quality factor of the resonator and more so when the junction becomes conductive. Typically one uses matching capacitors to tune the external quality factor to match the degraded internal quality factor (to ensure maximal signal transfer to the device lead) when no electrons shuttle across the junction and there is minimal junction conduction [31, 139, 146]. On achieving junction conduction, the internal quality factor degrades further (due to the dissipation across the tunnel junction) and the RF readout signal contrast moves from the critically-coupled regime to the under-coupled regime. That is, the readout signal decreases along the I-axis on the IQ plane and there is no phase change (as the resonant frequency of the resonator circuit remains unperturbed). Thus, one typically only measures the reduction in the reflected amplitude response [14, 33, 109].

However, in the case of measuring a quantum capacitance, there is no dissipation to perturb the resonator quality factor. Nonetheless, the resonant frequency is instead perturbed to a lower frequency by $\delta\omega$. The resulting shift in the signal reflectance $\Delta\rho$ is proportional to the qubit readout signal strength Υ given an input incident voltage signal of amplitude V_{in}:

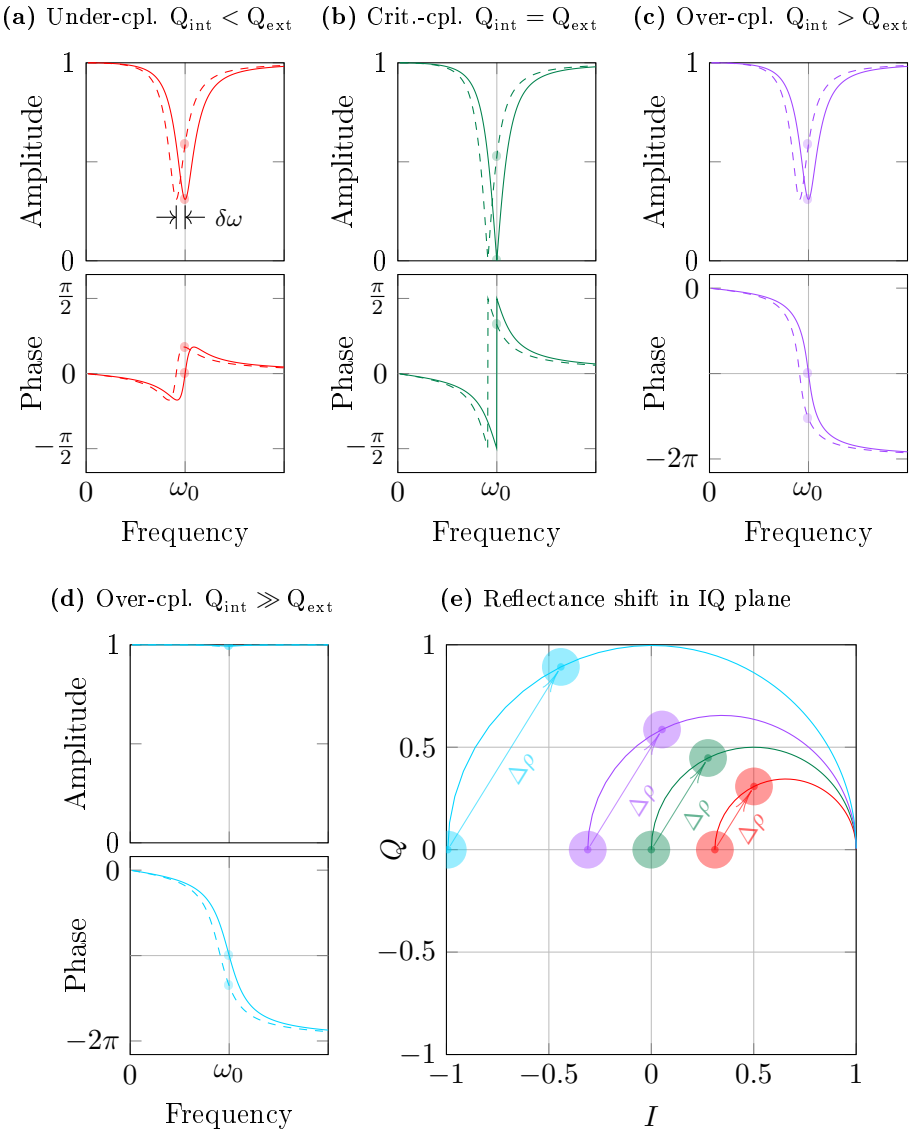

Figure 3.7: Shift in reflectance when measuring quantum capacitance over different quality factor coupling regimes. For each coupling regime, the reflected amplitude and phase responses are plotted as a function of frequency. The resonators have a resonant frequency ω_0 which shifts to $\omega_0 - \delta\omega$ on detecting a quantum capacitance as shown by the dashed curves. The markers indicate the shift in the reflected response on measuring a quantum capacitance while continuing to probe the incident voltage signal at ω_0. Note that the effective quality factor is kept the same across all four regimes for clarity (thus, the peak widths are all the same). **(a)** Under-coupled regime where the external quality factor dominates the internal quality factor. **(b)** Critically-coupled regime where the internal and external quality factors match. **(c)** Over-coupled regime where the internal quality factor dominates the external quality factor. **(d)** Far over-coupled regime where the internal quality factor is much higher than the external quality factor. **(e)** The responses in (a)-(d) are plotted in the IQ plane. The curves indicate the possible shifts in the reflectance that may occur for different frequency shifts. The markers indicate a typical shift with circles indicating the typical noise cloud measured in the I and Q channels. The SNR is proportional to the net change in the reflectance $\Delta\rho$ on the IQ plane.

$$\Upsilon = V_{\text{in}} \Delta\rho. \tag{3.9}$$

Since the input voltage signal is still at the initial resonant frequency, the reflected amplitude and phase responses effectively trace out the amplitude and phase responses at $\omega_0 + \delta\omega$ as shown in Figure 3.7. The shift in the reflected response for the different quality factor regimes are shown in Figure 3.7a-c, with Figure 3.7d showing the extreme case when the internal quality factor is much higher than the external quality factor where the initial response (when no quantum capacitance is present) lies in $(I, Q) = (-1, 0)$ on the IQ-plane. The combined shifted response in the amplitude and phase is best viewed in the IQ plane. When no quantum capacitance is present, the reflected signal (noting that the incident voltage input is set to the original resonant frequency ω_0) remains on the I-axis. The shaded circles illustrate the level of expected noise that would be typically seen in the I and Q channels during experiments[9]. The curves in the IQ-plane in Figure 3.7e show the points in which the shifted response may move on the IQ-plane due to a shift in the resonant frequency from a quantum capacitance. A larger quantum capacitance (larger shift in the resonant frequency) or a higher effective quality factor (a narrow peak) implies that the contrast in shifted reflected response is greater with the largest shift ending up at $(I, Q) = (1, 0)$. As there will still be noise at the shifted point, there are shaded circles drawn there too. The effective signal to noise ratio is the distance moved in the IQ-plane divided by the noise standard deviation in the IQ plane. For the same effective quality factor, the IQ plane responses from Figure 3.7a-c clearly show that having the external quality factor dominate the internal quality factor is undesirable as the shift in the reflectance is the smallest.

In the over-coupled regime (where the internal quality factor dominates the external quality factor), a small shift in the resonant frequency results in a shift in the reflected response that traverses a small portion of the semi-circles in the IQ-plane (purple and light blue curves in Figure 3.7e), with the amplitude remaining mostly unperturbed while the changes mostly occur in the phase. This leads to many authors only looking at the shifted phase response [30, 105, 110, 131, 132]. However, maximal signal strength is obtained when observing the overall shift in the reflected signal in the IQ-plane [29, 31, 32, 57, 139]. In addition, by only looking at the phase shift, one would incorrectly declare that being close to the critically coupled regime

[9] The noise comes from typical thermal Johnson noise, stochastic tunnelling noise [110, 148] or photon shot noise [149]. Photon shot noise affects the phase of the input RF voltage signal to cause noise in the phase relationship between the voltage and current signals (which gives rise to the quantum capacitance) to create a source of phase noise in the qubit readout signal.

yields the maximal signal response. For example, consider the over-coupled response given in purple with the severely over-coupled response in light blue given in Figure 3.7e. The purple curve has a greater phase signal response (approximately 49% more at 95.1° for the purple curve verses 63.7% for the light blue curve), but the light-blue curve has a greater shift (and thus, a greater signal to noise ratio) on the IQ-plane (approximately 52% more at 0.69 for the purple curve verses the 1.05 light blue curve).

As the shift in reflectance $\Delta\rho$ on the IQ-plane relates to the readout signal strength Υ, it is useful to find an analytic expression to use in finding the optimal quality factors for a given experiment. Now if a quantum capacitance C_q were present, due to electron oscillations between two sites, the resonant frequency will shift from $1/\sqrt{LC_p}$ to $1/\sqrt{L(C_p + C_q)}$. Taking this shift in resonant frequency to be perturbative, the change in reflectance, derived in Appendix D.1, is approximately:

$$\Delta\rho = \frac{2\mathrm{Q}_{\mathrm{ext}}\mathrm{Q}_{\mathrm{int}}^2}{(\mathrm{Q}_{\mathrm{ext}} + \mathrm{Q}_{\mathrm{int}})^2} \cdot \frac{C_q}{C_p}. \tag{3.10}$$

Thus, for an input signal voltage amplitude of V_{in}, the measured change in the reflected response is:

$$\Upsilon = K\eta_{\mathrm{loss}}V_{\mathrm{in}} \cdot \frac{2\mathrm{Q}_{\mathrm{ext}}\mathrm{Q}_{\mathrm{int}}^2}{(\mathrm{Q}_{\mathrm{ext}} + \mathrm{Q}_{\mathrm{int}})^2} \cdot \frac{C_q}{C_p}. \tag{3.11}$$

Here η_{loss} is the factor of the signal amplitude that remains when entering the resonant circuit and K is the net gain on the reflected signal amplification chain. One may obtain the measured signal response from the IQ demodulator. The point where there is no quantum capacitance, in the IQ plane, will shift by distance Υ upon its presence. Equation 3.11 neatly highlights the significance of reducing the parasitic capacitance C_p (due to $\Upsilon \propto 1/C_p$) and the benefits of having a high effective quality factor. However, in order to decide the optimal choice in quality factors, it is important to consider the role of quality factors when considering the net RF signal that reaches the gate lead of the nano-scale sensor V_{ac}. Finding the voltage on the device lead is also useful when calculating the quantum capacitance, as shown in later sections, since the quantum capacitance is nonlinear and depends on the voltage amplitude at the gate V_{ac}.

In the circuit model, V_{ac} is equivalent to the voltage division across the capacitor. To find the load voltage, consider the 'load' to be the entire RLC circuit. Taking the spatial phase as zero across the RLC circuit element (treated as a lumped element as the size of this circuit element is much smaller than the wavelength of the RF

drive), the total voltage deposited upon this load will be given by $V_{\text{in}}(1+\rho)$, where ρ is the reflection coefficient [150]. Now given the voltage across the lumped load, the voltage drop across the capacitor can be shown to be boosted by Q_{int}. Thus, writing ρ in terms of Q_{int} and Q_{ext}, the voltage at the gate of the device is:

$$V_{ac} = 2\eta_{\text{loss}}\text{Q}_{\text{eff}}V_{\text{in}}. \tag{3.12}$$

One immediate use for this equation is that one can calibrate the losses in sending a voltage signal to a given gate in the nano-scale device. That is, the RF broadening of a charge transition gives the voltage amplitude V_{ac} on the device lead for a given input voltage amplitude V_{in}. Thus, as the effective quality factor is known from characterising the resonator, the loss can be found by fitting the linear relation between V_{ac} and V_{in}.

Finally note that although the heavily over-coupled regime gives larger shifts in reflectance, one should not achieve this regime by solely decreasing Q_{ext} to zero for that would imply that no signal enters the resonant circuit to trigger the electron oscillations required to manifest the quantum capacitance. Figure 3.7d clearly shows that the majority of the input voltage signal does not reach the device in the severely over-coupled regime as most of the signal is reflected at resonance. If the severely over-coupled regime were to be reached by setting the external quality factor to zero, the effective quality factor becomes zero and by Equation 3.12, the voltage signal amplitude on the gate lead is zero. Thus, one typically sets the internal quality factor to be as high as physically possible in the over-coupled regime (usually via the use of low-resistance inductors such as superconducting inductors). The external quality factor is set as high as possible (by impedance matching the external transmission line to the resonator via capacitance networks [137, 139, 146]) with the limit set by the required circuit bandwidth, which approximately relates to the quality factor via $BW \sim \omega_0/\text{Q}_{\text{eff}}$ [147]. That is, having too high an effective quality factor limits the bandwidth of the readout signal to which one may measure. Given that the T_2^* is expected to be in the order of 10^{-7}-10^{-6} s [17, 34, 69], in the context of performing error detection, the readout time must be faster than 1 µs, leading to required bandwidths in the order of 1-10 MHz. Thus, with a resonant frequency of 100 MHz, the effective quality factor must not exceed 100. Note that the bandwidth cannot be readily increased by increasing the resonant frequency as the electron tunnel rates (whether in a SLQD or a single-gate RF sensor) may not be fast enough to respond such that the charge is perfectly in phase with the voltage to get a good quantum capacitance as shown in Figure 3.3. However, in the case of a single-gate RF

sensor operating in the tunnelling capacitance regime as shown in Figure 3.4, one may have resonant frequencies in the order of 5 GHz (to match the tunnel-coupling [133]) and thus, achieve 10 MHz bandwidths by using an effective quality factor of 500.

3.2.3 Summary of design considerations

The analysis presented in this section place certain design guidelines regarding optimal RF readout. The key guidelines are:

- The geometric parasitic capacitance C_p of the resonator must be made as small as possible. That is, the greatest percent change in the resonant frequency $1/\sqrt{LC_p}$ due to a quantum capacitance comes from making C_p small. One can minimise C_p by reducing the inductor footprint, reducing substrate electric permittivity and removing nearby copper ground planes.
- The internal quality factor $\mathrm{Q_{int}}$ must be made as large as possible (see below).
- The external quality factor $\mathrm{Q_{ext}}$ is set to the maximum value such that one still retains the required measurement bandwidth (given by the effective quality factor $\mathrm{Q_{eff}}$) while remaining in the over-coupled regime.

To increase the internal quality factor (for maximum readout signal strength), one usually reduces the resistance of the inductor. One may make the resistance zero by using a superconducting inductor, in which case, the losses limiting the internal quality factor are:

- Dielectric losses - RF signals interacting with the surrounding dielectric will undergo dissipation. One can reduce dielectric losses by etching away the surrounding substrate dielectric around the inductor [151].
- Radiative losses - source of loss due to the large inductor footprint acting as an antenna to radiate RF signals away. One can reduce radiative losses by using a smaller inductor footprint [145].
- Defects in film - source of loss due the RF signal exciting pools of charge trapped within substrate defects. Low defect superconducting films can be optimised at the fabrication level by varying the growth and etching strategies [144].
- Magnetic fields - large magnetic fields (as required for the typical operation of spin qubits) can cause the substrate electrons to align with the magnetic field and thus break superconductivity. One can reduce the impact of magnetic

fields by placing the superconducting inductor parallel with the magnetic field and by using a superconductor with a high critical field (maximum magnetic field before superconductivity breaks) such as NbTiN. In addition, the critical field is inversely proportional to the superconducting film thickness. Thus, thin NbTiN films are a good candidate for the detection resonators [152–154].

- Abrikosov vortices - stray magnetic fields can cause supercurrent vortices within the superconducting film that cause resistive losses and degrade the superconductivity. One may disrupt the formation of Abrikosov vortices by patterning meshed grids on the superconductor [154].

3.3 Theoretical model of a single-lead-quantum-dot sensor (SLQD)

Whilst the proposed singlet-triplet architecture aims to use single-gate RF sensors integrated into pre-existing gates for singlet-triplet readout, the utility of a charge sensor was highlighted in Figure 2.2.5 in the context of device characterisation and verification[10]. Thus, it is desirable to have compact charge sensors in the design of the overall architecture to act as diagnostic probes. The SLQD sensor can be inserted into Si-P devices without taking much space real-estate as it requires only one dedicated lead. In the scope of this thesis, the development of the SLQD sensor has paved the pathway to optimise the RF circuitry for the single-gate RF sensor.

In order to better understand the optimal operating conditions and the impact of all SLQD parameters (such as electron tunnel rates Γ_0, resonant frequency ω_0, input voltage amplitude V_{in}, resonator quality factors and electron temperature), an analytic model was built on previous theoretical ideas where one considers a rate equation describing the dot to reservoir electron oscillations in the SLQD sensor [109]. The key points addressed and improved in the modelling of the SLQD sensor, when compared to previous literature, include:

- A better metric for SLQD sensitivity. Previous works on the SLQD sensor have been in the context of 'charge-sensitivity' in detecting electrons oscillating between a reservoir and a dot in the SLQD sensor [109, 110]. However, the 'charge-sensitivity' metric is not the main metric in the context of qubit readout

[10] Single-gate RF sensors require fast electron tunnel rates. By design, to help isolate the double-dots hosting the singlet-triplet qubit, the only charge transition with a sufficient electron tunnel rate is the inter-dot transition. Thus, if one wished to count the electron number on the dots or view all charge transitions in general, a charge sensor is useful in the near vicinity.

where one is concerned with the ability to sense charge directly on nearby quantum dots rather than that solely across the reservoir and the quantum dot in the SLQD sensor. That is, nearby charging events shift the potential of the quantum dot in the SLQD sensor such that electron oscillations no longer occur directly on the SLQD. In the context of charge sensing (for example, in high-fidelity single-spin readout using spin-to-charge conversion), one therefore becomes more interested in the resulting signal contrast.

- Development of a full analytic model, including the readout signal strength at high powers in the nonlinear regime. Previous experiments typically operated at lower input powers $< -100\,\mathrm{dBm}$ and did not explore the high power nonlinear regime. This is because previous theory stated (correctly) that the quantum capacitance indeed reaches a peak value with respect to the input voltage amplitude V_{in}, such that the optimal readout signal might be obtained by setting V_{in} to maximise the quantum capacitance. However, our analytic modelling showed that the readout signal in fact, monotonically saturates at higher input voltage amplitudes rather than peaking - a fact that was experimentally verified as shown later in Section 3.4 [31]. This better understanding of the SLQD led to better optimisation and characterisation techniques (also discussed in Section 3.4).

- SLQD response at high powers in the nonlinear regime. The analytic solution also predicted high frequency harmonic nonlinearities in the reflected readout signal. One could exploit these nonlinearities to build exotic RF components such as an RF mixer as subsequently verified experimentally by a current PhD student, Mark R. Hogg [155].

This section will derive the analytic model for the SLQD sensor while discussing the theoretical predictions regarding the optimal operation of the SLQD sensor.

3.3.1 Developing a semi-classical model of the SLQD sensor

The operation of the SLQD sensor was modelled via a semi-classical rate equation as proposed previously in the literature. Here the solutions were found analytically to better study the functional trends in the SLQD parameters rather than simple numerical simulations [109, 110]. The analytic solution was found via a Fourier series. The Fourier series solution yielded the average steady state electron occupation probability, from which one finds the current and subsequently the nonlinear quan-

tum capacitance. This section shall present the Fourier series solution, while the following sections discuss the trends in key system parameters.

Now consider a quantum dot tunnel-coupled to a reservoir. The reservoir has a continuum of states with the electron filling probabilities given by the Fermi-Dirac distribution function. States below the reservoir's Fermi level are mostly filled while states above the Fermi level are mostly empty. By changing the voltage on a gate, one may periodically raise or lower the dot's energy level with respect to its reservoir's Fermi level as depicted in Figure 3.8. When the dot's energy level is above the Fermi level (I), the probability of finding an empty state on the reservoir with the dot's energy level is high, so the electron on the dot tunnels onto the reservoir. On lowering the dot's energy level to the reservoir's Fermi-level (II), the probability of finding a filled state with a free electron on the reservoir is 50% and the dot typically remains empty. On lowering the dot's energy level below the Fermi level (III), the probability of finding an electron with the same energy level as the dot is high and thus, an electron tunnels onto the dot from the reservoir. On raising the dot's energy level (IV), the probability of finding an empty state on the reservoir is 50% and the electron typically remains on the dot. The cycle repeats on raising the dot's energy level above the reservoir Fermi-level once more (I) to result in cyclic electron oscillations between the dot and its reservoir in synchrony with the input voltage signal. By considering the resulting current on the reservoir lead and its relationship to the input voltage signal, one may find the resulting AC quantum capacitance.

The schematic shown in Figure 3.8 can be realised mathematically via a classical rate equation. Now the electron tunnelling events are stochastic by nature with the rate given by the Fermi's golden rule. However, one may investigate the average steady-state behaviour over many cycles by considering the average tunnel rates of electrons moving from the reservoir to the dot Γ_+ and electrons moving from the dot to the reservoir Γ_-. Now one may write the classical rate equation governing the electron state probabilities (P_e being the probability that of an electron occupies the dot and P_0 being the probability that the dot is empty):

$$\begin{cases} \frac{d}{dt}P_e = \Gamma_+ P_0 - \Gamma_- P_e \\ \frac{d}{dt}P_0 = \Gamma_- P_e - \Gamma_+ P_0 \end{cases} . \tag{3.13}$$

The idea is that the change in the occupation probability changes with the tunnel rates. For example, the probability of occupying the dot P_e increases by the reservoir to dot tunnel rate if empty and decreases by the dot-to-reservoir tunnel-rate if full. Since probabilities must sum to unity, the equations simplify into:

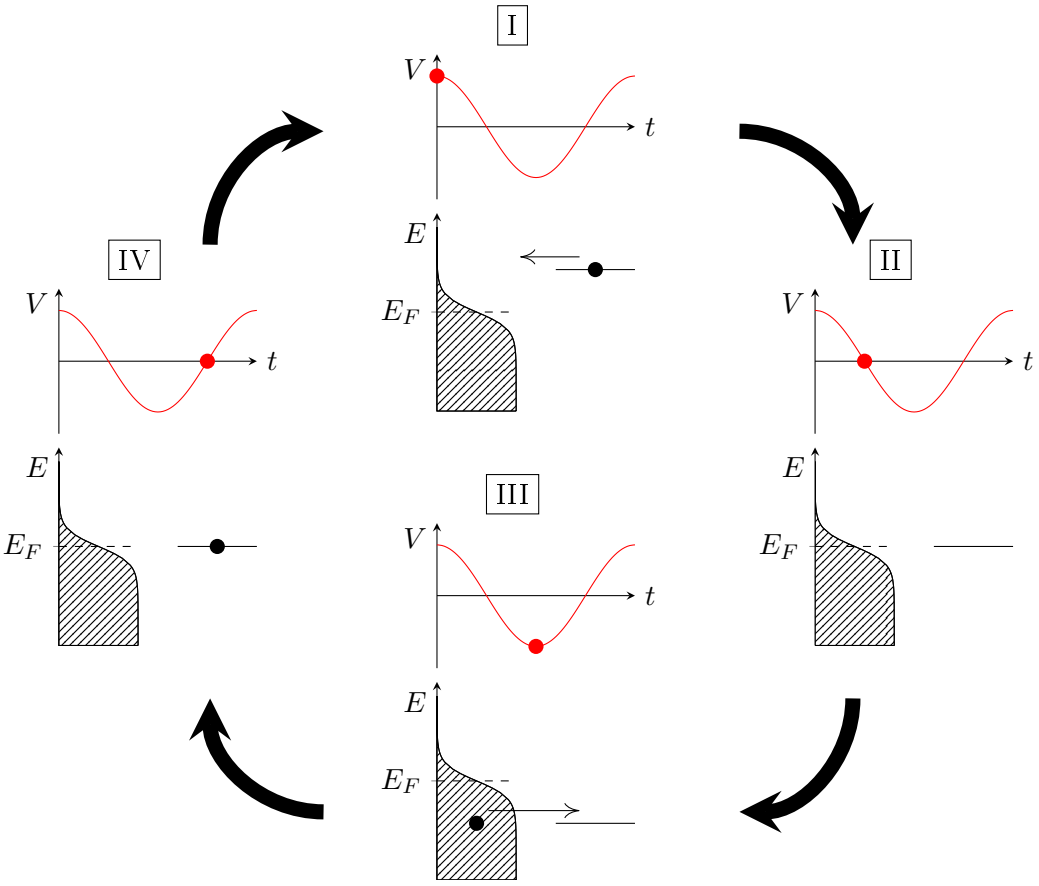

Figure 3.8: Electron oscillations between a reservoir and a quantum dot in a SLQD sensor. Electrons in the reservoir (shaded areas) are given by the Fermi-dirac distribution in which states below the Fermi level E_F are filled and states above are mostly empty. The dot has one discrete energy level to which the electron may occupy. The input voltage is applied to the reservoir lead; thus, positive voltages, push dot's energy level above the reservoir Fermi level. In the positive portion of the voltage cycle (top), the electron on the dot tunnels off the dot and onto the reservoir. On lowering the dot's energy level to the Fermi-level (right), no new electrons enter the dot as most of the states on the reservoir are filled. On lowering the dot's energy level below the Fermi-level (bottom), an electron tunnels onto the dot. Finally, the electron remains on the dot (left) on raising the dot's energy level back to the reservoir Fermi-level. On repeating the four stages, electrons oscillate between the reservoir and dot periodically with the incident voltage signal.

$$\frac{d}{dt}P_e = \Gamma_+(1-P_e) - \Gamma_- P_e = \Gamma_+ - (\Gamma_+ + \Gamma_-)P_e. \tag{3.14}$$

To find the tunnel rates, one applies Fermi's golden rule which states that transmission occurs when the two states (an electron state on the reservoir and the dot's energy state) are equal in energy. On applying Fermi's golden rule for a continuum of states in the reservoir and the single discrete state on the dot, one may calculate Γ_+ and Γ_- as derived in Appendix B.1:

$$\Gamma_\pm = \frac{\Gamma_0}{1+\exp\left(\pm\frac{\Delta E}{k_B T}\right)}, \tag{3.15}$$

where Γ_0 is twice the average tunnel rate of electrons through the tunnel barrier in between the reservoir and the dot. ΔE is the energy difference between the outer energy level on the dot (into and from which the electron tunnels) and the reservoir Fermi level. Since algebraically one notes that $\Gamma_+ + \Gamma_- = \Gamma_0$, the ordinary differential equation given in Equation 3.14 becomes:

$$\frac{dP_e}{dt} + \Gamma_0 P_e = \frac{\Gamma_0}{1+\exp\left(\frac{\Delta E}{k_B T}\right)}. \tag{3.16}$$

Now consider the dot's energy level to be aligned with the reservoir Fermi-level. By applying a voltage ΔV to a given gate in the device (with a lever-arm α_g to the quantum dot), one can change the energy level on the quantum dot by $\Delta E \equiv -e\alpha_g \Delta V$ (as shown by Equation A.8 in Appendix A.1). However, if the gate one which is changing the voltage is the reservoir itself, then the reservoir energy level must be drained of electrons and thus, the Fermi-level changes by $-e\Delta V$. Thus, in the case of applying the voltage to the reservoir, the net change in ΔE is $e(1-\alpha_g)\Delta V$. In summary:

$$\begin{aligned} \Delta E &= e\alpha_{rg}\Delta V \\ \alpha_{rg} &= \begin{cases} 1-\alpha_g & \text{Gate } g \text{ is reservoir to dot} \\ -\alpha_g & \text{Gate } g \text{ is not reservoir to dot} \end{cases}. \end{aligned} \tag{3.17}$$

Note that in typical operation of the SLQD, one will be applying the voltage signal to the reservoir (that is, $\alpha_{rg} = 1-\alpha_g$). However, if one were to feed the voltage signal via a different gate lead, then one should note this subtlety. Now the system shall be detuned (via manipulation of the gates) such that when $V = 0$, the reservoir and dot energy levels are degenerate. Now one applies a RF input voltage:

$$V(t) = V_0 + V_{ac}\cos(\omega t), \tag{3.18}$$

where V_0 is the DC voltage offset from the degeneracy point, V_{ac} is the RF driving amplitude and ω is the angular frequency of the RF drive. Note that $V_{ac} \gtrsim V_0$ for one cannot cyclically tunnel an electron on and off the dot without letting the dot's energy level cross the below and above Fermi-level respectively. Applying this RF excitation to the rate equation in Equation 3.16 yields:

$$\frac{dP_e}{dt} + \Gamma_0 P_e = \frac{\Gamma_0}{1 + \exp\left(\frac{e\alpha_{rg}}{k_B T}\left(V_0 + V_{ac}\cos(\omega t)\right)\right)}. \tag{3.19}$$

Now the right hand side is clearly periodic in time. Thus, the steady-state a.c. solution to this ordinary differential equation is naturally written in the Fourier basis as shown in Appendix B.2. Given the solution $P_e(t)$, one may construct the charge occupancy by simply noting that $Q(t) = -eP_e(t)$. To calculate the resulting current through the gate (to which the voltage signal is applied) one needs to calculate the charge per unit time on the gate $Q_g(t)$. Appendix A.1.6 explains how compensating charges must flow into gates when the charge state of a dot changes. First consider the case where the voltage signal is applied to the reservoir of the dot itself. In this case, the reservoir loses an electron each time an electron occupies the dot: $Q(t)$. However, on occupying the dot, a compensating charge of opposite sign must also flow: $-\alpha_g Q(t)$. This yields a net $(1-\alpha_g)Q(t) \equiv \alpha_{rg}Q(t)$. In the case of applying the voltage a gate lead that is not the reservoir of the dot, the only charge flow that occurs is the compensating charge: $-\alpha_g Q(t) \equiv \alpha_{rg}Q(t)$. Thus, in all cases, the net charge flow into the gate, to which the resonator is attached, is: $-e\alpha_{rg}P_e(t)$. Noting that the steady state current is simply the time-derivative of the charge, the probability of occupation and the currents are given as:

$$\begin{aligned} &P_e(t) = \textstyle\sum_{n=0}^{\infty} A_{n(p)}\cos(n\omega t + \phi_{n(p)}) \\ &\begin{cases} A_{n(p)} = \frac{1}{\sqrt{\Gamma_0^2+(n\omega)^2}} \cdot \frac{-e\alpha_{rg}\Gamma_0 V_{ac}}{4nk_BT} \cdot F\left(\frac{e\alpha_{rg}}{2k_BT}V_{ac}, \frac{e\alpha_{rg}}{2k_BT}V_0, n\right) \\ \phi_{n(p)} = -\arctan\left(\frac{n\omega}{\Gamma_0}\right) \end{cases}, \end{aligned} \tag{3.20}$$

$$\begin{aligned} &I(t) = \textstyle\sum_{n=1}^{\infty} A_{n(I)}\sin(n\omega t + \phi_{n(I)}) \\ &\begin{cases} A_{n(I)} = \frac{e\alpha_{rg}\omega}{2} \cdot \frac{\Gamma_0}{\sqrt{\Gamma_0^2+(n\omega)^2}} \cdot \frac{e\alpha_{rg}}{2k_BT}V_{ac} \cdot F\left(\frac{e\alpha_{rg}}{2k_BT}V_{ac}, \frac{e\alpha_{rg}}{2k_BT}V_0, n\right) \\ \phi_{n(I)} = \pi - \arctan\left(\frac{n\omega}{\Gamma_0}\right) \end{cases}, \end{aligned} \tag{3.21}$$

where $F(x, y, n)$ is defined in Appendix B.2.2:

$$F(x,y,n) \equiv \frac{1}{\pi}\int_{-\pi}^{\pi} \frac{\sin(t)\sin(nt)}{\cosh^2\left(y + x\cos(t)\right)}dt. \tag{3.22}$$

That is, for an injected voltage signal $V(t)$, the current response is nonlinear and has an infinite set of sinusoidal waveforms of frequency $n\omega$. Before discussing the properties of the AC current response in the next section, it is instructive to calculate the RF signal strength that would manifest when using a SLQD sensor. To find the response, the equivalent AC impedance must be found. Now expanding the current given in Equation 3.21 via the compound angle identity yields two orthogonal terms that will help find the effective capacitance and resistance of the dot:

$$I_n(t) \equiv -\underbrace{A_{n(I)}\frac{\Gamma_0}{\sqrt{\Gamma_0^2+(n\omega)^2}}}_{\text{Capacitive}}\sin(n\omega t) + \underbrace{A_{n(I)}\frac{n\omega}{\sqrt{\Gamma_0^2+(n\omega)^2}}}_{\text{Resistive}}\cos(n\omega t), \tag{3.23}$$

where one notes the identities: $\cos(\arctan(a/b)) \equiv b/\sqrt{a^2+b^2}$ and $\sin(\arctan(a/b)) \equiv a/\sqrt{a^2+b^2}$. The currents' phase relationship with the injected voltage wave $V(t)$ are 'capacitive' and 'resistive'. Note that the phase relationships only have meaning for the first harmonic $n = 1$. In the case of the 'capacitive' portion, taking $A_{1(I)}$ to be positive, is the portion of the current that 'leads' the voltage by 90°, while the 'resistive' portion of the current is in phase with the voltage. Thus, in a circuit-model description, the device acts as an AC capacitance and resistor in parallel[11]. It is of interest to note that the phase term $\phi_{1(I)}$ dictates the capacitive or resistive nature of the quantum dot to reservoir system. When $\Gamma_0 \gg \omega$, the dot-to-reservoir system is AC capacitive in nature and resistive otherwise. Now the equivalent nonlinear AC capacitance is given by: $\frac{1}{n\omega}\cdot\frac{I(n\omega)}{V(n\omega)}$. Thus the 'quantum capacitance' is:

$$C_{q(n)}(V_{ac},V_0) = \frac{e^2\alpha_{rg}^2}{4nk_BT}\cdot\frac{\Gamma_0^2}{\Gamma_0^2+(n\omega)^2}\cdot F\left(\frac{e\alpha_{rg}}{2k_BT}V_{ac},\frac{e\alpha_{rg}}{2k_BT}V_0,n\right), \tag{3.24}$$

where $V(n\omega) \equiv V_{ac}$. Note that the voltage at $n\omega$ is zero for all $n > 1$; thus, this effective capacitance at $n > 1$ is a harmonic-based distortion metric showing the ratio of the current response, to a given voltage input, at some higher frequency. Now similarly, one may find the equivalent nonlinear AC resistance by taking: $\frac{V(n\omega)}{I(n\omega)}$. Thus, by utilising the same methods, the 'Sisyphus resistance' is:

[11] Note that for $n > 1$, this description is the current response at a given frequency $n\omega$ for an injected voltage wave of frequency ω

$$R_q = \left[\frac{e^2\alpha_{rg}^2}{4k_BT} \cdot \frac{n\omega^2\Gamma_0}{\Gamma_0^2 + (n\omega)^2} \cdot F\left(\frac{e\alpha_{rg}}{2k_BT} V_{ac}, \frac{e\alpha_{rg}}{2k_BT} V_0, n \right) \right]^{-1}, \tag{3.25}$$

The quantum dot thus, acts as a capacitor C_q in parallel with a resistor R_q due to the quantum capacitance and Sisyphus resistance respectively. Under typical operation of the SLQD sensor in Si-P, the quantum capacitance term dominates the mostly negligible Sisyphus resistance. For example, consider some typical experimental parameters [30, 31, 155]: $f = 250\,\text{MHz}$, $\Gamma = 10\,\text{GHz}$, $\alpha_{rg} = 0.5$, $T = 0.25$. Taking $V_0 = V_{ac} = 0$ to give the maximum quantum capacitance (since the integral of sine-squared is π, $F(0,0,1) = 1$) of $C_q \approx 460\,\text{aF}$ (an AC impedance of $1/(\omega C_q) = 1.4\,\text{M}\Omega$) and a Sisyphus resistance of $R_q \approx 55\,\text{M}\Omega$. Thus, the Sisyphus resistance is an order of magnitude larger than the AC impedance of the quantum capacitance term. Thus, the SLQD sensor predominantly operates in the quantum capacitance regime and one may ignore the Sisyphus resistance term when calculating the readout signal strength as done so in the previous calculations in Section 3.2. Nonetheless, the Sisyphus resistance is important when calculating the power dissipation of the SLQD sensor as discussed in Section 3.3.4.

Finally, one may input the expression for C_q into Equation 3.11 to obtain the RF signal strength as discussed in the next section. It shall be shown that the point of maximum quantum capacitance is not necessarily the point of maximum readout signal strength.

3.3.2 Quantum capacitance and measured RF signal response

The quantum capacitance given in Equation 3.24 (taken for $n = 1$) has several key factors. The $\Gamma_0^2/(\Gamma_0^2 + \omega^2)$ factor implies that the quantum capacitance is only significant when the tunnel rate is much greater than the driving frequency: $\Gamma_0 \gg \omega$. Another key factor is the spectral function $F(x, y, 1)$ defined in Equation 3.22. The spectral function, plotted in Figure 3.9a, governs the nonlinearity as a function of the detuning offset V_0 and the input voltage amplitude V_{ac}. The spectral response is non zero within the conical region defined by $V_{ac} > V_0$ as expected when realising that the voltage amplitude V_{ac} must be large enough to sweep past the degeneracy point $V_0 = 0$ during each cycle. Similarly, as expected the quantum capacitance peaks at zero voltage offset ($V_0 = 0$) for this maximally cycles the voltage into the regions where electrons are more likely to move onto and off the quantum dot as illustrated in Figure 3.8. The spectral function drops the quantum capacitance monotonically downwards with increasing V_{ac} as shown in Figure 3.9b when plotting

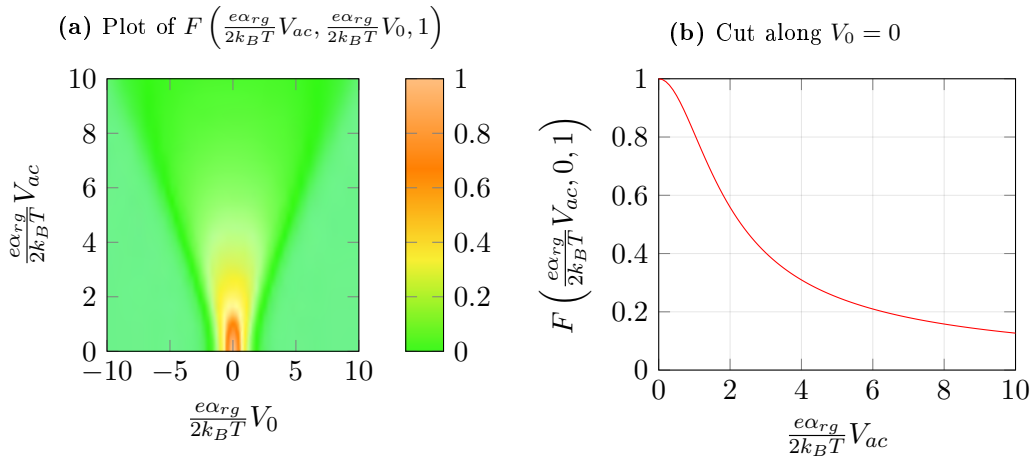

Figure 3.9: Theoretical model of the quantum capacitance of a SLQD sensor as a function of DC offset from Fermi-level V_0 and RF voltage amplitude V_{ac}. **(a)** The quantum capacitance drops monotonically with increasing RF voltage amplitude. The peak quantum capacitance (plotted in proportion to the maximum capacitance that occurs when $V_{ac} \to 0$) occurs when the quantum dot in the SLQD sensor is aligned with the reservoir Fermi-level: $V_0 = 0$. The quantum capacitance is null outside the cone $V_{ac} > |V_0|$ as the RF voltage amplitude must be large enough to sweep the dot's energy level past the Fermi-level to oscillate electrons on and off the dot in the SLQD sensor. **(b)** The quantum capacitance shows a monotonic decrease when plotting of the peak capacitance (at $V_0 = 0$) as a function of increasing RF voltage amplitude V_{ac}.

the peak response at $V_0 = 0$. Most papers in the literature declared that the best response therefore, occurred with perturbative input voltage amplitudes ($V_{ac} \to 0$), in which the capacitance maximum is approximately constant with V_{ac} (the linear regime). A consequence of this viewpoint is that one may indefinitely obtain a larger signal response (by maximising the capacitance) by setting the temperature T close to zero (as $C_q \propto 1/T$).

It is important to understand that the quantum capacitance should not be considered by itself in isolation as maximising the capacitance does not give the best results. One should instead maximise the readout signal strength Υ (as it directly relates to signal to noise ratio of the sensor readout and ultimately the fidelity of qubit readout). By taking the expression for the quantum capacitance in Equation 3.24 and substituting it into the expression for the readout signal strength in Equation 3.11, one obtains:

$$\Upsilon = \underbrace{\frac{2\mathrm{Q}_{\mathrm{ext}}\,\mathrm{Q}_{\mathrm{int}}^2}{(\mathrm{Q}_{\mathrm{ext}}+\mathrm{Q}_{\mathrm{int}})^2}\cdot\frac{K\eta_{\mathrm{loss}}}{C_p}}\cdot\underbrace{\frac{\Gamma_0^2}{\Gamma_0^2+\omega^2}}\cdot\underbrace{\frac{e^2\alpha_{rg}^2 V_{\mathrm{in}}}{4k_BT}\cdot F\left(\frac{e\alpha_{rg}}{2k_BT}V_{ac}, \frac{e\alpha_{rg}}{2k_BT}V_0, 1\right)}. \quad (3.26)$$

The first factor expresses the resonator circuit parameters where one maximises the internal quality factor and sets the external quality factor to suit the desired circuit bandwidth as discussed in Section 3.2.2. Similarly, the gain K, input cable loss factor η_{loss} and the parasitic capacitance C_p are separate circuit parameters concerning the resonator. The second factor signifies the degree to which the SLQD sensor provides a capacitive load with $\Gamma_0 \gg \omega$ being the limit where the factor becomes unity. To better view the trends in the readout signal strength, one may write the input voltage amplitude V_{in} in terms of the input voltage amplitude on the gate of the SLQD sensor:

$$\Upsilon = \underbrace{\frac{\mathrm{Q}_{\text{int}}}{\mathrm{Q}_{\text{ext}} + \mathrm{Q}_{\text{int}}} \cdot \frac{K}{C_p}}_{} \cdot \underbrace{\frac{e\alpha_{rg}}{2} \cdot \frac{\Gamma_0^2}{\Gamma_0^2 + \omega^2}}_{} \cdot \underbrace{\frac{e\alpha_{rg}}{2k_B T} V_{\text{ac}} \cdot F\left(\tfrac{e\alpha_{rg}}{2k_B T} V_{ac}, \tfrac{e\alpha_{rg}}{2k_B T} V_0, 1\right)}_{}. \quad (3.27)$$

Now the first factor now clearly highlights how a large ratio of the internal to external quality factors is favourable for maximal readout signal strength. With the second factor being similar to before, the last factor is of interest. The spectral function is now in the form of $x \cdot F(x, y, 1)$ as plotted in Figure 3.10a. As with the quantum capacitance trends, the peak readout signal strength occurs at $V_0 = 0$ with the non-zero response being approximately within the cone $V_{ac} > V_0$. The readout signal strength however, in contrast to before with the quantum capacitance, does not monotonically decrease but in fact, monotonically increases and saturates at high V_{ac} as shown by the plot in Figure 3.10b (cutting the maximal response across $V_0 = 0$).

The saturating response of the readout signal strength at high RF input voltage amplitude is contrary to that discussed in prior literature [110]. When considering the diagram of the SLQD sensor's operation in Figure 3.8, on each cycle of the input voltage signal, one needs to bring the dot's energy level well above the reservoir Fermi level to ensure the electron can tunnel off the dot and well below the reservoir Fermi level to ensure a new electron can tunnel onto the dot. The voltage amplitude therefore must be large enough such that one sweeps past the smearing of the Fermi-level due to a finite temperature. Thus, the ratio of the swept energy scale $e\alpha_{rg}V_{ac}$ must be greater than the temperature-smeared energy scale $2k_BT$ on the reservoir. Table 3.2 highlights some ratios of the two energy scales (RF amplitude sweeping the dot's chemical potential $e\alpha_{rg}V_{ac}$ to the thermal energy of the electrons in the reservoir $2k_BT$) and the resulting fraction of the maximum possible signal. When the voltage amplitude energy scale (to which the dot energy levels move) equals the

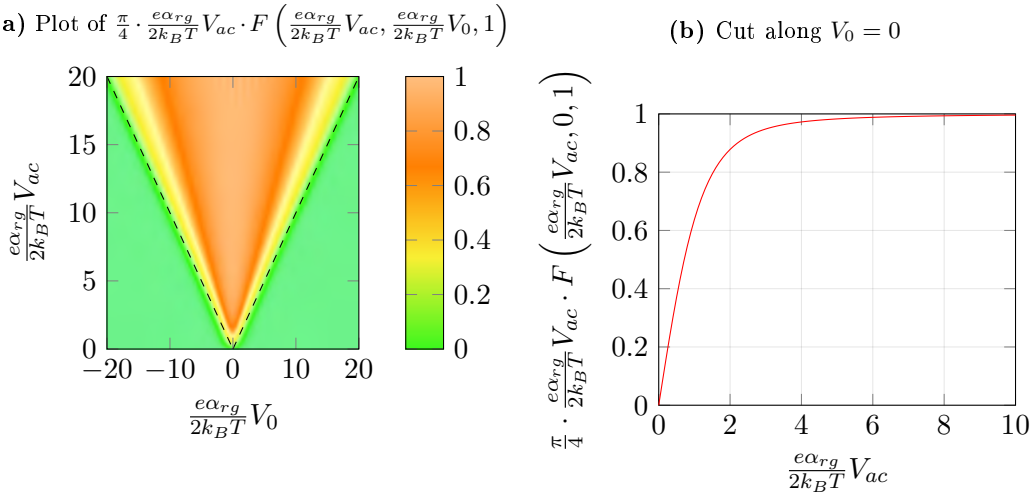

Figure 3.10: Theoretical model of the RF readout signal strength of a SLQD sensor as a function of DC offset from Fermi-level and RF voltage amplitude. **(a)** The readout signal strength (plotted as a function of the maximum possible signal strength) increases monotonically with increasing RF voltage amplitude. The peak readout signal occurs when the quantum dot in the SLQD sensor is aligned with the reservoir Fermi-level: $V_0 = 0$. The readout signal is null outside the cone $V_{ac} > |V_0|$ as the RF voltage amplitude must be large enough to sweep the dot's energy level past the Fermi-level to oscillate electrons on and off the dot in the SLQD sensor. Note that the factor of $\pi/4$ is to normalise the peak signal strength since $\lim_{x \to \infty} x \cdot F(x, 0, 1) = 4/\pi$ as shown in Appendix B.2.3. **(b)** The RF readout signal shows a monotonic increase when plotting of the peak RF readout signal (at $V_0 = 0$) as a function of increasing RF voltage amplitude V_{ac}.

thermal energy smearing of the reservoir, the signal is only 64% of its maximum possible value, while having the voltage amplitude being 4 times larger yields a fraction of approximately 97%. Typically in experiments one would not want to indefinitely increase the input voltage as the charge transition would continually broaden as shown in Figure 3.10 across the V_0 axis. A broader charge transition implies that charge detection (on a nearby quantum dot) would require a larger shift in the SLQD quantum dot's transition peak (that is, a need for stronger electrostatic coupling which would typically reduces the range of the SLQD sensor).

Ratio $\frac{e\alpha_{rg}}{2k_BT}V_{ac}$	$\Upsilon_{\text{peak}}/\Upsilon_{\text{max}}$
1	0.637
4	0.972
7	0.991
21	0.999

Table 3.2: Obtaining the maximum possible readout signal strength by increasing the input RF voltage with respect to the electron temperature. The ratios of the peak RF readout signal Υ_{peak} (which occurs at $V_0 = 0$) and the maximum possible readout signal Υ_{max} (which occurs at $V_0 = 0$ and $V_{ac} \to \infty$) are calculated by noting that the form of the RF response at $V_0 = 0$ is $xF(x, 0, 1)$ where $x = (e\alpha_{rg}V_{ac})/(2k_BT)$ with the maximum value being $4/\pi$.

At low RF input voltages, the RF readout response holds information that may be used to extract experimental parameters. At low voltage amplitudes, the RF response is linear with respect to the input voltage amplitude:

$$\frac{\Upsilon}{V_{\text{ac}}} = \frac{\text{Q}_{\text{int}}}{\text{Q}_{\text{ext}} + \text{Q}_{\text{int}}} \cdot \frac{K}{C_p} \cdot \frac{\Gamma_0^2}{\Gamma_0^2 + \omega^2} \cdot \frac{e^2\alpha_{rg}^2}{4k_BT} \cdot \text{sech}^2\left(\frac{e\alpha_{rg}}{2k_BT}V_0\right), \quad V_{\text{ac}} \to 0. \tag{3.28}$$

In this limit, the spectral function gives a profile for the SLQD charge transition. The width of the RF readout response across V_0 follows the usual $\text{sech}^2(e\alpha_{rg}V_0/2k_BT)$ relationship expected with Coulomb peaks inferred with DC readout [31, 156, 157]. One may take the low V_{ac} profiles across V_0 and fit a sech^2 function to deduce the ratio α_{rg}/T. Analysing α_{rg}/T across a range of temperatures enables one to deduce α_{rg} as shown later in the experimental demonstration in Section 3.4.2. Another feature of the linear regime (but not that of the maximum response) is that the gradient is inversely proportional to the temperature. Thus, a linearly decreasing V_{ac} offsets the response peak height at lower temperatures as discussed earlier.

At large input voltage amplitudes, the RF readout response follows a cone-like shape as seen by the semi-circular profile at large values of V_{ac}:

$$\Upsilon_{\text{large}} = \frac{\text{Q}_{\text{int}}}{\text{Q}_{\text{ext}} + \text{Q}_{\text{int}}} \cdot \frac{K}{C_p} \cdot \frac{2e\alpha_{rg}}{\pi} \cdot \frac{\Gamma_0^2}{\Gamma_0^2 + \omega^2} \cdot \sqrt{1 - \left(\frac{V_0}{V_{ac}}\right)^2}, \quad V_{ac} \to \infty. \tag{3.29}$$

If one takes the maximal response at $V_0 = 0$, voltage amplitudes much larger than the temperature energy scale and tunnel rates much larger than the driving frequency; the readout signal strength tends to:

$$\Upsilon_{\text{max}} = \frac{\text{Q}_{\text{int}}}{\text{Q}_{\text{ext}} + \text{Q}_{\text{int}}} \cdot \frac{K}{C_p} \cdot \frac{2e\alpha_{rg}}{\pi}, \quad \frac{e\alpha_{rg}}{2k_BT} V_{\text{ac}} \gg 1. \tag{3.30}$$

The first two factors once again simply involve circuit elements describing the resonator. The third factor describes a fundamental limit that states that the readout response will be limited to the current of a single electron moving between the reservoir and the quantum dot of the SLQD sensor. The lever-arm factor $\alpha_{rg} < 1$ simply states that the readout signal is proportional to the gate's coupling to the quantum dot.

The analysis in this section has a few key conclusions regarding the optimal readout signal strength:

- The fundamental limit to the readout signal strength is limited by the current of a single electron moving between the reservoir and the quantum dot in the SLQD sensor: $\Upsilon_{\text{max}} \propto e\alpha_{rg}$.
- Maximal signal strength is obtained when $e\alpha_{rg}V_{ac} \gg 2k_BT$ with $e\alpha_{rg}V_{ac} = 8k_BT$ yielding 97.2% the maximum signal strength.
- The maximal signal strength can be obtained at lower input voltage amplitudes if the one engineers the electron temperature on the reservoir to be proportionally smaller. However, the value of the maximum readout signal strength does not change with temperature.
- One should not keep increasing V_{ac} as the SLQD peak broadens by V_{ac}. Thus, if the shift in the SLQD peak due to sensing charging event is small, one may not obtain sufficient contrast in the qubit readout signal.

The analytic solution additionally yielded predictions on the nonlinearities of the SLQD current as well as the eventual power dissipation of the SLQD sensor as discussed in the following sections.

3.3.3 Nonlinear current response of the SLQD sensor

The nonlinear harmonics in the current do not affect the SLQD readout strength as the resonator's band-pass filtering effectively removes the higher harmonics. Whilst it is not the outcome of the thesis, the results became useful in guiding future experiments (involving the use of the higher harmonics for an on-chip frequency multiplier) done by a PhD student in UNSW: Mark R. Hogg [155].

The current harmonics of the SLQD system are proportional to the spectral function in the form:

$$\begin{aligned} &I_n(t) = A_{n(I)}\cos(n\omega t + \phi_{n(I)}) \\ &\begin{cases} A_{n(I)} = \frac{e\alpha_{rg}\omega}{2} \cdot \frac{\Gamma_0}{\sqrt{\Gamma_0^2+(n\omega)^2}} \cdot \frac{e\alpha_{rg}}{2k_BT}V_{ac} \cdot F\left(\frac{e\alpha_{rg}}{2k_BT}V_{ac}, \frac{e\alpha_{rg}}{2k_BT}V_0, n\right) \\ \phi_{n(I)} = \frac{\pi}{2} - \arctan\left(\frac{n\omega}{\Gamma_0}\right) \end{cases} \end{aligned} \tag{3.31}$$

Figure 3.11 shows the harmonic behavior of the current. Similar to the RF readout signal, all the current harmonics tend to zero outside the voltage cone when $V_{ac} < |V_0|$. That is, when one tunes the degeneracy point V_0 (where the dot's energy level equals the Fermi-level) beyond the voltage oscillation amplitude V_{ac}, one will not cycle between the two states (electron on or off the dot) to create current flow. With the higher harmonics n, there are n lobes in the current response which change sign. At high input voltage amplitudes, the current lobes saturate to values given by the Chebyshev polynomial of the second kind $U_n(x)$ enveloped by a semi-circular cone like with the RF readout response:

$$I_{n(\text{large})} = \frac{2e\alpha_{rg}}{\pi} \cdot \frac{\omega\Gamma_0}{\sqrt{\Gamma_0^2+(n\omega)^2}} \cdot \sqrt{1-\left(\frac{V_0}{V_{ac}}\right)^2} \cdot U_{n-1}\left(\frac{V_0}{V_{ac}}\right), \quad V_{ac} \to \infty. \tag{3.32}$$

The current is also attenuated at higher harmonics via the second factor $\sim 1/(n\omega)$ as expected for otherwise the sum of all the current harmonics would be divergent. Albeit, the factor saturates at larger drive frequencies. Asymptotic zeroes (shown by the dashed lines in Figure 3.11) occur at the higher current harmonics along lines given by the zeroes of the Chebyshev polynomial of the second kind $U_{n-1}(V_0/V_{ac})$:

$$V_0 = V_{ac}\cos\left(\frac{k\pi}{n}\right), \quad k < n, k \in \mathbb{N}, V_{ac} \to \infty, \tag{3.33}$$

with the peak current on each lobe (enumerated by $k < n$) being:

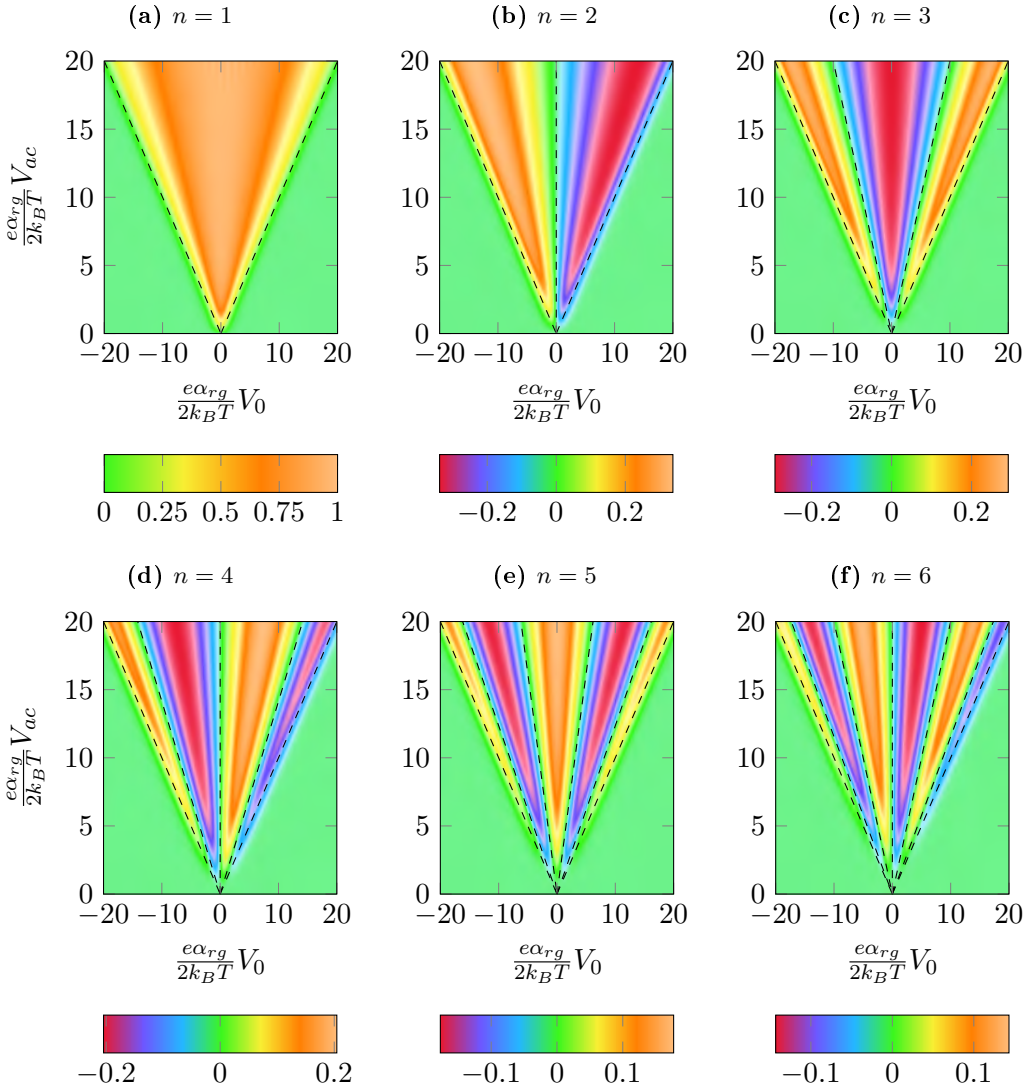

Figure 3.11: Higher harmonics in the SLQD current. The plots show the spectral function shaping the first 6 harmonics in the current response; specifically $\frac{\pi}{4} \cdot \frac{e\alpha_{rg}}{2k_BT}V_{ac} \cdot F\left(\frac{e\alpha_{rg}}{2k_BT}V_{ac}, \frac{e\alpha_{rg}}{2k_BT}V_0, n\right)$. The net current across the SLQD tunnel junction is the sum of all Fourier harmonics n. The harmonics all have non-zero responses within the cone $V_{ac>V_0}$. The dashed lines indicate the slopes of the asymptotic zeroes in the current response at $V_{ac} \to \infty$.

$$I_n^{\text{peak-}k} = \frac{2e\alpha_{rg}}{\pi} \cdot \frac{\omega\Gamma_0}{\sqrt{\Gamma_0^2 + (n\omega)^2}} \cdot (-1)^{k-1}, \quad k < n, k \in \mathbb{N}, V_{ac} \to \infty. \tag{3.34}$$

In the context of exploiting higher current harmonics, it is clear that the maximal current occurs at the lobes closer to $V_0 = 0$ as expected by the semi-circular envelope.

3.3.4 Power dissipation of the SLQD sensor

A parameter rarely considered in the design of qubit sensors is the subsequent power dissipation of the qubit sensor. If one were to place 10^8 qubit sensors (for modest qubit numbers prescribed by the surface code [8]) on the nano-scale device (operating to sense single-spin qubits via spin-to-charge conversion), the total power dissipation must be considered in the context of having sufficient cooling power in the dilution refrigerator to ensure that the electron temperatures remain low for high-fidelity qubits. The SLQD sensor operated in a capacitive regime ($\Gamma_0 \gg \omega$) offers the possibility of low power dissipation (as capacitive AC loads do not dissipate real power) and thus, is a viable candidate for large scale implementation [109, 110]. This section will outline the equation for the power dissipation of the SLQD sensor to show that the power dissipation is indeed low.

The power dissipation is defined as the average AC power per cycle:

$$P_{ac} = \frac{1}{T}\int_0^T V_{ac}(t) \cdot I_{ac}(t)dt \tag{3.35}$$

where T is the time for one period $T = 2\pi/\omega$. For example, if the load is purely capacitive, the net power dissipation is zero as there is no component of the current that is in phase with the voltage. Noting the orthogonality of sine and cosine, the only term that persists is the first harmonic of the current and specifically its in-phase component given by the Sisyphus resistance:

$$P_{\text{avg}} = \frac{1}{2} \cdot V_{ac} \cdot \frac{e\alpha_{rg}}{2} \cdot \frac{\omega^2\Gamma_0}{\Gamma_0^2 + \omega^2} \cdot \frac{e\alpha_{rg}}{2k_BT}V_{ac} \cdot F\left(\frac{e\alpha_{rg}}{2k_BT}V_{ac}, \frac{e\alpha_{rg}}{2k_BT}V_0, 1\right). \tag{3.36}$$

Like the current, the power saturates with increasing ω, however, the asymptotic form of the power grows linearly with increasing voltage amplitude V_{ac}:

$$P_{\text{asym.}} = \frac{e\alpha_{rg}}{\pi} \cdot \frac{\omega^2\Gamma_0}{\Gamma_0^2 + \omega^2} \cdot V_{ac}, \quad \frac{e\alpha_{rg}}{2k_BT}V_{\text{ac}} \gg 1. \tag{3.37}$$

However, the net power dissipation is in fact very low [110]. For example, consider a setup with $\Gamma_0 = 2\pi{\cdot}10\,\text{GHz}$, $\omega_0 = 2\pi{\cdot}1\,\text{GHz}$ and $\alpha_{rg} = 0.1$. With a voltage amplitude at the gate set to $45\,\mu\text{V}$, for a low temperature the power dissipation is approximately $1\,\text{fW}$. Thus, with 10^8 SLQD charge sensors, the average power dissipation would be approximately $100\,\text{nW}$. Thus, the nano-scale device contribution to the dissipated power is much less than the typical $>1\,\mu\text{W}$ cooling power at the mixing chamber of a dilution fridge. Whereas, if one were to use 10^8 SET sensors the net dissipation is an order of magnitude higher at $4.6\,\mu\text{W}$ (taking the source-drain bias voltage and current of $170\,\mu\text{V}$ and $270\,\text{pA}$ respectively for a typical Si-P SET [56]) and may exceed the cooling power of the dilution fridge.

3.4 Experimental demonstration of the SLQD

Section 3.3 has described the modelling behind the SLQD sensor by considering dot-to-reservoir transitions probed with RF reflectometry. A SLQD device was created both to demonstrate the operation of the SLQD sensor in Si-P devices and to verify the theoretical predictions. The theoretical framework has provided a pathway for SLQD device characterisation and optimisation. The techniques developed in characterising the SLQD sensor were different to that used in conventional charge sensors [31, 86, 101]. For example, the technique of Coulomb diamonds to deduce the lever-arm of the gate to the quantum dot in a SET cannot work with a charge sensor that does not contain source and drain leads.

To demonstrate the operation of the SLQD sensor an STM-patterned Si-P device was fabricated by Matthias Koch and Eldad Peretz. Characterisation of the RF circuitry involving the resonators attached to SLQD sensor was performed by Ian S. Bartlett as a part of his honours thesis. The characterisation of the SLQD sensor using the theory developed in the previous section was performed by the author with valuable assistance from Ian S. Bartlett.

3.4.1 SLQD device design

The STM image of the fabricated SLQD device is shown in Figure 3.12a. The lighter regions in the STM image indicate regions that were P-doped. The Si-P device had two charge sensors: the SLQD (consisting of reservoir R and the SLQD quantum dot) and the SET (consisting of a SET quantum dot, source S, drain D and tuning gate G). The SLQD charge sensor can be used to detect charge transitions onto the SET and vice versa to enable one to compare the conventional three-lead sensor

with the more compact SLQD sensor. The dimensions of the SET were taken from previously working SET designs [80]. The SET quantum dot was 10×24 nm in size with a 15 nm separation between the SET quantum dot and its source/drain leads. The dimensions of the SLQD sensor were taken to be nominally the same geometry as the SET quantum dot and its source. That is, the SLQD quantum dot was 10×24 nm in size with a 15 nm separation between itself and the reservoir R. The electron states of the SLQD and SET were probed via reflectometry on two LC resonators multiplexed onto a single RF line [31, 139]. The resonator on its own was characterised by Ian S. Bartlett as a part of a honours thesis. For the resonator connected to the reservoir R, the resonant frequency was 244.8 MHz with an effective quality factor of approximately 100. The parasitic capacitance C_p, was thus 0.68 pF. For the second resonator connected to the source terminal S, the resonant frequency was 283.6 MHz with an effective quality factor of approximately 45 (lower than that of R due to the dissipative nature of the SET). The parasitic capacitance was thus, 0.67 pF. Unlike the quality factors, which were different due to the resistive load of the SET, the parasitic capacitances were consistent. This suggests that the parasitic capacitances mainly depended on the surrounding PCB geometry (for example, nearby copper ground planes or a high electric permittivity PCB laminate both increase C_p) as opposed to the sensor on the device to which the associated inductor was connected.

On sending in a 244 MHz RF voltage signal to address the resonator attached to gate R, there was change in the reflectance when sweeping the gate voltages on R and G. Figure 3.12b shows the resulting RF response measured on the output of the IQ demodulator. The dataset has had its background subtracted, in both the I and Q channels individually, by taking an average of a region far from charge transitions (as seen bright lines). Then the RF response plot was generated by via $\sqrt{I^2 + Q^2}$; that is, one is interested in the net change (relative to the default background level) in the RF response in the IQ plane on measuring a charge transition between R and the SLQD quantum dot as opposed to naively observing the amplitude and phase response alone.

The bright lines in Figure 3.12b indicate a change in the signal reflectance caused by electron oscillations occurring when the given quantum dot (SLQD or SET) aligns with its reservoir Fermi-level such that the input RF voltage sweeps the dot's energy level above and below its Fermi-level (as shown in Figure 3.8). The vertical lines indicate charge transitions of positive slope and thus, indicate that the electrons came from either G or R; in this case it is R as indicated by the steep slope indicating a stronger coupling to gate R (the gate on the x-axis). On crossing a SLQD transition

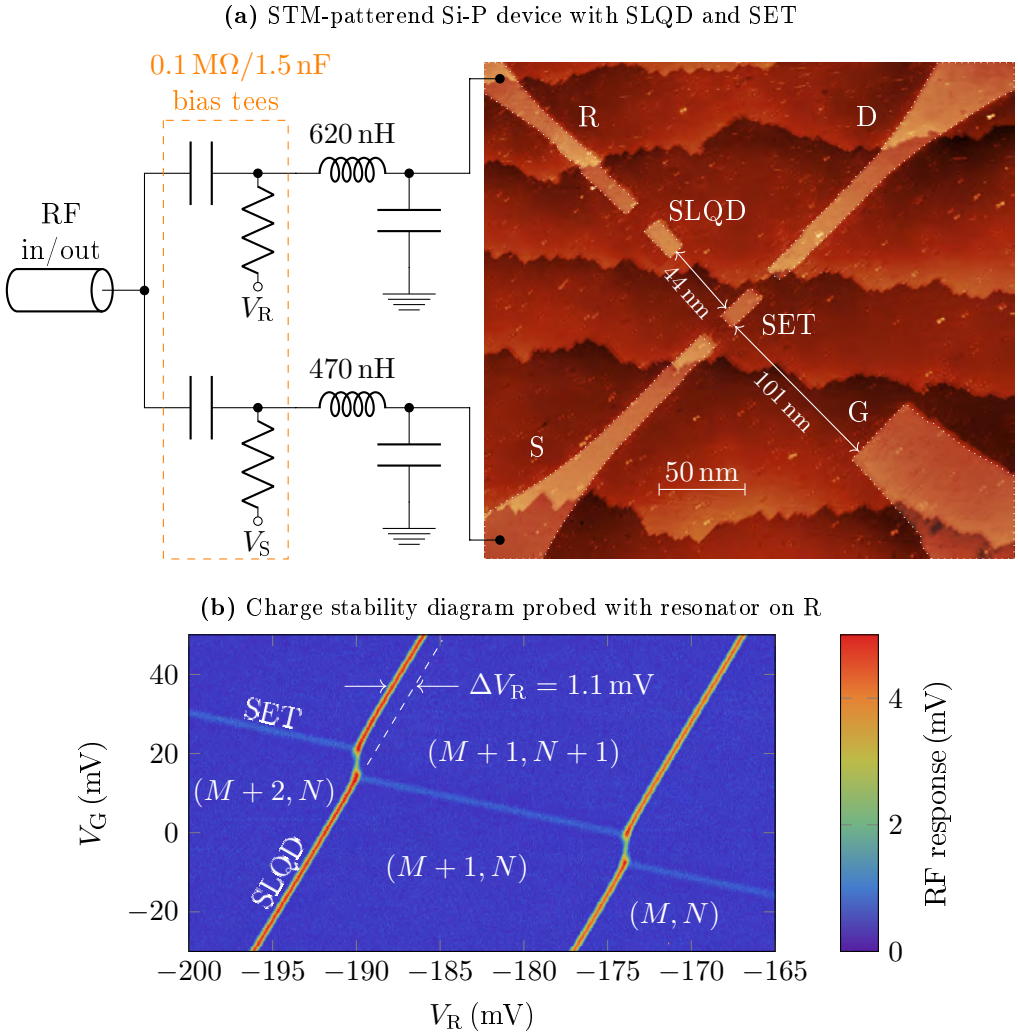

Figure 3.12: Demonstration of a SLQD sensor in a Si-P device. **(a)** STM image of the device. The lighter regions highlighted on the STM image were dosed with phosphine to incorporate P-donors. The terrace steps on the image are different layers of the silicon substrate. The SLQD sensor was formed by a reservoir R patterned 15 nm away from a large quantum dot SLQD (10×24 nm in size). The SLQD sensor detected electrons filling onto the SET quantum dot (10×24 nm in size; tuned via its source S and drain D leads each spaced 15 nm away and a gate G). The state of the SLQD and SET was sensed using RF reflectometry via two chip-inductor LC resonators multiplexed onto a single input RF line. Bias tees were placed on each resonator to set the DC voltage on the gates R and S. **(b)** Charge stability diagram, of the SLQD and SET charge transitions, using the RF response on resonator R. The vertical lines indicate charge transitions onto the SLQD quantum dot, while the faint horizontal lines indicate charge transitions onto the SET quantum dot. The ordered pairs indicate the ground-state charge states of the SLQD and SET quantum dots respectively in the charge-stable regions. The shift of $\Delta V_R = 1.1$ mV along V_R in the SLQD line indicates the ability of the SLQD sensor to detect the presence of charge entering or leaving the SET quantum dot.

line to a more negative voltage on the reservoir, more electrons enter the SLQD dot. The resonator also detects electron movement between the SET and its source/drain leads as seen by the horizontal lines of negative slope. Electrons enter the SET quantum dot when crossing the SET charge transition line to a more positive voltage on the reservoir R (or SET gate G). The RF response is weaker (fainter) on the SET charge transitions as the lever-arm α of reservoir R to the SET quantum dot is lower when compared to the SLQD which is of closer proximity. It would appear that there is a line linking the SET and SEB lines like that of an inter-dot transition. However, the distance between the SET and SLQD would prohibit the fast tunnel rates (greater than the driving frequency) required for RF readout. Thus, the inter-linking transition line is attributed to simultaneous charge movement between the SLQD to its reservoir R and the SET to its source/drain leads.

One key figure of merit is the shift in the SLQD charge transition ΔV_{R} due to the detection of nearby charge movement; in this case that is the addition of charge in the SET quantum dot. Using the shift in the charge transition to detect nearby charges is identical to the operation of an SET or QPC as a charge detector [12, 80, 111, 112]. That is, one sets the voltages on R and G such that one probes the maximum point in the SLQD transition. On a charging event causing a shift in the SLQD line, one then measures the background level. The resulting change in the readout signal strength indicates the presence of a real-time charging event.

Now to maximise the efficacy of the SLQD sensor, the two parameters that need optimising are the shift in the SLQD charge transition (1.1 mV along the V_{R} axis on sensing charge movement on the SET quantum dot as shown in Figure 3.12b) and the magnitude of the peak RF response of the SLQD charge transition. The shift in the SLQD charge transition must be at least beyond that of the half peak width of the SLQD charge transition (approximately the amplitude of the sweeping RF voltage V_{ac}) as otherwise the contrast on detecting charge will not be that of the peak RF response and the zero background level, but rather some finite non-zero value above the background level. The larger magnitude in the peak RF response implies more signal (a greater signal to noise ratio implies faster measurement times). Optimisation of the peak RF amplitude requires characterisation of the SLQD sensor to maximise the peak height (as discussed in Section 3.4.2) and careful device design to maximise the peak shift (as discussed in Section 3.4.3).

3.4.2 Demonstration and characterisation of the SLQD sensor

This section looks to maximise the readout signal strength by optimising the RF input power upon measurement of the SQLD reservoir-to-dot lever-arm and the electron temperature of the electrons in the reservoir (since the two parameters give the ratio $(e\alpha_{rg}V_{ac})\,/\,(2k_BT)$ as discussed in Table 3.2). The outlined methods first consider the readout signal strength as a function of input RF power; from which one may estimate the net loss in the transmission lines from the room temperature apparatus to the device. The net attenuation is an important parameter to diagnose. If the attenuation is much higher than expected, this could imply a broken coaxial cable or RF signal leakage. On measuring the power dependence, one measures the SLQD peak profiles at low powers over different temperatures to deduce the electron temperature and SLQD reservoir-to-dot lever-arm. Finally, given all the system parameters, one may estimate the signal's return gain. Once again, if the return gain is lower than expected, the diagnostic suggests that there may be a broken coaxial line or a malfunctioning amplifier. In the end, one obtains a calibrated RF peak height and peak width as a function of input voltage amplitude; an important calibration plot one may use in optmising the SLQD sensor. Knowing this, one can tune the input RF power to attain the maximum possible signal without inputting too much RF power that broadens the SLQD peak.

Now the input RF power sent to the PCB can be calculated by considering the different intentional attenuations [139]. The RF source (a *SRS SG386*) was set to output 11 dBm. The RF signal was sent through a splitter to yield the 5 dBm coherent local reference required for the IQ demodulator. The second portion of the split signal, 5 dBm, was sent to the device via a 30 dB *Minicircuits* attenuator and a variable *Pasternack PE7033* attenuator (that could be tuned from 0-90 dB over 1 dB steps) to help tune the input RF amplitude. The signal was then sent through a directional coupler that additionally couples the signal down by another 14.7 dB. Summing all the attenuations, the estimated signal power in dBm fed into device PCB was:

$$P_{\text{in(est)}} = -39.7 - A_S, \tag{3.38}$$

where A_S is the attenuator setting on the tunable attenuator. Noting that the signal generator is connected to a 50 Ω line, the estimated voltage level sent at the transmission line before the resonant circuit is[12]:

[12] Found by noting that $P = V^2/Z$ where $Z = 50\,\Omega$ is the transmission line impedance.

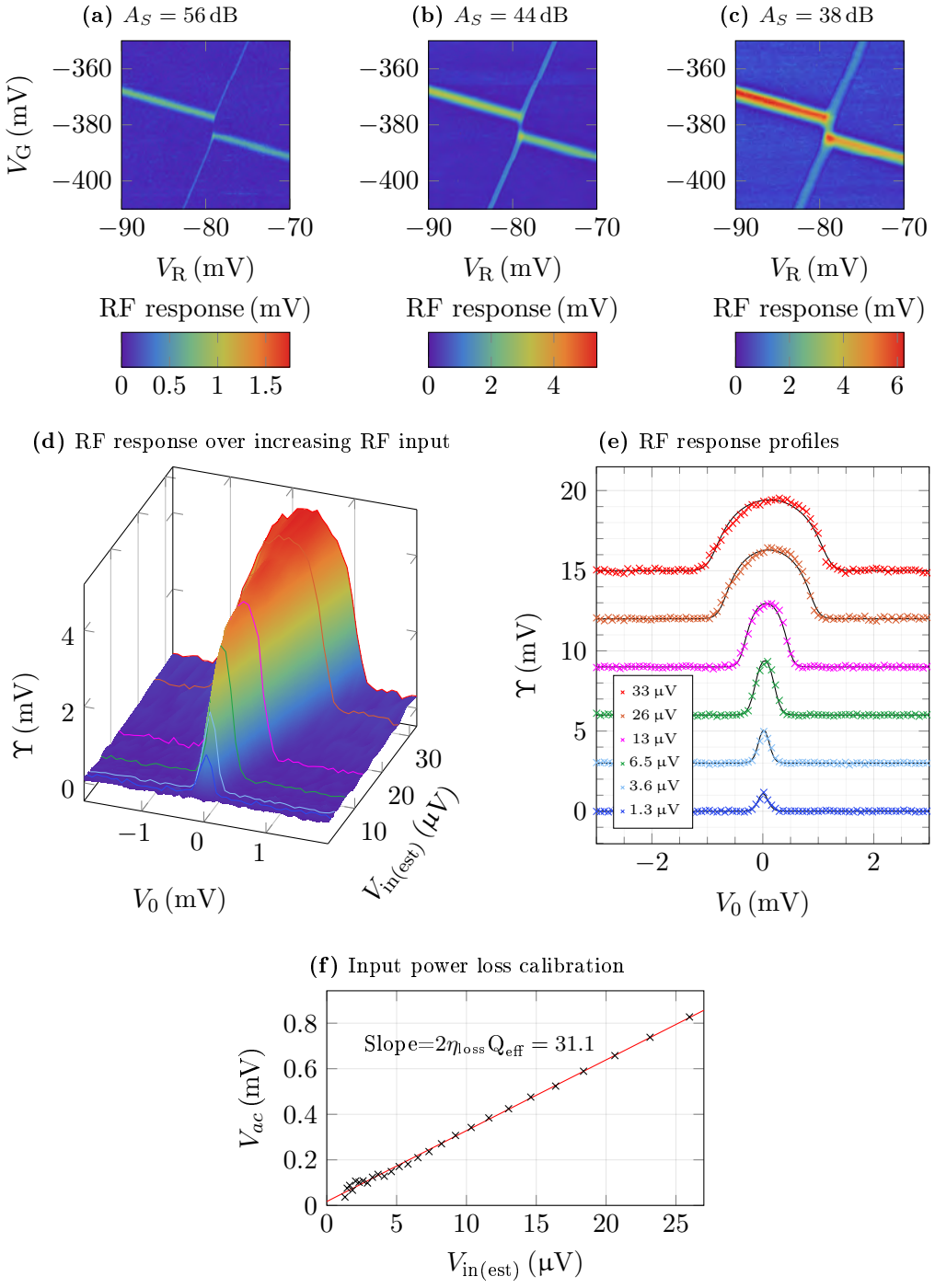

Figure 3.13: RF response of the SLQD sensor as a function of RF input power. **(a)-(c)** The stability diagram in Figure 3.12b can be plotted for different input attenuations A_S. With lower attenuation, as the RF input power increases, the RF response gets larger and broadens as seen by the thicker lines. **(d)** The SLQD response peak across V_R plotted as a function of V_0 (V_R offset to zero at the peak for clarity) and the estimated input voltage amplitude at the resonant circuit. The RF response saturates as expected. **(e)** The RF response profile plotted as a function of V_0 for selected input voltage amplitudes as highlighted in (d). The black lines indicate the RF response fitting function shown in Equation 3.40. The datasets are offset by 3 mV for clarity. **(f)** From the fits in (e), one may infer the RF voltage amplitude at the reservoir R itself: V_{ac}. From the linear fit in red, it is possible to estimate the RF input losses η_{loss} by noting the slope $dV_{ac}/dV_{in(est)} = 2\eta_{loss}Q_{eff} = 31.1$.

$$V_{\text{in-(est)}} = \sqrt{50 P_{\text{in-(est)}}}. \tag{3.39}$$

Figures 3.13a-c show charge stability diagrams, when setting the tunable attenuator A_S to 56 dB, 44 dB and 38 dB respectively. From the three plots, it is clear that the peak RF response of the SLQD transition line increases with increasing RF input power. However, as discussed in Section 3.3, the peak RF response of the SLQD charge transition must saturate with increasing RF input power as the fundamental limit to the maximal response is that when shuttling one electron between the reservoir and the SLQD quantum dot. One reaches the saturation in the RF response once the RF input voltage amplitude is large enough to start sweeping the SLQD energy level far beyond that of the temperature smearing on the reservoir. Figure 3.13d shows the measured saturating behaviour via a 3D plot of the RF response (of the SLQD peak) as a function of V_0 (the voltage offset tuning the SLQD energy level away from its reservoir Fermi-level[13]) and the estimated input voltage at the PCB $V_{\text{in-(est)}}$. The sliced profiles of the 3D plot (across V_0) at selected input $V_{\text{in-(est)}}$ values are shown in Figure 3.13e. As predicted, on increasing the RF input power, the peak RF response Υ saturates, while the peak width across V_0 continues to increase on increasing the RF input power. The RF signal response is non-zero when the RF voltage can sweep SLQD dot past the Fermi-level of its reservoir. Thus, the peak width (at larger input voltage amplitudes) is proportional to the extent to which the RF voltage moves the SLQD energy level and as expected, the peak width will continue to increase indefinitely with increasing RF input power.

The black fitting lines plotted on the RF response in Figures 3.13e were created by fitting the RF response for a given RF input power to the five parameter fitting function where V_0 is the dependent variable:

$$\Upsilon = a_0 \int_{-\pi}^{\pi} \frac{\sin^2(\tau)}{\cosh^2\left(a_w \left(V_0 - a_\delta + a_{ac}\cos(\tau)\right)\right)} d\tau + a_c. \tag{3.40}$$

This function comes from the analytic model for the RF response developed in Section 3.3.2 (specifically Equation 3.27). The fitting parameter a_δ may be zeroed if the dataset for the charge transition peak is post-processed such that it is centred at $V_0 = 0$. In addition, a_c may be zeroed if the RF response background level has been properly zeroed. The parameter a_0 determines peak RF response at $V_0 = 0$. The parameter a_w is the $e\alpha_{rg}/(2k_BT)$ factor common to V_0 and V_{ac} in the RF response. Thus, a_{ac} is the AC voltage amplitude at the gate used to move electrons between

[13] V_0 is simply V_R shifted such that $V_0 = 0$ at the peak of the RF response profile.

the SLQD dot and its reservoir. Since a_{ac} is the actual measured voltage at the gate of the device $a_{ac} \equiv V_{ac}$, one may infer the extra losses in the transmission of the RF input signal by comparing the fitted V_{ac} with the estimated voltage at the PCB $V_{\text{in-(est)}}$. Figure 3.13f shows a plot of V_{ac} as a function of $V_{\text{in(est)}}$. Now given the voltage amplitude input at the PCB $V_{\text{in(est)}}$ (that is, before the resonator), the expected voltage on the device gate is given by Equation 3.12:

$$V_{ac(\text{est})} = 2\eta_{\text{loss}} \text{Q}_{\text{eff}} \cdot V_{\text{in(est)}} \tag{3.41}$$

Since the effective quality factor of the resonator connected to R was approximately 100 [139], the slope of the fitted line (approximately 31.1) in Figure 3.13f is $200\eta_{\text{loss}}$. Thus, the measured voltage amplitude loss factor was $\eta_{loss} = 0.16$ (or approximately 16.1 dB in power loss). The transmission line loss was attributed to possible insertion losses at the PCB and general losses in the coaxial cable. One can obtain the actual input RF power at the PCB (that is, before the resonator) by subtracting loss η_{loss} from the estimated power:

$$P_{\text{in}} = P_{\text{in(est)}} - 16.1, \tag{3.42}$$

with all powers given in dB or dBm.

Using a similar approach, the return gain can also be calibrated if one knows the reservoir-to-SLQD lever-arm α_{R}. Usually with a SET sensor, the gate lever-arm to the sensor quantum dot can be found via Coulomb diamond measurements [15, 156]. Coulomb diamonds yield gate lever-arms by matching the known source-drain voltage bias to the SET quantum dot's energy level being tuned by a gate voltage via the gate lever-arm. However, for the SLQD sensor, there are no source-drain leads to provide a local energy reference. An alternate energy reference to which one may calibrate the gate lever-arm α_{R} is the temperature of the electrons in the reservoir. The reservoir electron temperature experimentally manifests as a broadening of the measured SLQD charge transition. As discussed before in Section 3.3.2 (specifically Equation 3.28), in the limit of low input voltage amplitudes (the so-called linear regime), the profile of the RF response as a function of V_0 tends towards a shape of constant width broadened by the temperature:

$$\begin{aligned} &\frac{\Upsilon}{V_{ac}} = b_0 \cdot \text{sech}^2\left(\frac{V_0}{b_w}\right) \\ &\begin{cases} b_0 = \left(\frac{\text{Q}_{\text{int}}}{\text{Q}_{\text{ext}}+\text{Q}_{\text{int}}} \cdot \frac{e(1-\alpha_{\text{R}})K}{2C_p} \cdot \frac{\Gamma_0^2}{\Gamma_0^2+\omega^2}\right) \cdot \frac{e(1-\alpha_{\text{R}})}{2k_B T_e} \\ \frac{1}{b_w} = \frac{e(1-\alpha_{\text{R}})}{2k_B T_e} \end{cases} \end{aligned} \tag{3.43}$$

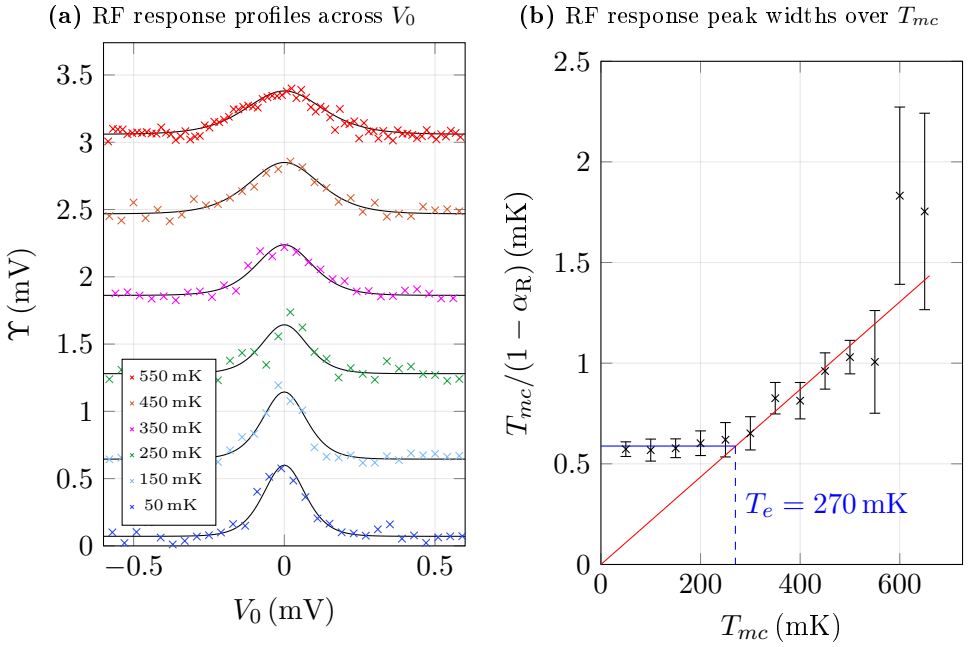

Figure 3.14: Temperature variation of the RF response in the linear regime used to determine the reservoir lever-arm and electron temperature. The RF response in the linear regime (low-V_{ac}) measured as a function of the mixing chamber temperature T_{mc} to deduce the lever-arm α_{rg} and the reservoir electron temperature T_e. **(a)** The RF response profiles are plotted over different mixing chamber temperatures. The fitted curves shown in black use the $\sim \text{sech}^2$ function given in Equation 3.43. The curves are offset by 0.6 mV for clarity. **(b)** The fitted widths, proportional to T_{mc}/α_{rg}, are then plotted as a function of temperature. When the mixing chamber temperature exceeds the electron temperature of the reservoir lead, the electrons equilibrate with the mixing chamber and thus, the peak widths linearly follow the mixing chamber temperature. The red line shows the linear fit for the portion of the data following the mixing chamber temperature; this yields $\alpha_{rg} = 0.46$. The blue line shows the linear fit for the widths when $T_e > T_{mc}$ to extract the reservoir electron temperature of 270 mK.

where b_0 controls the height of the fitted peak and b_w controls the peak width. Note that T_e is the temperature of the electrons in the reservoir R. Figure 3.14a shows this fitting function applied to the low-power RF response profiles[14] over different mixing chamber temperatures T_{mc}. Note that the peak RF response drops with higher temperatures as the RF response has a $1/T$ dependence (as shown in Section 3.3.2 when discussing the equation for the RF response Υ). Noting the expression for b_w, one may plot $T_{mc}/(1-\alpha_{\mathrm{R}})$ as a function of the mixing chamber temperature T_{mc} as shown in Figure 3.14b. In the bath-temperature raising experiment, the electron temperature T_e is typically higher than the mixing chamber temperature T_{mc} due to the difficulty in fully thermalising the silicon crystal with the mixing chamber when warm electrons are flowing into the device from the room temperature apparatus. Thus, for mixing chamber temperatures below the minimum temperature of the electrons in the reservoir, the peak width of the RF response remains constant as highlighted by the solid blue constant line fitted to the first six points. Eventually the mixing chamber temperature rises above the electron temperature and the reservoir electrons now become thermally excited by both the wires (the SMA cables and looms connected to the device) and the mixing chamber itself. The minimum reservoir electron temperature is no longer limited by the wires and thus, it equilibrates to the mixing chamber temperature as indicated by the linear trend fitted by the red line. The intersection point where the electron temperature starts to follow the mixing chamber temperature is taken to be the minimum electron temperature: $T_e = 270\,\mathrm{mK}$ [31, 112]. That is, the reservoir electron temperature is $T_e = 270 \pm 30\,\mathrm{mK}$ even when the fridge is set to its minimum mixing chamber temperature of approximately 50 mK. Since the gradient of the fitted points along the linear trend (in red) is $1/(1-\alpha_{\mathrm{R}})$, the reservoir lever-arm was extracted: $1-\alpha_{\mathrm{R}} = 0.54 \pm 0.05$.

With the gate lever-arm known, one may calibrate the return signal gain by investigating the RF response in the linear response regime (with $T_{mc} = 50\,\mathrm{mK}$). Here, one first considers the peak height of the fitted RF response (shown in the power dependence shown in Figure 3.13e) over different RF input voltage amplitudes at the reservoir lead V_{ac}. The peak RF response is plotted via the green markers in Figure 3.15. Taking the points for low values of V_{ac} in the linear regime[15], one may fit the line shown in blue. The gradient of the peak RF response with respect to V_{ac} in the linear regime was discussed in Section 3.3.2 (specifically Equation 3.28):

[14] The low amplitude power (in which the peak width was dominated by temperature rather than the RF input voltage amplitude) applied at the PCB was $P_{\mathrm{in}} = -131\,\mathrm{dBm}$

[15] Many papers in the prior literature only considered the RF voltage amplitude in the linear regime [110] instead of exploring the RF response at higher input powers as discussed in our paper [31].

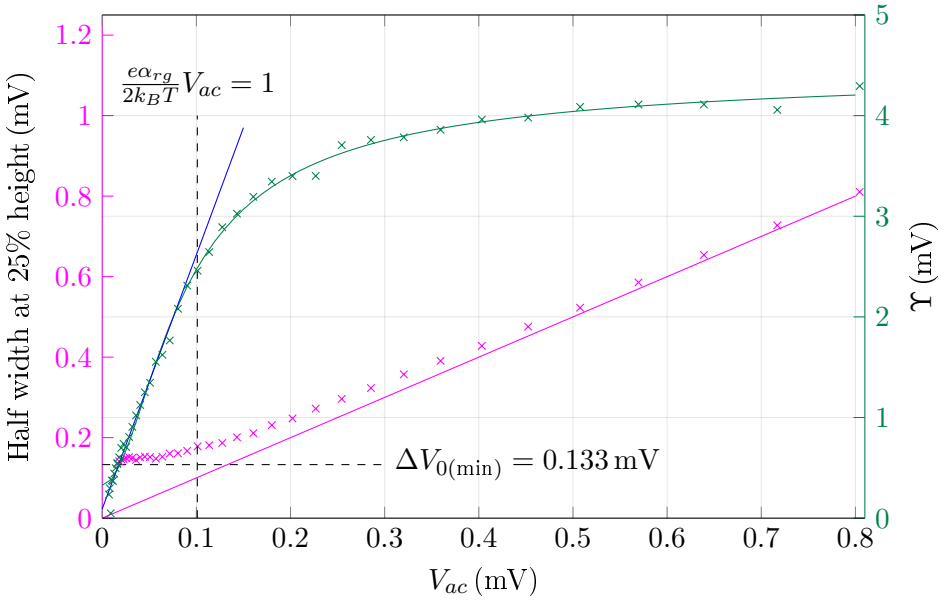

Figure 3.15: Experimentally measured RF response peak height (green) and peak width (magenta) of the SLQD sensor as a function of the input voltage amplitude. All the data points come from fitting the RF responses shown in Figures 3.13d-e as a function of V_{ac}. The magenta data points (with the left y-axis) indicate the half-width of each peak across V_0 where the response drops to 25% of the peak maximum for a given value of V_{ac}. The magenta line is the $V_{ac} = V_0$ line that indicates the asymptotic peak width as $V_{ac} \to \infty$. The green data points (with the right y-axis) indicate the peak RF response (at $V_0 = 0$) at any given value of V_{ac}. The solid green line is given by the fitting function in Equation 3.45. The slope of the peak RF response in the linear regime is highlighted by the blue line with the linear regime approximately stopping at the point where $e\alpha_{rg}V_{ac} = 2k_BT$. The minimum width of the RF response due to thermal broadening is also shown with $\Delta V_{0(\min)} = 0.133\,\text{mV}$.

$$\frac{\Upsilon_{\max}}{V_{ac}} = \frac{\mathrm{Q}_{\mathrm{int}}}{\mathrm{Q}_{\mathrm{ext}} + \mathrm{Q}_{\mathrm{int}}} \cdot \frac{K}{C_p} \cdot \frac{\Gamma_0^2}{\Gamma_0^2 + \omega^2} \cdot \frac{e^2\alpha_{rg}^2}{4k_BT} \approx \frac{\mathrm{Q}_{\mathrm{int}}}{\mathrm{Q}_{\mathrm{ext}} + \mathrm{Q}_{\mathrm{int}}} \cdot \frac{K}{C_p} \cdot \frac{e^2\alpha_{rg}^2}{4k_BT}. \tag{3.44}$$

The approximation in the second equality assumes that the electron tunnel rate is much larger than the driving frequency $\Gamma_0 \gg \omega$, where the SLQD operates mostly in the capacitive regime. The measured gradient of the RF response Υ with respect to V_{ac} in the linear regime was 25.256. Noting that, $(1 - \alpha_{\mathrm{R}})/T = 0.46/0.270$, $\mathrm{Q}_{\mathrm{int}} = 253$ and $\mathrm{Q}_{\mathrm{ext}} = 165$ [139], the voltage gain factor K is approximately 78000 or 97.8 dB gain in terms of power. The measured return gain of 97.8 dB was close to the expected gain in the amplifier chain, which was calculated to include 35 dB from the cryogenic amplifier in the fridge, $50 + 20$ dB via room temperature amplifiers and a 7.5 dB conversion loss in the IQ demodulator to yield approximately 97.5 dB in net signal gain. Thus, from the return gain diagnostic, one can conclude that the amplifiers (specifically the cryogenic amplifier) were properly functioning without any unexpected measurable signal loss. To capture the nonlinear regime (in the RF response) as predicted by the theoretical models in Section 3.3, the peak heights were fitted with the green line Figure 3.15 using the fitting function:

$$\Upsilon_{\max} = k_0 k_w V_{ac} F(k_w V_{ac}, 0, 1), \tag{3.45}$$

where k_0 controls the magnitude of the overall RF response (as it saturates with increasing V_{ac}) while $k_w = e(1-\alpha_{\mathrm{R}})/(k_BT)$ controls the point in which the peak RF response leaves the linear regime as highlighted by the dashed line where $e\alpha_{rg}V_{ac} = 2k_BT$. Similarly, at approximately $e\alpha_{rg}V_{ac} = 4(2k_BT)$, the peak RF response reaches 97.2% of the maximum possible value (with minimal peak broadening) as predicted previously by the analytic model in Table 3.2.

In the context of detecting nearby charges with the SLQD, it is desirable to know both the RF signal strength (peak height) as well as the peak half-width for a given input voltage amplitude[16]. Thus, Figure 3.15 shows the peak half-widths (taking it as the half-width when the function was 25% of its maximum value to better gauge the width of the peak with respect to the background noise) as a function of V_{ac} via the magenta markers. The lowest RF response peak half-width, when in the linear regime, is given by Equation 3.43:

[16] Noting that the peak height increases the readout SNR while the peak half-width needs to be smaller than the peak-shift that occurs when sensing nearby charge to obtain full contrast between the peak RF signal strength and the zero background level.

$$\Delta V_{0(\min)} = \frac{2k_BT}{e(1-\alpha_R)}\text{arcsech}\left(\tfrac{1}{2}\right) = 0.133\,\text{mV}, \tag{3.46}$$

with the measured electron temperature of electrons in the reservoir as $270 \pm 30\,\text{mK}$ and the reservoir lever-arm $\alpha_R = 0.54 \pm 0.05$. The linear trend shown in magenta highlights the asymptotic trend when $e\alpha_{rg}V_{ac} \gg k_BT$. That is, the half-width of the response peak tends towards the RF input drive amplitude (noting that the RF response is non-zero when $V_{ac} > V_0$ to ensure that the SLQD dot's energy level sweeps past the reservoir Fermi-level). The extra width of the SLQD peak is due to the temperature broadening of the reservoir electrons. Otherwise, the RF response is approximately zero outside $V_0 > V_{ac}$ for large V_{ac}, as discussed in the analytic models.

As noted before, the maximum readout signal contrast of the SLQD charge sensor requires the SLQD charge transition to shift by at least half its peak width on sensing charge on the target dot. In this experiment, the SLQD peak shifted by 1.1 mV on sensing electrons on the SET as shown in Figure 3.12. This is important as one can use this peak shift to bound the maximum peak width of the RF response to be below 1.1 mV. Thus, the maximum input RF voltage amplitude at the reservoir V_{ac} will be approximately 1.1 mV; an input amplitude far into the nonlinear saturation regime. From Equation 3.45, at this amplitude, one reaches 99.7% of the maximum possible RF readout signal strength. Note that if one were content with 97.2% (approximate minimum amplitude to reach the peak signal strength in the nonlinear regime while minimising peak broadening) of the maximum possible signal strength ($V_{ac} = 0.4\,\text{mV}$ in this experiment), then the peak shift on sensing charges can be as low as 0.4 mV.

3.4.3 Improving the SLQD sensor

In the previous section, specifically Figure 3.12, the relationship between the SLQD response peak width and height was explored as a function of the input voltage amplitude. The model, verified experimentally, predicts that one requires $e(1-\alpha_R)V_{ac(\text{sat})} = 4(2k_BT)$, to achieve 97.2% of the maximum possible RF response. However, at this mostly saturated RF input amplitude $V_{ac(\text{sat})}$, the peak half-width will also be approximately $\Delta V_0 \approx V_{ac(\text{sat})}$. Noting that the peak shift due to sensing nearby charge must be greater than the response peak half-width (to ensure maximal readout signal contrast between the peak height and the zero background level), one requires that:

$$\Delta V_0 \approx V_{ac(\mathrm{sat})} = \frac{8k_BT}{e(1-\alpha_\mathrm{R})} < \Delta V_\mathrm{SLQD} \tag{3.47}$$

where ΔV_SLQD is the peak shift of the SLQD charge transition on sensing nearby charge. Now the shift one obtains on sweeping a given gate is given by Equation A.20 in Appendix A:

$$\Delta V_\mathrm{SLQD} = \frac{e(\mathbf{C}_\mathrm{DD}^{-1})_\mathrm{SLQD\text{-}Dot}}{1-\alpha_\mathrm{R}}, \tag{3.48}$$

where $(\mathbf{C}_\mathrm{DD}^{-1})_\mathrm{SLQD\text{-}Dot}$ relates to the mutual capacitance between the SLQD dot and the target dot. The mutual capacitance quantity relates to the shift in the SLQD's energy on placing a charge on the target dot. In the context of this experiment, $\Delta V_\mathrm{SLQD} = 1.1\,\mathrm{mV}$ and $V_{ac(\mathrm{sat})} = \Delta V_0 = 0.4\,\mathrm{mV}$. The mutual capacitance factor rolls off approximately as the inverse of the distance between the SLQD and the target dot (the SET placed approximately 44 nm). Therefore, one could approximately double the distance between the SLQD and the SET to 120 nm and still achieve full signal contrast in the charge sensing RF readout signal without any loss in the signal to noise ratio. When comparing the range of the SLQD sensor to the size of a typical double-quantum dot in Si-P (12 nm), a sensor range of 120 nm yields a normalised range of 10. The normalised range is large when compared against the normalised range of 1-2 when using QPCs with GaAs or SiGe quantum dots [14, 17]. With such large charge sensing ranges (above 50 nm), the SLQD therefore serves as an excellent diagnostic charge sensor that can be discreetly placed in a large scale architecture.

Now combining the previous two equations, one can obtain the ultimate requirement in achieving full contrast in the RF signal strength when sensing charge movement:

$$k_BT < \frac{e^2}{8}(\mathbf{C}_\mathrm{DD}^{-1})_\mathrm{SLQD\text{-}Dot}. \tag{3.49}$$

Satisfying this inequality implies that one makes maximal use of the available RF readout signal strength when charge sensing. To satisfy this inequality one may increase the mutual capacitance $\mathbf{C}_\mathrm{DD}$ between the SLQD and the target dot by shaping the SLQD dot to cover more parallel area with the dot. In addition, one may better thermalise the reservoir of the SLQD to the mixing chamber of the dilution fridge[17]. With lower temperatures, one can start maximally oscillating electrons in

[17] Typical thermalising strategies seek to thermally contact the inner core of the coaxial lines (carrying the signals) onto the cooling plates of the dilution fridge [33, 34]. Usual methods include multiple stages of attenuators and feeding the signal over gold striplines on a sapphire block strapped to the mixing chamber plate (as sapphire is a good thermal conductor while being a good electrical

the SLQD at lower RF input voltage amplitudes and thus, minimally broaden the RF peak response.

Note that on satisfying the inequality above, one should also increase the maximum possible RF signal strength. From the discussions in Section 3.3.2, the fundamental maximum peak signal strength is:

$$\Upsilon_{\text{peak}} = \frac{\text{Q}_{\text{int}}}{\text{Q}_{\text{ext}} + \text{Q}_{\text{int}}} \cdot \frac{K}{C_p} \cdot \frac{2e(1-\alpha_{\text{R}})}{\pi}, \quad \frac{e(1-\alpha_{\text{R}})}{2k_B T} V_{\text{ac}} \gg 1. \tag{3.50}$$

The first method to approach the fundamental maximum is to increase the internal quality factor of the resonator[18] as discussed in Section 3.2.3. The second method to approach the fundamental maximum signal strength is to decrease the reservoir to gate lever-arm by increasing the mutual capacitance between the SLQD dot and its target dot (an approach implemented in a later experiment performed by Mark R. Hogg [155]). Finally, like with all signals transmitted from a nano-scale device to the room temperature apparatus, greater signal to noise ratios can be realised via cryogenic amplification at even lower temperatures (Johnson noise is lower at lower temperatures).

3.5 Future of the SLQD sensor

Theoretical and experimental developments in the design and implementation of a SLQD sensor in Si-P yielded the following key results:

- A SLQD sensor (fabricated in Si-P) was successfully characterised and shown to sense charge movement on a SET patterned 44 nm away. The SLQD peak shifting $\Delta V_{\text{R}} = 1.1\,\text{mV}$ due to charge movement on the SET.
- The theoretical methods developed to characterise the SLQD sensor enabled us to determine the RF input losses, RF return gain, SLQD reservoir-to-dot lever-arm ($\alpha_{\text{R}} = 0.54 \pm 0.05$) and the temperature of electrons in the reservoir ($T_e = 270 \pm 30\,\text{mK}$).
- The predicted saturation of the RF response with increasing RF power (beyond the linear regime) was verified experimentally; reaching 97.2% of the peak RF response, as predicted, when setting the voltage amplitude at the reservoir of the SLQD to $V_{ac} = 4(2k_BT)/(e\alpha_{rg})$. In this experiment for an electron

insulator).

[18] The circuit model assumes that the load is purely capacitive. To make the SLQD act capacitive, the electron tunnel rate must be much larger than the driving frequency

temperature of $T_e = 270 \pm 30\,\text{mK}$ and the reservoir lever-arm $\alpha_\text{R} = 0.54 \pm 0.05$, the optimal RF amplitude for peak RF response was $V_{ac} = 0.4\,\text{mV}$.

- With a $\Delta V_\text{R} = 1.1\,\text{mV}$ shift in the SLQD peak, the SLQD sensor was capable of detecting charges approximately up to 120 nm with full signal contrast in the RF response, given that the RF voltage amplitude only needed to be 0.4 mV in this experiment.

The detection distance of the SLQD sensor with respect to the target quantum dot can be further increased by increasing the detection sensitivity of the resonator via the methods discussed in Section 3.2.3:

- Increasing the internal quality factor with respect to the external quality factor.
- Lowering the parasitic capacitance.

However, some SLQD specific improvements include:

- Lowering the electron temperature via better thermalisation of the device to the dilution fridge.
- Lowering the reservoir-to-dot lever-arm by increasing the mutual capacitance between the SLQD dot and the target quantum dot. One can increase the mutual capacitance by increasing the parallel area between the two dots by reshaping the dot during fabrication.

The results also highlighted that the SLQD sensor can not only be used as a compact diagnostic probe, but also be used as a single-spin qubit sensor (via the spin-to-charge conversion method) that could replace the 3-lead SET. A current PhD student Mark R. Hogg continued this project and has already shown high-fidelity single-shot single-spin readout of single spin electrons via a SLQD sensor. Therefore, the SLQD sensor is a viable replacement for the larger SET sensor and should therefore be considered in future architectures using single-spin electron qubits in Si-P.

Chapter 4

Integrating RF singlet-triplet sensors for scalability

Although the SLQD sensor (outlined in Section 3) is compact, it still requires a dedicated gate and quantum dot[1]. A more compact sensor that integrates directly into a pre-existing gate in the device is the single-gate RF sensor as proposed for the scalable single-triplet architecture in this thesis. The single-gate RF sensor oscillates of one the two electron (of the singlet-triplet qubit) across the two dots hosting the qubit, with oscillations only occurring if the electrons are in a singlet state (lifting of Pauli blockade). As discussed in Section 3, resonant circuitry is used to detect an AC quantum capacitance resulting from the electron oscillations. There are two modes of inter-dot electron oscillations that may occur: tunnelling capacitance (electron oscillations via the ground and excited charge states) and adiabatic quantum capacitance (electron oscillations via adiabatic transfer across the ground-state eigenstates). The section will first model the single-gate RF sensor to investigate the optimal system parameters and tradeoffs of the two modes of operation with the the result that the adiabatic quantum capacitance is seen as the better pathway until further research is done on the tunnelling capacitance mode in the context of P-donor dots (for example, a sufficiently long excited singlet state coherence and spin lifetime to ensure a long enough measurement time). In particular, the modelling outlined in this section is performed to investigate the full nonlinearity of the quantum capacitance in the

[1] Although there was a demonstration of the SLQD taking form of one of the quantum dots hosting the singlet-triplet qubit and its reservoir, the implementation is not favourable in the long term [130]. This is because the large reservoir to dot tunnel rate required for SLQD operation will couple the quantum dot too strongly to its reservoir, thereby shortening the spin lifetime and coherence of the singlet-triplet qubit [30].

regime of higher RF powers as with the SLQD sensor. Although the RF power in fact decays at higher input RF powers (unlike the saturation that occurs with the SLQD sensor), the models help place bounds on the experimental parameters that are useful when operating in the tunnelling capacitance (driving frequency must match twice the tunnel coupling frequency) and adiabatic quantum capacitance regimes (driving frequency must be much less than the tunnel coupling frequency).

The device fabricated in Chapter 2 was then characterised using a single-gate RF sensor implemented with a chip-inductor resonator [29]. It was shown that the measurement time limiting singlet to triplet-t_- relaxation time was 2 ms. The value was many orders of magnitude better than a previous experiment which measured 60 ns due to the strong coupling of the dots to their reservoirs. This was weakened in the current experiment by moving the reservoirs further away (as discussed in the optimisation of the dot-to-reservoir distance d_r in Section 2.2.3). With long spin lifetime of 2 ms demonstrated, it was predicted that single-shot readout should be possible given an optimised setup. One of the key requirements to achieve high-fidelity single-gate RF readout was to utilise a resonator with a high internal quality factor. Thus, the chip-inductor resonator used in the initial device characterisation [29] was replaced with a low-loss superconducting inductor [32]. The single-gate RF sensor was then further optimised during the experiment (for example, by finding the optimal readout points). It was additionally shown that the single-gate RF sensor did not significantly affect the dynamics of the spins under measurement (important property of a qubit sensor is make a faithful representation of the qubit under measurement). Ultimately, the optimisation led to the first demonstration single-shot single-gate RF spin readout [32].

4.1 Modelling the single-gate RF sensor

The concept of a single-gate RF sensor has been demonstrated in gate-defined quantum dots (at 0 T [57] and 200 mT [105]) and recently with Si-P quantum dots [30] (at 2 T). Although the previous results showed spin-readout, the measurements were not achieved in single-shot. Nevertheless, the first attempt to use a single-gate RF sensor in a 4-dot device[2] yielded no RF signal response when activating the single-gate RF sensor as the electron tunnel rate between the two dots was too low when

[2]This was a device that was fabricated before the device discussed in Chapter 2. The device was fabricated as a training exercise and had a double quantum dot (approximately 2P-3P in size) with an inter-dot distance of 14 nm. The resulting tunnel coupling was too small to measure with the single-gate RF sensor using the adiabatic quantum capacitance mode.

compared to the driving frequency of 460 MHz. However, the exact conditions under which the single-gate RF sensor fails to produce a signal was unclear. As such, a better theoretical understanding of the single-gate RF sensor was needed to provide insights for future device designs, optimisations and experiments. It was hoped that by gaining a similar understanding to the effect of the nonlinear capacitances in the SLQD sensor experiments, the elusive single-shot readout with the single-gate RF sensor would be achievable.

The SLQD system was modelled using a rate equation that described the electron oscillations between a discrete state on a quantum dot and a continuum of states on the reservoir. However, with the single-gate RF sensor, the two sites are both discrete energy levels on separate quantum dots. Thus, the rate equation model is insufficient and the single-gate RF sensor must be modelled as a quantum system using the two-level system formalism. Although driven systems have been well-studied in the field of quantum optics, the application of the driven two-level system in the context of single-gate RF sensing leads to slightly different analytic techniques in finding the required solutions. For example, typically one is interested in the overall system dynamics in the rotating frame. However, in the context of single-gate RF sensing, one is interested in the probability density (proportional to the charge movement between the dots) at a particular frequency ω to then find the resulting current and quantum capacitance.

Our attempts at modelling the single-gate RF sensor started with perturbative methods (based on the rotating wave approximation) that revealed details surrounding the 'tunnelling capacitance' mode (where one utilises excited charge states to oscillate the electrons between the two dots). It was found that the perturbative methods could not capture the nonlinearities at higher RF input voltages and thus, a semi-quantum ansatz was used to analytically model the nonlinear capacitance when operating in the 'quantum capacitance' mode (where one adiabatically oscillates between the charge ground states to oscillate the electrons between the two dots). Collectively the modelling (developed in this thesis) provided insights into the conditions required to realise the single-gate RF sensor. These theoretical results helped pave the way to optimise the single-gate RF sensor in order to achieve single-shot single-gate RF spin readout as discussed in later in Section 4.2.

4.1.1 Initial Hamiltonian construction

The full Hamiltonian for a singlet-triplet qubit, derived in Appendix E, involves two electrons across two quantum dots in which the electrons interact via a tunnel

coupling term, the potentials across the dots may be tilted and magnetic fields break key spin degeneracies. However, in the context of single-gate RF readout, one may consider one of the electrons to remain on the second dot, while the other electron moves freely between the two dots if the electrons form a singlet state. If the electrons are in a triplet state, the electrons must remain on separate dots due to Pauli spin blockade. Thus, the analysis only considers the singlet state. Under the basis s_{11} (electrons on separate dots) and s_{02} (electrons both on the same dot), one may write the effective charge qubit Hamiltonian $\mathbf{H}_{\text{id}}$ [57, 158]:

$$\mathbf{H}_{\text{id}} = \begin{pmatrix} \Delta & -t_c \\ -t_c & -\Delta \end{pmatrix} \equiv \Delta\sigma_z - t_c\sigma_x, \tag{4.1}$$

where t_c is the inter-dot tunnel coupling and Δ is the detuning. The detuning is a tilting potential. The detuning is defined as half the energy splitting when the electrons (in the absence of a tunnel coupling), for a given applied voltage ΔV_g on gate g satisfies:

$$2\Delta = -e\alpha_{g1}\Delta V_g + e\alpha_{g2}\Delta V_g \equiv e\Delta\alpha \cdot \Delta V, \tag{4.2}$$

where α_{g1} and α_{g2} are the gate lever-arms to the first and second dots respectively, with $\Delta\alpha$ termed the differential lever-arm. The differential lever-arm is a geometric factor that is greater than zero and at most one (it is typically 5-10% in planar Si-P devices [82, 86, 92]). In the context of single-gate RF readout, the detuning is varied sinusoidally with a gate voltage amplitude of V_{ac} and frequency ω along with a possible detuning offset voltage V_0:

$$\Delta = \tfrac{e\Delta\alpha}{2}\left(V_0 + V_{ac}\cos(\omega t)\right) \equiv V_0' + V_{ac}'\cos\left(\omega t\right). \tag{4.3}$$

When the detuning drive causes the electron to oscillate adiabatically between the two ground-state charge states, one operates in the 'quantum capacitance' mode of operation shown in Figure 3.4a. When the detuning drive causes the electron to oscillate between the ground and excited charge states, one operates in the 'tunnelling capacitance' mode of operation shown in Figure 3.4b. The goal is to find the quantum capacitance and find the resulting readout signal strength in the two modes of operation. To find the quantum capacitance, the solution first finds the probability of occupation $p(t)$ at frequency ω. Similar to the modelling of the SLQD in Section 3.3, here we can obtain the charge occupation $Q(t) = e \cdot p(t)$. Noting that the current can be obtained by taking the time-derivative of the charge, one can obtain the quantum capacitance C_q by noting that $V_{ac}/I_{ac} = 1/(\omega C_q)$ (where

V_{ac} and I_{ac} are the voltage and current amplitudes at frequency ω). The solutions to the Hamiltonian in Equation 4.1 are given in Appendix C with the tunnelling capacitance behaviour solved via the rotating wave approximation and the adiabatic quantum capacitance behaviour solved via a semi-quantum approach. The next section summarises the key results from the theoretical modelling in the context of final design considerations along with the advantages and disadvantages of the adiabatic quantum capacitance and tunnelling capacitance modes.

4.1.2 Summary of design considerations for single-gate RF sensing

Two modes were explored in the theoretical study: the resonant 'tunnelling capacitance' and the adiabatic 'quantum capacitance'. Both modes require different LC resonator frequencies to achieve maximal RF readout signal strength. That is, the adiabatic quantum capacitance mode requires a resonator frequency much lower than the tunnel coupling frequency, while the tunnelling capacitance mode requires the driving frequency to match two times the tunnel coupling frequency.

The first mode of operation investigated was the tunnelling capacitance regime. Operation in the tunnelling capacitance regime requires voltage amplitudes V'_{ac} to be perturbative with respect to the tunnel coupling t_c to satisfy the rotating wave approximation. The RF readout signal for the resonant tunnelling mode of operation was found to be:

$$\Upsilon_{\text{res. tunl.}} = \frac{\mathrm{Q}_{\text{int}}}{\mathrm{Q}_{\text{ext}} + \mathrm{Q}_{\text{int}}} \cdot \frac{K}{C_p} \cdot \frac{e\Delta\alpha}{2} \cdot \frac{t_c}{\sqrt{V_0'^2 + t_c^2}} \tag{4.4}$$

with the resonant frequency ω of the RF drive set to the energy splitting:

$$\hbar\omega = 2\sqrt{t_c^2 + V_0'^2} \tag{4.5}$$

Maximal RF signal strength is clearly obtained when $V'_0 = 0$. That is, the resonant frequency should match twice the tunnel coupling frequency: $\omega = 2t_c$. Since, singlet-triplet qubit operation in Si-P (as discussed in Section 2.2.3) requires a large tunnel coupling of at least 1-2 GHz, operation in the tunnelling capacitance regime will require large resonant frequencies. Therefore, the required inductances for the resonators will be smaller by approximately a factor of ten[3]. A smaller inductance usually implies smaller footprint inductors (when using high-quality factor super-

[3] Current resonators operate at approximately ~100 MHz [29–31]. An increase in ω to 1-10 GHz will result in (noting that $\omega = 1/\sqrt{LC}$) an smaller inductance by a factor of approximately 10 (if the parasitic capacitance is approximately the same order of magnitude).

conducting inductors) and subsequently lower parasitic capacitances C_p (therefore, greater RF readout signal strength). From a scalability perspective a smaller inductor footprint is desirable. However, one should note that one of the key challenges is that the resonant frequency must precisely match $2t_c$ as any non-zero adjustments on the detuning offset V_0' to bring the RF drive into resonance will diminish the readout signal strength. For Si-P systems where the tunnel coupling is fixed on fabrication, one will require extremely precise tunnel couplings to match the resonant frequencies of the fabricated resonators. If one finds a precise regime where the qubits' tunnel couplings are all uniform, resonator multiplexing will be an issue as the resonant frequencies will not be different (as required for individual frequency addressibility). One solution to this conundrum is to set the resonant frequencies of adjacent resonators to progressively higher resonant frequencies (as V_0' can be adjusted to achieve resonance). That is, one can sacrifice readout signal strength to achieve frequency multiplexing. Finally, one needs to balance the possibly lower measurement times that may occur due to the fast decay and decoherence of the excited charge states (although not measured in Si-P, one may expect decoherence times of 100 ns-1 µs when comparing results from SiGe quantum dots [135]). Thus, as a long-term solution, the tunnelling capacitance mode was not recommended for the singlet-triplet architecture proposed in this thesis. However, the precise nature of the resonant tunnelling method gives an idea of why the tunnelling capacitance was not detected in the first quadruple quantum dot device. Here, the tunnel couplings were too small to be measured via the adiabatic quantum capacitance mode and most likely did not match half the driving frequency 460 MHz, to enable the tunnelling capacitance mode of operation.

The second mode of operation investigated (to find the conditions for peak RF readout signal strength) was the adiabatic quantum capacitance regime. Note that the readout point is set to zero detuning ($V_0' = 0$) to obtain the maximum readout signal strength. Here, the initial charge state of the qubit (that is, the superposition of s_{11} and s_{02}) was shown to affect the measured RF readout signal strength. If one starts in the exact ground state on initiating readout, the resulting RF readout strength is:

$$\Upsilon_g = \frac{\mathrm{Q_{int}}}{\mathrm{Q_{ext}} + \mathrm{Q_{int}}} \cdot \frac{K}{C_p} \cdot \frac{e\Delta\alpha}{2} \cdot \frac{V_{ac}'}{\sqrt{t_c^2 + V_{ac}'}} \left(1 - \exp\left(\frac{t_c^2}{\omega V_{ac}'/\sqrt{2}}\right)\right). \tag{4.6}$$

Disregarding the final factor (the LZSM envelope), the readout signal strength increases and saturates at input voltage amplitudes V_{ac}' larger than the tunnel coupling

t_c. A similar RF response occurs when the initial state of the qubit is fully in s_{11} charge state (as might be the case when performing singlet-triplet qubit operations), but slightly smaller at lower RF input amplitudes:

$$\Upsilon_0 = \frac{\mathrm{Q_{int}}}{\mathrm{Q_{ext}} + \mathrm{Q_{int}}} \cdot \frac{K}{C_p} \cdot \frac{e\Delta\alpha}{2} \cdot \frac{V_{ac}'^2}{t_c^2 + V_{ac}'^2} \left(1 - \exp\left(\frac{t_c^2}{\omega V_{ac}'/\sqrt{2}}\right)\right). \tag{4.7}$$

The slightly smaller response should be noted if one is optimising the signal to noise ratio (for example, using lower input RF powers to lower photon shot noise). One may mitigate the smaller readout signal strength by adiabatically moving (with respect to the tunnel coupling) from the qubit operating point to the readout point at zero detuning to ensure that one starts in the true charge ground state (at detuning $\Delta = -V_{ac}'$) at the beginning of the RF cycle. However, if one starts in $|-\rangle = (s_{11} - s_{02})/\sqrt{2}$ (the ground state found at zero detuning; that is, starting with the ground state 90° out of phase with the detuning of the RF drive), the readout signal strength reaches a peak at $V_{ac}' = t_c$:

$$\Upsilon_- = \frac{\mathrm{Q_{int}}}{\mathrm{Q_{ext}} + \mathrm{Q_{int}}} \cdot \frac{K}{C_p} \cdot \frac{e\Delta\alpha}{2} \cdot \frac{V_{ac}' t_c}{t_c^2 + V_{ac}'^2} \left(1 - \exp\left(\frac{t_c^2}{\omega V_{ac}'/\sqrt{2}}\right)\right). \tag{4.8}$$

The maximum RF response is in fact half the maximum possible peak value when compared to loading the state completely in s_{11}. Physically one may visualise this as a 50% efficiency in the electron oscillations. That is, when starting with the oscillating electron partially on both dots, the detuning sweep effectively oscillates only half an electron every cycle. Finally, in all cases, the readout signal strength for the adiabatic quantum capacitance mode of operation has a LZSM factor which places an upper bound on the resonant frequency of the LC resonator. Here, to maintain adiabatic operation, one must ensure that $\omega \ll t_c$ to ensure that the LZSM envelope appears at much higher values of V_{ac}' such that one may successfully find a point close to the fundamental maximum (that is, by satisfying $\omega \ll t_c$, one adiabatically stays in the ground state):

$$\Upsilon_{\max} = \frac{\mathrm{Q_{int}}}{\mathrm{Q_{ext}} + \mathrm{Q_{int}}} \cdot \frac{K}{C_p} \cdot \frac{e\Delta\alpha}{2}. \tag{4.9}$$

Note that the fundamental maximum is the same for both the resonant tunnelling (which occurs when exactly at resonance) and adiabatic modes of operation. The fundamental limit in the RF readout response occurs when oscillating a single electron between two dots and may be achieved in the two modes via:

- Tunnelling capacitance - setting $\omega = 2t_c$ and $V'_{ac} \ll t_c$.

- Adiabatic quantum capacitance - setting $\omega \ll t_c$ and $V'_{ac} \gtrsim t_c$. In addition, one must ensure that the RF drive begins readout with the singlet state close to the true ground singlet charge state.

The remaining experimental considerations required to reach the fundamental limit of the RF readout response (for both the adiabatic quantum capacitance and tunnelling capacitance modes) are similar to the SLQD sensor. That is, one should increase the internal quality factor with respect to the external quality factor and use cryogenic amplification at lower temperatures (where Johnson noise is smaller) to obtain larger signal to noise ratios as discussed in Section 3.2.3.

4.2 Single-gate RF characterisation and single-shot spin readout

The singlet-triplet architecture proposed in this thesis uses the compact single-gate RF sensor (which probes electron oscillations between the two dots hosting the qubit) for qubit readout. Although the single-gate RF sensor had been demonstrated before [30, 57, 105], it had not yet performed single-shot readout due to an insufficient RF readout signal to noise ratio. Experiments performed on the Si-P quadruple quantum dot device (characterised in Section 2.2.4) suggested that single-shot readout should be viable given that the available measurement time, set by the singlet to triplet t_- relaxation time (that is, the qubit decaying away from the qubit subspace), was 2 ms [29]. From the theory outlined in the previous sections, it was shown that to enhance the readout sensitivity for single-shot readout, it was important to increase the resonator's internal quality factor. The internal quality factor of the chip-inductor resonator (used initially for the electrostatic characterisation of the device) was $Q_{int} = 370$. This was increased in this chapter to $Q_{int} = 750$ by replacing the surface mount chip inductor with a NbTiN superconducting spiral inductor. The following sections highlight the experimental development in achieving single-shot single-gate RF spin readout as well as techniques for characterising both the RF circuitry and the double quantum dot hosting the singlet-triplet spin state.

4.2.1 Improving the resonator

To achieve single-shot readout, the spin readout signal strength needed to be maximised. For a LC resonator, as discussed in Section 3.2.2, the readout signal strength can be maximised by minimising the parasitic capacitance C_p of the resonator and maximising the internal quality factor Q_{int}. The LC resonator used in the initial experiment was formed by a *Coilcraft 1206CS-821XJE* surface mount chip-inductor (specified to be 820 nH at 35 MHz) along with the resulting geometric parasitic capacitance. The geometric parasitic capacitance C_p was reduced by removing all copper tracks and ground planes near the inductor and by using a thinner 0.5 mm *Rogers RO4003C* PCB laminate with a lower relative permittivity of 3.38 as opposed to 1 mm FR4 laminates (with a relative permittivity of 4.7) in previous experiments [159]. The changes collectively resulted in a drop in the parasitic capacitance from ∼0.72 pF to 0.45 pF, to yield an approximately 60% increase in the readout signal strength.

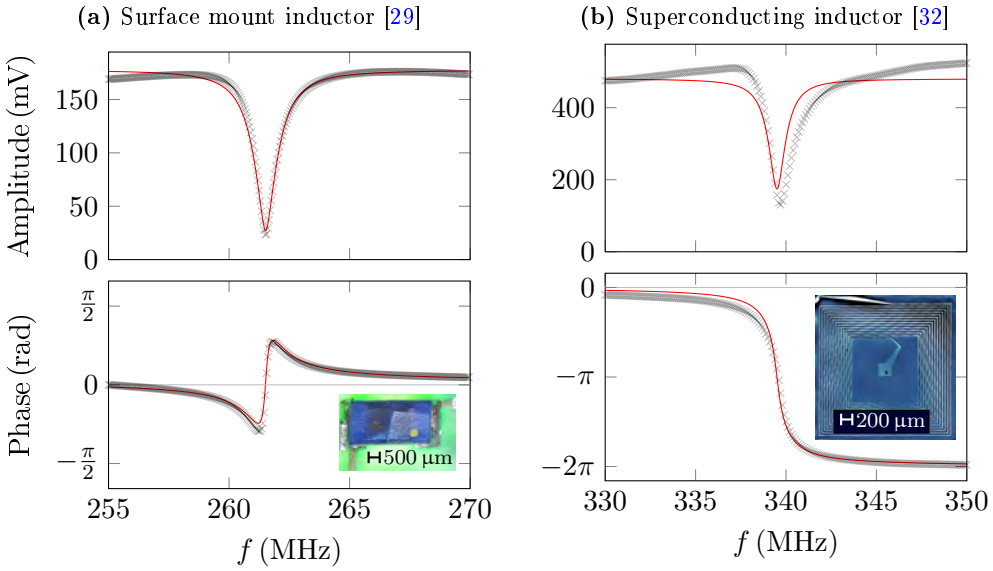

Figure 4.1: Resonator responses when using a surface mount and a superconducting inductors. The curves show the reflected amplitude and phase as a function of frequency about the respective resonant frequencies. **(a)** The resonator reflectance when using a SMD inductor. The resonant frequency was 261.5 MHz while the internal and external quality factors were 370 and 570 respectively. The inset shows an optical image of the SMD inductor. **(b)** The resonator reflectance when using the NbTiN superconducting spiral inductor. The resonant frequency was 339.5 MHz while the internal and external quality factors were 750 and 350 respectively. The difference in the external quality factors is likely to be due to the different geometry in coupling the inductor to the transmission line. The inset shows an optical false-colour image of the NbTiN superconducting inductor.

When fitting the reflectance (the methods discussed in Appendix D) response of the chip-inductor LC circuit, in Figure 4.1a, the internal and external quality factors were measured to be 370 and 570 respectively. The internal quality factor of the chip-inductor LC circuit was limited by the resistance of its coil windings. A natural step to reduce the coil resistance is to replace the chip-inductor with a super-conducting inductor which should have zero resistance in principle. Thus, the second round of experiments had the chip-inductor replaced by a 100 nm thick NbTiN, on Si subtrate, superconducting spiral inductor. The superconducting inductor was a 14-turn spiral, with a length of 78 mm, trace width of 10 µm and a trace gap of 30 µm between each turn. Typically superconducting lines lose their superconductivity, degrading the internal quality factor, when applying magnetic fields past their critical field. As spin qubits typically require high magnetic field operation, the substrate was chosen to be NbTiN due to its high critical field and subsequent ability to retain superconductivity when applying the magnetic fields parallel with the substrate [144, 154, 160, 161]. The inductor was fabricated by Takashi Kobayashi with a nominal geometric inductance of 440 nH and kinetic inductance of 98 nH. With the resonant frequency of the LC circuit measured to be 339.5 MHz, as shown in Figure 4.1b, the resulting parasitic capacitance was approximately 0.4 pF. The internal and external quality factors were approximately 750 and 350 respectively. Given the $Q_{int}/(Q_{int} + Q_{ext})$ pre-factor in the RF readout signal strength, one would expect a signal increase of approximately 73% when replacing the SMD chip inductor with the superconducting spiral inductor.

4.2.2 Characterisation of the singlet-triplet state hosted on P-donor dots

Before performing spin readout on a singlet-triplet state hosted on a double quantum dot, one needs to calibrate the energy landscape of the electrons on the double quantum dot. The two relevant parameters that required characterisation were the inter-dot tunnel coupling t_c and the inter-dot differential gate lever-arm $\Delta\alpha$.

To demonstrate a single-gate RF sensor, there needs to be a double quantum dot hosting a singlet-triplet state. Two possible candidates were present in the quadruple quantum dot device characterised in Section 2.2.5 (the double quantum dots D1L/D1U and D2L/D2U). However, the first pair of dots D1L/D1U formed an approximately symmetric 2P-2P double quantum dot and thus, presented no accessible singlet-triplet charge states (that is, even parity inter-dot transitions) within the available range of gate voltages. The second pair dots D2L/D2U (forming an

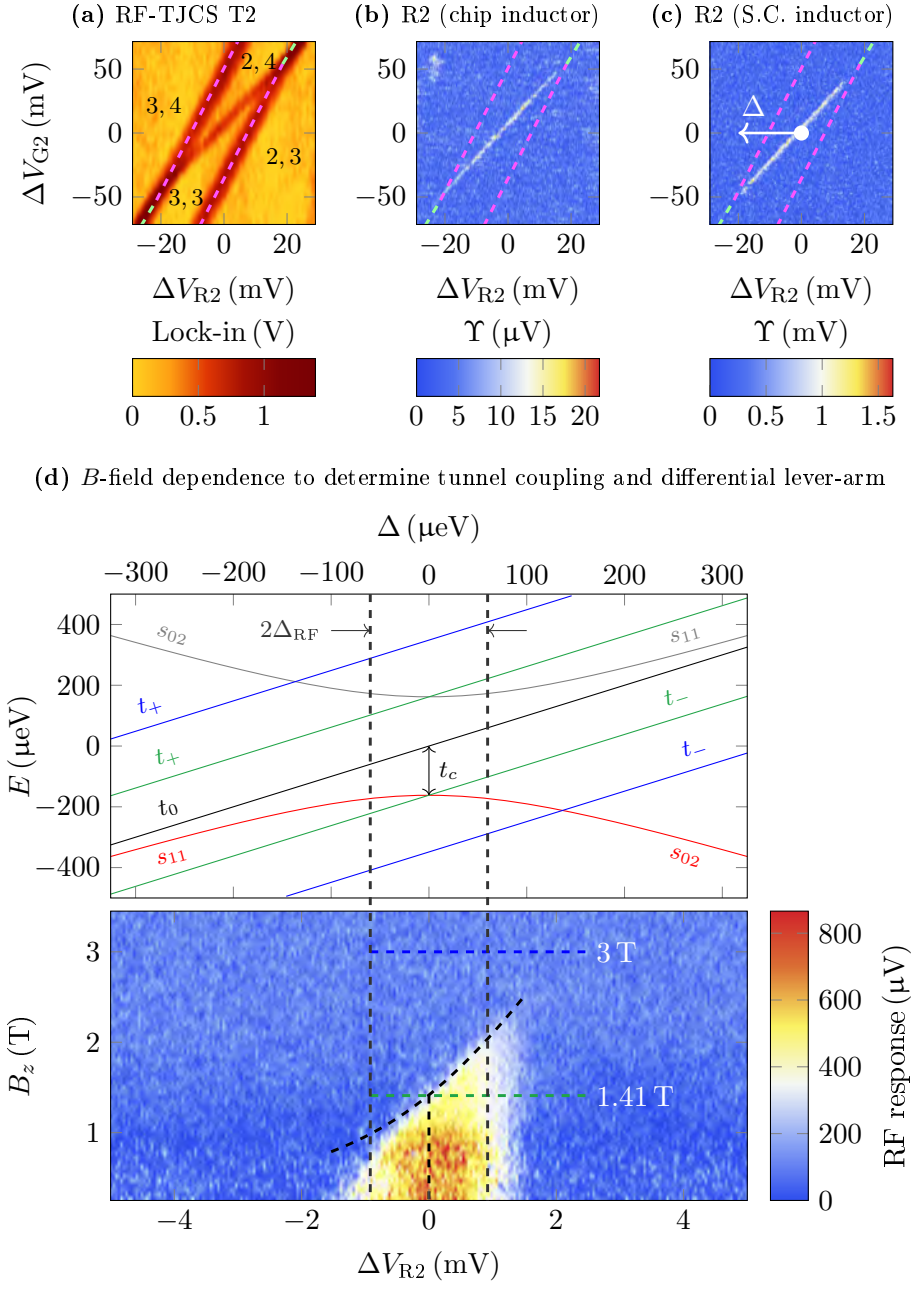

Figure 4.2: Single-gate RF sensor measurements with different inductors and device tunnel-coupling characterisation. The measurements concern the $(3,3) \leftrightarrow (2,4)$ inter-dot transition (across dots D2L/D2U shown in Figure 2.10) observed on sweeping the gate voltages on R2 and G2. **(a)** Differential TJCS response taken with the T2 sensor as measured with a 4 mV lock-in excitation applied to R2. **(b)** Single-gate RF response Υ of R2 using the chip-inductor at a resonant frequency of 261.5 MHz [29]. **(c)** Single-gate RF response Υ of R2 using the superconducting inductor at a resonant frequency of 339.5 MHz [32]. The direction of positive detuning Δ is labelled on the inter-dot transition. **(d)** Response when taking a 1D cut of the inter-dot transition from the single-gate RF response across R2 as shown in (c) and changing the magnetic field (applied in-plane as shown in Figure 2.10). A scale energy diagram is shown to highlight the energy scale and distribution of singlet-triplet energy states. Δ_{RF} is the input RF signal amplitude. The magnetic field dependence yields the tunnel coupling 39 ± 6 GHz as seen by the t_- triplet line at 1.41 T and differential lever-arm of R2 from fitting the envelope (the s_0/t_- anti-crossing like in a spin-funnel).

approximately asymmetric 3P-4P double quantum dot) provided several accessible singlet-triplet charge states (the electrostatic rationale is discussed in Section 2.2.3). Here, we accessed the inter-dot singlet-triplet transition across the dots D2L/D2U with the minimum number of electrons[4] in which single-gate RF readout was still possible (that is, a large enough tunnel coupling to yield a non-zero RF response). This was the $(3,3) \leftrightarrow (2,4)$ transition (with the electron numbers given for dots D2L and D2U respectively). Note that the 6-electron transition is equivalent to the $(1,1) \leftrightarrow (0,2)$ transition with two spin-paired electrons on each dot not affecting the singlet-triplet state formed by the valence electrons. The $(3,3) \leftrightarrow (2,4)$ inter-dot transition was first realised in a charge stability diagram, taken by sweeping the designated gates R2 and G2, using the charge sensor T2 as shown in Figure 4.2a (the electrons were counted via the characterisation techniques discussed in Section 2.2.5). The charge sensor response was useful due to the ability to show charge transitions of electrons leaving or entering the double quantum dot D2L/D2U. For example, the dashed magenta and green lines show electrons moving onto/from the reservoir from/to the dots D2L and D2U respectively. Figure 4.2b shows the same stability diagram taken using the single-gate RF sensor formed by the chip-inductor on R2 [29]. The RF stability diagram was taken with the input RF signal switched on while sweeping the gate voltages on the axes and measuring the reflected RF response. When the voltages are set to points across charge transitions, the input RF voltage can cause electrons to oscillate between a reservoir and a dot like in a SLQD sensor or between dots like that in a single-gate RF sensor. However, only the inter-dot charge transition is observed. By noting the SLQD theory from the previous sections, one readily confirms that by design the charge loading lines are not seen due to reservoir-to-dot tunnel rates being much smaller than the driving resonator frequency of 261.5 MHz. When switching to the superconducting inductor, there was a marked improvement in the signal strength as shown in Figure 4.2c where the peak RF readout signal strength of the inter-dot transition after amplification on average went from $\sim 20 \mu V$ to $\sim 800 \mu V$ [32].

Single-gate RF readout on the inter-dot transition can be used to measure the inter-dot tunnel coupling and the gates' differential lever-arm. The differential lever-arm calibrates the applied gate voltage to the shift in the electron's energy and when combined with the extracted inter-dot tunnel coupling, one may evaluate the potential to form a qubit as well as provide experimental guidance in future device

[4] The higher electron transitions were not chosen as increasing the electron number causes weaker confinement. Long spin lifetimes are found with tighter confinement of electrons onto their quantum dots as the electrons will interact less with the surrounding environment [56].

fabrication. To find the tunnel-coupling, one typically requires an absolute energy scale such as the bath temperature or magnetic field as a reference. Typically for singlet-triplet states measured with a charge sensor, one performs a so-called 'spin-funnel' measurement where one tracks the s_0-t_- anti-crossing as a function of magnetic field [13, 162, 163]. A similar spin-funnel measurement can be obtained using single-gate RF spin readout [29, 30, 105]. Here, one first takes a line-cut across the inter-dot crossing by sweeping one gate across the inter-dot crossing in the direction of positive detuning Δ (that is, towards the region where both valence electrons are brought onto the same quantum dot) as shown in Figures 4.2c. Now consider the energy diagram in Figures 4.2d when the applied field is 0 T. The triplet t_+ and t_- states are degenerate with the t_0 energy eigenstate and the singlet branch (shown in red) is the ground state. When one places the DC offset in Δ at the zero-detuning position, the RF voltage oscillates between positive and negative detuning and thereby oscillates the electrons between the two singlet states s_{11} and s_{02}. That is, there is a non-zero RF response at low magnetic fields as the singlet ground state allows one of the electrons to oscillate between both dots. The width of the RF response is given by the RF amplitude Δ_{RF}. The non-zero RF response requires electron oscillations and thereby requires the full cycle of the RF voltage to pass zero detuning to ensure that one cycles between the two singlet states s_{11} and s_{02}; a condition only satisfied if the DC offset in detuning is less than the RF amplitude. Now consider the magnetic field being slowly increased with each line-scan across detuning. Due to Zeeman splitting, the triplet degeneracy breaks and the triplet t_- state eventually becomes the ground state (as shown by the blue line at 3 T). Due to Pauli blockade, the triplet states prevent electrons oscillating between dots and thus, the RF response is null. The smoothly varying trajectory of the RF response going from low to high magnetic fields thus, tracks the t_-/s_0 anti-crossing just like a spin-funnel. However, since the zero-detuning point is well-known, one may find the point where the RF response is partitioned equally into a region of null response and non-zero response as shown by the green triplet lines at 1.41 T. Here, the Zeeman splitting of the triplet t_- line equals the energy splitting of the singlet branches; that is, the inter-dot tunnel-coupling. Now the Zeeman splitting for two spin-down electrons (that is, a triplet t_- state) is:

$$E_{t-} = 2 \cdot \tfrac{1}{2} g_e \mu_e B_z, \tag{4.10}$$

where $g_e = 2$ is the gyromagnetic ratio of electrons in silicon [16, 38, 50] and $\mu_e = 13.996\,\mathrm{GHz/T}$ is the Bohr magneton. Thus, taking the triplet t_- Zeeman

splitting at 1.41 T, the tunnel-coupling of the inter-dot transition was measured to be approximately 39 ± 6 GHz. Now the boundary between null response and a non-zero response, that is the spin-funnel, is found by solving the intersection between the singlet energies and the triplet t_- energies:

$$B_z = \frac{1}{g_e \mu_e} \left(\Delta + \sqrt{\Delta^2 + t_c^2} \right). \tag{4.11}$$

Note that the detuning relates to the applied voltage on R2 via:

$$2\Delta = e \Delta \alpha_{\mathrm{R2}} \Delta V_{\mathrm{R2}}, \tag{4.12}$$

where α_{R2} is the differential lever-arm of R2 across the dots D2L/D2U and ΔV_{R2} is the voltage distance from the zero-detuning point pointed towards the charge state where both valence electrons reside on the same dot (that is, the $(2, 4)$ charge state). Thus, one may relate the s_0/t_- anti-crossing trajectory (the boundary shaving off the signal in the magnetic field dependence in Figure 4.2) to the inter-dot differential lever-arm of R2 given that the tunnel coupling is known. The curve of best fit yielded $\alpha_{\mathrm{R2}} = 0.13 \pm 0.05$. The energy scale linking the applied gate voltage to the qubit detuning is important when gauging qubit control. For example, in this device, the tunnel-coupling and differential lever-arm parameters were not favourable for qubit control as the Hadamard point (where the qubit axis on the Bloch sphere is at least tilted to 45° from the z-axis) requires voltage pulses of up to 480 mV (if one were to send fast pulses on R2). In this device, the tunnel-coupling was too big for viable qubit control as the required voltage pulses of 480 mV was too large (that is, the tunnel coupling needed to be smaller). However, the tunnel coupling of 39 GHz was certainly much larger than the driving resonator frequency 339.5 MHz and thus, presented itself as a viable candidate for RF spin readout in the adiabatic quantum capacitance mode. Note that the tunnel coupling need not be that large; that is, one could have gotten the same high-fidelity spin readout with a tunnel coupling of $5\,\mathrm{GHz} \gg 339.5\,\mathrm{MHz}$.

Although the large inter-dot tunnel coupling makes the inter-dot crossing a viable candidate for single-gate RF spin readout, one still requires a sufficient measurement time to make a judgement on whether the two-electron spin state is a singlet or triplet. The relevant time scale is set by the $s_0 \to t_-$ relaxation time as t_- is the ground state. The t_- is the relevant ground state when the system is readied for qubit operations; that is, applying a magnetic field to break the triplet degeneracy and to place the s_0/t_- anti-crossing away from negative detuning such that it does not interfere with single-qubit gate operations. In addition, the s_0/t_- anti-crossing must

be placed away from the RF amplitude window about zero detuning for one should not mix the spin state via the s_0/t_- anti-crossing during the measurement [40]. Thus, on applying a magnetic field the triplet t_- is now the ground state and the singlet-state is now a higher energy state at zero detuning. Thus, with the measurements occurring at zero detuning (to oscillate the singlet state between the s_{11} and s_{02} states), one needs to ensure that any relaxation mechanisms that bring the singlet state into the lower triplet t_- state occur at a sufficiently long time scale in order to perform spin readout. In previous experiments (where the double quantum dots were approximately 11.7 nm from their reservoirs) the $s_0 \rightarrow t_-$ relaxation time at zero detuning was 60 ns due to the quantum dots having too strong a coupling to their reservoirs [30]. To weaken the coupling of the dots to their reservoirs, the control gates (G1 and G2) were made further away from the dots (52 nm and 55 nm respectively) and the reservoirs (R1 and R2) were placed further away from the dots (18 nm and 17 nm respectively). Although one may not assert that the changes resulted in an improvement (to the measured $s_0 \rightarrow t_-$ relaxation time), the measured relaxation time of 2 ms [29] in this experiment was many orders of magnitude larger than the previously measured time of 60 ns [30].

Figure 4.3 shows the singlet to triplet t_- relaxation that limits the measurement time. In the initial experiment, using the chip inductor for the resonator, the singlet states were loaded by pulsing (1D pulses on gate G2) into point L 100 mV into positive detuning for 100 µs and then pulsing back to zero detuning to perform the single-gate RF spin measurement as shown in Figure 4.3a. When taking 10^5 time averages, one obtains an ensemble decay that is attributed to the singlet states relaxing into the triplet t_- spin states at zero detuning. The fitted decay time was approximately 2 ms allowing us to show that with a better resonator single-shot single-gate RF spin readout should be possible [29]. The device was therefore taken out and the inductor was replaced with a superconducting spiral inductor as described in Section 4.2.1. The device reproduced the same stability diagrams with identical inter-dot crossings and singlet triplet relaxation times as shown in Figure 4.3b. This suggests that the relaxation mechanism is intrinsic to the P-donors rather than the surrounding environment. Nonetheless, the signal to noise ratio was much better as the trace in Figure 4.3b only required 10^4 averages to resolve.

4.2.3 Optimising the input RF amplitude

To achieve maximal signal strength in the readout signal of the single-gate RF sensor, the input voltage amplitude was optimised. When operating in the adiabatic

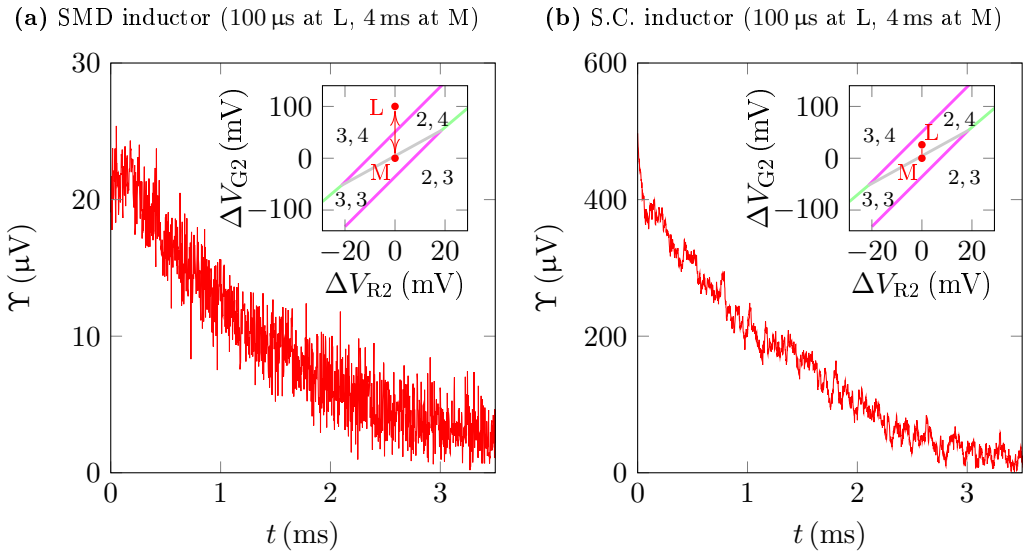

Figure 4.3: Singlet to triplet-t_- relaxation time (limits spin readout time). The insets show the pulse sequence on the charge stability diagram used to load singlet states at point L (for 100 µs) by moving into a region of positive detuning where the ground state is s_{02} and measuring the spin state at M (for 4 ms) at zero detuning. The resulting ensemble decay in the singlet readout signal Υ, using the single-gate RF sensor on R2, is due to the relaxation of the singlet state into the triplet t_- state. **(a)** First experiment performed with the surface mount (SMD) inductor. The spin trace shown is the average of 10^5 time traces and the fitted decay time was approximately 2 ms [29]. **(b)** Second experiment performed using a superconducting (S.C.) inductor reproduces the same decay but with a better signal to noise ratio. The time trace was taken with only 10^4 averages. In the second experiment with the superconducting inductor, the loading pulse was only 26 mV (instead of 100 mV as in (a)) into positive detuning since moving further into the (3, 4) charge state does not aid in speeding up the singlet initialisation (as discussed later when measuring the singlet-initialisation fidelity in Section 4.2.6).

quantum capacitance regime, the theory outlined previously in Section 4.1 suggested optimising the power to obtain the peak readout signal. The measured peak RF response is plotted (black markers) in Figure 4.4. The RF input voltage amplitude V'_{ac} on the x-axis was calibrated from the injected RF powers by considering the peak width at zero magnetic field in Figure 4.2d.

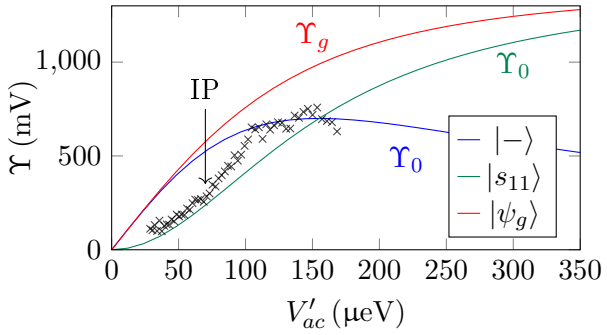

Figure 4.4: Finding the optimal RF input voltage amplitude V'_{ac} to achieve the maximal RF readout signal strength Υ. The measurements taken at zero magnetic field. The black markers show the measured peak height in the RF response (at zero detuning). The lines indicate the RF response as expected from the theory developed in Section 4.1 with the tunnel coupling taken as 39 GHz (161 μeV). The three lines (blue, green and red) are those when taking the initial state (before performing readout) to be $|-\rangle = (s_{11} - s_{02})/\sqrt{2}$, s_{11} and ψ_g (the ground-state eigenstate on starting readout). IP labels the approximation of the inflection point in the RF response.

From Figure 4.4, one observes that the RF response appears to have an inflection point (shown by the label IP) before coming to a maximum value at approximately the tunnel coupling energy of approximately 161 μeV before dropping. To understand this measured response, the data was analysed using three different theoretical models developed for the adiabatic quantum capacitance operation in Section C.5. All three fitting functions for the adiabatic quantum capacitance readout involve a LZSM factor that could explain the drop in the RF response at higher amplitudes. However, at 39 GHz and a driving frequency of 339.5 MHz, the LZSM envelope is irrelevant until the RF amplitudes exceed 10 meV. That is, the tunnel coupling was large enough (compared to the drive frequency) to ensure adiabatic passage (during readout) for voltage drive amplitudes of up to 10 meV. Thus, for the three possible initial conditions on performing readout ($|-\rangle = (s_{11} - s_{02})/\sqrt{2}$, s_{11} and ψ_g), the fitting functions were taken to be:

$$\Upsilon_- = A_0 \frac{V'_{ac} t_c}{t_c^2 + V'^2_{ac}} \tag{4.13}$$

$$\Upsilon_0 = A_0 \frac{V'^2_{ac}}{t_c^2 + V'^2_{ac}} \tag{4.14}$$

$$\Upsilon_g = A_0 \frac{V'_{ac}}{\sqrt{t_c^2 + V'^2_{ac}}}. \tag{4.15}$$

Υ_- is the peak RF response when the initial state is the $|-\rangle$ state, Υ_0 is the peak RF response when the initial state is s_{11} and Υ_g is the RF response when the electrons take on the ground-state eigenstate before performing readout. In the fitting functions, the tunnel-coupling was fixed at 39 GHz. Thus, the only fitting parameter was A_0; which was fitted to be 1.4 mV across all three curves. The fitting function taking the initial state to be s_{11} (green) appears to explain the RF response at lower RF amplitudes. At higher input RF amplitudes, the response maximum and subsequent downward trend appears to be better explained when taking the initial state to be the $|-\rangle$ (blue). The red curve, which assumes that the electrons always occupy the ground-state charge state, appears to not explain the data at all.

The conclusion we can make about which charge state initialisation we should employ needs to consider the manner in which the dataset was taken. The peak response was found by taking the RF response (with the RF drive continuously switched on) whilst sweeping the gate V_{R2} at approximately 1.5 mV/s. On sweeping the voltage past zero detuning, the initial state (at far negative detuning) will be s_{11}. At low amplitudes, the initial state is most likely s_{11} and thus, the green fitted curve explains the data in Figure 4.4. However, at higher amplitudes, on sweeping towards zero detuning, the large RF drive will sample zero detuning before the DC offset voltage has reached zero detuning. In doing so, there is the possibility that any excited charge state (with a larger energy splitting than at zero detuning) far from zero detuning (as the DC voltage has not reached zero detuning yet) quickly decays into the average ground-state eigenstate closer to zero detuning (the $|-\rangle$ state) explaining the transition to the blue curve as $V'_{ac} \gtrsim 100\,\mu\mathrm{eV}$. Higher RF amplitudes could not be accessed as the RF drive starts to be strong enough to start sweeping the dots' energy levels above and below their Fermi-level. Broadening of the charge loading lines is undesirable as one opens up the possibility of exchanging electrons with the reservoir R2 (thereby, destroying the spin-state of interest). The RF power was thus, set to $\sim$160 μeV for the maximal signal strength obtained in this experiment.

4.2.4 Optimising the signal to noise ratio

Even with the improved resonator yielding greater signal strength, as seen in Figures 4.2 and 4.3, single-shot readout was still elusive due to technical noise found in the apparatus surrounding the dilution fridge. Thus, several measures were taken to improve the SNR and eliminate the detection of technical noise not pertaining to the device under test.

The first source of technical noise was found when performing measurements via reflectometry using the directional coupler where the RF readout signal showed periodic oscillations at the same frequency as the pulse tubes. Although the true source was never diagnosed definitively, a trick to eliminate detection of the pulse tubes arose from discussions with Lucas Orona (from Harvard) when measuring a similar Si-P quadruple quantum dot device. The trick was to not send the RF input voltage signal via reflectometry (that is, via the directional coupler), but rather via the nearby gate G2 designed to send in high frequency pulses. The RF voltage signal sent through G2 will still oscillate the detuning across the dots to induce electron oscillations; the resulting current is picked up via the resonator and readout is performed as in reflectometry. The act of bypassing the directional coupler resulted in no pulse tube oscillations coupling into the measurements.

The second source of technical noise resulted in high frequency peaks present in the laboratory presumably due to power supply peaks induced by the pulse tube compressors (of the dilution fridge) linked to the same power supply circuit as the measurement apparatus. The straightforward method to eliminate these noise peaks was to move the signal bandwidth to frequencies far from the technical noise peaks via a lock-in amplifier. The input voltage signal was first modulated with a 21.361 kHz excitation. Any signal changes (for example, the presence or lack of a quantum capacitance due to a singlet or triplet) are now mapped around the lock-in frequency. The readout signal was then demodulated with the lock-in amplifier to extract the required singlet-triplet readout signal. The lock-in amplifier was filtered with a 3.3 kHz bandwidth and thus, the detection of technical noise peaks was eliminated. Note that the measurement bandwidth was not limited by the high quality factor of the superconducting resonator but was set below the 1.4 MHz limit to enhance the signal-to-noise ratio.

4.2.5 Optimising the readout position

On optimising the overall SNR of the readout signal, the final parameter to optimise was the optimal readout position in detuning. This section highlights how spin relaxation times were investigated as a function of detuning to find the optimal readout position. It will also be shown that the RF qubit sensor does not interfere with the spin dynamics of the spin state under measurement.

On choosing the optimal power from the previous section, the optimal position in detuning was also investigated. Since the RF readout signal is stronger with larger electron oscillations, one intuitively expects the optimal readout signal to occur at around zero detuning where the applied RF voltage maximally oscillates the detuning equally towards the s_{11} and s_{02} eigenstates. However, the readout signal strength should be considered along with the available measurement time (limited by the $s_0 \rightarrow t_-$ decay discussed the in previous section in Figure 4.3). Assuming additive white Gaussian noise, SNR is proportional to the square root of the measurement time. That is, one may filter the signal to a lower cut-off frequency to lower the overall noise power. Thus, the $s_0 \rightarrow t_-$ decay was investigated along with the singlet readout signal strength as a function of detuning Δ as shown in Figure 4.5.

The pulse sequence used to measure the $s_0 \rightarrow t_-$ decay as a function of detuning, shown in Figure 4.5a, was similar to that performed in the previous experiment shown in Figure 4.3. However, in this experiment, the significance of the $t_- \rightarrow s_{02}$ decay time was realised. That is, on repeating the pulse sequence, the measurement phase leaves the spin-state in the t_- ground state. Thus, to load a new singlet, one needs to wait at point L, for the triplet t_- state (now an excited state in far positive detuning) to decay into the singlet s_{02} ground state. As shown later, waiting at point L (far positive detuning) for approximately 4 ms was sufficient to ensure high singlet initialisation probabilities. The pulse sequence then proceeds into the measurement phase at point M where upon the singlet spin state decays into the triplet t_- state. Point M was varied around zero detuning and the subsequent decays are shown in Figure 4.5b. The top plot shows a scale energy diagram about zero detuning, while the centre plot shows the singlet population (given by a non-zero RF readout signal) during the measurement phase as a function of detuning (position of point M) and time waited at point M. Each vertical time averaged time trace (over 10,000 shots) was fitted to an exponential curve and the resulting fitting parameters are shown in the bottom plot: the peak RF readout signal strength in black and the relaxation times shown in orange. As expected zero detuning yielded the peak signal strength. However, the relaxation time was shown to decrease when moving towards positive

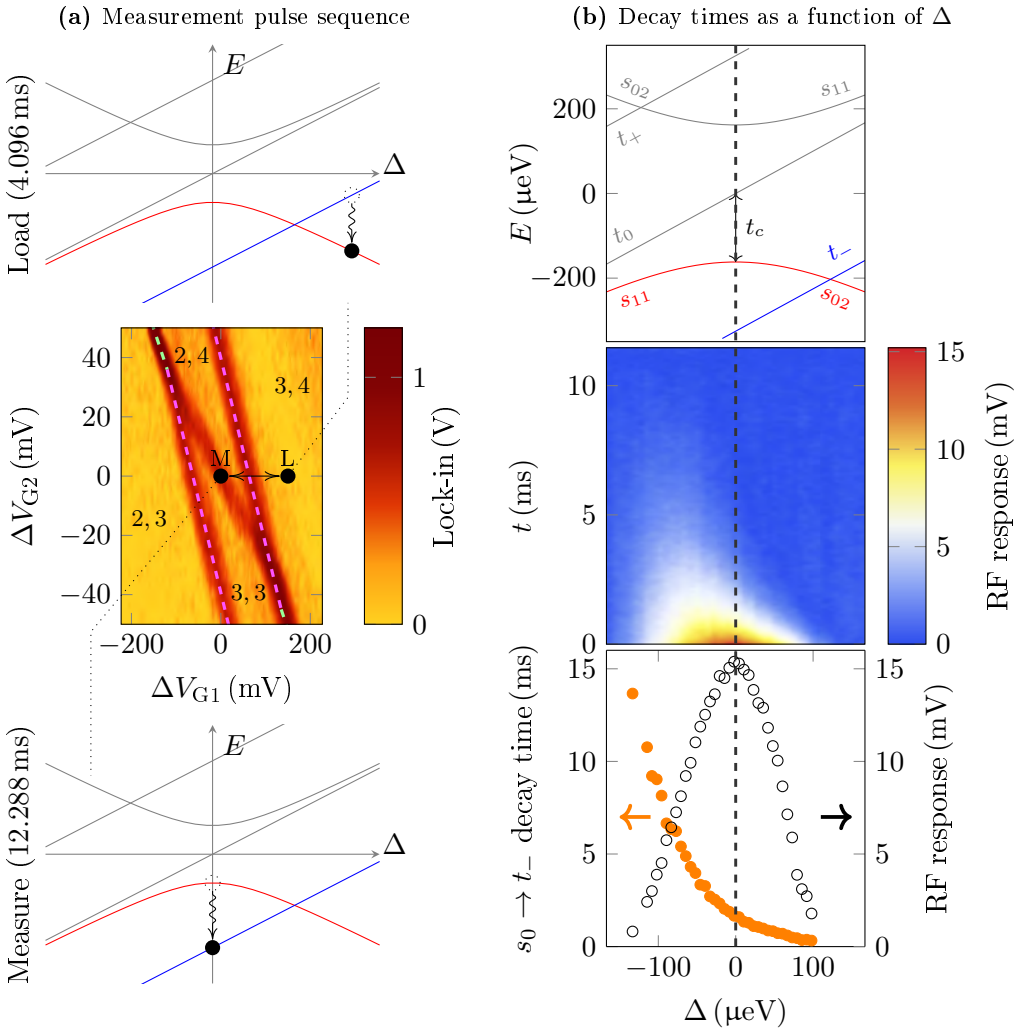

Figure 4.5: Finding the optimal measurement point in detuning. Different measurement points about zero detuning offered a compromise in the readout signal strength and available measurement time. **(a)** Repeated pulse sequence on the charge stability diagram. The load phase was performed in positive detuning with a 4.096 ms wait time (to ensure that the spins decay to the singlet s_{02} ground state, if the spins were in t_- due to the previous measurement phase). The measurement phase was performed at zero detuning, where the singlet spin-state decayed into the triplet t_- ground state, thereby limiting the measurement time of the singlet spin-state. **(b)** The measurement point M was varied about zero detuning to obtain the decay times as a function of detuning Δ. The top section shows a to-scale energy diagram of the spin states, the middle section shows the singlet-population as a function of detuning at point M and the time waited at point M (each vertical time trace is an average of 10,000 shots), while the bottom section shows the associated fitted exponential decay times (orange) and the peak RF singlet readout signals (black). Peak RF readout signal occurs at zero-detuning, while the available measurement time appears to reduce towards positive detuning and increase when moving towards negative detuning.

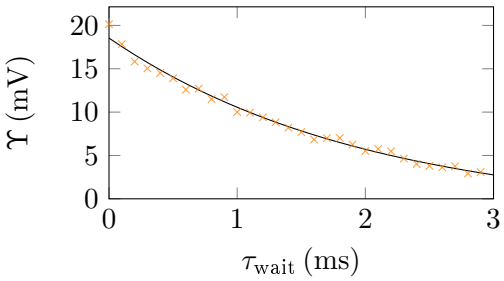

Figure 4.6: Singlet to triplet relaxation time when switching off the RF input voltage. The same pulse sequence used in Figure 4.5a was applied with the exception that the RF input voltage was only switched on during the measurement phase after waiting a certain time τ_{wait} at zero-detuning. The resulting measurement signal for a given wait-time was fitted with an exponential decay and the maximum readout signal (like in Figure 4.5bn) was extracted. Thus, the resulting trend in the singlet readout signal as a function of τ_{wait} indicates the $s_0 \rightarrow t_-$ decay in the absence of an applied RF input voltage. The resulting decay was still fitted to be approximately 2 ms; thus, the RF input voltage did not significantly affect the spin dynamics of the sensed electrons.

detuning due to the RF voltage signal now sweeping the detuning past the s_{02}/t_- anti-crossing and accelerating the decay to the t_- ground state via $s_0/t-$ mixing [97]. Although the decay time increases when moving towards negative detuning, the RF signal strength diminishes at a rate such that the SNR remains approximately the same. Thus, the optimal readout position was chosen to remain at zero detuning.

Before one can utilise the optimised single-gate RF sensor for spin readout, it is important to verify that the sensor is not affecting the spin-dynamics of the system under measurement. That is, one may posit that the $s_0 \rightarrow t_-$ decay was due to the RF voltage used by the RF readout sensor. To verify that the sensor was non-invasive, the measurement protocol was modified such that the RF input voltage was only switched on during the measurement phase and only after waiting a certain time period at point M (in all results shown so far, the RF input voltage was permanently switched on). The idea was that one idly waits a certain time period at point M to give the opportunity for the singlet spin-state to decay into the triplet t_- ground state before switching on the RF input voltage signal to execute the measurement. On measuring the peak RF readout signal as a function of the time waited at point M (before executing the measurement), one can observe the bare relaxation time when no RF excitation is applied to the electrons. If the $s_0 \rightarrow t_-$ decay was due to the single-gate RF sensor's input RF voltage excitation, the bare relaxation time should be longer. However, the bare relaxation time, plotted in Figure 4.6, was shown to be the same approximate 2 ms are zero detuning. Thus, one affirms that the single-gate RF sensor does not affect the spin dynamics of the qubit under measurement.

4.2.6 Single-shot spin readout using the single-gate RF sensor

With the single-gate RF sensor calibrated and optimised, the sensor was set to perform single-shot spin readout. Triplet t_- states were measured by simply waiting at zero detuning (where the ground state is t_-) as shown in Figure 4.7a. The readout signal for triplet states remained at the zero background level. Singlet states were measured using the same pulse sequence in Figure 4.5a. That is, to measure singlet states, the detuning was pulsed into positive-detuning by applying 150 mV on G2 for 4.096 ms and then pulsing to zero detuning to perform the measurement. The singlet traces, as shown in Figure 4.7b, initially displayed a signal above the zero background level indicating the presence of a quantum capacitance (that is, electron oscillations between the dots due to the lifting of Pauli-blockade). The readout signal later drops back to the zero background level indicating the measurement of triplet states. That is, the singlet traces show the time-resolved stochastic decay of singlet spins into the triplet t_- ground state.

To quantify the fidelity of the single-shot spin readout, one must discriminate between a fully null signal (triplet) and one with a non-zero readout signal (singlet). The singlet signal on average follows an exponential decay function and thus, the singlet signal contrast is concentrated at the beginning of the measurement. Thus, an exponential window was applied over the portion of the signal where the measurement began and a histogram was compiled of the maximum value of each trace [164]. The histogram shown in Figure 4.7c was created from 10,000 traces taken after waiting at point L for 4.096 ms (initialising singlet) and without pulsing to L (initialising triplet t_-) to measure the distribution for singlets and triplets respectively. Taking a threshold (shown by the dotted line in Figure 4.7c) to optimally partition the distributions such that values above are assigned as singlet states and values below are triplet states. This yielded an average single-shot readout fidelity of 85.77% (where the singlet and triplet readout fidelities were 80.02% and 91.52% respectively). The fidelities were in fact higher than that quoted in the publication as the exponential window was not adjusted for the line delays in acquisition and triggering [32]. That is, the analysis in the publication applied the exponential window approximately 75 µs too early. Thus, the maximum signal strength of the singlet signals were prematurely attenuated by 4% (that is, $\exp(-75/2000) \approx 0.96$). The lower singlet signal (due to the exponential window filter) led to a slightly smaller singlet-triplet signal contrast and thus, a lower fidelity. The analysis here correctly accounts for the 75 µs line delay between setting the pulse generator to zero detuning (for readout) and the actual point in time, during the signal acquisition, when readout truly begins.

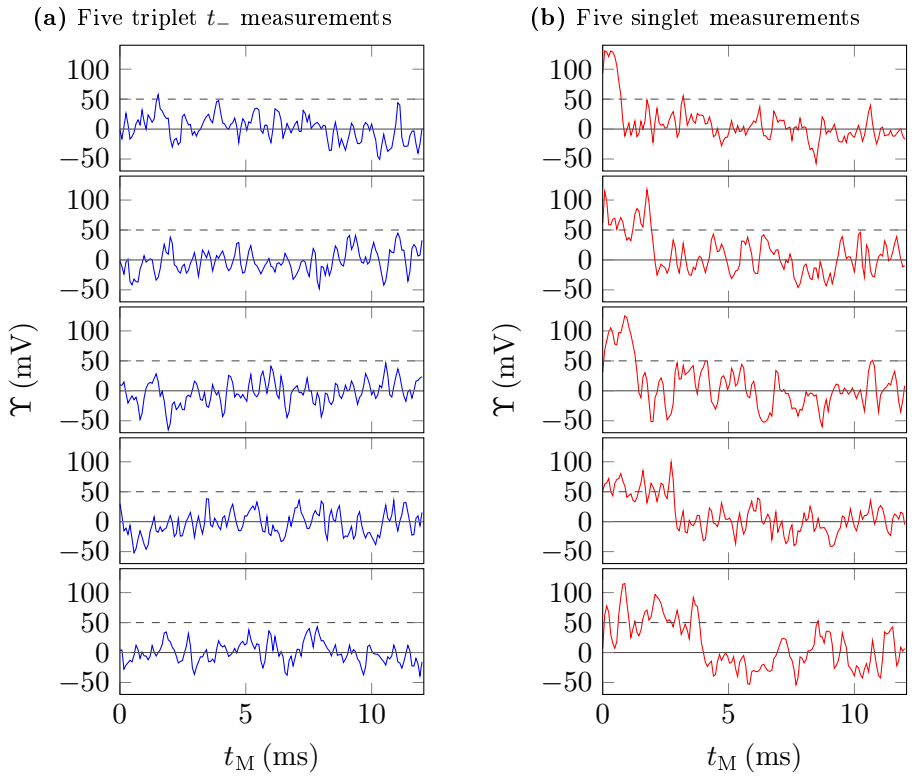

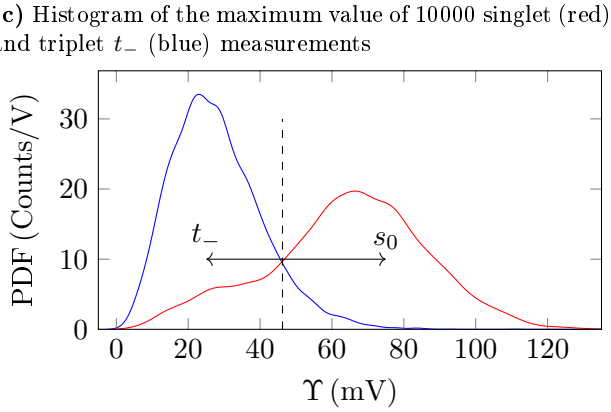

Figure 4.7: Single-shot single-spin readout. Using the superconducting resonator on R2, single spin states could be resolved with single shot. **(a)** Single-shot traces measuring a single spin in the singlet state when waiting at L for 4.1 ms. **(b)** Single-shot spin traces measuring triplet states where the detuning was never pulsed to L. **(c)** A histogram (a probability density function (PDF) from 10,000 traces) of the maximum value of the RF response when waiting at point L for 0 s and 4.1 ms shown in blue and red respectively. The dashed line shows the selected threshold that maximises the readout fidelity at 85.77%.

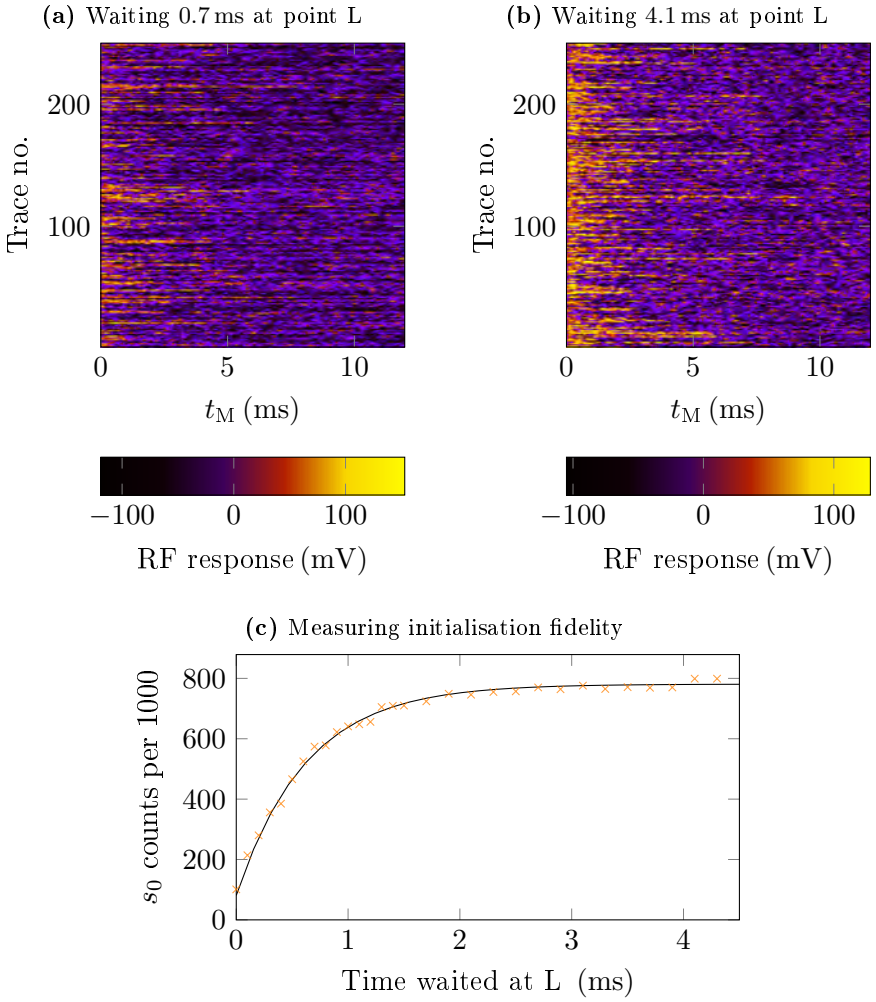

Figure 4.8: Observing singlet initialisation via the triplet t_- to singlet decay. **(a)** 250 single shot traces when waiting at the loading point L were taken after waiting at the loading point L (see Figure 4.5) for 0.7 ms to partially load singlet states. The traces indicate singlet states (yellow blips) decaying into triplet states (purple) during the measurement stage. **(b)** More singlet counts are present when waiting at point L for for 4.1 ms to fully load singlet states. The shorter wait time at L yields lower singlet counts as insufficient time was given for the t_- state to decay into the s_0 state before measurement. **(c)** To observe the dependence on wait time at L 1000 single-shot traces were taken, using the optimal readout threshold, to measure the singlet population on varying the time spent at point L. The exponential fit of the t_- to s_0 relaxation time at $\Delta \sim 1$ meV was approximately 0.62 ms.

With single-shot readout sensor characterised, the singlet initialisation was investigated in detail by measuring the t_- to s_0 decay at far positive detuning $\Delta = 1\,\text{meV}$ by varying the time the pulse spends at point L. After every measurement at point M, the electrons decay into the triplet t_- state. On initially pulsing to point L, the electrons remain in t_- via the $(3,3)$ charge state. Since the electron tunnel rate from R2 to D2U is slow, the system cannot immediately enter the $(3,4)$ charge ground state. The triplet t_- state must decay into the singlet state (the $(2,4)$ charge state) before an electron can move from R2 to D2L to leave system in the $(3,4)$ state [29, 102]. Figure 4.8a shows 250 traces taken when waiting 0.7 ms at point L while Figure 4.8b 250 traces when waiting 4.1 ms at point L. The lengths of each non-zero signal are exponentially distributed with a time constant of 2 ms and represent singlet states (yellow) decaying into triplet t_- states (purple). When waiting a lower time at L, there is clearly a smaller proportion of singlet states. Figure 4.8c shows the singlet counts over 1000 traces taken at different wait times at point L. When viewing the singlet counts as a function of the wait time at point L and fitting to the resulting exponential rise in the singlet counts, the decay time was measured to be 0.62 ms. Thus, waiting 4.1 ms at point L ensures high-fidelity initialisation of singlet states. Note that the approximately 100-count offset at zero wait time and 200-count offset at high wait times (as opposed to 0 counts and 1000 counts) is due to the readout infidelities of detecting triplets and singlets respectively (that is, dark counts where triplets are incorrectly declared as singlets and missed counts where singlet states are incorrectly declared as triplets).

4.3 Outlook

Key results came together to culminate in single-shot readout of the single-gate RF sensor:

- The theory was developed to better understand the conditions required for maximal readout signal strength when using the adiabatic quantum capacitance ($\omega \ll t_c$) and tunnelling capacitance regimes ($\omega \approx t_c$). After fully optimising the resonant circuitry and the tunnel couplings, the readout strength was ultimately found to be limited by the movement of a single electron between two quantum dots.
- The modelling suggested that increasing the internal quality factor aids in increasing the readout signal strength. Thus, the surface mount chip inductor ($Q = 370$) was replaced with a NbTiN spiral inductor ($Q = 750$).

- The single-gate RF sensor was shown to operate without significantly affecting the spin state under measurement. That is, the $s_0 \rightarrow t_-$ relaxation time of 2 ms (which limits the available readout time) was not due to the RF drive of the single-gate RF sensor.

- Single-shot electron spin readout in the singlet-triplet basis was demonstrated for the first time using a single-gate RF sensor[5] with an average readout fidelity of 85.77% (where the singlet and triplet readout fidelities were 80.02% and 91.52% respectively) at a 3.3 kHz measurement bandwidth.

The result forms a key pillar in the proposed singlet-triplet architecture by proving that single-shot readout (required for real-time error correction in modern error correction codes) is possible using the compact integrated single-gate RF sensor.

The average fidelity was measured to be 85.77% at a 3.3 kHz measurement bandwidth. The fidelity can be improved in future experiments by the usual techniques discussed in Section 3.2.3. This includes:

- Increasing the internal quality factor, which may be limited by dielectric losses, radiative losses and/or defects in the 100 nm NbTiN films. These parameters can be improved by using an uniform NbTiN film and substrate [144] and by reducing the overall size of the inductor [145].

- The external quality factor can be optimized by re-designing the superconducting resonator geometry to achieve the ideal coupling to the transmission line [165].

One of the challenges in scaling to many qubits using superconducting resonators is the space real-estate needed for the extra matching circuitry. Whilst the results in this thesis used a superconducting spiral inductor of a fairly large footprint (4 mm^2), the size was mainly limited by the need for a central bond pad and to keep the fabrication simple (that is, not using multi-layer superconducting inductors in which the bond pad can be placed away from the centre of the inductor spiral). Recent proposals have shown that the superconducting spiral inductors can be further scaled with thinner tracks and tighter spacings to achieve a density of thousands of resonators per square centimeter [137]. Another option is to use higher inductor frequencies if one commits to using resonant tunnelling capacitance readout as opposed to adiabatic quantum capacitance readout. Future work in developing the single-gate RF sensor include:

[5] Other groups have since posted single-shot single-gate RF spin readout results [132, 133] with one group using a SLQD sensor [130].

- Increase the internal quality factor to approximately above 1600 to push the readout fidelity past 99%.
- Investigate the spin life-times for lower electron numbers. With tighter electron confinement, one may indeed get singlet to triplet t_- lifetimes beyond 2 ms, thereby yielding longer integration times and thus, greater readout fidelity.
- Investigate the feasibility of the tunnelling capacitance mode of operation using high-frequency resonators in Si-P quantum dots (for example, the spin lifetimes and coherence times must be long enough to resolve the spin state with the single-gate RF sensor). If one can attain high fidelity readout with smaller inductances, the smaller footprint alone may warrant its use in the singlet-triplet architecture. Given that for N qubits, one requires N coaxial lines for the control gate lines, an extra N non-multiplex lines may be a worthwhile compromise.
- Implementing a digital solution to the RF electronics when simultaneously addressing a multiplexed array of resonators. The current analogue RF electronics enabled adequate RF signal synthesis and demodulation. However, if one performs simultaneous RF readout across more than N qubits, one will require N separate IQ demodulators and N separate signal generators. The separate signal generators are required (as opposed to outputting the summed waveform) as each frequency tone needs to provide a coherent local oscillator source for the IQ demodulator. A digital solution will enable synthesis via a single DAC (outputting the summed waveform) and demodulation via a single ADC as the digital fabric can keep track of the phase of each tone in the summed output signal.

Chapter 5

A scalable singlet-triplet quantum information processor

The phosphorus in silicon system in the form of Si-P quantum dots offer unique advantages for hosting singlet-triplet qubits ranging from low lead counts (2 per qubit) to stronger inter-qubit couplings (exceeding order of typical tunnel couplings of several gigahertz). Ultimately it is important to show the feasibility in leveraging these advantages to create a large-scale many-qubit quantum processor. The geometric architecture shown in Section 2 highlighted how a 4-dot device can work towards the demonstration of a coupled singlet-triplet two-qubit gate using only two gates per qubit. However, this particular design has flaws when attempting to tessellate the qubit unit-cell across a larger array of qubits. Ultimately, one must consider the optimal choice of the system parameters, such as inter-qubit coupling and tunnel coupling, to achieve high-fidelity two-qubit gates. In particular these parameters are required to be optimised for a high-fidelity CZ gate (since a high fidelity CZ or CX gate can ultimately be used to perform the parity measurements required for the surface code). During the time-frame of this thesis, parallel results from our group also demonstrated the ability to perform atomic-scale multi-layer Si-P fabrication, opening up the possibility for more complex singlet-triplet architecture proposals beyond that of a 1D linear array [76]. This chapter covers the following topics:

- Section 5.1 gives an overview of methods proposed to scale up solid state qubits.
- Section 5.2 shows the conversion of the fundamental double dot Hamiltonian (Hubbard model) into the singlet-triplet qubit Hamiltonian. This overview highlights the importance of a large tunnel coupling of at least 1 GHz (to over-

come thermal excitations), the minimum distance between dots to ensure the exchange J can be turned off and the role of global magnetic fields in isolating the singlet and triplet-t_0 qubit subspace.

- Section 5.3 gives an overview of the operation of single-qubit gates using singlet-triplet qubits. The analysis shows how the minimum exchange J for an accurate Pauli-z gate (as a non-zero ΔB_z will always tilt the qubit rotation axis away from the Pauli-z axis) is 810 MHz (for a typical $\Delta B_z = 29$ MHz expected for a 1P-2P double dot in Si-P). The analysis concludes with an upper bound on the tunnel coupling of approximately 10 GHz for Si-P as beyond this, the voltage pulses required for qubit gate control (to toggle between Pauli-z and Pauli-x rotations) will be too large. In addition, the influence of charge noise on the Pauli-z gate is discussed where one finds that if we operate in negative detuning (where $dJ/d\Delta$ is small), high-fidelity Pauli-z gates should be possible as previously observed in singlet-triplet qubit experiments in GaAs [34].

- Section 5.4 gives an overview of the requirements for a singlet-triplet two-qubit gate in Si-P in the presence of strong inter-qubit coupling. The CZ gate is presented with an analysis of charge noise (taken as a Gaussian variation on the qubit detuning). The analysis concludes that the regime of optimal operation (with worst case error rates below the fault-tolerant threshold of 0.5% and largest tolerance to noise of up to 810 neV detuning noise) is when the inter-qubit coupling is approximately six times the tunnel coupling, giving an optimal tunnel coupling of ∼6.5 GHz and an inter-qubit coupling of ∼39 GHz. The native CX and CH gates (although not required as there is a high-fidelity CZ gate) are briefly discussed for completeness.

- Section 5.5 finally concludes with an electrostatic optimisation of a linear 1D array of singlet-triplet qubits that can implement a high-fidelity CZ gate between adjacent singlet-triplet qubits. By appealing to recent developments in multilayer Si-P fabrication, electrostatic optimisation was also performed, in 3D, for the 2D surface code architecture in which one stacks many 1D arrays on top of one another.

5.1 Scalable architecture proposals for solid-state qubits

The promised speed-up in solving a certain class of algorithms that a quantum processor may provide, hinges on the Quantum Fourier transform (for example, in Shor's

integer factorisation algorithm [3]) and, to a lesser extent, the amplitude amplification algorithm [166] (as used in the Grover's search algorithm [4]). The algorithms are well-understood in terms of the operations that need to be performed over a few qubits [167]. Indeed a proof of concept of the Grover's search algorithm was recently demonstrated on a two-qubit processor using two single-spin qubits [55]. One may envisage extending the two-qubit demonstration to a 1D array of qubits to run multi-qubit algorithms. However, in practice device performance will be compromised by imperfect qubits. Qubit errors comprise of control errors (yielding imperfect qubit rotations), bit-flip errors (state changing due to a T_1 relaxation mechanism) and phase-errors (due to T_2^* processes that cause random fluctuations in the precession frequency). To summarise the impact of all these infidelities of qubit operations, one can introduce the quantity called the operational fidelity:

$$F = |\langle \psi_m \mid \psi_e \rangle|^2 , \tag{5.1}$$

where ψ_e is the expected state, while ψ_m is the measured state. The fidelity is the probability that one arrives at the correct resulting state. The qubit error rate per qubit operation (or per unit time) is the worst case infidelity $(1 - F)$.

One may improve operational fidelity due to control errors from imperfect control pulses via pulse compensation [66, 168–170]. The pulse imperfections arise from finite output bandwidth, voltage resolution and sample rates of the waveform generators. By realising that the phase accumulation of a qubit is given by both the qubit precession frequency and the time spent performing the gate, one may adjust the qubit precession frequency by pushing the qubit into a region of faster or slower frequency to account for the discrete time-base given by the sample rate.

One may improve operational fidelity due to bit-flip and phase errors by using qubits with longer lifetimes. Within the realm of solid-state spin qubits, P-donor qubits have demonstrated extremely long T_1 times. Electrons hosted on P-donor dots have been shown to have lifetimes (specifically the spin-up to spin-down relaxation time of single electron spins) of up to 30 s [56]. Theoretical predictions suggest that by correctly orienting the global magnetic field with respect to the electric field in the device, spin-orbit coupling can be minimised giving rise to spin lifetimes as long as 18 minutes [171, 172].

Although the T_1 time places an upper bound on T_2^*, this longer spin lifetime is irrelevant if the decoherence times are much shorter than T_1, causing phase errors to dominate the overall error rate. Precession due to magnetic fields (such as the global magnetic field used for Pauli-z rotations in single-spin qubits or the magnetic field

gradient used for Pauli-x rotations on singlet-triplet qubits) can have noise due to non-zero nuclear spins in the substrate. Some solutions to mitigating the magnetic field noise, discussed in Section 2.1.6, include dynamic nuclear spin polarisation as demonstrated in GaAs qubits where nuclear spin isotopes are present in both Ga and As [40, 41]. A solution for qubits in silicon is to use isotopic purification of the nuclear spins by using ^{28}Si instead of natural silicon [16, 39]. When using isotopically purified silicon, the single electron spin decoherence time T_2^* increased from 55 ns to 270 µs. Singlet-triplet decoherence times[1] for Pauli-x rotations (mediated by ΔB_z) have yet to be measured in isotopically purified silicon. However, GaAs implementations have noted that when stabilising the background nuclear spins, the singlet-triplet qubit's T_2^* increased from 10 ns [13] to 2µs [41] and the intrinsic charge noise becomes the dominating factor for operational qubit fidelities [69]. That is, by stabilising the nuclear spins (and using AC driving of the singlet-triplet qubit) GaAs singlet-triplet qubits showed single-qubit gate fidelities of up to 99.3%, but the two-qubit gate fidelity was limited to 90% by charge noise [34].

Even with these mitigation strategies, solid-state quantum dot qubits currently do not have sufficiently low error rates (both for single qubit and two qubit gates) to perform useful algorithms. Thus, one appeals to facets of classical error correction theory in telecommunication channels by utilising information redundancy. That is, one utilises multiple qubits to represent the information of a single 'logical qubit'. Given the proposal highlighted in Figure 2.1 in Section 2, one could envision extending the singlet-triplet qubit unit-cell (requiring two gates per qubit) into a linear array of singlet triplet qubits. Here a given qubit's state can be protected by redundant ancilla qubits on either side. However, previous research has shown that for this to work, qubit error rate thresholds need to be in the range of 10^{-7} to 10^{-5} [173]. Given that, for solid-state spin qubits, the best single qubit gate error rates are approaching $\sim 10^{-3}$ [18, 34] and two-qubit gate error rates (limited by charge noise) ranging 0.02-0.10 [34, 66], a 1D array will not be compatible with a many-qubit processor.

The state-of-the-art implementation of a logical qubit architecture revolves around the use of a 2D array of qubits. Here, additional redundancy in the number of physical qubits helps overcome the individual qubit error rates, while logical qubits are formed as topological particle excitations (or holes) in the code. The logical qubits are then moved around in braiding operations to perform two-qubit gates [174]. Com-

[1] It is not trivial to convert single spin coherence times into two electron singlet-triplet qubit coherence times. This is because the coupling of magnetic field noise couple directly to single-spin qubits, while singlet-triplet qubits couple to magnetic field gradient noise while rejecting global magnetic field noise.

(a) Arrangement of qubits and stabilisers in the surface code [8]

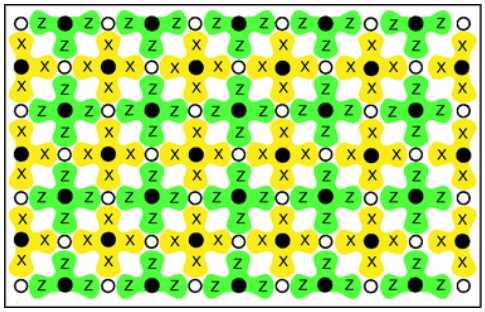

(b) Operation of the ZZZZ and XXXX stabilisers [8]

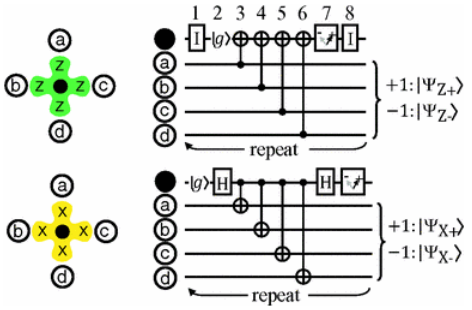

Figure 5.1: Arrangement of qubits in forming the 2D surface code. The white dots represent physical data qubits, while the black dots represent physical measurement (or ancilla) qubits. The green plaquettes represent 4-fold ZZZZ parity measurement cycle, while the yellow plaquettes represent 4-fold XXXX parity measurements. (a) The measurement qubits are interleaved with the data qubits such that each measurement qubit has four surrounding data qubits. (b) The ZZZZ parity measurement is performed via 4 CNOT gates in which the measurement qubit (initialised to spin-down) is flipped for every spin-up data qubit. The XXXX parity measurement is similar with the exception of the Hadamard gates in the beginning and end required to tip and un-tip the spins onto/off the Pauli-x axis before performing the Pauli-z axis measurement.

mon implementations include the colour code (following anyon physics [175]) and the surface code [8, 176]. Due to the ease of realising local nearest neighbour interactions arranged in a square grid, solid-state qubit proposals have typically adopted the surface code. The surface code consists of a network of X and Z stabilisers (a stabiliser constituting a parity measurement along the Pauli-x or Pauli-z axes between two qubits) as shown in Figure 5.1a. In simple terms, one realises that to protect a qubit state, one must protect two degrees of freedom. Thus, one may use redundant qubits to test for qubit errors along the X and Z axes. For example, if two qubits were set to $|\uparrow\rangle$ and a bit-flip error occurred, a weak parity[2] measurement along the Pauli-z axis would yield a change in the parity from even to odd; thus, the detection of an error. In addition, the ZZ-parity measurement is a weak measurement[3] that will likely project the state back into $|\uparrow\rangle$ if a small error had accumulated to rotate the qubit from the main state. To enhance redundancy, one may stabilise

[2] A parity measurement measures whether, for a given set of qubits, an odd or even number of qubits are in $|0\rangle$ or $|1\rangle$. A ZZ-parity measure distinguishes the parity along the Pauli-z axis ($|0\rangle$ or $|1\rangle$) while an XX-parity measurement measures along the Pauli-x axis (counting the number of qubits in the $(|0\rangle + |1\rangle)/\sqrt{2}$ or $(|0\rangle - |1\rangle)/\sqrt{2}$ states).

[3] A weak measurement on a set of qubits extracts information without fully collapsing the qubit states. For example, a parity measurement between two qubits gives information on the relative qubit orientations (parallel/even or anti-parallel/odd) but not the individual state of the qubits.

a given qubit with many Z-stabilisers along one axis and many X-stabilisers along an orthogonal axis. Then the new qubits (placed to stabilise the initial qubit) need to be also individually stabilised; upon which one attains a grid. The surface code continually stabilises its qubits via repeated stabiliser measurements. Figure 5.1b shows how the measurement (or ancilla) qubits (highlighted as black dots) are interleaved in between the data qubits (highlighted in white dots) to continually perform ZZZZ (green plaquettes) or XXXX (yellow plaquettes) parity measurements. The ZZZZ-parity measurement consists of a series of CNOT gates (or CZ gates preceded and followed by Hadamard gates [167]) where the measurement qubit (initialised as spin-down) is flipped for every data qubit that is spin-up. If final the state of the measurement qubit is spin-up, then the data qubits have an odd parity of spins, while spin-down indicates that the data qubits have an even parity of spins. Note that the XXXX stabiliser also has Hadamard gates to tip/un-tip the spin onto/off the Pauli-x axis as the measurements are performed on the Pauli-z axis.

Note that the the qubit errors only need to be detected and catalogued. After a given algorithm ends, one must then infer the true qubit states given the catalogued errors. As detailed in the Fowler review [8], logical qubits can be formed by stopping the stabiliser at a given point in the surface code to create a 'hole' or topological particle in the code. Gate operations between logical qubits are performed by moving the qubits (a qubit at a given site is moved by stopping the stabiliser on the adjacent site and starting the stabiliser on the current site) along the grid relative to each other to perform topologically braided operations. The basic X, Y, Z and CNOT gates may be performed by braiding the qubits. However, by the Gottesman-Knill theorem, stabilisers yielding such a gate-set can be efficiently simulated in polynomial time by a classical computer and thus, one needs to have qubit operations that take the qubit state away from the the Pauli x, y and z axes [177]. To generate states away from the Pauli basis, one needs to generate the qubit state via an iterative probabilistic 'magic state distillation' where upon each iteration, one distils the states converging towards the intended target state [178]. The cost of magic state distillation (in lowering the number of iterations to attain the target state) severely increases the required physical qubit count. For example, for a processor demonstrating the Shor's algorithm to factorise a 2000-bit number, one requires $\sim 10^8$ physical qubits at an error rate of 0.001-0.005 (to form approximately 4000 logical qubits). Therefore, with physical qubit error rates starting to reach 0.005, there is a greater focus on creating large scalable 2D arrays of solid-state qubits.

One of the earliest 2D array proposals was to use GaAs singlet-triplet qubits coupled over a long-distance via metallic floating gates [179]. The metallic floating

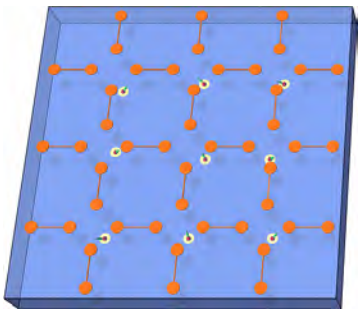

Figure 5.2: Surface code with GaAs singlet-triplet qubits and metallic floating gates [179]. A 2D grid of singlet triplet qubits (shown as the white disks) can exist despite the large gate-density of 11 gates per qubit (see Figure 2.3a) as the qubits are spaced apart thanks to the metallic floating-gates (orange) mediating the electric dipole coupling of the qubits to enable two-qubit gates over a longer distance.

gates, shown in orange in Figure 5.2, sought to extend the distance of the electric dipole coupling (between qubits) used in two-qubit gates [14]. However, the long-distance coupling was never realised experimentally since the metallic nature of the gates caused significant charge noise and decoherence. That is, a perturbation of an electron on one singlet-triplet qubit would be ideally transferred to the next qubit via the floating gate. However, the resulting charge rearrangement (of the many electrons in the metallic gate) causes the first singlet-triplet qubit to entangle information onto many electrons in the metal with resulting information loss. If one replaces the metallic gate with a single macroscopic wavefunction like a superconductor, then the floating gate approach might work while potentially offering stronger inter-qubit couplings for higher fidelity two-qubit gates [70].

A later proposal for a 2D surface code using single spin qubits in silicon involved the use of STM-patterned donor qubits measured with SETs [28]. The device has three layers as shown in Figure 5.3. The middle layer consists of SET islands, each surrounded by 4 P-donors. Here, the physical qubits for the surface code comprise of the P-donor nuclear spins, while the electrons on the donors are used to perform parity operations between adjacent qubits. The parity measurements between the nuclear spins occur by first transferring the information to the electron spins via global ESR/NMR pulses [39]. Since the global ESR/NMR pulses address the energy splittings given by the electron Zeeman splitting plus/minus the hyperfine splitting, the P-nucleus is only addressed when an electron resides on the donor. To perform the parity measurement between two electrons on adjacent P-donors (holding the nuclear spin information), one relies on the magnetic dipole exchange interaction. The top and bottom layers have source and drain terminals, for the SET islands,

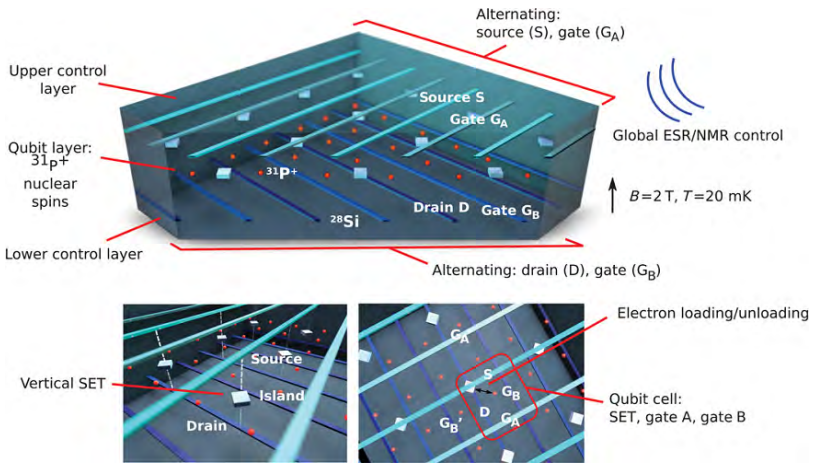

Figure 5.3: 2D Surface code with multi-layer STM-patterned Si-P single-spin qubits [28]. The device has three vertically separated layers. The middle layer consists of a grid of P-donors separated by ∼30 nm to form the physical qubits for the surface code. SET islands interleaved within the grid enable spin readout. The SET quantum dots (shown as the small squares) share criss-crossed source (along a column) and drain (along a row) leads with other SET quantum dots. The source and drain leads are interleaved with gate leads to enable gate control for qubits along a given row or column. The P-nuclei act as the physical qubits while the electrons are used for inter-qubit interactions and qubit readout. Single-qubit operations are performed via global ESR/NMR pulses, while two-qubit gates are ultimately mediated via the magnetic dipole interaction between two electron spins.

interleaved with control gates. Each SET island can be addressed by using the associated source and drain lines. During typical operation, multiple qubits along a given row are controlled via a single gate and similarly read-out via a single drain lead. The readout is performed by time-correlating the current signals on the source and drain leads with coincidences on multiple SETs eliminated via multiple qubit measurements. The advantage of this proposal is that the gate density scales as $2\sqrt{N}$ for an N qubits arranged in a square. Thus, the resulting wire density per qubit is smaller than one and results in favourable routing topologies [37]. However, several issues remain in this architecture. Firstly, the ability to globally address all the spins via a single ESR/NMR antenna requires uniform field homogeneity (across the full 2D array of qubits) that has not yet been demonstrated experimentally. Secondly, the individual electrons on the P-donors must have the same hyperfine splitting; that is, if the wavefunction on any given donor is perturbed, it might not be addressed resonantly via a single global ESR/NMR frequency. Thirdly, the sharing of the gate leads across many qubits and SETs requires a large degree of uniformity where there are no local charge traps or background potentials that may shift the dot's energies. The necessity for uniformity enables one to have less than one lead for every dot

in the system with a corresponding sacrifice in tunability. Finally, the architecture requires the so-called phase-matched loading. Here when electrons are loaded on the P-nuclei, the nuclear spins precess at a different frequency compared to when there are no electrons. Thus, when electrons are being read via the SET (via the spin to charge conversion method as discussed in the overview of conventional charge sensors in Section 3.1.1), the stochastic tunnelling process of some electrons hopping off the P-donor dots before others leads to nuclei, with electrons still on their dots, accumulating a phase difference; that is, performing an unintentional Pauli-z gate. A solution for this, as outlined in the original proposal, is to pulse the gates into the readout point (where an electron may unload) periodically (in time) at multiples of the precession frequency. Now the window for electrons to hop off the dot is only allowed when the net phase accumulation is a multiple of a full rotation. Whilst a novel concept, the concept of phase-matched loading to eliminate unintentional phase accumulation has also not yet been demonstrated.

(a) Device structure [180] **(b)** Parity measurement [180]

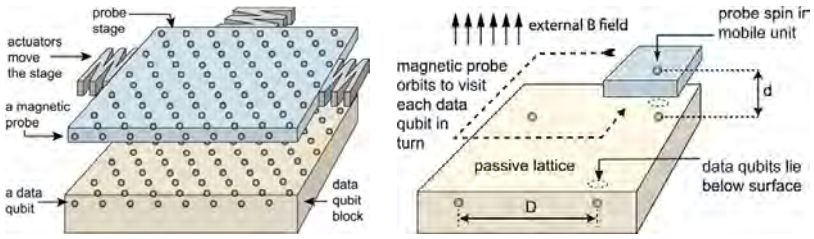

Figure 5.4: Surface code with a grid of electrons on P-donors (separated by 400±12 nm) measured with a piezoelectric stage holding a grid of NV centres [180]. **(a)** Electrons hosted on a grid of ion-planted P-donors form the slab of data qubits, while a grid of NV-centres magnetically probe the data qubit spins. **(b)** The data qubits are spaced 400 nm. The magnetic probe (moved via piezoelectric actuators) interacts with the electron spins via a magnetic dipole moment to accumulate a state-dependent phase to be used in the parity measurement.

A later proposal using donors (note this could be P or any other donor) considered using a moveable stage [180]. Here, a grid of donors was implanted into a silicon substrate as shown in Figure 5.4a. Another grid of magnetic probes (for example, NV centres) lies parallel above the grid of donors. The magnetic probes are movable via a piezoelectric stage (as in a STM). Using the magnetic dipole moment interaction between two spins, one may move the magnetic probe around four donor spins while accumulating a state-dependent phase on the magnetic probe spin to thereby perform the required parity measurement as sketched in Figure 5.4b. The spacings between donor qubits is more relaxed so that one may use ion implantation techniques. Here,

the proposed spacing between the implanted donors is 400 nm as opposed to the ∼30 nm required for the P-donor SET proposal above. This is important for this proposal, as the lasers used for readout are at a wavelength (250 nm) within the diffraction limit for this spacing. Nonetheless, the allowable inaccuracy in placement must be better than 11.7 nm to enable sufficient coupling to the associated NV centre on the moving stage during the parity measurement shown in Figure 5.4b. The 2D surface code device in Figure 5.3 requires atomic precision placement of the donors with nanometre accuracy of the control electrodes; both of which are within experimental capability [15, 27]. The moveable stage proposal hints that one may also use atomic precision hydrogen mask STM patterning of donors onto the silicon substrate (instead of ion implantation) for accuracies much better than 11.7 nm. However, one of the challenges of this proposal is that the NV centres must also have a similar implantation accuracy. The proposal states that the current state of the art NV centre implantation methods are not accurate enough with lateral accuracies of ±12 nm at depths of 8±3 nm. In addition, the implantation probability is below 30% and thus, there will be many dead-pixels in the magnetic probe. Thus, one requires further evolution in the technologies surrounding the implantation of NV centres in diamond. Other logistical issues with the moving stage is that the piezoelectric stage may cause frictional heating that will raise the operating temperature above the required temperature, of 100 mK, to ensure high-fidelity qubit operation.

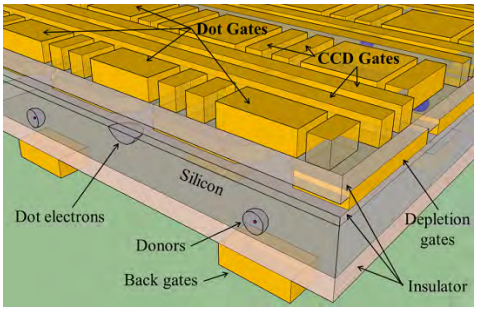

Figure 5.5: Surface code with a grid of gate-defined MOS quantum dots coupled to implanted Bi-donors [181]. The 2D grid consists of gate-defined MOS quantum dots (holding the electron data qubits) interleaved with Bi-donors. The Bi-donors hold an electron which has an exchange interaction with the MOS dot's electron controlled via a back-gate. The donors (and their hosted electrons) provide a method to perform CNOT gates on the data qubits; reading out the donor electron spin completes the parity measurement. CCD gates enable loading and moving of electrons on the MOS quantum dots across rows of qubits.

Another scalable architecture proposal involving donor qubits utilises a hybrid approach using Bi-donors and gate-defined quantum dots [181]. Here, MOS quan-

tum dots (quantum dots formed near the silicon oxide interface) act as data qubits, while interleaved with implanted Bi-donors that act as ancilla measurement qubits as shown in Figure 5.5. To perform a parity measurement, electrons on a row of quantum dot qubits are selectively moved in unison towards the Bi-donor dot's electron via CCD gates. The gate defined quantum dot electrons form a singlet-triplet state with the donor-confined electron such that one may adiabatically transfer spin information to perform a microwave-driven CNOT gate where the donor and its electron act as the target qubit. The CNOT mechanism involves the use of the back-gate (on the back of the silicon-on-insulator wafer) to control the exchange interaction between the donor electron and the MOS dot electron. The resulting exchange creates a singlet-triplet state [182]. When combined with the clock transitions of the Bi-donor (hyperfine transitions that are insensitive to magnetic field fluctuations), a subspace forms where donor electron spin flips are either allowed or forbidden. The three-spin system (MOS dot electron, donor dot electron and the donor nuclear spin) results in a controlled SWAP gate where the nuclear spin is the control qubit. When combined with a microwave field, one realises a CNOT gate. The advantages of using implanted Bi-donors is the back-gate mediated selective activation of the qubit measurement and the potential high-fidelity of the CNOT gate due to the qubit subspace being resistant to electric and magnetic field noise. The proposal allows the potential of high-fidelity readout of a donor electron spin when using a local SET and the spin-to-charge conversion method [112]. The SET should be possible to place near the donor dots as the qubits are spaced (that is, the distance between the MOS dot and the donor dots) by approximately 1 μm. The back-gates globally address a row of qubits by noting that the qubit subspaces do not require exact tuning of the exchange; thus, two discrete back-gate voltages indeed suffice in tuning all the qubits. Nevertheless, there is yet to be any experimental demonstration of the required Bi-donor control and the complex CNOT gate mechanism given in this proposal.

There is also a recent proposal extending the Kane mechanism to realise long-distance couplings between ion-implanted P-donor qubits by using electric dipole (rather than exchange) couplings [38, 78]. Here, the donors are implanted close to the surface of the silicon substrate as shown in Figure 5.6. Surface gates are then used to distort the electron cloud on the P-donor dot, without ionising it, to form a electron mushroom. The resulting hyperfine tuning leads to a second order ESR-driven flip-flop qubit where the qubit subspace (for electron spin $\downarrow$ / $\uparrow$ and nuclear spin $\Uparrow$ / $\Downarrow$) consists of $|\downarrow\Uparrow\rangle$ and $|\uparrow\Downarrow\rangle$. Similar to the single-spin qubit, the second-order driving yields Pauli-x rotations while off-resonant driving yields Pauli-z

(a) Flip-flop qubit formed between an electron and an implanted P-donor [78]

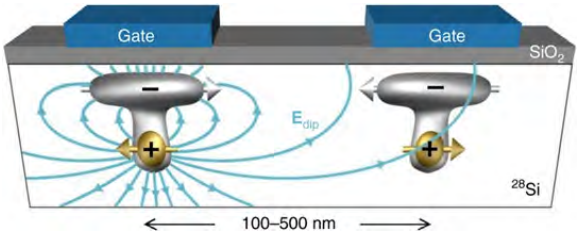

(b) Grid of flip-flop qubit cells interconnected with superconducting resonators [78]

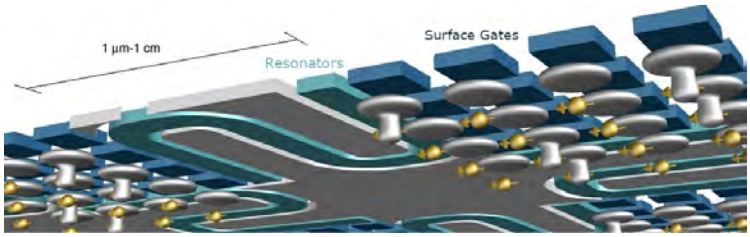

Figure 5.6: Surface code with a grid of ion-implanted P-donor flip-flop qubits [78]. The flip-flop qubit (for electron spin $\downarrow$ / $\uparrow$ and P-donor nuclear spin $\Uparrow$ / $\Downarrow$) is a qubit formed on the subspace: $|\downarrow\Uparrow\rangle$ and $|\uparrow\Downarrow\rangle$. **(a)** Each flip-flop qubit is tuned via a surface gate. The mushroom-like orbital state of the electron helps form an electric-dipole that can be used to couple adjacent qubits (spaced 100-500 nm apart) and perform a two-qubit gate. **(b)** Smaller grids of flip-flop qubits coupled via the electric dipole coupling are linked together via superconducting resonators (spaced 1 µm-1 cm apart) to form a large 2D array of qubits for the surface code.

rotations. When driving the qubit off-resonantly, one tunes the hyperfine splitting (between the P-donor nuclear spin and its electron) away from the resonant sweet-spot causing a change in height of the electron mushroom (with the ground and excited qubit states taking form of orbital wavefunctions being near the donor dot and the top of the mushroom respectively). To perform two-qubit gates, the proposal suggests using a similar electric dipole mechanism to that used with the singlet-triplet qubits in this thesis. That is, one pushes the qubits to an off-resonant drive where the electron (in the excited state) is spatially far from the P-donor dot and thus, forms a large electric dipole to the adjacent qubit. The electric dipole causes the adjacent qubit to have its off-resonant detuning shifted (to cause a change in its precession frequency) on the condition that the first qubit is in the excited state. Due to the long range of the electric dipole coupling due to the electron mushroom, the proposed distance between donors is in the range of 100-500 nm giving rise to an equivalent inter-qubit coupling is 10-100 MHz as opposed to the large gigahertz couplings targeted in this thesis. However, when one considers the density of local

surface gates and SET structures (to readout the electron spin to infer the state of the flip-flop qubit), it becomes difficult to route large arrays of flip-flop qubits. Thus, the proposal relies on using superconducting couplers (to extend the range of the electric dipole field), which have a coupling strength of 3 MHz, to interlink smaller arrays of flip-flop qubits. At the time of publishing this thesis, this proposal still required experimental demonstration of smooth hyperfine tuning with an electric field (that is, not immediately ionising the P-donor dot), before the subsequent demonstration of the flip-flop qubit. Afterwards, the electric-dipole coupling between adjacent flip-flop qubits must be shown to be sufficient to perform a two-qubit gate. Similarly, there needs to be experimental demonstration of the required cavity coupling between a flip-flop qubit and a superconducting resonator.

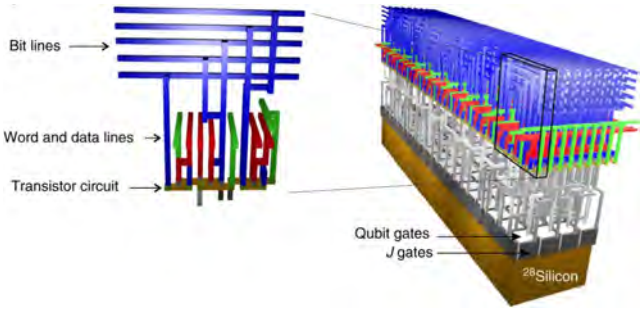

Figure 5.7: Surface code with in a silicon CMOS architecture [108]. The multi-layered CMOS architecture creates a 2D array of single-spin electron qubits (in gate-defined quantum dots) addressed via gates structured with addressable bit lines like in DRAM. Single-qubit gates and two-qubit gates are performed via ESR (with the exchange coupling J used to couple adjacent qubits). Qubit readout is done via single-gate RF sensors. The minimum feature size required for this architecture is $\sim$7 nm.

Finally, another potentially scalable solid-state qubit architecture proposal is the gate-defined quantum dot CMOS fabrication compatible qubit processor [108]. The proposal here forms an amalgamation of many previous concepts. That is, the processor, comprises single-spin electron qubits in a MOS architecture, utilises ESR for single-spin operations [52] and direct electron exchange J (along with ESR) for two-qubit (CX and CZ) operations [67]. With single-shot, single-gate RF readout recently demonstrated in solid-state qubits, the proposed readout structures use spin-down electron ancilla qubits to which one performs a singlet-triplet parity measurement to infer the single spin. These readout structures have also been recently demonstrated in single-shot [32, 132]. The proposal highlights a large scale 2D array of qubits in which different qubits are addressed via shared global transistor switched arrays similar to the addressing structure of DRAM modules in classical computing memory. The major hurdle in the realisation of this proposal is the required

Proposal	Qubits	Qubit spacing	Key benefits	Open issues
GaAs floating gates [179]	$(s_0/t_0)_{\mathrm{GD}}$	$\sim$1 µm	• Large spacing between qubits • Full individual qubit control	• Charge noise from substrate limits two-qubit gate fideties • Charge noise from metallic floating gates
STM P-donors [28]	D: $(\Uparrow / \Downarrow)_{\mathrm{P}}$ M: $(\uparrow / \downarrow)_{\mathrm{P}}$	$\sim$30 nm	• Low gate density • Long coherence times for P-nuclei	• Uniformity of ESR/NMR frequencies for all qubits • Gate limited tunability of dots • Phase-matched loading
P-donors and NV-centres [180]	D: $(\uparrow / \downarrow)_{\mathrm{P}}$ M: $(\uparrow / \downarrow)_{\mathrm{NV}}$	$\sim$400 nm	• Large qubit spacing • No leads	• Implantation inaccuracies in P-donors and NV-centres • Non uniform implanted dopant activation • Frictional heating of moving stage
MOS dots and Bi-donors [181]	D: $(\uparrow / \downarrow)_{\mathrm{GD}}$ M: $(\uparrow / \downarrow)_{\mathrm{Bi}}$ M: $(\Uparrow / \Downarrow)_{\mathrm{Bi}}$	$\sim$1 µm	• Large CCD gate spacing • CNOT gates are resistant to magnetic field and electric field noise	• The CNOT mechanism is unproven • Coherence times of the MOS dots may be low • Bi-donor control unproven
P-donor flip-flop [78]	$(\uparrow\Downarrow / \downarrow\Uparrow)_{\mathrm{P}}$	$\sim$100-500 nm & $\sim$1 µm-1 cm	• Large qubit spacing • Resistant to electric field noise near sweet-spot • Full individual qubit control	• Hyperfine tuning with a gate is unproven • Flip-flop qubit is unproven • Cavity coupling is unproven
CMOS [108]	$(\uparrow / \downarrow)_{\mathrm{GD}}$	$\sim$60 nm	• Compatible with CMOS fabrication • Full individual qubit control	• Simultaneous high-fidelity single-qubit and two-qubit gates unproven • Multilayer CMOS fabrication requires 7 nm feature sizes • High gate density

Table 5.1: Summary of the 2D surface code proposals in solid-state qubits. The proposals are given in terms of their key benefits and open issues. The $\uparrow$ / $\downarrow$ signifies electron spin qubits while $\Uparrow$ / $\Downarrow$ nuclear spin qubits. The subscripts signify the hosted location: GD=gate-defined quantum dot, P=P-donor nuclear spin, NV=NV-centre, Bi=Bi-donor. For some proposals, different qubit types act as the data (D) and measurement (M) qubits. Note that 'unproven' implies 'not realised experimentally'.

simultaneous fault-tolerant levels in both single and two qubit gate fidelities [66]. In fact, the proposed two-qubit gate is still limited by charge noise (as with most proposals highlighted above which rely also on specific values of direct exchange J). In addition, to claim compatibility with industrial CMOS fabrication techniques, the fabrication pipeline will require $\sim$7 nm feature sizes to cater for the smaller DRAM cells and gate structures.

A summary of the key 2D surface code proposals in semiconductor qubits are shown in Table 5.1. For quantum dot architectures which require many leads per qubit, one can observe a trend in the push for exploiting long-distance mechanisms to space the qubits further apart. Many of the proposals sacrifice individual qubit control to achieve lower gate-densities such as the STM P-donor and the MOS/Bi-donor proposals. The 2D array of singlet-triplet qubits proposed later in this chapter looks to retain individual qubit control while minimising gate-densities by exploiting the natural features of P-donor qubits (such as free-confinement).

5.2 Singlet-Triplet Hamiltonian from the Hubbard model

The singlet-triplet Hamiltonian describes the blueprint for the double quantum dot system in which a qubit is to be formed. In order to appreciate control operations required for full qubit control, it is useful to briefly overview the origin of the singlet-triplet Hamiltonian. The derivation of the Hamiltonian along with the functional properties are discussed in Appendix E. In this section, the Hamiltonians are discussed with emphasis on qubit gate operations.

5.2.1 Double quantum dots described by the Hubbard model

A singlet-triplet qubit is formed by taking the concatenated spin state of two electrons trapped across two adjacent quantum dots. To build up the Hamiltonian describing such a system it is useful to first consider the charge qubit Hamiltonian which consists of one electron across two quantum dots. The electron may reside on dot 1 or dot 2 (denoted by the wavefunctions φ_1 and φ_2). The associated potential energy of the electron when in either dot may be controlled by varying the electrostatic potential of the dots via local gate electrodes. The detuning parameter ε here shall be defined as half the energy separation between the two dots' potential energies as shown in Figure 5.8a-c. A negative ε implies that dot 1 is of lower energy, a positive detuning implies that 2 is of lower energy and zero detuning implies that both dots have equal potential energies.

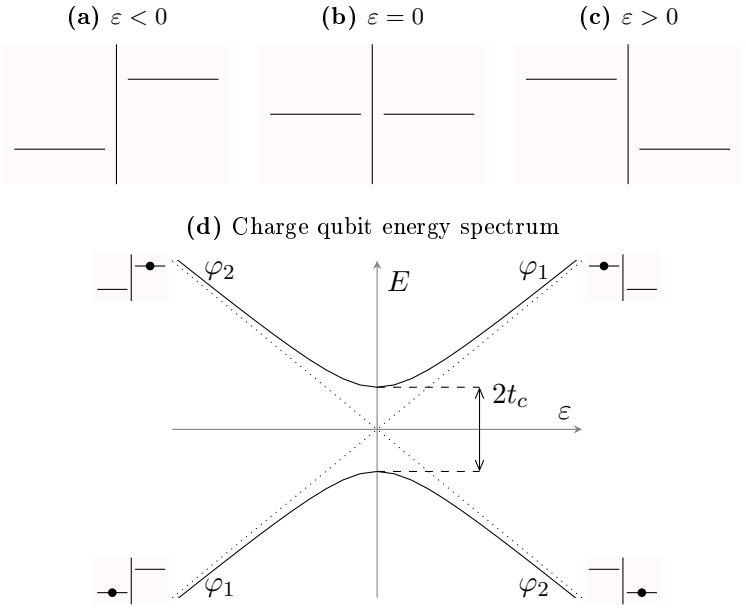

Figure 5.8: Charge qubit energy spectrum for the Hamiltonian given in Equation 5.2. **(a)-(c)** The structure of the electrostatic potential energy levels of electrons on the dots for different values of detuning ε. The two columns in each diagram reflect the energy level of dots 1 and 2 respectively. **(d)** The resulting energy diagram for a charge qubit. The dotted lines indicate the asymptotic energy levels when the tunnel coupling t_c is zero. The labels φ_1 and φ_2 indicate the approximate asymptotic energy eigenstates (electron residing entirely in dot 1 or dot 2 respectively) in those regions of detuning with the smaller energy diagrams showing the dot energy levels and the location of the electron given by the black dots.

Given the definition of ε, the excited and ground state energy levels would vary linearly as shown by the dotted lines in Figure 5.8d. However, this is only the case when the dots are well isolated and completely uncoupled. Now the energy eigenstates of the Hamiltonian are defined as those that are invariant under time evolution. If the two dots in the charge-qubit Hamiltonian were uncoupled (equivalently stated as the electron tightly confined to a given dot without any influence of the other dot's potential well), the electron on any given dot will remain there forever. However, with a non-zero tunnel coupling term t_c (equivalently stated as the electron wavefunction spreading onto the other dot such that it no longer solely occupies a single dot), the energies will be perturbed by virtue of the electron wavefunction overlapping with the other dot's potential landscape. When setting the voltages on the gates such that the detuning is negative, with zero tunnel coupling, φ_1 is the ground state as dot 1 is of lower energy. With a non-zero tunnel coupling, a wavefunction solely occupying φ_1 cannot be the stable ground state eigenstate (for the

ground state eigenstate would need to overlap with dot 2). Thus, if it were to be dot 1 and solely in φ_1, then it would be of a higher energy[4]. Thus, the energy of the φ_1 eigenstate must be an upper bound to the ground eigenstate. By similar argument, the excited state energy lower bounds the true excited energy eigenstate. Therefore, even at zero detuning, the energies may never be degenerate unless the coupling is zero. This avoided crossing or level repulsion is similar to that seen in coupled Harmonic oscillators. The continuous lines in Figure 5.8d illustrate this avoided crossing of energy levels across different values of the detuning ε. The dotted lines show the energy levels when the tunnel coupling is zero and how they form asymptotic bounds to the energy levels when the tunnel coupling is non-zero as shown by the two hyperbolas. The associated Hamiltonian (for the charge qubit) is derived in Appendix E.1:

$$\mathbf{H}_{\mathrm{CQ}} = -t_c\sigma_x + \varepsilon\sigma_z. \tag{5.2}$$

The tunnel coupling t_c is given by the energy overlap integral, a 'tunnelling amplitude', for the electron between the two dots and tends to be negative for Coulombic potential wells. The negative sign on the tunnel coupling is there for convenience so that t_c can be quoted as a positive value. The detuning is associated with the Pauli-z operator σ_z as it aligns with the measurement basis chosen to be the electron either in dot 1 or dot 2. The tunnel-coupling couples the two states via a Pauli-x term σ_x. At zero detuning, therefore, one obtains Pauli-x rotations while at far detuning $|\varepsilon| \gg 0$, one obtains Pauli-z rotations.

To complete the singlet-triplet Hamiltonian, one adds a second electron. When considering that there are two electron spins (that may each be spin-up or spin-down), two sites for each electron to reside, there are up to 16 possible spatial and spin state configurations. However, as shown in Appendix E.2, with no orbital degrees of freedom[5], the Pauli-exclusion principle places symmetry constraints on the 16 possible states so that the only states that have a non-zero probability density are the six electron singlet triplet states. The first three states are the three spatial singlet states s_{20}, s_{02}, s_{11}. These states have the electron anti-symmetric (entangled)

[4] This is simply a consequence of the spectral theorem. The two states (ground and excited) states are orthogonal and cover all possible states. Any state is therefore a linear combination of the ground and excited state and thus, bound between the two energy levels.

[5] An orbital degree of freedom means that the electrons may enter different electron orbital states to satisfy overall symmetry or anti-symmetry of the electron wavefunction [34, 42, 183]. For P-donors the higher orbital states are more than 10 meV higher in energy (the so-called $2p_0$ state) and are very short-lived at approximately 200 ps [184–187]. Thus, the orbital states are ignored in this analysis.

singlet spin configuration $\frac{1}{\sqrt{2}}(|\uparrow\downarrow\rangle - |\downarrow\uparrow\rangle)$. The indices indicate the two electron charge state on dots 1 and 2. That is, s_{20} indicates that both electrons are on dot 1, s_{02} indicates that both electrons are on dot 2, while s_{11} indicates that both electrons are on separate dots[6]. The remaining three states are the triplet states t_0, t_- and t_+. With no orbital degrees of freedom, the electrons in triplet states always remain on separate dots[7].

When the electron spins couple to external magnetic fields, the Hamiltonian is adjusted to include these magnetic field terms. The first magnetic field term is the globally applied, to both dots, magnetic field B_0. By choosing the z-axis as the direction of the average magnetic field (that is, the applied global magnetic field), there are no common-mode (same across both dots) magnetic field components perpendicular to B_0. The remaining differential magnetic field across the two dots is defined as $\Delta\mathbf{B} = \mathbf{B}_1 - \mathbf{B}_2 = (\Delta B_x, \Delta B_y, \Delta B_z)$ (with $\mathbf{B}_1$ and $\mathbf{B}_2$ denoting the net magnetic fields on dots 1 and 2 respectively). The portion of $\Delta\mathbf{B}$ parallel with the globally applied magnetic field is ΔB_z while the differential field component perpendicular to the globally applied magnetic field is:

$$\Delta B_\perp = \frac{\Delta B_x + i\Delta B_y}{\sqrt{2}}. \tag{5.3}$$

The differential magnetic fields (ΔB_z and $\Delta B_\perp$) come from the local magnetic field interactions on the two dots. For example, they can be formed via the polarisation of a bath of surrounding nuclear spins or from the addition of a local permanent micro-magnet as discussed in Section 2.1.5.

Figure 5.9 shows a sketch of the double quantum dot system with all the relevant double-dot interaction (t_c), two-electron repulsion (U_{02}), magnetic field (B_0, ΔB_z and $\Delta B_\perp$) and detuning terms. The blue line highlights the approximate potential landscape of the dots confining the electrons and how the individual potentials can be manipulated via the tilting potentials given by the detuning ε. The full Hamiltonian including all the outlined terms above is (noting that the overbar implies complex conjugation):

[6] Note that s_{11} is in a symmetric spatial state across the two dots as discussed in Appendix E.2
[7] Triplets have anti-symmetric spatial states across the two dots as discussed in Appendix E.2

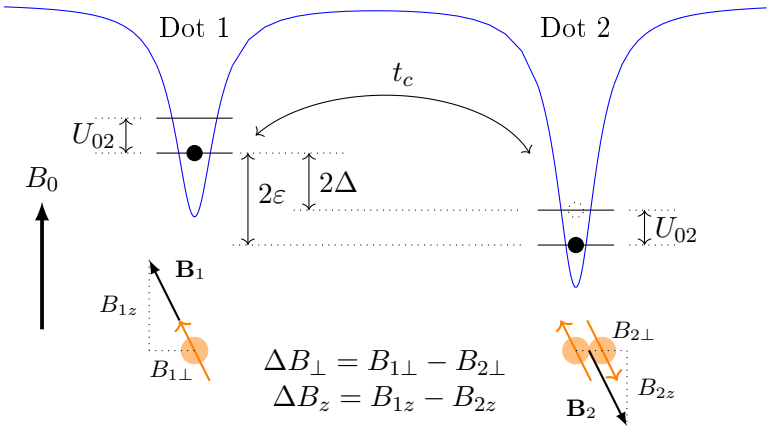

Figure 5.9: Schematic of two tunnel-coupled quantum dots (1P-2P) under different magnetic fields. The approximate potential landscape confining the electrons across two dots is sketched by the blue curve while the black dots represent electrons occupying the energy states on the dots (separated by the electron repulsion energy U_{02}). The dots are detuned by ε and Δ, and tunnel coupled via t_c. The average magnetic field across both dots is the global applied field B_0. Each dot has nuclear spins (in this example for Si-P, the first dot has 1 P-donor and the second dot has 2 P-donors) that when polarised produce net magnetic fields on each dot: $\mathbf{B}_1$ and $\mathbf{B}_2$ (the local magnetic field vectors omit B_0 in this diagram for clarity). The residual differential magnetic fields across both dots (ΔB_z and $\Delta B_\perp$) can be decomposed (with respect to the global magnetic field vector) into parallel components (B_{1z} and B_{2z}) and perpendicular components ($B_{1\perp}$ and $B_{2\perp}$).

$$\mathbf{H}_{\mathrm{ST}} \equiv \begin{pmatrix} U_{02}+2\varepsilon & 0 & -\sqrt{2}t_c & 0 & 0 & 0 \\ 0 & U_{02}-2\varepsilon & -\sqrt{2}t_c & 0 & 0 & 0 \\ -\sqrt{2}t_c & -\sqrt{2}t_c & 0 & \Delta B_z & \overline{\Delta B_\perp} & -\Delta B_\perp \\ 0 & 0 & \Delta B_z & 0 & 0 & 0 \\ 0 & 0 & \Delta B_\perp & 0 & -2B_0 & 0 \\ 0 & 0 & -\overline{\Delta B_\perp} & 0 & 0 & 2B_0 \end{pmatrix}. \tag{5.4}$$

under the basis of states: s_{20}, s_{02}, s_{11}, t_0, t_- and t_+. U_{02} is the on-site electron-to-electron repulsion energy. That is, U_{02} is the extra repulsive electrostatic potential energy that must be overcome to place two electrons on the same dot. The $\sqrt{2}$ factor that appears next to the tunnel coupling t_c (in the matrix) is significant as the tunnelling amplitude t_c was initially calculated for one electron across two dots. The inter-dot tunnelling event now couples entangled two-electron states across two dots and thus, requires a further two-body interaction to move the electrons between the spatial singlet states $s_{02} \leftrightarrow s_{11}$ and $s_{20} \leftrightarrow s_{11}$ [188]. The magnetic coupling terms $\Delta B_\perp$ couples the singlet s_{11} state to the triplet states t_+ and t_- (as seen by the off-diagonal positions). To suppress these couplings (between the qubit state s_{11} and the

non-qubit leakage states t_- and t_+) the Pauli-z like interaction B_0 must be set much larger than $\Delta B_\perp$ to suppress the interaction term $\Delta B_\perp$. That is, the rotation axis between the states $s_{11} \leftrightarrow t_-$ and $s_{11} \leftrightarrow t_+$ will point towards the Pauli-z axis when $B_0 \gg \Delta B_\perp$ where no population is interchanged between the states. Nonetheless, the presence of the $\Delta B_\perp$ coupling is important when considering dynamic nuclear spin polarisation protocols where nuclear spins are controllably flipped via adiabatic sweeps across the s_{11}-t_- anti-crossing [40, 41]. Finally, the last term ΔB_z couples the singlet s_{11} to triplet t_0 and is important in performing Pauli-x rotations in the s_0/t_0 qubit subspace.

The Hamiltonian shown in Equation 5.4 contains states that will not be accessed in practice. In typical configurations, when the system is tuned between a $(1,1)$ to $(0,2)$ charge transition, the $(2,0)$ state is separated very far from the charge transition. For example, the electron repulsion term U_{02} is approximately ∼1meV in GaAs quantum dots [189], ∼10meV for SiGe quantum dots [55], ∼10meV for Si-MOS quantum dots [132], and ∼100 meV for Si-P quantum dots [81]. The energy scale of U_{02} is much larger than the other dynamic parameters in the Hamiltonian. For example, the energy scale of tunnel couplings in quantum dot systems (for hosting singlet-triplet qubits or for performing two-qubit gates across two single-spin qubits) range at most $t_c \sim 100\,\mu\text{eV}$ [14, 17, 29, 30, 55, 82]. Similarly, at the larger magnetic fields used in typical experiments of 1 T yield energy scales of $B_0 \sim 100\,\mu\text{eV}$. Thus, the dynamics surrounding s_{11}, t_0 and s_{02} typically do not require consideration of s_{20} (in many cases, it may be inaccessible with the available range in gate voltages). Thus, without loss in generality, the s_{20} is culled from the Hamiltonian given in Equation 5.4 and the detuning ε shall be redefined (to Δ) to only consider to the local s_{11}-s_{02} anti-crossing:

$$2\Delta \equiv 2\varepsilon - U_{02}, \tag{5.5}$$

as shown by the labels in Figure 5.9. Although the tunnel coupling is referred to the wavefunction overlap integral, in the context of qubit control and typical experiments, one is more interested in the actual singlet-triplet energy splitting (when the magnetic fields are zeroed) at zero detuning [29, 30, 82]. Thus, the tunnel coupling is rescaled from $\sqrt{2}t_c$ to just t_c. In addition, the Hamiltonian is further simplified by taking one portion of Δ out of the Hamiltonian as a global offset $\Delta \cdot \mathbf{I}_6$ does not affect the qubit dynamics. The simplified Hamiltonian takes the following form [13, 14]:

$$\mathbf{H}_{\mathrm{ST}} \equiv \begin{pmatrix} -\Delta & -t_c & 0 & 0 & 0 \\ -t_c & \Delta & \Delta B_z & \overline{\Delta B_\perp} & -\Delta B_\perp \\ 0 & \Delta B_z & \Delta & 0 & 0 \\ 0 & \Delta B_\perp & 0 & \Delta - 2B_0 & 0 \\ 0 & -\overline{\Delta B_\perp} & 0 & 0 & \Delta + 2B_0 \end{pmatrix}, \tag{5.6}$$

under the basis states: s_{02}, s_{11}, t_0, t_- and t_+.

Although the Hamiltonians (in Equations 5.4 and 5.6) describe the same physics, the distinction between ε and Δ must be considered when viewing the shape of the resulting energy spectra. The energy eigenvalues of the Hamiltonians given in Equations 5.4 and 5.6 are plotted (with respect to ε and Δ respectively) in Figure 5.10. When plotting against ε, at zero detuning, the lowest energy levels on the respective dots are aligned as shown in Figure 5.10a. As one pushes ε away from zero, the electrons eventually occupy a single dot. Note that the higher energy level for a given dot is only considered when the lower electron energy level is filled. That is, this higher energy level is the Coulombic repulsion that one must overcome when spin-pairing two electrons (in the singlet state) onto the same dot[8]. The two anti-crossings mediated by the tunnel coupling are found either side of zero detuning: s_{20}-s_{11} and s_{11}-s_{02}. The anti-crossings are separated by $2U_{02}$. Another important anti-crossing is that between t_0 and s_{11} (coupled via ΔB_z to form Pauli-x rotations in singlet-triplet qubits) as seen in Figure 5.10b, while not visibly clear (as an 'anti-crossing') in the energy diagram when plotting against Δ as seen in Figures 5.10d. Nonetheless, when plotting against Δ, the superfluous s_{20} state disappears and one obtains the main inter-dot anti-crossing s_{11}-s_{02} symmetrically about zero detuning ($\Delta = 0$). In both cases, changing the detuning (either ε or Δ) changes the energy splitting between the lowest energy singlet state and the triplet t_0 state. As shown later, tuning this splitting (termed J) is important when toggling between Pauli-x and Pauli-z rotations.

5.2.2 Importance of tunnel coupling and temperature

The tunnel coupling t_c separates the ground and excited singlet states as shown in Figures 5.10c-d. One typically operates near zero-detuning $\Delta = 0$ when performing

[8] Electrons must be in an overall anti-symmetric state in order to obey the Pauli exclusion principle. Therefore, triplet states with both electrons on the same dot require an anti-symmetric orbital degree of freedom (typically too high in energy and subsequently discarded for Si-P quantum dots as discussed in Appendix E.2) as two electrons on the same dot in the triplet state implies that the both the spatial and spin states are symmetric (thus, the overall state is still symmetric).

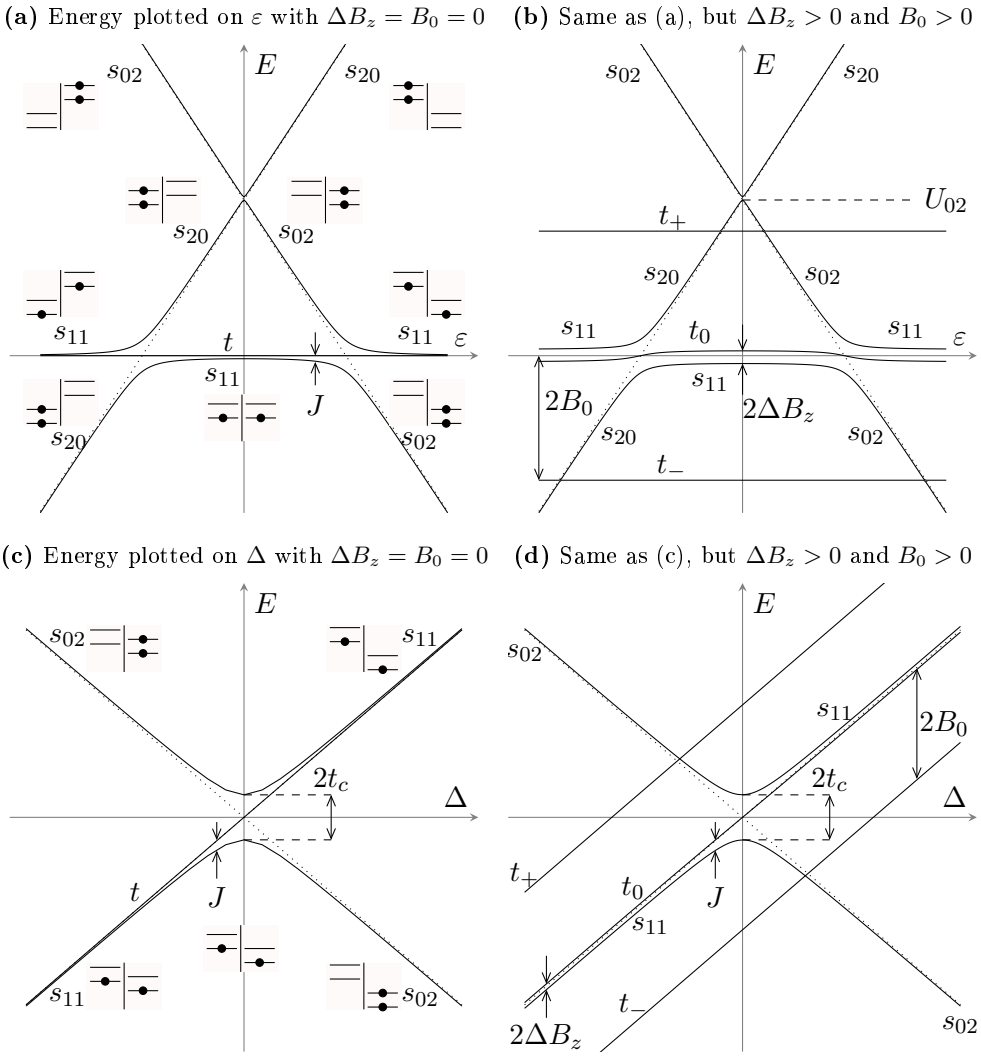

Figure 5.10: Energy spectra of the double quantum dot Hamiltonian for different detuning parameters ε and Δ. **(a)-(b)** Energy diagram given in terms of ε. The smaller energy level diagrams highlight the energy levels on the dots for different singlet states (s_{20}, s_{11} and s_{02}) across different points in detuning. **(c)-(d)** Energy diagram given in terms of the rescaled detuning Δ where the state s_{20} is discarded. Note that the state labels in all diagrams indicate the approximate asymptotic eigenstates. The magnetic field gradient across the dots ΔB_z creates an anti-crossing between the singlet s_{11} and triplet t_0 states as seen by the gap between s_{11} and t_0 at $\varepsilon = 0$ in (b) compared to (a). The global magnetic field B_0, Zeeman splits the triplet t_- and t_+ by $2B_0$. Note that the energy level t indicates three degenerate triplet states (t_-, t_0 and t_+) which split in a magnetic field $B_0 > 0$ in (b) and (d).

qubit operations and single-gate RF readout (where as discussed in Section 4.1, one oscillates between the s_{11} and s_{02} singlet ground states). In both cases, one needs to remain in the ground-state singlet state[9]. In this section, the role of the tunnel coupling in preventing thermal excitations into the excited singlet-state shall be investigated.

During the operation of the qubit, phonons in the lattice may excite the electron into the excited state at some prescribed rate. These electrons in the excited state would then decay at some prescribed rate. The phonon interaction can be modelled via the detailed balance equation [190] where the steady-state distribution is the definition of 'temperature' (used in statistical mechanics) of the electrons on the double-dot system (not necessarily the same 'temperature' of the electrons in the gate electrodes and perhaps closer to the lattice temperature). The ground state population distribution in this case is that akin to the Boltzmann distribution, where the population proportion of electrons in the ground state is given by [191]:

$$P_{\text{ground}} = \frac{\exp\left(-\frac{E_g}{k_B T}\right)}{\exp\left(-\frac{E_g}{k_B T}\right) + \exp\left(-\frac{E_e}{k_B T}\right)}, \tag{5.7}$$

where T is the temperature of the electrons, while E_g and E_e are the ground and excited state energies of the system. Taking the minimum gap in the singlet energy states (phonon excitation and decay does not change the spin state of the electrons), one may write $E_g = -t_c$ and $E_e = t_c$. Thus, the population becomes:

$$P_{\text{ground}} = \frac{1}{1 + \exp\left(-\frac{2t_c}{k_B T}\right)}. \tag{5.8}$$

Figure 5.11 shows the ground state population probabilities over different temperatures and tunnel couplings. Clearly low temperatures are required to obtain high ground state probabilities. Qubit devices usually operate in liquid helium dilution fridges that run at base temperatures as low as 10 mK. However, this temperature assumes perfect thermalisation of the silicon wafer with the mixing chamber of the fridge and perfect isolation from room temperature cabling connecting to the device. Thus, to maintain population probabilities above 99.5 %, a safe minimum bound for the tunnel coupling is 1 GHz, with 5 GHz comfortably reaching this probability at temperatures close to 100 mK.

[9] One may technically perform qubit operations if completely in the excited singlet branch. However, short excited state lifetimes and the stochastic nature of entering and leaving the excited state due to thermal effects makes it undesirable to use it in the qubit subspace.

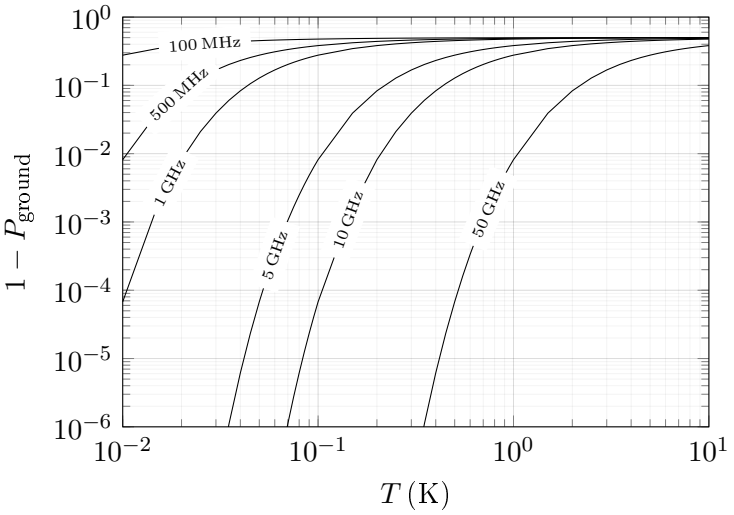

Figure 5.11: Importance of tunnel coupling and temperature on qubit operation. The plot shows the singlet ground state probability as a function of the electron temperature on the double quantum dot over different tunnel couplings as described by Equation 5.8. Larger ground state probabilities ($> 99.9\%$) are realised with lower temperatures (at least $\sim$1 GHz if the dilution fridge thermalises the device at 10 mK-20 mK) and higher tunnel couplings (for example, 5 GHz relaxes the maximum temperature to approximately 70 mK).

5.2.3 Double-dot to singlet-triplet qubit Hamiltonian

The full double-quantum dot Hamiltonian describes the dynamics of all four possible singlet-triplet states s_0, t_0, t_- and t_+. However, the singlet-triplet qubit is only formed on the s_0-t_0 subspace and thus, this section constructs a reduced Hamiltonian that can be used when evaluating gate operations and fidelities on singlet-triplet qubits.

Singlet-triplet qubits operate in the s_0-t_0 subspace. Thus, the coupling of the singlet-s_{11} state to the triplet t_- and t_+ states via the perpendicular magnetic field $\Delta B_\perp$ is undesirable as one will have state leakage away from the qubit subspace. To suppress these $\Delta B_\perp$ terms, one controls the on-diagonal Pauli-z terms given by the applied magnetic field B_0. By taking $B_0 \gg |\Delta B_\perp|$, one can suppress spin precession away from the qubit subspace into the triplet t_- and t_+ states. In typical experiments, $\Delta B_\perp$ is upper bounded by the magnitude of ΔB_z as the spins are likely to polarise and align mostly with the globally applied magnetic field. With ΔB_z typically in the order of $\sim$10-100 MHz for P-donors [50, 83] (as discussed earlier in Section 2.1.5), $\Delta B_\perp$ is approximately[10] $\sim$10 mT. With most spin qubit experiments

[10] The equivalent magnetic field is found by noting the Zeeman splitting of a single electron spin: $E_{B\perp} = \frac{1}{2} g_e \mu_e \Delta B_\perp$. Here $g_e = 2$ and $E_{B\perp} = 100$ MHz.

setting $B_0 > 100\,\mathrm{mT}$ to break the triplet degeneracy [14, 17, 29, 30, 55, 82], one can ignore the influence of $B_\perp$ in the following calculations. Note that the s_{11}-t_- anti-crossing (where the precession axis is such that the singlet may still interact and precess into the triplet t_-) is still useful in the context of dynamic nuclear spin polarisation where one may utilise the singlet state to flip nuclear spins to configure the value of ΔB_z [40, 41].

On suppressing the influence of $\Sigma B_\perp$, the triplet t_- and t_+ states do not participate in the qubit dynamics. This leaves three states of interest: s_{02}, s_{11} and t_0. The eventual qubit state is between the singlet s_0 and triplet t_0 states (with z-basis measurements performed along s_0 and t_0). However, the singlet state s_0 subdivides into two separate charge states (s_{02}, s_{11}), which makes it difficult to interpret the subspace as a two-level system as normally required for a qubit. To deduce the effective qubit state, the following analysis will look into the analytic eigenstates of the system. This is because the Hamiltonian eigenstates are invariant over time evolution. Since, two-level systems will indefinitely precess a given qubit state about a rotation axis given by the Pauli decomposition of the Hamiltonian, finding the eigenstates yields the rotation axes. From the rotation axes, one may deduce the effective two-level system Hamiltonian between the singlet s_0 and triplet t_0 states.

Now the tunnel coupling t_c is considered to be much larger in magnitude than the magnetic field gradient. In this regime $t_c \gg \Delta B_z$, the eigenvalue-eigenvector pairs are:

$$\begin{cases} \lambda_{t-} = \Delta - 2B_0 & |t_-\rangle \\ \lambda_{t+} = \Delta + 2B_0 & |t_+\rangle \\ \lambda_{t_0} = \Delta & |t_0\rangle \\ \lambda_{s+} = \sqrt{\Delta^2 + t_c^2} & \sqrt{\frac{1}{2} - \frac{\Delta}{2\sqrt{t_c^2+\Delta^2}}}\,|s_{02}\rangle - \frac{t_c}{\sqrt{2\left(t_c^2+\Delta^2-\Delta\sqrt{t_c^2+\Delta^2}\right)}}\,|s_{11}\rangle \\ \lambda_{s-} = -\sqrt{\Delta^2 + t_c^2} & \sqrt{\frac{1}{2} + \frac{\Delta}{2\sqrt{t_c^2+\Delta^2}}}\,|s_{02}\rangle + \frac{t_c}{\sqrt{2\left(t_c^2+\Delta^2+\Delta\sqrt{t_c^2+\Delta^2}\right)}}\,|s_{11}\rangle \end{cases} \tag{5.9}$$

The triplet states all remain on the $E = \Delta$ line with the $t_\pm$ states Zeeman split by $2B_0$. The singlet eigenstates split into excited and ground state branches with the eigenvalues λ_{s+} and λ_{s-} respectively. Taking the qubit state to be either in t_0 or the singlet ground state (s_{11}-s_{02}), the singlet-triplet splitting or 'exchange energy' is given by:

$$J \equiv \Delta + \sqrt{\Delta^2 + t_c^2}, \tag{5.10}$$

where J is the energy splitting between the two eigenstates lined up across the Pauli-z axis of the Bloch sphere. That is, it's the energy splitting attributed to a Pauli-z operator: $\frac{1}{2}J\sigma_z$. To deduce the qubit coupling term (between the singlet and triplet-t_0) one typically must go near the anti-crossing where the eigenstates fall onto the x-y plane on the Bloch sphere. From Figure 5.10d, this would be when $\Delta \to -\infty$. Thus, consider the eigendecomposition performed on Equation 5.6 at the far negative detuned region. Taking the characteristic polynomial and $|\Delta| \gg t_c$, the eigenvalue-eigenvector pairs are:

$$\begin{cases} \lambda_0 = -\Delta & |s_{02}\rangle \\ \lambda_- = \Delta - \Delta B_z & \frac{1}{\sqrt{2}}\left(|t_0\rangle - |s_{11}\rangle\right) \equiv |{\downarrow\uparrow}\rangle \\ \lambda_+ = \Delta + \Delta B_z & \frac{1}{\sqrt{2}}\left(|t_0\rangle + |s_{11}\rangle\right) \equiv |{\uparrow\downarrow}\rangle \end{cases} \tag{5.11}$$

The eigenvalues for the triplet t_- and t_+ have been omitted as they are the same as those in Equation 5.9. Clearly at far negative detuning, s_{02} is the excited state (that is, s_{02} is the highest energy state). The degeneracy between the two, lower energy, singlet s_{11} and triplet t_0 states is broken by the magnetic field gradient between the dots to create a splitting of: $2\Delta B_z$. Now this splitting is between two eigenstates that line up along the x-axis of the Bloch sphere[11]. Thus, this is the energy splitting attributed to a Pauli-x operator. Therefore, in the subspace restricted to t_0 and s_0, the two-level qubit sub-system of the singlet-triplet qubit Hamiltonian is:

$$\mathbf{H}_{\text{STQ}} \equiv \frac{1}{2}J\sigma_z + \Delta B_z\sigma_x = \begin{pmatrix} \frac{1}{2}J & \Delta B_z \\ \Delta B_z & -\frac{1}{2}J \end{pmatrix}. \tag{5.12}$$

The associated Bloch sphere for this qubit Hamiltonian is shown in Figure 5.12a. Typically the magnetic field gradient ΔB_z set to some fixed value. For example, if we use an integrated micro-magnet (fabricated by evaporating cobalt in a magnetic field), then the gradient will retain a fixed gradient [17, 47, 85]. In Si-MOS quantum dots, a difference in the on-site spin-orbit term interaction term (for example, due to local strain, local electric fields or oxides on the silicon crystal step edges on the surface) can give an effective ΔB_z-like term (albeit, due to spin-orbit contributions rather than magnetic fields) that is fixed on fabrication with slight tunability with applied electric fields [64, 192, 193]. In GaAs quantum dots, the substrate provides a bath of nuclear spins that one may polarise to create an in-situ magnetic field gradient; a technique known as 'dynamic nuclear spin polarisation' or DNP [40, 41]. It is proposed that a similar technique be employed to polarise the phosphorus nuclei

[11] These are the usual plus and minus qubit states. Note that this is also seen by the fact that in this regime of $\Delta \to -\infty$, the Pauli-z tends to zero for $J \to 0$ as seen by Equation 5.10

used to create quantum dots in Si-P systems [29]. However, the polarisation sequence used in DNP is much slower than the time-scale of individual qubit gate operations. Thus, ΔB_z can be considered to be fixed over a single qubit gate operation.

The rotation axis in a singlet-triplet qubit is therefore tuned purely by changing J, which is directly controlled by manipulating Δ or t_c as shown in Equation 5.10 and illustrated in Figure 5.12b. This manipulation of the rotation axis enables x-rotations when $J \approx 0$ at far negative detunings and z-rotations when $J \gg \Delta B_z$. Thus, one achieves 'all-electrical single-qubit control' in the sense that qubit rotations can be steered purely by applying a voltage on a local gate electrode. Importantly, the qubit rotations are not limited by slower magnetic field control in contrast to single-spin qubits [16].

5.2.4 Summary

Before one investigates the property of single-qubit gates with singlet-triplet qubits, it is important to note the required properties in attaining a singlet-triplet qubit across two P-donor quantum dots:

- The tunnel coupling t_c must be large enough to prevent thermal excitations into excited singlet-states. To maintain ground state probabilities above 99.9%, the tunnel coupling must be at least 1 GHz if the dilution fridge thermalises the device at 10 mK and 5 GHz if thermalised at 70 mK.

- The residual exchange J must be zero when the electrons are in separate dots ($\varepsilon = 0$) as otherwise one cannot turn off J (known as the weakly interacting tight-binding limit). For Si-P, the dots must be at least 9-10 nm apart (so that J is below the P-donor induced $\Delta B_z \sim$10-100 MHz [50, 83]) as estimated from numerical simulations of 1P-1P and 1P-2P double quantum dots [81, 84, 194].

- One must apply a global magnetic field B_0 to split the degeneracy of the three triplet states and ensure that the s_0-t_- anti-crossing is away from all single-qubit gate operating points to prevent state leakage into the triplet t_- and t_+ states. In experiments involving Si-P quantum dots, one typically needs $B_0 \gg 10$ mT.

(a) Singlet-triplet qubit Bloch sphere

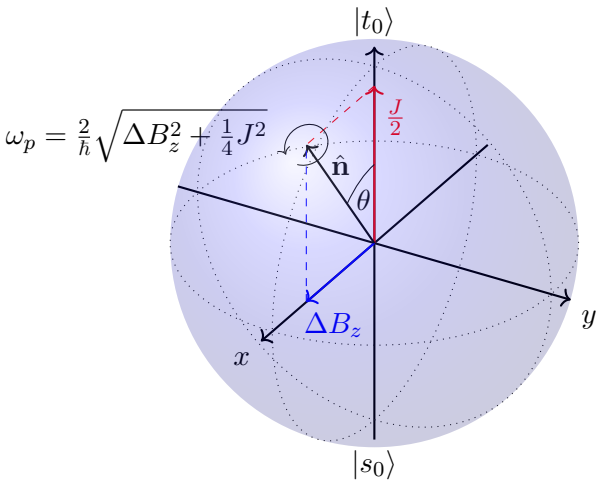

(b) Energy diagram of a 2-electron singlet-triplet across two quantum dots

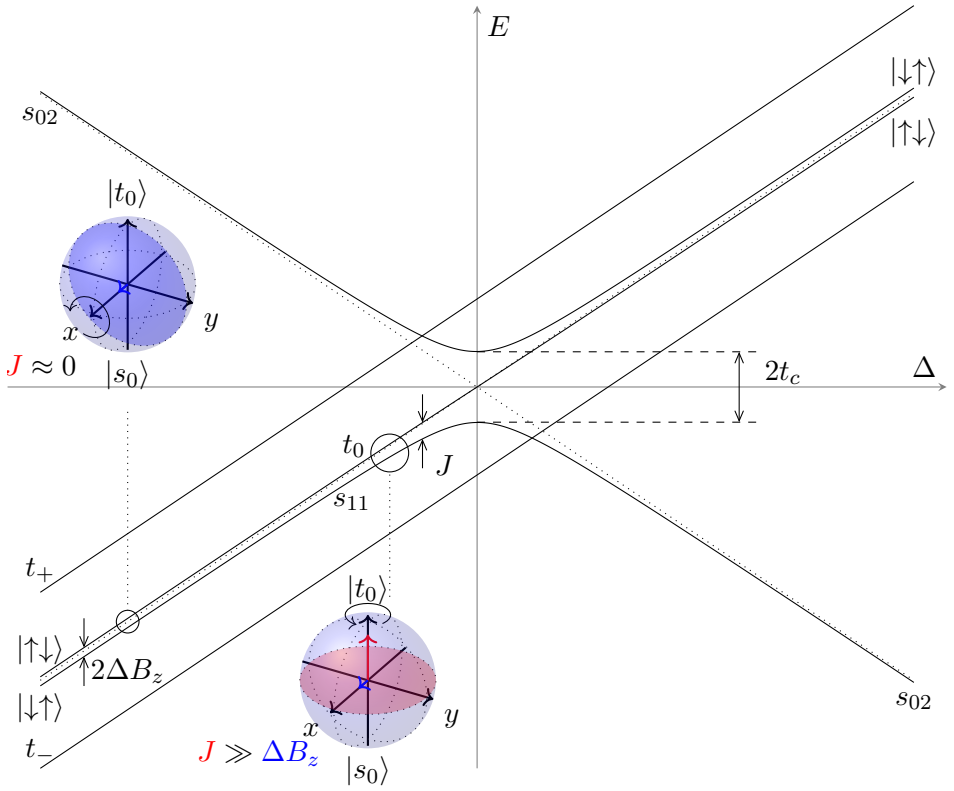

Figure 5.12: Singlet-triplet Hamiltonian qubit subspace and energy diagram. **(a)** Singlet-triplet qubit Bloch subspace mediated by J (twice the magnitude of red arrow) for Pauli-z rotations and ΔB_z (magnitude of the blue arrow) for Pauli-x rotations. Typically ΔB_z is fixed and J is tuned to change the qubit precession angle θ. **(b)** Energy spectrum of the double quantum dot Hamiltonian described in Equation 5.6. The state labels indicate the approximate eigenstate of the energy eigenvalue line at different points in detuning Δ. The tunnel coupling t_c highlights the singlet charge state anti-crossing. The label $2\Delta B_z$ indicates the anti-crossing seen clearly in Figure 5.10. In this region, the Hamiltonian is set for Pauli-x rotations as $J \approx 0$. At detunings away from far-negative detuning, J becomes appreciably larger than ΔB_z and subsequently, the system undergoes Pauli-z rotations. The dotted lines are guides that show the asymptotes and the small curvature seen in the t_0 eigenstate as it deviates from a simple linear trend.

5.3 Single-qubit gates on singlet-triplet qubits

Figure 5.12 shows the singlet-triplet qubit Hamiltonian on the Bloch sphere with $J/2$ yielding Pauli-z rotations and ΔB_z yielding Pauli-x rotations. The spherical angle (or the complementary angle of the altitude angle) of the rotation vector is simply:

$$\theta \equiv \arctan\left(\frac{2\Delta B_z}{J}\right) = \arctan\left(\frac{2\Delta B_z}{\Delta + \sqrt{\Delta^2 + t_c^2}}\right). \tag{5.13}$$

Evidently, one can smoothly toggle between Pauli-x rotations ($\theta = 90°$) and Pauli-z ($\theta = 0°$) by moving between $J \approx 0$ or $J \gg \Delta B_z$ respectively. With the speed of the precession, given by Equation 5.12:

$$\omega_p = \frac{2}{\hbar}\sqrt{\Delta B_z^2 + \tfrac{1}{4}J^2}, \tag{5.14}$$

one may also tune the precession frequency by changing J. In this section, each single-qubit gate shall be discussed in detail and then the optimal choice of J is discussed under the presence of charge noise.

5.3.1 Realising Pauli-x rotations via ΔB_z in Si-P

At large negative detunings where J is close to zero, the rotation axis points along the x-axis. The speed is fixed at approximately $\frac{2}{\hbar}\Delta B_z$. The magnitude of ΔB_z is taken to be 29 MHz as estimated for a 1P-2P double quantum dot (with the 2P donor dot holding two spin-paired electrons below the valence electron forming the singlet-triplet state). The 1P-2P configuration using the $(1,3) \leftrightarrow (0,4)$ singlet-triplet inter-dot crossing was shown in Section 2.2.3 to be favourable in the context of electrostatic control required to perform a singlet-triplet two-qubit gate. With one electron on the first dot, the hyperfine interaction of a 1P donor contributes approximately 29 MHz [50, 83]. With two electrons spin-paired below the valence electron on the 2P donor dot, one expects a small contribution that will shift ΔB_z by ± 5.25 MHz. Thus, the average ΔB_z will be taken to be approximately 29 MHz for the remainder of this thesis.

Now clearly $J = 0$ (as required for a Pauli-x gate) never happens as going to $\Delta \to -\infty$ will push the electrons towards the s_{20} state. By inspection of the full energy spectrum shown in Figure 5.10a and the Hamiltonian in Equation 5.4, the minimum singlet-triplet splitting J, occurring at $\varepsilon = 0$, is[12]:

[12] Note that the equation for J given in Equation 5.10 cannot be directly applied for large negative detunings as it does not account for the extra t_c term coupling s_{11} and s_{20}.

$$J_{\min} = \frac{-U_{02}}{2} + \frac{1}{2}\sqrt{8t_c^2 + U_{02}^2}, \tag{5.15}$$

where t_c refers to the rescaled version outlined in Equation 5.6. The minimum detuning one may traverse is:

$$\Delta_{\min} = -\frac{U_{02}}{2}. \tag{5.16}$$

At detunings below this point, the exchange J increases as the electrons start entering the s_{20} state. This minimum exchange puts an upper bound on the angle of the rotation axis θ. In Si-P, taking U_{02}~100 meV and $t_c = 5$ GHz, the minimum J is approximately 2.1 MHz. Given a typical ΔB_z of 29 MHz from a 1P donor (as discussed in Section 2.1.5), the maximum rotation angle is thus, approximately $\theta = 87.95°$. That is, one may need to compensate the slight inaccuracy in the Pauli-x rotations via echoes or dynamical decoupling pulse sequences to enhance the single-qubit gate fidelity [195, 196].

Finally in the context of setting up experiments, it is useful to gauge the magnitude of the voltage pulses to perform the gate operations. One useful measure is to find the detuning required to perform a Hadamard operation where $J/2 = \Delta B_z$ ($\theta = 45°$). If the Hadamard operation is accessible, then one may still attain Pauli-x rotations by appending Hadamard operations before and after a Pauli-z gate [167]. Using the expression for J in terms of Δ, the detuning point for a Hadamard gate is:

$$\Delta_{\text{Hadamard}} = \frac{2\Delta B_z^2 - t_c^2}{4\Delta B_z}. \tag{5.17}$$

Noting that $2\Delta = e\Delta\alpha_g \Delta V_g$, one may find the required amplitude of the voltage pulse ΔV_g (when applied on gate g with a differential lever-arm $\Delta\alpha_g$):

$$\Delta V_g = \frac{4\Delta B_z^2 - t_c^2}{2e\Delta\alpha_g \cdot \Delta B_z}. \tag{5.18}$$

Taking $\Delta B_z \approx 29$ MHz and a typical differential lever-arm of 5% (expected for the control gates in the proposed singlet-triplet architecture in this thesis), one finds that the tunnel coupling strongly affects the range of voltages one needs to pulse to achieve the Hadamard gate. For example, with a tunnel couplings of 5 GHz, 10 GHz and 30 GHz, the required voltage amplitudes reach −36 mV, −140 mV and −1.3 V respectively. High-speed arbitrary waveform generators have a limited voltage range of typically ±1.5 V with the range further limited to approximately ±470 mV due

to the minimum recommended 10 dB of thermalising attenuators placed along the coaxial lines going into the dilution fridge [33]. In addition, large voltage pulses near 1 V may cause gate-to-gate leakage current in the device. Thus, large tunnel couplings (above 10 GHz) make it difficult to perform Hadamard operations due to both equipment and device limitations.

5.3.2 Requirements for Pauli-z rotations

For approximate Pauli-z rotations, one may set $J \gg \Delta B_z$ with the speed of precession approximately at $J/\hbar$. When the qubits are idle, one sets them to precess about the Pauli-z axis. Here, the qubit population will not shift and no gates are induced as long as all qubits precess at the same frequency $J/\hbar$. A high-fidelity idle (or identity) gate is important in a many qubit processor. The gate here can be imperfect as a non-zero ΔB_z will tilt the rotation axis away from the Pauli-z axis. One can calculate the loss in fidelity due to imperfect Pauli-z gates[13]. The fidelity shall be taken as the projection of the final state upon the intended state. Consider a state ψ_i on the xy-plane of the Bloch sphere. Now a Z gate (a Pauli-z gate) with a finite J and ΔB_z shall be performed by waiting π/ω_p while at $J \gg \Delta B_z$. Geometrically, the phase rotation is perfect, but the state is now slightly off the xy-plane. For an axis rotation angle of θ, this imperfect state ψ_f is off the xy-plane by 2θ. Thus, taking the states on the Bloch sphere, converting to vector notation and taking the projection probability $|\langle \psi_{\text{actual}} \mid \psi_{\text{ideal}} \rangle|^2$, the Fidelity is simply:

$$F_{\text{Z}} = \cos^2(\theta) \equiv \frac{J^2}{J^2 + (2\Delta B_z)^2}. \tag{5.19}$$

Solving for J, one may then relate the required exchange to reach a certain fidelity threshold:

$$J_{\text{req}} = 2\Delta B_z \sqrt{\frac{F_{\text{Z}}}{1 - F_{\text{Z}}}}. \tag{5.20}$$

Table 5.2 lists the required ratio of $J/\Delta B_z$ to reach given Z-gate fidelities. Note that these fidelities arise simply from gate control when using J and do not yet consider the additional contribution from charge noise.

Given the values in Table 5.2, for a given ΔB_z, one may identify the minimum J required to realise to enable Pauli-z gates. As shown later, when considering the

[13] One could recast the algorithms to utilise the imperfect gates $\theta \neq 0$. The approach taken here is to achieve the conventional X and Z gate sets to later aid in performing the required surface code parity operations.

Z Fidelity	$J/\Delta B_z$	θ (°)
90 %	6	18
99 %	20	5.7
99.5 %	28	4.1
99.9 %	63	1.8
99.99 %	200	0.57
99.999 %	632	0.18

Table 5.2: Imperfection in Pauli-z rotations due to ΔB_z. For given Z (that is, a 180° Pauli-z rotation) fidelities, the required ratio of exchange to the magnetic field gradient $J/\Delta B_z$ are listed along with their associated spherical rotation angles. Note that $\theta = 0$ points along the z-axis of the Bloch sphere.

presence of charge noise in two-qubit gates in Section 5.4, the minimum J is also important since it impacts the choice in the tunnel coupling and the inter-qubit coupling. From Table 5.2, the exchange J would need to be 28 times bigger than the magnetic field gradient $\Delta B_z = 29\,\text{MHz}$ for Pauli-z gates with 99.5% fidelity. That is, the exchange when the qubit is in its idle Pauli-z rotating state must be at least $J_{\text{idle}} = 810\,\text{MHz}$.

5.3.3 Impact of charge noise on Pauli-z gates

The precession frequency of a singlet-triplet qubit given in Equation 5.14 is a function of J and ΔB_z. Any shot-to-shot perturbations on these parameters will cause the qubit precession frequency to alter from one logic gate to the next. Thus, for example, if one waits the nominal time for a π rotation, there will be instances where the trajectory either overshoots or undershoots the required rotation angle. Decoherence describes the ensemble average of the state vector as it is pushed away from the pure states. Mitigation of 'charge noise' affecting J and magnetic field gradient noise affecting ΔB_z is important when considering these qubits in the context of a large scale 2D surface-code quantum processor where qubit error rates must be at least below 0.5 % to achieve fault tolerance [8]. Magnetic field gradient noise can be mitigated by using isotopically purified ^{28}Si which has a low concentration of non-zero spins from ^{29}Si nuclei. The significant limiter for conventional solid state spin qubits (such as singlet-triplet qubits) is charge noise [34, 69]. Thus, this section will focus on the influence of charge noise that affects J. The results will show that it is desirable to keep the operating points far in negative detuning ($\Delta < 0$) to minimise decoherence of the qubits.

Qubit operations are controlled by changing Δ to control the exchange J as

shown in Sections 5.2 and 5.3. In this section, it is assumed that one is performing Pauli-z rotations, where $J \gg \Delta B_z$ and $\omega_p \approx J$. The noise source shall perturb Δ as any source of charge noise will fundamentally manifest as a perturbation on the dots' local electric fields resulting in an experimentally measurable shift in the detuning [17, 64, 197]. The electric field perturbation could be either due to noise on the gates (producing the tilting electric fields) or due to intrinsic charge fluctuators within the crystal; nonetheless, the source and its characteristics is a topic of ongoing research [18, 69]. This noise source shall be taken to be a Gaussian distribution[14] centred about the target detuning Δ_μ with a standard deviation 'amplitude' parameter Δ_σ:

$$P_{\mathrm{Z}}(\Delta) = A_0 \exp\left(-\frac{(\Delta - \Delta_\mu)^2}{2\Delta_\sigma^2}\right), \tag{5.21}$$

where A_0 parametrically normalises the distribution. Note if the noise standard deviation Δ_σ tends towards zero, one has a dirac-delta like frequency peak about the intended detuning Δ_μ, leading towards zero deviation in J as required for stable and coherent gate operations. Now given this probability distribution in terms of Δ, one may recast it in terms of J:

$$P_{\mathrm{Z}}(J) = A_0 \exp\left(-\frac{\left(\frac{J^2 - t_c^2}{2J} - \Delta_\mu\right)^2}{2\Delta_\sigma^2}\right). \tag{5.22}$$

The asymptotic forms away from zero detuning are:

$$P_{\mathrm{Z}}(J) \approx \begin{cases} A_0 \exp\left(-\frac{(J-2\Delta_\mu)^2}{2(2\Delta_\sigma)^2}\right) & \Delta_\mu \gg t_c \\ A_0 \exp\left(-\frac{\left(J+\frac{t_c^2}{2\Delta_\mu}\right)^2}{2\left(\frac{t_c}{2\Delta_\mu^2}\Delta_\sigma\right)^2}\right) & \Delta_\mu \ll -t_c \end{cases}. \tag{5.23}$$

This provides an approximate functional upper bound that overestimates the spread of the distribution. Although the asymptotic forms are approximated with Gaussians, the original distribution is asymmetric (seen easily by noting that one maps $\Delta \in [-\infty, \infty]$ to $J \in [0, \infty]$). From the asymptotic approximations, it is clear that the Gaussian standard deviation in J for working points on positive and negative detunings are:

[14] If the actual noise distributed itself via a different shape, one can tweak Δ_σ to match the actual distribution to ensure it overestimates the noise distribution, as the aim of this analysis is to give an worst-case upper-bound while using a typical realistic distributions.

$$J_\sigma \approx \begin{cases} 2\Delta_\sigma & \Delta_\mu \gg t_c \\ \frac{t_c}{2\Delta_\mu^2}\Delta_\sigma & \Delta_\mu \ll -t_c \end{cases}. \tag{5.24}$$

Here J_σ represents the spread of Pauli-z precession frequencies one may expect if taking an ensemble of many measurements. Since the inverse Fourier transform of a Gaussian is a Gaussian, the resulting precession in the time-domain rotations will have a decaying Gaussian envelope. The decay time-constant is the characteristic coherence time $T_2^*{\sim}J_\sigma$. At positive detunings ($\Delta > 0$), the coherence time saturates to a constant value as the gradient in J (that is, $dJ/d\Delta$), is constant. When going deeper into negative detuning, the coherence time gets larger as the change in J with respect to detuning tends to zero: $dJ/d\Delta{\sim}0$. The gate fidelity relates to the loss in population due to decoherence; that is, the gate fidelity relates to the number of possible gates one may perform (at a rate given by the mean J) within the given coherence time:

$$\frac{J}{J_\sigma} \approx \begin{cases} \frac{\Delta_\mu}{\Delta_\sigma} & \Delta_\mu \gg t_c \\ \frac{t_c}{\Delta_\sigma} & \Delta_\mu \ll -t_c \end{cases}. \tag{5.25}$$

The fidelity estimate implies that one may in fact, increase the gate fidelity when working away from zero detuning (either at positive or negative detuning). When going further into positive detuning, the speed of the gate increases while the exchange noise standard deviation J_σ saturates to a constant value. Thus, one may indefinitely increase the gate fidelity by going into positive detuning. However, experimental limitations limit the speed of J and thus, the maximum detuning Δ_μ. These experimental difficulties arise from the precise timing required for gate times below 1 ns (the state of the art arbitrary waveform generator at the time of writing this thesis was limited to 20 ps pulses). Whereas when working deeper into negative detuning, the gate speed can remain slow enough to be experimentally feasible (as $\Delta < 0$ implies that $J < t_c = 5\,\text{GHz}$, the pulses can be made much slower than 200 ps) and one may increase the tunnel coupling t_c to increase the gate fidelity. Larger tunnel couplings give larger gate fidelities as the desired J now appears deeper in negative detuning where $dJ/d\Delta$ is smaller and thus, variations in J are smaller for a given noise standard deviation Δ_σ.

The intuition from the analytic formulation above was confirmed with numerical simulations of the gate fidelities shown in Figure 5.13. The gate fidelities were calculated numerically using the method described in Appendix F. The method first takes a noise standard deviation Δ_σ and a nominal choice in J_μ to construct the proba-

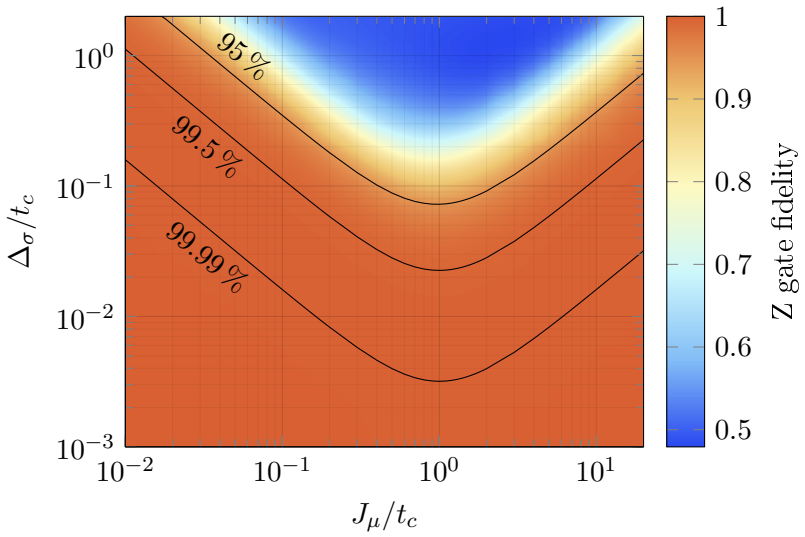

Figure 5.13: Fidelity of a single-qubit Z gate as a function of exchange J_μ and noise standard deviation Δ_σ. The plot shows the worst-case Z gate fidelities across different operating points J_μ and charge noise, given as the standard deviation in detuning, Δ_σ. The parameters are normalised to the tunnel coupling t_c. The dark lines signify the contours for fidelities of 95 %, 99.5 % and 99.99 %.

bility distribution of the precession frequency J given in Equation 5.22. It is noted that one may normalise J and Δ_σ conveniently in terms of the tunnel coupling t_c to reduce the parameter space. Given the spread in the precession frequency (that is, the spread in J), one may take the inverse Fourier transform to obtain the decaying cosine wave that represents the average loss in the coherence due to stochastic shot-to-shot perturbations in the precession frequency J. The worst case Z gate fidelity was extracted from the decay at one full period of rotation to both conservatively underestimate the π-rotation fidelity and to get the idle qubit fidelity. The idle qubit fidelity is a 2π Pauli-z rotation (or two Z gates) where the qubit performs an identity operation.

Figure 5.13 shows the resulting fidelities when varying the exchange J/t_c and noise standard deviation Δ_σ/t_c. Here J_μ is the precession frequency as expected when setting the associated point in detuning Δ_μ to perform the Pauli-z gate[15]. The key feature is that at zero detuning ($J = t_c$), the fidelities dramatically drop. As one traverses further into positive detuning, the saturation of the noise in J and the increasing precession frequency yields a monotonic increase in the resulting

[15]Here J_μ is not necessarily the mean J given the distribution of J from the Gaussian spread in Δ. As one may not be necessarily sampling the true mean frequency in J, the fidelity estimates underestimate the gate fidelity.

fidelities (as realised by the analytic asymptotic expressions for the gate fidelities). Similarly, as expected, at negative detuning ($J < t_c$), the Z-gate fidelities start to increase. The 99.5 % contour represents a hard boundary in which devices must satisfy by design and operation in order to satisfy the error thresholds for scalable quantum computing qubit arrays.

Now considering the minimum tunnel coupling bound of ∼5 GHz (for a general double quantum dot system measured in a typical dilution fridge), one would need the detuning noise standard deviation Δ_σ to be approximately $0.02t_c = 400\,\text{neV}$ to work at zero detuning. To date, Δ_σ has been experimentally measured to be 5 μeV in GaAs [197], 6.4 μeV in SiGe [17] and 2 μeV in Si-MOS [64] quantum dots. Although a recent experiment in Si-P reported a relatively large detuning noise of ∼10 μeV [198], the device operated close to voltages that would cause gate-to-gate leakage. In general, the noise in Si-P has been shown to be lower given that the P-donor qubits are embedded within an epitaxially grown bulk crystal far from the surface where there may be charge traps due to the oxide interface [199]. In addition, the smaller size of the qubits (12.5 nm as opposed to 70-100 nm of gate-defined quantum dots [14]) should also provide lower noise given that any electric field fluctuation from a source far away may not be necessarily different across the dots. That is, detuning noise requires a tilting of the dot's energy levels as opposed to raising or lowering both dots' energy levels simultaneously. In addition, the noise from any charge fluctuations in the nearby gates in P-doped delta layers have been measured to be much lower (3 orders of magnitude lower) compared to other wires in semiconductor systems [199, 200]. Thus, P-donor dots should approach the theoretical prediction of the background detuning noise in silicon of approximately 100-1000 neV [18, 201, 202]. Although 400 neV is above the theoretical minimum, it would be advisable to set J to negative detuning to obtain higher fidelities. For example, if one sets $J = 0.1t_c = 1\,\text{GHz}$, the allowable charge noise to obtain 99.5% fidelity is approximately $\Delta_\sigma = 0.1t_c \approx 2\,\mu\text{eV}$.

5.3.4 Summary

The discussion of single-qubit operation sets important experimental bounds on the choice of device parameters operating conditions. These key concepts include:

- The tunnel coupling should not exceed 10 GHz as typical values of $\Delta B_z = 29\,\text{MHz}$ (estimated for a 1P-2P double quantum dot) and $\Delta\alpha = 5\%$ (typical control gate differential lever-arms for the proposed singlet-triplet architecture) yield voltage pulses of $-140\,\text{mV}$ to perform a Hadamard gate (the pulses need

to be larger to reach $J \approx 0$). The voltage range is limited by the equipment to approximately $\sim \pm 0.5\,\mathrm{V}$ if using a typical waveform generator fed through attenuated coaxial cables in a dilution fridge. It is also limited by the device since large pulses of $\pm 1\,\mathrm{V}$ will likely cause gate-to-gate current leakage.

- The minimum J is approximately 810 MHz (given that $\Delta B_z = 29\,\mathrm{MHz}$) if one wishes to produce Pauli-z gates with 99.5% accuracy.
- Typical operation for maximal Pauli-z gate fidelity would involve setting the qubits to negative detuning. Negative detuning offers a smaller fluctuation in J for a given fluctuation in the detuning (that is, a small $dJ/d\Delta$).
- High-fidelity (greater than 99.5%) Pauli-z gates should be possible given typical detuning noise. For example, if one takes $t_c = 5\,\mathrm{GHz}$ and sets $J = 0.1t_c = 1\,\mathrm{GHz}$, the detuning noise needs to be below $\Delta_\sigma = 0.1t_c \approx 2\,\mu\mathrm{eV}$.

5.4 Two-Qubit gates on Si-P Singlet-Triplet qubits

The mainstream proposal for two-qubit gates amongst singlet-triplet qubits in the literature utilises electric dipole couplings also termed 'capacitive coupling' [14, 34, 42, 203]. Here the basic concept is that the triplet state always remains in a $(1,1)$ charge state with respect to detuning Δ, while the singlet state can change between charge states s_{11} and s_{02} with respect to Δ. This means that above zero detuning ($\Delta > 0$), a singlet-state will have most of its electric charge transferred onto a single dot, while for the same detuning, a triplet t_0 state will have both electrons occupying separate dots. The difference in charge state on the 'control' qubit will have a state-dependent difference in electric field on a second 'target' qubit. If configured correctly, this electric field can manipulate the Δ of the 'target' qubit to either precess faster along the z-axis or change its gate type from Pauli-z to a Pauli-x gate. The advantage of the electric-dipole induced two-qubit gate (adopted in the proposals in this thesis) is that the individual double dots forming the singlet-triplet qubits may be spaced far apart (more than an order of magnitude further than the individual dot-to-dot separation distance within a single singlet-triplet qubit). Thus, the method is conducive for a scalable architecture as the routing of control lines is less difficult since the qubits are not so tightly packed.

The two-qubit gates discussed and later optimised in this chapter utilise DC pulsing in the presence of large inter-qubit couplings (as opposed to the preturbative inter-qubit couplings required for AC-driven singlet-triplet qubits operating at $J{\sim}0$)

to realise faster high-fidelity two-qubit gates. Note that from previous works [34, 35], a perturbative inter-qubit coupling, conducive with AC-driven singlet-triplet qubits, in P-donor qubits can be realised by spacing the double-quantum-dots more than 120 nm apart as discussed in Section 2.3.

There is also a two-qubit gate proposal that utilises direct exchange between all four quantum dots forming the two singlet-triplet qubits [204]. Although this method promises faster gates, not only must it handle the higher probability of entering leakage states (that is, not in the s_0-t_0 subspace) but the fact that the dots must be exchange coupled implies that the double-dot singlet-triplet qubits need to be in close proximity (in the order of the individual dot-to-dot separation distance within a single singlet-triplet qubit). Such strongly coupled exchange-based singlet-triplet qubits are not considered in the large scale architecture proposals in this thesis.

5.4.1 CZ Gate

The CZ gate performs a Pauli-z rotation (by angle π) on the target qubit conditional on the state of the control qubit. The two qubits, control and target, are initially biased such that $J \gg \Delta B_z$; that is, performing a Pauli-z gate at the same frequency (thereby performing a mere identity operation every full rotation about the z-axis). Figure 5.14 shows how when biasing the control qubit towards positive detuning, the control qubit remains in the remains in the $(1,1)$ charge state if in the triplet t_0 state (a) due to Pauli-spin blockade. However, if the control qubit is in the singlet s_{11} state (b), it may enter the $(0,2)$ charge state via s_{02}. On the target qubit, there is no change if the control qubit is in the triplet t_0 state. However, if the control qubit is in the singlet s_{02} state, the target qubit's detuning shifts to a point of higher J and thus, a faster z-axis precession frequency. Thus for example, if one tunes this shift in J to double the precession frequency, then on waiting for a π z-axis rotation (with the control qubit in the t_0 state) would become an identity operation with the control qubit in the s_0 state as the rotation angle will be 2π. The resulting gate operation is a CZ gate where the target qubit undergoes a π rotation about the Pauli-z axis conditional on the control qubit being in the triplet t_0 state.

Ultimately for the CZ gate one needs to find the optimal choice in physical (tunnel coupling and inter-qubit coupling set by geometry upon fabrication) and operational parameters (exchange J on the qubits tuned by the voltages set on the gates) to maximise the two-qubit gate fidelity. The operation of a CZ gate depends on the following parameters (the optimal choice in the parameters for Si-P will be found in the end of the noise analysis in Section 5.4.2):

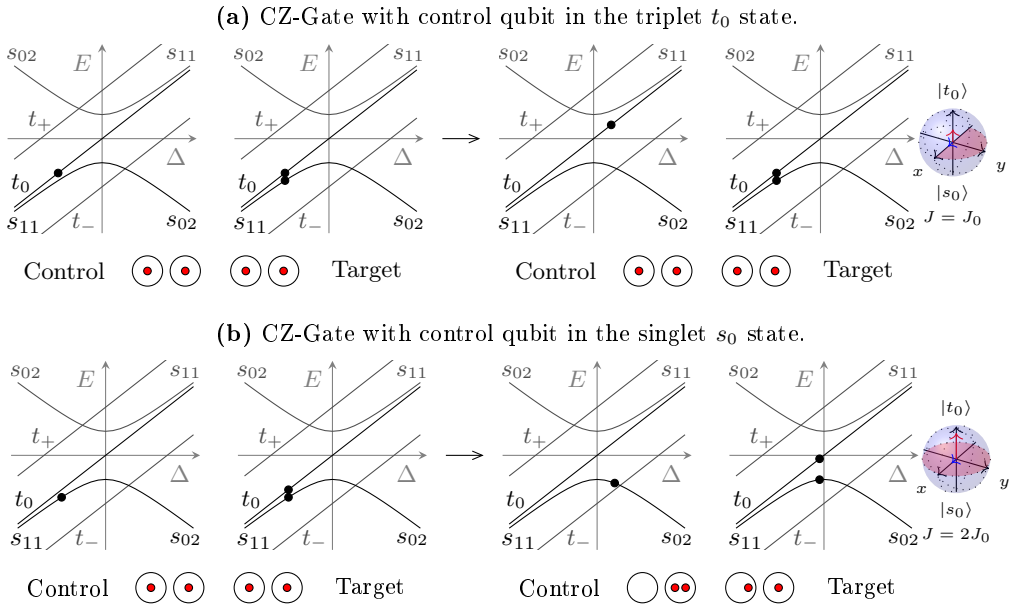

Figure 5.14: CZ gate for electric-dipole coupled singlet-triplet qubits. The energy diagrams (see Figure 5.12) and double-dots (red dots representing the two electrons forming each singlet-triplet qubit) represent the individual singlet-triplet qubits: the control and target qubits. To activate the gate, the control qubit is biased towards the region of positive detuning, where a triplet t_0 remains in the $(1,1)$ charge state as shown in **(a)**, while the singlet enters the $(0,2)$ charge state (via s_{02}) as shown in **(b)**. A control qubit in the singlet state causes the target qubit's detuning to shift and subsequently its exchange J increases from J_0 to $2J_0$. For a fixed time, this greater J causes a faster rotation, which if tuned right can yield an identity operation on the target qubit if the control qubit is a singlet and a Pauli-z flip if the control qubit is a triplet t_0. The Bloch spheres represent the operation performed on the target qubit with the red arrow representing the target qubit's J while the blue arrow represents its ΔB_z vector.

- Idle-qubit exchange J_t (set by idle-qubit detuning Δ_t). The qubits in their default idle state (and thus, the target qubit's initial state) is when $J = J_t \gg \Delta B_z$.
- Control-qubit exchange J_c (set by control-qubit detuning Δ_c). The exchange to which one sets on the control qubit to initiate the two-qubit coupling to run the CZ gate.
- Inter-qubit coupling Δ_Δ. The shift in the target qubit's detuning when completely moving the control qubit from $(1,1)$ to $(0,2)$ charge states. Note that the actual shift in the target qubit's detuning is $p_{02} \cdot \Delta_\Delta$ (where p_{02} is the fractional probability of being in the $(0,2)$ charge state as given in Equation 5.28).

Now when a CZ gate is performed between two qubits, one biases the control and target qubits to J_c and J_t respectively, where if the control qubit were in the singlet-state, the target qubit becomes biased at $J_t + \Delta J$. Thus, as one waits a certain period of time τ, the target qubit will accumulate phase at a different rate with the relative difference in phase being (taking Equation 5.14 for the qubit z-precession frequency):

$$\Delta \upsilon_z = \frac{J_t + \Delta J}{\hbar}\tau - \frac{J_t}{\hbar}\tau = \frac{\Delta J}{\hbar}\tau. \tag{5.26}$$

When the relative phase is π, then the gate is a CZ gate where one waits τ_{CZ}:

$$\tau_{\text{CZ}} = \frac{h}{2\Delta J}. \tag{5.27}$$

Before calculating ΔJ, one needs to find the shift in the target qubit's detuning via Δ_Δ. The shift in the target qubit's detuning only occurs when the control qubit is in the singlet s_{02} charge state. One can estimate the net shift to be $p_{02} \cdot \Delta_\Delta$, where p_{02} is the fraction of the control qubit in the s_{02} state [42]. One can find the fraction of the control qubit in the singlet s_{02} charge state via the eigendecomposition given in Equation 5.9:

$$p_{02} = \frac{1}{2} + \frac{\Delta}{2\sqrt{t_c^2 + \Delta^2}} \equiv \frac{J^2}{J^2 + t_c^2}. \tag{5.28}$$

Evidently at zero detuning, the dipole strength will be a half, maximal at an infinite positive detuning and nullified at infinite negative detuning. The change in exchange ΔJ due to the shift in the target qubit's detuning can be calculated from the definition of J in Equations 5.10:

$$\Delta J = \left(\Delta_t + p_{02}\Delta_\Delta + \sqrt{\left(\Delta_t + p_{02}\Delta_\Delta\right)^2 + t_c^2}\right) - \left(\Delta_t + \sqrt{\Delta_t^2 + t_c^2}\right). \tag{5.29}$$

That is, the shifted value of J is at the detuning $\Delta_t + p_{02}\Delta_\Delta$ where p_{02} is a scaling factor that determines the probability proportion of the control qubit in the $(0,2)$ charge state. Since, p_{02} is a function of J_c, one may rewrite the target qubit's exchange interaction in terms of J_c (noting tunnel-coupling normalised parameters: $\Delta J' = \Delta J/t_c$, $J'_c = J_c/t_c$, $\Delta'_t = \Delta_t/t_c$ and $\Delta'_\Delta = \Delta_\Delta/t_c$):

$$\Delta J' = \frac{J_c'^2}{J_c'^2+1}\Delta'_\Delta + \sqrt{1 + \left(\frac{J_t'^2-1}{2J'_t} + \frac{J_c'^2}{J_c'^2+1}\Delta'_\Delta\right)^2} - \frac{J_t'^2+1}{2J'_t} \tag{5.30}$$

The equation for $\Delta J'$ gives the relative speed of the gate given J'_c, J'_t and Δ'_Δ.

Figures 5.15a-c show the gate speeds for different inter-qubit couplings as a function of exchange on the control and target qubits. For all inter-qubit couplings, the larger CZ gate speeds appear at positive detuning on the control qubit (that is, $J_c \gtrsim t_c$) as one needs to be near positive detuning where the control qubit starts to enter the s_{02} charge state to activate the electric dipole required to trigger the CZ gate.

To interpret the trends in J_t consider an activated CZ gate where $J_c > 1$. At negative detuning on the target qubit ($J_t \ll 1$), the variation in J with respect to the target qubit detuning $dJ/d\Delta_t$ is small resulting in a small ΔJ when shifting from Δ_t to $\Delta_t + p_{02}\cdot\Delta_\Delta$. At positive detuning on the target qubit ($J_t \gg 1$), the target qubit exchange linearly increases to result in a constant $dJ/d\Delta_t$. Thus, at positive detuning, the gate speed ΔJ is constant when shifting from Δ_t to $\Delta_t + p_{02}\cdot\Delta_\Delta$.

For larger inter-qubit couplings (such as $\Delta_\Delta = t_c$ and $\Delta_\Delta = 10t_c$ in Figures 5.15b-c), the gate speeds start to saturate to the maximum speed at $J_t < 1$ as the larger jump in detuning enables a large change in the target qubit exchange. That is, the larger ΔJ occurs when shifting from $J_t \approx 0$ at negative detuning to $J_t \gg 0$ at positive detuning. Finally, since J_t monotonically increases with detuning Δ_t, a larger inter-qubit coupling enables a larger change in J_t and thus, gate speeds in general increase with larger inter-qubit couplings as seen by the scale-bars in Figures 5.15a-c. As with the analysis of Pauli-z gate fidelities, the area of maximum gate speed does not guarantee maximal gate fidelities when considering the presence of charge noise.

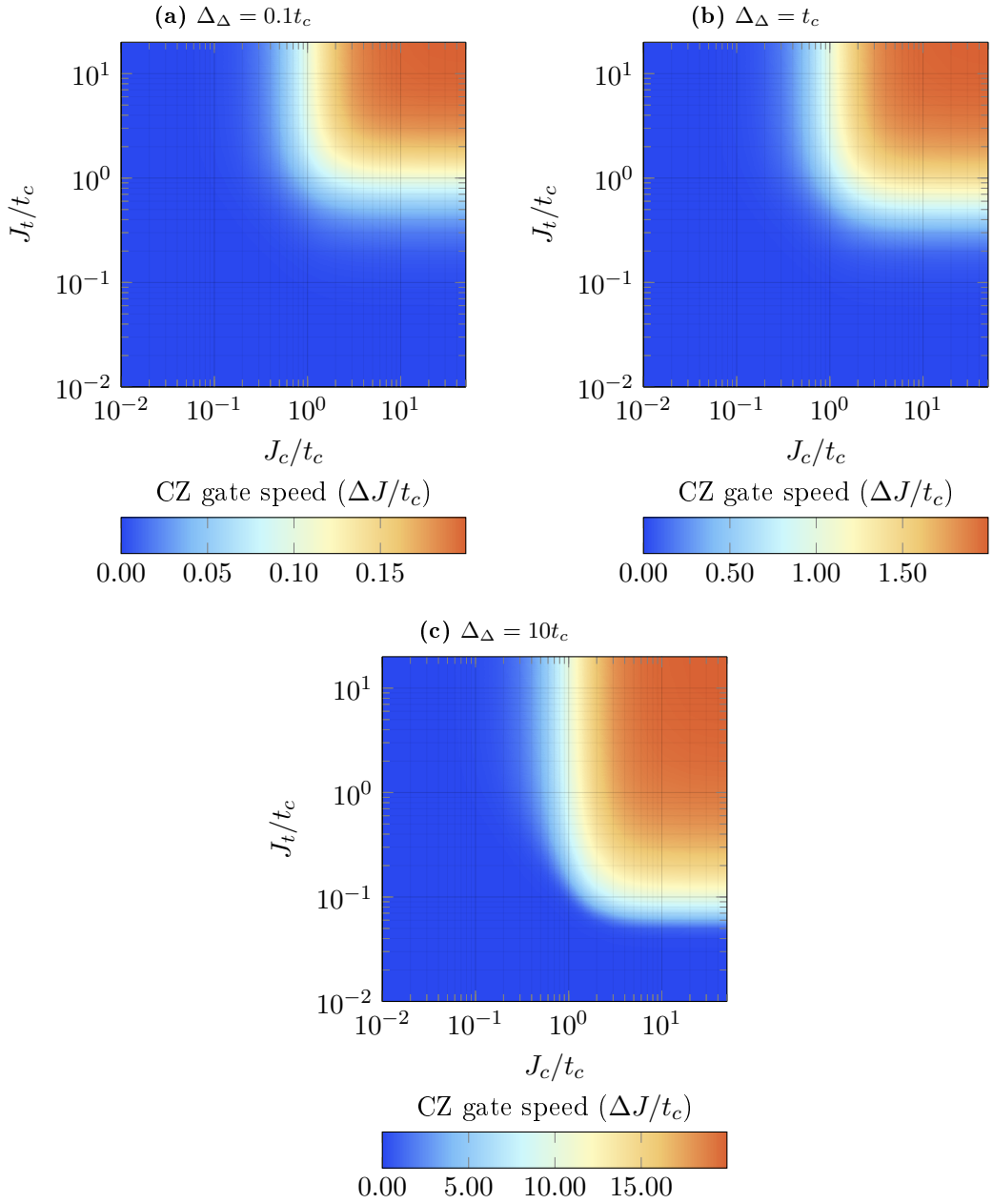

Figure 5.15: CZ gate speeds as a function of control qubit exchange J_c, target qubit exchange J_t and inter-qubit coupling Δ_Δ. The plots **(a)-(c)** show the CZ gate speeds, for different inter-qubit couplings Δ_Δ, normalised to the tunnel coupling: $\Delta J/t_c$ (note the different colour scales: 0.15, 1.5 and 15). Each plot shows the CZ gate speed as a function of the control and target qubit exchange (both normalised to the tunnel coupling). The CZ gate speed is close to zero for $J_c < 1$ as the CZ gate is inactive (as the control qubit is biased in negative detuning and thus, in the s_{11} state). The CZ gate speed only becomes non-zero when $J_c > 1$ (to activate the gate) and when there is an appreciable change in J_t when shifting the target detuning by $p_{02}\Delta_\Delta$ ($dJ_t/d\Delta_t \sim 0$ at far negative detuning). The general trend is that the CZ gate speed increases when increasing both J_c and J_t.

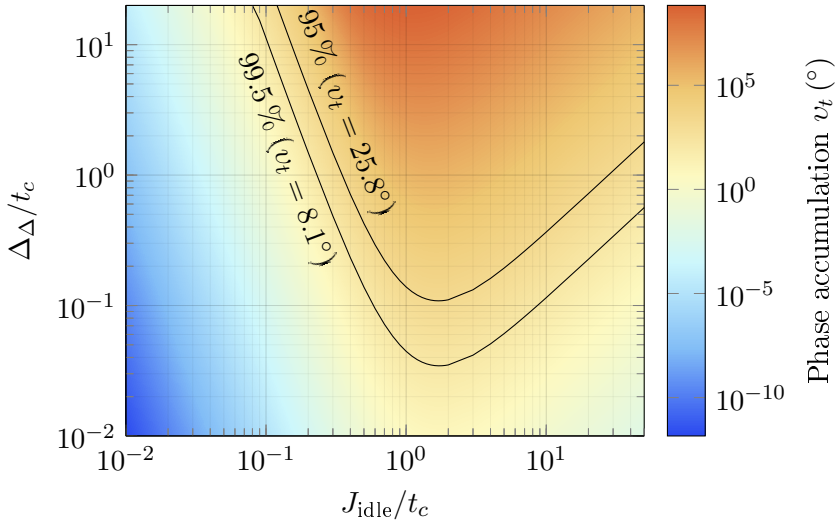

Figure 5.16: The ability to turn off the CZ gate by observing the phase accumulation υ_t from unintentional CPHASE gates on adjacent qubits. The plot shows the phase accumulation (over one full rotation at frequency J_{idle}) υ_t in radians, given in Equation 5.31, of a qubit due to an unintentional CHPASE gate with an adjacent qubit. A small phase accumulation implies a greater ability to switch off the CZ gate as the qubit remains idle without accumulating any Pauli z-axis phase due to the state of adjacent qubits. The phase accumulation is plotted against the idle point of exchange $J_{\text{idle}} \gg \Delta B_z$ and the shift in qubit detuning Δ_Δ when the adjacent qubit is in the $(0, 2)$ charge state as opposed to the $(1, 1)$ charge state. Both parameters are normalised to the tunnel coupling t_c. The dark lines signify the contours for idle qubit fidelities (that is, a measure of the qubits retaining their initial state) of 95 % and 99.5 %. Note that the diagram takes the shift in detuning (when the adjacent qubit enters the $(0, 2)$ charge state) to be from Δ to $\Delta + p_{02} \cdot \Delta_\Delta$. For $\Delta_\Delta < 0$, one simply waits at the idle $\Delta + |\Delta_\Delta|$ to be shifted to Δ to result in the same phase accumulation listed on the plot.

However, before investigating the influence of charge noise (to find the appropriate choices in J_c, J_t and Δ_Δ) in Section 5.4.2, it is important to realise the conditions in which the CZ gate may be completely toggled on and off. Now consider a set of many singlet-triplet qubits in the quantum processor. If the qubits were in the idle state, there should be no change in local qubit populations. Thus, one nominally places the qubits in the Paul-z rotation regime ($J \gg \Delta B_z$). All idle qubits must be tuned to the same frequency J_{idle} as any differences in the precession frequency results in an unintentional Pauli-z gate. To ensure no spurious gate, let alone entangling, operations occur, one must choose a qubit biasing position where no inter-qubit interactions are present. However, electric dipoles (used for the CZ gate) of other qubits will shift the detuning in adjacent qubits to an exchange away from J_{idle} and thereby initiate local CPHASE gates (a phase rotation on the target qubit dependent on the control-qubit-state). Since the induced CPHASE gate will accumulate phase at the speed ΔJ, the unintentional CPHASE rotation on the target qubit over one qubit Pauli-z rotation (at speed J_{idle}) is:

$$\frac{\upsilon_t}{2\pi} = \frac{\Delta J}{J_{\text{idle}}} = \frac{J'}{1+J'^2}\Delta'_\Delta - \frac{1+J'^2}{2J'^2} + \frac{1}{J'}\sqrt{1+\left(\frac{J'^2-1}{2J'} + \frac{J'^2}{1+J'^2}\Delta'_\Delta\right)^2} \tag{5.31}$$

where $J' \equiv J_{\text{idle}}/t_c$ and $\Delta'_\Delta = \Delta_\Delta/t_c$. Figure 5.16 shows a plot of the phase accumulation of the unintentional CPHASE gates for different J_{idle} and inter-qubit couplings Δ_Δ. The sensitivity to nearby qubits' electric-dipoles drops as one moves deeper into negative detuning ($J_{\text{idle}} \ll t_c$). That is, even at strong electric-dipole strengths, the state-dependent shift in detuning Δ_Δ causes too small a change in J_{idle} to result in significant phase accumulation. Similarly when traversing deep into positive detuning ($J_{\text{idle}} \gg t_c$), J_{idle} increases rapidly such that the percent change in J_{idle} due to the shift in detuning Δ_Δ is once again too small to result in phase accumulation per single rotation at J_{idle}. In general having larger inter-qubit couplings requires one to set the idle qubit J_{idle} to be further into negative detuning $J_{\text{idle}} = 1$ (as positive detuning yields Pauli-z precession frequencies too fast for the voltage pulse generators to track as discussed Section 5.3.4).

The unintentional CPHASE gate will not impact target qubits if the target qubit state is purely in either singlet or triplet-t_0 (as a Pauli-z rotation will not change the state). The worst case impact of the unintentional CPHASE gate will be when the adjacent qubit is in a state perpendicular to the Pauli-z axis, in which case the idle qubit fidelity (that is, the drop in fidelity due to an intentional phase accumulation

taking the qubit away from its initial state) is:

$$F_{\text{idle}} = \cos^2\left(\frac{\upsilon_t}{2}\right). \tag{5.32}$$

For the adjacent qubit to remain in the initial state to within 95% and 99.5% fidelity, the CPHASE must not accumulate above 25.8° and 8.1° respectively. Figure 5.16 plots the 99.5% and 95% idle qubit fidelity contours. The 99.5% contour (at $J_{\text{idle}} < 1$), for a given inter-qubit coupling, presents the minimum operating point in exchange for all qubits to ensure that the unintentional CPHASE gate does not move the adjacent qubits' states away from their initial states to within 99.5% fidelity. For example, in a Si-P device, if the tunnel coupling were 5 GHz, and the inter-qubit coupling was $0.035t_c = 175$ MHz (like the perturbative tunnel couplings seen in GaAs experiments [14]), then one may set the idle qubit exchange freely without worrying about loss in fidelity (below 99.5%) due to unintentional CPHASE gates. If the inter-qubit coupling was however, above 5 GHz, then one must set the idle qubit exchange below approximately $J_{\text{idle}} < 0.23t_c = 1.15$ GHz. Similarly, if the inter-qubit coupling were 40 GHz, then the idle qubit exchange must be below $J_{\text{idle}} < 0.11t_c = 550$ MHz to avoid unintentional CPHASE gates.

5.4.2 Impact of charge noise on CZ gate fidelities

With the CZ gate speed given by ΔJ, one may investigate the influence of charge noise on the two-qubit gate fidelities. The two-qubit gate fidelity is taken as the product of the control and target qubit fidelities. Thus, the investigation of the CZ gate-fidelity is broken up into two contributing elements:

- F_c - gate fidelity of Pauli-z rotations on the control qubit under the presence of charge noise (local to the control qubit) perturbing the value of J_c.
- F_t - gate fidelity of Pauli-z rotations on the target qubit under the presence of charge noise perturbing the value of $J_t + \Delta J$. Here, the charge noise is due to two sources. The first source is local charge noise on the target qubit perturbing the value of J_t. The second source is the local charge noise on the control qubit (that is, charge noise on J_c) perturbing the value of ΔJ.

Note that the charge noise on the control and target qubits are assumed to be independent (that is, uncorrelated noise) with a Gaussian noise standard deviation Δ_σ. If the noise were correlated (that is, any perturbations on the control qubit is applied equally on the target qubit), then one can exploit standard echoing techniques

to enhance the gate fidelity [14, 39]. In the following numerical simulations, F_c and F_t are calculated numerically assuming the worst case scenarios to find a lower-bound estimate on the overall fidelity (with the intent to create a more robust design that maximises the worst-case fidelities). In addition, the numerical simulations may leave the qubits in a different phase (as the simulations simply consider the optimal pathway that yields a π phase shift on the target qubit conditional on the control qubit state); thus, one will need to apply high-fidelity corrective single-qubit rotations to compensate.

This section will first calculate the CZ gate fidelities for a variety of operating points for the control and target qubit exchanges (J_c and J_t) and inter-qubit couplings Δ_Δ (both positive and negative). The results will then be put in the context of Si-P dots to find the optimal choices in J_c, J_t, Δ_Δ and the inter-dot tunnel coupling t_c.

Charge noise local to the control qubit: F_c

The first factor for the CZ gate fidelity is F_c due to local noise on the control qubit. Here, the control qubit precesses about the Pauli-z axis over the duration of the CZ gate and will decohere as single-qubit Pauli-z gate rotations. The simulations are identical to that used to gauge the gate fidelities of Pauli-z rotations in Section 5.3.3. However, the time waited for the gate, is taken to be that of the CZ gate time given by ΔJ (for the choice of exchange on the control J_c and target J_t qubits). Figure 5.17a shows the control qubit fidelities across a range of J_c and J_t for $\Delta_\Delta = t_c$ and $\Delta_\sigma = 0.01 t_c$. There appears to be a monotonic increase in the fidelities when increasing the target qubit exchange J_t. One may interpret this as a shortening of the gate time (as seen by the increasing speed on moving to larger J_t in Figure 5.15) counteracting the larger J-noise at positive detunings ($J_t > 1$). There is also a partial increase in the fidelities on moving towards positive control qubit exchange J_c (as seen by the curving down of the 99.5% fidelity contour at $J_c > 1$), which once again can be attributed to larger gate speeds on increased CZ gate activation. That is, p_{02} tends to unity for large $J_c \gg 1$ (in positive detuning) as there is a larger proportion of the control qubit in the $(0, 2)$ charge state. Although Figure 5.15 shows that the gate speed decreases when moving to negative control qubit detunings ($J_c < 1$), the control qubit's resistance to charge noise in negative detuning due to the smaller $dJ_c/d\Delta_c$ (as described in Section 5.3.3 in the context of Pauli-z gates) still yields a high control qubit fidelity.

The 99.5% contour in Figure 5.17a highlights the boundary for a fault-tolerant

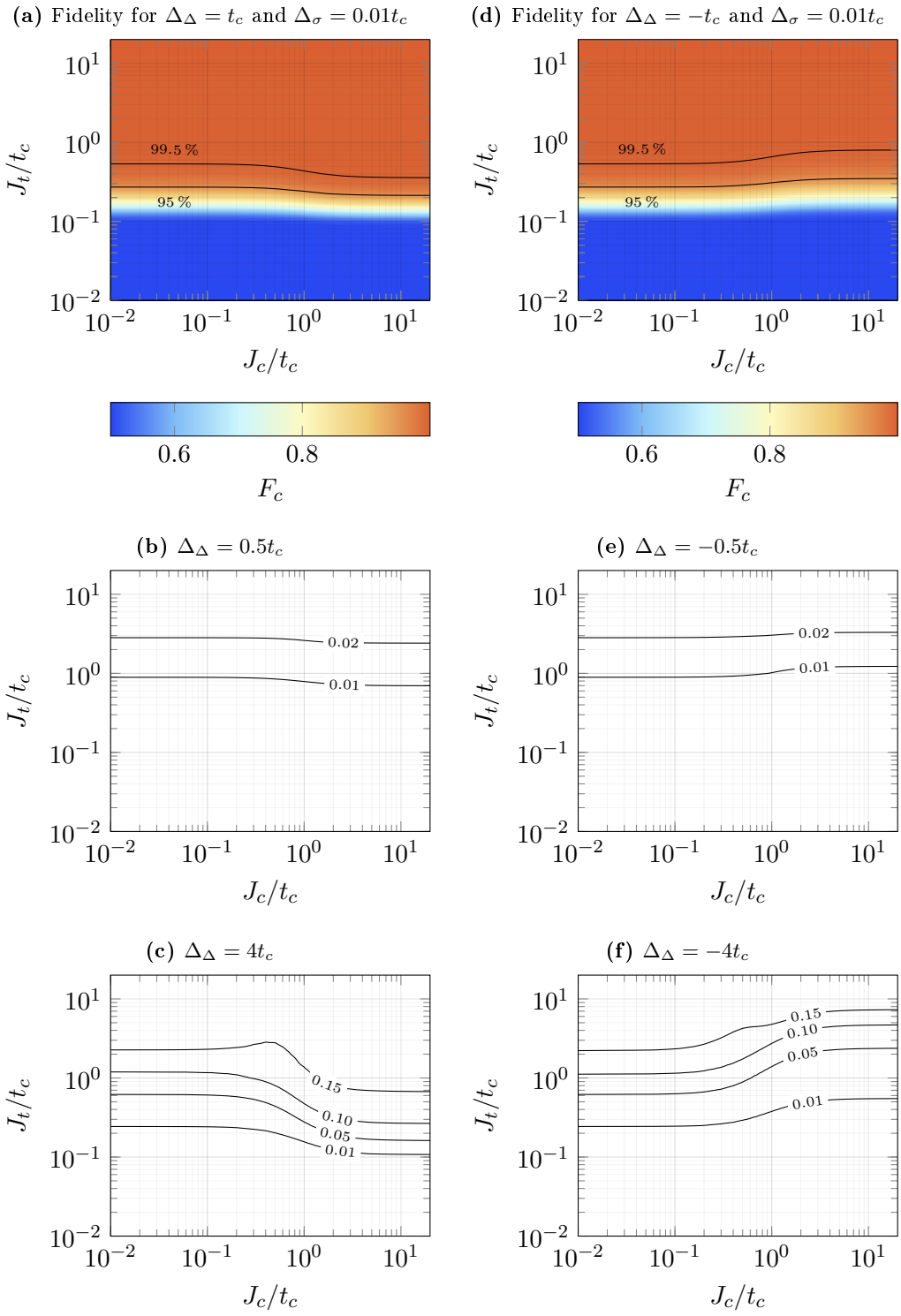

Figure 5.17: Fidelity of the control qubit (F_c) when performing a CZ gate. All plots are taken over exchange on the control and target qubits (J_c and J_t). **(a)** Contour plot of the control qubit fidelities (with the 95% and 99.5% contours highlighted). Fault tolerant fidelities are found above the 99.5% line at higher values of J_t. **(b)-(c)** Plots showing the 99.5% contour, shown in (a), for different noise amplitudes Δ_σ/t_c (as labelled on the lines). Higher inter-qubit couplings Δ_Δ push the 99.5% contours deeper into negative detunings on both the control ($J_c < 1$) and target ($J_t < 1$) qubits. **(d)-(f)** Same plots as in (a)-(c) but with negative inter-qubit couplings.

control qubit. For J_t above the contour the control qubit fidelity is larger than 99.5% (as indicated by the 95% contour below the 99.5% contour for reference). With the knowledge that the 99.5% contour shows the minimum J_t one may reach for fault tolerance, it is useful to investigate the trend in the 99.5% contour over different inter-qubit couplings and noise amplitudes. Figures 5.17b-c show the 99.5% contour lines for different inter-qubit couplings Δ_Δ/t_c (across the plots) and noise-amplitudes Δ_σ/t_c as shown by the labelled lines. Note that the lines indicate the minimum J_t boundary whereupon one still achieves fault-tolerance. Clearly on increasing the inter-qubit coupling, the 99.5% contour lines move downwards into more negative detuning ($J_t < 1$) on the target qubit. Similarly, the increased fidelity trend across J_c, seen in Figures 5.17a, becomes more exaggerated as seen by the lines curving downwards further into negative target qubit detuning ($J_t < 1$) in Figures 5.17c for $\Delta_\Delta = 4t_c$. Note that although the faster gate speeds yield higher fidelities for $J_c \gg 1$, the gate speeds may become too fast for the waveform generators similar to the discussion of Pauli-z gates in Section 5.3.3.

Figure 5.17d shows the same plot as in Figure 5.17a, but with a negative inter-qubit coupling $\Delta_\Delta = -t_c$. That is, when the control qubit moves into a singlet state, the target qubit shifts to a lower detuning. The functional trend appears to be similar at $J_c \ll 1$. However, the fidelities decrease on increasing J_c as seen by the curving up of the 99.5% fidelity contour. One may attribute the lower fidelity to the smaller change in ΔJ for the same J_t when shifting to a lower value of detuning as opposed to shifting to a higher value of detuning as with a positive inter-qubit coupling. Figures 5.17e-f similarly highlight the same trend where at $J_c \gg 1$, one needs to operate at a higher J_t to access the region of fault-tolerant control qubit fidelities (for a given detuning noise amplitude). Since the gate times may become too fast to experimentally realise in positive detuning ($J_c > 1$), one will typically operate in negative detuning where the control qubit appears to have similar fidelities for both the positive and negative inter-qubit couplings.

Charge noise on the target qubit: F_t

The second factor for the CZ gate fidelity is F_t. Here, the decoherence due to local noise on the target qubit and the local noise on the control qubit (resulting in noise on $p_{02}\Delta_\Delta$) are both considered. As shown in Appendix F, the gate fidelities can be found from the probability distribution of the precession frequencies $N(\omega)$. One finds $N(\omega)$ by first computing the probability distribution of detunings on the target qubit Δ_t' and then converting it into the associated distribution in J. The

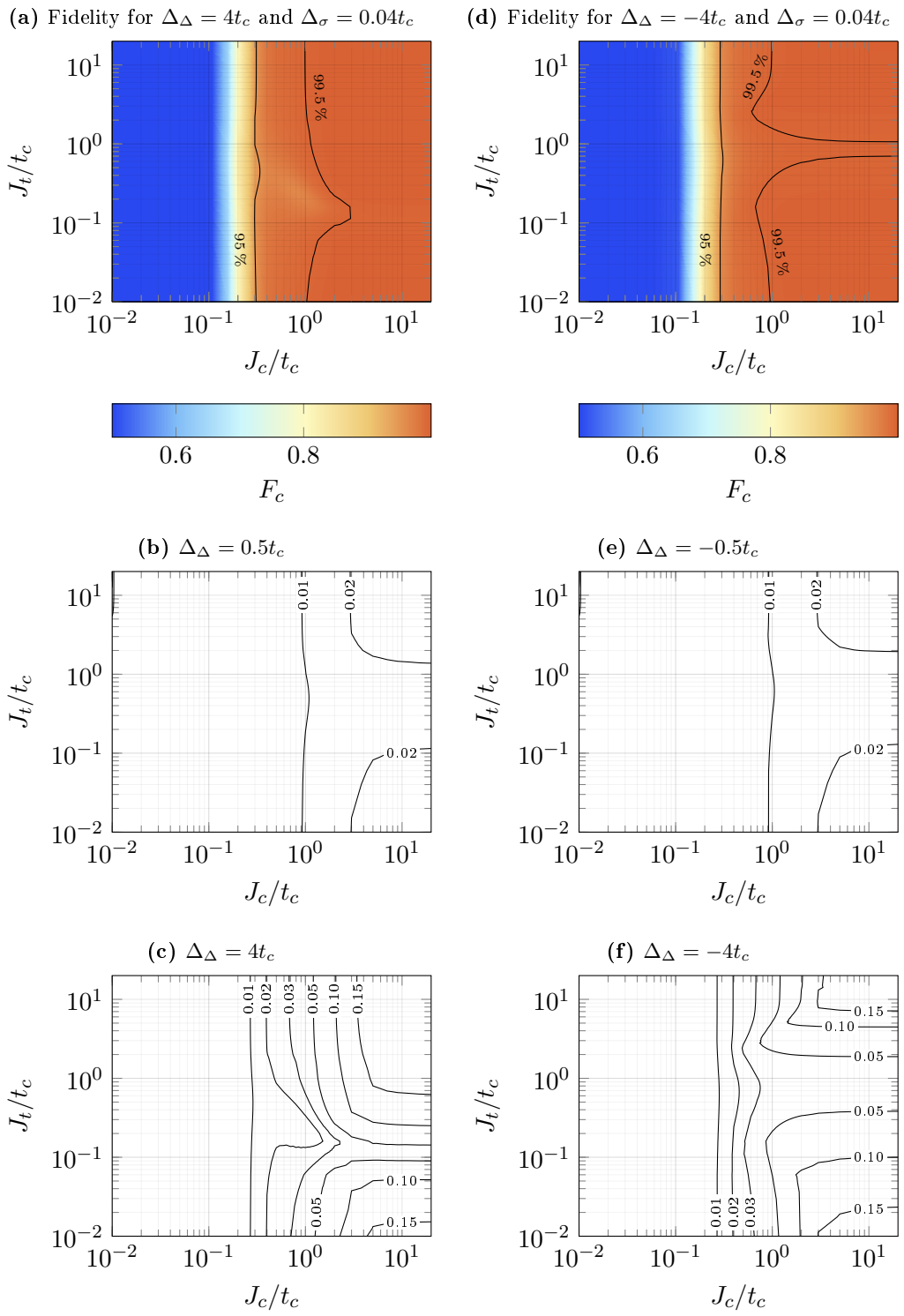

Figure 5.18: Fidelity of the target qubit (F_t) when performing a CZ gate. All plots are taken over exchange on the control and target qubits (J_c and J_t). **(a)** Contour plot of the control qubit fidelities (with the 95% and 99.5% contours highlighted). Fault tolerant fidelities are found above the 99.5% line at higher values of J_c. **(b)-(c)** Plots showing the 99.5% contour, shown in (a), for different noise amplitudes Δ_σ/t_c (as labelled on the lines). Higher inter-qubit couplings Δ_Δ push the 99.5% contours deeper into negative detunings on the target qubit. **(d)-(f)** Same plots as in (a)-(c) but with negative inter-qubit couplings.

probability distribution of the target-qubit detuning due to local noise (on the target qubit) is once again treated as a Gaussian distribution about target qubit detuning $\Delta'_t \equiv \Delta_t/t_c$ to get a set of points:

$$N_{\text{local}}(\Delta'_{(t)}) \sim \left(\Delta'_{(t)}, P_G(\Delta', \Delta'_t, \Delta'_\sigma)\right), \tag{5.33}$$

where $P_G(\Delta'_{(t)}, \mu, \sigma)$ is a normal distribution with mean μ and standard deviation σ. Note that $\Delta'_{(t)}$ represents a varying parameter across the target qubit detuning (divided by the tunnel coupling), Δ'_t represents the nominal mean value one sets on the target qubit detuning and $\Delta'_\sigma \equiv \Delta_\sigma/t_c$ is the noise standard deviation. To find the probability distribution on the target qubit due to noise from the control qubit, one starts with a normal distribution of points representing the detuning fluctuations on the control qubit:

$$N_{\text{inter}}(\Delta'_{(c)}) \sim \left(\Delta'_{(c)}, P_G(\Delta'_{(c)}, \Delta'_c, \Delta'_\sigma)\right). \tag{5.34}$$

Note that $\Delta'_{(c)}$ represents a continuous parameter along the control qubit detuning (divided by the tunnel coupling) while $\Delta'_c \equiv \Delta_c/t_c$ represents the nominal mean value one sets on the control qubit detuning. From Equation 5.28, one may convert the detuning $\Delta'_{(c)}$ into points in the target qubit's detuning $\Delta'_{(t)}$ (that is, the resulting shifts in the target qubit's detuning) via $p_{02}\Delta'_\Delta$ (where $\Delta'_\Delta \equiv \Delta_\Delta/t_c$):

$$\Delta'_{(t)} = \left(\frac{1}{2} + \frac{\Delta'_{(c)}}{2\sqrt{1+\Delta'^2_{(c)}}}\right)\Delta'_\Delta \tag{5.35}$$

to get the distribution of noise fluctuations on the target qubit due to the control qubit:

$$N_{\text{inter}}(\Delta'_{(t)}) \sim \left(\Delta'_{(t)}, P_G(\Delta'_{(c)}, \Delta'_c, \Delta'_\sigma)\right). \tag{5.36}$$

Now given the two distributions, one needs to combine them to get the net fluctuations on the target qubit's detuning. Noting that the probability distribution of the sum of two random variables[16] is the convolution, one may find the net probability distribution of the target qubit's detuning via:

$$N_{\text{target}}(\Delta'_{(t)}) = N_{\text{local}}(\Delta'_{(t)}) * N_{\text{inter}}(\Delta'_{(t)}) \tag{5.37}$$

[16] In this case N_{local} is a probability distribution centred on Δ'_t with a spread due to charge noise local to the target qubit, while N_{inter} is centred on $p_{02}\Delta'_\Delta$ with a spread due to charge noise local on the control qubit. Adding the two distributions yields a new distribution centred on $\Delta'_t + p_{02}\Delta'_\Delta$, with the combined spread of N_{local} and N_{inter}.

where the convolutions were taken numerically from the interpolated probability distributions. Given the distribution across $\Delta'_{(t)}$, one may find the distribution in the target qubit's exchange J by taking $\Delta'_{(t)} + \sqrt{1 + \Delta'^2_{(t)}}$ and subsequently calculate the target qubit fidelities as shown in Figure 5.18. Note that to calculate the worst-case fidelities, the initial state on the target qubit is taken to be perpendicular to the Pauli-z axis. During the CZ gate, the target qubit may precess in two modes where the target qubit's exchange is either J_t (when control qubit is t_0) or $J_t + \Delta J$ (when control qubit is s_0). When the control qubit is t_0, the noise on the target qubit is only given by $N_{\text{local}}(\Delta'_{(t)})$ as the control qubit remains in the $(1,1)$ charge state to result in no inter-qubit detuning shift on the target qubit. When the control qubit is s_0, the noise on the target qubit is given by $N_{\text{target}}(\Delta'_{(t)})$. To obtain the worst-case CZ gate fidelity, the numerical simulations in Figure 5.18 take the minimum fidelity of the two possible cases (for every point in J_c and J_t).

Figure 5.18a shows the target qubit fidelity as a function of J_c and J_t for a positive inter-qubit coupling $\Delta_\Delta = 4t_c$ and detuning noise amplitude $\Delta_\sigma = 0.01t_c$. There is a general monotonic increase in the target qubit fidelity on increasing J_c as seen by the 95% and 99.5% fidelity contours. One can attribute the fidelity increase to the faster gate speeds resulting in the full activation of the CZ gate (that is, bringing the control qubit into a more s_{02}-like state to realise a stronger shift on the target-qubit's detuning). A more subtle feature is the fidelity minima across J_t similar to that seen with the fidelity of single-qubit Pauli-z gates in Figure 5.13. Here, the minimum is formed at $J_t < t_c$ because $N_{\text{target}}(\Delta'_{(t)})$ dominates when the inter-qubit shift places the target qubit exchange at $J_t + \Delta J$ near at the zero-detuning point ($J_t = 1$) where single-qubit Pauli-z gate fidelities are minimal. Figures 5.18b-c show the 99.5% contours (which indicate the minimum J_c to which one can realise a fault-tolerant target-qubit) as a function of the inter-qubit coupling across the plots and the detuning noise amplitude as shown by the labelled lines within the plots. A clear feature is that on increasing the inter-qubit coupling (here from $\Delta_\Delta = 0.5t_c$ to $\Delta_\Delta = 4t_c$), the 99.5% fidelity contours move to lower values of J_c. In addition, the point in which the 99.5% fidelity contour curves across J_c (due to a fidelity minimum across J_t) shifts to a lower value of J_t corresponding to the point where $J_t + \Delta J$ is near zero-detuning.

Figure 5.18d shows the same target qubit fidelity plot as in Figure 5.18a but for a negative inter-qubit coupling $\Delta_\Delta = -4t_c$. There is still an overall monotonic increase in the target qubit fidelity with increasing J_c (as seen by the 95% and 99.5% contours). However, the target qubit fidelity minimum (across J_t) now occurs at zero detuning because $N_{\text{local}}(\Delta'_{(t)})$ dominates $N_{\text{target}}(\Delta'_{(t)})$ at zero detuning as

$J_t + \Delta J$ shifts the target qubit deep into negative detuning where single-qubit Pauli-z gates operate at a high fidelity. Figures 5.18e-f show the trend in the 99.5% fidelity contours (which once again signifies the minimum J_c in which one can obtain fault-tolerant target qubit fidelities) as a function of different inter-qubit couplings (across the plots) and detuning noise as shown by the labelled lines in the plots. Once again, a larger magnitude in the inter-qubit coupling (here from $\Delta_\Delta = -0.5t_c$ to $\Delta_\Delta = -4t_c$) pushes the 99.5% fidelity contours to lower values of J_c. The fidelity minimum across J_t however, remains close to zero detuning as seen by the 99.5% fidelity contours curving away at $J_t \sim t_c$.

Total impact of charge noise on the CZ gate

The overall CZ gate fidelity is taken to be the product of the worst-case control qubit and target qubit fidelities:

$$F_{\mathrm{CZ}} = F_c F_t \tag{5.38}$$

The CZ gate fidelities are plotted in Figure 5.19. Figure 5.19a shows the CZ fidelity as a function of J_c and J_t for a positive inter-qubit coupling $\Delta_\Delta = 4t_c$ and detuning noise amplitude $\Delta_\sigma = 0.04t_c$. Clearly, staying deep in negative detuning on either of the two qubits ($J_c < 1$ and $J_t < 1$) yields poor CZ gate fidelities due to the gates being too slow in overcoming the decoherence rates. Note that the bottom-left patch of 25% fidelity is due to 50% gate fidelities in both the target and control qubits as seen in Figures 5.17 and 5.18. Similarly, the top-left and bottom-right patches of 50% are due to the 50% fidelity in the target and control qubits respectively. There is nonetheless, a monotonic increase in F_{CZ} when increasing J_c and J_t as seen by the 95% and 99.5% fidelity contours. The trends in the 99.5% fidelity contour lines (here bounding the region of fault-tolerant operation to the upper-right quadrant) are shown in Figures 5.19b-c as a function of inter-qubit coupling (across the plots) and the detuning noise as shown by the labelled lines in the plots. A clear feature seen on increasing the inter-qubit coupling (here from $\Delta_\Delta = 0.5t_c$ to $\Delta_\Delta = 4t_c$), is that the 99.5% fidelity contours move to lower values of J_c and J_t.

Figure 5.19d shows the same plot as in Figure 5.19a, but with a negative inter-qubit coupling $\Delta_\Delta = -4t_c$. Once again, there is a monotonic rise in F_{CZ} with increasing J_c and J_t. Figures 5.19e-f show the trends in the 99.5% fidelity contour lines (once again bounding the region of fault-tolerant operation to the upper-right quadrant) as a function of inter-qubit coupling (across the plots) and the detuning noise as shown by the labelled lines in the plots. On increasing the magnitude of

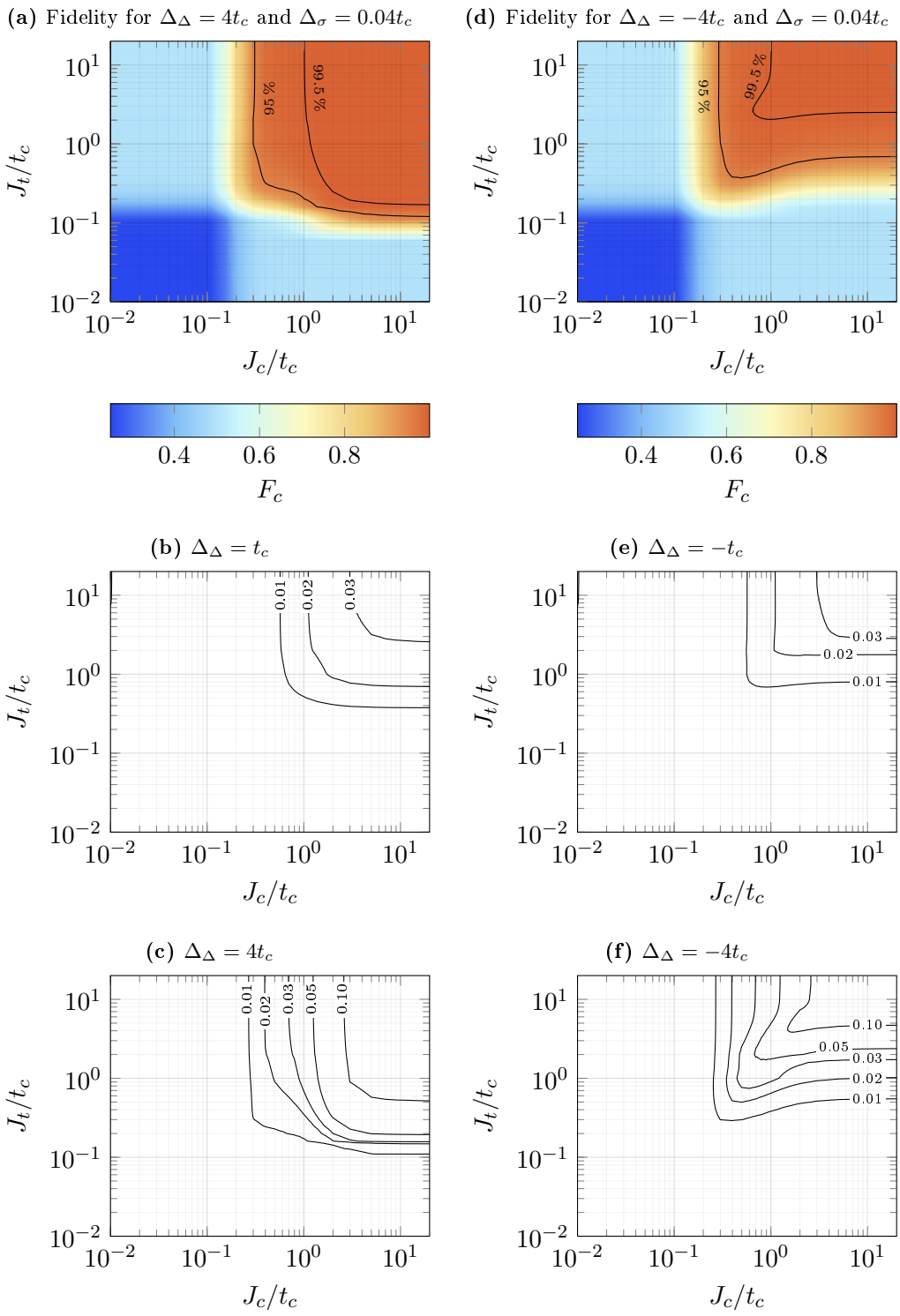

Figure 5.19: Total CZ gate Fidelity ($F_{\mathbf{CZ}}$) due to charge noise. All plots are taken over exchange on the control and target qubits (J_c and J_t). **(a)** Contour plot of the control qubit fidelities (with the 95% and 99.5% contours highlighted). Fault tolerant fidelities are found above the 99.5% line at higher values of J_c. **(b)-(c)** Plots showing the 99.5% contour, shown in (a), for different noise amplitudes Δ_σ/t_c (as labelled on the lines). Higher inter-qubit couplings Δ_Δ push the 99.5% contours deeper into negative detunings on the target qubit. **(d)-(f)** Same plots as in (a)-(c) but with negative inter-qubit couplings.

the inter-qubit coupling (here from $\Delta_\Delta = -0.5t_c$ to $\Delta_\Delta = -4t_c$), the 99.5% fidelity contours move to lower values of J_c and J_t. A key difference when compared against the positive inter-qubit coupling of $\Delta_\Delta = 4t_c$ in Figure 5.19c is that the regions of 99.5% fault-tolerant operation are concentrated along the $J_c = J_t$ line (rather than, for example, regions of low J_t and high J_c or vice versa).

Impact on CZ gate fidelities on the device parameters

Given the trends in the CZ gate fidelities (as a function of J_c, J_t, Δ_Δ and Δ_σ), it is now possible to identify and optimise critical device parameters (both affecting the geometry and experimental device operation) such as the tunnel coupling t_c and the inter-qubit coupling Δ_Δ. One may utilise the plots of the 99.5% fidelity contours in Figure 5.19 with additional overlays to account for the feasibility of operating under different inter-qubit couplings as shown in Figure 5.20:

- Preventing unintentional CPHASE gates (red) - overlay shows regions where the target-qubit would trigger unintentional CPHASE gates with its adjacent qubits (as discussed in Section 5.4.1). That is, assuming that all the qubits are coupled with the same inter-qubit coupling Δ_Δ, setting too high a J_t on the target qubit will trigger unintentional CPHASE gates on all adjacent qubits. Since unintentional CPHASE gates are undesirable, the operating points (J_c and J_t) must be outside the red region.
- Preventing pulses from being too fast for current waveform generators (grey ruled lines) - overlay shows regions where the gate times are below 20 ps. The gate times (and thus, the voltage pulse times) were calculated via the equation for ΔJ for a nominal tunnel coupling of 5 GHz. In the ruled region, the pulse generators will need to output detuning pulses faster than the best waveform generators. The dashed line indicates the boundary in which operating points above it (in the top-right quadrant) require pulse widths less than 1 ns (easily achieved with waveform generators).

Noting the minimum tunnel coupling of 5 GHz set to prevent thermal excitations destroying the singlet-triplet qubit (as discussed in Section 5.2.4), if the noise amplitude is 1% of the tunnel coupling (that is, $\Delta_\sigma = 0.01t_c$), then the resulting noise is 200 neV. Since this noise amplitude is extremely close to the theoretical minimum of 100 neV predicted in previous papers for silicon [18, 201, 202], at a bare minimum, one should select qubit operating points where the maximum allowable noise Δ_σ is well above $0.01t_c$. That is, one needs the 99.5% fidelity contours for larger noise

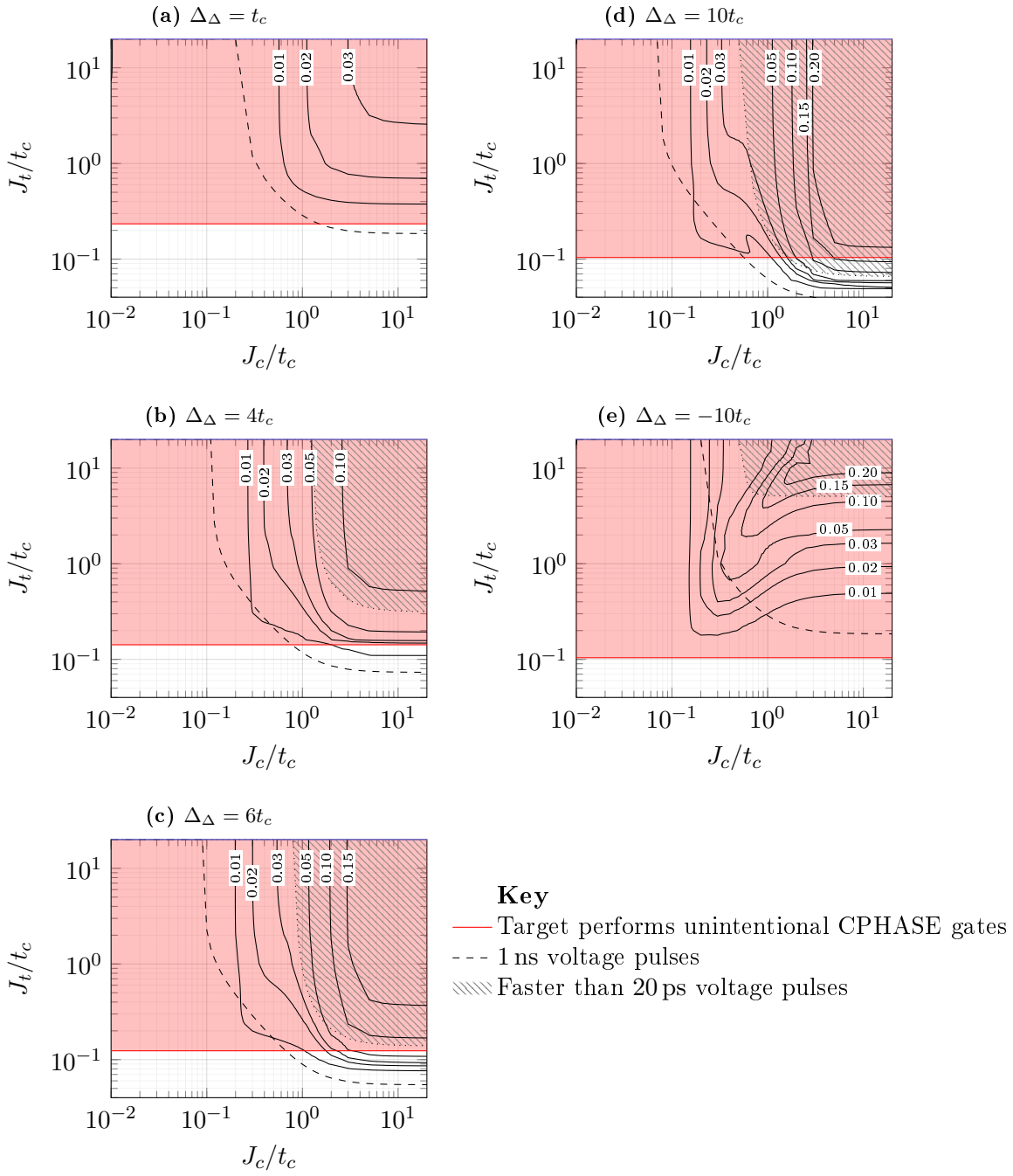

Figure 5.20: Finding the optimal choice of Δ_Δ that is most resistant to charge noise. **(a)-(e)** are plots of the 99.5 % CZ gate fidelity boundary contours as a function of the control and target qubit exchanges (J_c and J_t) for different inter-qubit couplings Δ_Δ. The solid contour lines (plotted for different noise amplitudes Δ_σ/t_c) represent the boundary enclosing regions (the top-right quadrant) where the CZ gate fidelity exceeds 99.5%. Thus, lower noise amplitudes Δ_σ enclose larger regions. The red region indicates restricted regions where the target qubit will start inadvertently forming two-qubit gates with adjacent qubits. The grey ruled region (bound by the dotted line) is a restricted domain where voltage pulses are too fast (quicker than 20 ps) given the current state of the art equipment (for a minimal tunnel coupling of 5 GHz). The dashed lines enclose a region where the voltage pulses are shorter than 1 ns. (c) shows the best operating regime with $\Delta_\Delta = 6t_c$ as one can access feasible regions (white) where the noise amplitude can be as large as $\Delta_\sigma = 0.05t_c$ without the voltage pulses being prohibitively fast like in (d) where $\Delta_\Delta = 10t_c$.

amplitudes in the feasible (white) region. Note that the labelled contours (signifying the noise amplitude Δ_σ/t_c) each signify the minimum J_c and J_t in which one may operate given the noise amplitude. That is, lower noise amplitudes enable smaller operating points in J_c and J_t.

The optimal choice in inter-qubit coupling (with respect to the tunnel coupling) is one where there are feasible operating points (for >99.5% fidelity, fault tolerant CZ gates) that can tolerate noise well above $\Delta_\sigma = 0.01t_c$. Figures 5.20a-b show that all feasible operating points require the noise to be below $0.02t_c$ for inter-qubit couplings up to $\Delta_\Delta = 4t_c$. Figure 5.20d shows that $\Delta_\Delta = 6t_c$ is the optimal choice as it offers good operating points where the noise amplitudes can be up to $\Delta_\sigma = 0.05t_c$. Going to higher inter-qubit couplings of $\Delta_\Delta = 10t_c$ yield no additional benefits as the gate times become too fast (below 20 ps) to be experimentally feasible. Finally, for negative inter-qubit couplings, all feasible operating points require noise amplitudes to be below $\Delta_\sigma = 0.01t_c$ even with strong inter-qubit couplings of $\Delta_\Delta = -10t_c$ as shown in Figure 5.20e. Thus, $\Delta_\Delta = 6t_c$ is a good choice for the inter-qubit coupling as it yields a good margin for noise amplitudes as large as $\Delta_\sigma = 0.05t_c$. Now we can map the feasible operating points to physical device parameters.

The maximum value of J_t/t_c that one may obtain from Figure 5.20d (for $\Delta_\Delta = 6t_c$) is 0.124. One should operate near the red region in order to be within the boundaries set by the 99.5% fidelity contours for $\Delta_\sigma = 0.02$-$0.03t_c$ in order to be maximally robust to charge noise. Given the minimum $J_t = 810$ MHz set to obtain accurate Pauli-z gates (given the typical $\Delta B_z = 29$ MHz as discussed in Section 5.3.1), one obtains the required tunnel coupling to be $t_c = 0.810/0.124 = 6.5$ GHz. Thus, the required inter-qubit coupling is $\Delta_\Delta = 6t_c = 39$ GHz. From Figure 5.20d, one may choose the operating point near $J_c \sim 2t_c$ (where the detuning noise needs to be approximately $\Delta_\sigma = 0.02t_c$-$0.03t_c$), thereby requiring a maximum charge noise amplitude of $\Delta_\sigma = 540$-810 neV. This is approximately 8 times the theoretical minimum expected charge noise in silicon [18, 201, 202]. Therefore, by utilising strong inter-qubit couplings ($\Delta_\Delta = 39$ GHz for $t_c = 6.5$ GHz), one may construct fault tolerant (>99.5% fidelity) CZ gates between singlet-triplet qubits in P-donor quantum dots.

5.4.3 CX Gate

Although a CX gate operation (as required for the surface code) can be formed via a CZ gate sandwiched between two single-qubit Hadamard gates as shown in Figure 5.21 [167], it is interesting to investigate whether a high-fidelity native CX can be

performed especially if it provides improvements to the geometry (for example, larger spacing between the leads due to the lower inter-qubit coupling required).

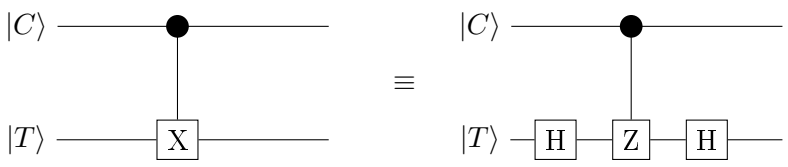

Figure 5.21: Circuit conversion of a CZ gate into a CX gate. The CX gate can be formed by concatenating two Hadamard gates (H) onto a CZ gate (for control and target qubits $|C\rangle$ and $|T\rangle$).

The CZ gate discussed in Section 5.4.1 relied on Δ_Δ being small enough such that it did not tilt the singlet-triplet rotation axis. However, if $\Delta_\Delta \gg t_c$, then the target detuning could shift far enough to make the rotation axis tilt away from the z-axis and point along the x-axis to help form a native CX gate. Figure 5.22 shows the operation of a two-qubit gate where one chooses a working point on the target qubit such that $J_t = J_0 \gg \Delta B_z$. If the control qubit were in the triplet t_0 state, the target qubit's axis of rotation remains along the z-axis. However, if the control qubit were in the singlet state, the electrostatic shift on the target qubit is to push it to a regime $J \ll \Delta B_z$. Now the target qubit undergoes Pauli-x rotations (giving rise to a CX gate) at a gate time given by Equation 5.14; thus, the gate time τ_x for a Pauli-x π-rotation is:

$$\tau_x = \frac{h}{4\Delta B_z}. \tag{5.39}$$

Here $J \approx 0$ for all detunings $\Delta \ll \Delta B_z$. Thus, there is very little impact in shifting the initial point's detuning Δ where $J = J_0$. This is important for J_0 must be carefully selected such that:

$$\frac{J_0}{4\Delta B_z} \in \mathbb{Z}. \tag{5.40}$$

That is, J_0 is chosen such that if the control qubit is in the triplet state, the target qubit undergoes exactly an integer number of full rotations to ensure that an identity operation is performed.

To physically perform the native CX gate, the inter-qubit shift Δ_Δ must be large enough to tilt the singlet-triplet qubit axis of precession from the z-axis onto the x-axis. Now from Table 5.2, a ratio of J to ΔB_z of 28 yields 99.5% fidelity in the accuracy of z-rotations. Similarly a ratio of ΔB_z to J being 28 yields 99.9% fidelity x-rotations. The shift required in the target qubit detuning Δ_t to perform the CX gate

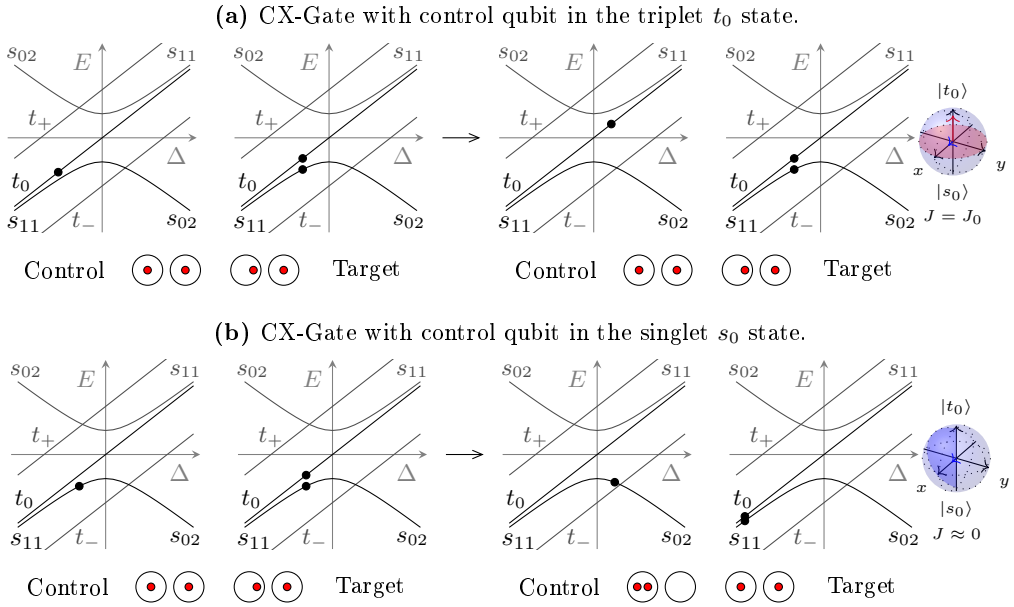

Figure 5.22: The native CX gate for singlet-triplet qubits. The energy diagrams (see Figure 5.12) and double-dots represent the individual singlet-triplet qubits: the control and target qubits. To activate the CX gate, the control qubit is biased towards the region of positive detuning, where a triplet t_0 remains in the $(1,1)$ charge state as shown in **(a)**, while the singlet s_{11} takes upon a s_{02}-like character to partially enter the $(0,2)$ charge state as shown in **(b)**. Note that in this example, the $(0,2)$ charge state on the control qubit moves the electron away target qubit. A control qubit in the singlet state causes the target qubit's detuning to shift and subsequently its exchange J decreases from J_0 to approximately zero. Now the wait-time is set to be the x-axis π-rotation time mediated by the fixed ΔB_z. The choice of J_0 must be such that during this time, an integer number of full rotations about the z-axis is performed if the control qubit is in the triplet state. Thus, if tuned right the above example yields an identity operation on the target qubit if the control qubit is a triplet and a Pauli-x flip otherwise. The Bloch spheres represent the operation performed on the target qubit with the red arrow representing the target qubit's J while the blue arrow represents its ΔB_z vector.

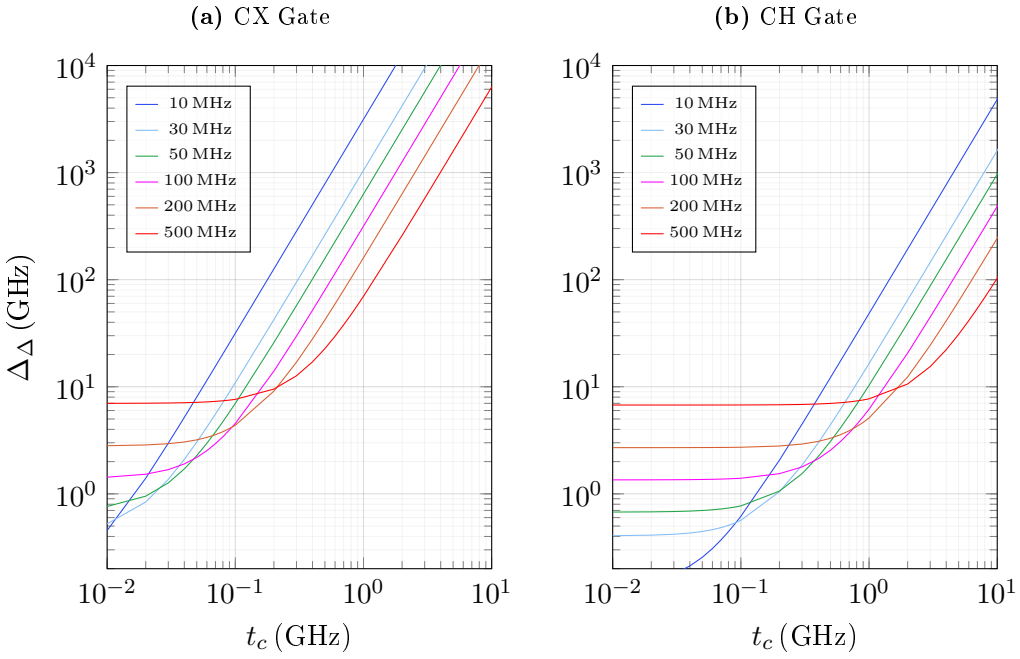

Figure 5.23: Required inter-qubit couplings to achieve native CX and CH gates. The plots show the required inter-qubit coupling Δ_Δ as a function of the inter-dot tunnel coupling t_c on the target qubit. The different curves on each plot represent different values of ΔB_z as shown in the legends. **(a)** The required Δ_Δ for a CX gate. Given that t_c needs to be at least 1 GHz to prevent thermal excitations (discussed in Section 5.2.2), the required inter-qubit coupling becomes prohibitively large (∼1 THz) for the expected $\Delta B_z = 29$ MHz. **(b)** The required inter-qubit coupling for the CH (controlled-Hadamard) gate is however lower with inter-qubit couplings as low as 17 GHz if one selects a tunnel coupling of 1 GHz.

can be calculated by taking the difference in detuning when $J = 28 \cdot \Delta B_z$ (performing a Pauli-z gate on target qubit) and $J = \Delta B_z/28$ (performing a Pauli-z gate on target qubit). Figure 5.23a shows a plot of the required inter-qubit couplings as a function of the target qubit tunnel coupling. The different curves represent different values of ΔB_z (arising from the different number of P-donors in the quantum dots as discussed in Section 5.3.1). From Figure 5.11, it is noted that if the base temperature of the fridge were 10-20 mK, to achieve 99.9% ground state probability, the tunnel coupling must be at least 1 GHz. It is clear from Figure 5.23a that for even 500 MHz magnetic field gradients, the required inter-qubit couplings exceed 70 GHz. Thus, the CX gate yields no improvement to the device geometry when considering the analysis in Section 2.2.3 as a 70 GHz coupling (being much larger than 39 GHz proposed for the CZ gate) would require closer inter-qubit distances. Thus, it is better to simply use CZ gates and Hadamard gates to realise a CX gate.

However, if one were to relax the need for a CX gate into a CH gate (a controlled-Hadamard gate shown in Figure 5.24), then the inter-qubit shift only needs to move J from $J = 28\Delta B_z$ (for accurate Pauli-z gates) to $J = \Delta B_z$ to perform the Hadamard gate. Thus, one requires smaller inter-qubit couplings Δ_Δ (to tilt the rotation axis from the Pauli-z axis to the 45° axis as opposed to all the way onto the Pauli-x axis). The required inter-qubit coupling Δ_Δ at 1 GHz is approximately 17 GHz for $\Delta B_z = 29$ MHz as plotted in Figure 5.23b. Although the smaller inter-qubit coupling can yield larger gate distances, one needs to analyse the CH gate under the presence of both charge noise and magnetic field noise. As the nature of magnetic field gradient noise is yet to be measured (for example, whether it is simply Gaussian fluctuations or large discrete jumps due to P-nuclei flips) in Si-P, the noise analysis is outside the scope of this thesis. If native CH gates are found to be feasible in the future, the geometry could be enhanced with larger gate distances (due to larger inter-qubit distances).

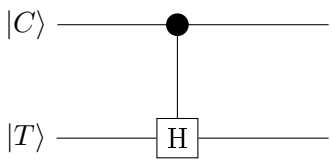

Figure 5.24: Circuit diagram of a controlled Hadamard gate. The CH gate is shown for control and target qubits $|C\rangle$ and $|T\rangle$.

5.4.4 Summary

Consideration of the two-qubit gate mechanisms and their susceptibility to charge noise yielded optimal parameters to use in the design of a large-scale singlet-triplet processor using Si-P. The key results include:

- Negative inter-qubit couplings yield no feasible working points for CZ gates as the required CZ operating points (in control and target qubit exchange: J_c and J_t) fall in regions where the qubits will start performing unintentional CPHASE gates.

- An inter-qubit coupling of $\Delta_\Delta = 6t_c$ yielded feasible CZ operating points (in control and target qubit exchange: $J_c \sim 2t_c$ and $J_t = 0.124t_c$) where the detuning noise can be up to $\Delta_\sigma = 0.02t_c$-$0.03t_c$, while triggering no unintentional CPHASE gates with adjacent qubits. Any higher inter-qubit coupling would

require voltage pulses that are faster than the state-of-the-art benchtop equipment (less than 20 ps).

- Given $J = 810\,\text{MHz}$ (for an accurate Pauli-z gate discussed in Section 5.3.4), for >99.5% fidelity CZ gates, the optimal tunnel coupling was found to be $t_c = 6.5\,\text{GHz}$ with an inter-qubit coupling of $\Delta_\Delta = 39\,\text{GHz}$. The maximum detuning noise must be below $\Delta_\sigma = 540\text{-}810\,\text{neV}$; approximately 8 times the theoretical minimum expected charge noise in silicon [18, 201, 202]

- The native CX gate (that is, not using a CZ gate sandwiched between two Hadamard gates applied on the target qubit) was found to require inter-qubit couplings in excess of 100 GHz and thus, discarded as an option for the final architecture.

- The native CH (controlled-Hadamard) gate was found to be technically feasible with inter-qubit couplings that can be made as low as $\Delta_\Delta = 17\,\text{GHz}$ for a 1 GHz tunnel coupling and $\Delta B_z = 29\,\text{MHz}$. The lower inter-qubit coupling yields the promise of spacing the qubits further apart than the CZ gate. However, further experimental work is required to characterise the magnetic field gradient noise and charge noise before the CH gate can be considered for a large-scale architecture.

5.5 Optimising the 1D and 2D singlet-triplet qubit arrays

The device described in Chapter 2 demonstrated a quadruple quantum dot device that could eventually be used to host singlet-triplet qubits. The device parameters originally chosen in the design of this 4-dot architecture were from insights provided from previous published data and experiments. During the experimental investigations, the theoretical framework of singlet-triplet qubits in Si-P (based on models from first principles) was further developed and, as outlined in this chapter, place more stringent bounds on device parameters. From this modelling, updated device parameters have been extracted for maximum resistance to charge noise when implementing the CZ gate (for an inter-qubit coupling much larger than the tunnel coupling). This section now collates the results from both Chapters 2 and 5 to design an optimal architecture for a 1D array of coupled singlet-triplet qubits.

Parameter	Value	Reason
B_0	$\gg$10 mT	Magnetic field must be large enough to suppress qubit state leakage via s_0-t_- and s_0-t_+ couplings.
P-donors	1P-2P	Asymmetric 1P-2P dots enable simultaneous access to even parity inter-dot transitions, $(1,3) \leftrightarrow (0,4)$, on adjacent qubits (as required for a two-qubit gate), with minimal voltages applied to the gates (to prevent gate-to-gate current leakage).
ΔB_z	29 MHz	Expected gradient from approximate hyperfine splittings for a 1P-2P cluster (with 2 spin-paired electrons in the 2P cluster as discussed in Section 5.3.1)
J_z	810 MHz	$J_z > 28\Delta B_z$ for 99.5% accurate z-rotations (see Table 5.2)
t_c	6.5 GHz	Approximate minimum t_c and Δ_Δ, where the CZ gate can be turned off while enabling high fidelity CZ gates with $\Delta_\sigma \lesssim 0.03\text{-}0.05 t_c$, is when $\Delta_\Delta = 6t_c$ and $J_z = 0.124 t_c$ (see Figure 5.20.)
Δ_Δ	39 GHz	

Table 5.3: Summary of physical parameters constraining the scalable qubit unit-cell. The physical parameters include the magnetic field gradient across the double-dot pair ΔB_z, the exchange J_z when doing z-rotations on the qubit, the inter-dot tunnel coupling t_c and the inter-qubit coupling Δ_Δ. The distances d_{rc} is the distance from the reservoir and the nearest dot in unit-cell c. Δ_σ denotes the noise standard deviation on the detuning.

5.5.1 Summary of optimal device parameters

The previous sections in this chapter covered modelling of the double quantum dots, single-qubit gates and two-qubit gates. The key collective results that now set future fabrication and operational device conditions are shown in Table 5.3.

The first parameter is an operational parameter that indicates that for singlet-triplet qubits, one needs to apply a global magnetic field to suppress s_0-t_- and s_0-t_+ coupling parameters given by the differential magnetic field $\Delta B_\perp$ perpendicular to the Pauli-z axis (chosen to be the direction of the applied magnetic field B_0). This is necessary to avoid qubit state leakage (into non-qubit states t_- and t_+). The second parameter is the number of P-donors in the individual dots. Electrostatic simulations in Section 2.2.3 showed that a 1P-2P double quantum dot enables simultaneous access of even-parity inter-dot charge transitions (specifically the $(1,3) \leftrightarrow (0,4)$ charge transition) on adjacent qubits (as required for a two-qubit gate). The 1P-2P configuration enables us to reach the even-parity inter-dot transitions with minimal

voltages applied to the gates, thereby preventing gate-to-gate current leakage. The third parameter is the nominal magnetic field gradient estimated from the hyperfine splittings of a 1P-2P double quantum dot; $\Delta B_z = 29\,\text{MHz}$ (when one electron is on the 1P dot and 3 electrons occupy the 2P dot) as discussed in Section 5.3.1. The fourth parameter is the minimum exchange J_z required for accurate Pauli-z gates. That is, at $J_z = 810\,\text{MHz}$, the exchange J is sufficiently larger than ΔB_z to obtain 99.5% accurate Pauli-z rotations. The final two parameters (tunnel coupling $t_c = 6.5\,\text{GHz}$ and inter-qubit coupling $\Delta_\Delta = 39\,\text{GHz}$) were obtained by considering the CZ gate fidelities under the influence of charge noise. The values obtained were those most resistant to charge noise; while still being able to turn off the CZ gate; and experimentally realise the gate operation with currently available voltage pulse generation technology (that is, the gates require voltage pulse times much larger than the fastest pulse time of 20 ps). Given these optimal parameters, one may redesign the geometry of the singlet-triplet qubit array.

5.5.2 Overcoming the shortcomings of the previous geometry to create a 1D qubit array

The overall geometric design in Section 2.2.3 was adequate for realising a two-qubit gate if the tunnel coupling and inter-qubit coupling were optimised. However, when expanding this 1D design (that is, the double-quantum dots splayed away from one another with a wedge angle ϑ) for an inter-qubit coupling of 39 GHz, the distance between adjacent unit-cell control gate leads (G2 and G3) becomes too small as shown in Figure 5.25a. Although small distances between reservoirs can be slightly tolerated (as they are usually fixed at similar voltages as shown in the stability diagram simulation in Figure 2.9), the control gates need to have maximal flexibility in voltage pulses of approximately $\pm 0.5\,\text{V}$ (without entering gate-to-gate current leakage) and thus, need to be uniformly spaced far apart. For example, consider 3 qubit unit-cells tessellated using the previous design as shown in Figure 5.25a. The gates G1 and G2 are spaced far apart while G2 and G3 are close together (vice versa for the reservoirs). Figure 5.25b shows the required lead distances (between adjacent reservoirs and adjacent control gates) to achieve 39 GHz for different double-dot angles ϑ (taken from the previous numerical simulations shown in Figure 2.7). Although for large angles ($\vartheta > 90°$), the control gates could be well-separated, they will be too close when considering the next unit-cell. For example, at $\vartheta = 135°$, the control gates are separated by 50 nm, but in the next unit-cell (with an angle of $\vartheta = 45°$) these control gates become less than 30 nm apart. Figure 5.25b shows

(a) 3 qubit unit-cells using the previous design for the singlet-triplet qubit array

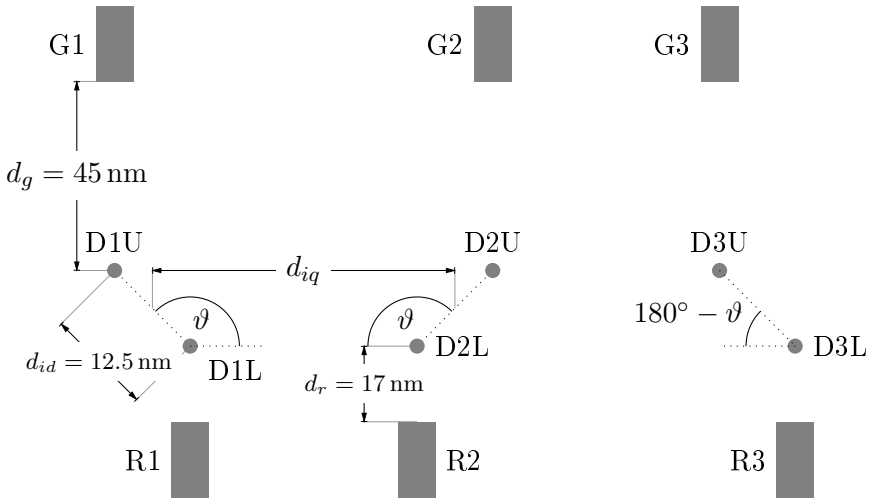

(b) Shortcoming of the previous architecture due to small inter-lead distances

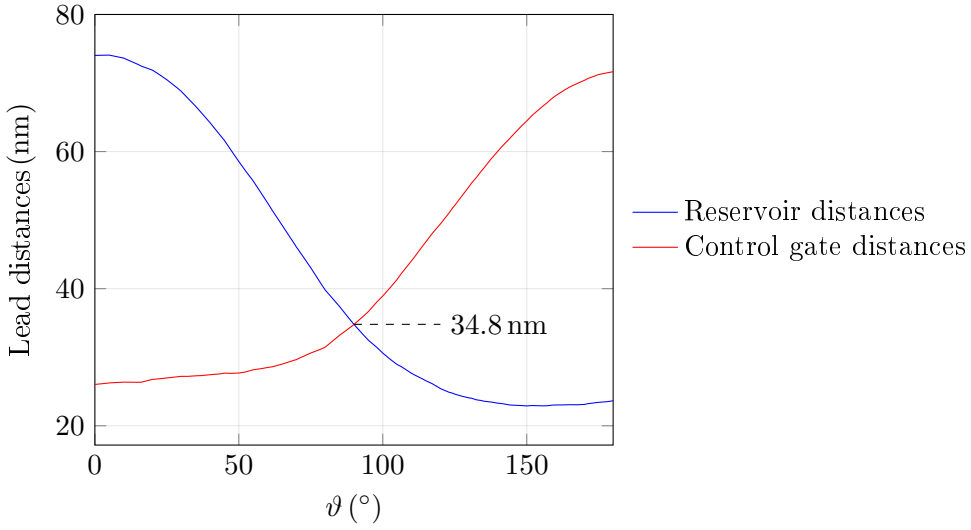

Figure 5.25: The shortening distances between control gates in the previous design for the singlet-triplet qubit unit-cell. **(a)** The previous design is illustrated for 3 qubit unit-cells with reservoirs (R1, R2 and R3), double quantum dots (D1L/D1U, D2L/D2U and D3L/D3U) and control gates (G1, G2 and G3). The dot angle ϑ and inter-qubit distance d_{iq} are left as free parameters as the inter-qubit coupling needs to be changed to $\Delta_\Delta = 39\,\mathrm{GHz}$. The key issue here is that although G1 and G2 are spaced far apart, the distance between the control gates on the next unit-cell (G2 and G3) become too small. **(b)** The resulting plot of the lead distances (between adjacent reservoirs and adjacent control gates) required to generate an inter-qubit coupling of $\Delta_\Delta = 39\,\mathrm{GHz}$. The distances were calculated from the numerical FEA simulation shown in Figure 2.7c. This is seen by the asymmetry about $\vartheta_1 = 90°$.

that the gates may be separated by a minimum of 34.8 nm when using the angle of $\vartheta = 90°$ (to achieve an inter-qubit coupling of 39 GHz). Noting that the singlet-triplet qubits are still separated further than the previous Si-P architecture proposal, at 30 nm [28], this separation may be adequate and is worth future work.

However, a more critical issue is that the inter-qubit coupling Δ_Δ for the previous design is always negative (that is, when the control qubit enters s_{02}, the target qubit shifts to a lower detuning). Here we pattern all dots further from their reservoir to be a 2P dot and the ones closer to their reservoir to be a 1P dot. We could instead make the inter-qubit coupling positive (as required for the proposed CZ gate) by alternating the dot which holds both electrons in the s_{02} charge state from qubit to qubit. One may achieve this by alternating the dot that is 2P across each qubit unit-cell (that is, the individual double quantum dots would be fabricated as: 1P-2P, 2P-1P, 1P-2P etc.). With this alternating donor size arrangement, the $(0, 2)$ charge state in each qubit will also alternate in direction (towards the 2P cluster as shown in the previous stability diagram simulations Figure 2.9). However, unlike the previous arrangement of P-donors (where the electrons were pushed in the same direction to enter the s_{02} charge state), the new P-donor arrangement will require large differential voltages between reservoirs and control gates to push electrons in different directions from qubit to qubit to obtain the s_{02} charge states simultaneously. That is, one can tolerate smaller distances between adjacent reservoirs and control gates if the adjacent reservoirs and gates are set to similar voltages as when pushing the electrons in the same direction across all qubit unit-cells. Thus, below we consider an alternate geometry for the 1D array.

Figure 5.26a shows an alternate geometry where the double quantum dots are arranged in an parallel Echelon formation. Due to the geometric similarities with the wedge-formation geometry, the results from the previous electrostatic optimisation carry over from Section 2.2.3. That is, the distances for the individual qubit unit-cell remain the same (that is, reservoir distance $d_r = 17$ nm, gate distance $d_g = 45$ nm and inter-dot distance $d_{id} = 12.5$ nm). The parameters that we change are the dot angle ϑ and the inter-qubit distance d_{iq} which, as with the previous optimisation, are set by the inter-qubit coupling which needs to be 39 GHz. Again we compare an analytic model of the inter-qubit coupling against the numeric finite-element simulations. Here we consider the four dots to be sites for electrons to occupy and subsequently calculate the inter-qubit coupling for dots arranged in the Echelon formation:

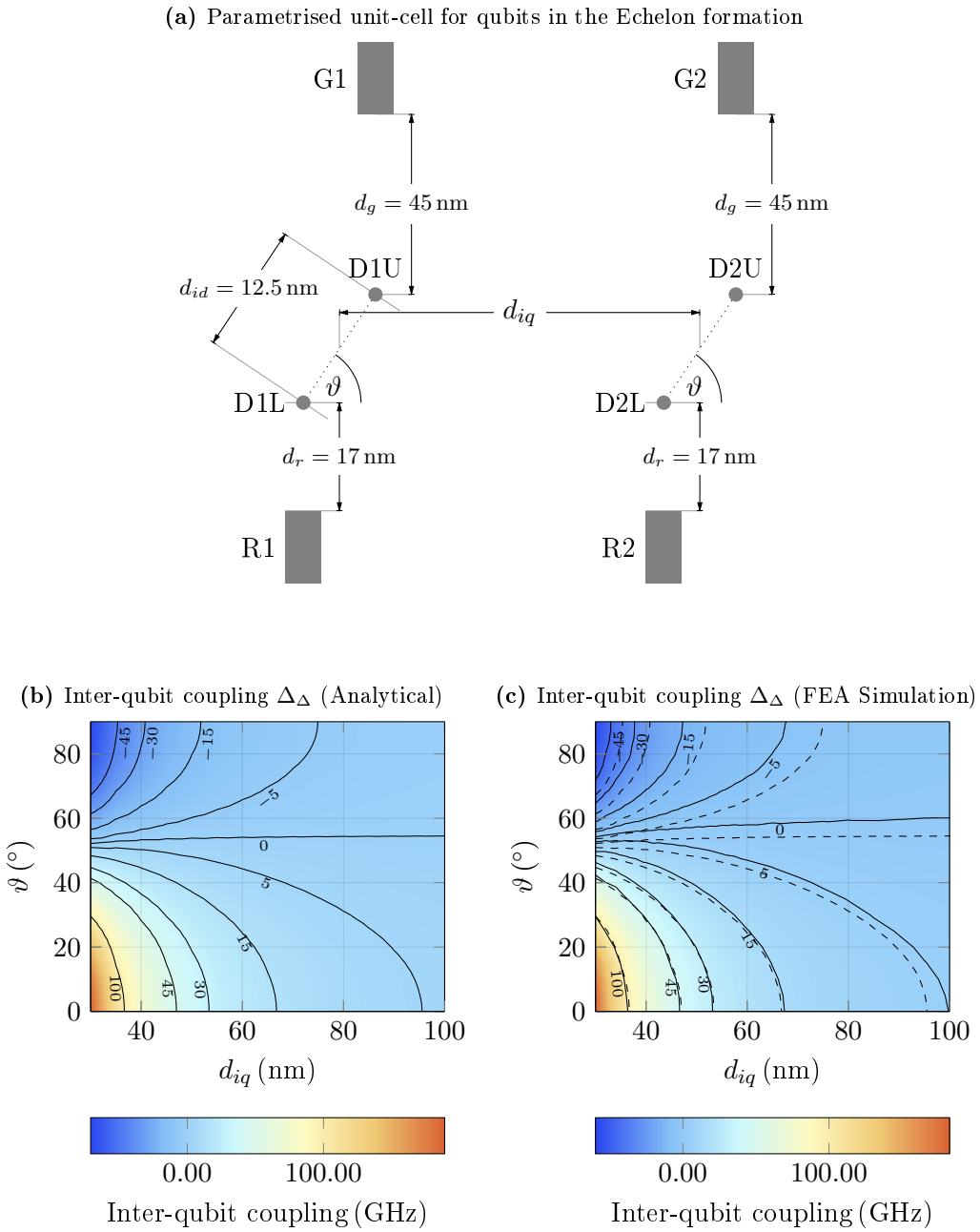

Figure 5.26: Optimising the inter-qubit distance d_{iq} and dot angle ϑ to achieve an inter-qubit coupling of $\Delta_\Delta = 39\,\text{GHz}$ on a more scalable singlet-triplet qubit unit-cell. **(a)** An improved qubit unit-cell structure with the dots in an Echelon formation. The key parameters to optimise are the inter-qubit distance d_{iq} and the dot-pair angle ϑ. The other distances are from optimisations performed in Section 2.2.3. **(b)** Plot of the analytic approximation of the inter-qubit coupling Δ_Δ given by using Coulomb's law in Equation 2.9 over different inter-qubit distances d_{iq} and dot-pair angles ϑ_1. The contours, highlighted for clarity, give the inter-qubit coupling in gigahertz. **(c)** Plot of the inter-qubit coupling when running a FEA simulation with an encapsulation layer thickness of 45 nm. Like in (b), the contours give the inter-qubit coupling in gigahertz. The dashed lines are contours from the analytic approximation in (b). The analytic model captures the FEA simulation at low angles where the contours overlap, while there is a slight discrepancy at higher angles where the analytic approximation overestimates the inter-qubit coupling for a given distance (since the numerical simulation captures the screening effect of the metallic reservoirs).

$$\Delta_{\Delta(\mathrm{E})} = \frac{e^2}{8\pi\varepsilon_0\varepsilon_r}\left(\frac{1}{\sqrt{d_{iq}^2 + d_{id}^2 - 2d_{iq}d_{id}\cos(\vartheta)}} + \frac{1}{\sqrt{d_{iq}^2 + d_{id}^2 + 2d_{iq}d_{id}\cos(\vartheta)}} - \frac{2}{d_{iq}}\right), \tag{5.41}$$

Figure 5.26b shows a plot of the inter-qubit coupling as predicted by the analytical model. The inter-qubit coupling does in fact change sign. To observe the reason for the change in sign, consider the two extremes $\vartheta = 90°$ and $\vartheta = 0°$. At $\vartheta = 90°$ the geometry is the same as the simulations performed on the previous design and thus, the sign of the inter-qubit coupling is already negative. However, at the other extreme $\vartheta = 0°$, if one enters the s_{02} charge states by either pushing both electrons onto D1L/D2L or D1U/D2U, the sign of the inter-qubit coupling will be positive as discussed earlier in Table 2.2.

The change in sign of the inter-qubit coupling leads to a region of null coupling as shown by the $\Delta_\Delta = 0$ contour in Figure 5.26b. When comparing against the numeric simulations in Figure 5.26c, the analytic model correctly predicts the inter-qubit coupling for low dot angles (as seen by the overlap of the analytic contours overlaid with the dashed lines). However, at larger angles, the screening effect of the dots' metallic reservoirs (in this case R1 and R2) perturbs the inter-qubit coupling away from the analytic approximation as seen by the numeric simulations which suggest that one needs to bring the dots closer than that predicted by the analytic model for larger angles ($\vartheta \gtrsim 50°$). Taking a nominal 40 nm separation between adjacent double quantum dots (10 nm more qubit and gate separation than that suggested previously in the single-spin Si-P architecture [28]), one can avoid gate-to-gate current leakage and choose the optimal angle (from Figure 5.26c) to achieve $\Delta_\Delta = 39$ GHz of $\vartheta = 32°$.

Figure 5.27 shows the geometry of the newly proposed 1D array of singlet-triplet qubits. The tighter angle of $\vartheta = 32°$ gives rise to a lower differential lever-arm (defined as $\alpha_{\mathrm{D1L}} - \alpha_{\mathrm{D1U}}$), when compared to $\vartheta = 45°$, from approximately -3.2% to -2.6% for the control gates and 8.6% to 7.5% for the reservoirs. The lower differential lever-arms however do not necessarily give concern as there are many control gates in close proximity to the qubits and one will likely obtain a greater effective differential lever-arm by using a linear combination of all the control gates; as found with gate-defined quantum dots [33, 55]. Nonetheless, one should verify that the new geometry can still obtain the required charge states to form the singlet-triplet qubit. That is, whether one can access the even-parity inter-dot crossings to form singlet-triplet states across the individual double quantum dots.

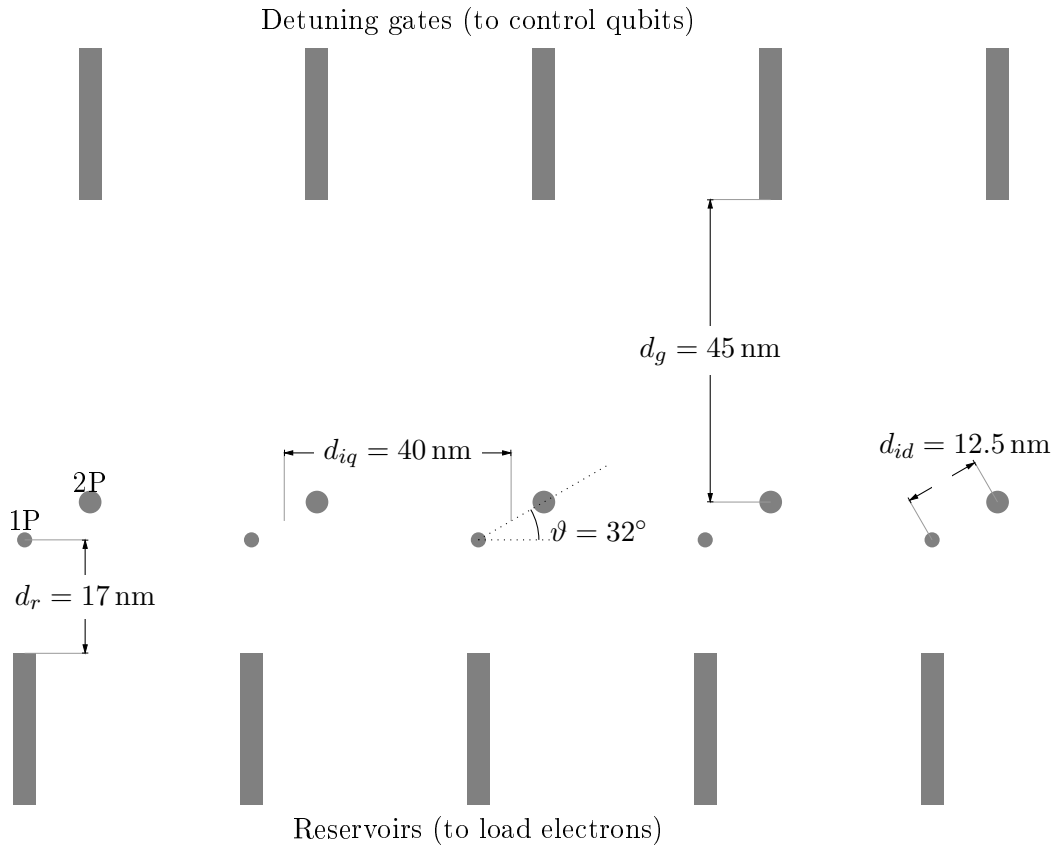

Figure 5.27: Proposed 1D array of singlet-triplet qubits using Si-P quantum dots. The double-quantum dots hosting the electrons for the singlet-triplet qubits are arranged vertically to maximise the differential lever-arms on the gates. The bigger dot (indicated by the larger circle) in each double-quantum dot is a 2P donor dot (holding both electrons when the qubit enters the s_{02} charge state) while the other dot is a 1P donor.

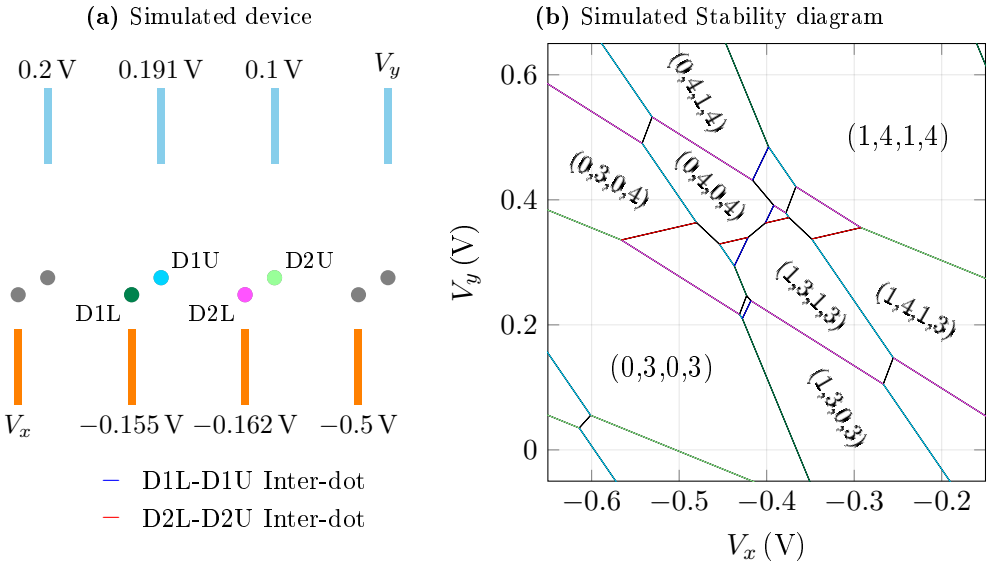

Figure 5.28: Stability diagram simulations for the newly proposed geometry for a 1D array of singlet-triplet qubits. The goal is to overlap singlet-triplet transitions on adjacent double quantum dots (red and blue and labelled EP) to setup a two-qubit gate. The electron numbers on dots are shown as (D1L, D1U, D2L, D2U). The simulated dots are colour-coded with the electron charge transitions the stability diagram. **(a)** Two adjacent qubit unit-cells sandwiched by two extra unit-cells used in the simulation. The reservoirs are shown in orange, while the control gates are shown in light blue. The dots close to their reservoirs are 1P, while the dots further from their reservoirs are 2P. The voltages on the gates required to overlap the inter-dot crossings are labelled along with the voltages swept in the simulated charge stability diagram (gate voltages V_x and V_y). **(b)** The resulting charge stability diagram where the even parity inter-dot crossings are made to overlap as required to perform two-qubit gates between singlet-triplet qubits hosted on the double quantum dots D1L/D1U and D2L/D2U.

To simulate the electrostatic accessibility, the newly proposed 1D array was simulated in FEA and analysed via the custom charge-stability diagram simulator described in Appendix A. Figure 5.28a shows an array of 4 qubit unit-cells in the proposed Echelon formation geometry. The model was numerically simulated, using the proposed geometric parameters, as before to obtain the capacitance matrix, from which we obtained the charge stability diagram shown in Figure 5.28b. The charge stability diagram shows the charge regions for the four interior dots D1L, D1U, D2L and D2U. The aim of the simulation is to show that one can obtain the required singlet-triplet charge states for qubits within the 1D array with all the gates set to similar voltage conditions. Here we remember that large differential voltages between adjacent gates can cause gate-to-gate current leakage. The simulations show that one can overlap the singlet-triplet inter-dot charge crossings required to perform two-qubit gates as discussed in the previous simulations in Section 2.2.3. The voltages required on the reservoirs close to the simulated qubits are similar at $\sim$0.36-0.37 V. Similarly the voltages on the control gates are a few 100 mV. The comparable voltage ranges not only ensure low lead-to-lead differential voltages (between adjacent control gates and reservoirs), but also confirms that one can find a stable pattern of voltages along the array when forming all the adjacent singlet-triplet qubits. The voltages on the reservoirs are mostly negative as expected to enable electrons to load the dots (a negative voltage applied on a reservoir brings down the dots' energy levels with respect to the reservoir), while the control gates perform fine corrections to obtain the required charge configurations. We note that the leads at the ends of the array (for example, x and y as swept on the stability diagram) require larger voltages (approximately $\pm$200 mV different for the reservoirs and -0.3 V for the control gate) as the translational symmetry of the qubit unit-cells along the array breaks down. Since the simulation suggests that the leads towards the end of the array may require large voltages to sustain the singlet-triplet charge states, the ends of the 1D array should be terminated with large gates to offset the lack of leads at the end of the array. One could in fact, use TJCS structures as used in the experiments in Section 2.2.4 to function as both diagnostic probes and as biasing gates for qubits near the end of the array [29].

5.5.3 A 2D singlet-triplet qubit array

The 1D array proposed in Section 5.5.2 provides a blue-print to further extend the proposal into a 2D array as required in forming a fault-tolerant quantum processor using a surface code. To translate the 1D array into a 2D array, one appeals to recent

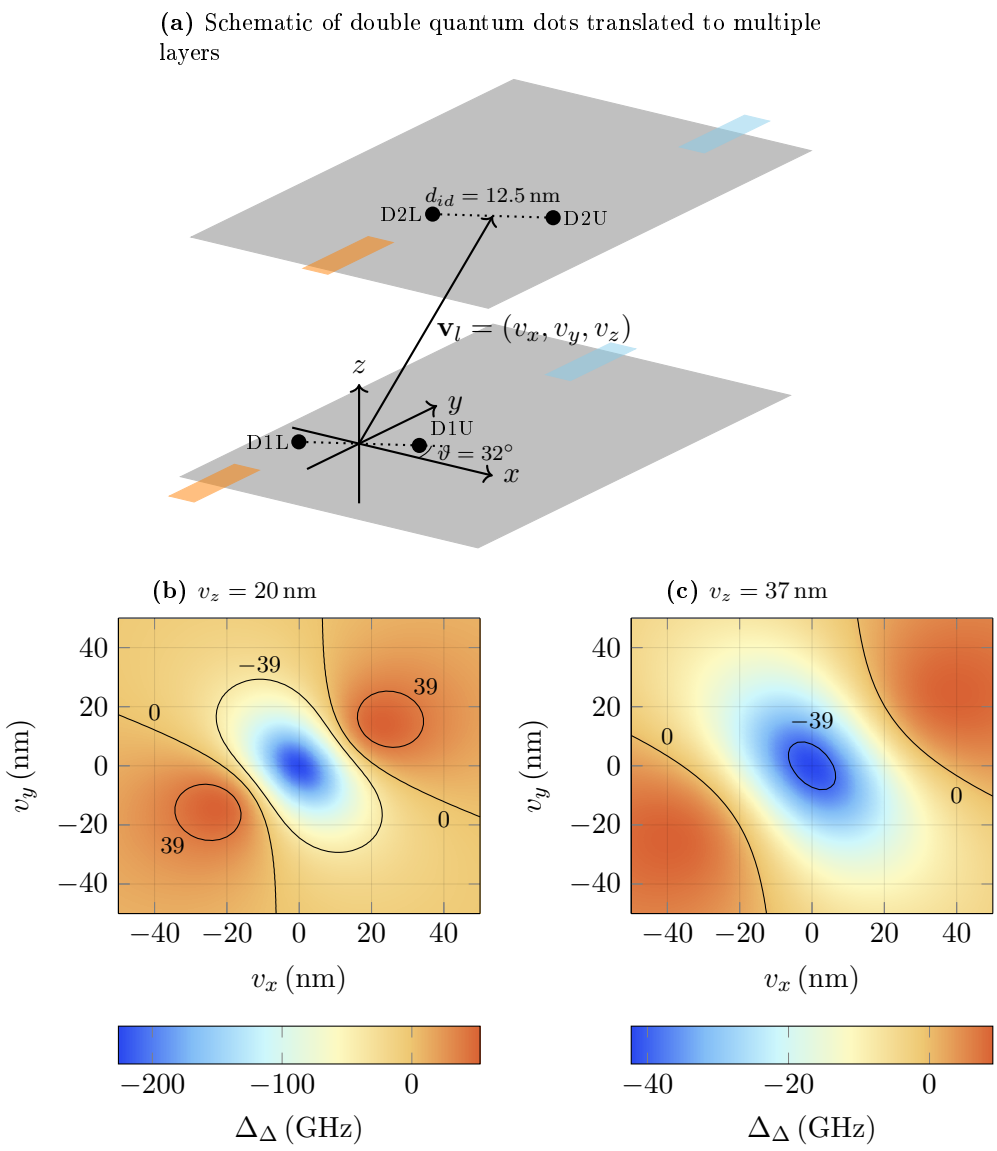

Figure 5.29: Analytic simulations of the inter-qubit couplings Δ_Δ between double quantum dots across different vertically separated STM-patterned layers. **(a)** Two double quantum dots D1L/D1U and D2L/D2U adopting the geometry of the proposed 1D array are spaced apart via a translation vector $\mathbf{v}_l = (v_x, v_y, v_z)$. The reservoirs (orange) and gates (light blue) are shown for reference but not included in the analytic calculation. **(b)** Plot of the inter-qubit coupling (as a function of the planar translation vector (v_x, v_y)) for vertically stacked layers separated by 20 nm of epitaxial silicon; the maximum separation where there is are regions where $\Delta_\Delta = 39\,\text{GHz}$ as required for the CZ gate. (c) Plot of the inter-qubit coupling for layers separated by 37 nm; the maximum separation in which one can access the region $-39\,\text{GHz}$. Although the sign (of the $-39\,\text{GHz}$ contour) is wrong, the arrangement of the dots proves useful in creating the final geometry due to the larger spacing (37 nm as opposed to 20 nm) between layers (important in reducing lead-to-lead current leakage between leads across adjacent vertically separated layers).

advancements in multilayer STM lithography developed in our group by Matthias Koch [76]. Here, the key advancement was that one can now perform lithography on the multiple vertically separated layers, as we have already shown on one layer of the silicon crystal. Previously, when encapsulating the first layer with silicon, it was found that the second layer was too rough to perform feasible lithography. However, with rapid-thermal-anneals (optimised via thermal Monte-Carlo simulations and experimental growth studies) performed on encapsulating the final few monolayers of silicon, one can flatten the second layer (ideal for lithography) without diffusing the incorporated phosphorus atoms in the first layer. In addition, it has been shown that one can indeed image buried P-dopants to help align the second layer with the layer below via lock-in excitations applied to the tip during the imaging process [205]. With advancements in feasible multilayer lithography, one can propose a multi-layered architecture where one stacks many 1D arrays on top of one another to create a 2D array of singlet-triplet qubits. Here, each qubit in the next layer interacts not only with its adjacent two qubits in its layer, but also the qubits directly above and below its layer.

The individual 1D arrays (one per layer) can retain the geometry of the optimised 1D array in Section 5.5.2. One method to stack the arrays is to simply translate the second layer from the first layer via the vector $\mathbf{v}_l = (v_x, v_y, v_z)$ as shown in Figure 5.29a. Here, if one investigates the 1D array, the vector is $\mathbf{v}_l = (\pm d_{iq}, 0, 0)$. The goal is to find a vector in a layer above $v_z > 0$ such that the double quantum dots are as far apart as possible to reduce the possibility of lead-to-lead current leakage. One can analytically investigate the inter-qubit coupling Δ_Δ between vertically separated layers via the coordinate positions of the dots D1L/D1U and D2L/D2U (where the reservoirs shown in orange is near D1L and D2L, while the gates shown in blue are further away and closer to D1U and D2U) via Equation 2.12 as plotted in Figures 5.29b-c for different layer separations v_z. At a layer separation of 20 nm, shown in Figure 5.29b, there are two loci in (v_x, v_y) shown by the 39 GHz contours where one can achieve the desired inter-qubit coupling. Note that the 39 GHz loci disappear at $v_z = 21$ nm. However, in choosing any of the positions (along the the 39 GHz loci), one has a lead-to-lead distance of approximately 28 nm (taking 20 nm across x and 20 nm across z) which may be too close to avoid lead-to-lead current leakage. Thus, we investigate another z-layer separation of 37 nm shown in Figure 5.29c. Here there is a region of -39 GHz coupling which disappears at 38 nm vertical separation. One can overcome the negative sign of the -39 GHz inter-qubit coupling if the s_{02} charge state occupies the dots further from the reservoir (D2U) in the second layer while occupying the dots closer to the reservoir in the first layer (D1L). One may

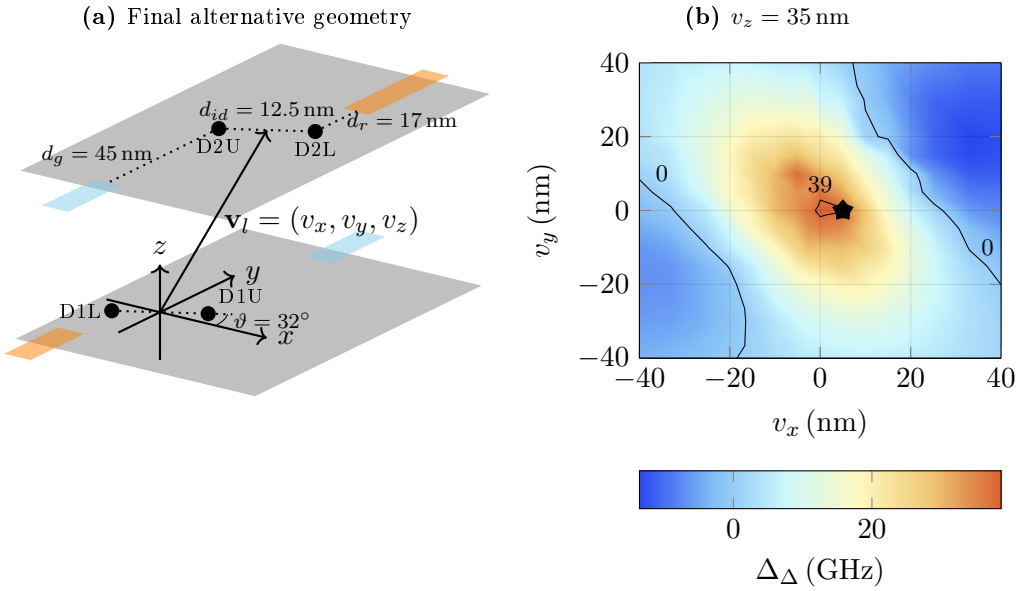

Figure 5.30: Numeric simulations of the inter-qubit couplings between double quantum dots across different vertically separated STM-patterned device layers in an alternating 1D array geometry. **(a)** Two double quantum dots D1L/D1U and D2L/D2U adopting the geometry of the proposed 1D array are spaced apart via a translation vector $\mathbf{v}_l = (v_x, v_y, v_z)$. The reservoirs (orange) and gates (light blue) are to alternate over every layer. The alternating geometry is used to help achieve a positive inter-qubit coupling without changing the, already optimised, electrostatic control amongst the individual 1D layers. **(b)** Plot of the FEA calculations of the inter-qubit coupling (as a function of the planar translation vector (v_x, v_y)) for layers separated by 35 nm; the maximum separation where there is are regions where $\Delta_\Delta = 39\,\text{GHz}$ as required for the CZ gate. The star highlights the final geometry $(v_x, v_y, v_z) = (5, 0, 35)\,\text{nm}$.

achieve this alternating charge state between layers, by alternating the dots that are 2P over every vertically separated layer (for example, D1L and D2U can be made 2P while D1U and D2L can be made 1P). Although electrostatically one may obtain the required interactions for qubits within the same layer, the swapped positions of the $(0, 2)$ charge state between layers make it difficult to tune the control gates to perform a two-qubit gate across two qubits on different layers. An alternative solution is to swap the positions of the reservoirs and gates on alternating layers by effectively flipping the 1D array from layer to layer.

Figure 5.30a shows a solution to achieve a positive inter-qubit coupling at larger vertical separations by swapping the positions of the reservoirs and gates on alternating layers. Note that D1L and D2L are 1P dots close to their respective reservoirs (orange) at a distance of $d_r = 17\,\text{nm}$. The dots D1U and D2U are 2P dots further from their respective reservoirs with inter-dot separations (between D1L/D1U and

between D2L/D2U) of $d_{id} = 12.5\,\text{nm}$. The dot to gate (light blue) separations are still 45 nm. To simulate the presence of the gates, the analytic approximation was replaced by a numeric simulation where for given vector translations $\mathbf{v}_l$, capacitance matrices were calculated like with the all the previous electrostatic simulations and the inter-qubit coupling was extracted from the capacitances via Equation 2.9. Note that there was no encapsulation layer in these simulations (that is, the device was immersed in infinite silicon) as the different layers are buried deep in the bulk silicon.

Figure 5.30b shows the result of the numeric simulations with a vertical separation of 35 nm. Note that at vertical separations greater than 35 nm, there was no loci along the xy-plane on the second layer where the inter-qubit coupling was 39 GHz. The lower vertical separation required to retain 39 GHz (when compared to numerical simulations suggesting 37 nm in Figure 5.29b) is due to the screening effect of the nearby reservoir leads causing a lower inter-qubit coupling. The chosen vector translation to get 39 GHz for the second layer was $\mathbf{v}_l = (5, 0, 35)\,\text{nm}$ as marked by the black star. Finally, one must ensure that the residual couplings to qubits adjacent to the first layer have a weak inter-qubit coupling with the qubit on D2U/D2L to avoid unintentional two-qubit gates. The inter-qubit coupling of the qubit on D2U/D2L with the qubits (spaced by $d_{iq} = 40\,\text{nm}$) either side of that hosted on D1U/D1L can be found by translating the $\mathbf{v}_l$ by $\pm 40\,\text{nm}$. The stray inter-qubit couplings of D2L/D2U with the qubits to the right and left (positive and negative x-axes) of D1L/D2U are $-1.0\,\text{GHz}$ and $-2.6\,\text{GHz}$ respectively. From Figure 5.16 showing the regions where where the target qubit exchange J_t may reside such that (for a given inter-qubit coupling) there is no two-qubit gate with at least 99.5% fidelity, the bounds on J_t to prevent unintentional two-qubit gates are subsequently $J_t < 3.1\,\text{GHz}$ and $J < 2.1\,\text{GHz}$ respectively. From Table 5.3, the CZ gate and idle qubit states are optimally at a lower exchange of 810 MHz. Thus, the stray couplings do not present significant unintentional two-qubit gates that will affect fault-tolerant control.

With sufficient inter-qubit couplings for the proposed geometry, it is important to show that one may perform a CZ gate via the overlap of even-parity charge transitions across adjacent qubits on different layers. Figure 5.31a shows two double quantum dots D1L/D2U and D2L/D2U across two layers. To simulate the translational symmetry of qubits deep within the 2D grid, the two vertically separated qubits are surrounded by six double quantum dots and gates. The layers follow the proposed geometry; that is, each layer (separated by 35 nm) has the reservoirs (orange) and gates (light blue) alternating while being shifted horizontally by 5 nm. For each quantum dot, the dot close to the reservoir is a 1P donor while the dot further

(a) Schematic of the simulated portion of the 2D array

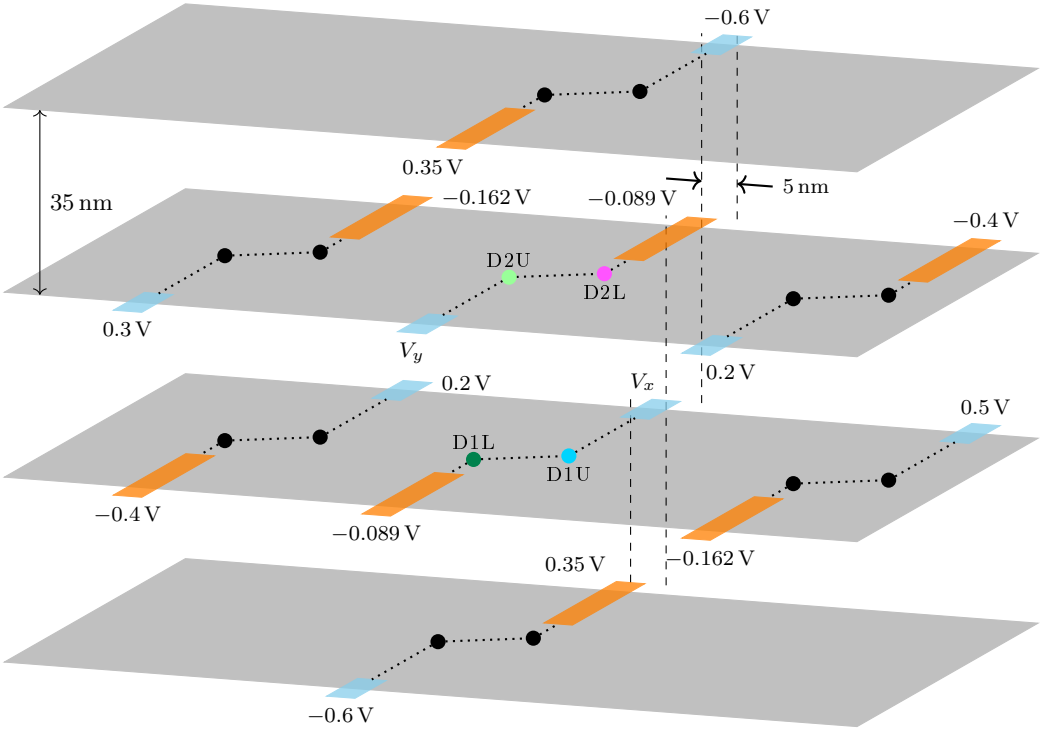

(b) Simulated Stability diagram

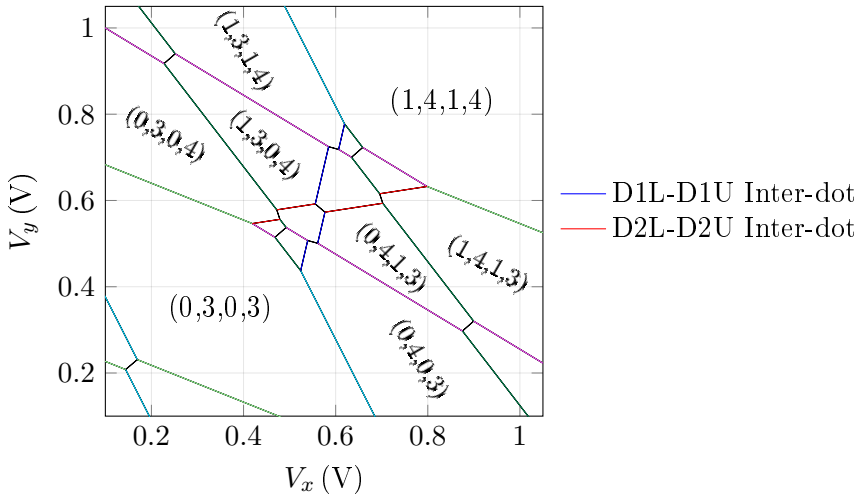

Figure 5.31: Stability diagram simulations of the proposed geometry for the 2D array of singlet-triplet qubits. The goal is to overlap singlet-triplet transitions on adjacent double quantum dots (red and blue and labelled EP) to setup a two-qubit gate. The electron numbers on dots are shown as (D1L, D1U, D2L, D2U). The simulated dots are colour-coded with the electron charge transitions the stability diagram. **(a)** Two adjacent qubit unit-cells (across different layers) are sandwiched by six extra unit-cells used in the simulation. The simulation used the six extra pairs of gates to emulate the translational symmetry of two vertically separated qubits within the 2D array. The reservoirs are shown in orange, while the gates are shown in light blue. The dots close to their reservoirs are 1P, while the dots further from their reservoirs are 2P. The voltages on the gates required to overlap the inter-dot crossings are labelled along with the voltages swept in the simulated charge stability diagram (gate voltages V_x and V_y). **(b)** The resulting charge stability diagram where the even parity inter-dot crossings are made to overlap as required to perform two-qubit gates between singlet-triplet qubits hosted on the double quantum dots D1L/D1U and D2L/D2U.

from the reservoir is a 2P donor dot. The device was once again simulated without an encapsulation layer (that is, immersed in infinite silicon) to create a capacitance matrix with the resulting simulated stability diagram on tuning the gate voltages is shown in Figure 5.31b. The two even-parity transitions on dots D1L/D1U and D2L/D2U (shown in blue and red) are overlapped such that one may perform a CZ gate. The reservoirs on the middle two layers are approximately $-0.3\,\mathrm{V}$ with the gates set to approximately $0.3\,\mathrm{V}$. Similar to the simulations on the 1D array, the reservoirs and gates on the ends require large negative voltages of up to $-0.6\,\mathrm{V}$. Once again, a larger array will stabilise the voltages to lower values as one can use more adjacent gates down the array to help tune the double quantum dots. However, one should note that the gates on the top and bottom of the stack of many layers may require extreme voltages when compensating for the lack of gates from further layers above or below the stack. Therefore, it is advisable to pattern gates (or diagnostic TJCS structures [29]) on the top and bottom layers that one may utilise the biasing gates for optimal qubit tuning of the inner layers.

Given the 2D grid of qubits, it is important to overview the typical operation in making the parity measurements. A unique feature of the proposed architecture is the ability to perform four CZZZZ gates; that is, on initiating a control qubit, the four adjacent qubits (along the left, right, top and bottom directions) will act as simultaneous target qubits upon which to perform the CZ gate. Noting that the surface code requires controlled phase flips on the auxiliary qubit given the state of its surrounding data qubits. The proposed mechanism to perform the CZ gate does not facilitate simultaneous CZ gates on the same target qubit. Thus, one requires four cycles of CZ operations to perform one cycle of the surface code as described by the quantum circuit diagrams in Figure 5.1b. In each cycle, a given data qubit will perform a CZ gate on four different auxiliary target qubits. Since the proposed architecture does not yet employ native CX gates, one needs to utilise the CZ gates sandwiched with Hadamard gates.

5.5.4 Summary

The design work outlined in this section were simply the application of the electrostatic models (developed in the previous sections) for the proposed optimal parameters in implementing the CZ gate. The theoretical simulations performed for the design of the newly proposed 1D array (a single row of the 2D grid) resulted in a few key observations:

- The previous 1D array design in Chapter 2, in which four quantum dots were

placed in a wedge formation, was shown to be inadequate for creating a scalable 1D array of singlet-triplet qubits as the lead distances (between adjacent reservoirs and adjacent control gates) become too small. In addition, the sign of the inter-qubit coupling was always negative (unless one alternated the dot containing the 2 P-donors for each qubit).

- The superior design choice was to place the double quantum dots in a parallel Echelon formation. With the inter-qubit distance (and subsequently the distance between adjacent leads) set to $d_{iq} = 40\,\mathrm{mV}$, the double-dot angles were set to $\vartheta = 32^\circ$ to obtain the required 39 GHz inter-qubit coupling.

- Capacitance model simulations showed that the Echelon arrangement still enables electrostatic accessibility of the even parity inter-dot transitions as required to form singlet-triplet qubits. In addition, the even parity inter-dot transitions amongst adjacent qubits could be overlapped as required to perform two-qubit gates.

- The capacitance model simulation suggested that the two ends of the 1D qubit arrays should be terminated with extra control gates to ensure that the required charge states on the dots can be achieved with as low a voltage on the control gates (to avoid gate-to-gate current leakage). One could implement the extra gates via TJCS structures to not only provide a biasing gate, but also on-board charge sensing diagnostics like with the quadruple quantum device experiment discussed in Section 2.2.4.

- A 2D grid of qubits for a surface code was investigated. It was shown that by stacking multiple 1D arrays in layers separated by 35 nm and offset horizontally by 5 nm, it was possible to extend this architecture into a 2D array of singlet-triplet qubits. To ensure that the sign of the inter-qubit coupling was positive, the 1D array was flipped (so that the side with the reservoirs and gates are alternated) over each subsequent layer. Similar to the 1D array, the top and bottom layers of the stack may need to be supplemented with additional gates to enable ease in electrostatic accessibility.

- Both the 1D and 2D qubit arrays have 2 gates per qubit. Therefore, unlike architectures that share one gate across many qubits [28], if there are nonuniform sections in the fabricated device (for example, a charge trap shifting the potentials of a cluster of qubits), one has enough gates to tune the device into satisfactory operation.

Although the theoretical designs described above show feasibility, there are certain long-term experimental challenges and milestones that must be met:

- Control of the nuclear spin dynamics of P-donor dots in forming a stable ΔB_z (over the course of a set of gate operations) must be shown experimentally. For example, recent results have shown that simply placing an electron on a P-donor dot decreases its nuclear spin coherence time and can affect the nuclear spin states by either tilting or flipping the nuclear spins [39, 50].

- High fidelity CZ gates (above 99.5%) must be shown across a 1D array of at least two singlet-triplet qubits. In addition, the high-fidelity CX gate (as required for the surface code) must be demonstrated (likely using isotopically purified ^{28}Si) using a CZ gate sandwiched in between two Hadamard gates.

- When stacking multiple 1D arrays, it must first be shown that there is sufficient gate voltage range between gates across adjacent vertical layers without gate-to-gate current leakage.

- If stacking multiple layers proves to be experimentally feasible (for example, sufficient gate voltage range before reaching gate-to-gate current leakage), one needs to address the contacting of the deep P-doped leads to the surface Ohmic gates. That is, typically the encapsulation layer in Si-P devices is $\sim$40 nm. However, if one were to make a 100×100 array of singlet-triplet qubits, the 100 vertical layers result in 3500 nm of encapsulated silicon that one must penetrate to contact the bottom layer.

Finally, if the proposed vertical layer separation results in gate-to-gate current leakage, one could investigate the applicability of slower AC driving techniques [33–35] where the inter-qubit couplings can be in the perturbative regime (with respect to the tunnel coupling). Thus, one may radically increase the separation between qubits both across the horizontal 1D array as well as the vertical separation in the 2D array.

Chapter 6

Conclusion and outlook

This thesis sought to develop a singlet-triplet unit-cell for a scalable singlet-triplet qubit architecture by leveraging the low gate densities provided by Si-P quantum dots with single-gate RF sensors. The thesis is set around three theoretical developments along with experimental demonstrations of RF control in the Si-P qubit system, allowing us to propose a scalable singlet-triplet architecture in the final results chapter.

The first set of results concentrated on the demonstration of a quadruple quantum dot device for hosting two singlet-triplet qubits [29]. Here we showed the following results:

- The development of a capacitance model tailored to Si-P quantum dots including a charge stability diagram simulator to simulate the impact of different P-donor dot sizes in silicon.

- The fabrication of a quadruple quantum dot Si-P device where 2P-2P and 3P-4P double quantum dots were separated by 75 nm.

- The successful cryogenic measurement to characterise the donor number and electronic charge states of a quadruple quantum dot device using a TJCS (tunnel-junction-charge-sensor) and single-gate RF sensor.

- The development of a triangulation technique to successfully pinpoint the exact locations of the four patterned P-donor dots in the device. This model was also used to identity the location and source of an unintentional charge trap; highlighting the utility of the model.

- Following this we successfully verified and benchmarked the electrostatic model via measurements of the gate lever-arms and inter-qubit coupling.
- We were able to experimentally extract the inter-qubit coupling of 5 GHz in agreement with theoretical capacitance models. Such a large inter-qubit coupling is important for fast high-fidelity CZ gates using Si-P quantum dots.

However, the key shortcoming in the experiment was the inter-dot tunnel coupling being too large to enable qubit control. Thus, the near-term pathway to be rectified in future experiments include:

- Demonstration of a singlet-triplet qubit. The tunnel coupling was too large at 39 GHz to enable one to tilt the qubit precession axis away from the Pauli-z axis. Further fabricated devices still had too large a tunnel coupling or too small a tunnel coupling. Nonetheless, the singlet-triplet qubit should be possible to realise if one can fabricate a device with the inter-dot tunnel coupling as it was partially demonstrated (Pauli-z rotation control) recently by members of the Simmons group [198].
- Demonstration of a two-qubit gate between singlet-triplet qubits.
- Benchmarking the AC driven two-qubit gate and the proposed CZ gate to determine the pathway to take in implementing the many-qubit architecture.

The second set of results concerned the development of a more compact charge sensor via RF reflectometry where the conventional 3-lead (and quantum dot) SET sensor was reduced to a single-lead quantum dot (SLQD) sensor. The key developments include [31]:

- An analytic model of the SLQD sensor, using previous works done using rate equations, extended to the nonlinear regime. The peak RF signal strength was predicted to saturate at higher RF input powers (beyond the linear capacitance regime). In addition, the model gave a better understanding of the nonlinearities in the SLQD current (exploited later by Mark R. Hogg in the context of an RF mixer [155]) and the low power dissipation of the SLQD sensor.
- Fabrication and successful model verification of the SLQD sensor. The SLQD sensor showed the response predicted by the theoretical modelling.
- Development of new characterisation techniques to measure the reservoir-to-dot lever arm (in the SLQD) and the electron temperature. Conventionally

with an SET, the lever-arms were measured via Coulomb oscillations, but the SLQD lacks the source and drain contacts to perform this measurement. Thus, the analytic responses developed in the SLQD theory (for example, the conical shape of the RF readout signal strength with respect to the input RF voltage amplitude), were applied to the experiment to deduce the reservoir-to-dot lever-arm, electron temperature, input RF power loss and net output return gain.

- Successful detection of electron charge movement (at peak RF signal strength) over 44 nm away from the SLQD sensor with predicted ranges exceeding 100 nm. Noting that the size of Si-P qubits is less than 12.5 nm, the normalised range (ratio of sensor range to the qubit size) in which one can still perform high-fidelity spin readout is far greater than qubits in gate-defined quantum dots (10 as opposed to 1-2). That is, the SLQD sensor leads to a significant reduction in gate density as the sensor does not need to be too close to the qubits.

The work done in this thesis paved the way for further experimental development of the SLQD sensor as shown by a current PhD student Mark R. Hogg. Here, the SLQD nonlinearities were used to create an RF mixer device along with single-shot readout of single electron spins using a SLQD sensor.

The third results chapter further developed the compact single-gate RF sensor by removing the dedicated lead and quantum dot (in comparison to the SLQD sensor). The sensor was once again first modelled to find the optimal modes of operation and then demonstrated experimentally. The key results include [32]:

- Hamiltonian modelling to better understand the operation of the SLQD sensor. The model covered the operation in both the tunnelling capacitance and adiabatic quantum capacitance regimes. One unique trait of the models (similar to the SLQD modelling) is that the quantum capacitance was investigated in the regime of large RF input powers (where the readout response was found to eventually decay) to better understand the optimal operating regimes.

- By replacing the surface mount chip inductor (internal quality factor of $\sim$370) used in previous experiments with a low-loss NbTiN superconducting inductor (internal quality factor of $\sim$800), we were able to improve the readout signal strength.

- Successful characterisation of the RF sensor in measuring key qubit parameters such as the inter-dot tunnel coupling of 39 GHz and singlet to triplet-t_- lifetime as a function of detuning (2 ms at zero detuning). In addition, the single-gate

RF sensor was shown to make faithful measurements of the electron spins without affecting the dynamics of the spins under measurement.

- First experimental demonstration of single-shot, single-gate RF spin readout. The average readout fidelity was 85.77% at a 3.3 kHz measurement bandwidth.

The fidelity of single-shot single-gate RF spin readout was still limited by the internal quality factor of the resonator and thus, the next steps in improving the sensor involve the engineering, development and integration of higher quality internal factor (above 1600) superconducting spiral inductors with the Si-P quantum dots.

Finally, the last results chapter undertakes theoretical modelling of single and two qubit gates in singlet-triplet qubits that integrate in a scalable Si-P architecture. Particular attention was paid to the CZ gate under the influence of charge noise due to its importance in the surface code in performing the required XX and ZZ parity measurements. The key highlights of this work were:

- Development of simple noise models to optimise the device parameters for high-fidelity CZ gates. The modelling looked at the CZ gate fidelities when applying Gaussian charge noise on the qubit detuning. The modelling was unique in that it investigates the CZ gates in the strong inter-qubit coupling (with respect to the inter-dot tunnel coupling) regime to realise CZ gates with worst-case error rates smaller than 0.5%.

- Combining the noise and electrostatic models, we showed the way to create a scalable 1D array of singlet-triplet qubits in Si-P.

- Combining recent developments in 3D multi-layer Si-P fabrication to stack 1D arrays vertically above each other, we showed an architecture containing a large 2D array of singlet-triplet qubits that can implement a fault-tolerant surface code. Unlike previous single-spin qubit proposals in Si-P [28], gates are not shared amongst qubits. Since each qubit in the 2D grid can be individually tuned, one can actively counter potential offsets due to fabrication defects.

Given the success of the results to date, several key objectives remain in order to realise the singlet-triplet architecture proposed in this thesis:

- The measurement of charge noise spectra affecting the qubit detuning. The actual magnitude (that is, measurement of Δ_σ) and possible noise distribution helps evaluate and fine-tune the feasibility of the CZ gate.

- The measurement of the stability of the magnetic field gradient ΔB_z when using the P-donor dots and possible demonstration of dynamic nuclear spin polarisation. No experiments to date have exploited the use of P-donors to form a magnetic field gradient. It will be important to see if one can form a stable and repeatable magnetic field gradient across the P-donor dot qubits. Recent experiments have shown that nuclear spins can flip when loading electrons onto the dots, thus, further investigation is required [39, 50].

- The measurement of coherence times and spin lifetimes. Evidently any long-term proposal requires long spin coherence times and lifetimes.

- The development of higher internal quality factor (above 1600) superconducting resonators for high fidelity single-gate RF spin readout along with their eventual miniaturisation to ensure many superconducting resonators can fit near the device.

- The development of deterministic incorporation techniques will enable reproducible dots, reliable dot sizes and precise locations of individual P-donors. In achieving all three facets, one should be able to reliably set the tunnel couplings on all qubits during fabrication.

- The experimental measurement of gate-to-gate current leakage profiles for leads across multiple vertically separated device layers as proposed for the 2D array. If the available gate voltage range is consistently too small, then one needs to redesign the proposed architecture.

- The experimental measurement of the gate lever-arms and potential offsets due to different P-donor clusters and distances from their reservoir. Better modelling of the offsets and gate lever-arms will enable more optimal geometries with smaller voltages on the gates to access the required charge states for qubit operation.

Despite the many experimental milestones that lie ahead, the results and theoretical work in this thesis have validated the feasibility in pursuing a many-qubit singlet-triplet architecture using Si-P quantum dots.

Bibliography

[1] Gene H. Golub and Charles F. Van Loan. *Matrix Computations (Johns Hopkins Studies in the Mathematical Sciences)*. Johns Hopkins University Press, 2013.

[2] Richard P. Feynman. Simulating physics with computers. *International Journal of Theoretical Physics*, **21**, 467 (1982). DOI: 10.1007/bf02650179.

[3] P.W. Shor. Algorithms for quantum computation: discrete logarithms and factoring. In *Proceedings 35th Annual Symposium on Foundations of Computer Science*. IEEE Comput. Soc. Press. DOI: 10.1109/sfcs.1994.365700.

[4] Lov K. Grover. A fast quantum mechanical algorithm for database search. In *Proceedings of the twenty-eighth annual ACM symposium on Theory of computing - STOC '96*. ACM Press, 1996. DOI: 10.1145/237814.237866.

[5] Lieven M. K. Vandersypen, Matthias Steffen, Gregory Breyta, Costantino S. Yannoni, Mark H. Sherwood, and Isaac L. Chuang. Experimental realization of Shor's quantum factoring algorithm using nuclear magnetic resonance. *Nature*, **414**, 883 (2001). DOI: 10.1038/414883a.

[6] Erik Lucero, R. Barends, Y. Chen, J. Kelly, M. Mariantoni, A. Megrant, P. O'Malley, D. Sank, A. Vainsencher, J. Wenner, T. White, Y. Yin, A. N. Cleland, and John M. Martinis. Computing prime factors with a Josephson phase qubit quantum processor. *Nature Physics*, **8**, 719 (2012). DOI: 10.1038/nphys2385.

[7] T. Monz, D. Nigg, E. A. Martinez, M. F. Brandl, P. Schindler, R. Rines, S. X. Wang, I. L. Chuang, and R. Blatt. Realization of a scalable Shor algorithm. *Science*, **351**, 1068 (2016). DOI: 10.1126/science.aad9480.

[8] Austin G. Fowler, Matteo Mariantoni, John M. Martinis, and Andrew N. Cleland. Surface codes: Towards practical large-scale quantum computation. *Physical Review A*, **86** (2012). DOI: 10.1103/physreva.86.032324.

[9] Christopher Monroe. IonQ. Quantum for Business), 2018.

[10] Dario Gil. The Future of Computing: AI and Quantum. IEEE Industry Summit (IEEE Rebooting Computing), 2017.

[11] Julian Kelly, Zijun Chen, Ben Chiaro, Brooks Foxen, and John M. Martinis. Operating and Characterizing of a 72 Superconducting Qubit Processor "Bristlecone". APS March meeting, 2019.

[12] A. C. Johnson, J. R. Petta, J. M. Taylor, A. Yacoby, M. D. Lukin, C. M. Marcus, M. P. Hanson, and A. C. Gossard. Triplet–singlet spin relaxation via nuclei in a double quantum dot. *Nature*, **435**, 925 (2005). DOI: 10.1038/nature03815.

[13] J. R. Petta. Coherent Manipulation of Coupled Electron Spins in Semiconductor Quantum Dots. *Science*, **309**, 2180 (2005). DOI: 10.1126/science.1116955.

[14] M. D. Shulman, O. E. Dial, S. P. Harvey, H. Bluhm, V. Umansky, and A. Yacoby. Demonstration of Entanglement of Electrostatically Coupled Singlet-Triplet Qubits. *Science*, **336**, 202 (2012). DOI: 10.1126/science.1217692.

[15] Martin Fuechsle, Jill A. Miwa, Suddhasatta Mahapatra, Hoon Ryu, Sunhee Lee, Oliver Warschkow, Lloyd C. L. Hollenberg, Gerhard Klimeck, and Michelle Y. Simmons. A single-atom transistor. *Nat Nano*, **7**, 242 (2012). DOI: 10.1038/nnano.2012.21.

[16] Jarryd J. Pla, Kuan Y. Tan, Juan P. Dehollain, Wee H. Lim, John J. L. Morton, David N. Jamieson, Andrew S. Dzurak, and Andrea Morello. A single-atom electron spin qubit in silicon. *Nature*, **489**, 541 (2012). DOI: 10.1038/nature11449.

[17] X. Wu, D. R. Ward, J. R. Prance, D. Kim, J. K. Gamble, R. T. Mohr, Z. Shi, D. E. Savage, M. G. Lagally, M. Friesen, S. N. Coppersmith, and M. A. Eriksson. Two-axis control of a singlet-triplet qubit with an integrated micromagnet. *Proceedings of the National Academy of Sciences*, **111**, 11938 (2014). DOI: 10.1073/pnas.1412230111.

[18] Jun Yoneda, Kenta Takeda, Tomohiro Otsuka, Takashi Nakajima, Matthieu R. Delbecq, Giles Allison, Takumu Honda, Tetsuo Kodera, Shunri Oda, Yusuke

Hoshi, Noritaka Usami, Kohei M. Itoh, and Seigo Tarucha. A quantum-dot spin qubit with coherence limited by charge noise and fidelity higher than 99.9%. *Nature Nanotechnology*, **13**, 102 (2017). DOI: 10.1038/s41565-017-0014-x.

[19] T. Hensgens, T. Fujita, L. Janssen, Xiao Li, C. J. Van Diepen, C. Reichl, W. Wegscheider, S. Das Sarma, and L. M. K. Vandersypen. Quantum simulation of a Fermi–Hubbard model using a semiconductor quantum dot array. *Nature*, **548**, 70 (2017). DOI: 10.1038/nature23022.

[20] M. A. McCord. Lithography with the scanning tunneling microscope. *Journal of Vacuum Science & Technology B: Microelectronics and Nanometer Structures*, **4**, 86 (1986). DOI: 10.1116/1.583400.

[21] Ph. Avouris, R.E. Walkup, A.R. Rossi, T.-C. Shen, G.C. Abeln, J.R. Tucker, and J.W. Lyding. STM-induced H atom desorption from Si(100): isotope effects and site selectivity. *Chemical Physics Letters*, **257**, 148 (1996). DOI: 10.1016/0009-2614(96)00518-0.

[22] J.W. Lyding. UHV STM nanofabrication: progress, technology spin-offs, and challenges. *Proceedings of the IEEE*, **85**, 589 (1997). DOI: 10.1109/5.573743.

[23] Lars Oberbeck, Neil J. Curson, Steven R. Schofield, Toby Hallam, Michelle Y. Simmons, and Robert G. Clark. Challenges in Surface Science for a P-in-Si Quantum Computer — Phosphine Adsorption/Incorporation and Epitaxial Si Encapsulation. *Surface Review and Letters*, **10**, 415 (2003). DOI: 10.1142/s0218625x03005098.

[24] Michelle Y. Simmons, Steven R. Schofield, Jeremy L. O'Brien, Neil J. Curson, Lars Oberbeck, T. Hallam, and Robert G. Clark. Towards the atomic-scale fabrication of a silicon-based solid state quantum computer. *Surface Science*, **532-535**, 1209 (2003). DOI: 10.1016/s0039-6028(03)00485-0.

[25] Frank J. Ruess, Lars Oberbeck, Michelle Y. Simmons, Kuan Eng J. Goh, Alex R. Hamilton, Toby Hallam, Steven R. Schofield, Neil J. Curson, and Robert G. Clark. Toward Atomic-Scale Device Fabrication in Silicon Using Scanning Probe Microscopy. *Nano Letters*, **4**, 1969 (2004). DOI: 10.1021/nl048808v.

[26] Toby Hallam, Neil J. Curson, Lars Oberbeck, and Michelle Y. Simmons. STM characterization of phosphine adsorption on STM-patterned H:Si(001)surfaces. In Jung-Chih Chiao, David N. Jamieson, Lorenzo Faraone, and Andrew S.

Dzurak, editors, *Micro- and Nanotechnology: Materials, Processes, Packaging, and Systems II*. SPIE (2005). DOI: 10.1117/12.583316.

[27] B. Weber, S. Mahapatra, H. Ryu, S. Lee, A. Fuhrer, T. C. G. Reusch, D. L. Thompson, W. C. T. Lee, G. Klimeck, L. C. L. Hollenberg, and M. Y. Simmons. Ohm's Law Survives to the Atomic Scale. *Science*, **335**, 64 (2012). DOI: 10.1126/science.1214319.

[28] Charles D. Hill, Eldad Peretz, Samuel J. Hile, Matthew G. House, Martin Fuechsle, Sven Rogge, Michelle Y. Simmons, and Lloyd C. L. Hollenberg. A surface code quantum computer in silicon. *Science Advances*, **1**, e1500707 (2015). DOI: 10.1126/sciadv.1500707.

[29] Prasanna Pakkiam, Matthew G. House, Matthias Koch, and Michelle Y. Simmons. Characterization of a Scalable Donor-Based Singlet–Triplet Qubit Architecture in Silicon. *Nano Letters*, **18**, 4081 (2018). DOI: 10.1021/acs.nanolett.8b00006.

[30] M. G. House, T. Kobayashi, B. Weber, S. J. Hile, T. F. Watson, J. van der Heijden, S. Rogge, and M. Y. Simmons. Radio frequency measurements of tunnel couplings and singlet–triplet spin states in Si:P quantum dots. *Nature Communications*, **6** (2015). DOI: 10.1038/ncomms9848.

[31] M. G. House, I. Bartlett, P. Pakkiam, M. Koch, E. Peretz, J. van der Heijden, T. Kobayashi, S. Rogge, and M. Y. Simmons. High-Sensitivity Charge Detection with a Single-Lead Quantum Dot for Scalable Quantum Computation. *Physical Review Applied*, **6** (2016). DOI: 10.1103/physrevapplied.6.044016.

[32] P. Pakkiam, A. V. Timofeev, M. G. House, M. R. Hogg, T. Kobayashi, M. Koch, S. Rogge, and M. Y. Simmons. Single-Shot Single-Gate rf Spin Readout in Silicon. *Physical Review X*, **8** (2018). DOI: 10.1103/physrevx.8.041032.

[33] Michael Dean Shulman. *Entanglement and Metrology with Singlet-Triplet Qubits*. PhD thesis, Harvard School of Physics, Cambridge, Massachusetts (2015).

[34] John M. Nichol, Lucas A. Orona, Shannon P. Harvey, Saeed Fallahi, Geoffrey C. Gardner, Michael J. Manfra, and Amir Yacoby. High-fidelity entangling gate for double-quantum-dot spin qubits. *npj Quantum Information*, **3** (2017). DOI: 10.1038/s41534-016-0003-1.

[35] R. K. L. Colmenar and J. P. Kestner. Stroboscopically robust gates for capacitively coupled singlet-triplet qubits. *Physical Review A*, **99** (2019). DOI: 10.1103/physreva.99.012347.

[36] S. Blanvillain, J. I. Colless, D. J. Reilly, H. Lu, and A. C. Gossard. Suppressing on-chip electromagnetic crosstalk for spin qubit devices. *Journal of Applied Physics*, **112**, 064315 (2012). DOI: 10.1063/1.4752863.

[37] D.P. Franke, J.S. Clarke, L.M.K. Vandersypen, and M. Veldhorst. Rent's rule and extensibility in quantum computing. *Microprocessors and Microsystems*, **67**, 1 (2019). DOI: 10.1016/j.micpro.2019.02.006.

[38] B. E. Kane. *Nature*, **393**, 133 (1998). DOI: 10.1038/30156.

[39] Juha T. Muhonen, Juan P. Dehollain, Arne Laucht, Fay E. Hudson, Rachpon Kalra, Takeharu Sekiguchi, Kohei M. Itoh, David N. Jamieson, Jeffrey C. McCallum, Andrew S. Dzurak, and Andrea Morello. Storing quantum information for 30 seconds in a nanoelectronic device. *Nature Nanotechnology*, **9**, 986 (2014). DOI: 10.1038/nnano.2014.211.

[40] J. R. Petta, J. M. Taylor, A. C. Johnson, A. Yacoby, M. D. Lukin, C. M. Marcus, M. P. Hanson, and A. C. Gossard. Dynamic Nuclear Polarization with Single Electron Spins. *Physical Review Letters*, **100** (2008). DOI: 10.1103/physrevlett.100.067601.

[41] M. D. Shulman, S. P. Harvey, J. M. Nichol, S. D. Bartlett, A. C. Doherty, V. Umansky, and A. Yacoby. Suppressing qubit dephasing using real-time Hamiltonian estimation. *Nature Communications*, **5** (2014). DOI: 10.1038/ncomms6156.

[42] J. M. Taylor, H.-A. Engel, W. Dür, A. Yacoby, C. M. Marcus, P. Zoller, and M. D. Lukin. Fault-tolerant architecture for quantum computation using electrically controlled semiconductor spins. *Nature Physics*, **1**, 177 (2005). DOI: 10.1038/nphys174.

[43] Samuel Earnshaw. On the Nature of the Molecular Forces which Regulate the Constitution of the Luminiferous Ether. *Trans. Camb. Phil. Soc.*, **7**, 97, 1842.

[44] Wolfgang Paul and Helmut Steinwedel. Notizen: Ein neues Massenspektrometer ohne Magnetfeld. *Zeitschrift für Naturforschung A*, **8** (1953). DOI: 10.1515/zna-1953-0710.

[45] C. Monroe and J. Kim. Scaling the Ion Trap Quantum Processor. *Science*, **339**, 1164 (2013). DOI: 10.1126/science.1231298.

[46] J. Zhang, G. Pagano, P. W. Hess, A. Kyprianidis, P. Becker, H. Kaplan, A. V. Gorshkov, Z.-X. Gong, and C. Monroe. Observation of a many-body dynamical phase transition with a 53-qubit quantum simulator. *Nature*, **551**, 601 (2017). DOI: 10.1038/nature24654.

[47] Yasuhiro Tokura, Wilfred G. van der Wiel, Toshiaki Obata, and Seigo Tarucha. Coherent Single Electron Spin Control in a Slanting Zeeman Field. *Physical Review Letters*, **96** (2006). DOI: 10.1103/physrevlett.96.047202.

[48] E. Zavoisky. Spin-magnetic resonance in paramagnetics. *J Phys USSR*, **9**, 211, 1945.

[49] P. London, P. Balasubramanian, B. Naydenov, L. P. McGuinness, and F. Jelezko. Strong driving of a single spin using arbitrarily polarized fields. *Physical Review A*, **90** (2014). DOI: 10.1103/physreva.90.012302.

[50] Samuel J. Hile, Lukas Fricke, Matthew G. House, Eldad Peretz, Chin Yi Chen, Yu Wang, Matthew Broome, Samuel K. Gorman, Joris G. Keizer, Rajib Rahman, and Michelle Y. Simmons. Addressable electron spin resonance using donors and donor molecules in silicon. *Science Advances*, **4**, eaaq1459 (2018). DOI: 10.1126/sciadv.aaq1459.

[51] H. Malissa, D. I. Schuster, A. M. Tyryshkin, A. A. Houck, and S. A. Lyon. Superconducting coplanar waveguide resonators for low temperature pulsed electron spin resonance spectroscopy. *Review of Scientific Instruments*, **84**, 025116 (2013). DOI: 10.1063/1.4792205.

[52] M. Veldhorst, J. C. C. Hwang, C. H. Yang, A. W. Leenstra, B. de Ronde, J. P. Dehollain, J. T. Muhonen, F. E. Hudson, K. M. Itoh, A. Morello, and A. S. Dzurak. An addressable quantum dot qubit with fault-tolerant control-fidelity. *Nature Nanotechnology*, **9**, 981 (2014). DOI: 10.1038/nnano.2014.216.

[53] Jarryd James Pla. *Single atom spin qubits in silicon*. PhD thesis, 2013.

[54] D. M. Zajac, A. J. Sigillito, M. Russ, F. Borjans, J. M. Taylor, G. Burkard, and J. R. Petta. Resonantly driven CNOT gate for electron spins. *Science*, **359**, 439 (2017). DOI: 10.1126/science.aao5965.

[55] T. F. Watson, S. G. J. Philips, E. Kawakami, D. R. Ward, P. Scarlino, M. Veldhorst, D. E. Savage, M. G. Lagally, Mark Friesen, S. N. Coppersmith, M. A. Eriksson, and L. M. K. Vandersypen. A programmable two-qubit quantum processor in silicon. *Nature*, **555**, 633 (2018). DOI: 10.1038/nature25766.

[56] Thomas F. Watson, Bent Weber, Yu-Ling Hsueh, Lloyd C. L. Hollenberg, Rajib Rahman, and Michelle Y. Simmons. Atomically engineered electron spin lifetimes of 30 s in silicon. *Science Advances*, **3**, e1602811 (2017). DOI: 10.1126/sciadv.1602811.

[57] K. D. Petersson, C. G. Smith, D. Anderson, P. Atkinson, G. A. C. Jones, and D. A. Ritchie. Charge and Spin State Readout of a Double Quantum Dot Coupled to a Resonator. *Nano Letters*, **10**, 2789 (2010). DOI: 10.1021/nl100663w.

[58] Takeshi Ota, Kenichi Hitachi, and Koji Muraki. Landau-Zener-Stückelberg interference in coherent charge oscillations of a one-electron double quantum dot. *Scientific Reports*, **8** (2018). DOI: 10.1038/s41598-018-23468-2.

[59] E. A. Laird, J. M. Taylor, D. P. DiVincenzo, C. M. Marcus, M. P. Hanson, and A. C. Gossard. Coherent spin manipulation in an exchange-only qubit. *Physical Review B*, **82** (2010). DOI: 10.1103/physrevb.82.075403.

[60] Zhan Shi, C. B. Simmons, J. R. Prance, John King Gamble, Teck Seng Koh, Yun-Pil Shim, Xuedong Hu, D. E. Savage, M. G. Lagally, M. A. Eriksson, Mark Friesen, and S. N. Coppersmith. Fast Hybrid Silicon Double-Quantum-Dot Qubit. *Physical Review Letters*, **108** (2012). DOI: 10.1103/physrevlett.108.140503.

[61] Mark Friesen, Joydip Ghosh, M. A. Eriksson, and S. N. Coppersmith. A decoherence-free subspace in a charge quadrupole qubit. *Nature Communications*, **8**, 15923 (2017). DOI: 10.1038/ncomms15923.

[62] Timothy B. Boykin, Gerhard Klimeck, M. A. Eriksson, Mark Friesen, S. N. Coppersmith, Paul von Allmen, Fabiano Oyafuso, and Seungwon Lee. Valley splitting in strained silicon quantum wells. *Applied Physics Letters*, **84**, 115 (2004). DOI: 10.1063/1.1637718.

[63] Srijit Goswami, K. A. Slinker, Mark Friesen, L. M. McGuire, J. L. Truitt, Charles Tahan, L. J. Klein, J. O. Chu, P. M. Mooney, D. W. van der Weide,

Robert Joynt, S. N. Coppersmith, and Mark A. Eriksson. Controllable valley splitting in silicon quantum devices. *Nature Physics*, **3**, 41 (2006). DOI: 10.1038/nphys475.

[64] Ryan M. Jock, N. Tobias Jacobson, Patrick Harvey-Collard, Andrew M. Mounce, Vanita Srinivasa, Dan R. Ward, John Anderson, Ron Manginell, Joel R. Wendt, Martin Rudolph, Tammy Pluym, John King Gamble, Andrew D. Baczewski, Wayne M. Witzel, and Malcolm S. Carroll. A silicon metal-oxide-semiconductor electron spin-orbit qubit. *Nature Communications*, **9** (2018). DOI: 10.1038/s41467-018-04200-0.

[65] Rifat Ferdous, Kok W. Chan, Menno Veldhorst, J. C. C. Hwang, C. H. Yang, Harshad Sahasrabudhe, Gerhard Klimeck, Andrea Morello, Andrew S. Dzurak, and Rajib Rahman. Interface-induced spin-orbit interaction in silicon quantum dots and prospects for scalability. *Physical Review B*, **97** (2018). DOI: 10.1103/physrevb.97.241401.

[66] W. Huang, C. H. Yang, K. W. Chan, T. Tanttu, B. Hensen, R. C. C. Leon, M. A. Fogarty, J. C. C. Hwang, F. E. Hudson, K. M. Itoh, A. Morello, A. Laucht, and A. S. Dzurak. Fidelity benchmarks for two-qubit gates in silicon. *Nature*, **569**, 532 (2019). DOI: 10.1038/s41586-019-1197-0.

[67] M. Veldhorst, C. H. Yang, J. C. C. Hwang, W. Huang, J. P. Dehollain, J. T. Muhonen, S. Simmons, A. Laucht, F. E. Hudson, K. M. Itoh, A. Morello, and A. S. Dzurak. A two-qubit logic gate in silicon. *Nature*, **526**, 410 (2015). DOI: 10.1038/nature15263.

[68] Andreas V. Kuhlmann, Julien Houel, Arne Ludwig, Lukas Greuter, Dirk Reuter, Andreas D. Wieck, Martino Poggio, and Richard J. Warburton. Charge noise and spin noise in a semiconductor quantum device. *Nature Physics*, **9**, 570 (2013). DOI: 10.1038/nphys2688.

[69] O. E. Dial, M. D. Shulman, S. P. Harvey, H. Bluhm, V. Umansky, and A. Yacoby. Charge Noise Spectroscopy Using Coherent Exchange Oscillations in a Singlet-Triplet Qubit. *Physical Review Letters*, **110** (2013). DOI: 10.1103/physrevlett.110.146804.

[70] S. P. Harvey, C. G. L. Bøttcher, L. A. Orona, S. D. Bartlett, A. C. Doherty, and A. Yacoby. Coupling two spin qubits with a high-impedance resonator. *Physical Review B*, **97** (2018). DOI: 10.1103/physrevb.97.235409.

[71] Jessica van Donkelaar, C Yang, A D C Alves, J C McCallum, C Hougaard, B C Johnson, F E Hudson, A S Dzurak, A Morello, D Spemann, and D N Jamieson. Single atom devices by ion implantation. *Journal of Physics: Condensed Matter*, **27**, 154204 (2015). DOI: 10.1088/0953-8984/27/15/154204.

[72] S. R. McKibbin, W. R. Clarke, A. Fuhrer, T. C. G. Reusch, and M. Y. Simmons. Investigating the regrowth surface of Si:P δ-layers toward vertically stacked three dimensional devices. *Applied Physics Letters*, **95**, 233111 (2009). DOI: 10.1063/1.3269924.

[73] S. R. McKibbin, C. M. Polley, G. Scappucci, J. G. Keizer, and M. Y. Simmons. Low resistivity, super-saturation phosphorus-in-silicon monolayer doping. *Applied Physics Letters*, **104**, 123502 (2014). DOI: 10.1063/1.4869111.

[74] Joris G. Keizer, Sarah R. McKibbin, and Michelle Y. Simmons. The Impact of Dopant Segregation on the Maximum Carrier Density in Si:P Multilayers. *ACS Nano*, **9**, 7080 (2015). DOI: 10.1021/acsnano.5b01638.

[75] Joris G. Keizer, Sebastian Koelling, Paul M. Koenraad, and Michelle Y. Simmons. Suppressing Segregation in Highly Phosphorus Doped Silicon Monolayers. *ACS Nano*, **9**, 12537 (2015). DOI: 10.1021/acsnano.5b06299.

[76] Matthias Koch, Joris G. Keizer, Prasanna Pakkiam, Daniel Keith, Matthew G. House, Eldad Peretz, and Michelle Y. Simmons. Spin read-out in atomic qubits in an all-epitaxial three-dimensional transistor. *Nature Nanotechnology* (2019). DOI: 10.1038/s41565-018-0338-1.

[77] Fahd A. Mohiyaddin, Rajib Rahman, Rachpon Kalra, Gerhard Klimeck, Lloyd C. L. Hollenberg, Jarryd J. Pla, Andrew S. Dzurak, and Andrea Morello. Noninvasive Spatial Metrology of Single-Atom Devices. *Nano Letters*, **13**, 1903 (2013). DOI: 10.1021/nl303863s.

[78] Guilherme Tosi, Fahd A. Mohiyaddin, Vivien Schmitt, Stefanie Tenberg, Rajib Rahman, Gerhard Klimeck, and Andrea Morello. Silicon quantum processor with robust long-distance qubit couplings. *Nature Communications*, **8** (2017). DOI: 10.1038/s41467-017-00378-x.

[79] Mukunda P. Das and Frederick Green. Comments on "Ohm's Law Survives to the Atomic Scale" by Weber et al, 2012.

[80] H. Büch, S. Mahapatra, R. Rahman, A. Morello, and M. Y. Simmons. Spin readout and addressability of phosphorus-donor clusters in silicon. *Nature Communications*, **4** (2013). DOI: 10.1038/ncomms3017.

[81] Bent Weber, TanY H. Matthias, Suddhasatta Mahapatra, Thomas F. Watson, Hoon Ryu, Rajib Rahman, HollenbergLloyd C. L., Gerhard Klimeck, and Michelle Y. Simmons. Spin blockade and exchange in Coulomb-confined silicon double quantum dots. *Nat Nano*, **9**, 430 (2014). DOI: 10.1038/nnano.2014.63.

[82] M. A. Broome, S. K. Gorman, M. G. House, S. J. Hile, J. G. Keizer, D. Keith, C. D. Hill, T. F. Watson, W. J. Baker, L. C. L. Hollenberg, and M. Y. Simmons. Two-electron spin correlations in precision placed donors in silicon. *Nature Communications*, **9** (2018). DOI: 10.1038/s41467-018-02982-x.

[83] Yu Wang, Chin-Yi Chen, Gerhard Klimeck, Michelle Y. Simmons, and Rajib Rahman. Characterizing Si:P quantum dot qubits with spin resonance techniques. *Scientific Reports*, **6** (2016). DOI: 10.1038/srep31830.

[84] Yu Wang, Archana Tankasala, Lloyd C L Hollenberg, Gerhard Klimeck, Michelle Y Simmons, and Rajib Rahman. Highly tunable exchange in donor qubits in silicon. *npj Quantum Information*, **2** (2016). DOI: 10.1038/npjqi.2016.8.

[85] E. Kawakami, P. Scarlino, D. R. Ward, F. R. Braakman, D. E. Savage, M. G. Lagally, Mark Friesen, S. N. Coppersmith, M. A. Eriksson, and L. M. K. Vandersypen. Electrical control of a long-lived spin qubit in a Si/SiGe quantum dot. *Nature Nanotechnology*, **9**, 666 (2014). DOI: 10.1038/nnano.2014.153.

[86] Thomas Francis Watson. *Multi-qubit architectures for donor-based quantum computing*. PhD thesis, University of New South Wales, Sydney (2016).

[87] Gerhard Klimeck, Fabiano Oyafuso, Timothy Boykin, R. Bowen, and Paul Allmen. Development of a Nanoelectronic 3-D (NEMO 3-D) Simulator for Multimillion Atom Simulations and Its Application to Alloyed Quantum Dots (INVITED). *Computer Modeling in Engineering and Science*, **3**, 2002.

[88] P.A. Maksym, L.D. Hallam, and J. Weis. Models of quantum dots. *Physica B: Condensed Matter*, **212**, 213 (1995). DOI: 10.1016/0921-4526(95)00035-8.

[89] W. G. van der Wiel, S. De Franceschi, J. M. Elzerman, T. Fujisawa, S. Tarucha, and L. P. Kouwenhoven. Electron transport through double quantum dots. *Reviews of Modern Physics*, **75**, 1 (2002). DOI: 10.1103/revmodphys.75.1.

[90] Jonathan P. Bird, editor. *Electron Transport in Quantum Dots*. Springer US, 2003. DOI: 10.1007/978-1-4615-0437-5.

[91] N. F. Johnson and M. C. Payne. Many-body effects in resonant tunneling through quantum dots. *Physical Review B*, **45**, 3819 (1992). DOI: 10.1103/physrevb.45.3819.

[92] Bent Weber. *Towards scalable planar donor-based silicon quantum computing architectures*. PhD thesis, University of New South Wales, Sydney (2013).

[93] Travis S Humble, M Nance Ericson, Jacek Jakowski, Jingsong Huang, Charles Britton, Franklin G Curtis, Eugene F Dumitrescu, Fahd A Mohiyaddin, and Bobby G Sumpter. A computational workflow for designing silicon donor qubits. *Nanotechnology*, **27**, 424002 (2016). DOI: 10.1088/0957-4484/27/42/424002.

[94] Belita Koiller, Xuedong Hu, and S. Das Sarma. Exchange in Silicon-Based Quantum Computer Architecture. *Physical Review Letters*, **88** (2001). DOI: 10.1103/physrevlett.88.027903.

[95] J. S. Smith, A. Budi, M. C. Per, N. Vogt, D. W. Drumm, L. C. L. Hollenberg, J. H. Cole, and S. P. Russo. Ab initio calculation of energy levels for phosphorus donors in silicon. *Scientific Reports*, **7** (2017). DOI: 10.1038/s41598-017-06296-8.

[96] S. K. Gorman, Y. He, M. G. House, J. G. Keizer, D. Keith, L. Fricke, S. J. Hile, M. A. Broome, and M. Y. Simmons. Tunneling Statistics for Analysis of Spin-Readout Fidelity. *Physical Review Applied*, **8** (2017). DOI: 10.1103/physrevapplied.8.034019.

[97] S. K. Gorman, M. A. Broome, M. G. House, S. J. Hile, J. G. Keizer, D. Keith, T. F. Watson, W. J. Baker, and M. Y. Simmons. Singlet-triplet minus mixing and relaxation lifetimes in a double donor dot. *Applied Physics Letters*, **112**, 243105 (2018). DOI: 10.1063/1.5021500.

[98] M. Fuechsle, J. A. Miwa, S. Mahapatra, H. Ryu, S. Lee, O. Warschkow, L. C. L. Hollenberg, G. Klimeck, and M. Y. Simmons. Spectroscopy of a deterministic single-donor device in silicon. In *Quantum Information and Computation X*. SPIE (2012). DOI: 10.1117/12.919763.

[99] M. G. House, E. Peretz, J. G. Keizer, S. J. Hile, and M. Y. Simmons. Single-charge detection by an atomic precision tunnel junction. *Applied Physics Letters*, **104**, 113111 (2014). DOI: 10.1063/1.4869032.

[100] Wilson Pok. *Atomically Abrupt, Highly-Doped, Coplanar Nanogaps in Silicon*. PhD thesis, University of New South Wales, Sydney (2011).

[101] Martin Maximilian Fuechsle. *Precision few-electron silicon quantum dots*. PhD thesis, University of New South Wales, Sydney (2011).

[102] C. H. Yang, A. Rossi, N. S. Lai, R. Leon, W. H. Lim, and A. S. Dzurak. Charge state hysteresis in semiconductor quantum dots. *Applied Physics Letters*, **105**, 183505 (2014). DOI: 10.1063/1.4901218.

[103] Ted Thorbeck and Neil M. Zimmerman. Determining the location and cause of unintentional quantum dots in a nanowire. *Journal of Applied Physics*, **111**, 064309 (2012). DOI: 10.1063/1.3692387.

[104] Patrick Harvey-Collard, Benjamin D'Anjou, Martin Rudolph, N. Tobias Jacobson, Jason Dominguez, Gregory A. Ten Eyck, Joel R. Wendt, Tammy Pluym, Michael P. Lilly, William A. Coish, Michel Pioro-Ladrière, and Malcolm S. Carroll. High-Fidelity Single-Shot Readout for a Spin Qubit via an Enhanced Latching Mechanism. *Physical Review X*, **8** (2018). DOI: 10.1103/physrevx.8.021046.

[105] M. D. Schroer, M. Jung, K. D. Petersson, and J. R. Petta. Radio Frequency Charge Parity Meter. *Physical Review Letters*, **109** (2012). DOI: 10.1103/physrevlett.109.166804.

[106] Qin Liu, Yanhua Lei, Xiji Shao, Fangfei Ming, Hu Xu, Kedong Wang, and Xudong Xiao. Controllable dissociations of PH3molecules on Si(001). *Nanotechnology*, **27**, 135704 (2016). DOI: 10.1088/0957-4484/27/13/135704.

[107] David P. DiVincenzo. The Physical Implementation of Quantum Computation. *Fortschritte der Physik*, **48**, 771 (2000). DOI: 10.1002/1521-3978(200009)48:9/11<771::aid-prop771>3.0.co;2-e.

[108] M. Veldhorst, H. G. J. Eenink, C. H. Yang, and A. S. Dzurak. Silicon CMOS architecture for a spin-based quantum computer. *Nature Communications*, **8** (2017). DOI: 10.1038/s41467-017-01905-6.

[109] F. Persson, C. M. Wilson, M. Sandberg, G. Johansson, and P. Delsing. Excess Dissipation in a Single-Electron Box: The Sisyphus Resistance. *Nano Letters*, **10**, 953 (2010). DOI: 10.1021/nl903887x.

[110] M. F. Gonzalez-Zalba, S. Barraud, A. J. Ferguson, and A. C. Betz. Probing the limits of gate-based charge sensing. *Nature Communications*, **6** (2015). DOI: 10.1038/ncomms7084.

[111] J. M. Elzerman, R. Hanson, L. H. Willems van Beveren, B. Witkamp, L. M. K. Vandersypen, and L. P. Kouwenhoven. Single-shot read-out of an individual electron spin in a quantum dot. *Nature*, **430**, 431 (2004). DOI: 10.1038/nature02693.

[112] Andrea Morello, Jarryd J. Pla, Floris A. Zwanenburg, Kok W. Chan, Kuan Y. Tan, Hans Huebl, Mikko Möttönen, Christopher D. Nugroho, Changyi Yang, Jessica A. van Donkelaar, Andrew D. C. Alves, David N. Jamieson, Christopher C. Escott, Lloyd C. L. Hollenberg, Robert G. Clark, and Andrew S. Dzurak. Single-shot readout of an electron spin in silicon. *Nature*, **467**, 687 (2010). DOI: 10.1038/nature09392.

[113] Frederico Martins, Filip K. Malinowski, Peter D. Nissen, Saeed Fallahi, Geoffrey C. Gardner, Michael J. Manfra, Charles M. Marcus, and Ferdinand Kuemmeth. Negative Spin Exchange in a Multielectron Quantum Dot. *Physical Review Letters*, **119** (2017). DOI: 10.1103/physrevlett.119.227701.

[114] Takashi Nakajima, Akito Noiri, Jun Yoneda, Matthieu R. Delbecq, Peter Stano, Tomohiro Otsuka, Kenta Takeda, Shinichi Amaha, Giles Allison, Kento Kawasaki, Arne Ludwig, Andreas D. Wieck, Daniel Loss, and Seigo Tarucha. Quantum non-demolition measurement of an electron spin qubit. *Nature Nanotechnology* (2019). DOI: 10.1038/s41565-019-0426-x.

[115] T. A. Fulton and G. J. Dolan. Observation of single-electron charging effects in small tunnel junctions. *Physical Review Letters*, **59**, 109 (1987). DOI: 10.1103/physrevlett.59.109.

[116] Henk van Houten and Carlo Beenakker. Quantum Point Contacts. *Physics Today*, **49**, 22 (1996). DOI: 10.1063/1.881503.

[117] D. J. Reilly, C. M. Marcus, M. P. Hanson, and A. C. Gossard. Fast single-charge sensing with a rf quantum point contact. *Applied Physics Letters*, **91**, 162101 (2007). DOI: 10.1063/1.2794995.

[118] B. J. van Wees, H. van Houten, C. W. J. Beenakker, J. G. Williamson, L. P. Kouwenhoven, D. van der Marel, and C. T. Foxon. Quantized conductance of point contacts in a two-dimensional electron gas. *Physical Review Letters*, **60**, 848 (1988). DOI: 10.1103/physrevlett.60.848.

[119] Tsuneya Ando, Alan B. Fowler, and Frank Stern. Electronic properties of two-dimensional systems. *Reviews of Modern Physics*, **54**, 437 (1982). DOI: 10.1103/revmodphys.54.437.

[120] D A Wharam, T J Thornton, R Newbury, M Pepper, H Ahmed, J E F Frost, D G Hasko, D C Peacock, D A Ritchie, and G A C Jones. One-dimensional transport and the quantisation of the ballistic resistance. *Journal of Physics C: Solid State Physics*, **21**, L209 (1988). DOI: 10.1088/0022-3719/21/8/002.

[121] M. J. Matragrano, D. G. Ast, G. P. Watson, and J. R. Shealy. Measurement of the mean free path of dislocation glide in the InGaAs/GaAs materials system. *Journal of Applied Physics*, **79**, 776, 1996. DOI: 10.1063/1.360824.

[122] K. E. J. Goh, L. Oberbeck, M. Y. Simmons, A. R. Hamilton, and M. J. Butcher. Influence of doping density on electronic transport in degenerate Si:Pδ-doped layers. *Physical Review B*, **73** (2006). DOI: 10.1103/physrevb.73.035401.

[123] L. A. Tracy, D. R. Luhman, S. M. Carr, N. C. Bishop, G. A. Ten Eyck, T. Pluym, J. R. Wendt, M. P. Lilly, and M. S. Carroll. Single shot spin readout using a cryogenic high-electron-mobility transistor amplifier at sub-Kelvin temperatures. *Applied Physics Letters*, **108**, 063101 (2016). DOI: 10.1063/1.4941421.

[124] C R Cosens. A balance-detector for alternating-current bridges. *Proceedings of the Physical Society*, **46**, 818 (1934). DOI: 10.1088/0959-5309/46/6/310.

[125] Walter C. Michels and Norma L. Curtis. A Pentode Lock-In Amplifier of High Frequency Selectivity. *Review of Scientific Instruments*, **12**, 444 (1941). DOI: 10.1063/1.1769919.

[126] R. J. Schoelkopf. The Radio-Frequency Single-Electron Transistor (RF-SET): A Fast and Ultrasensitive Electrometer. *Science*, **280**, 1238 (1998). DOI: 10.1126/science.280.5367.1238.

[127] C. Barthel, D. J. Reilly, C. M. Marcus, M. P. Hanson, and A. C. Gossard. Rapid Single-Shot Measurement of a Singlet-Triplet Qubit. *Physical Review Letters*, **103** (2009). DOI: 10.1103/physrevlett.103.160503.

[128] Joseph Cheney Bardin. *Silicon-Germanium Heterojunction Bipolar Transistors For Extremely Low-Noise Applications*. PhD thesis, California Institute of Technology, Pasadena, California (2009).

[129] A. Wallraff, D. I. Schuster, A. Blais, L. Frunzio, J. Majer, M. H. Devoret, S. M. Girvin, and R. J. Schoelkopf. Approaching Unit Visibility for Control of a Superconducting Qubit with Dispersive Readout. *Physical Review Letters*, **95** (2005). DOI: 10.1103/physrevlett.95.060501.

[130] Matias Urdampilleta, David J. Niegemann, Emmanuel Chanrion, Baptiste Jadot, Cameron Spence, Pierre-André Mortemousque, Christopher Bäuerle, Louis Hutin, Benoit Bertrand, Sylvain Barraud, Romain Maurand, Marc Sanquer, Xavier Jehl, Silvano De Franceschi, Maud Vinet, and Tristan Meunier. Gate-based high fidelity spin readout in a CMOS device. *Nature Nanotechnology* (2019). DOI: 10.1038/s41565-019-0443-9.

[131] J. I. Colless, A. C. Mahoney, J. M. Hornibrook, A. C. Doherty, H. Lu, A. C. Gossard, and D. J. Reilly. Dispersive Readout of a Few-Electron Double Quantum Dot with Fast rf Gate Sensors. *Physical Review Letters*, **110** (2013). DOI: 10.1103/physrevlett.110.046805.

[132] Anderson West, Bas Hensen, Alexis Jouan, Tuomo Tanttu, Chih-Hwan Yang, Alessandro Rossi, M. Fernando Gonzalez-Zalba, Fay Hudson, Andrea Morello, David J. Reilly, and Andrew S. Dzurak. Gate-based single-shot readout of spins in silicon. *Nature Nanotechnology* (2019). DOI: 10.1038/s41565-019-0400-7.

[133] Guoji Zheng, Nodar Samkharadze, Marc L. Noordam, Nima Kalhor, Delphine Brousse, Amir Sammak, Giordano Scappucci, and Lieven M. K. Vandersypen. Rapid gate-based spin read-out in silicon using an on-chip resonator. *Nature Nanotechnology* (2019). DOI: 10.1038/s41565-019-0488-9.

[134] Alexandre Blais, Ren-Shou Huang, Andreas Wallraff, S. M. Girvin, and R. J. Schoelkopf. Cavity quantum electrodynamics for superconducting electrical circuits: An architecture for quantum computation. *Physical Review A*, **69** (2004). DOI: 10.1103/physreva.69.062320.

[135] X. Mi, J. V. Cady, D. M. Zajac, P. W. Deelman, and J. R. Petta. Strong coupling of a single electron in silicon to a microwave photon. *Science*, **355**, 156 (2016). DOI: 10.1126/science.aal2469.

[136] X. Mi, J. V. Cady, D. M. Zajac, J. Stehlik, L. F. Edge, and J. R. Petta. Circuit quantum electrodynamics architecture for gate-defined quantum dots in silicon. *Applied Physics Letters*, **110**, 043502 (2017). DOI: 10.1063/1.4974536.

[137] J. M. Hornibrook, J. I. Colless, A. C. Mahoney, X. G. Croot, S. Blanvillain, H. Lu, A. C. Gossard, and D. J. Reilly. Frequency multiplexing for readout of spin qubits. *Appl. Phys. Lett.*, **104**, 103108 (2014). DOI: 10.1063/1.4868107.

[138] Imtiaz Ahmed, James A. Haigh, Simon Schaal, Sylvain Barraud, Yi Zhu, Chang-min Lee, Mario Amado, Jason W. A. Robinson, Alessandro Rossi, John J. L. Morton, and M. F. Gonzalez-Zalba. Radio-Frequency Capacitive Gate-Based Sensing. *Phys. Rev. Applied*, **10**, 014018 (2018). DOI: 10.1103/PhysRevApplied.10.014018.

[139] Ian Stuart Bartlett. Radio-frequency detection of electron charge in silicon-based qubits. Master's thesis, University of New South Wales, Sydney (2015).

[140] Jacques Carolan, Jasmin D. A. Meinecke, Peter J. Shadbolt, Nicholas J. Russell, Nur Ismail, Kerstin Wörhoff, Terry Rudolph, Mark G. Thompson, Jeremy L. O'Brien, Jonathan C. F. Matthews, and et al. On the experimental verification of quantum complexity in linear optics. *Nature Photonics*, **8**, 621–626 (2014). DOI: 10.1038/nphoton.2014.152.

[141] J. Carolan, C. Harrold, C. Sparrow, E. Martin-Lopez, N. J. Russell, J. W. Silverstone, P. J. Shadbolt, N. Matsuda, M. Oguma, M. Itoh, and et al. Universal linear optics. *Science*, **349**, 711–716 (2015). DOI: 10.1126/science.aab3642.

[142] Earl T. Campbell, Barbara M. Terhal, and Christophe Vuillot. Roads towards fault-tolerant universal quantum computation. *Nature*, **549**, 172–179 (2017). DOI: 10.1038/nature23460.

[143] T. F. Watson, B. Weber, M. G. House, H. Büch, and M. Y. Simmons. High-Fidelity Rapid Initialization and Read-Out of an Electron Spin via the Single DonorD-Charge State. *Physical Review Letters*, **115** (2015). DOI: 10.1103/physrevlett.115.166806.

[144] R. Barends, N. Vercruyssen, A. Endo, P. J. de Visser, T. Zijlstra, T. M. Klapwijk, P. Diener, S. J. C. Yates, and J. J. A. Baselmans. Minimal resonator loss for circuit quantum electrodynamics. *Applied Physics Letters*, **97**, 023508, 2010. DOI: 10.1063/1.3458705.

[145] Jonas Zmuidzinas. Superconducting Microresonators: Physics and Applications. *Annual Review of Condensed Matter Physics*, **3**, 169–214 (2012). DOI: 10.1146/annurev-conmatphys-020911-125022.

[146] N. Ares, F. J. Schupp, A. Mavalankar, G. Rogers, J. Griffiths, G. A. C. Jones, I. Farrer, D. A. Ritchie, C. G. Smith, A. Cottet, G. A. D. Briggs, and E. A. Laird. Sensitive Radio-Frequency Measurements of a Quantum Dot by Tuning to Perfect Impedance Matching. *Physical Review Applied*, **5** (2016). DOI: 10.1103/physrevapplied.5.034011.

[147] Peter Russer. *Electromagnetics, Microwave Circuit, And Antenna Design for Communications Engineering, Second Edition*. Artech House, Inc., Norwood, MA, USA, 2006.

[148] S. F. Babiker and R. Naeem. Shot Noise Suppression in Single Electron Transistors. *IEEE Transactions on Nanotechnology*, **11**, 1267 (2012). DOI: 10.1109/tnano.2012.2223713.

[149] A. P. Sears, A. Petrenko, G. Catelani, L. Sun, Hanhee Paik, G. Kirchmair, L. Frunzio, L. I. Glazman, S. M. Girvin, and R. J. Schoelkopf. Photon shot noise dephasing in the strong-dispersive limit of circuit QED. *Physical Review B*, **86** (2012). DOI: 10.1103/physrevb.86.180504.

[150] Tony J. Rouphael. *Wireless Receiver Architectures and Design: Antennas, RF, Synthesizers, Mixed Signal, and Digital Signal Processing*. Academic Press, 2018.

[151] Martin Sandberg, Michael R. Vissers, Jeffrey S. Kline, Martin Weides, Jiansong Gao, David S. Wisbey, and David P. Pappas. Etch induced microwave losses in titanium nitride superconducting resonators. *Applied Physics Letters*, **100**, 262605 (2012). DOI: 10.1063/1.4729623.

[152] R. Meservey and P. M. Tedrow. Properties of Very Thin Aluminum Films. *Journal of Applied Physics*, **42**, 51 (1971). DOI: 10.1063/1.1659648.

[153] Francesco Borsoi. Magnetic field resilient superconducting circuitelements for Majorana parity detection. Master's thesis, TU Delft, Delft, 2016.

[154] J.G. Kroll, F. Borsoi, K.L. van der Enden, W. Uilhoorn, D. de Jong, M. Quintero-Pérez, D.J. van Woerkom, A. Bruno, S.R. Plissard, D. Car, E.P.A.M. Bakkers, M.C. Cassidy, and L.P. Kouwenhoven. Magnetic-Field-Resilient Superconducting Coplanar-Waveguide Resonators for Hybrid Circuit

Quantum Electrodynamics Experiments. *Physical Review Applied*, **11** (2019). DOI: 10.1103/physrevapplied.11.064053.

[155] M. R. Hogg, M. G. House, P. Pakkiam, and M. Y. Simmons. A Cryogenic Semiconductor Microwave Modulator for Qubit Control. *Paper in review*, 2019.

[156] C. W. J. Beenakker. Theory of Coulomb-blockade oscillations in the conductance of a quantum dot. *Physical Review B*, **44**, 1646 (1991). DOI: 10.1103/physrevb.44.1646.

[157] Martin Füchsle. *Precision Few-Electron Silicon Quantum Dots*. PhD thesis, University of New South Wales, Sydney (2011).

[158] S. Das Sarma, Xin Wang, and Shuo Yang. Hubbard model description of silicon spin qubits: Charge stability diagram and tunnel coupling in Si double quantum dots. *Physical Review B*, **83** (2011). DOI: 10.1103/physrevb.83.235314.

[159] Samuel J. Hile, Matthew G. House, Eldad Peretz, Jan Verduijn, Daniel Widmann, Takashi Kobayashi, Sven Rogge, and Michelle Y. Simmons. Radio frequency reflectometry and charge sensing of a precision placed donor in silicon. *Applied Physics Letters*, **107**, 093504 (2015). DOI: 10.1063/1.4929827.

[160] J. R. Gavaler, D. W. Deis, J. K. Hulm, and C. K. Jones. Superconducting properties of Niobium-Titanium-Nitride thin films. *Applied Physics Letters*, **15**, 329 (1969). DOI: 10.1063/1.1652846.

[161] A. Klimov, W. Słysz, M. Guziewicz, V. Kolkovsky, M. Węgrzecki, J. Bar, M. Marchewka, and B. Seredyński. Critical current and electric transport properties of superconducting epitaxial Nb(Ti)N submicron structures. In Barbara Swatowska, Wojciech Maziarz, Tadeusz Pisarkiewicz, and Wojciech Kucewicz, editors, *Electron Technology Conference 2016*. SPIE (2016). DOI: 10.1117/12.2258216.

[162] B. M. Maune, M. G. Borselli, B. Huang, T. D. Ladd, P. W. Deelman, K. S. Holabird, A. A. Kiselev, I. Alvarado-Rodriguez, R. S. Ross, A. E. Schmitz, M. Sokolich, C. A. Watson, M. F. Gyure, and A. T. Hunter. Coherent singlet-triplet oscillations in a silicon-based double quantum dot. *Nature*, **481**, 344 (2012). DOI: 10.1038/nature10707.

[163] M. A. Broome, T. F. Watson, D. Keith, S. K. Gorman, M. G. House, J. G. Keizer, S. J. Hile, W. Baker, and M. Y. Simmons. High-Fidelity Single-Shot

Singlet-Triplet Readout of Precision-Placed Donors in Silicon. *Physical Review Letters*, **119** (2017). DOI: 10.1103/physrevlett.119.046802.

[164] B. D'Anjou and W. A. Coish. Optimal post-processing for a generic single-shot qubit readout. *Physical Review A*, **89** (2014). DOI: 10.1103/physreva.89.012313.

[165] Omid Noroozian. *Superconducting microwave resonator arrays for submillimeter/far-infrared imaging*. PhD thesis, California Institute of Technology (2012).

[166] G. Brassard and P. Hoyer. An exact quantum polynomial-time algorithm for Simon's problem. In *Proceedings of the Fifth Israeli Symposium on Theory of Computing and Systems*. IEEE Comput. Soc. DOI: 10.1109/istcs.1997.595153.

[167] Michael A. Nielsen and Isaac L. Chuang. *Quantum Computation and Quantum Information: 10th Anniversary Edition*. Cambridge University Press, New York, NY, USA, 10th edition, 2011.

[168] Christoph Dankert, Richard Cleve, Joseph Emerson, and Etera Livine. Exact and approximate unitary 2-designs and their application to fidelity estimation. *Physical Review A*, **80** (2009). DOI: 10.1103/physreva.80.012304.

[169] C. H. Yang, K. W. Chan, R. Harper, W. Huang, T. Evans, J. C. C. Hwang, B. Hensen, A. Laucht, T. Tanttu, F. E. Hudson, S. T. Flammia, K. M. Itoh, A. Morello, S. D. Bartlett, and A. S. Dzurak. Silicon qubit fidelities approaching incoherent noise limits via pulse engineering. *Nature Electronics*, **2**, 151 (2019). DOI: 10.1038/s41928-019-0234-1.

[170] Joseph Emerson. Designer pulses for better qubit gate operations. *Nature Electronics*, **2**, 140 (2019). DOI: 10.1038/s41928-019-0238-x.

[171] D. K. Wilson and G. Feher. Electron Spin Resonance Experiments on Donors in Silicon. III. Investigation of Excited States by the Application of Uniaxial Stress and Their Importance in Relaxation Processes. *Physical Review*, **124**, 1068 (1961). DOI: 10.1103/physrev.124.1068.

[172] Bent Weber, Yu-Ling Hsueh, Thomas F. Watson, Ruoyu Li, Alexander R. Hamilton, Lloyd C. L. Hollenberg, Rajib Rahman, and Michelle Y. Simmons. Spin–orbit coupling in silicon for electrons bound to donors. *npj Quantum Information*, **4** (2018). DOI: 10.1038/s41534-018-0111-1.

[173] Austin G. Fowler, Charles D. Hill, and Lloyd C. L. Hollenberg. Quantum-error correction on linear-nearest-neighbor qubit arrays. *Physical Review A*, **69** (2004). DOI: 10.1103/physreva.69.042314.

[174] Robert Raussendorf and Jim Harrington. Fault-Tolerant Quantum Computation with High Threshold in Two Dimensions. *Physical Review Letters*, **98** (2007). DOI: 10.1103/physrevlett.98.190504.

[175] Markus S. Kesselring, Fernando Pastawski, Jens Eisert, and Benjamin J. Brown. The boundaries and twist defects of the color code and their applications to topological quantum computation. *Quantum*, **2**, 101 (2018). DOI: 10.22331/q-2018-10-19-101.

[176] Austin G. Fowler. Two-dimensional color-code quantum computation. *Physical Review A*, **83** (2011). DOI: 10.1103/physreva.83.042310.

[177] Daniel Gottesman. The Heisenberg Representation of Quantum Computers. 1998.

[178] Sergey Bravyi and Alexei Kitaev. Universal quantum computation with ideal Clifford gates and noisy ancillas. *Physical Review A*, **71** (2005). DOI: 10.1103/physreva.71.022316.

[179] Luka Trifunovic, Oliver Dial, Mircea Trif, James R. Wootton, Rediet Abebe, Amir Yacoby, and Daniel Loss. Long-Distance Spin-Spin Coupling via Floating Gates. *Physical Review X*, **2** (2012). DOI: 10.1103/physrevx.2.011006.

[180] Joe O'Gorman, Naomi H Nickerson, Philipp Ross, John JL Morton, and Simon C Benjamin. A silicon-based surface code quantum computer. *npj Quantum Information*, **2** (2016). DOI: 10.1038/npjqi.2015.19.

[181] G. Pica, B. W. Lovett, R. N. Bhatt, T. Schenkel, and S. A. Lyon. Surface code architecture for donors and dots in silicon with imprecise and nonuniform qubit couplings. *Physical Review B*, **93** (2016). DOI: 10.1103/physrevb.93.035306.

[182] Patrick Harvey-Collard, N. Tobias Jacobson, Martin Rudolph, Jason Dominguez, Gregory A. Ten Eyck, Joel R. Wendt, Tammy Pluym, John King Gamble, Michael P. Lilly, Michel Pioro-Ladrière, and Malcolm S. Carroll. Coherent coupling between a quantum dot and a donor in silicon. *Nature Communications*, **8** (2017). DOI: 10.1038/s41467-017-01113-2.

[183] Nakul Shaji, C. B. Simmons, Madhu Thalakulam, Levente J. Klein, Hua Qin, H. Luo, D. E. Savage, M. G. Lagally, A. J. Rimberg, R. Joynt, M. Friesen, R. H. Blick, S. N. Coppersmith, and M. A. Eriksson. Spin blockade and lifetime-enhanced transport in a few-electron Si/SiGe double quantum dot. *Nature Physics*, **4**, 540 (2008). DOI: 10.1038/nphys988.

[184] N. Q. Vinh, P. T. Greenland, K. Litvinenko, B. Redlich, A. F. G. van der Meer, S. A. Lynch, M. Warner, A. M. Stoneham, G. Aeppli, D. J. Paul, C. R. Pidgeon, and B. N. Murdin. Silicon as a model ion trap: Time domain measurements of donor Rydberg states. *Proceedings of the National Academy of Sciences*, **105**, 10649 (2008). DOI: 10.1073/pnas.0802721105.

[185] S. Chick, N. Stavrias, K. Saeedi, B. Redlich, P. T. Greenland, G. Matmon, M. Naftaly, C. R. Pidgeon, G. Aeppli, and B. N. Murdin. Coherent superpositions of three states for phosphorous donors in silicon prepared using THz radiation. *Nature Communications*, **8**, 16038 (2017). DOI: 10.1038/ncomms16038.

[186] R. L. Aggarwal and A. K. Ramdas. Optical Determination of the Symmetry of the Ground States of Group-V Donors in Silicon. *Phys. Rev.*, **140**, A1246 (1965). DOI: 10.1103/PhysRev.140.A1246.

[187] H.-W. Hübers, S. G. Pavlov, S. A. Lynch, Th. Greenland, K. L. Litvinenko, B. Murdin, B. Redlich, A. F. G. van der Meer, H. Riemann, N. V. Abrosimov, P. Becker, H.-J. Pohl, R. Kh. Zhukavin, and V. N. Shastin. Isotope effect on the lifetime of the $2p_0$ state in phosphorus-doped silicon. *Phys. Rev. B*, **88**, 035201 (2013). DOI: 10.1103/PhysRevB.88.035201.

[188] Neil W. Ashcroft and N. David Mermin. *Solid State Physics*. Brooks Cole, 1976.

[189] T. Takakura, A. Noiri, T. Obata, T. Otsuka, J. Yoneda, K. Yoshida, and S. Tarucha. Single to quadruple quantum dots with tunable tunnel couplings. *Applied Physics Letters*, **104**, 113109 (2014). DOI: 10.1063/1.4869108.

[190] L. Couture and R. Zitoun. *Statistical Thermodynamics and Properties of Matter*. Routledge, 2000.

[191] L. DiCarlo, H. J. Lynch, A. C. Johnson, L. I. Childress, K. Crockett, C. M. Marcus, M. P. Hanson, and A. C. Gossard. Differential Charge Sensing and Charge Delocalization in a Tunable Double Quantum Dot. *Physical Review Letters*, **92** (2004). DOI: 10.1103/physrevlett.92.226801.

[192] M. A. Fogarty, K. W. Chan, B. Hensen, W. Huang, T. Tanttu, C. H. Yang, A. Laucht, M. Veldhorst, F. E. Hudson, K. M. Itoh, D. Culcer, T. D. Ladd, A. Morello, and A. S. Dzurak. Integrated silicon qubit platform with single-spin addressability, exchange control and single-shot singlet-triplet readout. *Nature Communications*, **9** (2018). DOI: 10.1038/s41467-018-06039-x.

[193] M. Veldhorst, R. Ruskov, C. H. Yang, J. C. C. Hwang, F. E. Hudson, M. E. Flatté, C. Tahan, K. M. Itoh, A. Morello, and A. S. Dzurak. Spin-orbit coupling and operation of multivalley spin qubits. *Physical Review B*, **92** (2015). DOI: 10.1103/physrevb.92.201401.

[194] J. Salfi, J. A. Mol, R. Rahman, G. Klimeck, M. Y. Simmons, L. C. L. Hollenberg, and S. Rogge. Quantum simulation of the Hubbard model with dopant atoms in silicon. *Nature Communications*, **7** (2016). DOI: 10.1038/ncomms11342.

[195] Joakim Bergli and Lara Faoro. Exact solution for the dynamical decoupling of a qubit with telegraph noise. *Physical Review B*, **75** (2007). DOI: 10.1103/physrevb.75.054515.

[196] Michael J. Biercuk, Hermann Uys, Aaron P. VanDevender, Nobuyasu Shiga, Wayne M. Itano, and John J. Bollinger. Experimental Uhrig dynamical decoupling using trapped ions. *Physical Review A*, **79** (2009). DOI: 10.1103/physreva.79.062324.

[197] K. D. Petersson, J. R. Petta, H. Lu, and A. C. Gossard. Quantum Coherence in a One-Electron Semiconductor Charge Qubit. *Physical Review Letters*, **105** (2010). DOI: 10.1103/physrevlett.105.246804.

[198] Y. He, S. K. Gorman, D. Keith, L. Kranz, J. G. Keizer, and M. Y. Simmons. A two-qubit gate between phosphorus donor electrons in silicon. *Nature*, **571**, 371 (2019). DOI: 10.1038/s41586-019-1381-2.

[199] Saquib Shamim, Bent Weber, Daniel W. Thompson, Michelle Y. Simmons, and Arindam Ghosh. Ultralow-Noise Atomic-Scale Structures for Quantum Circuitry in Silicon. *Nano Letters*, **16**, 5779 (2016). DOI: 10.1021/acs.nanolett.6b02513.

[200] Saquib Shamim, Suddhasatta Mahapatra, Craig Polley, Michelle Y. Simmons, and Arindam Ghosh. Suppression of low-frequency noise in two-dimensional

electron gas at degenerately doped Si:Pδlayers. *Physical Review B*, **83** (2011). DOI: 10.1103/physrevb.83.233304.

[201] E. Paladino, Y. M. Galperin, G. Falci, and B. L. Altshuler. 1/fnoise: Implications for solid-state quantum information. *Reviews of Modern Physics*, **86**, 361 (2014). DOI: 10.1103/revmodphys.86.361.

[202] Peihao Huang and Xuedong Hu. Electron spin relaxation due to charge noise. *Physical Review B*, **89** (2014). DOI: 10.1103/physrevb.89.195302.

[203] V. Srinivasa and J. M. Taylor. Capacitively coupled singlet-triplet qubits in the double charge resonant regime. *Physical Review B*, **92** (2015). DOI: 10.1103/physrevb.92.235301.

[204] Matthew P. Wardrop and Andrew C. Doherty. Exchange-based two-qubit gate for singlet-triplet qubits. *Physical Review B*, **90** (2014). DOI: 10.1103/physrevb.90.045418.

[205] Georg Gramse, Alexander Kölker, Tingbin Lim, Taylor J. Z. Stock, Hari Solanki, Steven R. Schofield, Enrico Brinciotti, Gabriel Aeppli, Ferry Kienberger, and Neil J. Curson. Nondestructive imaging of atomically thin nanostructures buried in silicon. *Science Advances*, **3**, e1602586 (2017). DOI: 10.1126/sciadv.1602586.

[206] James Clerk Maxwell. *A treatise on electricity and magnetism*. Oxford Clarendon Press, 1873.

[207] M. L. Balinski. An Algorithm for Finding All Vertices of Convex Polyhedral Sets. *Journal of the Society for Industrial and Applied Mathematics*, **9**, 72 (1961). DOI: 10.1137/0109008.

[208] M. E. Dyer and L. G. Proll. An algorithm for determining all extreme points of a convex polytope. *Mathematical Programming*, **12**, 81 (1977). DOI: 10.1007/bf01593771.

[209] J. J. Shirron. *Solution of Exterior Helmholtz Problems Using Finite and Infinite Elements*. PhD thesis, University of Maryland College Park, 1995.

[210] E.T. Jaynes and F.W. Cummings. Comparison of quantum and semiclassical radiation theories with application to the beam maser. *Proceedings of the IEEE*, **51**, 89, 1963. DOI: 10.1109/proc.1963.1664.

[211] L. Allen and J. H. Eberly. *Optical Resonance and Two-Level Atoms*. Dover Publications (1987).

[212] Russell Anderson. *Nonequilibrium dynamics and relative phase evolution of two-component Bose-Einstein condensates*. PhD thesis, Swinburne University of Technology, Melbourne (2010).

[213] K. Rama Koteswara Rao and Dieter Suter. Nonlinear dynamics of a two-level system of a single spin driven beyond the rotating-wave approximation. *Physical Review A*, **95** (2017). DOI: 10.1103/physreva.95.053804.

[214] L. D. Landau. Zur Theorie der Energieubertragung II. *Z. Sowjetunion*, **2**, 46, 1932.

[215] C. Zener. Non-Adiabatic Crossing of Energy Levels. *Proceedings of the Royal Society A: Mathematical, Physical and Engineering Sciences*, **137**, 696 (1932). DOI: 10.1098/rspa.1932.0165.

[216] E.C.G. Stueckelberg. Theorie der unelastischen Stösse zwischen Atomen. 1932. DOI: 10.5169/seals-110177.

[217] Ettore Majorana. Atomi orientati in campo magnetico variabile. *Il Nuovo Cimento*, **9**, 43 (1932). DOI: 10.1007/bf02960953.

[218] Francesco Di Giacomo and Evgenii E Nikitin. The Majorana formula and the Landau–Zener–Stückelberg treatment of the avoided crossing problem. *Physics-Uspekhi*, **48**, 515 (2005). DOI: 10.1070/pu2005v048n05abeh002804.

[219] Angbo Fang. *Quantum computation with electron spins of phosphorous donors in silicon*. PhD thesis, University of Illinois, Urbana-Champaign (2005).

[220] K. D. Petersson, J. R. Petta, H. Lu, and A. C. Gossard. Quantum Coherence in a One-Electron Semiconductor Charge Qubit. *Phys. Rev. Lett.*, **105**, 246804 (2010). DOI: 10.1103/PhysRevLett.105.246804.

[221] Stephen Blundell. *Magnetism in Condensed Matter (Oxford Master Series in Physics)*. Oxford University Press, 2001.

[222] Etienne Lacheisserie. *Magnetism: Fundamentals*. Springer, New York, 2004.

[223] Alexander Altland and Ben D. Simons. *Condensed Matter Field Theory*. Cambridge University Press, 2010.

[224] J. Hubbard. Electron correlations in narrow energy bands. *Proceedings of the Royal Society of London. Series A. Mathematical and Physical Sciences*, **276**, 238 (1963). DOI: 10.1098/rspa.1963.0204.

Appendix A

Electrostatic simulations of Si-P devices

STM-patterned Si-P devices offer a reduced gate density when compared to gate-defined quantum dots because of the free confinement potential from the P-donor dots. As with all quantum dot devices, the device operation relies on achieving particular charge states (number of electrons) on the individual dots (for example, an even-parity inter-dot transition for a singlet-triplet qubit). To achieve a given charge state in a Si-P device, one manipulates the potentials on the P-donor dots by applying voltages to the local metallic P-doped leads. However, the voltages between leads should not exceed $\pm 1\,\mathrm{V}$ as typical lead structures (spaced apart by $\sim 50\,\mathrm{nm}$) will undergo gate-to-gate device leakage [86, 92, 101]. Thus, it is of interest to fabricate devices that can achieve the desired charge states with a minimal voltage applied to the gates. The simulation methods highlighted in this section adopt finite element solvers to calculate a capacitance matrix. From the capacitance matrix, one can extract key device parameters and simulate a charge stability diagram to test whether one can achieve the desired charge states with minimal voltages.

This section shall highlight key details of the electrostatic modelling adapted and improved upon for Si-P dots:

- Appendix A.1 gives an overview of the capacitance matrix and links it to physical electrostatic device parameters (such as gate to dot lever-arms and mutual capacitance) that one may utilise in designing Si-P devices.

- Appendix A.2 highlights the stability diagram simulator developed in this thesis. Here, one feeds a capacitance matrix (describing the dots and gates in the Si-P device) and the gate voltages set on the individual gates to obtain a simulated charge stability diagram. In addition, this section highlights how

one may simulate the effect of different P-donor dot sizes by feeding in data from previous tight-binding simulations [81].

- Appendix A.3 describes the improved method in finding the capacitance matrices via a FEA simulation. Here, the method no longer simulates P-donors as metallic spheres like in previous device designs [86, 92, 157] as P-donor dots will most likely not display the electrostatic screening as seen by perfect metallic spheres. The lever-arms to the P-donors are inferred from electrostatic potential simulations.

A.1 Electrostatic parameters from capacitance matrix

The capacitance matrix describes the geometric network of dots and local metallic gates in the Si-P device via a circuit network of capacitors as discussed in Section 2.2.2. One can simulate the capacitance matrix via finite element solvers such as *COMSOL* or *FastCap* [86, 92, 157]. A better methodology in simulating the capacitance matrix is described later in Appendix A.3, whereas this section highlights the key experimental device parameters that one may extract from a simulated capacitance matrix.

A.1.1 Definition of the Maxwell's capacitance matrix

The capacitance matrix derived here is that well-established in literature [206]. It is an algebraic construct that has strong analogues to the scalar equation $Q = CV$ that relates charge and the voltage across a capacitor. Now consider a network of N nodes with nodal voltages given by the vector $\mathbf{V}$ with its components labelled as V_i (with $0 < i \leqslant N$). Consider a network of interlinking capacitors between all node c_{ij} where $i = j$ is the self capacitance of node i to ground while $i \neq j$ is the interlinking capacitance between nodes i and j. Now taking the charges on the nodes to be the vector $\mathbf{Q}$ with its components given by Q_i, the charge on a given node is simply given summing all the charges on the capacitors (noting that $Q = CV$):

$$Q_i = c_{ii}V_i + \sum_{j=1,j\neq i}^{N} c_{ij}(V_i - V_j) = \left(\sum_{j=1}^{N} c_{ij}\right) V_i + \sum_{j=1,j\neq i}^{N} (-c_{ij})V_j. \tag{A.1}$$

By definition of matrix multiplication, one may write:

$$\mathbf{Q} = \mathbf{CV} \tag{A.2}$$

$$C_{ij} = \begin{cases} \sum_{j=1}^{N} c_{ij} & i = j \\ -c_{ij} & i \neq j \end{cases}. \tag{A.3}$$

That is, the diagonal components of the capacitance matrix $\mathbf{C}$ are the sum of all capacitances stemming off the node (including the self-capacitance), while the off-diagonal components are the negation of the inter-nodal capacitances.

A.1.2 Energy Difference between two charge states

The charge-stable ground state is the charge configuration on the dots (for a given set of gate voltages) that minimises the global potential energy. However, when considering charge transitions, it is useful to know the energy difference between the two charge states. As discussed later in Appendix A.2, the charge transition occurs along the set of voltages where the energy difference between two charge configurations is zero.

A network of quantum dots and voltage sources (powering the gates, source or drain electrodes) can be modelled as an interconnected capacitive network [89]. The network is defined by the capacitance matrix $\mathbf{C}$ linking the node voltages $\mathbf{V}$ and node charges $\mathbf{Q}$ as $\mathbf{Q} = \mathbf{CV}$ as discussed in Appendix A.1.1. Now the components of $\mathbf{V}$ are partitioned into the dot voltages $\mathbf{V}_\mathrm{D}$, offset voltages $\mathbf{V}_\mathrm{O}$ and the applied voltages $\mathbf{V}_\mathrm{G}$. The offset voltages correspond to the unintentional links from the given node to some nearby defect (for example, a charge trap from an oxide defect). Thus, one gets:

$$\begin{pmatrix} \mathbf{Q}_\mathrm{D} \\ \mathbf{Q}_\mathrm{O} \\ \mathbf{Q}_\mathrm{G} \end{pmatrix} = \begin{pmatrix} \mathbf{C}_\mathrm{DD} & \mathbf{C}_\mathrm{DO} & \mathbf{C}_\mathrm{DG} \\ \mathbf{C}_\mathrm{OD} & \mathbf{C}_\mathrm{OO} & \mathbf{C}_\mathrm{OG} \\ \mathbf{C}_\mathrm{GD} & \mathbf{C}_\mathrm{GO} & \mathbf{C}_\mathrm{GG} \end{pmatrix} \begin{pmatrix} \mathbf{V}_\mathrm{D} \\ \mathbf{V}_\mathrm{O} \\ \mathbf{V}_\mathrm{G} \end{pmatrix}. \tag{A.4}$$

Now the dot voltages may be found (by considering that $\mathbf{Q} = \mathbf{CV}$) via the following relation:

$$\mathbf{V}_\mathrm{D} = \mathbf{C}_\mathrm{DD}^{-1} \left(\mathbf{Q}_\mathrm{D} - \mathbf{C}_\mathrm{DO}\mathbf{V}_\mathrm{O} - \mathbf{C}_\mathrm{DG}\mathbf{V}_\mathrm{G} \right), \tag{A.5}$$

where $\mathbf{Q}_\mathrm{D}$ is the charge in the dots. Let the addition or removal of charges on the dots be given as: $\Delta\mathbf{Q} = \mathbf{Q}_{\mathrm{D}(f)} - \mathbf{Q}_{\mathrm{D}(i)}$ (where $\mathbf{Q}_{\mathrm{D}(i)}$ and $\mathbf{Q}_{\mathrm{D}(f)}$ are the initial and

final charge states on the dots). All analysis from now on presume that the total charge difference is at most 1 electron[1]. Taking the charge offset voltages $\mathbf{V}_{\mathrm{O}}$ and $\mathbf{V}_{\mathrm{G}}$ to be constant on the transfer of charges on the dots (as the voltage sources will sustain a constant voltage on the gates), the net work done to move charges onto the dots is:

$$\Delta U = \int_{\mathbf{Q}_{\mathrm{D}(i)}}^{\mathbf{Q}_{\mathrm{D}(f)}} \mathbf{V}_{\mathrm{D}}(\mathbf{Q}_{\mathrm{D}}) d\mathbf{Q}_{\mathrm{D}}. \tag{A.6}$$

Noting some simple matrix calculus[2], this integral evaluates to:

$$\Delta U = \frac{\mathbf{Q}_{\mathrm{D}(f)}^T \mathbf{C}_{\mathrm{DD}}^{-1} \mathbf{Q}_{\mathrm{D}(f)} - \mathbf{Q}_{\mathrm{D}(i)}^T \mathbf{C}_{\mathrm{DD}}^{-1} \mathbf{Q}_{\mathrm{D}(i)}}{2} - \left(\mathbf{V}_{\mathrm{O}}^T \mathbf{C}_{\mathrm{OD}} + \mathbf{V}_{\mathrm{G}}^T \mathbf{C}_{\mathrm{GD}}\right) \mathbf{C}_{\mathrm{DD}}^{-1} \Delta\mathbf{Q}, \tag{A.7}$$

noting that the second term has been transposed for notational convenience. Now taking $\mathbf{V}_0 \equiv \mathbf{C}_{\mathrm{DD}}^{-1} \mathbf{C}_{\mathrm{DO}} \mathbf{V}_{\mathrm{O}}$ (where the parameter $\mathbf{V}_0$ is a voltage offset vector that adds to the energy when adding an electron to a given dot), the equation for ΔU takes a simpler form:

$$\Delta U = \tfrac{1}{2} \left(\mathbf{Q}_{\mathrm{D}(f)}^T \mathbf{C}_{\mathrm{DD}}^{-1} \mathbf{Q}_{\mathrm{D}(f)} - \mathbf{Q}_{\mathrm{D}(i)}^T \mathbf{C}_{\mathrm{DD}}^{-1} \mathbf{Q}_{\mathrm{D}(i)} \right) + \mathbf{V}_{\mathrm{G}}^T \boldsymbol{\alpha} \Delta\mathbf{Q} - \mathbf{V}_0^T \Delta\mathbf{Q}. \tag{A.8}$$

The first (bracketed) term is due to the intrinsic electrostatic charging energies of loading an electron onto the dots. That is, the repulsive energy due to electrons on other dots and the charging energy due to the dot's self-capacitance. The second term describes the energy shift due to electric fields from the gates, where $\boldsymbol{\alpha}$ is the gate-to-dot lever-arm matrix discussed in the next section. The third term describes the offset energies on the dots.

A.1.3 Gate to dot lever-arm matrix

Given a dot d and a gate g, the lever-arm α is defined as:

$$\alpha_{gd} = \frac{1}{-e} \cdot \frac{\Delta U_d}{\Delta V_g}, \tag{A.9}$$

[1] The assumption here is that the thermal energies and electron momenta are small. Consider a dot of capacitance C. The charging energy is $E_c = e^2/(2C)$, where the electron energies must be lower than twice the charging energy to ensure only one electron enters the dot at a time: $E < 2E_c$. Thus, the thermal energy must be smaller than the charging energy: $\frac{1}{2} k_B T \ll 2E_c$. Similarly, electron tunnel rates Γ onto the dot must obey the Heisenberg limit: $\frac{\hbar}{2}\Gamma \ll 2E_c$.

[2] That is, $\frac{\partial}{\partial \mathbf{x}} \left(\mathbf{x}^T \mathbf{M} \mathbf{x}\right) = (\mathbf{M} + \mathbf{M}^T)\mathbf{x} = 2\mathbf{M}\mathbf{x}$ (if $\mathbf{M}$ is symmetric).

where ΔU_d is the change in the potential energy of the dot (with respect to its Fermi level) on changing the gate voltage by ΔV_g. Now Equation A.7, gives the energy requirement ΔU for a given charge transition $\Delta\mathbf{Q}$ and a gate voltages $\mathbf{V}_\mathrm{G}$. The energy shifts when changing $\mathbf{V}_\mathrm{G}$ to $\mathbf{V}_\mathrm{G} + \Delta\mathbf{V}$ (due to the influence of the gate voltages). Subtracting the two energies now yields the energy difference due to the change in gate voltages:

$$\Delta U_{\Delta\mathbf{V}} = \Delta\mathbf{V}^T(-\mathbf{C}_\mathrm{GD}\mathbf{C}_\mathrm{DD}^{-1})\Delta\mathbf{Q}. \tag{A.10}$$

By selecting charge vectors $\Delta\mathbf{Q}$ to be the change of one electron on dot d so that is is simply a vector of zeroes except for the $-e$ in the d^th entry, one realises by Equation A.9 that the lever-arm matrix is simply:

$$\boldsymbol{\alpha} = -\mathbf{C}_\mathrm{GD}\mathbf{C}_\mathrm{DD}^{-1}, \tag{A.11}$$

where the number of rows in $\boldsymbol{\alpha}$ equals the number of gates and the number of columns in $\boldsymbol{\alpha}$ equals the number of dots. The entry α_{gd} in the matrix $\boldsymbol{\alpha}$ is the lever-arm of gate g to dot d.

A.1.4 Finding the charge transition hyperplanes

To find the charge transition boundaries, it is important to realise the significance of ΔU. A negative ΔU implies that the final charge state is electrostatically lower in energy and thus favourable (once again noting that $\Delta\mathbf{Q}$ is restricted to at most one unit of charge in total). Thus, the region described by $\Delta U < 0$ would be that where $\mathbf{Q}_{\mathrm{D}(f)}$ is the ground state charge state. Thus, $\Delta U = 0$ describes the charge transition boundary. However, $\Delta U = 0$ is only the charge transition boundary if the electron added or removed comes from an infinite distance away, or equivalently the zero-potential ground, and thereby describing the Fermi level (of the reservoir holding the electrons) to be at zero potential. Now consider the possibility that the electron in fact came from a reservoir that is one of the gates in the system. By the electrostatic superposition principle, one can decompose the energy change for an electron entering the dot from the reservoir to be the difference between adding the electron (from zero-potential ground) to the dot against adding it to the reservoir E_F. The energy required to add charge onto the reservoir is given by (noting that the potential energy is simply the product of potential and charge):

$$\Delta U_\mathrm{res} = \mathbf{V}_\mathrm{G}^T\mathbf{K}\Delta\mathbf{Q}. \tag{A.12}$$

The number of rows and columns in $\mathbf{K}$ equals the number of gates and dots respectively. The entry K_{mn} is 1 if the lead m is tunnel coupled to dot n (that is, charges can jump onto or off this dot n from the given reservoir m) and 0 otherwise. For the charge transition boundary, if adding the electron to the dot lowers the system energy more than adding it to the reservoir, then an electron will flow from the reservoir onto the dot to enter the lower ground-state charge state ($\Delta U < \Delta U_{\text{res}}$). Thus, by Equation A.8

$$\tfrac{1}{2}\left(\mathbf{Q}_{\mathrm{D}(f)}^{T}\mathbf{C}_{\mathrm{DD}}^{-1}\mathbf{Q}_{\mathrm{D}(f)} - \mathbf{Q}_{\mathrm{D}(i)}^{T}\mathbf{C}_{\mathrm{DD}}^{-1}\mathbf{Q}_{\mathrm{D}(i)}\right) + \mathbf{V}_{\mathrm{G}}^{T}\left(\boldsymbol{\alpha} - \mathbf{K}\right)\Delta\mathbf{Q} - \mathbf{V}_{0}^{T}\Delta\mathbf{Q} \leqslant 0. \quad \text{(A.13)}$$

The inequality gives a region bounded by a voltage hyperplane where the final charge configuration $\mathbf{Q}_{\mathrm{D}(f)}$ is of a lower energy than the charge configuration $\mathbf{Q}_{\mathrm{D}(i)}$.

Note that by definition $\mathbf{K}$ only affects the charge transition boundary when the charge transition involves a new addition or removal of an electron onto the dot from its reservoir. For example, if there is an inter-dot transition between two dots (both individually loaded or unloaded from the same reservoir), the contribution of $\mathbf{K}$ cancels out. However, if there is an inter-dot transition between two dots in which each dot has a different reservoir, then the position of the charge transition boundary becomes non-trivial as it is not possible to distinguish the original reservoir of that electron. In fact, there is no unique ground-state charge stability diagram as the stability diagram becomes hysteretic. That is, the position of the charge transitions will now depend on the history regarding the order in which one loads or moves the electrons in the network of quantum dots and their reservoirs. In the scope of devices simulated in this thesis, all inter-dot transitions are between dots that share the same reservoir. Thus, the charge transition boundaries are well-defined and unique.

A.1.5 Virtual gates

For a given device, the lever-arm matrix $\boldsymbol{\alpha}$ links the input gate voltages to the dot energies. Ideally, the gate voltages should independently a given dot's energy without affecting the other dots. However, since there will always be cross-coupling between gates and dots, one will need to use a linear combination of gate voltages to create a set of 'virtual gates' where each individual virtual gate only affects one dot [14, 55]. Now consider the total energy shift for a given network of gates and dots on changing the voltages on the gates by $\Delta\mathbf{V}_{\mathrm{G}}$:

$$\Delta U_d = \Delta\mathbf{V}_{\mathrm{G}}^{T}\boldsymbol{\alpha}\Delta\mathbf{Q}. \quad \text{(A.14)}$$

Now to have independent access such that the voltage in a virtual gate directly changes the energy if an electron is in that associated dot, one can immediately define the virtual gates to be:

$$\Delta \mathbf{V}'^{T} = \Delta \mathbf{V}_{\mathrm{G}}^{T} \boldsymbol{\alpha}. \tag{A.15}$$

Where changing the voltage of the n^{th} virtual gate in $\Delta \mathbf{V}'$ only shifts the energy of the n^{th} dot. Now one needs to solve for $\Delta \mathbf{V}_{\mathrm{G}}$ to find the physical voltages to apply on the gates for a given set of virtual gate voltages $\Delta \mathbf{V}'$. Now if the number of gates is less than the number of dots, there system does not have enough degrees of freedom to control the potentials of all the dots independently. However, if the number of gates equals the number of dots, then one may simply invert the lever-arm matrix to obtain:

$$\Delta \mathbf{V}^{T} = \Delta \mathbf{V}'^{T} \boldsymbol{\alpha}^{-1}. \tag{A.16}$$

If the number of gates exceeds the number of dots, then $\boldsymbol{\alpha}$ is no longer a square matrix. In this case, one may find the optimal usage of the gates (to tune the dots' potentials individually) in a least-squares sense by first taking the singular value decomposition (SVD) of $\boldsymbol{\alpha}$:

$$\boldsymbol{\alpha} = \mathbf{X} \boldsymbol{\Sigma} \mathbf{Y}^{*}, \tag{A.17}$$

where $\mathbf{X}$ is a $G \times G$ matrix, $\boldsymbol{\Sigma}$ is a $G \times D$ matrix and $\mathbf{Y}$ is a $D \times D$ matrix (for G gates and D dots). Now one may apply the pseudo-inverse of $\boldsymbol{\alpha}$ to find the optimal set of physical gate voltages to realise a set of virtual gates:

$$\Delta \mathbf{V}^{T} = \Delta \mathbf{V}'^{T} \boldsymbol{\alpha}^{+} \equiv \Delta \mathbf{V}'^{T} \mathbf{Y} \boldsymbol{\Sigma}^{+} \mathbf{X}^{*}, \tag{A.18}$$

where $\boldsymbol{\Sigma}^{+}$ indicates usual the transpose matrix of the reciprocal singular values.

A.1.6 Charge transitions causing compensating charge flow in gates

For a network of gates (connected to voltage sources) and dots, the device operates such that voltage sources keep the gates at a fixed potential and charges move to minimise the total potential energy of the system. Now consider the case where one electron moves onto the dot. By definition of the electrostatic potential (that is, the energy required to move a unit test charge from infinity to a given point) of a given gate must change due to the presence of said electron (as the positive unit test charge

moved from infinity will require less energy due to the electric field of the electron). Since the voltage sources must maintain a fixed potential on all gates, compensating charge must flow from the sources onto the gates to counter the effect of the electron (so that the energy required to move the test charge to the given gate remains the same). This compensating charge can be found by considering Equations A.4, A.5 and A.11; the change in the gate charge is:

$$\Delta \mathbf{Q}_{\mathrm{G}} = \mathbf{C}_{\mathrm{GD}} \mathbf{C}_{\mathrm{DD}}^{-1} \mathbf{Q}_{\mathrm{D}} \equiv -\boldsymbol{\alpha} \Delta \mathbf{Q}, \tag{A.19}$$

given that the change in the gate and offset voltages is zero on some charge transfer $\Delta \mathbf{Q}$ onto the dots. Now the implication is that gates far away from the influence of a given dot require less compensating charge as the potential environment around that gate is less affected. In addition, the negative sign implies that the compensating charge must be of opposite sign to counteract the electrostatic potential of charges entering or leaving the dots.

A.1.7 Mutual capacitance

Now given a transition line for an electron entering a given dot, it is interesting to note the shift in this transition line, in voltage space, on adding an electron to a neighbouring dot. To find this shift, consider the two hyperplanes describing the charge transitions $(0,0) \leftrightarrow (1,0)$ and $(1,0) \leftrightarrow (1,1)$ with the numbers indicating the number of electrons in dots m and n. Note that the net change in charge is $(1,0)$ with the only difference being the presence of charge in dot n in the second case. By Equation A.13, on walking across a voltage unit-vector $\mathbf{V}_{\mathrm{vec}}$, the distance between the two hyperplanes across this vector is:

$$\Delta V = \frac{e(\mathbf{C}_{\mathrm{DD}}^{-1})_{mn}}{\mathbf{V}_{\mathrm{vec}}^{T}(\boldsymbol{\alpha}_{*m} - \mathbf{K}_{*m})}. \tag{A.20}$$

Thus, the distance is large if the gates used along the voltage vector $\mathbf{V}_{\mathrm{vec}}$ have weak lever-arm α values as a greater voltage swing is required to exact the required change in energy. However, the key element of concern is the mutual capacitance between dots m and n.

A.1.8 On-site interaction

The inter-dot charge crossing is that when an electron hops between two dots. One particular archetype is of heavy interest is the singlet-triplet crossing where one

investigates a charge crossing of $(1,1)$ to $(0,2)$. Now taking Equation A.13, the hyperplane for a $(1,1)$ to $(0,2)$ inter-dot transition on dots m and n is:

$$\mathbf{V}_{\mathrm{G}}^{T}\left((\boldsymbol{\alpha})_{*n}-(\boldsymbol{\alpha})_{*m}\right)=\left(\mathbf{V}_{0}^{T}\right)_{n}+e^{2}\left(\mathbf{C}_{\mathrm{DD}}^{-1}\right)_{mn}-\tfrac{1}{2}e^{2}\left(\mathbf{C}_{\mathrm{DD}}^{-1}\right)_{nn}+\tfrac{1}{2}e^{2}\left(\mathbf{C}_{\mathrm{DD}}^{-1}\right)_{mm}, \tag{A.21}$$

where $(\boldsymbol{\alpha})_{*d}$ is the list of lever-arm alphas of all the gates to dot d, $\left(\mathbf{V}_{0}^{T}\right)_{n}$ is the voltage offset placed upon dot n and $\left(\mathbf{C}_{\mathrm{DD}}^{-1}\right)_{mn}$ is the mn-component of C_{DD}^{-1}. Note that for the sake of having a memoryless stability diagram in which the electrons on both dots load from the same reservoir, the terms involving $\mathbf{K}$ disappear. Now taking the hyperplane for the $(1,1)$ to $(2,0)$ transition, the distance between said hyperplanes (that is, the two inter-dot transitions) is:

$$V_{0,2\leftrightarrow 2,0}=\frac{\left|\left(\mathbf{V}_{0}^{T}\right)_{n}+\left(\mathbf{V}_{0}^{T}\right)_{m}+2e^{2}\left(\mathbf{C}_{\mathrm{DD}}^{-1}\right)_{mn}\right|}{\left\|(\boldsymbol{\alpha})_{*n}-(\boldsymbol{\alpha})_{*m}\right\|}. \tag{A.22}$$

Now evident from the plane equations (with respect to $\mathbf{V}_{\mathrm{G}}$):

$$\mathbf{n}_{0,2\leftrightarrow 2,0}=\frac{(\boldsymbol{\alpha})_{*n}-(\boldsymbol{\alpha})_{*m}}{\left\|(\boldsymbol{\alpha})_{*n}-(\boldsymbol{\alpha})_{*m}\right\|} \tag{A.23}$$

is the normal vector. Thus, from Equation A.11, it is clear that the total energy spent in moving between the two hyperplanes is:

$$U_{0,2\leftrightarrow 2,0}=e\left|\left(\mathbf{V}_{0}^{T}\right)_{n}+\left(\mathbf{V}_{0}^{T}\right)_{m}+2e^{2}\left(\mathbf{C}_{\mathrm{DD}}^{-1}\right)_{mn}\right|. \tag{A.24}$$

A.1.9 Electrostatic detuning

The detuning Δ in this section shall be that defined in Section 5.2. The detuning is defined as zero at the $(1,1)$ to $(0,2)$ charge anti-crossing where both charge states are degenerate (under the constant interaction model where interaction terms are considered to be zero). Away from inter-dot charge crossing, the detuning is the energy separation between the $(1,1)$ and $(0,2)$ charge states with positive detuning being when $(0,2)$ is the lower energy state. By Equation A.8, the change in energy (or rather the energy splitting between the two charge states) is:

$$2\Delta=-e(\mathbf{V}_{\mathrm{G}}-\mathbf{V}_{\mathrm{id}})^{T}\left((\boldsymbol{\alpha})_{*m}-(\boldsymbol{\alpha})_{*n}\right)=e(\mathbf{V}_{\mathrm{G}}-\mathbf{V}_{\mathrm{id}})^{T}\left((\boldsymbol{\alpha})_{*n}-(\boldsymbol{\alpha})_{*m}\right), \tag{A.25}$$

where the voltage vector $\mathbf{V}_{\text{id}}$ is that when the detuning is zero. That is, $\mathbf{V}_{\text{id}}$ is any point on the inter-dot crossing hyperplane (in gate voltage space) where the energy splitting between the the $(1,1)$ and $(0,2)$ charge states is zero. Note that it matters not where $\mathbf{V}_{\text{id}}$ is chosen. The indices m and n represent the dots upon which n is the dot where both electrons reside when in the $(0,2)$ state. Finally note that the splitting is 2Δ if taking the simplified singlet-triplet Hamiltonian definition introduced in Section 5.2 where the energy difference between the $(1,1)$ and $(0,2)$ charge states is 2Δ.

A.1.10 Summary

A summary of the physical parameters (derived in this section) that one may extract from the capacitance matrix is given in Table A.1. The corresponding summary of the physical parameters (such as the on-site interaction or the electrostatic detuning) specific to double quantum dots is given in Table A.2.

Parameter	Expression
Capacitance matrix	$C_{ij} = \begin{cases} \sum_{m=1}^{N} c_{im} & i = j \\ -c_{ij} & i \neq j \end{cases}$
Lever-arm alpha	$\boldsymbol{\alpha} = -\mathbf{C}_{\text{GD}}\mathbf{C}_{\text{DD}}^{-1}$ $\alpha_{ij} = \alpha$ of gate i to dot j
Charging energies	$\text{diag}\left(\frac{1}{2}e^2\mathbf{C}_{\text{DD}}^{-1}\right)$
Virtual gates to physical gates	$\Delta\mathbf{V}^T = \begin{cases} \Delta\mathbf{V}'^T\boldsymbol{\alpha}^{-1} & G = D \\ \Delta\mathbf{V}'^T\boldsymbol{\alpha}^{+} & G > D \end{cases}$
Mutual capacitance voltage shift	$\Delta V = \dfrac{e(\mathbf{C}_{\text{DD}}^{-1})_{mn}}{\mathbf{V}_{\text{vec}}^T(\boldsymbol{\alpha}_{*m} - \mathbf{K}_{*m})}$

Table A.1: Summary of the capacitance model parameters derived in Appendix A. The capacitances c_{ij} are raw capacitances between nodes i and j, while c_{ii} is the capacitance of the node to ground. In all expressions it is presumed that there are G gates and D dots for a total of $N = G + D$ elements. Note that $\mathbf{C}_{\text{GD}}$ is a $G \times D$ matrix block matrix from $\mathbf{C}$ where each entry ij is the negation of the capacitance between gate i and dot j. Similarly, $\mathbf{C}_{\text{DD}}$ is the $D \times D$ capacitance block matrix of the dots. The charging energies are given as a D-vector where diag takes the diagonal elements of a matrix. The change in the virtual gate voltage vector $\Delta\mathbf{V}'$ (a D-dimensional vector) corresponds to the change in the physical gate vector $\Delta\mathbf{V}$ (also a D-dimensional vector). The mutual capacitance voltage shift (when moving in the direction of the unit-vector $\mathbf{V}_{\text{vec}}$ in voltage space) is the shift in the charge transition on dot m due to an electron entering another dot n.

Parameter	Expression
On-site interaction	$U_{02} = e\left\lvert \left(\mathbf{V}_0^T\right)_n + \left(\mathbf{V}_0^T\right)_m + 2e^2\left(\mathbf{C}_{\mathrm{DD}}^{-1}\right)_{mn}\right\rvert$
Detuning	$\Delta = \frac{e}{2}\Delta V \cdot \mathbf{V}_{\mathrm{vec}}^T \Delta\boldsymbol{\alpha} \equiv \frac{e}{2}\Delta V \Delta\alpha_{\mathrm{eff}}$ $\begin{cases} \Delta V \cdot \mathbf{V}_{\mathrm{vec}} = \mathbf{V}_{\mathrm{G}} - \mathbf{V}_{\mathrm{id}} \\ \Delta\boldsymbol{\alpha} = (\boldsymbol{\alpha})_{*n} - (\boldsymbol{\alpha})_{*m} \end{cases}$
Hadamard Detuning	$\Delta V_{\mathrm{Hadamard}} = \dfrac{4\Delta B_z^2 - t_c^2}{2e\Delta B_z \Delta\alpha_{\mathrm{eff}}}$

Table A.2: Relating the double quantum dot parameters to physical parameters in the capacitance model as derived in Appendix A. The capacitances c_{ij} are raw capacitances between nodes i and j, while c_{ii} is the capacitance of the node to ground. In all expressions it is presumed that there are G gates and D dots for a total of $N = G + D$ elements. $\mathbf{C}_{\mathrm{DD}}$ is the $D \times D$ capacitance block matrix of the dots while $\boldsymbol{\alpha}$ is the lever-arm matrix defined in Table A.1. $\mathbf{V}_{\mathrm{G}}$ is a G-vector for an arbitrary configuration of gate voltages while $\mathbf{V}_{\mathrm{id}}$ is a G-vector representing any point on the $(1,1)$ to $(0,2)$ inter-dot crossing hyperplane on dots m and n where n is the dot where both electrons reside when in the $(0,2)$ charge state. $\mathbf{V}_{\mathrm{vec}}$ is the unit-vector of the voltage direction in which one pulses to alter the detuning with α_{eff} being the effective differential lever-arm when pulsing along this direction.

A.2 Charge stability diagram simulator

A.2.1 Finding charge stable regions

Now Equation A.13 describes the hyperplane for a given charge transition. A charge stable region $\mathbf{Q}_{\mathrm{D}(f)}$ is simply the feasible region that results in satisfying all the hyperplane inequalities over all neighbouring charge states $\mathbf{Q}_{\mathrm{D}(i)}$ (that is, the net change in charge is at most 1 unit charge). For the sake of generating 2D stability diagrams where one sweeps two gates, it is useful to write down the line inequalities. Without loss of generality, let the first two entries in $\mathbf{V}_{\mathrm{G}}$ be the sweeping gates on the x and y axes in the charge stability diagram[3]. Let the gate voltages and the reservoir matrix be partitioned as follows:

[3] One may always permute the indices in the capacitance matrix to make other gates be the sweeping gates

$$\mathbf{V}_{\mathrm{G}} = \begin{pmatrix} g_x \\ g_y \\ \mathbf{V}_{\mathrm{N}} \end{pmatrix} \tag{A.26}$$

$$\boldsymbol{\alpha} = \begin{pmatrix} \boldsymbol{\alpha}_x \\ \boldsymbol{\alpha}_y \\ \boldsymbol{\alpha}_{\mathrm{N}} \end{pmatrix} \tag{A.27}$$

$$\mathbf{K} = \begin{pmatrix} \mathbf{K}_x \\ \mathbf{K}_y \\ \mathbf{K}_{\mathrm{N}} \end{pmatrix}. \tag{A.28}$$

Here (g_x, g_y) are the sweeping gate voltages on the 2D stability diagram. $\boldsymbol{\alpha}_m$ is a row vector containing the lever arm alphas of gate m to all the dots along its columns. $\mathbf{K}_m$ is a row vector that contains zeroes and one if dot corresponding to the column is coupled to gate m. Note that N enumerates all the remaining gates that are held constant over the 2D charge stability diagram. The line inequalities are thus:

$$\begin{aligned} &a \cdot g_x + b \cdot g_y \geqslant c \\ &\begin{cases} a = (\mathbf{K}_x - \boldsymbol{\alpha}_x)\,\Delta\mathbf{Q} \\ b = (\mathbf{K}_y - \boldsymbol{\alpha}_y)\,\Delta\mathbf{Q} \\ c = \frac{\mathbf{Q}^T_{\mathrm{D}(f)}\mathbf{C}^{-1}_{\mathrm{DD}}\mathbf{Q}_{\mathrm{D}(f)} - \mathbf{Q}^T_{\mathrm{D}(i)}\mathbf{C}^{-1}_{\mathrm{DD}}\mathbf{Q}_{\mathrm{D}(i)}}{2} - \left(\mathbf{V}^T_{\mathrm{N}}\left(\mathbf{K}_{\mathrm{N}} - \boldsymbol{\alpha}_{\mathrm{N}}\right) + \mathbf{V}^T_0\right)\Delta\mathbf{Q} \end{cases} \end{aligned}. \tag{A.29}$$

A.2.2 Simulating different P-donor dot sizes

The parameter $\mathbf{V}_0$ is a voltage offset designated for other charge sources in the device (for example, unintentional 'charge traps'). However, one may utilise the offset to simulate the charge transition offsets due to different P-donor dot sizes by decomposing the offset voltage vector into V_0 into two parts:

$$\mathbf{V}_0 = \mathbf{V}_{\mathrm{ct}} + \mathbf{V}_{\mathrm{pdd}}, \tag{A.30}$$

where $\mathbf{V}_{\mathrm{ct}}$ is the offset due to unintentional charge reservoirs and $\mathbf{V}_{\mathrm{pdd}}$ is the offset due to the number of P-donors in a given dot. In the simulations, $\mathbf{V}_{\mathrm{ct}}$ is set to zero. However, the potential offset $\mathbf{V}_{\mathrm{pdd}}$ can be matched to be the charging energies one would expect for the an electron loaded onto a P-donor dot with m electrons (where $m \geqslant 0$). The associated potential energy offset $U_{\mathrm{pd(m)}}$ for the $(m+1)^{th}$ electron

loaded onto a P-donor d can be found via Equation A.8 (taking the voltages on the gates to be zeroed, $\mathbf{Q}_{\mathrm{D}(f)}$ to be a zero vector with $-(m+1)e$ in the d^{th} entry and to be $\mathbf{Q}_{\mathrm{D}(i)}$ a zero vector with $-me$ in the d^{th}):

$$U_{\mathrm{pdd}(m)} = \tfrac{e^2}{2}\,(2m+1)\left(\mathbf{C}_{\mathrm{DD}}^{-1}\right)_{dd} + e(\mathbf{V}_{\mathrm{pdd}}^{T})_{d}, \tag{A.31}$$

where $(\mathbf{V}_{\mathrm{pdd}}^{T})_{d}$ is the d^{th} entry in the voltage offset vector $\mathbf{V}_{\mathrm{pdd}}$. Note that the associated voltage offset $\mathbf{V}_{\mathrm{pdd}}$ does not negate the mutual charging energies. That is, the voltage offset effectively overwrites the charging energy value from the capacitance matrix to equal the expected potential offset $U_{\mathrm{pd(m)}}$.

No. Donors	$U_{\mathrm{pdd(CB)(0)}}$ (meV)	$U_{\mathrm{pdd(0)}}$ (meV)
1	-50	45
2	-150	-55
3	-285	-190
4	-425	-330

Table A.3: The estimated potential energy offsets for the first electron loaded onto different P-donor dots. The quantity $U_{\mathrm{pdd(CB)(0)}}$ refers to the potential energy (from tight-binding simulations) of the electron as referenced to the conduction band, while $U_{\mathrm{pdd(0)}}$ refers to the approximate potential energy referenced to the Fermi-level.

Tight-binding simulations of different P-donor sized dots (averaged over many P-donor arrangements for dots larger than 1 P-donor) give estimations of the offset potential energy [81] with respect to the conduction band $U_{\mathrm{pdd(CB)}(m)}$ as shown in Table A.3 for $m = 0$. To calibrate the offset potential energies to the conduction band offset, a standard calibration was used from the single-donor transport device that had reproducible offsets between multiple cool-downs in the dilution fridge [15]. Here, for a 1P dot, the first electron only entered the dot when applying 0.45 V onto the gates with an effective lever-arm of 0.1 [101]. Thus, the absolute energy offset for the first electron maps (from the zero-potential energy point) maps to $U_{\mathrm{pd}} = 45\,\mathrm{meV}$ as shown in Table A.3. Thus, from the simulations, one may recalibrate the approximate energy offsets that one may measure for different P-donor dot sizes via:

$$U_{\mathrm{pdd}(m)} = 95 + U_{\mathrm{pdd(CB)}(m)}, \tag{A.32}$$

where the units are in meV. Assuming that the conduction band offset is the same for all P-donor dot sizes (can be individually calibrated via further experimental data on different donor cluster sizes), one may take the remaining potential energy offsets

(from tight-binding simulations [81]) for different electron numbers on different sizes of P-donor dots to get the expected potential energy offsets for different electron numbers as shown in Table A.4. That is, for a given charge transition, the entries in $\mathbf{V}_{\text{pdd}}^{T}$ are varied appropriately to match $U_{\text{pdd}(m)}$ given m electrons on a given dot.

No. Donors	$U_{\text{pdd}(0)}$ (meV)	$U_{\text{pdd}(1)}$ (meV)	$U_{\text{pdd}(2)}$ (meV)	$U_{\text{pdd}(3)}$ (meV)
1	45	75	-	-
2	-55	20	70	90
3	-190	-55	15	65
4	-330	-165	-80	-15

Table A.4: Estimated potential energy offsets of P-donor dots as a function of electron number. The quantities $U_{\text{pdd}(m)}$ were calculated by simply adding 95 meV to the average potential energies (from tight-binding simulations) referenced to the conduction band [81] to reference them to the Fermi-level as before in Table A.3. Note that the data for a 1P donor is restricted to just 2 electrons.

A.2.3 Tracing the Charge Configuration Regions

With the constructions in the previous sections, one may now generate the stability diagram given a capacitance matrix. The algorithm takes the capacitance matrix and four inequalities bounding the gate range of g_x and g_y to simulate. Then one starts with a state $\mathbf{Q}_{\text{D}(f)}$ that exists within the gate voltage space (for example, the state with zero electrons on all the dots). Since, the stability diagram assumes that all charge transitions have their total electron numbers differ by at most one electron[4], the state will be bound by the charge transitions to the states $\mathbf{Q}_{\text{D}(i)}$ that differ by one electron in total. That is, one has a set of inequalities to the neighbouring charge states via Equation A.29. The convex polygon forming the charge stable region $\mathbf{Q}_{\text{D}(f)}$ satisfies all the inequalities (both from the four voltage bounds and the neighbouring charge transitions) and can be found via typical algorithms designed to find convex polytopes [207, 208]. On finding the polygon to the current charge stable region, one may iterate over all neighbouring charge regions (that clearly exist within the current gate voltage space) to find the resulting polygons of those charge stable regions until the gate voltage space is filled with all possible charge stable regions.

[4] Thus, this includes cases where the electrons may shift and enter the dots simultaneously (for example, $(0,1,0) \to (1,0,1)$)

A.3 Numerically generating the capacitance matrix

The self capacitances and inter-element capacitances of the gates and dots in the device can be numerically simulated via any finite element solver. To simulate Si-P gates, the individual structures are considered to be planar structures with a thickness of 3.6 nm. The thickness derives from the effective Bohr radius of electrons on phosphorus atoms in a silicon crystal [94, 95]. The gates in the simulations are considered to be perfect electrical conductors as verified experimentally by the metallic nature of densely doped phosphorus gates [15, 27, 81]. For large quantum dots, one may apply a similar treatment to the gates. To improve the accuracy for smaller dots, one may model the P-donor dots as metallic spheres with a radius chosen to match the experimentally measured charging energy. That is, the equivalent self-capacitance of a single P-donor dot for a nominal 45 meV charging energy is:

$$C_{\text{donor}} = \frac{e^2}{2U} = \frac{e^2}{2 \cdot 45 \cdot 10^{-3} \cdot e} \approx 1.8\,\text{aF}. \tag{A.33}$$

Using the equation for the self-capacitance of a sphere, the effective radius of the metallic sphere is:

$$r_{\text{donor}} = \frac{C_{\text{donor}}}{4\pi\varepsilon_0\varepsilon_{\text{Si}}} \approx 1.4\,\text{nm}, \tag{A.34}$$

where $\varepsilon_{\text{Si}} = 11.7$ is the relative permittivity of the silicon crystal surrounding the P-donor. This yields results should yield accurate results when estimating the lever-arm alphas between the surrounding gates to the P-donor dot. However, model becomes inaccurate when multiple P-donor dots are lined up in a row. This is because the dots, simulated as metallic spheres, start screening adjacent dots from other gates' electric fields for the electric field inside a metallic sphere must be zero. This distortion of the electrostatic scalar potential around the dots is illustrated in Figure A.1a where the potential on the dots is fixed at a nominal 0 V, while the potential on the gate is set to 1 V. Figure A.1b shows the resulting electrostatic scalar potential when ignoring the presence of the dots.

Now the P-donor dots are not metallic structures that will distort the electric fields in such a manner. In fact, the dots are structurally the same size as neighbouring silicon atoms when no electrons are trapped within them. Thus, it is more appropriate to consider the scalar potential field strengths at the positions of the dots in the absence of the dots to infer the associated gate to dot couplings. This point-like approximation holds when considering small donor clusters. In fact, the following analysis shows that one only needs to find the lever-arm matrix α and the

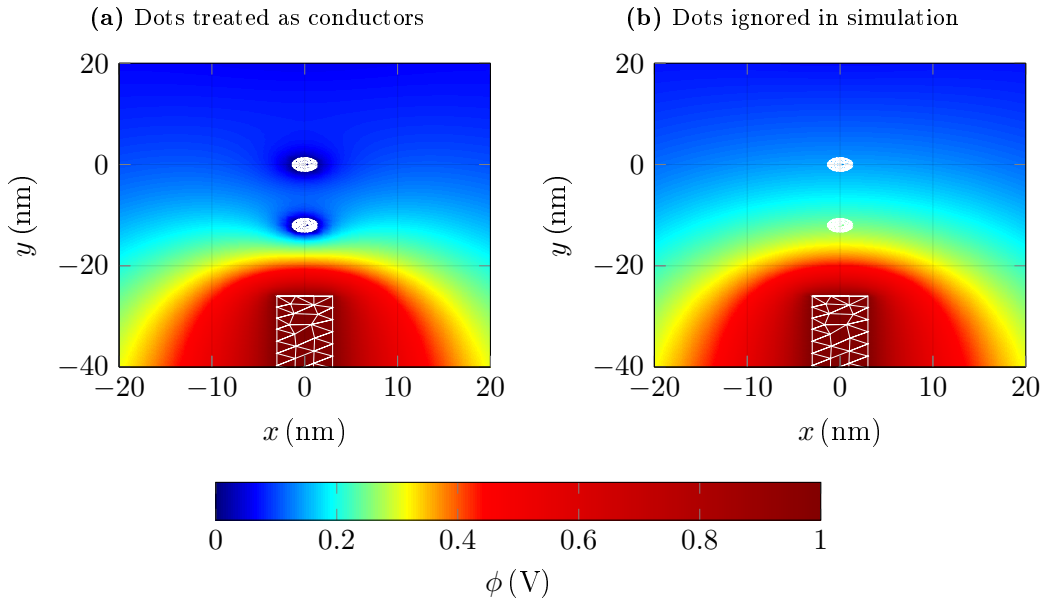

Figure A.1: Screening effects seen when modelling dots as perfect electrical conductors. The white lines show the meshing of the gate below and the two dots above. The two plots show a top view of the electrostatic scalar potential maps when applying 1 V to a 3.6 nm thick metallic gate (on the bottom) in the presence of the two dots. **(a)** shows the potential map when treating the dots as metallic spheres, while **(b)** ignores the presence of the dots. Clearly treating the dots as metallic spheres causes the potential field bend around the bottom dot such that the potential at the top dot is much lower than that when ignoring the presence of the bottom dot. Treating the dots as metallic spheres in this case leads to underestimations of the lever-arm alpha of the top dot with respect to the gate below.

inverse inter-dot matrix $\mathbf{C}_{\mathrm{DD}}^{-1}$ as explained in Section A.2.1. The gate-to-gate couplings are irrelevant to the electrostatics of electrons on the quantum dots. Thus, one need not simulate the gate structures beyond the close proximity of the quantum dots. That is, structures far away from the dots will not contribute to the gate to dot capacitances or affect the inter-dot capacitances.

In the following simulations, the gates and large quantum dots (such as an SET which will likely retain its metallic and subsequent electric-field screening properties) are simulated with the same parameters as the previous capacitance simulations. Thus, for this section, $\mathbf{C}_{\mathrm{DD}}$ refers to the inter-dot matrix between the small P-donor clusters only. To infer the large quantum dot to P-donor cluster capacitances in the C_{DD} matrix, one needs to consider the entries of the inferred $\mathbf{C}_{\mathrm{GD}}$ matrix where the 'gate' in this case is the large quantum dot (that is, one iterates over the large quantum dots as though they were gates). However, the dots are completely omitted and replaced with point charges when appropriate.

A.3.1 Numerically simulating $\boldsymbol{\alpha}$ for P-donor clusters

To infer the gate-to-dot couplings, one first generates potential maps for every gate g. In each map associated with gate g, one applies 1 V to gate g and 0 V to all remaining gates. Now consider a potential map when 1 V is applied to gate g; the potential energy to bring one electron from an infinite distance away (zero potential reference) to a site where a P-donor cluster dot d resides, is simply $e\phi_g(\mathbf{r} = \mathbf{r}_d)$ (where $\phi_g(\mathbf{r} = \mathbf{r}_d)$ is the potential at site g). Taking Equation A.11 (with $\Delta\mathbf{Q}$ having $1e$ for dot index d and 0 for all other entries and $\Delta\mathbf{V}$ having 1 for gate index g and 0 elsewhere), it becomes evident that:

$$\alpha_{gd} = \phi_g(\mathbf{r} = \mathbf{r}_d). \tag{A.35}$$

Although it is not required in generating stability diagrams, one may generate $\mathbf{C}_{\mathrm{GD}}$ by simply considering the definition of $\boldsymbol{\alpha}$ in Equation A.11.

A.3.2 Numerically simulating $\mathbf{C}_{\mathrm{DD}}^{-1}$ for P-donor clusters

Now from Equation A.8, when the gate voltages and offsets are zeroed:

$$\Delta U_{V=0} = \tfrac{1}{2}\left(\mathbf{Q}_{\mathrm{D}(f)}^T \mathbf{C}_{\mathrm{DD}}^{-1} \mathbf{Q}_{\mathrm{D}(f)} - \mathbf{Q}_{\mathrm{D}(i)}^T \mathbf{C}_{\mathrm{DD}}^{-1} \mathbf{Q}_{\mathrm{D}(i)}\right). \tag{A.36}$$

Now taking the initial charge state to be empty on all the dots (that is, $\mathbf{Q}_{\mathrm{D}(i)} = \mathbf{0}$) and the final charge state to individually populate each dot d, the resulting energy

change is:

$$\Delta U_d = \tfrac{1}{2} e^2 \left(\mathbf{C}_{\mathrm{DD}}^{-1}\right)_{dd}. \tag{A.37}$$

This is in fact the charging energy of the dot[5] and set to be $\Delta U_d = 45\,\mathrm{meV}$ (the offsets for other dot sizes are taken care of by the offsets on $\mathbf{V}_0$).

Now to find the off-diagonal components, consider the same process as before (that is, an electron enters dot d) but with another dot $c \neq d$ occupied during the entire transaction. The resulting energy change (with all voltages gate zeroed as before) is:

$$\Delta U_{cd} = \tfrac{1}{2} e^2 \left(\mathbf{C}_{\mathrm{DD}}^{-1}\right)_{dd} + e^2 \left(\mathbf{C}_{\mathrm{DD}}^{-1}\right)_{cd}, \tag{A.38}$$

where one makes use of the symmetry of the capacitance matrix. Now the energy shift considered here is that when moving an electron to dot d in the presence of an electron on dot c. That is, one calculates the potential map due to an electron situated at dot c and evaluates it at the point on dot d: ϕ_{dc}. Now the energy payment is simply $e\phi_{dc}$. Note that the charging energy term also contributes an additional 45 meV. Thus:

$$e^2 \left(\mathbf{C}_{\mathrm{DD}}^{-1}\right)_{cd} = e\phi_{dc}. \tag{A.39}$$

Thus, one can evaluate all the terms in the matrix $\mathbf{C}_{\mathrm{DD}}^{-1}$; the inverse yielding $\mathbf{C}_{\mathrm{DD}}$ as required.

A.3.3 Summary of the FEA method

To incorporate the methods shown in the previous section, one translates the device to be modelled into a FEA software package such as *COMSOL*. The gates are modelled as perfect electrical conductors. That is, the electric field inside the gates is zero and it matters not what material type is set on the surface and within the gate structures. The gates reside in material silicon with the key parameter being the relative permittivity of 11.7. The device plane is separated from the surface via an encapsulation layer of silicon and then vacuum (relative permittivity of 1). This simulates the effect of the finite encapsulation layer thickness on the devices. Finally, the zero potential boundary condition is set at all elements an infinite distance away

[5] This has been posited to be a function of intrinsic nature of phosphorus in bulk as well as the nearby gate geometry [98]. Such effects may only be captured in a full tight-binding simulation and therefore, the simulations here utilise the nominal value taken from experimental results [15].

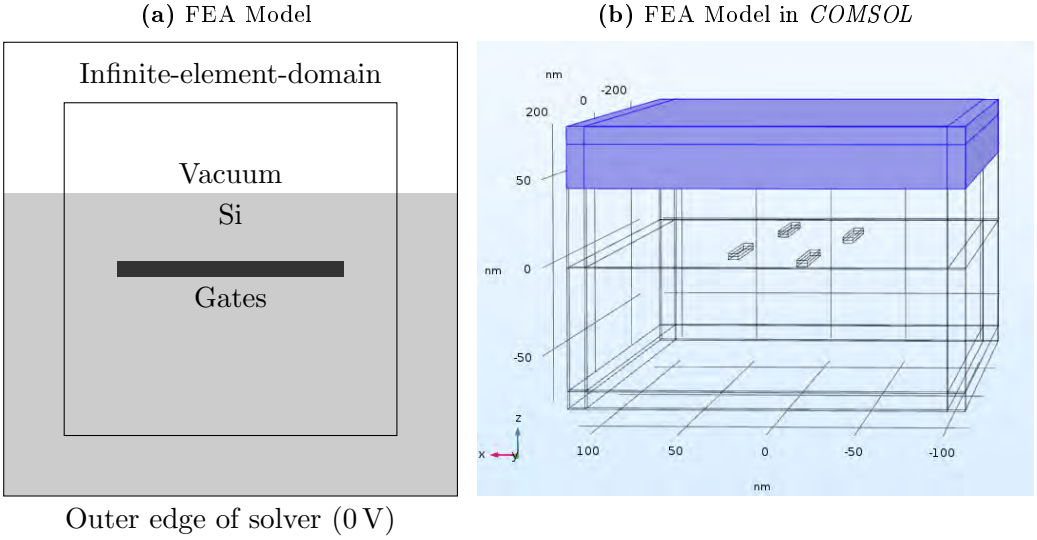

Figure A.2: The electrostatic FEA model used to generate the capacitance matrix. **(a)** Schematic of the cuboid to be modelled. The cuboid is subdivided into a silicon and vacuum portion to simulate the finite encapsulation layer on the device. Gates are modelled as perfect electrical conductors. The outer boundary is set to zero potential and exists at an infinite distance away from the inner cuboid of the model via an infinite-element-domain boundary condition. **(b)** An example FEA model done in *COMSOL* with the vacuum portion of the device highlighted for convenience.

from the device as shown in Figure A.2a. If this were not set, the elements will have zero self-capacitance and thus, provide incorrect entries to a Maxwellian capacitance matrix [206]. The infinite distance is simulated via a special infinite-element-domain boundary condition [209]. Figure A.2b shows the associated model in *COMSOL*.

With the model set up with the appropriate boundary conditions in Figure A.2, the algorithm to integrate the methods of the previous sections is as follows:

procedure CAPMAT($\{g_1, ..., g_G\}, \{r_1, ...r_D\}$) ▷ G gates and D dot coordinates
  $\mathbf{C} \leftarrow \mathbf{0}_{(G+D)\times(G+D)}$
  ZEROALLGATES ▷ Set all gates to 0 V
  $\mathbf{C}_{\text{DD-INV}} \leftarrow \mathbf{0}_{D\times D}$
  for $m \leftarrow 1$ to D **do** ▷ Compute $\mathbf{C}_{\text{DD}}^{-1}$
    CLEARPOINTCHARGES ▷ Clear all point charges in model
    POINTCHARGE(e,r_m) ▷ Place 1e of charge at dot r_m
    for $n \leftarrow 1$ to D, $n \neq m$ **do**
      SOLVEFEA ▷ Mesh and solve model
      $\mathbf{C}_{\text{DD-INV}}(m,n) \leftarrow \phi(r_n)/e$ ▷ Take electrostatic potential at r_n
    $\mathbf{C}_{\text{DD-INV}}(m,m) \leftarrow 2 \times 45/e$
  CLEARPOINTCHARGES
  $\boldsymbol{\alpha} \leftarrow \mathbf{0}_{G\times D}$

14: **for** $m \leftarrow 1$ to G **do** ▷ Compute $\boldsymbol{\alpha}$-matrix
15: ZeroAllGates
16: GateVoltage(m,1 V) ▷ Set gate m to 1 V
17: SolveFEA
18: **for** $n \leftarrow 1$ to D **do**
19: $\boldsymbol{\alpha}(m, n) \leftarrow \phi(r_n)$
20: $\mathbf{C}(1..G, 1..D) \leftarrow -\boldsymbol{\alpha} \times \mathbf{C}_{\text{DD-INV}}$
21: $\mathbf{C}((G+1)..(G+D), 1..G) \leftarrow (-\boldsymbol{\alpha} \times \mathbf{C}_{\text{DD-INV}})^T$
22: $\mathbf{C}((G+1)..(G+D), (G+1)..(G+D)) \leftarrow (\mathbf{C}_{\text{DD-INV}})^{-1}$
23: **return C**

The algorithm is divided into three sections. The first section (lines 5-11) calculates $\mathbf{C}_{\text{DD}}^{-1}$ using the methods outlined in Section A.3.2. The second section (lines 14-19) calculates the alpha matrix $\boldsymbol{\alpha}$ using the methods outlined in Section A.3.1. The final section (lines 20-22) computes the required elements to fill in the capacitance matrix. Note that the inter-element matrix between the gate elements $\mathbf{C}_{\text{GG}}$ is left zeroed for this does not affect the electrostatics of electrons loading or unloading onto the quantum dots.

Appendix B

RF probing of nonlinear capacitance between reservoir and dot

The SLQD sensor involves the RF probing of electron oscillations between a reservoir and a quantum dot as discussed in Chapter 3. This appendix details the solutions surrounding the resulting RF response of the electrons (across the reservoir and quantum dot) by solving the corresponding rate equation discussed in Section 3.3.

B.1 Tunnel rates from Fermi's golden rule

Now consider an electron entering the dot from the reservoir. The tunnel rate, equivalently the transition probability per unit time, as given by the Fermi's golden rule is:

$$\Gamma_{\mathrm{D}\leftrightarrow\mathrm{R}} = \frac{2\pi}{\hbar} T_{DR}^2 \delta\left(E_D - E_R\right), \tag{B.1}$$

where E_R is the energy of electrons in the reservoir and T_{DR} is the transmission probability of an electron tunnelling between the reservoir to the dot. E_D is the lowest unfilled energy level in the quantum dot; that is, all energy levels below E_D are assumed to be filled (that is, the dot is in its ground state). Thus, E_D is the energy of the electron once it tunnels onto the dot. Note that the net tunnel rate is given as a Dirac δ-function for tunnelling only occurs between two states of the same energy.

The energy states in the reservoir and the dot may follow a weighted probability distribution. Thus, to get the net tunnel-rate, one must sum over all possible

reservoir and dot energy states. Thus, letting g_D and g_R be the state energy density distributions of the electrons in the dot and reservoir respectively, the net tunnel rate is:

$$\Gamma = \Gamma_0 \int_{-\infty}^{+\infty}\int_{-\infty}^{+\infty} g_D(E_d) g_R(E_r) \delta\left(E_d - E_r\right) dE_r\, dE_d, \tag{B.2}$$

where one assumes that the transmission probability is constant over all state transitions; thus, all the constants are compactly defined as $\Gamma_0 \equiv \frac{2\pi}{\hbar} T_{DR}^2$. The energy states on the reservoir are given by the Fermi-Dirac distribution (with $g_{R(\pm)}$ being that when electrons move onto and off the dot respectively):

$$\begin{cases} g_{R(+)}(E) \equiv \frac{1}{1+\exp\left(\frac{E-E_F}{k_B T}\right)} \\ \\ g_{R(-)}(E) \equiv 1 - \frac{1}{1+\exp\left(\frac{E-E_F}{k_B T}\right)} = \frac{1}{1+\exp\left(-\frac{E-E_F}{k_B T}\right)} \end{cases}, \tag{B.3}$$

where k_B is the Boltzmann constant, T is the temperature of the electrons in the reservoir and E_F is the reservoir Fermi-Energy level (tunable by the voltage applied to the reservoir). Now $g_{R(+)}$ describes the filled energy states (mostly filled below the Fermi-level E_R and mostly empty above the Fermi level) on the reservoir from which an electron may tunnel onto the dot. The distribution is inverted for $g_{R(-)}$ to describe the empty energy states to which the electron may occupy when moving off the dot. Now by Equation B.2 the tunnel rates for an electrons moving on or off the dot (defined as Γ_+ and Γ_- respectively) are:

$$\Gamma_\pm = \Gamma_0 \int_{-\infty}^{+\infty} \frac{g_D(E_d)}{1 + \exp\left(\pm\frac{E_d - E_F}{k_B T}\right)} dE_d. \tag{B.4}$$

Note that one assumes that the variation between the Fermi-level and a given dot energy state is small enough such that only one energy state, in the dot, crosses the Fermi-level. All dot states below this state remain filled. As there is only one available energy level on the dot, the distribution of states (assuming no lifetime broadening) is $g_D(E_d) \equiv \delta(E_d - E_D)$ where E_D is the energy of the energy electron when it tunnels onto the dot. Thus, the net tunnel rates are given by:

$$\Gamma_\pm = \frac{\Gamma_0}{1 + \exp\left(\pm\frac{E_D - E_F}{k_B T}\right)}. \tag{B.5}$$

B.2 Solving the rate equation

Electrons oscillating between a dot-to-lead transition can be modelled via a simple ordinary differential equation as described in Section 3.3.1. As the ODE is periodic, the natural solution is a Fourier series as shown in this section.

B.2.1 Main solution

Applying a sinusoidal gate voltage on a gate can induce shuttling of an electron between a reservoir and a quantum dot. Now the ODE governing the electron occupation is given by Equation 3.19 (constructed in Section 3.3.1):

$$\frac{dP_e}{dt} + \Gamma_0 P_e = \frac{\Gamma_0}{1 + \exp\left(\frac{e\alpha_{rg}}{k_B T}\left(V_0 + V_{ac}\cos(\omega t)\right)\right)} \equiv \Gamma_+(t) \tag{B.6}$$

As the right hand side is clearly periodic, the natural basis to write the steady-state solution is the Fourier basis:

$$P_e(t) = \sum_{n=1}^{\infty} P_n \equiv \sum_{n=1}^{\infty} A_{n(p)} \cos\left(n\omega t + \phi_{n(p)}\right) \tag{B.7}$$

$$\Gamma_+(t) = \sum_{n=1}^{\infty} F_n \equiv \sum_{n=1}^{\infty} \left(\frac{\omega}{\pi}\int_{-\frac{\pi}{\omega}}^{\frac{\pi}{\omega}} \Gamma_+ \cos(n\omega\tau) d\tau\right) \cdot \cos\left(n\omega t\right) \tag{B.8}$$

Note that $\Gamma_+(t)$ is an even function and thus, expressible as a Fourier cosine series. Now noting the linearity of the ODE and orthogonality of cosines, one may write an equation concerning the n^{th} harmonic by simply matching the coefficients of the cosines:

$$A_{n(p)}\left(\Gamma_0 \cos\left(n\omega t + \phi_{n(p)}\right) - n\omega \sin\left(n\omega t + \phi_{n(p)}\right)\right) = F_n \cos\left(n\omega t\right) \tag{B.9}$$

Now by the compound trigonometric identity:

$$A_{n(p)}\sqrt{\Gamma_0^2 + (n\omega)^2}\cos\left(n\omega t + \phi_{n(p)} + \arctan\left(\frac{n\omega}{\Gamma_0}\right)\right) = F_n \cos\left(n\omega t\right) \tag{B.10}$$

The integral F_n on the right hand side is solved in Section B.2.2. Now one may match the amplitude and phase terms on both sides (noting that the phase offset on

the RHS is zero) to yield the probability of the electron being on the dot:

$$P_n = A_{n(p)}\cos(n\omega t + \phi_{n(p)}), n \in \mathbb{N}$$
$$\begin{cases} A_{n(p)} = \frac{1}{\sqrt{\Gamma_0^2+(n\omega)^2}} \cdot \frac{-e\alpha_{rg}\Gamma_0 V_{ac}}{4nk_BT} \cdot F\left(\frac{e\alpha_{rg}}{2k_BT}V_{ac}, \frac{e\alpha_{rg}}{2k_BT}V_0, n\right) \\ \phi_{n(p)} = -\arctan\left(\frac{n\omega}{\Gamma_0}\right) \end{cases} . \tag{B.11}$$

B.2.2 Special function $F(x, y, n)$

A particular function required in solving the ODE given in Equation 3.19 shall be constructed in this section. Now the integral of concern is:

$$F_n = \frac{\omega}{\pi}\int_{-\frac{\pi}{\omega}}^{\frac{\pi}{\omega}} \frac{\Gamma_0\cos(n\omega t)}{1+\exp\left(\frac{e\alpha_{rg}}{k_BT}\left(V_0+V_{ac}\cos(\omega t)\right)\right)}dt \tag{B.12}$$

Using integration by parts[1]:

$$\begin{aligned} F_n =& \frac{\Gamma_0}{n\pi}\cdot\left[\frac{\sin(n\omega t)}{1+\exp\left(\frac{e\alpha_{rg}}{k_BT}\left(V_0+V_{ac}\cos(\omega t)\right)\right)}\right]_{-\frac{\pi}{\omega}}^{\frac{\pi}{\omega}} \\ &- \frac{\Gamma_0}{n\pi}\int_{-\frac{\pi}{\omega}}^{\frac{\pi}{\omega}} \frac{-\sin(n\omega t)\exp\left(\frac{e\alpha_{rg}}{k_BT}\left(V_0+V_{ac}\cos(\omega t)\right)\right)\frac{-e\omega\alpha_{rg}V_{ac}}{k_BT}\sin(\omega t)}{\left(1+\exp\left(\frac{e\alpha_{rg}}{k_BT}\left(V_0+V_{ac}\cos(\omega t)\right)\right)\right)^2}dt \\ =& 0 - \frac{e\omega\alpha_{rg}\Gamma_0 V_{ac}}{4nk_BT}\cdot\frac{1}{\pi}\int_{-\frac{\pi}{\omega}}^{\frac{\pi}{\omega}} \frac{\sin(n\omega t)\sin(\omega t)}{\cosh^2\left(\frac{e\alpha_{rg}}{2k_BT}\left(V_0+V_{ac}\cos(\omega t)\right)\right)}dt \end{aligned} \tag{B.13}$$

Applying the transformation: $\omega t \to t$ yields:

$$F_n = \frac{-e\alpha_{rg}\Gamma_0 V_{ac}}{4nk_BT}\cdot\frac{1}{\pi}\int_{-\pi}^{\pi} \frac{\sin(nt)\sin(t)}{\cosh^2\left(\frac{e\alpha_{rg}}{2k_BT}\left(V_0+V_{ac}\cos(t)\right)\right)}dt \tag{B.14}$$

$$\equiv \frac{-e\alpha_{rg}\Gamma_0 V_{ac}}{4nk_BT}\cdot F\left(\frac{e\alpha_{rg}}{2k_BT}V_{ac}, \frac{e\beta}{2k_BT}V_0, n\right), \tag{B.15}$$

where the function $F(x, y, n)$ is defined as:

[1] Taking $u = \left(1+\exp\left(\frac{e\alpha_{rg}}{k_BT}\left(V_0+V_{ac}\cos(\omega t)\right)\right)\right)^{-1}$ and $dv = \cos(n\omega t)$

$$F(x,y,n) \equiv \frac{1}{\pi}\int_{-\pi}^{\pi} \frac{\sin(t)\sin(nt)}{\cosh^2(y + x\cos(t))}dt. \tag{B.16}$$

The behaviour of this function is shown below in Figure B.1.

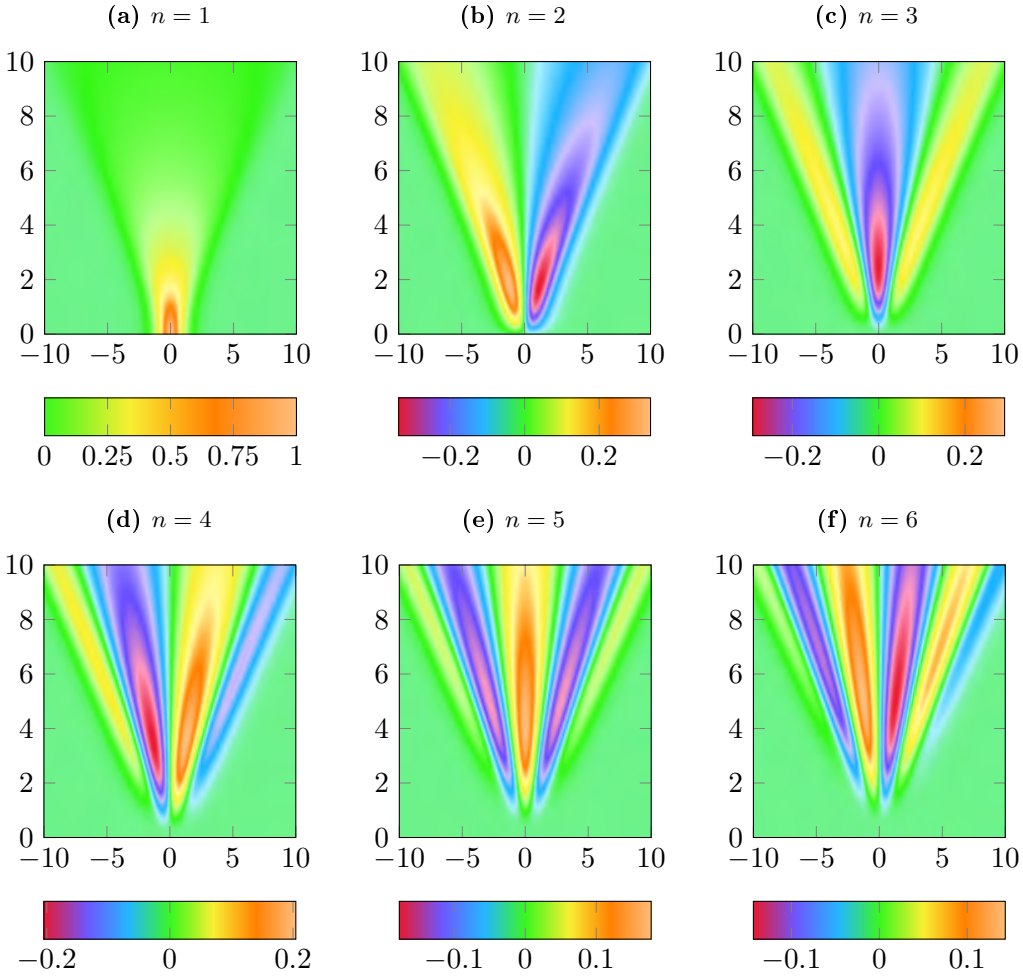

Figure B.1: Plot of $F(x,y,n)$ over $n = 1$ to $n = 6$. Note that both the quantum capacitance and Sisyphus resistance terms are proportional to $\sim F(V_{ac}, V_0, n)$.

B.2.3 Properties of $F(x,y,n)$

The special function $F(x,y,n)$ is plotted in Figure B.1. The first harmonic shows a monotonic decrease with increasing x, while the higher harmonics show peaking responses. The function also changes sign along the $y = 0$ for every odd harmonic while being zero for the even harmonics. Finally, the function accumulates a number

of lobes (that alternate in sign) equal to the harmonic number with the overall height of the lobes decreasing monotonically with harmonic number.

Now taking $x \to 0$, the special function F in Equation B.16 for $n = 1$ becomes:

$$\lim_{x\to 0} F(x,y,1) \equiv \frac{1}{\pi}\int_{-\pi}^{\pi} \frac{\sin^2(t)}{\cosh^2(y)}dt \equiv \int_{-\pi}^{\pi} \frac{1-\cos(2t)}{2\pi\cosh^2(y)}dt = \operatorname{sech}^2(y). \tag{B.17}$$

Similarly, one may take the limit $x \to \infty$:

$$x\cdot F(x,y,n) = \frac{2}{\pi}\int_{y-x}^{y+x} \frac{\sin(nt)}{\cosh^2(u)}du = \frac{2}{\pi}\int_{y-x}^{y+x} \frac{\sqrt{1-\left(\frac{u-y}{x}\right)^2}U_{n-1}\left(\frac{u-y}{x}\right)}{\cosh^2(u)}du, \tag{B.18}$$

where the substitution $u = y + x\cos(t)$ was made and one realises that F is even. In addition, one realises that $\sin(nt) \equiv \sin(t)\cdot U_{n-1}(\cos(t))$ with $U_n(t)$ being the Chebyshev polynomial of the second kind. Now separately letting u vary finitely, while letting x tend to infinity (with y being allowed to vary in a similar order of magnitude) yields:

$$\lim_{x\to\infty} x\cdot F(x,y,n) = \frac{2}{\pi}\int_{-\infty}^{\infty} \frac{\sqrt{1-\left(\frac{y}{x}\right)^2}U_{n-1}\left(\frac{-y}{x}\right)}{\cosh^2(u)}du = \frac{4\sqrt{1-\left(\frac{y}{x}\right)^2}U_{n-1}\left(\frac{-y}{x}\right)}{\pi}. \tag{B.19}$$

Thus, the asymptotic profile of $xF(x,y,n)$ over y is a Chebyshev polynomial with a circularly envelope. Now to find the asymptotic zeroes (that is, points of null response), one may expand U_{n-1}:

$$\lim_{x\to\infty} x\cdot F(x,y,n) = \frac{4\sqrt{1-\left(\frac{y}{x}\right)^2}}{\pi}2^{n-1}\prod_{k=1}^{n-1}\left(\frac{-y}{x} - \cos\left(\frac{k\pi}{n}\right)\right) \tag{B.20}$$

Now in the integral, the first fraction is always positive. Thus, if any zeroes exist, it must be due to the product on the right:

$$y = -x\cos\left(\frac{k\pi}{n}\right), \quad k < n, k \in \mathbb{N}. \tag{B.21}$$

Note that the minus sign can be dropped on noting the symmetry of the cosine and $F(x,y,n)$ about x and y. An intriguing idea now is that the saturating extrema of $x\cdot F(x,y,n)$ as $x \to \infty$ are centred on $y_{k_0} = -x\cos((k_0 + \frac{1}{2})\pi/n)$ for $0 \leqslant k < n$.

Taking this value for y and substituting it into Equation B.19 yields:

$$\lim_{x\to\infty} x \cdot F(x, y_{k_0}, n) = \frac{4\sin\left(\frac{(k_0+\frac{1}{2})\pi}{n}\right) U_{n-1}\left(\cos\left(\frac{(k_0+\frac{1}{2})\pi}{n}\right)\right)}{\pi}, \tag{B.22}$$

Applying the properties of U_n, this limit simplifies to:

$$\lim_{x\to\infty} x \cdot F(x, y_{k_0}, n) = \frac{4\sin\left((k_0+\frac{1}{2})\pi\right)}{\pi} = \frac{4}{\pi}(-1)^{k_0}, \quad k < n, k \in \mathbb{W}. \tag{B.23}$$

B.3 Summary

Table B.1 shows a summary of the physical parameters surrounding the SLQD sensor on combining the discussions in this appendix and in Section 3.3.

Parameter	Expression
Spectral Function	$F(x,y,n) \equiv \frac{1}{\pi}\int_{-\pi}^{\pi} \frac{\sin(t)\sin(nt)}{\cosh^2(y+x\cos(t))}dt$
Gate voltage	$V(t) = V_0 + V_{ac}\cos(\omega t)$
Current	$I(t) = \sum_{n=1}^{\infty} A_{n(I)}\cos(n\omega t + \phi_{n(I)})$ $\begin{cases} A_{n(I)} = \frac{e\alpha_{rg}\omega}{2} \cdot \frac{\Gamma_0}{\sqrt{\Gamma_0^2+(n\omega)^2}} \cdot \frac{e\alpha_{rg}}{2k_BT}V_{ac} \cdot F\left(\frac{e\alpha_{rg}}{2k_BT}V_{ac}, \frac{e\alpha_{rg}}{2k_BT}V_0, n\right) \\ \phi_{n(I)} = \frac{\pi}{2} - \arctan\left(\frac{n\omega}{\Gamma_0}\right) \end{cases}$
Maximum current ($V_0 = 0$)	$I_n^{\max} = \begin{cases} \frac{2e\alpha_{rg}}{\pi} \cdot \frac{\omega\Gamma_0}{\sqrt{\Gamma_0^2+(n\omega)^2}} \cdot (-1)^{\frac{n-1}{2}} & n \in \mathbb{N}_{\text{odd}} \\ 0 & n \in \mathbb{N}_{\text{even}} \end{cases}, \quad V_{ac} \to \infty$
High power current	$A_{n(I)} = \frac{2e\alpha_{rg}}{\pi} \cdot \frac{\omega\Gamma_0}{\sqrt{\Gamma_0^2+(n\omega)^2}} \cdot \sqrt{1-\left(\frac{V_0}{V_{ac}}\right)^2} \cdot U_{n-1}\left(\frac{V_0}{V_{ac}}\right), \quad V_{ac} \to \infty$
Peak lobe current	$I_n^{\text{peak-}k} = \frac{2e\alpha_{rg}}{\pi} \cdot \frac{\omega\Gamma_0}{\sqrt{\Gamma_0^2+(n\omega)^2}} \cdot (-1)^{k-1}, \quad k < n, k \in \mathbb{N}, V_{ac} \to \infty$
Zeroes in I_n	$V_0 = V_{ac}\cos\left(\frac{k\pi}{n}\right), \quad k < n, k \in \mathbb{N}, V_{ac} \to \infty$
RF response	$\Upsilon = V_{\text{in}} \cdot \frac{2\text{Q}_{\text{ext}}\text{Q}_{\text{int}}^2}{(\text{Q}_{\text{ext}}+\text{Q}_{\text{int}})^2} \cdot \frac{K\eta_{\text{loss}}}{C_p} \cdot \frac{e^2\alpha_{rg}^2}{4k_BT} \cdot \frac{\Gamma_0^2}{\Gamma_0^2+\omega^2} \cdot F\left(\frac{e\alpha_{rg}}{2k_BT}V_{ac}, \frac{e\alpha_{rg}}{2k_BT}V_0, 1\right)$ $\Upsilon = \frac{\text{Q}_{\text{int}}}{\text{Q}_{\text{ext}}+\text{Q}_{\text{int}}} \cdot \frac{K}{C_p} \cdot \frac{e\alpha_{rg}}{2} \cdot \frac{\Gamma_0^2}{\Gamma_0^2+\omega^2} \cdot \frac{e\alpha_{rg}}{2k_BT}V_{\text{ac}} \cdot F\left(\frac{e\alpha_{rg}}{2k_BT}V_{ac}, \frac{e\alpha_{rg}}{2k_BT}V_0, 1\right)$ $\Upsilon_{\text{large}} = \frac{\text{Q}_{\text{int}}}{\text{Q}_{\text{ext}}+\text{Q}_{\text{int}}} \cdot \frac{K}{C_p} \cdot \frac{2e\alpha_{rg}}{\pi} \cdot \frac{\Gamma_0^2}{\Gamma_0^2+\omega^2} \cdot \sqrt{1-\left(\frac{V_0}{V_{ac}}\right)^2}, \quad V_{ac} \to \infty$
Max. RF response	$\Upsilon_{\max} = \frac{\text{Q}_{\text{int}}}{\text{Q}_{\text{ext}}+\text{Q}_{\text{int}}} \cdot \frac{K}{C_p} \cdot \frac{2e\alpha_{rg}}{\pi} \cdot \frac{\Gamma_0^2}{\Gamma_0^2+\omega^2}, \quad \frac{e\alpha_{rg}}{2k_BT}V_{\text{ac}} \gg 1$
Linear RF response	$\frac{\Upsilon}{V_{\text{ac}}} = \frac{\text{Q}_{\text{int}}}{\text{Q}_{\text{ext}}+\text{Q}_{\text{int}}} \cdot \frac{K}{C_p} \cdot \frac{\Gamma_0^2}{\Gamma_0^2+\omega^2} \cdot \frac{e^2\alpha_{rg}^2}{4k_BT} \cdot \text{sech}^2\left(\frac{e\alpha_{rg}}{2k_BT}V_0\right), \quad V_{\text{ac}} \to 0$
Power	$P_{\text{avg}} = \frac{1}{2} \cdot V_{ac} \cdot \frac{e\alpha_{rg}}{2} \cdot \frac{\omega^2\Gamma_0}{\Gamma_0^2+\omega^2} \cdot \frac{e\alpha_{rg}}{2k_BT}V_{ac} \cdot F\left(\frac{e\alpha_{rg}}{2k_BT}V_{ac}, \frac{e\alpha_{rg}}{2k_BT}V_0, 1\right)$
Asymptotic Power	$P_{\text{asym.}} = \frac{e\alpha_{rg}}{\pi} \cdot \frac{\omega^2\Gamma_0}{\Gamma_0^2+\omega^2} \cdot V_{ac}, \quad \frac{e\alpha_{rg}}{2k_BT}V_{\text{ac}} \gg 1$

Table B.1: Comparison of the experimentally deduced α values with an FEA simulation. The experimental measurements were only possible on the right-hand dot pair D2L and D2U. The differential alpha $\Delta\alpha_{\text{G}}$ for a given gate G is defined as $V_{ac} = \eta_{\text{loss}}\text{Q}_{\text{eff}}V_{\text{in}}$

.

Appendix C

RF probing of nonlinear capacitance between two quantum dots

Section 4.1.1 introduced a Hamiltonian construction describing a double quantum dot system being measured with a single-gate RF sensor:

$$\mathbf{H}_{\text{id}} = \begin{pmatrix} \Delta & -t_c \\ -t_c & -\Delta \end{pmatrix} \equiv \Delta\sigma_z - t_c\sigma_x, \tag{C.1}$$

$$\Delta = \tfrac{e\Delta\alpha}{2}\left(V_0 + V_{ac}\cos(\omega t)\right) \equiv V_0' + V_{ac}'\cos\left(\omega t\right). \tag{C.2}$$

where t_c is the inter-dot tunnel coupling, Δ is the detuning and $\Delta\alpha$ is the differential lever-arm. The applied voltage (at the gate of the device) is a sum of the detuning offset voltage V_0 (voltage offset from the inter-dot crossing where $\Delta = 0$) and the applied RF sensor drive amplitude V_{ac}. The aim is to find the probability of occupation with respect to time $p(t)$. From which one obtains the current to ultimately deduce the quantum capacitance.

Given the foundation laid out by the Hamiltonian, the following sections outline the pathway taken to find the quantum capacitance:

- Appendix C.1 gives a general overview for the solution by the rotating wave approximation. The general solution is applicable to other driven systems (for example, ESR on single-spin qubits [16, 50] or AC driving of singlet-triplet qubits [34]).
- Appendix C.2 outlines a solution to the Hamiltonian using the rotating wave approximation (RWA). Given the periodic Hamiltonian, this seemed to be a

natural approach. This section highlights a general solution utilised by the following two sections.

- Appendix C.3 applies the RWA solution to the resonant tunnelling capacitance regime where the driving frequency matches the energy splitting between the ground and excited states. The solution yielded conditions required for maximum readout signal strength when using the tunnelling capacitance mode.
- Appendix C.4 briefly discusses the limitation of RWA when applied to the adiabatic quantum capacitance mode.
- Appendix C.5 thus provides a semi-classical approach to solving the Hamiltonian for the adiabatic quantum capacitance mode of operation.

C.1 Rotating wave approximation

In this section, one shall consider a common time-dependent Hamiltonian on a two-level system and the subsequent rotating wave approximation [210–213]. The Hamiltonian is a sum of a bare Hamiltonian (free precession due to a z-directional magnetic field) and that of a driving Hamiltonian:

$$\mathbf{H} = \frac{E_z}{2}\sigma_z + \mathbf{H}_{\text{drive}}, \tag{C.3}$$

where the driving Hamiltonian $\mathbf{H}_{\text{drive}}$ is defined as the sum of two orthogonal time-dependent fields (that are also orthogonal to the z-axis; thus, chosen to be along the x and y axes):

$$\mathbf{H}_{\text{drive}(\pm)} = \frac{E_{ac}}{2}\left(\cos(\omega t)\sigma_x \pm \sin(\omega t)\sigma_y\right) = \frac{E_{ac}}{2}\begin{pmatrix} 0 & \mathrm{e}^{\mp i\omega t} \\ \mathrm{e}^{\pm i\omega t} & 0 \end{pmatrix} \tag{C.4}$$

The two orthogonal driving fields create two circularly polarised driving fields termed co-rotating for $\mathbf{H}_{\text{drive}(+)}$ and counter-rotating for $\mathbf{H}_{\text{drive}(-)}$. The co-rotating term follows the rotation prescribed by the bare Pauli-z rotation term. In resonant driving (where the frequency of the drive equals the Pauli-z energy splitting) if one were in the rotating frame that followed the co-rotating term, the Pauli-z term will effectively disappear to enable a simple solution that yields x-rotations.

Now consider the co-rotating drive. To solve the behaviour of the co-rotating component, it is convenient to work in the frame that rotates with the circularly polarised axis:

$$\mathbf{T}_+ = R_z(-\omega t) = \mathrm{e}^{i\frac{\omega t}{2}\sigma_z}. \tag{C.5}$$

The applied transformation makes the co-rotating circularly polarised vector appear to be of a constant magnitude without any oscillations; the removal of the time-dependence enables a simple solution. Now applying the transformation to the Schrödinger's equation yields:

$$i\hbar\mathbf{T}_+\frac{\partial}{\partial t}\left(\mathbf{T}_+^\dagger\mathbf{T}_+\Psi\right) = \mathbf{T}_+\mathbf{H}_{\mathrm{drive}(+)}\mathbf{T}_+^\dagger\mathbf{T}_+\Psi. \tag{C.6}$$

Simplifying the equation while taking taking $\Psi' = \mathbf{T}_+\Psi$ to be the transformed state vector, one may write the effective Hamiltonian in the co-rotating frame to be:

$$\mathbf{H}_{+(\mathrm{rot})} = \frac{E_z - \hbar\omega}{2}\sigma_z + \frac{E_{ac}}{2}\sigma_x. \tag{C.7}$$

The co-rotating Hamiltonian describes a simple two level system where the precession in the rotating frame is purely about the x-axis when $E_z = \hbar\omega$. That is, one resonantly drives the two-level system at a frequency matching the splitting given by E_z. If the driving frequency ω fails to match $E_z/\hbar$, then the rotation axis tilts as per the detuning $E_z - \hbar\omega$ compared with E_{ac}.

Now consider the driving field being counter-rotating circularly polarised field. It is convenient to work in the frame that rotates with the circularly polarised axis:

$$\mathbf{T}_- = R_z(\omega t) = \mathrm{e}^{-i\frac{\omega t}{2}\sigma_z}. \tag{C.8}$$

Similar to before, applying the rotating transformation removes the oscillatory time dependence of the counter-rotating term. Applying the transformation to the Schrödinger's equation like before, taking $\Psi' = \mathbf{T}_-\Psi$ to be the transformed state vector and simplifying the resulting equation yields the effective Hamiltonian in the counter-rotating frame to be:

$$\mathbf{H}_{-(\mathrm{rot})} = \frac{E_z + \hbar\omega}{2}\sigma_z + \frac{E_{ac}}{2}\sigma_x. \tag{C.9}$$

The counter-rotating Hamiltonian describes a simple two level system where the precession in the rotating frame now lies on an axis prescribed by E_{ac} and $E_z + \hbar\omega$. One could induce pure x-rotations by using $-\omega$, but this is trivially the definition of the co-rotating waveform described in the previously.

During resonant driving ($\hbar\omega = E_z$), the co-rotating solution yields neat rotations, while the counter-rotating solution yields rotates about an axis given by E_{ac} and

$E_z + \hbar\omega$. It is as if one drives the co-rotating solution resonantly ($\hbar\omega = E_z$), while driving the counter-rotating solution a detuning away from the splitting at twice the z-splitting. That is, the axis of rotation for the counter-rotating solution is given by E_{ac} and $2\hbar\omega$. Now assume that one drives the two-level system resonantly with $\hbar\omega = E_z$. One way to get good rotations about the x-axis would be if the counter-rotating solution were to produce clean rotations about the x-axis with $E_{ac} \ggg E_z + \hbar\omega$; that is, the 'strong driving regime'. An alternative method is to suppress all rotations, then one can work in the regime where $E_{ac} \lll E_z + \hbar\omega$; that is, the 'weak driving regime'. The weak driving regime is the basis of the 'rotating wave approximation' where one neglects this high frequency z-axis contribution.

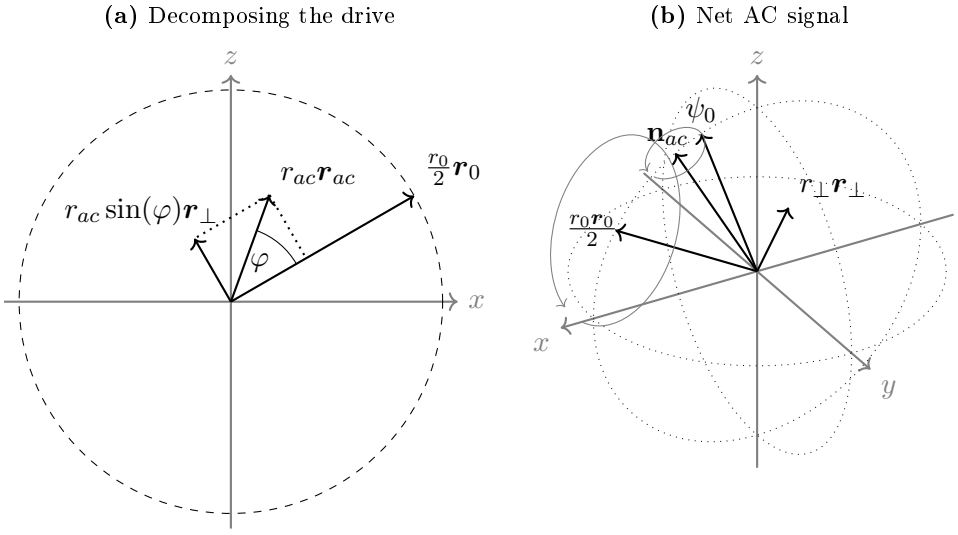

Figure C.1: Bloch sphere representation of the general rotating wave Hamiltonian. Here, the driving term r_{ac} (the $\cos(\omega t)$ is omitted for clarity) is non-orthogonal to the stationary term $r_0/2$. **(a)** Under a perturbative approximation, the component of the driving term parallel with the stationary term can be ignored to leave $r_{ac}\sin(\varphi)\boldsymbol{r}_\perp$ be the only time-dependent term taken into consideration. **(b)** The net dynamics is that of precession about the axis $\mathbf{n}_{ac}$, noting that $\mathbf{n}_{ac}$ is parallel to $\mathbf{r}_\perp$ if driven at resonance, and then precession at frequency ω about the stationary axis $\mathbf{r}_0$.

A more general problem is when the driving term is not orthogonal to the main stationary component. Figure C.1a describes one such Hamiltonian where the stationary term sets the axis of rotation at $\boldsymbol{\sigma}_0$ at a precession frequency of $r_0/2$. The driving term $r_{ac}\boldsymbol{\sigma}_{ac}/2$ is applied at an angle φ from the stationary term. The full non-orthogonal Hamiltonian is:

$$\mathbf{H}_{\mathrm{NO}} = \frac{r_0}{2}\boldsymbol{\sigma}_0 + r_{ac}\cos(\omega t)\boldsymbol{\sigma}_{ac} \approx \frac{r_0}{2}\boldsymbol{\sigma}_0 + r_{ac}\sin(\varphi)\cos(\omega t)\boldsymbol{\sigma}_{ac}. \tag{C.10}$$

Note that $\boldsymbol{\sigma}_0$ and $\boldsymbol{\sigma}_{ac}$ are the Pauli vector matrices corresponding to the rotation vectors $\boldsymbol{r}_0$ and $\boldsymbol{r}_{ac}$ respectively. The approximation made here is that the driving amplitude r_{ac} is pertubative and thus, does not significantly affect the magnitude stationary term. Therefore, one may simply consider the portion of the driving term orthogonal to the stationary term. Taking the frame co-rotating about $\boldsymbol{\sigma}_0$ and applying the rotating wave approximation, the dynamics are given approximately by rotations about the axis (the magnitude relating to the frequency of precession):

$$\mathbf{n}_{ac} = \frac{r_0 - \hbar\omega}{2}\boldsymbol{r}_0 + \frac{r_{ac}\sin(\varphi)}{2}\boldsymbol{r}_{\perp}. \tag{C.11}$$

In the lab frame, the dynamics translate to nutation akin to a precessing gyroscope. That is, the initial state vector ψ_0, highlighted in Figure C.1b, precesses about $\mathbf{n}_{ac}$ (the nutation) while the axis itself precesses about $\mathbf{r}_0$ (the overall precession) at frequency ω.

C.2 Solving the Hamiltonian using RWA

The periodic driving of the Hamiltonian given by the detuning drive in Equation C.1 lends itself to the application of the rotating wave approximation. However, the driving term is not necessarily orthogonal to the stationary term as illustrated in Bloch sphere diagrams in Figure C.2. The driving term (shown in blue) of amplitude V'_{ac} occurs along the Pauli-z axis. The stationary term (shown in red) is given by the tunnel coupling along the Pauli-x axis and the detuning offset V'_0 along the Pauli-z axis. Thus, the stationary term is not orthogonal to the driving term and forms an angle φ with the driving term as shown in Figure C.2a.

Now one invokes a perturbative approximation where only the orthogonal component of the driving term $\mathbf{r}_{\perp}$ is considered for the precession dynamics. As discussed in Appendix C.1, the remaining component (the portion of the driving term parallel with $\mathbf{r}_0$) will not affect the dynamics if the stationary term $\mathbf{r}_0$ is really large. Experimentally, this implies that the voltage amplitude of the RF drive V'_{ac} is perturbative with respect to the energy splitting (if $V'_0 = 0$, it implies that $V'_{ac} \ll t_c$ as seen in previous experiments [133]). Now the orthogonal component of the driving term (shown in green) is:

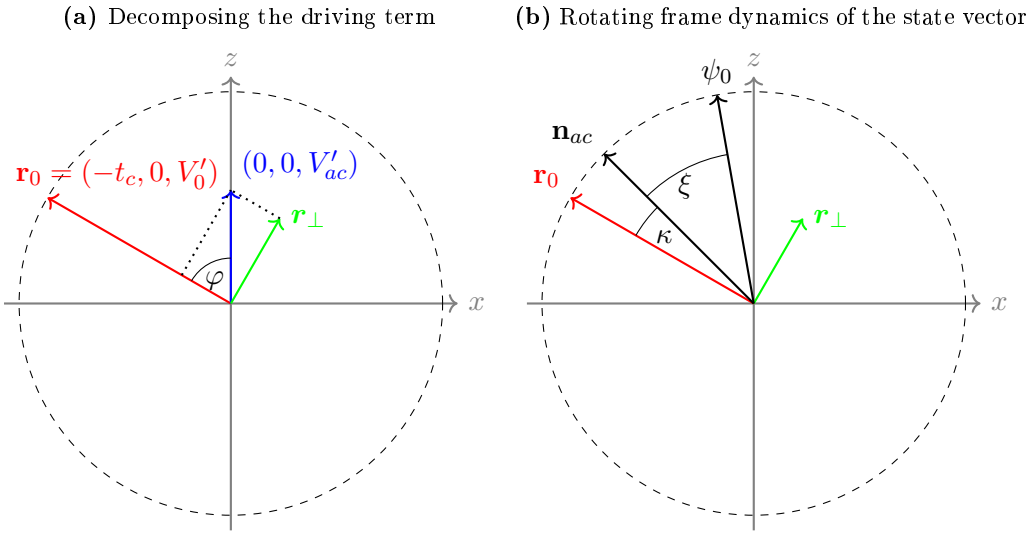

Figure C.2: Bloch sphere representation of a driving Hamiltonian modelling single-gate RF readout. The driving term V_{ac}' (the $\cos(\omega t)$ is omitted for clarity) is non-orthogonal to the stationary term r_0. **(a)** Under a perturbative approximation, the component of the driving term parallel with the stationary term can be ignored to leave $V_{ac}' \sin(\varphi)\hat{\boldsymbol{r}}_\perp$ be the only time-dependent term taken into consideration. **(b)** The axis of rotation in the rotating frame (rotated about the stationary axis $\mathbf{r}_0$) is given by the driving amplitude and the amount the driving frequency is off resonant from the tunnel coupling as given in Equation C.13 ($\mathbf{n}_{ac}$ is parallel to $\mathbf{r}_\perp$ if driven at resonance). The net result is that the initial state precesses about the axis $\mathbf{n}_{ac}$ in the rotating frame. When returning to the lab frame (by rotating about the axis $\mathbf{r}_0$), said precession becomes a nutation to the overall precession at frequency ω about the stationary axis $\mathbf{r}_0$.

$$\mathbf{r}_\perp \equiv V_{ac}' \sin(\varphi) \cdot \frac{(V_0', 0, t_c)}{\sqrt{t_c^2 + V_0'^2}} = \frac{V_{ac}' t_c}{t_c^2 + V_0'^2} \cdot (V_0', 0, t_c)\,. \tag{C.12}$$

Now one enters the frame that rotates about the stationary term $\mathbf{r}_0$ (the rotating frame) as shown in Figure C.2b. From Equation C.11, the time-dependent dynamics are such that the initial state vector ψ_0 precesses about the rotation axis (in the frame rotating about the $\mathbf{r}_0$-axis):

$$\mathbf{n}_{ac} = \frac{2\sqrt{t_c^2 + V_0'^2} - \hbar\omega}{2} \boldsymbol{r}_0 + \frac{V_{ac}' t_c}{2\sqrt{t_c^2 + V_0'^2}} \boldsymbol{r}_\perp. \tag{C.13}$$

Note that the result is the same as in any driving system; that is, the rotations are purely about the $\mathbf{r}_0$-axis if one drives resonantly and matches the energy splitting of the stationary term $\hbar\omega = 2\sqrt{t_c^2 + V_0'^2}$. Nonetheless, in the rotating frame, ψ_0 rotates about $\mathbf{n}_{ac}$ at an angle ξ. Back in the lab-frame, the resulting dynamics is precession

of the initial state vector ψ_0 about $\mathbf{n}_{ac}$ (the nutation) and precession about the vector $\mathbf{r}_0$. Decomposing ψ_0 into a parallel and orthogonal component with respect to $\mathbf{n}_{ac}$, the parts orthogonal to $\mathbf{n}_{ac}$ will produce oscillations at $\omega \pm |\mathbf{n}_{ac}|$, while the parallel component will oscillate at ω (the frequency of concern when deducing the eventual quantum capacitance).The component of the state vector parallel with the rotation axis (in the rotating frame) is $\psi_{\parallel} = \cos(\xi)$. The parallel component then precesses about $\mathbf{r}_0$ in the lab frame; the circular trajectory can be described as:

$$\psi_{\parallel}(t) = \cos(\xi)\sin(\kappa)\left(\cos(\omega t)\frac{\mathbf{r}_{\perp}}{|\mathbf{r}_{\perp}|} + \sin(\omega t)(0,1,0)\right) \tag{C.14}$$

Given the relevant trajectory at ω, one simply needs to find the z-probability of occupying the charge state s_{11}. Now consider the associated 2×2 density matrix in the rotating frame for a Bloch vector $\mathbf{P}$: $P \equiv \frac{1}{2}(\mathbf{I}_2 + \boldsymbol{\sigma} \bullet \mathbf{P})$, with the elements P_{ij} (for row i and column j). Measuring along $|0\rangle$, the probability of occupation is:

$$p(t) \equiv \mathrm{tr}\left(P \cdot \begin{pmatrix} 1 & 0 \\ 0 & 0 \end{pmatrix}\right) = P_{11} \equiv \frac{1}{2} + \frac{P_z}{2}, \tag{C.15}$$

where P_z is the z-component of $\mathbf{P}$. Thus, only the z-component matters; isolating the z component of the Bloch vector evolution:

$$p_{\omega}(t) = \frac{1}{2} + \frac{\cos(\xi)\sin(\kappa)}{2} \cdot \frac{t_c}{\sqrt{V_0'^2 + t_c^2}} \cdot \cos(\omega t), \tag{C.16}$$

where one may note that:

$$\sin(\kappa) = \frac{\frac{V'_{ac} t_c}{2\sqrt{t_c^2 + V_0'^2}}}{\sqrt{\left(\frac{V'_{ac} t_c}{2\sqrt{t_c^2 + V_0'^2}}\right)^2 + \left(\frac{2\sqrt{t_c^2 + V_0'^2} - \hbar\omega}{2}\right)^2}}. \tag{C.17}$$

Now similar to the SLQD analysis, one may calculate the net charge flow into the gate, to which the resonator is attached: $-e\Delta\alpha \cdot p_e(t)$. Thus, the current, the derivative of the charge flow, on the lead is:

$$I_{\omega}(t) = e\omega\Delta\alpha \cdot \frac{\cos(\xi)\sin(\kappa)}{2} \cdot \frac{t_c}{\sqrt{V_0'^2 + t_c^2}} \cdot \sin(\omega t). \tag{C.18}$$

The resulting ac capacitance[1] shall be defined, like in the SLQD analysis, crudely as $\frac{1}{\omega} \cdot \frac{I}{V_{ac}}$:

[1] If the term turns out to be negative, then one may find the equivalent inductance by taking $L \equiv -\frac{1}{\omega^2 C_q}$

$$C_q = \frac{e\Delta\alpha}{V_{ac}} \cdot \frac{\cos(\xi)\sin(\kappa)}{2} \cdot \frac{t_c}{\sqrt{V_0'^2 + t_c^2}}. \tag{C.19}$$

With the ac capacitance known, one may deduce the RF readout signal strength. The following sections shall investigate two different operating conditions: the resonant tunnelling capacitance mode and the adiabatic quantum capacitance mode.

C.3 Resonant tunnelling capacitance

Towards the end of the thesis, single-shot single-gate RF spin readout was shown using the tunnelling capacitance mode [133]. The experiment reported an RF drive frequency of 5.7 GHz with an inter-dot tunnel coupling of only 2 GHz. With the drive frequency greater than the tunnel coupling, electrons on the double quantum dot will be too slow to respond to the fast drive frequency to operate in the adiabatic quantum capacitance regime. Thus, the experimenters declared that they operated in the tunnelling capacitance regime. This raised two key questions:

- If one can operate at frequencies higher than the tunnel coupling via the tunnelling capacitance regime, why did initial experiments on a quadruple quantum dot device (where the drive frequency was much higher than the tunnel coupling) yield zero RF response?
- What are the conditions that must be satisfied to operate in the tunnelling capacitance regime?

To better understand the high-frequency operation of the single-gate RF sensor in the tunnelling capacitance regime, the RWA solution from the previous section was solved for the resonant tunnelling capacitance regime.

For resonant tunnelling, one sets the detuning offset, tunnel-coupling and drive-frequency such that:

$$\hbar\omega = 2\sqrt{t_c^2 + V_0'^2} \tag{C.20}$$

The resonant condition simplifies the required trigonometric terms in equation for the ac capacitance given in Equation C.19 to:

$$\sin(\kappa) = 1 \tag{C.21}$$

$$\cos(\xi) = 1. \tag{C.22}$$

Note that $\kappa = \pi/2$ is self-evident given that one demands resonant driving implies that $\mathbf{n}_{ac}$ is parallel with $\mathbf{r}_\perp$. Similarly, $\xi = 0$ implies that the initial state vector settles onto the eigenstate[2] given by $\mathbf{r}_\perp$. The quantum capacitance is thus:

$$C_q = \frac{e\Delta\alpha}{V_{ac}} \cdot \frac{1}{2} \cdot \frac{t_c}{\sqrt{V_0'^2 + t_c^2}}. \tag{C.23}$$

Thus, given the ac capacitance term, the equation for RF readout signal strength can be found via Equation 3.11:

$$\Upsilon = \frac{\mathrm{Q_{int}}}{\mathrm{Q_{ext}} + \mathrm{Q_{int}}} \cdot \frac{K}{C_p} \cdot \frac{e\Delta\alpha}{2} \cdot \frac{t_c}{\sqrt{V_0'^2 + t_c^2}}. \tag{C.24}$$

The peak RF readout response is similar to that of the SLQD system; the readout signal strength is ultimately limited by the charge movement of a single electron between the two dots. The $t_c/\sqrt{V_0'^2 + t_c^2}$ factor becomes unity when $t_c \gg V_0'$. That is, the working point for readout is ideally close to zero detuning when compared to the tunnel coupling. Thus, if one wishes to use the resonant tunnelling capacitance to perform single-gate RD readout, the driving frequency must be as close as possible to the tunnel coupling frequency. Note that if the driving frequency is below the tunnel coupling, one cannot achieve the resonance condition and thus, the RF readout signal is further diminished. That is, if the drive frequency is above the tunnel coupling, one can adjust V_0' to increase the energy splitting and bring the RF drive into resonance.

Finally, the readout signal strength has no dependence on the input voltage amplitude. However, to minimise decoherence (important when driving between excited states of a short-lived charge-qubit states), one should minimise photon shot-noise by operating at as low a signal strength as possible.

C.4 Adiabatic quantum capacitance - limitation of RWA

In the adiabatic quantum capacitance mode (as demonstrated and optimised in this thesis) shown in Figure 3.4b, one stays in the ground state as much as possible. Thus, to ensure adiabatic passage between the two charge states (that is, the electron moving between the two sites), one drives the qubit with as slow a driving frequency as possible via: $\hbar\omega \ll t_c$. As in the previous section, the required trigonometric terms in equation for the ac capacitance given in Equation C.19 become:

[2] In the case $t_c \gg V_0'$, the stationary term $\mathbf{r}_0$ lies on the Pauli-x axis, while the driving term $\mathbf{r}_\perp$ lies on the z-axis. Thus, one starts fully in the s_{11} or s_{02} charge states to make $\xi = 0$.

$$\sin(\kappa) = \frac{V'_{ac}}{\sqrt{\frac{4\left(t_c^2+V'_0\right)^2}{t_c^2} + V'^2_{ac}}} \tag{C.25}$$

$$\cos(\xi) = 1. \tag{C.26}$$

Once again, $\xi = 0$ implies that the initial state vector settles onto the $\mathbf{n}_{ac}$. The quantum capacitance is thus:

$$C_q = \frac{e\alpha_\Delta}{V_{ac}} \cdot \frac{1}{2} \cdot \frac{V'_{ac}}{\sqrt{\frac{4\left(t_c^2+V'_0\right)^2}{t_c^2} + V'^2_{ac}}} \cdot \frac{t_c}{\sqrt{V'^2_0 + t_c^2}}. \tag{C.27}$$

Thus, by Equation 3.11, the RF readout signal strength is:

$$\Upsilon = \frac{\mathrm{Q_{int}}}{\mathrm{Q_{ext}} + \mathrm{Q_{int}}} \cdot \frac{K}{C_p} \cdot \frac{e\alpha_\Delta}{2} \cdot \frac{V'_{ac}}{\sqrt{\frac{4\left(t_c^2+V'_0\right)^2}{t_c^2} + V'^2_{ac}}} \cdot \frac{t_c}{\sqrt{V'^2_0 + t_c^2}}. \tag{C.28}$$

Now the maximum readout signal is achieved at around zero-detuning where $V'_0 = 0$ as expected since this equally oscillates the electrons completely into both dots. In addition, however the readout signal strength now depends on the driving voltage amplitude V'_{ac} with the prediction that the maximal readout signal strength occurs at infinitely large amplitudes. The perturbative approximation required for RWA used here however, breaks down at large voltage amplitudes $V'_{ac} \gtrsim t_c$. In fact, the predicted response does not match numerical Hamiltonian simulations at non-perturbative powers. Thus, we have adapted a different approach in the next section to find the readout signal strength at higher RF powers.

C.5 Adiabatic quantum capacitance - semi-classical solution

The response given by Equation C.28 only applies for perturbative input voltage amplitudes; specifically $V'_{ac} \ll t_c$. However, larger input voltage amplitudes (at a magnitude equal to or exceeding the tunnel coupling) have been shown to yield better RF responses [29–31]. Whilst the model using the RWA mimics the appropriate functional trend, there are incorrect factors that makes the model fail in replicating numeric simulations when using large input voltage amplitudes. However, the RWA model does provide useful insights that may help derive a more accurate model. The

adiabatic quantum capacitance approach seeks to track the ground-state eigenstate (in the s_{11}-s_{02} basis):

$$\psi_g = \left(\sqrt{\frac{1}{2}\left(1 - \frac{\Delta}{\sqrt{t_c^2 + \Delta^2}}\right)}, \sqrt{\frac{1}{2}\left(1 + \frac{\Delta}{\sqrt{t_c^2 + \Delta^2}}\right)} \right). \tag{C.29}$$

One can intuitively break down the eigenvector by realising that the ground state is s_{11} when $\Delta \to -\infty$ and s_{02} when $\Delta \to \infty$. Now one sets the detuning offset to zero ($V_0' = 0$) for maximal RF readout response as suggested by the previous analysis. When the voltage signal sweeps the detuning sinusoidally one enters the s_{11} and s_{02} ground-state charge-states. The extent in probability to which one reaches one of the charge states varies sinusoidally with the variation being largest at the trough and peak in the detuning. Now the probability of being in s_{11} is $|\langle s_{11} \mid \psi_0 \rangle|^2$. Taking the difference in probabilities at $\Delta = -V_{ac}'$ and $\Delta = V_{ac}'$ and halving the result (to find the amplitude), the probability $p_\omega(t)$ oscillates at frequency ω:

$$p_\omega(t) = \frac{1}{2} + \frac{V_{ac}' \chi_{gs}}{2\sqrt{t_c^2 + V_{ac}'^2}} \cdot \cos(\omega t). \tag{C.30}$$

The χ_{gs} term describes the degree to which one is in the ground state (as to be discussed later). Here, $\chi_{gs} = 1$ implies that one has settled onto the ground-state eigenstate before performing the measurement. Thus, as before, one may calculate the current and find the quantum capacitance to be:

$$C_q = \frac{e\Delta\alpha}{V_{ac}} \cdot \frac{V_{ac}' \chi_{gs}}{2\sqrt{t_c^2 + V_{ac}'^2}}. \tag{C.31}$$

Thus, as before, the readout signal strength can be found:

$$\Upsilon = \frac{\mathrm{Q_{int}}}{\mathrm{Q_{ext}} + \mathrm{Q_{int}}} \cdot \frac{K}{C_p} \cdot \frac{e\Delta\alpha}{2} \cdot \frac{V_{ac}' \chi_{gs}}{\sqrt{t_c^2 + V_{ac}'}}. \tag{C.32}$$

One may set $\chi_{gs} = 1$ and obtain an initial solution to the readout response. However, the readout signal strength on setting $\chi_{gs} = 1$ has two important caveats. Firstly, the initial charge state is presumed to be the ground-state eigenstate and secondly, the apparent saturation of the RF readout signal at high V_{ac}' is unphysical (infinitely large V_{ac}' will result in an infinitely faster Landau velocity at zero detuning; thus, the state no longer adiabatically tracks the ground state). The first case shall be addressed before alleviating the second issue.

Now if one starts with an arbitrary initial state ψ_i, if the electrons start fully in the ground state, the electron oscillations at frequency ω will fully contribute to the

readout signal. On the other extreme, if the electrons were fully in the excited state, then the resulting current will be 180° out of phase when comparing to the current resulting from being in the ground state. The phase difference occurs because the charge is 180° out of phase with the voltage. That is, when the detuning is set such that the electron should enter a given dot, the electron enters the opposite dot. Now a 180° phase difference is a destructive interference effect. Assuming that the electrons move between eigenstates states (on negative and positive detuning) adiabatically (therefore, maintaining ground and excited state probabilities), the ground-state factor χ_{gs} describes the diminishing readout signal (due destructive interference from being partially in the excited state) via:

$$\chi_{gs} = P_{gs} - P_{ex}, \tag{C.33}$$

where P_{ex} and P_{gs} are the excited and ground-state probabilities at the start of the readout cycle. The parameter χ_{gs} shall be calculated for the two cases where the initial ground state is $|s_{11}\rangle$ (as expected if one has performed singlet-triplet qubit operations with the electrons in the s_{11} state) and $|-\rangle$ (the ground state at zero detuning). Thus, calculating the ground-state factor via $|\langle\psi_i \mid \psi_g\rangle|$ where ψ_g is the ground state on initiating readout at $\pm V'_{ac}$:

$$\begin{cases} \chi_{gs} = \frac{V'_{ac}}{\sqrt{t_c^2+V'^2_{ac}}}, & \psi_i = s_{11} \\ \chi_{gs} = \frac{t_c}{\sqrt{t_c^2+V'^2_{ac}}}, & \psi_i = |-\rangle = \frac{1}{\sqrt{2}}\left(s_{11} - s_{02}\right) \end{cases} \tag{C.34}$$

Thus, if the initial states were s_{11} or $|-\rangle$ respectively, the RF readout response is:

$$\Upsilon_0 = \frac{\mathrm{Q_{int}}}{\mathrm{Q_{ext}} + \mathrm{Q_{int}}} \cdot \frac{K}{C_p} \cdot \frac{e\Delta\alpha}{2} \cdot \frac{V'^2_{ac}}{t_c^2 + V'^2_{ac}} \tag{C.35}$$

$$\Upsilon_- = \frac{\mathrm{Q_{int}}}{\mathrm{Q_{ext}} + \mathrm{Q_{int}}} \cdot \frac{K}{C_p} \cdot \frac{e\Delta\alpha}{2} \cdot \frac{V'_{ac} t_c}{t_c^2 + V'^2_{ac}}. \tag{C.36}$$

The RF response appears to monotonically saturate at large V'_{ac} if the initial state is $|s_{11}\rangle$. However, the RF response has a maximum at $V'_{ac} = t_c$ if the initial state is the superposed ground-state eigenstate at zero detuning: $|-\rangle$. Now for the case where the initial state is $|s_{11}\rangle$ (relevant when performing readout immediately after singlet-triplet qubit operations), the readout signal Υ_0 appears to be similar monotonic response to when $\chi_{gs} = 1$. However, at lower voltage amplitudes, the RF readout response is lower; a fact must note if one wishes to use smaller RF drive powers to lower the photon shot noise. The issue is that on moving to the readout point at

zero-detuning, the state $|s_{11}\rangle$ will have a non-zero probability of being in the excited state and thus, $\chi_{gs} < 1$. One may enter the true ground state (to make $\chi_{gs} = 1$) by using adiabatic sweeps to arrive at the readout point to ensure that the singlet is completely in the ground state charge state. However, one should note that using too slow an adiabatic sweep may lead to unwanted qubit evolution (thereby changing the qubit state) before performing readout.

The second caveat to address is that one intrinsically assumes that the RF readout keeps the electrons in the ground state even at high input voltage amplitudes. Although the input drive frequency ω is still taken to be smaller than the tunnel coupling t_c, a large voltage amplitude will lead to faster detuning sweeps that will make the passage non-adiabatic. To account for the non-adiabatic progressions at higher input voltage amplitudes, one may use the formula for linear sweeps in Landau-Zener-Stuckelberg-Majorana interferometry [214–218]:

$$\Upsilon = \frac{\mathrm{Q_{int}}}{\mathrm{Q_{ext}} + \mathrm{Q_{int}}} \cdot \frac{K}{C_p} \cdot \frac{e\Delta\alpha}{2} \cdot \frac{V'_{ac}\chi_{gs}}{\sqrt{t_c^2 + V'_{ac}}} \underbrace{\left(1 - \exp\left(\frac{t_c^2}{\omega V'_{ac}/\sqrt{2}}\right)\right)}_{\text{LZSM factor}}. \tag{C.37}$$

Here, the LZSM factor involves an exponential where the sweeping velocity was approximated as the gradient of a cosine curve: $\omega V'_{ac}$. The LZSM factor is an empirical factor that ensures that any solution for the RF response obeys the adiabatic approximation. The LZSM factor requires that the driving frequency is much lower than the tunnel coupling in order for the exponential envelope to start its attenuation (of the RF response) beyond the voltage amplitudes where the RF readout signal either saturates to its maximum value (for example, in the case where the initial state upon readout is $|s_{11}\rangle$) or reaches a maximum (in the case where the initial state upon readout is $|-\rangle$).

Appendix D

RF Reflectometry

This appendix outlines the methods used to derive the equations describing the resonant circuit used in RF reflectometry. Section D.1 outlines the derivation for the equation describing the RF readout signal strength given circuit parameters of the resonant circuit (such as, the resonator quality factors, geometric parasitic capacitance and the quantum capacitance). Section D.2 highlights the method used to fit the RF reflectance curves to extract the appropriate internal and external quality factors.

D.1 Change in the reflectance

Now consider the reflectance defined in Equation 3.8 for the *RLC* circuit coupled to a transmission line shown in Figure 3.5:

$$\rho \equiv -\frac{1-\frac{\mathrm{Q_{ext}}}{\mathrm{Q_{int}}}\left(1+j\mathrm{Q_{int}}\left(\frac{\omega}{\omega_0}-\frac{\omega_0}{\omega}\right)\right)}{1+\frac{\mathrm{Q_{ext}}}{\mathrm{Q_{int}}}\left(1+j\mathrm{Q_{int}}\left(\frac{\omega}{\omega_0}-\frac{\omega_0}{\omega}\right)\right)}, \tag{D.1}$$

where $\mathrm{Q_{int}}$ and $\mathrm{Q_{ext}}$ are the internal and external quality factors. Now on measuring the quantum dot's response, one tunes the circuit to resonance at $\omega_0 = 1/\sqrt{LC_p}$. Then as the quantum capacitance manifests, the resonant frequency is $\omega_c = 1/\sqrt{LC_c}$ (where $C_c \equiv C_p + C_q$). Now during this change, the quality factors remain constant. Thus, the shift in reflectance is:

$$\Delta\rho = -\frac{1-\frac{\mathrm{Q_{ext}}}{\mathrm{Q_{int}}}\left(1+j\mathrm{Q_{int}}\left(\frac{\omega}{\omega_c}-\frac{\omega_c}{\omega}\right)\right)}{1+\frac{\mathrm{Q_{ext}}}{\mathrm{Q_{int}}}\left(1+j\mathrm{Q_{int}}\left(\frac{\omega}{\omega_c}-\frac{\omega_c}{\omega}\right)\right)}+\frac{1-\frac{\mathrm{Q_{ext}}}{\mathrm{Q_{int}}}\left(1+j\mathrm{Q_{int}}\left(\frac{\omega}{\omega_0}-\frac{\omega_0}{\omega}\right)\right)}{1+\frac{\mathrm{Q_{ext}}}{\mathrm{Q_{int}}}\left(1+j\mathrm{Q_{int}}\left(\frac{\omega}{\omega_0}-\frac{\omega_0}{\omega}\right)\right)}. \quad \text{(D.2)}$$

Note that the first term contains ω_c for that is the resonant frequency in that case. Now one drives the circuit with the initially tuned frequency $\omega = \omega_0$. Now simplifying the expression yields:

$$\Delta\rho = \frac{2\mathrm{Q_{ext}}\mathrm{Q_{int}^2}}{\left(\mathrm{Q_{ext}}+\mathrm{Q_{int}}\right)^2+\mathrm{Q_{ext}^2}\mathrm{Q_{int}^2}\nu^2}\left(\mathrm{Q_{eff}}\nu+j\right)\nu, \quad \text{(D.3)}$$

where $\nu = \omega_0/\omega_c - \omega_c/\omega_0$. Now noting that the change in the resonant frequency $\delta\omega \equiv \omega_0 - \omega_c$ is very small compared to the numerical value of the resonant frequency itself:

$$\nu \equiv \frac{\delta\omega}{\omega_0}+\frac{\delta\omega}{\omega_0-\delta\omega_0} \approx \frac{2\delta\omega}{\omega_0} = 2\left(1-\frac{\omega_c}{\omega_0}\right). \quad \text{(D.4)}$$

Now expressing the change in frequency via the circuit parameters:

$$\nu = 2\left(1-\sqrt{\frac{LC_p}{L(C_p+C_q)}}\right) = 2-\frac{2}{\sqrt{1+\frac{C_q}{C_p}}} \approx 2-2\left(1-\frac{C_q}{2C_p}\right) = \frac{C_q}{C_p}, \quad \text{(D.5)}$$

where one utilises the Binomial approximation after noting that $C_q \ll C_p$. Since $C_p \sim 1000C_q$, $\nu \sim 10^{-3}$. Taking Q in the order of 100 (both internal and external), this implies that $\mathrm{Q}\nu \sim 0.1$. Thus, the first term in the denominator is approximately 100 times greater than the second term. Thus, the change in the reflection coefficient simplifies to approximately:

$$\Delta\rho \approx \frac{2\mathrm{Q_{eff}}\mathrm{Q_{int}}}{\mathrm{Q_{ext}}+\mathrm{Q_{int}}}\left(\mathrm{Q_{eff}}\left(\frac{C_q}{C_p}\right)^2+j\left(\frac{C_q}{C_p}\right)\right). \quad \text{(D.6)}$$

Note that the real part (in-phase) is of a much smaller magnitude than the imaginary part (quadrature-phase) due to the squaring of the quantum capacitance term. In addition, note that for a fixed internal quality factor, the (tunable) external quality factor must be equal for a maximal dispersive (that is, the quadrature component) signal[1]. However, an optimal dissipative signal (that is, the in-phase component)

[1] Seen by noting: $F_Q = \frac{\mathrm{Q_{eff}}\mathrm{Q_{int}}}{(\mathrm{Q_{int}}+\mathrm{Q_{ext}})^2}$, $\frac{\partial F_Q}{\partial \mathrm{Q_{ext}}} = \frac{\mathrm{Q_{int}^2}}{(\mathrm{Q_{int}}+\mathrm{Q_{ext}})^2} - \frac{2\mathrm{Q_{ext}}\mathrm{Q_{int}^2}}{(\mathrm{Q_{int}}+\mathrm{Q_{ext}})^3} = 0 \implies \mathrm{Q_{ext}} = \mathrm{Q_{int}}$

occurs when the external quality factor is twice that of the internal quality factor[2]. Now given equal quality factors, where typical experiments operate, the imaginary term is at least, 10 times greater than the real part. Thus, in further analysis, only the imaginary part shall be considered. That is, for a signal of amplitude V_{in} injected into the circuit, the resulting measured response is simply given by the magnitude of the reflectance:

$$\Upsilon = K\eta_{\text{loss}} V_{\text{in}} \cdot \frac{2\text{Q}_{\text{ext}}\text{Q}_{\text{int}}^2}{(\text{Q}_{\text{ext}} + \text{Q}_{\text{int}})^2} \cdot \frac{C_q}{C_p}, \tag{D.7}$$

where η_{loss} is the factor of the signal amplitude that remains when entering the resonant circuit and K is the net gain on the reflected signal amplification chain.

D.2 Analysing RF Reflectometry Data

This section outlines an automated fitting method to analyse the measured in-phase and quadrature phase (that is, I and Q) signals to extract the internal circuit quality factor Q_{int}, the external quality factor Q_{ext} and the resonant frequency of the resonant circuit ω_0.

D.2.1 The Fitting Model

Now from Equation 3.8, the reflectance of a resonant circuit of resonance ω_0 coupled to a transmission line of impedance Z_e can be given in terms of the internal and external quality factors (Q_{int} and Q_{ext} respectively):

$$\rho \equiv -\frac{1 - \frac{\text{Q}_{\text{ext}}}{\text{Q}_{\text{int}}}\left(1 + j\text{Q}_{\text{int}}\left(\frac{\omega}{\omega_0} - \frac{\omega_0}{\omega}\right)\right)}{1 + \frac{\text{Q}_{\text{ext}}}{\text{Q}_{\text{int}}}\left(1 + j\text{Q}_{\text{int}}\left(\frac{\omega}{\omega_0} - \frac{\omega_0}{\omega}\right)\right)}. \tag{D.8}$$

Now this provides the reflectance when the viewer treats the transmission line as a lumped element, when in fact the transmission line length L is much greater than the typical wavelength of the signal. In addition, the measured data appears as a complex voltage vector that must be scaled (to convert to ρ) by a reference voltage amplitude of the injected signal. Thus, model to which one fits the data is:

$$V = -k \cdot \frac{1 - \frac{\text{Q}_{\text{ext}}}{\text{Q}_{\text{int}}}\left(1 + j\text{Q}_{\text{int}}\left(\frac{\omega}{\omega_0} - \frac{\omega_0}{\omega}\right)\right)}{1 + \frac{\text{Q}_{\text{ext}}}{\text{Q}_{\text{int}}}\left(1 + j\text{Q}_{\text{int}}\left(\frac{\omega}{\omega_0} - \frac{\omega_0}{\omega}\right)\right)} \cdot \text{e}^{j\frac{2\omega L}{c}}, \tag{D.9}$$

[2] Seen by noting: $F_I = \frac{\text{Q}_{\text{eff}}^2\text{Q}_{\text{int}}}{(\text{Q}_{\text{int}}+\text{Q}_{\text{ext}})^2}$, $\frac{\partial F_I}{\partial \text{Q}_{\text{ext}}} = \frac{2\text{Q}_{\text{ext}}\text{Q}_{\text{int}}^3}{(\text{Q}_{\text{int}}+\text{Q}_{\text{ext}})^3} - \frac{3\text{Q}_{\text{ext}}^2\text{Q}_{\text{int}}^3}{(\text{Q}_{\text{int}}+\text{Q}_{\text{ext}})^4} = 0 \implies \text{Q}_{\text{ext}} = 2\text{Q}_{\text{int}}$

where k is a positive real-valued scaling factor and c is the speed of light. Now since this is a nonlinear fit, one utilises a simple least-squares minimiser[3]. The minimiser requires good initial conditions to ensure convergence. The following section will show how one may obtain good guesses for the initial parameters.

D.2.2 Parameter Estimation

Now the initial estimate for ω_0 can be done by simply taking the frequency at which the amplitude plot is at a minimum. Similarly, one may estimate k by taking the maximum magnitude of measured voltage[4]. Now ignoring the effect of L (that is, take $L = 0$), one may estimate $\mathrm{Q}_{\mathrm{int}}$ and $\mathrm{Q}_{\mathrm{ext}}$ by observing the derivative of the phase plot at the resonant frequency and the peak height in the amplitude plot. Now one shall first note that the derivative of the phase $\phi \equiv \arg(V)$ is:

$$p = \left.\frac{d\phi}{d\omega}\right|_{\omega=\omega_0} = \frac{\mathrm{Q}_{\mathrm{ext}}\mathrm{Q}_{\mathrm{int}}^2}{\omega_0\left(\mathrm{Q}_{\mathrm{ext}}^2 - \mathrm{Q}_{\mathrm{int}}^2\right)}, \tag{D.10}$$

while the peak height (that is, the vertical size of the peak when viewing the plot of $|\rho|$ vs. ω) is given as:

$$h = \frac{2\mathrm{Q}_{\mathrm{int}}}{\mathrm{Q}_{\mathrm{int}} + \mathrm{Q}_{\mathrm{ext}}}. \tag{D.11}$$

Now one may algebraically solve this to obtain the internal and external quality factors. Noting that the quality factor must be positive:

$$\mathrm{Q}_{\mathrm{ext}} = \begin{cases} -\frac{(h-1)\omega_0}{h^2} \cdot \frac{d\phi}{d\omega} & \frac{d\phi}{d\omega} > 0 \\ \frac{(h-1)\omega_0}{(h-2)^2} \cdot \frac{d\phi}{d\omega} & \frac{d\phi}{d\omega} < 0 \end{cases} \tag{D.12}$$

$$\mathrm{Q}_{\mathrm{int}} = \begin{cases} \frac{(h-1)\omega_0}{h(h-2)} \cdot \frac{d\phi}{d\omega} & \frac{d\phi}{d\omega} > 0 \\ -\frac{(h-1)\omega_0}{h(h-2)} \cdot \frac{d\phi}{d\omega} & \frac{d\phi}{d\omega} < 0 \end{cases}. \tag{D.13}$$

It is worth noting that the phase slope indicates whether the external transmission line is 'over-coupled' ($\frac{d\phi}{d\omega} > 0$), 'under-coupled' ($\frac{d\phi}{d\omega} < 0$) or 'critically-coupled' ($\frac{d\phi}{d\omega} = 0$). Finally, to estimate L, one may look at the phase slope and algebraically show that when taking the limit where $\omega \ll \omega_0$:

[3] The actual minimisation of the kernel can be done via any of the common methods such as Monte-Carlo, Simplex sampling, Steepest-Descent etc.

[4] This can be further normalised by referencing it to the value when one can ensure that it corresponds to nearly perfect reflection like that when tuning the bias of a varactor connected in parallel to the RLC circuit to effectively negate the presence of the RLC circuit.

$$L = \lim_{\omega \to 0} \frac{c}{4\pi} \cdot \frac{d\phi}{d\omega}. \tag{D.14}$$

Table D.1 summarises the procedures used to find the initial estimates.

Parameter	Estimation
ω_0	ω that minimises $\lvert V(\omega)\rvert$
k	$\max \lvert V\rvert$
h	$\frac{1}{k} \cdot (\max \lvert V\rvert - \min \lvert V\rvert)$
p	Finite Difference about ω_0
Q_{int}	$\frac{(h-1)\omega_0}{h(h-2)} \cdot \lvert p\rvert$
Q_{ext}	$\begin{cases} -\frac{(h-1)\omega_0}{h^2} \cdot p & p > 0 \\ \frac{(h-1)\omega_0}{(h-2)^2} \cdot p & p < 0 \end{cases}$
p_0	Finite Difference about $\omega \ll \omega_0$
L	$\frac{c}{4\pi} \cdot p_0$

Table D.1: Initial parameter estimates when fitting the RF reflectometry resonance data to the model in Equation D.9.

Appendix E

Derivation of the Singlet-Triplet qubit Hamiltonian

I remember that when someone had started to teach me about creation and annihilation operators, that this operator creates an electron, I said, "how do you create an electron? It disagrees with the conservation of charge", and in that way, I blocked my mind from learning a very practical scheme of calculation.

- Richard P. Feynman, *Nobel Lecture 1965*

In this section, the singlet-triplet Hamiltonian of interest shall be constructed in simple language without invoking any second quantisation formalism[1]. The singlet-triplet qubit is formed by taking the effective spin state between two electrons settled across two quantum dots. Sections E.1, E.2 and E.3 build up the associated Hamiltonian from simple fundamental arguments and left there for completeness and left for interested readers. Section E.4 brings all the derivations together to build up a general model for singlet-triplet states across two dots. The details of qubit operation are discussed in Chapter 5.

E.1 One electron, two dots - charge qubit Hamiltonian

Consider an electron that resides in a Coulombic potential well $V(\mathbf{r}-\mathbf{r}_1)$ centred at $\mathbf{r}_1$ due to a quantum dot. The electron is in the ground state orbital level of the dot.

[1] For a more complete overview that includes silicon valley contributions, refer to Fang's thesis [219]

The Hamiltonian of an electron on this single dot is thus:

$$\mathbf{H}_{1e,\mathbf{r_1}} = \frac{-\hbar^2}{2m_e}\nabla^2 + V(\mathbf{r}-\mathbf{r}_1), \tag{E.1}$$

where $\nabla^2 = \left(\frac{\partial^2}{\partial x^2} + \frac{\partial^2}{\partial y^2} + \frac{\partial^2}{\partial z^2}\right)$ is the Laplacian operator, m_e is the effective mass of the electron when interacting with the dot and the surrounding crystal. Now consider an identical potential well centred at $\mathbf{r}_2$. Although the potential wells tightly confine the electrons, the wavefunction probability of the electron is still finite everywhere and thus, non-zero at $\mathbf{r}_2$. The tight-binding approximation demands that the wavefunction probability at this point is small and that the new wavefunction is still the original wavefunction that solves $\mathbf{H}_{1e,\mathbf{r}_1}$, but with a slight perturbation in the energy of the electron due to $V(\mathbf{r}-\mathbf{r}_2)$:

$$\mathbf{H}_{1e,\mathbf{r}_1,\mathbf{r}_2} = \frac{-\hbar^2}{2m_e}\nabla^2 + V(\mathbf{r}-\mathbf{r}_1) + V(\mathbf{r}-\mathbf{r}_2). \tag{E.2}$$

Now consider the basis of states to be the wavefunctions when the electron resides in either dot[2] 1 or 2 to be $\varphi_1(\mathbf{r})$ and $\varphi_2(\mathbf{r})$. Now one can find the two-level Hamiltonian describing such an interaction[3]:

$$\begin{cases} \langle\varphi_1|\,\mathbf{H}_{1e,\mathbf{r_1},\mathbf{r_2}}\,|\varphi_2\rangle = -t_c \\ \langle\varphi_1|\,\mathbf{H}_{1e,\mathbf{r_1},\mathbf{r_2}}\,|\varphi_1\rangle = U_1 \equiv U_0 + \varepsilon \\ \langle\varphi_2|\,\mathbf{H}_{1e,\mathbf{r_2},\mathbf{r_2}}\,|\varphi_2\rangle = U_2 \equiv U_0 - \varepsilon \end{cases}. \tag{E.3}$$

Note that U_1 and U_2 may not be necessarily equal. The inequality stems from differing on-site electrostatic potentials created by an electric field from a local gate. In the literature, the idea of using a gate to create a difference in the on-site potentials is termed a 'tilting potential' or 'tilting gate'. The, resulting the Hamiltonian over the φ_1, φ_2 basis is the 'charge-qubit' Hamiltonian [57, 58, 220]:

$$\mathbf{H}_{\mathrm{CQ}} = U_0 I_2 - t_c\sigma_x + \varepsilon\sigma_z. \tag{E.4}$$

Under the charge state basis, one has full-axis control of the resulting two-level system by tuning the so-called 'detuning' parameter ε and the tunnel coupling t_c.

[2] That is, $\varphi_i(\mathbf{r})$ solves $\mathbf{H}_{1e,\mathbf{r}_i}$ and gets perturbed by the potential $V(\mathbf{r}-\mathbf{r}_j)$ of the other dot $j \neq i$.
[3] Note that the Bra-Ket notation implies: $\langle\varphi_1 \mid \varphi_2\rangle \equiv \int \varphi_1(\mathbf{r})\varphi_2(\mathbf{r})d\mathbf{r}$

E.2 Two electrons, two dots

Now one considers adding another electron to this double-well system. This adds an electron-electron interaction term $V_{ee}(\mathbf{r}_1, \mathbf{r}_2) \propto 1/|\mathbf{r}_2 - \mathbf{r}_1|$ to the Hamiltonian to give a complete two-electron, two-dot Hamiltonian:

$$\mathbf{H}_{\mathrm{DQD}} = \frac{-\hbar^2}{2m_e}\nabla^2 + V(\mathbf{r} - \mathbf{r}_1) + V(\mathbf{r} - \mathbf{r}_2) + V_{ee}(\mathbf{r}_1, \mathbf{r}_2). \tag{E.5}$$

To find the two-electron wavefunction that solves this Hamiltonian, one considers that, individually, each electron will have a spatial component (it either resides in dot 1 or 2) and a spin component; the product of which must yield a wavefunction that is antisymmetric under exchange[4]. With two possible sites (φ_1 and φ_2) per dot and two spins ($\uparrow$ and $\downarrow$) per electron, this yields a state space of 16 possible states. Now before proceeding, one shall label the states as $|\Phi\xi\rangle$, where Φ and ξ are the combined spatial and spin states of the two electrons respectively (formally the tensor product of the individual spatial and spinful states: $\Phi_1 \otimes \Phi_2 \otimes \xi_1 \otimes \xi_2$). The combined spatial or spin states shall be in the eigenbasis suitable for the application of the particle-exchange operator; namely the singlet-triplet basis:

$$|\Phi\rangle \in \begin{cases} \Phi_- = \frac{1}{\sqrt{2}}\left(|\varphi_1\varphi_2\rangle - |\varphi_2\varphi_1\rangle\right) \\ \Phi_+ = \frac{1}{\sqrt{2}}\left(|\varphi_1\varphi_2\rangle + |\varphi_2\varphi_1\rangle\right) \\ \Phi_1 = |\varphi_1\varphi_1\rangle \\ \Phi_2 = |\varphi_2\varphi_2\rangle \end{cases}, \qquad |\xi\rangle \in \begin{cases} s_0 = \frac{1}{\sqrt{2}}\left(|\uparrow\downarrow\rangle - |\downarrow\uparrow\rangle\right) \\ t_0 = \frac{1}{\sqrt{2}}\left(|\uparrow\downarrow\rangle + |\downarrow\uparrow\rangle\right) \\ t_- = |\downarrow\downarrow\rangle \\ t_+ = |\uparrow\uparrow\rangle \end{cases} \tag{E.6}$$

where the two labels Φ and ξ in each Ket refer to the spatial or spin state of the first and second electrons respectively. The electron spin state s_0 is termed the 'singlet' state while t_0, t_+ and t_- are termed the 'triplet' states. With 16 states, there are 256 terms in the Hamiltonian. However, when one demands the property of antisymmetry, many of the states will become zero. For example, $|\Phi_1 t_-\rangle$ involves a symmetric spatial state and a symmetric triplet spin state; thus, under exchange

[4] By the spin-statistics theorem, the application of the particle exchange operator, where one exchanges two particles in the system, must result in an eigenvalue of -1 if the particles are Fermions.

such a state will be symmetric and thus, the probability density of such a state must be zero or equivalently of infinite energy[5]. Now the states with non-zero probability density are: $|\Phi_1 s_0\rangle$, $|\Phi_2 s_0\rangle$, $|\Phi_+ s_0\rangle$ and $|\Phi_- t\rangle$ (where t refers to any triplet spin state). Under the $|\Phi\xi\rangle$ basis, the Hamiltonian can be recast as the charge qubit Hamiltonian acting individually on each electron (that is, the first three terms in $\mathbf{H}_{\mathrm{DQD}}$ are single-electron terms) coupled with a multi-electron interaction term:

$$\mathbf{H}_{\mathrm{DQD}} = \mathbf{H}_{\mathrm{CQ}} \otimes I_2 \otimes I_2 \otimes I_2 + I_2 \otimes \mathbf{H}_{\mathrm{CQ}} \otimes I_2 \otimes I_2 + V_{ee}. \tag{E.7}$$

On expanding the tensor products, the resulting energy-offset terms (diagonal matrix components) are:

$$\langle \Phi_1 s_0 | \, \mathbf{H}_{\mathrm{DQD}} \, | \Phi_1 s_0 \rangle = 2U_0 + 2\varepsilon + U_{02} \tag{E.8}$$

$$\langle \Phi_2 s_0 | \, \mathbf{H}_{\mathrm{DQD}} \, | \Phi_2 s_0 \rangle = 2U_0 - 2\varepsilon + U_{02} \tag{E.9}$$

$$\langle \Phi_+ s_0 | \, \mathbf{H}_{\mathrm{DQD}} \, | \Phi_+ s_0 \rangle = 2U_0 - 2t_c \langle \varphi_1 \mid \varphi_2 \rangle + U_{11} + J_{12} \tag{E.10}$$

$$\langle \Phi_- t | \, \mathbf{H}_{\mathrm{DQD}} \, | \Phi_- t \rangle = 2U_0 + 2t_c \langle \varphi_1 \mid \varphi_2 \rangle + U_{11} - J_{12}. \tag{E.11}$$

The term $U_{11} \equiv \langle \varphi_1 \varphi_2 | \, V_{ee} \, | \varphi_1 \varphi_2 \rangle \equiv \langle \varphi_2 \varphi_1 | \, V_{ee} \, | \varphi_2 \varphi_1 \rangle$ is taken to be independent of the spin state of the electrons for the charge states are equal and the term simply describes the energy due to electrostatic repulsion between the two electrons. Similarly, $J_{12} \equiv \langle \varphi_1 \varphi_2 | \, V_{ee} \, | \varphi_2 \varphi_1 \rangle \equiv \langle \varphi_2 \varphi_1 | \, V_{ee} \, | \varphi_1 \varphi_2 \rangle$ describes the shift in the energy due to spatial wavefunction overlap between the two electrons (that is, the amount the electron wavefunction occupies a given point in space if swapped and made to live in the adjacent potential well). The interaction term J_{12} is described in literature as the 'electron-exchange interaction' term that breaks the degeneracy between the singlet and triplet spin states of electrons amongst adjacent potential wells and leads to the origin of ferromagnetism in metals [221–223]. However, in the case of operating singlet-triplet qubits in quantum dots, this intrinsic exchange term is taken to be zero as one places the dots sufficiently far apart in order to operate in the 'tight-binding' limit where the individual electron wavefunctions φ_1 and φ_2 have negligible overlap. In this limit, one formally takes:

[5] One can make this probability density non-zero (hence of finite energy) if one introduces an anti-symmetric (or symmetric) orbital state where one of the electrons may occupy a higher orbital to still obey the overall antisymmetry for electrons [34, 42, 183]. This is ignored in this analysis as the orbital energy spacing in phosphorus is large and if an electron somehow enters the higher orbital state (the so-called $2p_0$ state which is more than 10 meV higher), it is very short lived at approximately 200 ps [184–187]

$$U_{11} \approx 0 \tag{E.12}$$

$$J_{12} \approx 0 \tag{E.13}$$

$$\langle \varphi_1 \mid \varphi_2 \rangle \approx 0. \tag{E.14}$$

With this approximation, it remains that the only two-electron term that manipulates the z-energy splitting is $U_{02} \equiv \langle \varphi_1\varphi_1 | \, V_{ee} \, | \varphi_1\varphi_1 \rangle \equiv \langle \varphi_2\varphi_2 | \, V_{ee} \, | \varphi_2\varphi_2 \rangle$, which describes the energy due to the strong electrostatic repulsion between two electrons on the same dot. Thus, this Hamiltonian has a ground state where the electrons prefer to be in separate dots, while the two excited states has them both occupying one of the two dots.

Now continuing the expansion of the tensor products, one may find the interacting terms (off-diagonal matrix components) of the Hamiltonian:

$$\langle \Phi_1 s_0 | \, \mathbf{H}_{\mathrm{DQD}} \, | \Phi_+ s_0 \rangle = \sqrt{2}(U_0 + 2\varepsilon) \langle \varphi_1 \mid \varphi_2 \rangle - \sqrt{2} t_c \approx -\sqrt{2} t_c \tag{E.15}$$

$$\langle \Phi_2 s_0 | \, \mathbf{H}_{\mathrm{DQD}} \, | \Phi_+ s_0 \rangle = \sqrt{2}(U_0 - 2\varepsilon) \langle \varphi_1 \mid \varphi_2 \rangle - \sqrt{2} t_c \approx -\sqrt{2} t_c \tag{E.16}$$

$$\langle \Phi_1 s_0 | \, \mathbf{H}_{\mathrm{DQD}} \, | \Phi_2 s_0 \rangle = -2 t_c \langle \varphi_1 \mid \varphi_2 \rangle \approx 0 \tag{E.17}$$

$$\langle \Phi_1 s_0 | \, \mathbf{H}_{\mathrm{DQD}} \, | \Phi_- t \rangle = 0 \tag{E.18}$$

$$\langle \Phi_2 s_0 | \, \mathbf{H}_{\mathrm{DQD}} \, | \Phi_- t \rangle = 0 \tag{E.19}$$

$$\langle \Phi_+ s_0 | \, \mathbf{H}_{\mathrm{DQD}} \, | \Phi_- t \rangle = 0. \tag{E.20}$$

Note that the contributions of V_{ee} are not seen here because $\langle \varphi_i\varphi_i | \, V_{ee} \, | \varphi_i\varphi_j \rangle \ll U_{11} \approx 0$ (for $i \neq j$). This is simply a statement that the spatial overlap between wavefunctions of electrons on separate dots is negligible. Now noting the charge state of triplet states is always $\Phi_\pm$ have one electron on each dot, for simplicity the labels are rewritten in terms of charge states in the subscripts (where i, j refers to the number of electrons in dot 1 and 2 respectively):

$$|\Phi_1 s_0\rangle \equiv s_{20} \tag{E.21}$$

$$|\Phi_2 s_0\rangle \equiv s_{02} \tag{E.22}$$

$$|\Phi_+ s_0\rangle \equiv s_{11}. \tag{E.23}$$

For the triplet states t_0, t_+ and t_-, the charge states are dropped and implicitly

presumed to be in the $(1,1)$ charge state. With that, the full double-dot Hamiltonian can be rewritten in its matrix form over the basis of states s_{20}, s_{02}, s_{11}, t_0, t_- and t_+ as:

$$\mathbf{H}_{\mathrm{DQD}} \equiv 2U_0 I_6 + \begin{pmatrix} 2\varepsilon + U_{02} & 0 & -\sqrt{2}t_c & \\ 0 & -2\varepsilon + U_{02} & -\sqrt{2}t_c & \mathbf{0}_3 \\ -\sqrt{2}t_c & -\sqrt{2}t_c & 0 & \\ & \mathbf{0}_3 & & \mathbf{0}_3 \end{pmatrix}, \tag{E.24}$$

where $\mathbf{0}_3$ is a 3×3 matrix of zeroes. This Hamiltonian corresponds to the basic tight-binding or Hubbard model [221, 222, 224].

E.3 Adding in a Magnetic Field

The general singlet-triplet Hamiltonian refers to a two-electron double-dot system immersed in a magnetic field. Now the Hamiltonian for a spin in a magnetic field is:

$$\mathbf{H}_{\mathrm{B}} = \frac{g_e \mu_e}{2} \mathbf{B}(\mathbf{r}) \bullet (\boldsymbol{\sigma}_1 + \boldsymbol{\sigma}_2), \tag{E.25}$$

where g_e is the electron Landé g-factor, μ_e is the Bohr Magneton and $\boldsymbol{\sigma}_{1|2}$ are the Pauli spin operators for the first and second electrons across x, y and z (or simply $(\sigma_x, \sigma_y, \sigma_z)$ in the up-down spin basis). Note that the magnetic field vector $\mathbf{B}(\mathbf{r})$ is not necessarily homogeneous across both dots and the 'dot-product' is merely abuse of notation for convenience (that is, not a scalar inner product). In fact, the Hamiltonian above is an abbreviation for the following:

$$\begin{aligned} \mathbf{H}_{\mathrm{B}} \equiv \frac{g_e \mu_e}{2} \big[& |\varphi_1\rangle \langle\varphi_1| \otimes I_2 \otimes (B_{1(x)}\sigma_x + B_{1(y)}\sigma_y + B_{1(z)}\sigma_z) \otimes I_2 + \\ & |\varphi_2\rangle \langle\varphi_2| \otimes I_2 \otimes (B_{2(x)}\sigma_x + B_{2(y)}\sigma_y + B_{2(z)}\sigma_z) \otimes I_2 + \\ & I_2 \otimes |\varphi_1\rangle \langle\varphi_1| \otimes I_2 \otimes (B_{1(x)}\sigma_x + B_{1(y)}\sigma_y + B_{1(z)}\sigma_z) + \\ & I_2 \otimes |\varphi_2\rangle \langle\varphi_2| \otimes I_2 \otimes (B_{2(x)}\sigma_x + B_{2(y)}\sigma_y + B_{2(z)}\sigma_z) \big]. \end{aligned} \tag{E.26}$$

The result is that electrons on the first dot experience a different magnetic field vectors to that in the second dot:

$$\mathbf{B}_1 = \frac{g_e \mu_e}{2}(B_{1(x)}, B_{1(y)}, B_{1(z)}) \tag{E.27}$$

$$\mathbf{B}_2 = \frac{g_e \mu_e}{2}(B_{2(x)}, B_{2(y)}, B_{2(z)}). \tag{E.28}$$

The magnetic field contribution to the overall system Hamiltonian is relatively perturbative in that the states already relegated from the analysis of $\mathbf{H}_{\mathrm{DQD}}$ need not be considered. Before continuing it's useful to write down the spin component of the Hamiltonian in the Singlet-Triplet basis[6] ($|s_0\rangle$, $|t_0\rangle$, $|t_-\rangle$, $|t_+\rangle$):

$$\mathbf{B}_1 \bullet \boldsymbol{\sigma}_1 + \mathbf{B}_2 \bullet \boldsymbol{\sigma}_2 = \begin{pmatrix} 0 & \Delta B_z & \frac{\Delta B_x - i\Delta B_y}{\sqrt{2}} & -\frac{\Delta B_x + i\Delta B_y}{\sqrt{2}} \\ \Delta B_z & 0 & \frac{\Sigma B_x - i\Sigma B_y}{\sqrt{2}} & \frac{\Sigma B_x + i\Sigma B_y}{\sqrt{2}} \\ \frac{\Delta B_x + i\Delta B_y}{\sqrt{2}} & \frac{\Sigma B_x + i\Sigma B_y}{\sqrt{2}} & -\Sigma B_z & 0 \\ -\frac{\Delta B_x - i\Delta B_y}{2} & \frac{\Sigma B_x - i\Sigma B_y}{\sqrt{2}} & 0 & \Sigma B_z \end{pmatrix}, \tag{E.29}$$

where $\mathbf{B}_1 \bullet \boldsymbol{\sigma}_1 \equiv (\mathbf{B}_1 \bullet \boldsymbol{\sigma}) \otimes I_2$, $\mathbf{B}_1 \bullet \boldsymbol{\sigma}_2 \equiv I_2 \otimes (\mathbf{B}_2 \bullet \boldsymbol{\sigma})$, $\Delta\mathbf{B} = \mathbf{B}_1 - \mathbf{B}_2$ and $\Sigma\mathbf{B} = \mathbf{B}_1 + \mathbf{B}_2$. Expanding the tensor products once more to find the matrix terms yields:

$$\langle \Phi_- t | \, \mathbf{H}_{\mathrm{B}} \, | \Phi_+ s_0 \rangle \approx \tfrac{1}{2} \langle t | \, (\mathbf{B}_1 \bullet \boldsymbol{\sigma}_1 + \mathbf{B}_2 \bullet \boldsymbol{\sigma}_2) - (\mathbf{B}_2 \bullet \boldsymbol{\sigma}_1 + \mathbf{B}_1 \bullet \boldsymbol{\sigma}_2) \, | s_0 \rangle \tag{E.30}$$

$$\langle \Phi_- t | \, \mathbf{H}_{\mathrm{B}} \, | \Phi_- t' \rangle \approx \tfrac{1}{2} \langle t | \, (\mathbf{B}_1 \bullet \boldsymbol{\sigma}_1 + \mathbf{B}_2 \bullet \boldsymbol{\sigma}_2) + (\mathbf{B}_2 \bullet \boldsymbol{\sigma}_1 + \mathbf{B}_1 \bullet \boldsymbol{\sigma}_2) \, | t' \rangle \tag{E.31}$$

$$\langle \Phi_m s_0 | \, \mathbf{H}_{\mathrm{B}} \, | \Phi_- t \rangle \approx 0 \tag{E.32}$$

$$\langle \Phi_m s_0 | \, \mathbf{H}_{\mathrm{B}} \, | \Phi_+ s_0 \rangle \approx 0 \tag{E.33}$$

$$\langle \Phi_m s_0 | \, \mathbf{H}_{\mathrm{B}} \, | \Phi_n s_0 \rangle \approx 0, \tag{E.34}$$

where $t, t' \in \{t_0, t_-, t_+\}$ and $\Phi_m, \Phi_n \in \{\Phi_1, \Phi_2\}$. The approximations invoke $\langle \varphi_1 \mid \varphi_2 \rangle \approx 0$ as discussed in Section E.2. The matrix forms of the non-zero terms yields the magnetic field contribution:

[6] Apply the transformation: $\mathbf{THT}^{-1}$ to convert from the computational ($|\uparrow\uparrow\rangle$, $|\uparrow\downarrow\rangle$, $|\downarrow\uparrow\rangle$, $|\downarrow\downarrow\rangle$) basis to singlet-triplet ($|s_0\rangle$, $|t_0\rangle$, $|t_-\rangle$, $|t_+\rangle$) basis, where $\mathbf{T} = \begin{pmatrix} 0 & 1/\sqrt{2} & -1/\sqrt{2} & 0 \\ 0 & 1/\sqrt{2} & 1/\sqrt{2} & 0 \\ 0 & 0 & 0 & 1 \\ 1 & 0 & 0 & 0 \end{pmatrix}$

$$\langle t|\,\mathbf{H}_{\mathrm{B}}\,|s_{11}\rangle = \langle t|\begin{pmatrix} 0 & \Delta B_z & \frac{\Delta B_x - i\Delta B_y}{\sqrt{2}} & -\frac{\Delta B_x + i\Delta B_y}{\sqrt{2}} \\ \Delta B_z & 0 & 0 & 0 \\ \frac{\Delta B_x + i\Delta B_y}{\sqrt{2}} & 0 & 0 & 0 \\ -\frac{\Delta B_x - i\Delta B_y}{2} & 0 & 0 & 0 \end{pmatrix}|s_0\rangle \tag{E.35}$$

$$\langle t|\,\mathbf{H}_{\mathrm{B}}\,|t'\rangle = \langle t|\begin{pmatrix} 0 & 0 & 0 & 0 \\ 0 & 0 & \frac{\Sigma B_x - i\Sigma B_y}{\sqrt{2}} & \frac{\Sigma B_x + i\Sigma B_y}{\sqrt{2}} \\ 0 & \frac{\Sigma B_x + i\Sigma B_y}{\sqrt{2}} & -\Sigma B_z & 0 \\ 0 & \frac{\Sigma B_x - i\Sigma B_y}{\sqrt{2}} & 0 & \Sigma B_z \end{pmatrix}|t'\rangle\,. \tag{E.36}$$

Note that only the states in the (1,1) charge state have non-zero magnetic field contributions. The physical interpretation for the zero coupling term between S_{02} or S_{20} and t is the state transition requires two events to occur: a change in angular momentum and a change in the charge state. Since quantum tunnelling is generally spin-conserving, this sort of transition would require a second-order effect and thus, one would expect such couplings to be zero. Similarly, the coupling between singlet states is purely a tunnelling effect (captured by the analysis in section Section E.2). Finally, an important point of interest is that the coupling terms between the singlet s_{11} and t_0 has no dependence on the overall magnetic field and instead just the difference in the magnetic fields across the two dots.

E.4 The general singlet-triplet Hamiltonian

The full singlet-triplet Hamiltonian is the sum of double-dot tunnelling physics $\mathbf{H}_{\mathrm{DQD}}$ and the magnetic field contributions $\mathbf{H}_{\mathrm{B}}$:

$$\mathbf{H}_{\mathrm{ST}} = \mathbf{H}_{\mathrm{DQD}} + \mathbf{H}_{\mathrm{B}}. \tag{E.37}$$

To investigate the behaviour of the singlet-triplet Hamiltonian, first consider a zero magnetic field environment in which the Hamiltonian is simply the pure double-quantum dot Hamiltonian given in Equation E.24. Figure E.1a shows the resulting energy spectrum when the two-electron on-site energy U_{02} is four times larger than the tunnel coupling t_c. In this regime, there is a gap between the two highest energy eigenstates at zero detuning due to an anti-crossing between the s_{20} and s_{02} states. Similarly there is a large non-zero energy gap between the two lowest energy states due to an anti-crossing between the s_{11} and the three degenerate triplet states t.

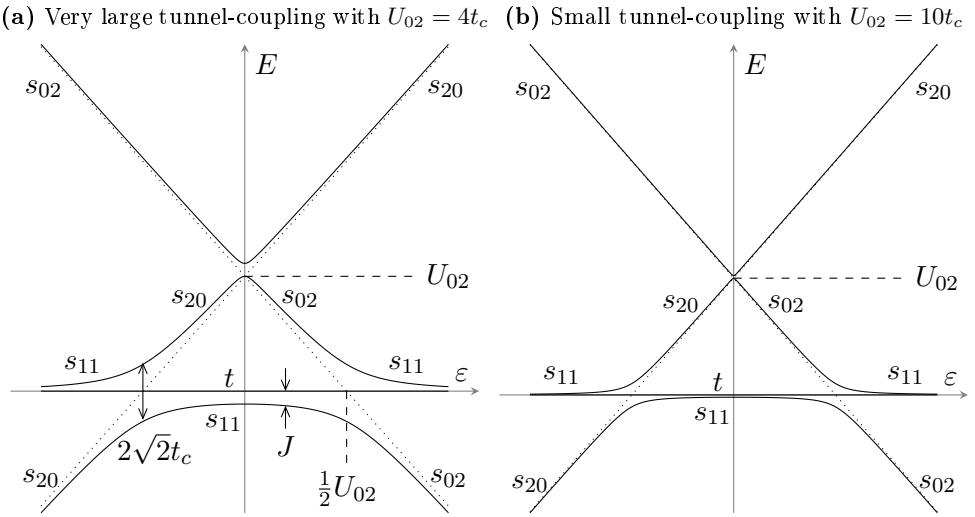

Figure E.1: The energy spectrum of the double quantum dot Hamiltonian given in Equation E.24. The singlet labels (s_{11}, s_{20} and s_{02}) indicate the approximate asymptotic eigenstate of the energy eigenvalue line at different points in detuning ε. The triplet label t indicates all three degenerate triplet states (t_0, t_- and t_+) that remain invariant with ε and stay at the zero energy line. Two points of interest are the s_{11}-s_{02} and s_{11}-s_{20} anti-crossings; both split by $2t_c$. J is the exchange energy (or the singlet-triplet splitting) and is appreciable across all points in detuning in (a) where $U_{02}/t_c = 4$. However, in (b), J tends towards zero at zero detuning as opposed to approximately $0.449t_c$ like in (a) as given by Equation 5.15. The global offsets have been omitted for clarity.

The gap between the singlet ground state and the triplet state is the 'singlet-triplet splitting' (also by definition the 'exchange coupling' or 'exchange energy' in the literature) and symbolised with J. In the regime where the tunnel coupling t_c is comparable in magnitude to the two-electron on-site energy U_{02}, the singlet-triplet splitting J does not approach zero; even at zero detuning. This is because the weak confinement energy U_{02}, when compared to the tunnel coupling t_c, leads to a stronger interaction (and greater wavefunction overlap) between the two electrons across the two quantum dots.

However, in practice, the system usually operates with $U_{02} \gg t_c$ and thus, J can tend towards zero when taken at zero detuning as shown in Figure E.1b. This is because the eventual qubit control relies on the ability to tune the exchange J to zero. Now consider the magnetic field contributions. In the matrix form this is:

$$\mathbf{H}_{\mathrm{ST}} \equiv \begin{pmatrix} U_{02}+2\varepsilon & 0 & -\sqrt{2}t_c & 0 & 0 & 0 \\ 0 & U_{02}-2\varepsilon & -\sqrt{2}t_c & 0 & 0 & 0 \\ -\sqrt{2}t_c & -\sqrt{2}t_c & 0 & \Delta B_z & \overline{\Delta B_\perp} & -\Delta B_\perp \\ 0 & 0 & \Delta B_z & 0 & \overline{\Sigma B_\perp} & \Sigma B_\perp \\ 0 & 0 & \Delta B_\perp & \Sigma B_\perp & -2B_0 & 0 \\ 0 & 0 & -\overline{\Delta B_\perp} & \overline{\Sigma B_\perp} & 0 & 2B_0 \end{pmatrix}, \tag{E.38}$$

once again under the basis of states: s_{20}, s_{02}, s_{11}, t_0, t_- and t_+. The global offset $2U_0$ has been omitted for clarity and holds no significance in the system dynamics. For clarity the following substitutions were made:

$$\Delta B_\perp = \frac{\Delta B_x + i\Delta B_y}{\sqrt{2}} \tag{E.39}$$

$$\Sigma B_\perp = \frac{\Sigma B_x + i\Sigma B_y}{\sqrt{2}} \tag{E.40}$$

$$B_0 = \frac{\Sigma B_z}{2}. \tag{E.41}$$

The system shall have its quantisation z-axis aligned parallel with an externally applied magnetic field. Note that the quantisation axis is taken to be in the direction of the net common-mode field across the two dots. That is, the net field (summing the individual field vectors on both dots) along the x-y plane given by ΣB_x and ΣB_y is zero. This leaves the magnetic field component $\Delta B_\perp$ which is the contribution perpendicular to the main applied field B_0. In addition, there is a magnetic field gradient ΔB_z in the direction of the applied field across the two dots. The non-zero ΔB_z creates an anti-crossing between the t_0 and s_{11} states as shown in Figure E.2a. A large ΔB_z compared to the tunnel coupling t_c causes multiple anti-crossings and the t_0 state starts to mix heavily with the other states causing it to have a strong dependence on the detuning ε as shown in Figure E.2b. As shown later, this regime is undesirable and the system is usually tuned to $t_c \gg \Delta B_z$. In all cases, the global field B_0 breaks the triplet degeneracy by only affecting the energy of the triplet t_- and t_+ states ('Zeeman splitting').

A non-zero $\Delta B_\perp$ yields an anti-crossing between the s_{11} and the triplet states: t_+ and t_-. The triplets do not couple to the singlet s_{02} and s_{20} states and thus, form no anti-crossing[7].

[7] There can however, be an anti-crossing mediated by another Hamiltonian term such as a spin-orbit coupling term that links between the electron charge states and spin states [192].

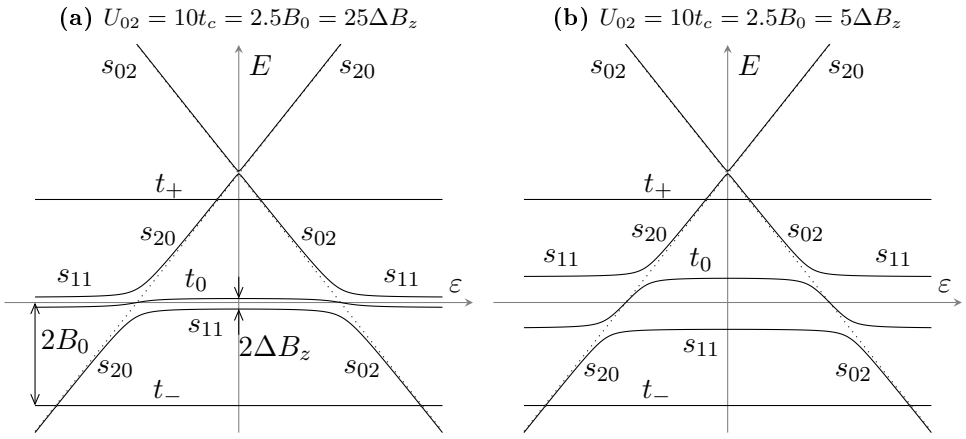

Figure E.2: The energy spectrum of the double quantum dot Hamiltonian given in Equation E.38. The state labels indicate the approximate asymptotic eigenstate of the energy eigenvalue line at different points in detuning ε. The magnetic field gradient across the dots ΔB_z creates an anti-crossing between the singlet s_{11} and triplet t_0 states, while the global magnetic field Zeeman splits the triplet t_- and t_+ by $2B_0$. In (a), $t_c = 2.5\Delta B_z$ and the t_0 eigenstate has very little dependence with ε. However, when $\Delta B_z = 2t_c$, multiple anti-crossings form on the t_0 state causing a strong detuning dependence on the t_0 eigenstate.

Appendix F

Numerical simulations of gate fidelity

Numerical methods were used to evaluate the approximate fidelities for the single and two-qubit gates under the influence of charge noise. The basic method shall be discussed in this section.

Consider a qubit rotation such as that described in Figure F.1a where one rotates an initial state about some axis by π from ψ_0 to ψ_π. One calculates the time required to achieve a π rotation by taking the nominal precession frequency. However, noise in the environment may randomly perturb the precession frequency such that one sometimes undershoots the final state rotation (if the frequency is too slow) or overshoots the final state rotation (if the frequency is too fast). If one takes the average of all the randomly distributed final states, one gets an average state ψ_{av} that is no longer a pure state (that is, unit magnitude on the Bloch sphere). The decay of the Bloch vector is termed information loss due to decoherence. One may plot the z-projection of the averaged final state vector as shown in Figure F.1b. One can convert the z-projection p_z into a measurement probability via:

$$P_z = \frac{1}{2}\left(1 + p_z\right) \equiv \frac{1}{2}\left(1 + \gamma(t) \cdot \cos(\omega_p t)\right), \tag{F.1}$$

where ω_p is the average precession frequency and $\gamma(t)$ is the decay function describing the average information loss due to perturbations in ω_p. The metric to describe the decay of the state vector into the centre of the Bloch sphere (that is, a measurement probability of 1/2) is typically a sinc, Gaussian or exponential decay envelope where T_2^* is the time-constant. The fitted envelope depends on the distribution of the precession frequencies as given by the noise distribution (for example, a Gaussian distribution of precession frequencies yields a Gaussian envelope in the time-domain probabilities). One may attach fidelities to the decay by noting that a gate operation

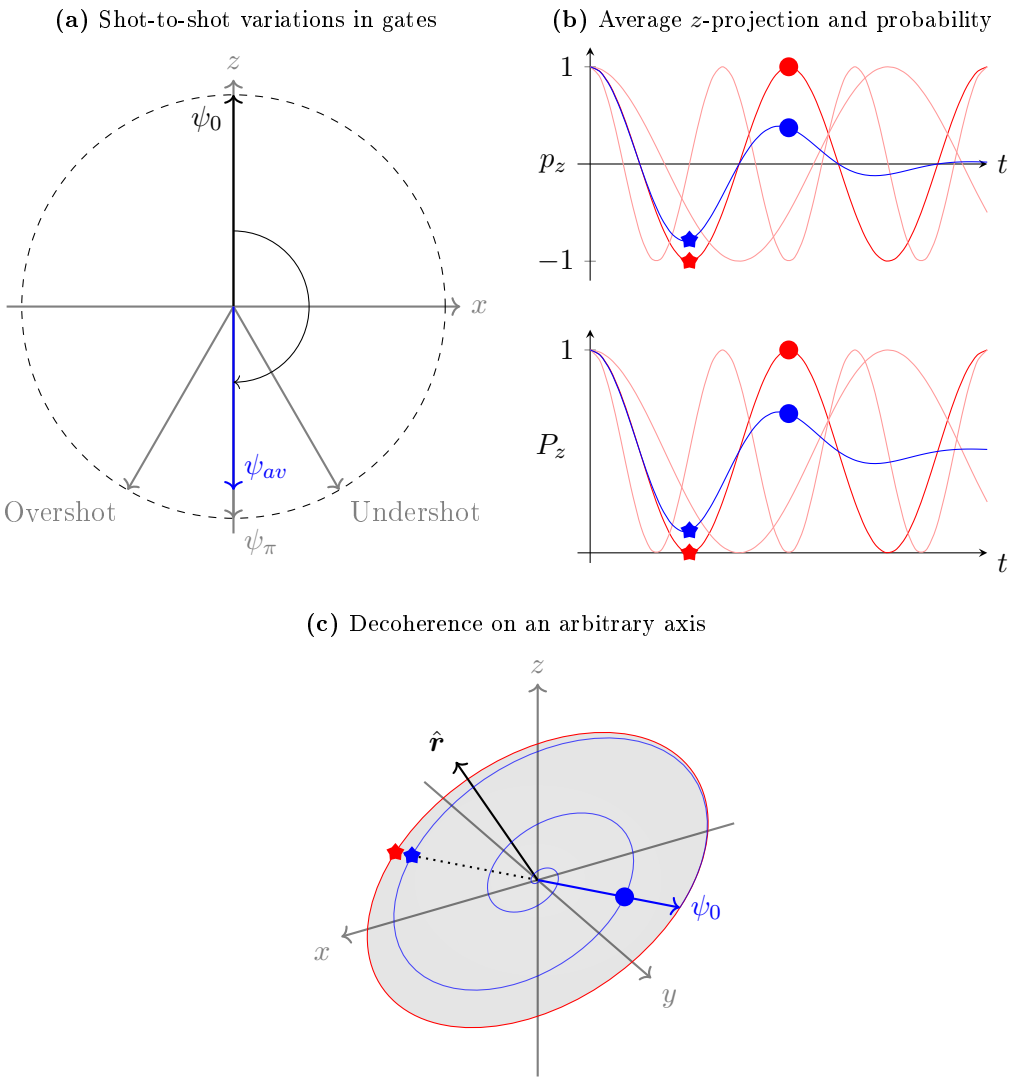

Figure F.1: Visualising decoherence and the resulting link to gate fidelities. Decoherence is decay of the state vector when taking the average of many gate operation events where the precession frequency randomly varies each time due to noise. (a) In a simple example, the initial state ψ_0 is to rotate from the z-axis by π to ψ_π. However, sometimes the gate will under-rotate (precession frequency too slow) or over-rotate (precession frequency too fast) with the average state vector being ψ_{av}. (b) The z projection of the average state vector (in blue) over time is shown relative to the intended state vector (in red). The average state vector is the weighted sum of all other state vector trajectories when the precession frequency is too fast or slow (lighter red). The resulting z-probability measurement P_z, when compared against the ideal probability yields the fidelity. For example, the stars and circles indicate the state vectors on π and 2π rotations respectively (with the ideal state vectors in red and the decohered state vectors signifying the fidelity in blue). (c) Given that the worst-case fidelity is the projection of a state vector ψ_0 perpendicular to the rotation axis $\hat{\mathbf{r}}$ as measured along the ψ_0-axis, one may simply find the decay envelope to estimate the resulting gate fidelities.

should yield ψ_π for π-rotations (shown by the red stars) and ψ_0 for 2π-rotations (shown by the red circles), but instead yield the trajectory given by the ensemble average ψ_{av} (the blue stars and circles); the resulting fidelity estimates are:

$$F_\pi = |\langle \psi_{av} \mid \psi_\pi \rangle|^2 \equiv 1 - P_z \tag{F.2}$$

$$F_{2\pi} = |\langle \psi_{av} \mid \psi_0 \rangle|^2 \equiv P_z. \tag{F.3}$$

Note that the 2π rotations are important when considering identity or idle operations on the qubits. Now the z-projection is simply that of a cosine wave at a frequency given by the precession frequency and a decay given by the decay due to decoherence. The decay of the cosine wave at a half rotation is the gate fidelity. One may extend this fidelity calculation to any arbitrary axis of rotation. For example, consider an arbitrary rotation axis $\hat{\mathbf{r}}$ given in Figure F.1c. Now take any pure state ψ_0 on the plane perpendicular to the rotation axis. The state must be perpendicular to achieve the worst-case fidelity estimate (a state parallel with the rotation axis will undergo no precession and thus, no suffers decoherence). Now to find the fidelity, one can take the inner-product along the ψ_0-axis to realise that the fidelity is simply the decay envelope $\gamma(t)$ evaluated at $t = t_\pi$ (the time taken to perform a half rotation as given by the precession frequency):

$$F_\pi = \frac{1}{2}\left(1 + \gamma(t_\pi)\right) \tag{F.4}$$

$$F_{2\pi} = \frac{1}{2}\left(1 + \gamma(2t_\pi)\right). \tag{F.5}$$

Thus, estimation of the decay envelope given the distribution of precession frequencies directly yields the fidelities.

Now one seeks the decay envelope in the time-domain given a probability distribution of precession frequencies. Note that taking the inverse Fourier transform of the probability spread of precession frequencies in the frequency domain yields the average time-domain decaying cosine wave as required when averaging many shot-to-shot variations in the precession frequency. Now consider a probability distribution of the precession frequencies $N(\omega)$ where the distribution is symmetric $N(-\omega) = N(\omega)$ and has a mean frequency of interest at $\omega = \omega_p$. Now taking the inverse Fourier transform to get the time-domain decaying sine wave:

$$p_0(t) = \mathcal{F}^{-1}[N(\omega)] = \frac{1}{2\pi}\int_{-\infty}^{\infty} \mathrm{e}^{i\omega t} N(\omega) d\omega = \frac{1}{\pi}\int_{0}^{\infty} \cos(\omega t) N(\omega) d\omega. \tag{F.6}$$

The cosine integral was numerically evaluated using a 1000-point trapezium rule across the probability distribution $N(\omega)$. The resulting function $p_0(t)$ is a decaying sine wave with frequency ω_p. The decay associated envelope can be found by simply taking:

$$\gamma(t_\pi) = \frac{p_0(t_\pi)}{p_0(0)} \tag{F.7}$$

$$\gamma(2t_\pi) = \frac{p_0(2t_\pi)}{p_0(0)}. \tag{F.8}$$

From the decay function, one may immediately extract the gate fidelities as shown above.